



---

**Forschungszentrum Karlsruhe**  
in der Helmholtz-Gemeinschaft

---

**Wissenschaftliche Berichte**

FZKA 7210

EUR 22253 EN

**Nuclear Fusion Programme  
Annual Report of the  
Association Forschungszentrum  
Karlsruhe/EURATOM  
January 2005 - December 2005**

**Programm Kernfusion**

**April 2006**



# **Forschungszentrum Karlsruhe**

in der Helmholtz-Gemeinschaft

Wissenschaftliche Berichte

FZKA 7210  
EUR 22253 EN

Nuclear Fusion Programme  
Annual Report of the  
Association Forschungszentrum Karlsruhe/  
EURATOM  
January 2005 – December 2005

compiled by I. Pleli  
Programm Kernfusion

Forschungszentrum Karlsruhe GmbH, Karlsruhe  
2006

This work, supported by the European Communities under the contract of Association between EURATOM and Forschungszentrum Karlsruhe, was carried out within the framework of the European Fusion Development Agreement. The views and opinions expressed herein do not necessarily reflect those of the European Commission.

Für diesen Bericht behalten wir uns alle Rechte vor

Forschungszentrum Karlsruhe GmbH  
Postfach 3640, 76021 Karlsruhe

Mitglied der Hermann von Helmholtz-Gemeinschaft  
Deutscher Forschungszentren (HGF)

ISSN 0947-8620

urn:nbn:de:0005-072101

## Introduction

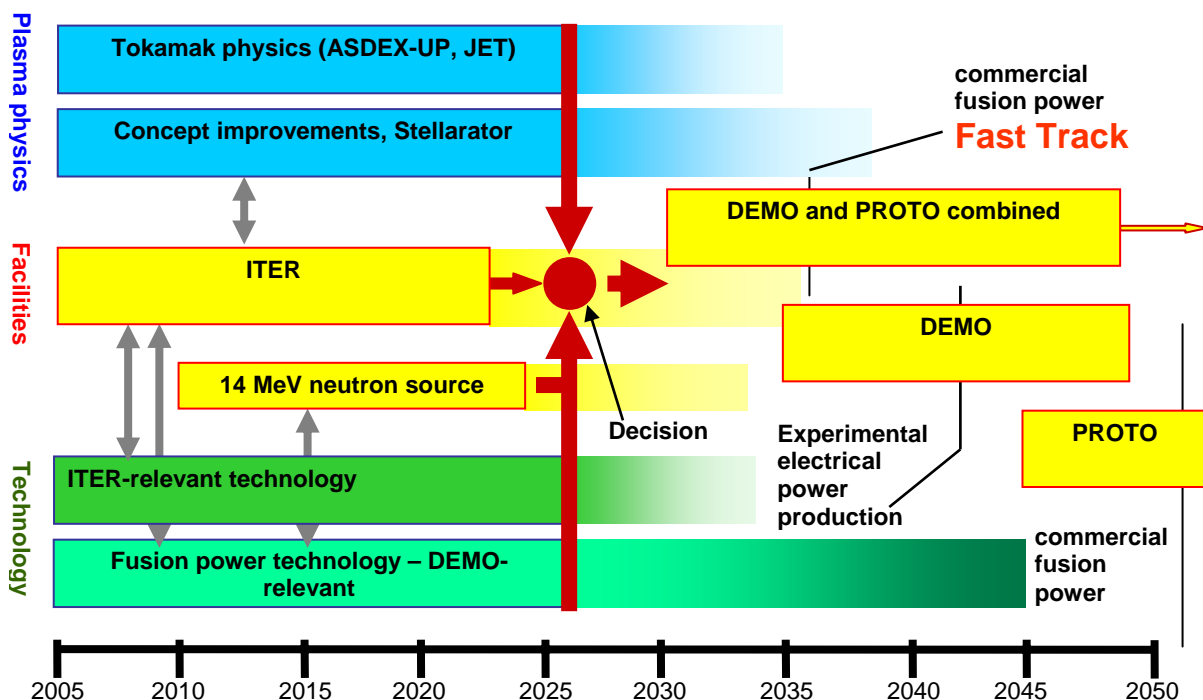
Nuclear fusion represents a most promising option for a safe, sustainable energy source which can be made inherently safe and which, even with a substantial contribution to a future global energy supply will not meet resource limits and should not leave burdens for future generations. Fusion research therefore has to fully explore this option as to provide a complete basis of proven information whether energy production by fusion is technically feasible, ecologically tolerable and finally, economically meaningful.

The FZK fusion research programme is fully integrated in the European Fusion Programme which follows a road map towards commercial fusion energy. At present the so-called Fast Track is intensively discussed in Europe which would reduce the time span to commercial fusion power by ten years (Fig. 1). Three major elements of research and development are required in order to generate the know-how for the construction of a fusion power station DEMO/PROTO:

A base physics programme targeted to improve capabilities to simulate plasma confinement concepts while making use of existing experimental facilities.

A major facilities programme including ITER as the most important next step, IFMIF for the qualification of materials for DEMO and a component test facility.

A base technology programme comprising plasma support technologies such as superconducting magnets, fuelling systems, high heat flux components, remote maintenance, reactor relevant steady state plasma heating systems etc., and fusion power technologies such as breeding blankets, helium cooled divertor and tritium extraction systems.



The activities of all the European fusion laboratories (known as EURATOM Associations) and industry are combined into one organisational structure via the European Fusion Development Agreement (EFDA). EFDA has a leader and two associate leaders (one for

JET and one for fusion technology). It is guided by a steering committee, consisting of the heads of association laboratories, which has to approve the major strategy and annual work programmes as well as large contracts with industry or associations.

Within this framework FZK is developing key technologies in the areas of superconducting magnets, microwave heating systems (Electron-Cyclotron-Resonance-Heating, ECRH), the deuterium-tritium fuel cycle, He-cooled breeding blankets, a He-cooled divertor and structural materials as well as refractory metals for high heat flux applications including a major participation in the international IFMIF project. Furthermore investigations on plasma wall interactions and core and divertor modelling are carried out and a global plasma model is being developed.

The results from experimental activities such as the tests of high temperature superconducting current leads in the test facility TOSKA, the quasi-stationary gyrotron operation and the operation of fuel cycle subsystems and components with deuterium-tritium have already been utilised for the design work for ITER. In addition large progress has been made in the engineering design of test blanket modules for ITER.

With regard to DEMO design integration of blanket modules taking into account requirements of remotely controlled handling has been started and the conceptual design of a He-cooled divertor considering two alternatives of cooling the target plate has been elaborated. Both activities will serve as an input to the planned DEMO study.

The detailed design and construction of ITER components and subsystems needs to be supported by experiments such as prototype testing, validation of scale up factors and additional R&D. For this purpose a helium loop HELOKA has been designed which not only serves for experimental investigations but also as a pilot loop in view of the loops to be installed in ITER for the cooling of test blanket modules. HELOKA Construction will start in 2006.

In order to efficiently manage these tasks a project-oriented approach is required involving a quality assured and quality controlled exploitation of R&D results. Subsequently the development of a quality control system has been started. This process shall result in the development of complete licensable components and systems. In a later phase support has to be provided to industrial partners who shall produce, assemble and finally install the components or systems into ITER, taking quality control and licensing aspects into account. However, the responsibility for the performance and the overall management of the procurement, installation and commissioning shall remain with the designers.

In order to meet this challenge, a project-oriented organisation structure is maintained in the FZK fusion programme by means of task forces in the areas Blanket/Divertor, HELOKA, Microwave Heating, Superconducting Magnets, Fuel Cycle and IFMIF (14 MeV neutron source). A task force which is responsible for a large component or subsystem to be delivered to ITER can be seen as a design and development division with a division head and several groups, each of them having a group leader. A team of design engineers supported by CAD constitutes the nucleus of each group in the task force. Besides the above-mentioned task forces materials research is oriented at engineering requirements.

About 220 professionals and technicians are involved in the fusion programme of the Association FZK-EURATOM with additional support of the technical departments.

Progress from January 2005 to December 2005 is reported here. More information is available from the programme management and from the responsible scientists. The website [www.fzk.de/fusion](http://www.fzk.de/fusion) offers further access to the fusion activities of FZK.

# Contents

Page

## Introduction

<b>Plasma Edge</b> .....	1
EFDA/03-1080      Characterisation of Material Damage for EU W and CFC ITER Divertor Materials under Repetitive Plasma Energy Fluxes by Modelling and Experimental Validation .....	3
TW5-TPP/ITERTRAN      Modelling of ITER Divertor Target Damage and Plasma Contamination following ELMs and Disruptions .....	8
TW4-TPP-TRIDEP      Studies of Hydrocarbon Formation and Redeposition under ITER Relevant Divertor Chamber Conditions .....	12
Divertor and Core Plasma Modelling for ITER .....	16
<b>Heating and Current Drive</b> .....	21
TW5-TPHE-ECHULA      Detailed Design and Analysis of the Upper Launcher for the ITER ECH&CD System: Torus Window Design and Development .....	23
EFDA/05-1230      Detailed Design and Analysis of the Upper Launcher for the ITER ECH&CD System: Launcher Structural Design Integration .....	32
TW4-TPDC-IRR CER      Irradiation Effects in Ceramics for Heating and Current Drive, and Diagnostics Systems .....	39
<b>Vessel/In-Vessel</b> .....	43
TW5-TVV-EBWO      Demonstration of Overhead E-Beam Welding .....	45
<b>Magnet Structure and Integration</b> .....	49
EFDA/03-1105      Cryogenic Laboratory Tests for V-I Characterisation of Subcable Samples .....	51
EFDA/05-1250      HTS Current Lead Operation with Liquid Nitrogen .....	56
TW4-TMSF-HTSCOM      Conceptual Design of External HTS Busbars .....	60
EFDA/04-1216      Cryogenic Testing of Materials and Welds for Magnet Structures .....	65
EFDA/04-1198      European Dipole Design .....	69
TW5-TMSF-HTSMAG      Scoping Study of HTS Fusion Magnets .....	72
TW5-TMSC-HTSPER      HTS Materials for Fusion Magnets .....	74
<b>Breeding Blanket – HCPB Blanket Concept</b> .....	79
TTBB-001      Helium Cooled: TBM Design, Integration and Analysis .....	81
TW3-TTBB-001 D 1      HCPB TBM System Safety and Licinsing .....	81
TW3-TTBB-001 D 2      Review of HCPB Blanket Design .....	82
TW4-TTBB-001 D 1      Detailed Design of the First ITER EM-TBM-Module .....	86
TW4-TTBB-001 D 2      Review of the Material Data Base and Assessment Reports for the Breeder and Multiplier Materials for the HCLL and HCPB Concept .....	90
TW5-TTBB-001 D 1      Design and Analysis for the HCPB TBM including Design of Supporting System, Connections and Instrumentation Integration .....	92
TW5-TTBB-001 D 2      Detailed Design of Sub-components and Prototypical Mock-ups for the HCPB TBM Qualification .....	101

	<b>Page</b>
TW5-TTBB-001 D 8	Detailed HCPB TBM Development Work Plan and First Technical Specification Document ..... 103
TW5-TTBB-001 D 9	Study with Experimental Verification of the Pebbles Filling in the HCPB TBM ..... 104
TTBB-002b	Helium Cooled. Blanket Manufacturing Technologies ..... 106
TW2-TTBB-002b D 4	Procurements of Beryllium Materials and Quality Control of Procuded Material ..... 106
TW2-TTBB-002b D 5	FW Manufacturing by HIPing..... 109
TTBB-006	Helium Cooled: Breeder and Neutron Multiplier Materials ..... 114
TW5-TTBB-006 D 3	Procurements and Quality Control of Orthosilicate Ceramic Pebbles ..... 114
TW5-TTBB-006 D 5	Development of Beryllium Alloy Pebbles with Improved Tritium Release Characteristics..... 118
EFDA/04-1176	Helium Cooled Pebble Bed: Production and Characterization of Breeder and Neutron Multiplier Materials in Support of the HELICA and HEXCALIBER Experiments..... 124
TTBB-006b	Helium Cooled: Thermo-mechanical Modelling of Pebble Bed Assembly ..... 132
TW2-TTBB-006b D 2	Development of Pebble Beds Models ..... 132
<b>Breeding Blanket – HCLL Blanket Concept</b> ..... 135	
TTBA-006b	Water-Cooled: Magneto-Hydrodynamics ..... 137
TW2-TTBA-006b D 1	Test and Modeling of Forces Convection MHD..... 137
TTBC-006	Helium-Cooled Lithium Lead: Magneto-Hydrodynamics and Liquid Metal Materials..... 140
TW5-TTBC-006 D 1	MHD Experiments on a 3D Relevant Mock-up of the HCLL TBM..... 140
<b>High Pressure He-Loop – HELOKA</b> ..... 143	
TW5-TTB-001	Construction of the High Pressure He Loop (HELOKA-HP/TBM) for Testing of TBMs ..... 145
<b>Materials Development – Structural Materials</b> ..... 151	
TTMS-001	Irradiation Performance ..... 153
TW2-TTMS-001b D 5	Tensile, Charpy and Fatigue Specimen Testing after Neutron Irradiation up to 15 dpa in the Range of 250°C – 450°C, Completion of the Irradiation and PIE..... 153
TW2-TTMS-001b D 9	Fast Reactor Irradiation up to 30 dpa, at 340°C of Tensile, Charpy and LCF RAF/M Specimens, Completion of the PIE ..... 157
TW4-TTMS-001 D 1 TW5-TTMS-001 D 2	Fabrication and Irradiation of Fe-54 enriched Samples to Study the Influence of He/dpa Ratio on Materials Degradation up to Medium Dose Level..... 160
TW5-TTMS-001 D 10	Mechanical Post Irradiation Examinations of FZK-Specimens Irradiated in the ARBOR-2 Experiment in the BOR 60 Reactor ..... 163
TW5-TTMS-001 D 11	Assessment of Irradiations performed on EUROFER 97 ..... 164
TW5-TTMS-001 D 14	Assessment of Irradiated Fracture Mechanic Samples on EUROFER, F82H (and OPTIFER) to Study the Size Effect ..... 166
TTMS-002	Metallurgical and Mechanical Characterisation ..... 168
TW2-TTMS-002a D 19	Creep-Fatigue Testing at 550°C on EUROFER, Continuation to Longer Times Preferably under Controlled Atmosphere ..... 168



	<b>Page</b>
TTMS-003	Compatibility with Hydrogen and Liquids ..... 170
	TW4-TTMS-003 D 1 Development of Modeling Tools to Describe the Corrosion Behavior of Uncoated EUROFER in Flowing Pb-17Li and their Validation by Performing of Corrosion Tests at T up to 550°C ..... 170
TTMS-004	Qualification Fabrication Processes..... 175
	TW4-TTMS-004 D 1 Improve Design Limits of Welded Components through Improved Post Weld Heat Treatments ..... 175
	TW5-TTMS-004 D 1 Diffusion Welding Techniques – One Step HIP ..... 180
TTMS-005	Rules for Design, Fabrication and Inspection ..... 182
	TW2-TTMS-005b D 1 TBM Design Rules..... 182
	TW2-TTMS-005b D 2 Evaluation of the Material Design Limits for TBM's Application ..... 185
	TW2-TTMS-005b D 4 Creep-fatigue Lifetime Prediction Rules for Irradiated EUROFER ..... 190
	TW2-TTMS-005b D 7 Small-scale Fracture Mechanics Specimens ..... 191
	TW4-TTMS-005 D 2 Mechanical and Structural Characterization of EUROFER 97-2 Acceptance Tests of the 2003 Procured EUROFER Batch..... 193
	TW5-TTMS-005 D 4 Experiments in Support of Modelling Activities on Size Effects ..... 198
	TW5-TTMS-005 D 5 High Temperature Fracture Mechanical (Creep-fatigue) Rules: Formulation and Implementation ..... 200
	TW5-TTMS-005 D 6 Accompanying Experiments for the Formulation of High Temperature Fracture Mechanical Rules ..... 201
	TW5-TTMS-005 D 7 General Implementation of HT Rules (including Creep Fatigue Interaction Rules) ..... 203
	TW5-TTMS-005 D 8 Definition of an Experimental Programme for Validation of HT Creep-fatigue Rules at Fusion Relevant Conditions..... 204
	TW5-TTMS-005 D 9 Experimental Programme for Verification of HT Creep-fatigue Rules from Uniaxial Experiments (e.G. LCF tests with long dwell time) and/or Multi-step LCF Tests ..... 209
TTMS-006	High Performance Steels ..... 212
	TW3-TTMS-006 D 1 EU ODS Steel Specification and Production ..... 212
	TW4-TTMS-006 D 1 Optimisation of Fabrication Parameters of Current EUROFER ODS Plate Material ..... 215
	TW5-TTMS-006 D 6 Characterisation of Reference EU ODS-EUROFER Batch (Tensile, Creep and Charpy) ..... 217
	TW5-TTMS-006 D 10 Characterisation of Reference EU-ODS-EUROFER Batch: Optimisation of Heat Treatment, Ageing Behaviour and Microstructural Characterisation..... 219
	TW5-TTMS-006 D 5 Nano Compositing Ferritic Steels for HT Application: Identification of Promising Candidate Alloy Compositions and Respective Fabrication Routes According to the outcome of the 2004 Study. Production of Different Laboratory Batches (14%Cr) ..... 222
TTMS-007	Modelisation of Irradiation Effects ..... 224
	TW5-TTMS-007 D 5, D 7, D 10 and D 22 ..... 224
EFDA/01-622	Order of EUROFER Heats ..... 228
EFDA/05-1244	Investigation of Options to Reduce Critical Elements in Low Activation Ferritic/Martensitic Steels ..... 230



TW4-TTMI-003 D 7	HFTM Component Manufacturing, Up-grading of the Helium-Loop .....	293
TW4-TTMI-003 D 9	Evaluation and Validation of D-Li Cross Section Data .....	298
TW5-TTMI-003 D 3	Design of a Horseshoe Type Neutron Shielding Block Enveloping all Test Modules to Reduce further the Nuclear Inventory and the Gamma Dose Rate in the Rooms Surrounding the Test Cell .....	303
TW5-TTMI-003 D 4	Calculation of Complete Nuclear Response through the Entire Test Cell with Consideration of an Additional Shielding Block .....	309
TTMI-004	IFMIF – Design Integration .....	314
TW5-TTMI-004 D1	3D Radiation Shielding Analysis of all Rooms Surrounding the Test Cell using State-of-the-Art Computational Tools .....	314
<b>Fuel Cycle</b>	.....	<b>317</b>
GB8-VP 1	Cryopump Development and Testing.....	319
GB8-VP 1 D 6	Effect of Strongly Sorbed Substances .....	319
TW3-TTFF-VP 35	Study of Cryopump Compatibility with Carbon Erosion Products .....	322
TW1-TTF/VP 11	Torus Exhaust Cryopump Development Testing .....	327
TW1-TTF/VP 11 D 8	Design Modification of ITER-Scale Pump .....	327
EFDA/04-1173	Design and Procurement Specification for ITER Prototype Torus Exhaust Cryopump .....	331
TW5-TTFF-VP 51	Mechanical Tests and Post-operational Examination of TIMO .....	333
TW1-TTF/VP 12	Performance Evaluation of Roots Blower with Ferrofluidic Seal System .....	335
EFDA/03-1095	Design of an ITER-sized Mechanical Pump Train .....	338
TW4-TTFF-VP 45	Performance Assessment of Mechanical Pumps in Tritium Plant .....	342
EFDA/04-1141	ITERVAC Conductance Modelling of ITER Torus Exhaust Pumping Ducts .....	343
TW5-TTFF-VP 57	ITERVAC Validation Test .....	346
TW0-T 450/01	Detection and Localisation of Leaks from Cooling Circuits.....	349
TW1-TTF/VP 13	Compatibility of Leak Localisation Tracers with Cryopumps.....	351
TW4-TTFD-TR 42	Analysis of Gases from Fusion Devices with Carbons PFCs .....	354
EFDA/04-1217	Operation of the Tritium Laboratory Karlsruhe (TLK).....	355
TW1-TTF/TR 11 and TW4-TTFD/TR 41 and TW4-TTFD/TR 43	Gas Processing during in-situ Tritium Recovery from PFC's..... Experimental Investigation of Undesired Side-reactions in PERMCAT Comparison of Batch and Continuous Operation Modes for the Impurity Processing Stage of the Tokamak Exhaust Processing System	357
TW1-TTF/TR 31	Improvements to the Mechanical Design of the PERMCAT Component.....	363
TW1-TTF/TEP 13A and TW3-TTFD/TR 33	Self-Assay, Fast Delivery Tritium Storage Bed Development..... Determination of Isotopic Effect during Rapid Delivery from Storage Beds	365
TW4-TTFD/TR 44	Inactive Tests of Selected Composition Control Loop Performance under Typical ITER Operating Conditions.....	368
TW1-TTF/TR 13	Extended Lifetime Tests of Specified Tritium Plant Components .....	369
TW1-TTF/TR 16	Tritium Recovery from Ceramic Breeder Test Blanket Module.....	371
TW4-TTFD/TR 46	Design, Experimental Plan and Procurement of Cryogenic Distillation System for Isotope Separation Tests for ITER .....	372

	<b>Page</b>
TW4-TTFD/TR 47	Upgrading of LPCE (Liquid Phase Catalytic Exchange) Column for Trade-off Studies between WDS and ISS ..... 376
EFDA/04-1142	Development of a Procedure for Global Fuel Cycle Tritium Inventory Determination..... 378
EFDA/04-1172	Dynamic Modelling of ITER Tritium Inventory (TRIMO)..... 382
EFDA/05-1237	Development of ITER PRM and Standard Parts Catalogues in CATIA V5 for Tritium-containing Systems and Components ..... 385
EFDA/05-1239	Development of a Resource-loaded Schedule for the Overall ITER Tritium Plant Integration ..... 387
EFDA/05-1240	Definition of the Interfaces between the Tritium Plant and the Torus Pumping, Neutral Beam Injection Pumping, and Fuelling Systems..... 389
EFDA/05-1251	Development of a Tritium Manual for ITER..... 391
<b>Safety Analysis and Environmental Impact</b>	..... 393
TW5-TSS-SEA 3.5	In-vessel Safety: Mitigation of Hydrogen and Dust Explosions..... 395
EFDA/04-1194	Hydrogen Deflagration/Detonation Analyses in ITER Cryopumps, Heating Neutral Beam, and Diagnostic Neutral Beam Boxes ..... 399
TSS-SEA 5.4	Busbar Arcs Behavior and Consequences ..... 405
	TW5-TSS-SEA 5.4 D 1-3 Experimental Simulation in the VACARC Facility..... 405
	TW3-TSS-SEA 5.4 D 4 Busbar Arcs Behavior and Consequences – Final Report ..... 407
and TSS-SEA 5.5	Validation of EU Safety Computer Codes and Models ..... 407
	TW4-TSS-SEA 5.5 D 8 Report on Busbar Arc Model Development and TW4-TSS-SEA 5.5 D 9 Report on Arc Experiments for Support of Arc Model Development and Validation
	TW4-TSS-SEA 5.5 D 7 Report on MAGS Recalculation of EVITA Experiments including Noncondensables ..... 410
	and TW5-TSS-SEA 5.5 D 5 Final Report on MAGS Recalculation of the EVITA Experimental Campaign 2005
TW5-TSS-SEP 2	Dosis to the Public and Validation of UFOTRI ..... 412
<b>Power Plant Conceptual Study</b>	..... 415
TRP-001	He-cooled Divertor Concepts..... 417
	TW4 + TW5-TRP-001 D 2 Conceptual Design Design, Analysis, and Tests..... 417
TRP-002	DEMO Physics Studies ..... 425
	TW5-TRP-002 D 2 Analysis of Total Radiation in Tokamak Reactor Scenarios..... 425
TRP-009	He-cooled Divertor Test Module for ITER ..... 428
	TW5-TRP-009 D 2 Testing suitable HEMS/HEMJ Prototypes in ITER ..... 428
<b>Tritium Inventory Control</b>	..... 431
TW3-TI-VP 31	High Temperature Regeneration Tests of the ITER Model Torus Cryopump ..... 433
EFDA/02-1019	Detailed Design of Water Detritiation Systems for JET ..... 434
<b>Design Support and Procurement</b>	..... 439
EFDA/03-1100	Detailed Engineering and Manufacturing Studies of the ITER Magnet System: Toroidal Field (TF) and Poloidal Field (PF) Coil Windings, Structure and Cold Test Facility ..... 441

	<b>Page</b>
<b>JET Technology</b> .....	445
JW2-FT-2.9 Tritium Removal from JET Tiles.....	447
JW4-FT-2.19 Endurance Test for the Catalyst-packing Mixture Proposed for Water Detritiation System at JET with FZK Mixture.....	452
JW5-FT-3.11 Assessment of in-situ Detritiation in JET – OPL Tile Analysis .....	455
JW4-FT-3.18 Assessment of in-situ Detritiation in JET .....	459
JW5-FT-4.7 CAD to MCNP Interface .....	462
JW4-FT-5.15 Fully Automated Interface in Convert CATIA Files into MCNP Geometry Surfaces and Cells .....	463
JW4-FT-5.17 Simulation of Tritium Spreading in Controlled Areas after a Tritium Release Considering Inner Obstacles.....	464
JW5-FT-5.20 Shutdown Dose Rate at JET Tokamak – Code Benchmark .....	467
JW0-FT-6.1 Impact of Tritium on the Performance of a Prototype Cryosorption Pumping Panel.....	468
<b>Heating Systems Technology Project</b> .....	471
TW5-THHE-CCGDS2 EC Coaxial Cavity Gyrotrons and Test Facility: Design, Support to the Industrial Development and Preparation of Technical Specifications.....	473
TW5-THHE-CCGDS2 D 1 Supervision of the Industrial Partner during the Procurement Contracts .....	473
TW5-THHE-CCGDS2 D 6 Upgrading of the Gyrotron Test Facility at FZK.....	478
TW3-THHN-NB-RFS Cryopumps for the NBI-Testbed at IPP Garching .....	479
EFDA/04-1185 The First ITER NB Injector and the ITER NB Test Facility: Progress in the Design .....	483
<b>Physics Integration</b> .....	487
ECR Heating and Current Drive – Step-Tunable Gyrotron Development .....	489
Microwave Heating for Wendelstein 7-X .....	493
<b>Underlying Technology</b> .....	503
Operation of the Fusion Materials Laboratory .....	505
Appendix I FZK Departments Contributing to the Fusion Programme.....	507
Appendix II Fusion Programme Management Staff .....	509
Appendix III Glossary .....	511



## **Plasma Edge**





## EFDA/03-1080

# Characterisation of Material Damage for EU W and CFC ITER Divertor Materials under Repetitive Plasma Energy Fluxes by Modelling and Experimental Validation

## 1. Introduction

Operation of ITER in the ELMy H-mode will be accompanied by repetitive pulses of hot deuterium-tritium plasma impacts on the divertor armour with an anticipated frequency up to a few Hz. The heat loads of the energy density  $Q \sim 1\text{-}3 \text{ MJ/m}^2$  on the time scale  $\tau \sim 0.1 - 0.5$  ms will deteriorate the armour performance. The main parts of the armour of the ITER vertical divertor will be covered by tungsten and CFC. This report describes joint numerical and experimental investigations of erosion mechanisms of CFC and tungsten targets at ITER relevant conditions carried out in FZK, TRINITY<sup>1</sup> and KIPT<sup>2</sup>. The modelling in FZK uses the anisotropic thermomechanic codes PEGASUS and PHEMOBRID and the surface melt motion code MEMOS. The experiments aimed at the characterisation of material damage for tungsten and CFC targets manufactured in the EU and also at the validation of the mentioned codes have been set up at the plasma guns MK-200UG and QSPA-T (TRINITY) and QSPA-Kh50 (KIPT). These facilities produce pulses of hydrogen plasma with  $Q$  and  $\tau$  of the values relevant to the ELM loads expected in ITER.

## 2. Codes applied for the modelling

The main application of PEGASUS, PHEMOBRID and MEMOS is to make predictions of the behaviour of CFC and tungsten divertor materials under ITER transient loads. To confirm the suitability of the calculations for ITER, the codes are validated using results of dedicated experiments at plasma guns.

In PEGASUS, the matrix and the fibres of the CFC structure are described by means of several millions of numerical cells of one micrometer size. Some grains combining different groups of cells are implemented to simulate the graphite structure. Neighbour grains contact each other by means of mechanical and heat conduction bonds. The complicated composition of CFC is simulated by varying material properties of the cells, which are the thermal conductivity, the coefficient of thermal expansion and the Young's modulus.

The code PHEMOBRID is based on a phenomenological model which assumes that the brittle destruction (BD) is a threshold phenomenon of heated graphite with a specific threshold enthalpy of 10 kJ/g. The results of the PEGASUS investigation obtained on the microscopic scale are used in the macroscopic scale code PHEMOBRID for simulation of large CFC armour samples. The effective heat conductivities of the CFC matrix, accounting for cracks and bunches of carbon fibres obtained with PEGASUS, are implemented in PHEMOBRID.

In MEMOS, surface melting in the frame of the 'shallow water' model is implemented, accounting for the viscosity of molten metal and surface tension, and the radiative losses from the surface. The gradient of plasma pressure and the gradient of surface tension as well as the Lorentz force of the currents crossing the melt layer in the strong magnetic field produce an acceleration of the melt along the divertor plate. A two-dimensional heat transport equation with two boundary conditions at the moving vapour-liquid and liquid-solid interfaces describes the temperature inside the target.

---

<sup>1</sup> State Research Centre of Russian Federation Troitsk Institute for Innovation and Fusion Research

<sup>2</sup> Institute of Plasma Physics of the National Science Centre "Kharkov Institute of Physics and Technology", Ukraine

### 3. Experimental facilities

The collaboration with the research centres TRINITI and KIPT is going on in the frame of the WTZ projects RUS 99/566 and UKR 04/002, respectively. In previous years, the TRINITI experiments provided important information about BD of CFC NB31 and NS31 at high heat loads relevant to ITER disruptions and also at minimal plasma heat loads for the melting of tungsten targets (in particular the macrobrushes) [1-5]. The results have been used for the validation of PEGASUS and MEMOS. The joint work with KIPT has been focused at the experimental investigations of melt motions at the surface of tungsten targets aiming at the validation of MEMOS. The time dependencies of the target surface pressure during plasma pulses have been measured and surface analysis of the samples has been performed. It was shown that the melt motion driven by the pressure gradient dominates in the macroscopic erosion of metallic targets, confirming the numerical simulations with MEMOS.

In the MK-200UG, a magnetic pressure gradient accelerates a plasma cloud in the gap between two coaxial electrodes of the gun. The magnetic field and the plasma appear after applying a high pulse electric field  $E$  at the electrodes, which causes an electric current through the hydrogen gas previously injected into the gap. The accelerated plasma propagates in a long vacuum tube along the guiding magnetic field  $B$  up to 3 T and then hits the target. A pulse duration  $\tau$  of 0.05 ms, a heat load  $Q$  up to 15 MJ/m<sup>2</sup>, a plasma radius 6-7 cm, ion impact energies  $E_i$  up to 2.5 keV, and electron temperatures  $T_e$  up to 300 eV are achieved. However, for the material tests  $Q$  was drastically decreased. A thin plate of CFC or W was placed in the tube under the angle of 20 degrees to the tube axis.

In the QSPA-T and QSPA-Kh50 a plasma of 5 cm radius moves quasi-stationary due to the  $E \times B$  drift, which allows much longer pulses compared to MK-200UG:  $\tau = 0.25$  ms in QSPA-Kh50 and 0.5 ms in QSPA-T. However, the large plasma conductivity prevents fast penetration of the fields into the stream; therefore only the regime with low ion and electron energies was reached:  $E_i$  up to 0.2 keV and  $T_e$  of a few eV.

### 4. Recent experimental results

**MK-200UG:** The energy threshold of intense vaporisation of tungsten and CFC surfaces and spectra of evaporated carbon have been obtained. The targets were exposed in the heat load range  $Q = 0.1$  to  $0.9$  MJ/m<sup>2</sup>. Calorimetric, pyrometric and spectral measurements have been arranged.

For the CFC target, the ionization states, temperature and density of carbon vapour were measured near the exposed CFC surface at ITER ELM relevant heat fluxes. The CFC surface was heated to the maximum temperature  $T_{\max} = 4000$  °K at  $Q = 0.2$  MJ/m<sup>2</sup>. If  $Q$  is increased further,  $T$  does not raise more, i.e., intense evaporation of the CFC surface and formation of a carbon vapour plasma shield occurs at  $Q \geq 0.2$  MJ/m<sup>2</sup>. Heat loads  $Q < 0.1$  MJ/m<sup>2</sup> do not cause measurable vaporisation, but at  $Q$  in the range  $0.1 - 0.2$  MJ/m<sup>2</sup>, some CFC evaporation occurs. The maximal energy absorbed by the CFC sample is 0.31 MJ/m<sup>2</sup>. According to the spectroscopic measurements, the ionized carbon vapour moves from the target surface along the magnetic field lines with a velocity about  $10^4$  m/s.

For tungsten targets at MK-200UG, the temperature of the exposed surface reaches the boiling point  $T = 6000$  °K at  $Q = 0.65$  MJ/m<sup>2</sup> (see Fig. 1). At larger plasma heat loads, a vapour plasma forms near the surface and it shields the surface from the incoming energy flux<sup>3</sup>. The maximal energy which can be absorbed by the tungsten target is limited to 0.67 MJ/m<sup>2</sup>. The tungsten plasma remains near the exposed surface at distances of 1-2 cm.

---

<sup>3</sup> The curve in Fig. 1 that separates the cases with and without vapour shield corresponds to the ITER high temperature impacting plasma (not to that of the plasma guns).

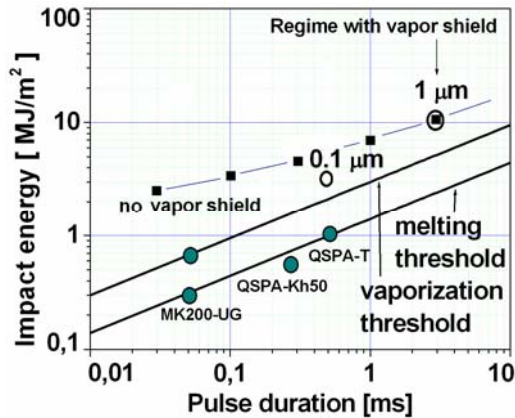


Fig. 1: Composite  $Q$ - $\tau$  diagram for tungsten surface under pulsed loads. Experimental results are shown with small filled circles. The continuous lines represent MEMOS simulations.

cracking. A large number of exposures resulted in lowering the melt threshold down to  $0.45 \text{ MJ/m}^2$ . Fig. 3 demonstrates the behaviour of the erosion rates as a function of pulse number.

**QSPA-T:** The latest experiments at this facility have been carried out with European CFC and W materials at  $Q < 1.65 \text{ MJ/m}^2$  and  $\tau = 0.5 \text{ ms}$ . The absorbed energy is linearly correlated with the applied voltage in the explored range both for W (up to  $\sim 1.1 \text{ MJ/m}^2$ ) and CFC (up to  $1.2 \text{ MJ/m}^2$ ). For an extrapolated impinging energy of  $1.65 \text{ MJ/m}^2$  (based on the linear dependence for W), the absorbed power on CFC is  $1.45 \text{ MJ/m}^2$ , which indicates the onset of strong carbon vaporisation.

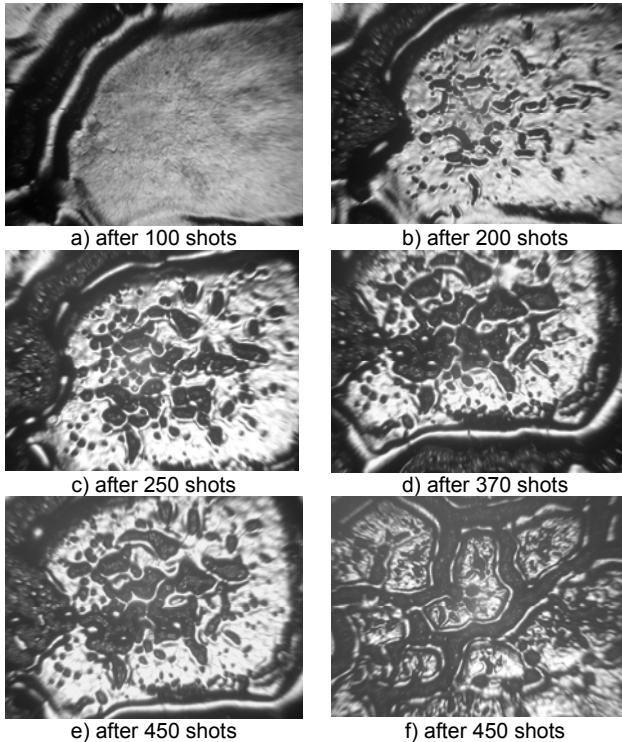


Fig. 2: W surface after multiple pulse plasma irradiations. Sizes: a) to e)  $0.9 \text{ mm}$ , f)  $1.7 \text{ mm}$ .

**QSPA-Kh50:** During the last two years, a surface degradation experiment with  $Q \sim 1 \text{ MJ/m}^2$  and  $\tau = 0.25 \text{ ms}$  has been carried out with tungsten plates of the sizes  $5 \times 5 \times 1 \text{ cm}^3$ , of the EU trademark delivered by FZK. The aim was to get insight into complicated plasma wall interaction physics for adequate future simulations of the damage to tungsten targets undergoing multiple ITER ELM loads. To measure the plasma stream parameters, calorimetric and spectroscopic techniques have been used. Complicated structures of W erosion profiles appeared after a large number of pulses (up to 450, Fig. 2)<sup>4</sup>. Tungsten boiling is observed on the exposed target surface at  $Q$  of  $1.1 \text{ MJ/m}^2$ , which is 30% less than in numerical modelling.

The surface roughness is caused mainly by

The codes PEGASUS and PHEMOBRID have been engaged for checking the experimental results. The temperature dependences of the CFC thermophysical parameters available elsewhere in the range  $0^\circ\text{C}$  to  $2200^\circ\text{C}$  have been extrapolated up to  $4000^\circ\text{C}$  (Fig. 4).

Assuming a constant impacting heat flux during  $0.5 \text{ ms}$  and neglecting the vapour shield, the dependences of the vaporization erosion on  $Q$  are obtained (Fig. 5). The experiments are in excellent agreement with the numerical curve of bulk-absorbed energy for the pitch direction. At increased pressure up to  $5 \text{ bar}$ , the code PHEMOBRID predicted the onset of brittle destruction at  $Q = 1.5 \text{ MJ/m}^2$ , which is not yet experimentally confirmed.

<sup>4</sup> Each year about 200 plasma shots were performed.

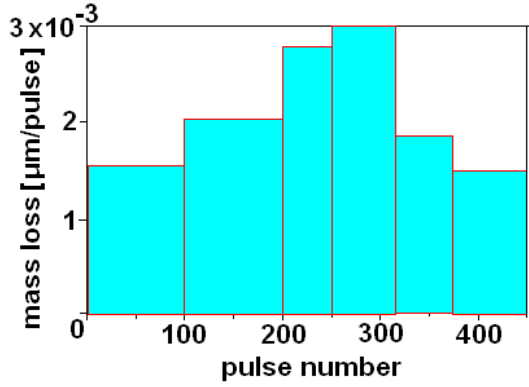


Fig. 3: Erosion rate of W sample under QSPA-Kh50 heat loads at  $Q = 1.1 \text{ MJ/m}^2$ .

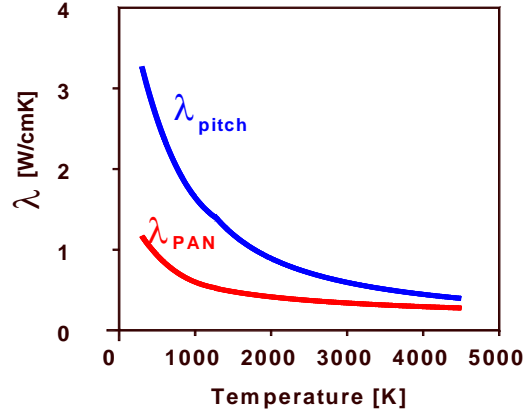


Fig. 4: Thermal conductivities used in CFC modelling are shown. The pitch direction is perpendicular and the PAN direction is parallel to the irradiated surface.

### 5. Conclusions

The experimental results allowed a validation of the FZK codes. For MK-200UG and QSPA-T a good agreement between the simulations and the experiments is obtained. The W surface degradation experiments at QSPA-Kh50 demonstrated a very complex violent surface cracking of bulk tungsten, even below the melting threshold. The tungsten and CFC vaporisation thresholds obtained in experiments on MK-200UG and QSPA-T were successfully compared with the calculations and justify the application of the codes for investigations on the damage of tokamak armours. It is to note that the new results of QSPA-Kh50 cannot be reproduced by the available numerical tools but they promote the development of new adequate modelling approaches. These results are going to be used in further development of FZK modelling.

#### Staff:

I.S. Landman  
 B.N. Bazylev  
 S.E. Pestchanyi

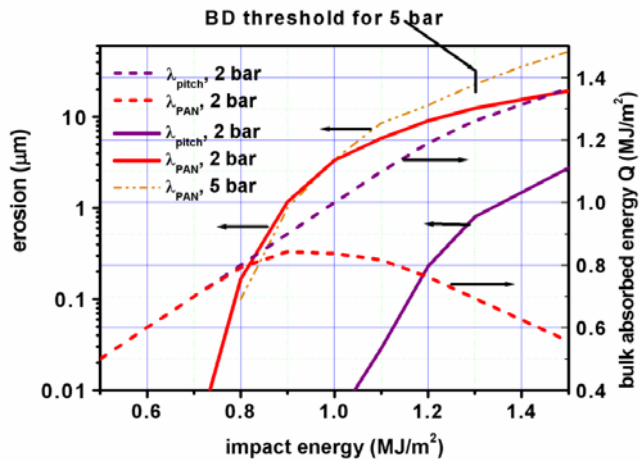


Fig. 5: Calculated CFC erosion rate and absorbed energy as functions of  $Q$ .

#### Literature:

[1] I.S. Landman, B.N. Bazylev, I.E. Garkusha, A. Loarte, S.E. Pestchanyi, V.M. Safronov, "Simulation of tokamak armour erosion and plasma contamination at intense transient heat fluxes in ITER", J. Nucl. Mater. 337-339 (2005) 761-765

[2] G. Federici, A. Zhitlukhin, N. Arkhipov, R. Giniyatulin, N. Klimov, I. Landman, V. Podkovirov, V. Safronov, A. Loarte, M. Merola, "Effects of ELMs and disruptions on ITER divertor armour materials", J. Nucl. Mater. 337-339 (2005) 684-690

- [3] B.N. Bazylev, I.S. Landman, S.E. Pestchanyi, "Erosion of ITER divertor armour and contamination of SOL after transient events by erosion products", Problems of Atomic Science and Technology, 2005, No. 1 Series: Plasma Physics (10) p. 49-53
- [4] I.S. Landman, S.E. Pestchanyi, B.N. Bazylev, "Numerical Simulations for ITER Divertor Armour Erosion and SOL Contamination due to Disruptions and ELMs", 20th IAEA Fusion Energy Conference, Vilamoura, Portugal, 1-6 November 2004, Paper IT/P3-26; IAEA-CSP-25/CD; ISBN 92-0-100405-2; ISSN 1562-4153
- [5] A. Zhiluckhin, G. Federici, R. Giniyatulin, I. Landman, J. Linke, A. Loarte, M. Merola, V. Podkovyrov, V. Saffronov, "Experimental assessment of the effects of ELMs and disruptions on ITER divertor armour materials", 20th IAEA Fusion Energy Conference, Vilamoura, Portugal, 1-6 November 2004, Paper IT/P3-30; IAEA-CSP-25/CD; ISBN 92-0-100405-2; ISSN 1562-4153

## TW5-TPP/ITERTRAN Modelling of ITER Divertor Target Damage and Plasma Contamination following ELMs and Disruptions

### 1. Introduction

In this report, numerical modelling carried out in FZK-IHM in 2005 for the ITER tokamak armour damages after transient events such as Edge Localised Modes (ELMs) and disruptions and the consequent contamination of the Scrape-Off Layer (SOL) is described. Any intense transient process results in a complicated self-consistent plasma wall interaction [1]. Hot deuterium-tritium plasma lost from the confinement region hits the surfaces of the divertor and the first wall. The armour erosion occurs mainly due to evaporation, brittle destruction in the case of carbon fibre composite (CFC), and melt motion for tungsten targets. The eroded material propagates back along the magnetic field lines in the SOL, intensively reradiating energy. The main computational tools for modelling these complicated processes are the radiation-magneto-hydrodynamic code FOREV that calculates the plasma processes and wall loads, the incompressible fluid dynamic code MEMOS applied for the calculation of the damage to tungsten surfaces, and the thermomechanic codes PEGASUS and PHEMOBRID applied for the calculation of CFC erosion.

### 2. Modelling of plasma and radiation transport with the code FOREV

The code FOREV models the hot plasma lost across the separatrix into the SOL during a transient event, its propagation towards the wall and impact on the armour, accounting for a self-consistent evaporation and ionization of carbon atoms, the radiation transport in the contaminated plasma and backward propagation of the erosion products into the SOL. In previous years, the geometry of the ITER magnetic field and the plasma description were implemented including the toroidal magnetic field with single poloidal field null and one divertor, the whole SOL, inner and outer divertor plates as well as the ion fluids of D, T, He, He<sup>+</sup> and impurity charge states C<sup>+1-6</sup>.

In 2005, in accordance with the task objectives, FOREV was applied for transient loads of the size of  $Q = 1 \text{ MJ/m}^2$  and pulse duration  $\tau = 0.1 - 0.2 \text{ ms}$  (see Fig. 1). A phenomenological model for an ELM scenario is implemented [2]. Hot plasma from the pedestal moves both convectively and diffusively across the field lines and simultaneously flows to the target. The process is simulated artificially by increasing the plasma cross diffusion coefficient in the pedestal and the SOL. The diffusion coefficient linearly rising up to  $2\text{-}5 \text{ m}^2/\text{s}$  at  $0.25 \text{ ms}$  is obtained by fitting the time dependence of the heat flux to the divertor and the pedestal plasma parameters such as the pedestal temperature  $T_{\text{ped}}$ . The plasma parameters were measured at the tokamaks JET and D-IIIID and scaled to ITER sizes. The influx of the DT plasma from the pedestal to the SOL was stopped after  $0.3 \text{ ms}$ , but the simulation for the evaporated carbon plasma continued. The evaporation produces  $5 \cdot 10^{21}$ -  $2 \cdot 10^{22}$  carbon ions which fill the SOL during  $1\text{-}2 \text{ ms}$  with a density of  $10^{20}\text{-}10^{21} \text{ m}^{-3}$ .

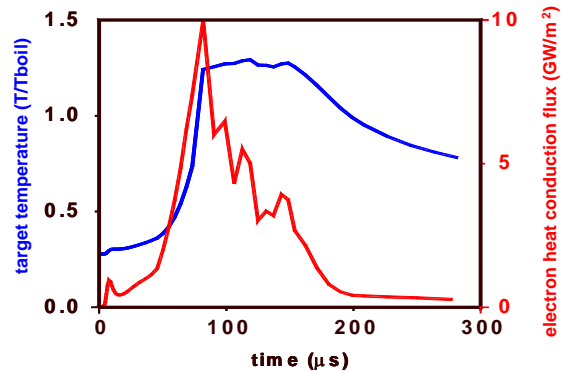


Fig. 1: Time dependence of temperature and heat flux at the ITER divertor surface ( $T_{\text{ped}} = 3 \text{ keV}$ ).

### 3. Melting of oblique W-brush surfaces and melt splashing criterion

The main disadvantage of bulk tungsten as armour material is surface cracking under the high heat loads typical for intense transient events with  $Q > 1 \text{ MJ/m}^2$  and  $\tau > 0.1 \text{ ms}$ . One possibility to mitigate it is using a tungsten macrobrush armour structure (W-brush, Fig. 2). The most important remaining damage mechanism is surface melting. Plasma pressure gradients induce a motion of the melt layer along the target surface. The melt layer erosion of the W-brush armour under the transient heat loads was numerically investigated using the code MEMOS [3]. The melt motion is described in the "shallow water" approximation, accounting for the surface tension, viscosity of the molten metal, and the radiative losses from the hot surface. A heat transport equation with two boundary conditions at the moving vapour-liquid and liquid-solid interfaces describes the temperature inside the target. For avoiding sharp brush edges, their shape is modelled as an arc with a radius  $R$  of 1 mm. It is assumed that the melt moves always along the surface without separation from the melt bottom and without droplet formation, including the arc segments between the tops of the W-brushes and their lateral surfaces. Previous simulations demonstrated that the macrobrush structure prevents violent melt motion: the melt motion velocity drops more than 3 times in comparison with that of a bulk armor, which significantly decreases the final magnitude of the melt erosion.

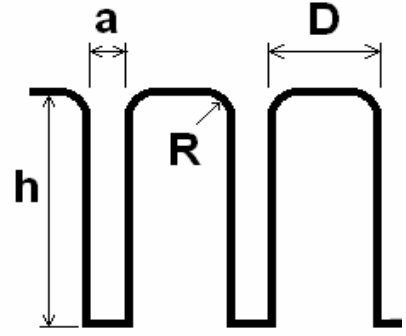


Fig. 2: Macro-brush target schematically.

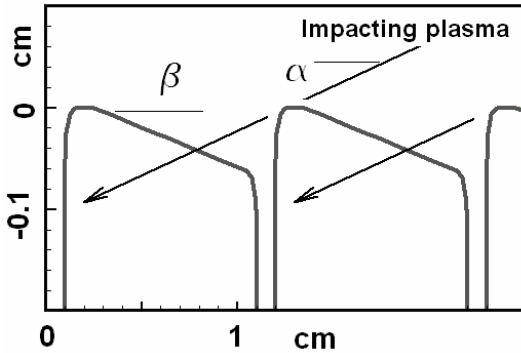


Fig. 3: W-brushes with oblique surfaces shadowed by neighbor elements.

Following the objectives, in 2005 the optimal angle of the brush surface inclination that provides a minimum of surface roughness was estimated for given inclination angles of the impacting plasma stream and given parameters of the macrobrush target. The criterion of melt splashing at the brush surface was estimated. It is shown that for most of the important cases no melt splashing will occur in conditions relevant for ITER ELMs. As in 2004 it was shown that the overheating of the macrobrush edges faced to the plasma stream leads to a significant increase of the melt roughness up to  $1 \mu\text{m}$  of magnitude, the effect of shadowing of the gaps by the neighbour upstream element was investigated in

detail (see Fig. 3). It is demonstrated that the shadowing decreases the final roughness down to  $0.2\text{-}0.4 \mu\text{m}$ . With a given plasma impact angle  $\alpha$ , the optimal surface inclination angle  $\beta$  is calculated to be approximately given by  $\beta \approx \alpha/2$ . Typical sizes of the macrobrush armour elements used in the modelling are the following: the diameter of the brushes  $D$  is  $0.5\text{-}1 \text{ cm}$ , the depth of the gaps between the brushes  $h$  is  $1 \text{ cm}$ , the width of the gaps  $a = 0.2\text{-}1 \text{ mm}$ ; the radius of the edge arc  $R = 0.1\text{-}0.5 \text{ mm}$ .

The droplet splashing melt velocity threshold was estimated based on the Taylor criterion for the instability of moving thin liquid films. The motion of the film along the macrobrush edge of a radius  $R$  will be stable if the centrifugal force is smaller than the capillary force. The balance of these forces gives the stability criterion:

$$\rho \frac{V_{\max}^2}{R} h = \frac{2\sigma}{R} \quad \Rightarrow \quad V < V_{\max} = \sqrt{\frac{2\sigma}{\rho h}} \quad (1)$$

The centrifugal force is in the left side and the capillary force in the right hand side of Eq.(1)<sub>1</sub>. The surface tension is  $\sigma$ , the liquid density  $\rho$  and the melt thickness  $h$ . The splashing of the melt layer occurs as soon as the velocity of the melt motion exceeds  $V_{\max}$ . For the tungsten armour ( $\sigma = 2200 \text{ din/cm}$ ,  $\rho = 17 \text{ g/cm}^3$ ) and ITER transient events, the maximum velocities estimated from the Taylor criterion are  $V_{\max} = 0.8 \text{ m/s}$  for typical disruptions ( $h \sim 400 \mu\text{m}$ ) and  $V_{\max} = 2.5 \text{ m/s}$  for typical ELMs ( $h \sim 40 \mu\text{m}$ ). Typical melt velocities obtained with MEMOS are below 1.5 m/s for the bulk target and below 0.5 m/s for the W-brushes. Thus for ELMs splashing doesn't occur. For disruptions the splashing may occur in the case of the bulk target, and it doesn't occur for W-brushes.

#### 4. Modelling of CFC damage under ITER ELM and disruption loads

CFC of NB31 and NS31 grades developed for the ITER divertor armour have shown high erosion rates by brittle destruction (BD) in the temperature range of 3000 - 4000 K, which occurs during the transient processes. The CFC materials have a complex structure consisting of a carbon fibre skeleton immersed into a carbon matrix. The main component of the skeleton, the pitch fibres perpendicular to the armour surface, provides the high thermal conductivity of CFC. They are weaved and needled by the PAN fibres arranged parallel to the heated surface. A theoretical analysis on the  $\mu\text{m}$  scale of the erosion mechanism specific for CFC has been carried out earlier using the code PEGASUS. The increase of the erosion rate at high temperatures is explained by the new BD mechanism called the local overheating (LOEM) of CFC surface. The PAN fibres undergo the largest LOEM damage.

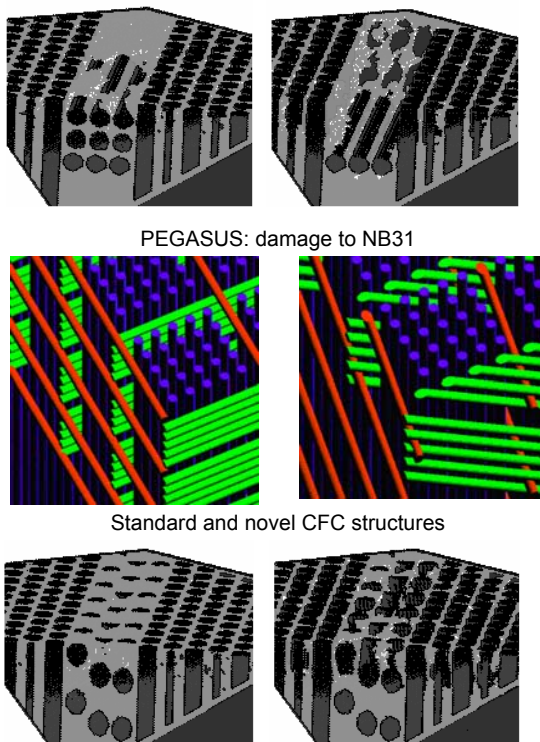


Fig. 4: Damage to the novel CFC.

In 2005, this EFDA task activity focused on the numerical simulation of BD erosion aiming at a comparison of the standard NB31 CFC with a modified one. The PAN fibres of the novel CFC are proposed to be inclined under an angle for instance of 45 degrees in respect to the irradiated surface in order to decrease their damage under high heat loads (Fig. 4). It was shown that the erosion rate of the improved CFC is 5 times smaller than that of NB31 under ELM-like heat loads [4]. As the result, this CFC structure modification is proposed for future CFC technology involving transient high heat fluxes.

Additionally, the code PHEMOBRID based on a phenomenological model which assumes that BD is a threshold phenomenon with specific enthalpy of heated graphite having a threshold 10 kJ/g for BD has been applied for the same purpose. The results of the PEGASUS investigation on a microscopic scale are used in the macroscopic scale code PHEMOBRID for the simulation of large CFC armour samples. Earlier, this approach was success-

fully verified by conducting numerical simulations for the experiments at the electron beam test facilities JEBIS (Japan) and JUDITH (FZJ Jülich). Now, the effective heat conductivities of the graphite matrix with cracks and bunches of carbon fibres obtained with PEGASUS are implemented in PHEMOBRID. Numerical simulations with PHEMOBRID demonstrated on the macroscopic scale of a few mm that the local overheating significantly influences the onset of BD. The code is available to simulate inhomogeneous substances arranged in the structures similar to the NB31 fibre frame. A first comparison of the microscopic code



PEGASUS and the phenomenological code PHEMOBRID on the surface temperature distribution is being performed.

## 5. Conclusions

Enhanced plasma diffusion in the pedestal and SOL allowed the simulation of ELMs and the following SOL contamination using the code FOREV. The density of carbon impurities in the SOL within a few ms after an ITER ELM is estimated. For further validation of FOREV, the measurements of the amount of vaporized carbon and the electron temperature in the JET tokamak during ELMs with a time resolution of  $\sim 10 \mu\text{s}$  are necessary.

The code MEMOS was further developed implementing arbitrary surface geometry of the macrobrushes, which allowed optimization of the design of the W armour. The shadowing prevents large overheating of the brush edges and significantly decreases the surface roughness. The melt splashing criterion for the macrobrush geometry is roughly estimated based on the Taylor criterion. For most important cases, melt splashing will not occur for ITER relevant conditions. Further numerical simulations should be performed to clarify in more detail the optimal geometry of the W macrobrush armour.

For adequate calculation of the surface erosion of CFC samples showing the structure of the surface erosion on the macroscopic scale, detailed numerical simulations with PHEMOBRID are needed. The theoretical prediction made using the code PEGASUS about the good BD resistance of modified CFC needs to be confirmed experimentally. However, the production of CFC with the improved fibre structure is very difficult; therefore, initially one has to use indirect experimental evidences for the real erosion mechanism. For this reason, an investigation of the CFC erosion under repetitive pulsed heat load simulating the Type I ELMs in ITER is going to be performed experimentally at the plasma gun facilities MK-200UG and QSPA. An NB31 sample is to be cut under a 45 degree angle with respect to the PAN fibres and the erosion rate has to be compared with that of the standard layout.

### Staff:

B.N. Bazylev  
I.S. Landman  
S.E. Pestchanyi

### Literature:

- [1] I.S. Landman, B.N. Bazylev, I.E. Garkusha, A. Loarte, S.E. Pestchanyi, V.M. Safronov, "Simulation of tokamak armour erosion and plasma contamination at intense transient heat fluxes in ITER", J. Nucl. Mater. 337-339 (2005) 761-765
- [2] S. Pestchanyi, I. Landman, "Simulation of ELMs and impurity plasma transport in SOL", European Fusion Theory Conference EFTC-11, September 26-28, 2005, Aix-en-Provence, France
- [3] B.N. Bazylev, G.Janeschitz, I.S. Landman, S.E. Pestchanyi, "Erosion of macrobrush tungsten armor after multiple intense transient events in ITER", 23<sup>rd</sup> Symp. on Fusion Technology (SOFT), Venice, I, Sept. 20-24, 2004. To be published in Fus. Eng. Design
- [4] S. Pestchanyi, I. Landman, "Improvement of the CFC structure to withstand high heat flux", The ISFNT-7 conference, May 22-26, Tokyo, Japan, to be published in Fus. Eng. Design

## TW4-TPP-TRIDEP Study of Hydrocarbon Formation and Redeposition under ITER- relevant Divertor Chamber Conditions

The understanding of hydrocarbon generation, transport and sticking is a matter of salient importance in fusion research. The experimental investigations addressing this topic being started in 2004 at the Humboldt-University in Berlin (supported by theoretical studies at IPP Greifswald) were continued in 2005.

In the experiments hydrocarbons (methane  $\text{CH}_4$ , ethene  $\text{C}_2\text{H}_4$  and acetylene  $\text{C}_2\text{H}_2$ ) are injected into stationary plasmas produced in PSI-2 plasma generator and the formation of a:C-H layers on a cooled collector probe is recorded. The results are compared with Monte Carlo modelling including all relevant data. The aim of these investigations is to assess the quality of modelling before applying it to ITER conditions. The experimental setup is shown in Fig. 1.

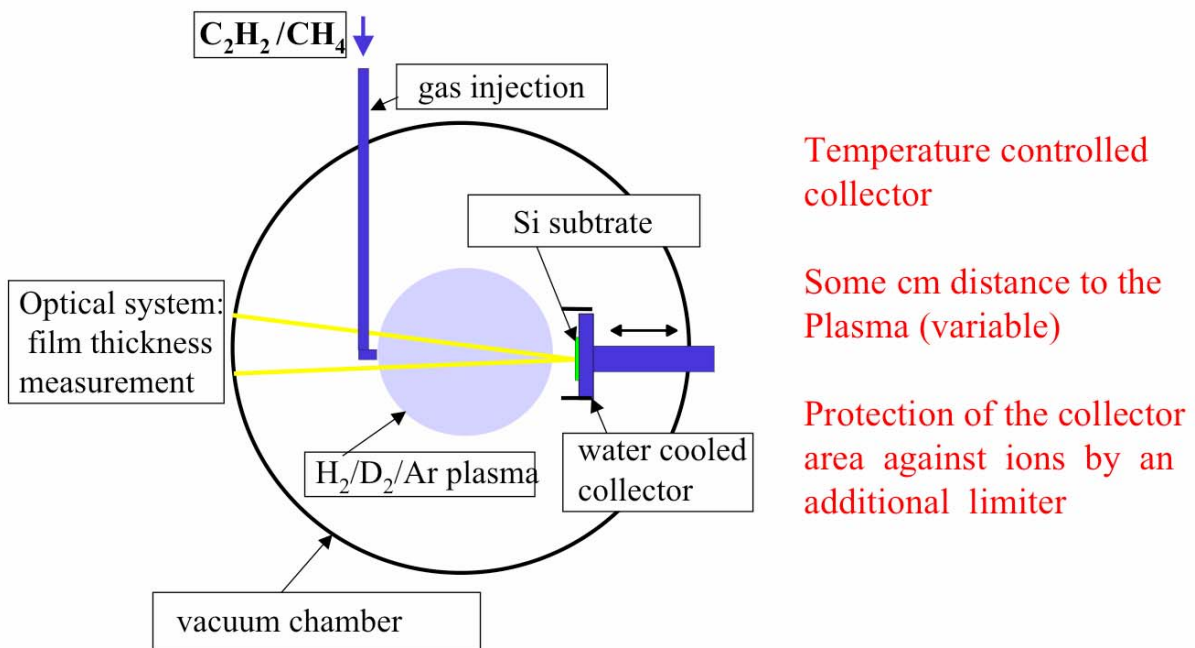


Fig. 1: Experimental arrangement used to determine the growth rates of amorphous hydrocarbon layers.

A temperature controlled collector is arranged near the plasma edge and opposite to the nozzle used for hydrocarbon injection. By means of an optical system the deposition rate for different plasma conditions can be determined in situ. Noticing that in hydrogen or deuterium plasmas the deposition is strongly influenced by erosion due to atomic hydrogen complementary measurements were done in helium and argon plasmas. Some results are depicted in Fig. 2.

As it is to be seen, the deposition rate increases nearly linearly with electron density (up to  $3 \cdot 10^{18} \text{ m}^{-3}$ ) with some ten-

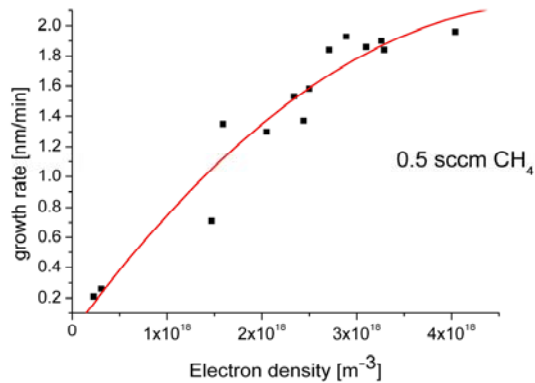


Fig. 2: Experimentally determined growth rate of a:C-H films on a Si collector for  $\text{CH}_4$  injection into an argon discharge with varying electron density.

dency to saturation at higher densities. Several scenarios were assessed by ERO modelling to explain this behaviour. At higher densities the reactive particles are formed in a volume very close to the nozzle, i.e. the carbon source is moving away from the collector with increasing plasma density. In addition, the enhanced ionization of the hydrocarbons in high density plasmas leads to a loss of produced ions from the collecting area via transport along the magnetic field lines. Both effects lead finally to a reduction of the growth rate and a maximum rate of about 2.5 nm/min is predicted for  $n_e \approx 1 \cdot 10^{19} \text{ m}^{-3}$ . Unfortunately, we not able yet to pass this value in the experiments. In Fig. 3 we compare the simulation results with the measurements.

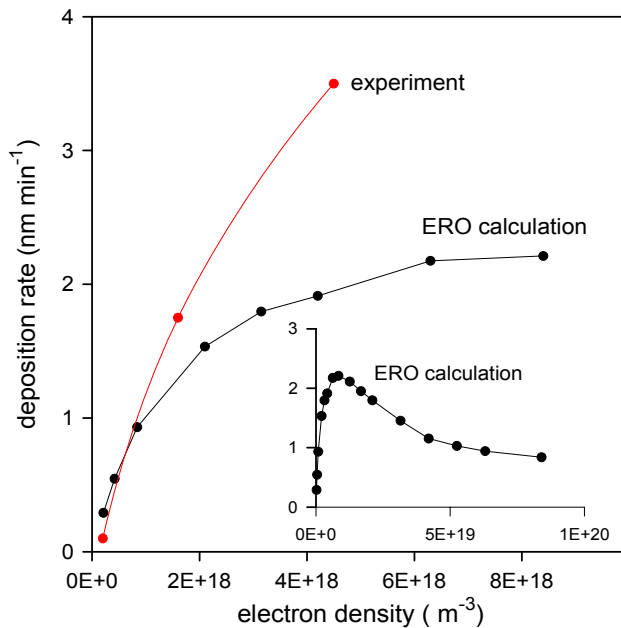


Fig. 3: Comparison of experimentally determined growth rates and ERO-results for  $\text{C}_2\text{H}_4$  injection (0.5 sccm) into argon discharges. The inserted graph shows that, according to ERO calculations, the growth rate should attain a maximum at  $n_e \approx 1 \cdot 10^{19} \text{ m}^{-3}$ .

Consistent with earlier studies [1] the experimentally determined growth rates are seen in Fig. 3 to be larger than those predicted by ERO modelling. Actually, this statement holds for all kind of injected hydrocarbons and all plasmas. Some additional experiments were performed to reveal the possible reasons for such discrepancies. The spatial extension of the carbon source in the plasma can be visualised by taking photos in the light of the CH-band emission around  $\lambda = 430 \text{ nm}$ . The results are presented in Fig.4 for  $\text{C}_2\text{H}_4$  (left) and  $\text{CH}_4$  (right) injection by means of the nozzle ("Düse", indicated by an arrow) into helium plasmas. The two pictures on top refer to a relatively low electron density of  $n_e = 2.0 \cdot 10^{17} \text{ m}^{-3}$ . As to be seen from Fig. 4 the emission is then rather homogeneously distributed over the cross-section, roughly reproducing the weakly hollow electron density

profile. When increasing the electron density by an order of magnitude (bottom part in Fig. 4) the pattern changes considerably and the CH-band emission is restricted to the region close to the nozzle. This concentration of the emission is found for floating conditions of the nozzle as well as for negative biasing but not in case of positive biasing thus indicating that plasma ions play an essential rôle in the molecular decomposing processes. The occurrence of the CH radicals in the immediate vicinity of the injection position can so far not be reproduced by ERO simulations.

Another parameters that strongly influences the deposition rates in the modelling is the list of sticking coefficients of the various hydrocarbons being produced within the plasma (see [2] for a discussion of the disintegration processes in case of  $\text{CH}_4$ ). In general ERO predicts relatively large flux densities of hydrocarbons impinging on the collector plate, but only a small fraction of those contribute to film formation. With the sticking data used in the modelling the film formation is dominated by species having sticking coefficients between 0.05 (CH) and 1 (C).

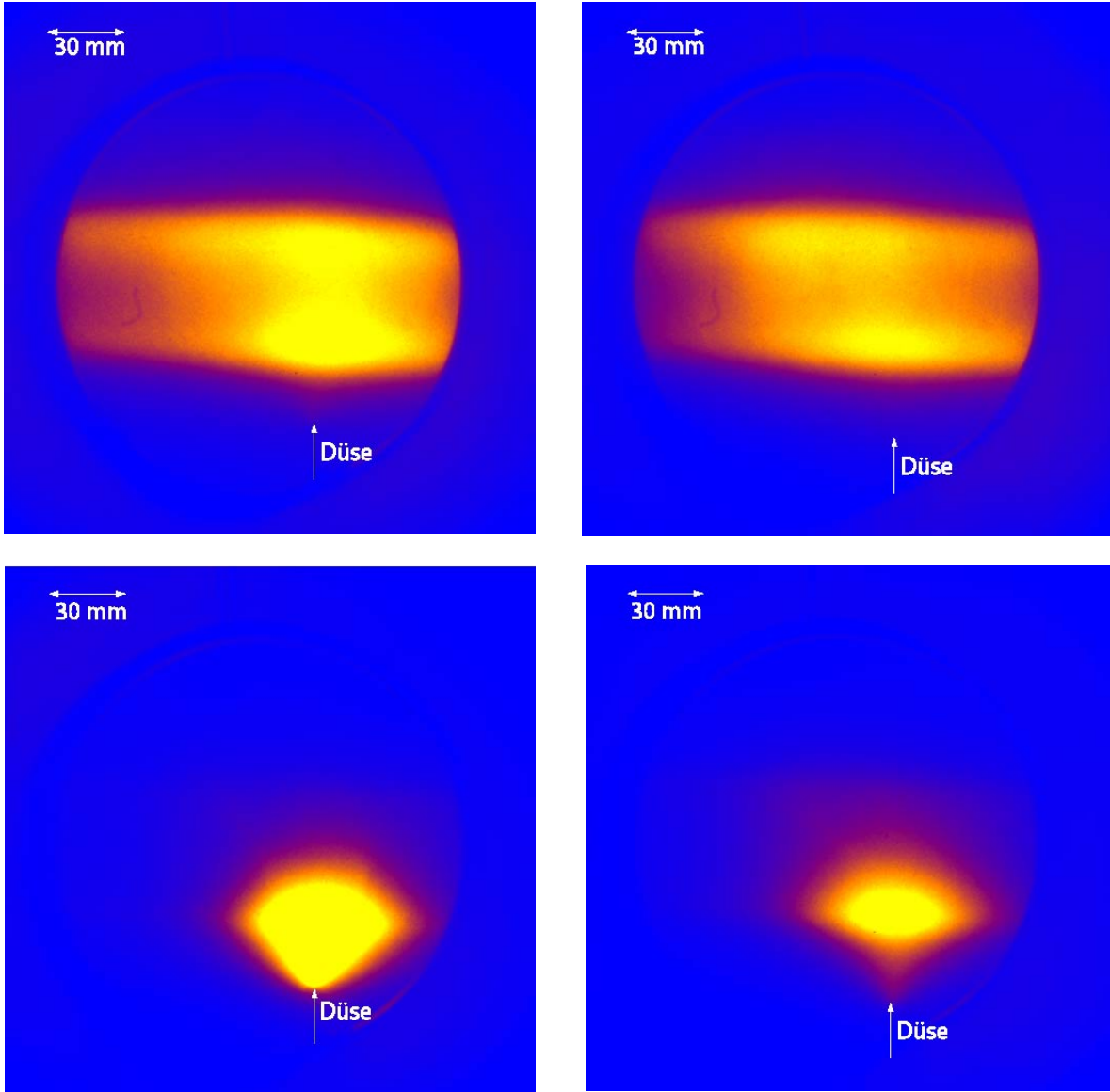


Fig. 4: CH emission pattern in helium discharges taken with a CCD camera equipped with an interference filter for two different electron densities; top:  $n_e = 2.0 \cdot 10^{17} \text{ m}^{-3}$ , bottom:  $n_e = 2.51 \cdot 10^{18} \text{ m}^{-3}$ . Left: ethene injection, Right: methane injection. The position of the injection nozzle is indicated by an arrow.

After having studied the layer formation in argon and helium plasmas we analysed the situation in hydrogen and deuterium discharges where the erosion on account of hydrogen atoms must be included. At high densities the experimental determination of the carbon sticking flux renders difficult as the erosion rate (at room temperature) becomes comparable to the deposition rate. Our attempts to derive sticking coefficients from deposition measurements in cavities have therefore not been successful so far. In Fig. 5 some examples of the net deposition in cavities are shown.

In case of a discharge with 100 A plasma current (Fig. 5, top/left) the density of atomic hydrogen is obviously so low that no erosion opposite to the entrance slit is noticeable. The deposition profile on the bottom plate is then nearly a Gaussian. However, for currents  $I \geq 200 \text{ A}$  (i.e. increasing electron density) the profiles attain a more complicated structure (Fig. 5, bottom and top/right). Such profiles can be explained in terms of erosion by a parallel beam of H-atoms reducing the original profiles by a factor of about 5 to 10 over the slit range.

The correlation between the densities of electrons ( $n_e$ ) and H-atoms ( $n_H$ ) could be substantiated by Lyman- $\alpha$  absorption measurements. These measurements will be improved further to allow absolute determination of  $n_H$  as a function of the distance to the plasma.

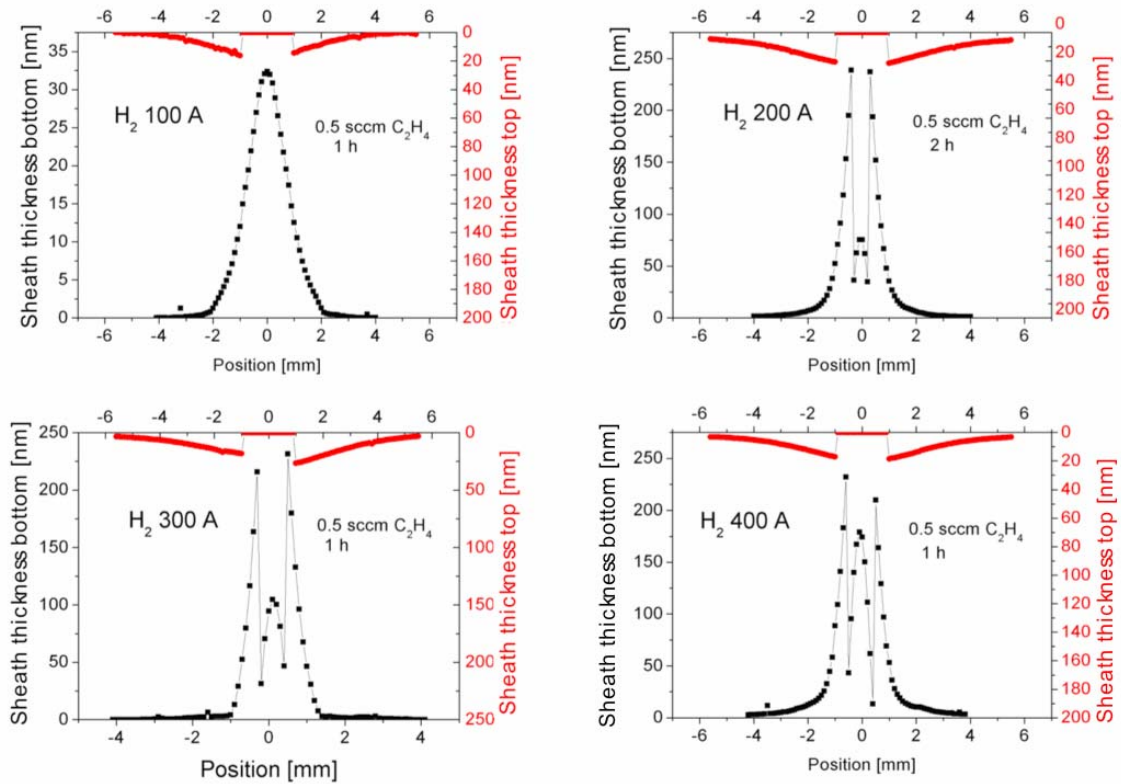


Fig. 5: Deposition profiles on the top and bottom plates of a cavity with the plasma current ( $\sim n_e$ ) as a parameter.

Staff:

W. Bohmeyer  
D. Naujoks  
Association Euratom - Max-Planck Institut für Plasmaphysik (IPP), Germany

G. Fussmann  
G. Krenz  
Humboldt Universität zu Berlin, Institut für Physik

A. Markin  
Institute of Physical Chemistry, Russian Academy of Sciences, Moscow, Russia

Literature:

[1] D. Naujoks, W. Bohmeyer, A. Markin, I. Arkhipov, P. Carl, B. Koch, H.-D. Reiner, D. Schröder and G. Fussmann, "Physica Scripta Vol.IXX, 1-6, (2004)

[2] A. B. Erhardt and W. D. Langer, Rep.PPPL-2477, Princeton (1987)

## **Divertor and Core Plasma Modelling for ITER**

### **Introduction**

The goal of the core and divertor plasma modelling program is the development, improvement, and application to ITER of a set of modelling codes which describe the ITER plasma from the core to the divertor plates in a coherent way so as to permit a consistent prediction of ITER plasma operating modes, operating windows, performance, and scenarios. Two separate codes are used for this purpose: the 2D coupled fluid & Monte Carlo code B2-EIRENE for two-dimensional modelling of the ITER divertor and scrape-off layer, and the Integrated Core-Pedestal-Sol (ICPS) model incorporated into the 1D ASTRA transport code for one-dimensional modelling of the ITER core and pedestal. The two codes communicate by means of scaling laws derived for the separatrix parameters from stand-alone runs of the codes. A variant of the model, which uses a simpler two-point model for the scrape-off and divertor plasma, is used to fit results from the experiments. Quantitative predictive modelling of ITER is done with the more complete model.

ITER performance modelling, crucial to establish the expected performance of ITER and to define the operating scenarios to obtain this performance, can be carried out only with such an integrated plasma model which describes in a coherent way the entire plasma from the centre via the pedestal and the scrape-off layer to the divertor plate. Our model has been developed in the framework of a quadripartite collaboration (FZ Karlsruhe, ITER International Team, Hydro-Québec, Varennes, Québec, Canada, and INRS-EMT, Varennes, Québec, Canada), as described in previous Annual Reports.

The previous version of the model and the results obtained were described in the previous Annual Reports and references therein, as well as in [1]. Several contributions described there have now been published [2], [3]. Initial results obtained in 2005 were described in [1]. Advances in ITER 2D divertor modelling were described in [4], [5], with particular emphasis on the application of improved neutral modelling including radiation transports and [6], in which theoretically proposed scalings are compared to modelling results for Asdex Upgrade (AUG). Advances in 1D modelling of the plasma core were described in [7], with particular emphasis on modelling improved H-modes. Work with the integrated model was reviewed in [8], and also formed part of the presentation in [9]. Additional work on limiter power lower loads was presented in [10]. Recent work in all these areas and in modelling of DEMO is presented in [11], and the DEMO modelling is also described briefly in a separate section of this Annual Report [12].

### **2. Divertor Plasma Modelling**

As reported in the previous Annual Reports and [1], a more complete neutral model than used earlier was introduced to include neutral-neutral collisions and molecular dynamics, particularly the ion conversion process (MAR) and elastic collisions of molecules with the plasma ions. The initial results indicated that (a) introduction of the molecular dynamics package leads to plasma detachment of the inner divertor at a higher neutral pressure, (b) the operational window of the ITER divertor retains the same width but shifts to higher neutral pressure in the PFR, and (c) the parameters of the interface to the core at the transition point remain approximately the same.

In the present reporting period, this model has been applied to a study of the consequences of removing the divertor "dome" structure between the inboard and outboard divertor regions [4]. A major effect is a factor 3 increase of the pumping speed necessary to replace the neutral compression by the dome. Removal of the dome leads to similar scaling as domed operation with power and divertor pressure (the temperature at the inner divertor follows the same curve). The separatrix densities are 20% higher and the separatrix temperatures 20% lower. The peak power load at the divertor plates is 30% lower at the same normalised pres-

sure. Some of these parameters are shown in Fig. 1. The carbon radiation at the X-point is 3x larger upon removal of the dome, but not dangerously, since the level remains low,  $0.05 \text{ MW/m}^3$ . There is therefore no indication of the occurrence of an X-point MARFE when the dome is removed. In contrast to ITER, a simulation for AUG parameters with the same model reveals a peak in carbon radiation at the X-point, due to a peak in deuterium (and therefore electron) density there and a dip in average impurity  $Z$  to 4.2, i.e. present-day device may be more susceptible to the occurrence of X-point MAFES than larger, higher-power devices such as ITER. The neutral density inside the separatrix remains unimportant for ITER even when the dome is removed,  $< 1.10^{15} \text{ m}^{-3}$ , i.e. a factor 20 lower than present devices such as AUG because of the lower neutral penetration in ITER (lower temperature, larger distance).

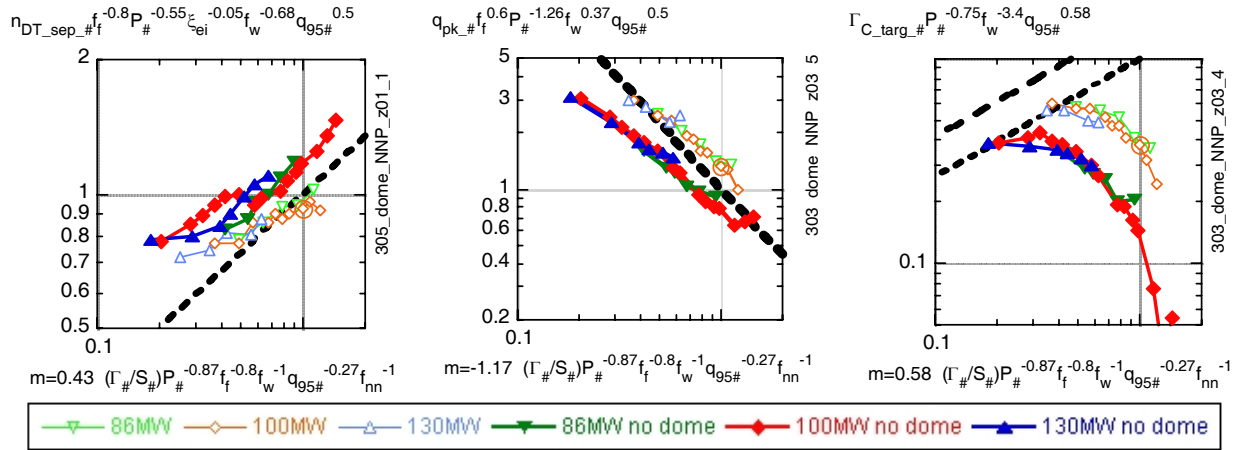


Fig. 1: a) Average DT density at the separatrix, b) Normalised peak power loading of the outer divertor and c) Normalised net target erosion, vs. normalised divertor neutral pressure, for cases with "dome" structure (light colours) and without (dark colours). See [4] for definitions, normalisation and scalings.

A further advance in the present reporting period was the introduction of Lyman alpha radiation transport. This was shown in [4] to cause strongly enhanced local ionisation, which is largely compensated by strongly enhanced local recombination, leading to similar global divertor parameters. More detailed results were reported in [5].

The model has also been applied to an extensive series of investigations of ASDEX Upgrade for two different divertor geometries (Divertor II and Divertor IIb), and more recently to JET. Further modelling is required, and conclusions will be drawn in the next reporting period. The model has also been applied to initial runs of a prototypical DEMO geometry [12].

In a further study, we examined an interesting statistical approach to determine the underlying SOL transport from a comparison of the experimentally measured width of the power deposition profile on the outer divertor target with that predicted by various theoretical models of plasma transport along and across the magnetic field in the scrape-off layer (SOL) (see references in [5]). In the study [5], we tested this approach by applying the same technique to a set of 2D simulation results rather than to actual experimental data. Our analysis shows that the statistical approach, when applied to our modelling data for AUG parameters rather than to experiment, does not ensure discrimination in favour of the simple model having the same transport mechanisms as the full modelling. Since the analysis is not able to recover the model that was actually used to generate the modelling data, we infer that conclusions based on such an analysis when applied to experimental data may not be warranted.

### 3. Core Plasma Modelling

As reported in previous Annual Reports and [1], the Integrated Core-Pedestal-SOL (ICPS) model now models core energy transport with the MMM95 transport coefficients, stabilized by a combination of ExB velocity flow shear and magnetic shear in order to obtain an edge

pedestal. For ITER modelling, the boundary conditions (separatrix parameters) for the core model are self-consistently determined by scaling relationships derived from database of B2-Eirene runs for the ITER SOL and divertor.

The model as described has been applied to JET and AUG conditions, and reasonable agreement with the experimental results had been demonstrated for normal tokamak discharges. Subsequently, a study of improved H-modes ("hybrid scenarios") had been initiated, in which a stabilization function depending on the sparseness of low-order rational surfaces produced conditions similar to those obtained in AUG hybrid scenarios. This model and the results obtained are described in the preceding annual report. In the course of developing the improved H-mode model, various tests indicated the possibility that the partition of power transport between electron and ion channels as described by the MMM transport coefficients was different from that obtained experimentally, so that a readjustment of the MMM model or its replacement by another transport model should be investigated.

In the first half of the present reporting period, the major emphasis was placed on modelling of hot-ion H-modes in JET, for which the discrepancy noted above had been observed. Still using the MMM model, it was found that a large part of the problem resulted from comparing the experimental data with the fully-relaxed conditions obtained from the model. When the transient behaviour of the discharge was correctly modelled and compared with the transients obtained experimentally, the agreement was much better, as shown in fig. 2.

Further work during the first part of the present period has concentrated on implementing the GLF23 model and contrasting results obtained with the GLF23 model with those obtained using the MMM95 model for hot-ion H-modes.

Results of a comparison of four models (critical gradient, MMM, GLF, GLF with adjusted edge temperature) are shown in Fig. 2. Two models (MMM95 and GLF) then produce central ion temperatures reasonably similar to those observed; CG is a bit higher. The central electron temperature evolution, however, is

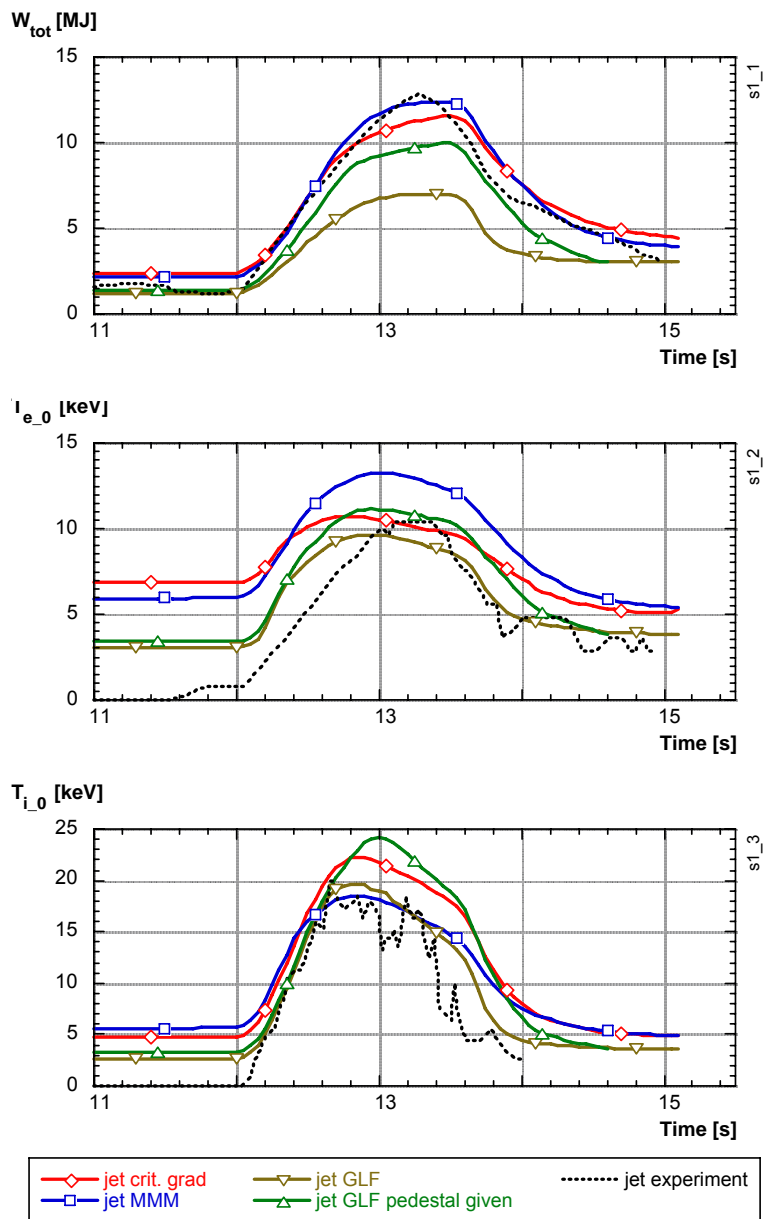


Fig. 2: Time evolution of energy content and central  $T_e$  and  $T_i$  for hot-ion H-mode simulation for the following simulations: CG (red), MMM95 (blue), GLF (khaki), and GLF with adjusted edge temperature (green). Experimental curves are black dashed.



best reproduced with the GLF simulation. MMM95 energy transport results in electron temperatures appreciably higher than those observed. In contrast, the energy content obtained with the GLF model remains appreciably below that of the experiment, whereas the two other models fit relatively well. Examination of the profiles showed that the discrepancy in energy content may result from the lower pedestal obtained with the GLF model. For comparison, we thus carried out simulations with GLF core transport for which the temperatures near the edge (and thus the pedestal energy content) were forced to be similar to those obtained in the MMM simulation. The discrepancy in energy is then seen to be strongly reduced, albeit at the cost of degrading the comparison of central ion temperature. As to the modelling of improved H-modes, simulations carried out for JET with the two models show that the confinement improvement obtained with the stabilization function for the MMM model is not found in the GLF simulations because the stiffness of the latter model increases the transport coefficients in such a way as to compensate the reduction due to the stabilization function. Similarly, for ITER, no notable improvement of net transport is obtained in the region where the stabilization function due to low rational surfaces is active with the GLF model.

In summary of the results obtained in the first part of the reporting period, a transient hot-ion H-mode shot in JET could be satisfactorily simulated with the MMM95 model when the transient behaviour of the discharge was correctly modelled, and with the GLF model when the pedestal height was adjusted to that obtained in the MMM95 simulation. Improved H-modes could not be simulated with GLF using the same approach as had been employed previously, because the extreme stiffness of the GLF transport model strongly reduced the improvement. Therefore, for the GLF model, both the stabilisation responsible for the pedestal and that yielding the improved H-mode require that stabilisation of the individual unstable modes be implemented, resulting in modified critical gradients.

The main thrust of work carried out in the second part of the reporting period concerned modelling of DEMO [12].

#### **4. Limiter Power Loads**

At the request of ITER, an evaluation of the power loads on ITER blanket modules used as inboard and outboard startup limiters was done. Three scenarios were investigated and contrasted: toroidally extended first wall limiter limited by alignment, toroidally local first wall limiter, and port limiter. Both inboard and outboard startup was investigated. It was concluded that the first option required excessive cooling capability of the whole first wall and that in the second option three wall modules had to be specifically configured as limiters to obtain similar heat loads as those of the port limiters. It was concluded that from the point of view of peak power loads, cooling, and ease of replacement and adjustment, the port limiters remained preferable.

#### **5. Perspectives**

Work on divertor and core modelling for ITER is continuing, particularly:

- In two-dimensional modelling of the ITER scrape-off and divertor plasma with walls having realistic carbon erosion-deposition, extension of the model to include temperature- and flux-dependent variation of the carbon erosion at the target, further development of the neutral model by improvements of the molecular package as required and the investigation of Lyman alpha radiation transport in the divertor plasma, continuation of the study of variations of the ITER geometry (influence of the dome), further simulations and generation of scaling relations for ASDEX Upgrade and/or JET, and initial application of the current model to a highly radiating prototypical reactor plasma.
- In one-dimensional modelling of the plasma core, the work will concentrate on modifications of the model to include transport modules which better describe hot ion modes and

advanced scenarios for present devices, the validation of the model against present experiments, the evaluation of the impact of advanced operation on ITER using the improved model, and initial application of the current model to a highly radiating prototypical reactor plasma.

- Validation of the model will include application of the scaling law approach to coupling of the core and edge to existing experiments.

### Staff:

H. D. Pacher (INRS-EMT, Varennes, Québec, Canada)  
G. W. Pacher (Hydro-Québec, Varennes, Québec, Canada)  
A. S. Kukushkin (ITER International Team)  
G. Janeschitz  
I. Landman  
S. Pestchanyi - with the collaboration of G. Pereverzev (IPP Garching).

### Literature:

- [1] Pacher H.D., Pacher G.W., in collaboration with ITER IT Garching, FZ Karlsruhe, Max-Planck-Institut für Plasmaphysik Garching, EFDA CSU Garching, "Divertor and core plasma modelling for ITER - Final Report June 2005", INRS Energie, Mat. et Télécom. Report, 2004, INRS-EMT-021-0605, June, 2005
- [2] Kukushkin, A. S., Pacher, H. D., Kotov, V., Reiter, D., Coster, D., Pacher, G. W., "Effect of neutral transport on ITER divertor performance", Nucl. Fusion 45, 608-616, 2005
- [3] Pacher, G. W., Pacher, H. D., Janeschitz, G., Kukushkin, A. S., Pankin, A., Pereverzev, G., Voitsekhovitch, I., "Modelling of ITER Improved H-mode Operation with the Integrated Core Pedestal SOL Model", Nucl. Fusion 45, 581-587, 2005
- [4] Kukushkin A.S., Pacher H.D., Kotov V., Reiter D., Coster D., Pacher G.W., "Improved modelling of neutrals and consequences for the divertor performance in ITER", Proc. 32nd EPS Conf. on Plasma Physics, Tarragona, Spain, 2005
- [5] Kotov, V., Reiter, D., Kukushkin, A.S., Pacher, H.D., Börner, P., Wiesen, S., "Radiation absorption effects in the B2-EIRENE divertor modelling", presented at Conference on Plasma Edge Theory (PET), Jülich 2005
- [6] Kukushkin A.S., Pacher H.D., "Critical Evaluation of the Determination of the SOL Transport Mechanism from a Statistical Examination of Experimental Data", presented at Conference on Plasma Edge Theory (PET), Jülich 2005, to be publ.
- [7] Pacher G.W., Pacher H.D., Janeschitz G., Kukushkin A.S., Pereverzev G., Pankin A., Voitsekhovitch I., "Simulation of ITER Improved H-mode Operation with the Integrated Core Pedestal SOL Model Using MMM95 and GLF23 Core Transport Models", Proc. 32nd EPS Conf. on Plasma Physics, Tarragona, Spain, 2005
- [8] Pacher, G.W., Janeschitz, G., Pacher, H.D., Kukushkin, A.S., "Development of the Integrated Core Pedestal SOL (ICPS) Approach", presented at Symposium on the Future of Integrated Modeling, Princeton, USA, July 2005
- [9] Lönroth, J.S., Becoulet, M., Beyer, P., Corrigan, G., C. Figarella, Fundamenski, W., Garcia, O.E., Garbet, X., Huysmans, G., Janeschitz, G., Johnson, T., Kiviniemi, T., Kuhn, S., Loarte, A., Naulin, V., Pacher, G.W., Pacher, H.D., Parail, V., Pitts, R., Saibene, G., Snyder, P., Spence, J., Tskhakaya, D., Wilson, H., "Integrated ELM modelling", presented at Conference on Plasma Edge Theory (PET), Jülich 2005
- [10] Pacher H.D., Pacher G.W., "Power loads on ITER blanket modules used as inboard and outboard startup limiters", INRS Energie, Mat. et Télécom. Report, EMT-015-0105-a, 2005
- [11] Pacher H.D., Pacher G.W., in collaboration with ITER IT Garching, FZ Karlsruhe, Max-Planck-Institut für Plasmaphysik Garching, EFDA CSU Garching, "Divertor and core plasma modelling for ITER - Intermediate Report December 2005", INRS Energie, Mat. et Télécom. Report, INRS-EMT-025-1205, December, 2005, in preparation
- [12] Pacher H.D., Pacher G.W., "Analysis of total radiation in tokamak reactor scenarios", this Annual Report (Systems Studies Section, Task TW5-TRP-002.D2 DEMO Physics Studies)

## **Heating and Current Drive**



## **TW5-TPHE-ECHULA**

### **Detailed Design and Analysis of the Upper Launcher for the ITER ECH&CD System: Torus Window Design and Development**

#### **Objectives**

For NTM stabilisation at ITER, a mm-wave launching system ("launcher") based on the remote steering (RS) concept had been considered until recently as the reference design at the ITER upper port level. For the separation between the primary (plasma) and secondary vacuum in the RS Upper launcher, a torus window unit was designed and manufactured as a compact structure which allows off-axis transmission of 2 MW beams at 170 GHz. Off-axis transmission was a particular challenge, which had to be implemented to provide the substantial angular input steering range of  $\pm 12^\circ$  required for the in-vessel square mm-wave waveguide system. The location of the window called for an asymmetric cooling structure at the diamond disks allowing the window aperture to be maximised. Given a diameter for the CVD diamond disk of 106 mm, an aperture of 95 mm could be realised. For this prototype design of a RS window unit, specific experiments were conducted to demonstrate the feasibility of the torus window concept based on the CVD-diamond window technology including remote handling procedures. Thus, for modelling the thermo-hydraulic performance of the torus window cooling circuit, a heated copper dummy disk simulating the CVD diamond disk was studied. Furthermore, exploratory studies to define suitable cutting/re-welding tools and procedures were performed where a dummy window housing was to be joined and removed from metallic rings that represent typical window sockets. In cooperation with the lead team for the mm-wave design of the RS launcher (FOM Rijnhuizen, NL), a beam line mock-up was set up at the high power gyrotron test facility of FZK/IHM to demonstrate the transmission characteristics of the waveguides with ITER dimensions at high power/short pulse together with the specific mm-wave components (steerable mirror unit, RS torus window prototype and front mirror).

#### **Deliverable d3**

##### **Experimental study of thermal-hydraulic performance of the torus window cooling circuit**

The torus window prototype [1] which was manufactured by the FZK technical services (cf. Fig. 1) was based on a large area CVD diamond disk (106 mm dia. x 1.85 mm) grown by Element Six (Ascot, UK). The metallic parts (copper cuffs) were joined to the disk by a Ag-Cu braze which was realised at Thales Electron Devices (Velizy, F). For studies of the cooling efficiency of the RS torus window unit, a dummy window structure was manufactured which was identical to the prototype CVD torus window except that the CVD diamond was substituted by an electrically heated copper disk (cf. Fig. 2) [2]. The cooling circuit was configured to provide the parameters of the component cooling water system at ITER which is the projected cooling system for the torus window. This means that a water pressure of up to 1.0 MPa and a water temperature of up to 40°C were made available. From the temperature rise between the input and output channel, it could be concluded that 85 ( $\pm 10$ )% of the electrical power was extracted by the coolant for flow rates of 5 -10 l/min. The remaining power was inferred to be dissipated by convection in air or thermal conduction in the solid parts. The temperature profile over the disk was measured by an infrared camera and, at selected positions, by thermocouples. It was found that the temperature profile did not differ for the horizontal and vertical arrangement of coolant input, thus excluding gravitational effects. The temperature difference determined between the disk at the edge of the window aperture ( $T_{\text{aper}}$ ) and the coolant ( $T_{\text{W}}$ ) characterises the cooling efficiency of the cooling chamber which is the product of the heat transfer coefficient and the effective cooling area. Experiments showed that only minor differences occur in  $T_{\text{aper}} - T_{\text{W}}$  for flow rates of 5 l/min and 10 l/min in cooling tests performed with a heating power of 500 W, yet much higher values for 2 l/min (cf. Tab.1). The same observation was made for the temperature at the centre of the disk

( $T_{\text{cent}}$ ). Studies with alternative water inlet temperature (ambient and 35°C) produced comparable results when scaled with  $T_w$ .

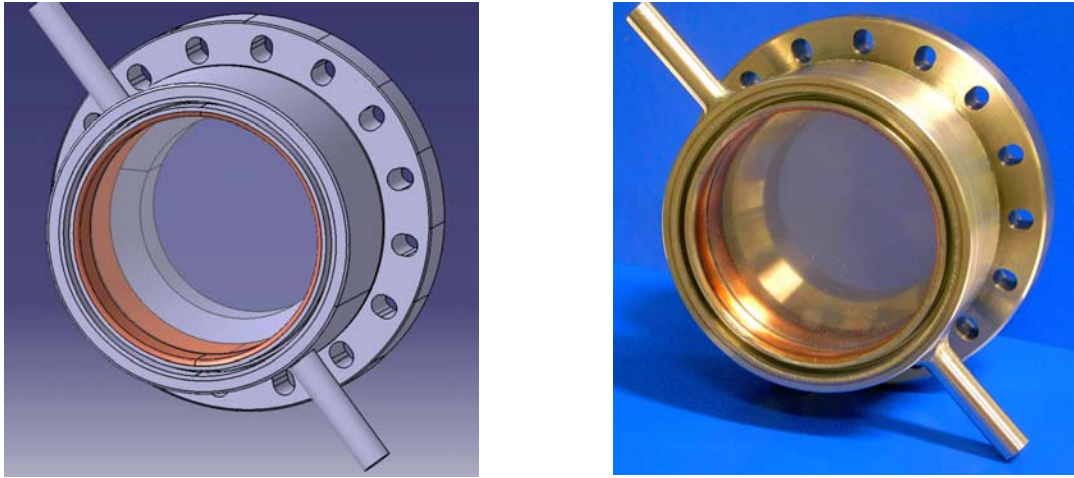


Fig. 1: The torus window prototype developed for the 3/8 RS reference launcher as a 3D-CATIA model (left) and as a manufactured component (right).

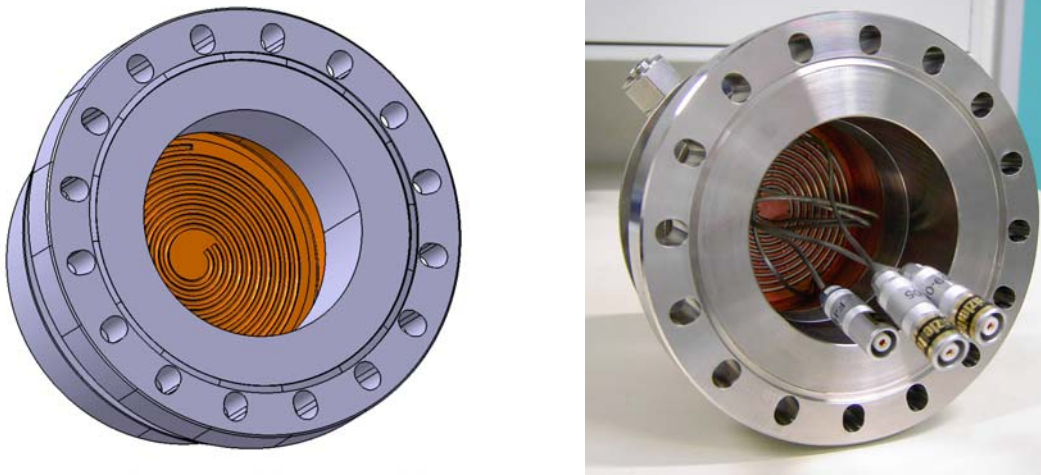


Fig. 2: The torus window dummy set up for the thermo-hydraulic window tests as a 3D-CATIA model (left) and as a manufactured component including thermocoax cables for ohmic heating.

The experiments showed that the insensitivity of the cooling efficiency to the water flow rate which was set during the previous design development to be given for 10 l/min and above could be extended to the flow rate 5 l/min. As a consequence of the experiments, an efficient cooling operation of the RS window prototype is now estimated to be fulfilled when the temperature difference between the edge of the disk aperture and the coolant is below 15 K. The FEM modelling of the structure allows to estimate then the required heat transfer coefficient to be  $\alpha_T > 6000 \text{ Wm}^{-2}\text{K}^{-1}$ .

Table 1: Experimental results of the heating test for the window structure and corresponding values of the heat transfer coefficient assigned by FEM modelling of the window and cooling configuration.

Water inlet temperature: ambient or 35 °C (alternatively)			
Water flow rate	2 l/min	5 l/min	10 l/min
$T_{\text{cent}} - T_w$ [K]	56-66	~ 44	39-44
$T_{\text{aper}} - T_w$ [K]	24-27	~ 11	9-13
$\alpha_T$ [ $\text{Wm}^{-2}\text{K}^{-1}$ ]	1500-2500	> 10000	> 13000

Very recently, the reference concept for the ITER upper ECRH launcher has been shifted to the front steering (FS) option in which the mm-wave beam can be transmitted on axis through the disk. Therefore the aperture can be reduced, and there is the potential to provide indirect cooling through the cooling chambers fixed to the metallic cuffs ("indirect face cool-

ing”) alternative to edge cooling which provides the safety relevant advantage of separating the coolant from the diamond disk forming the tritium barrier. An explorative version of a related FS window prototype will be manufactured and corresponding cooling tests will be performed on dummy structures to determine the limits for the flow rates of the cooling water accordingly.

#### **Deliverable d4**

#### **Exploratory tests for cutting/re-welding of the torus window structure to window sockets**

The torus window is connected by a window socket to an isolation valve fixed at the closure plate. This configuration had been introduced into the upper ECRH launcher design during the preceding development for the “3-port/8-beam” RS reference launcher which was transferred in 2004 to the ITER design office. This design allows the requested hands-on maintenance of a failed torus window with a cracked CVD diamond disk. With the isolation valve closed, the replacement of the window unit by automated cutting and welding tools must be feasible on site. Nuclear radioactivation analysis has shown that for both the RS and the FS launcher options, the limiting dose rate of 100  $\mu\text{Sv/h}$  for hands-on maintenance is fulfilled. The open key design aspect was to demonstrate the availability of automated cutting and welding tools and the definition of space reserves to be respected in the mm-wave design for access to the joint between the window socket and the window housing.

Among the commercial tools on the market, an adequate product spectrum for automated cutting was found at Protem GmbH (Dettenheim, D) and for automated welding at Arc Machines (Much, D). For exploratory tests, dummy structures for typical cutting and welding configurations were fabricated for testing with available demonstrator tools (cf. Fig. 3). Common to both structures are outer diameters of 120 mm of the window housing of the RS window prototype and the 141 mm of flange to the window socket.

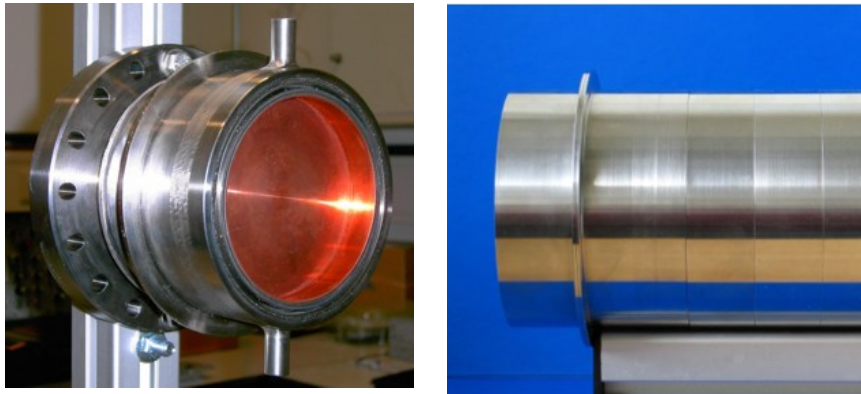


Fig. 3: The dummy window structure fabricated for tests of automated cutting (left) of automated welding (right).

The cutting was successfully demonstrated with a slightly oversized tool (cf. Fig.4). Yet this allowed to identify the type TSS-NG 141 with a working area of 73 – 141.3 mm to be suited for the RS window design and the type TSS-NG 114 with a working area of 60 – 114 mm to be suited for the FS window design. The outer dimensions of the tools (220 mm and 193 mm resp.) exceed the diameters of the window housings by 100 mm and 90 mm resp., which means that a perimeter of 50 mm has to be reserved around each window for giving access to the tool. The cutting tool TSS-NG 141 has been procured for detailed RS window maintenance tests. These will be performed in 2006 together with tests of the FS window demonstrator that can be cut with the same tool even though with non-optimum space requests.

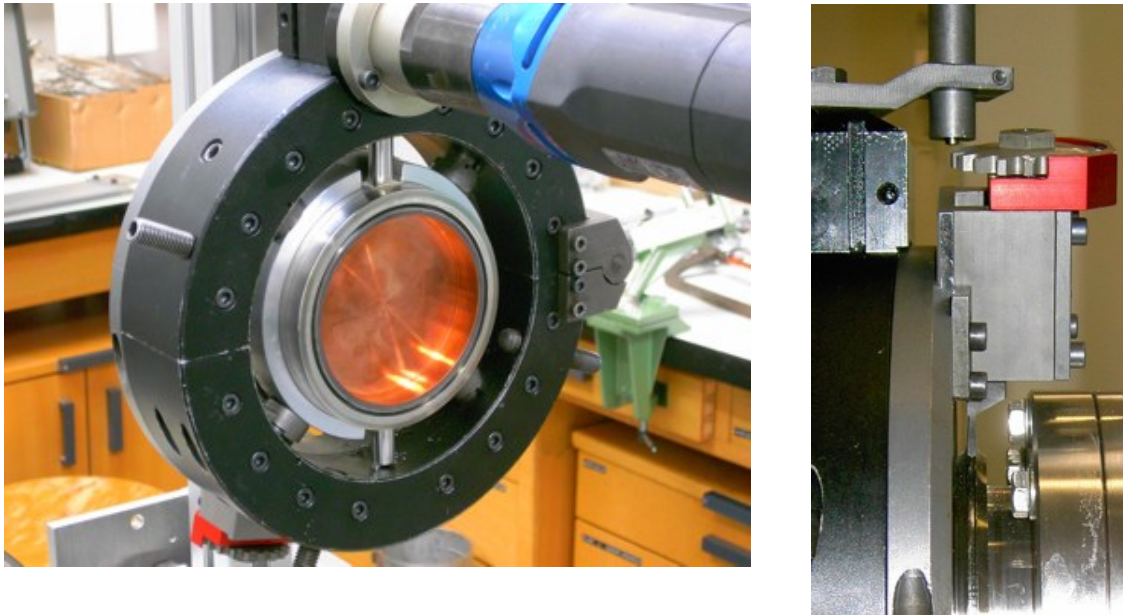


Fig. 4: The dummy window structure with positioned automated cutting (left) and the blade acting on the welded flange connection (right).

The experiments for studying the performance of the automated welding tool produced evidence of substantial deformation of the mm-wave structures for butt welding configurations, whereas satisfactory quality could be obtained by lip welding (cf. Tab. 2).

Table 2: Weld characteristics of selected welding options studied with automated orbital welding tool as compared to regular electron beam welding.

Welding type	Butt welding		Lip welding	
	Orbital welding (Arc-welding)		Electron beam welding	Orbital welding (Arc-welding)
Welding depth (ca.)	full	2mm	2mm	2mm
Welding width (ca.)	8mm	5mm	2mm	3.5mm
Deformation (inner diameter)	large (> 0.5mm)	large (> 0.5 mm)	small (< 0.5mm)	small (< 0.5mm)

Following the goal of reducing the size of the window socket in order to gain reserves for beam steering angles with respect to beam vignetting at the window housing, the welding area was shifted close to the window housing, for which a minimum attachment zone for the welding tool of 40 mm was to be reserved. Therefore, a special modification, compatible with the plate-to-tube configuration characteristic for the narrow joint of the window to the isolation flange, was ordered from the tool manufacturer. This is in contrast to the tube-to-tube configuration characteristic for the axial beam arrangement of the front steering mm-wave system (cf. Fig. 5). Therefore, the welding tests planned after the delivery of the dedicated welding head will be applicable to the RS torus window design only. A dedicated welding tool for the future FS torus window demonstrator will have to be designed separately based on the initial exploratory tool.



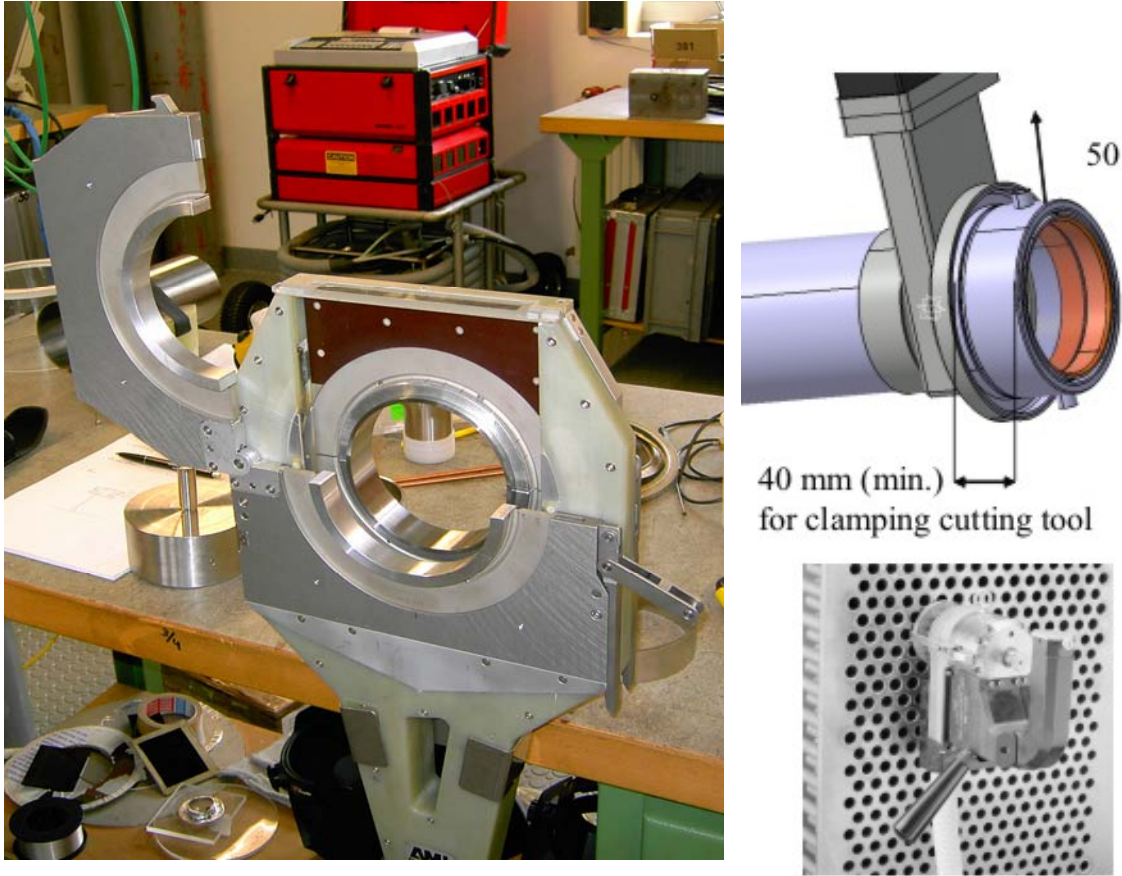


Fig. 5: The tube-to-tube configuration used for the exploratory automated orbital welding tool (left) and plate-to-tube configuration used for the adapted welding tool for the remote steering torus window (right).

Staff:

I. Danilov  
R. Heidinger  
A. Meier

**Deliverable e6**

**Preparation of the housing for the test facility for steering tests with the mock-up square waveguide system**

To perform the tests with the beam line mock-up of the RS launcher, several modifications at the gyrotron test facility had to be provided. The modifications included the microwave box the microwave beam was radiated into, as well as building up a special diagnostic box for measuring the properties of the microwave beam from the remote launcher. Fig. 6 gives an overview over the test arrangement. Because of the length of the launcher, some mechanical modifications as, e.g., a microwave tight opening in the wall of the box, were necessary for the installation inside the microwave box. In addition, a set of mirrors forming the matching optic unit (MOU) was installed inside the microwave box for converting the gyrotron output beam into a suitable beam for injection into the waveguide system.

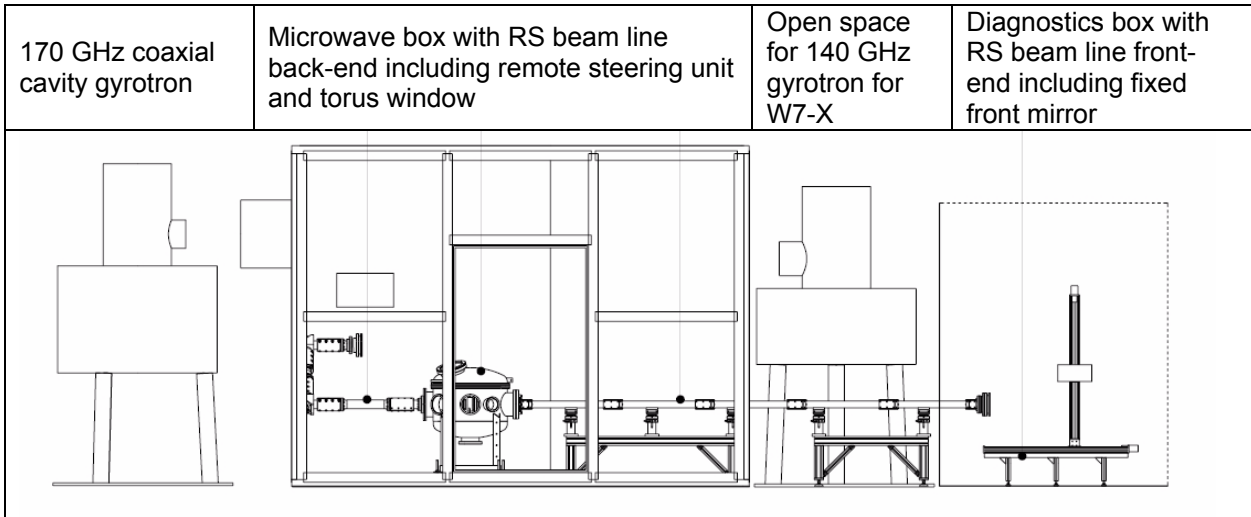


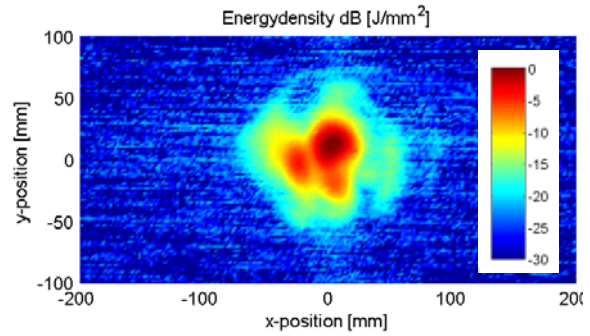
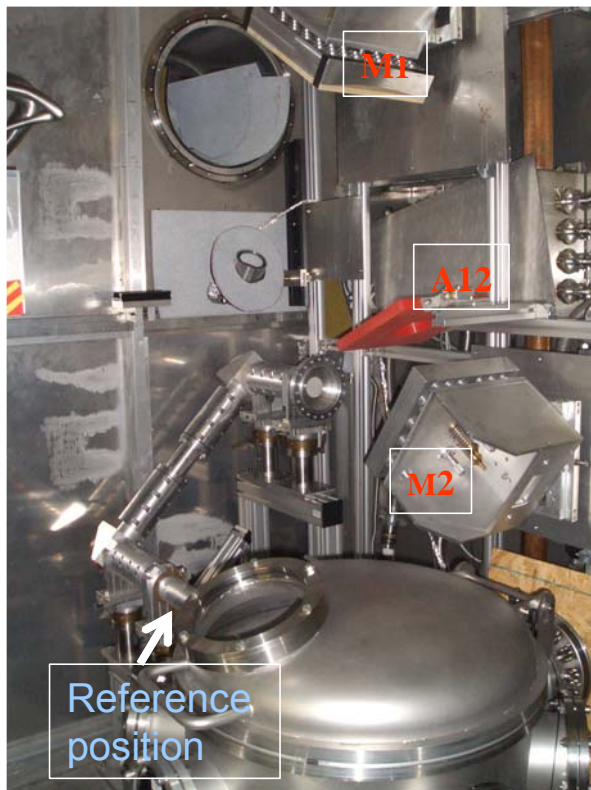
Fig. 6: Schematic lay-out of the test facility for steering tests with the mock-up beam line for the RS launcher at the ITER upper port.

**Deliverable e7  
Fabrication of the mirror supports for the MOU**

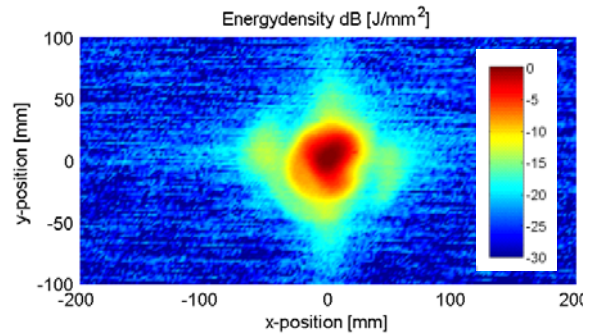
The microwave beam from the gyrotron was converted into a Gaussian beam suitable for injection into the remote launcher system. This beam conversion is done with a matching optic unit (MOU) consisting of two mirrors designed and fabricated at IPF Stuttgart. The mirrors were installed inside the existing microwave box, where special supports have been designed and manufactured for at FZK. By means of the MOU, the input beam was improved from 58 % to 87 % lowest order Gaussian content. This fraction could be further increased to 96% by placing extra vignette absorbers in front of mirror M1 and between mirrors M1 and M2 (A12).

**Deliverable e8  
Provision of additional quartz glass window (for square waveguide end in microwave box)**

A disc made of fused silica was ordered (thickness: 6.805 mm) and a window unit was designed and manufactured to complete, together with another already existing one, a set of vacuum windows. By mounting the windows at the entry of the RS launcher back-end and the exit of the RS launcher front end, the steering capabilities could be tested under vacuum. The vacuum obtained in the waveguide system was better than  $3 \cdot 10^{-6}$  mbar. A typical temperature rise of 10 K was observed in the centre of the quartz glass window at the launcher front end for a 170 GHz/300 kW/6 msec pulse ( $0^\circ$  steering angle).



Beam pattern without vignetting absorbers: Gaussian content: 87.2 %



Beam pattern with vignetting absorbers: Gaussian content: 96.0%

Fig. 7: Mirror arrangement (M1,M2) of the Matching Optic Unit (MOU) fixed in the microwave box and the filtering of the Gaussian beam by insertion of vignette absorbers (A12, and in front of M1) with patterns observed at the input of the remote steering unit (reference position).

### Deliverable e9

#### Built-up of the outer structure of the diagnostics box

The diagnostic box was constructed, manufactured and installed to house the launcher front end and the diagnostic screen. The box is microwave tight with the inner walls lined with wood as mm-wave absorber and with a controlled access via integration into the safety system. The diagnostic screen was made of PVC absorber foil, the lateral temperature distribution of which was registered from the backside by an infrared camera, to provide (after calibration of the integrated power with a calorimeter) a quantitative measure of the power profile in the beam pattern (cf. Fig. 8).

### Deliverable e10

#### Execution of the high power/short pulse tests at FZK

The coaxial gyrotron was operated for 3 months for the tests with the beam line mock-up of the RS launcher. The maximum output power delivered by the gyrotron was slightly above 1 MW. The frequency of the generated microwave was very close to 170 GHz. However, the Gaussian content of the beam was only about 58 %, reducing thus significantly the usable part of the microwave power. It was possible to extend the pulse length up to about 9 ns. Within these parameters, the gyrotron operation was very reliable during the whole test period.

In the tests of the overall steering performance, it was found in the joint experiments together with FOM Rijnhuizen, that despite of the non-optimal behaviour of the coaxial gyrotron both in power level and Gaussian content, the steering performance at high power could be demonstrated to be in conformity with the ITER specifications. The near field output patterns of the RS square waveguide show that the starting position of the steered beam and the shifts behave as expected. The far field output patterns of the RS square waveguide (also with the front mirror included) show good quality output beams and the expected steering range.



Fig. 8: View into the diagnostics box with the fixed mirror at the launcher front end (left) and the arrangement of the diagnostic screen relative to launcher front end (right).

In the experiments, one measurement campaign was dedicated to the investigation of the potential influence of the RS torus window prototype on the transmission performance of the beam line mock-up. In a measurement series with the beam line operated in ambient atmosphere, it was found that the patterns of the steered beams were neither degraded in shape nor in amplitude over the full steering range of  $-12^\circ$  to  $+12^\circ$  (cf. Fig. 9). Arc formation was never observed at the window, neither during operation in atmosphere nor in vacuum. The main difference between both types of operation was the occurrence of a few light emitting spots at the CVD diamond surface under vacuum, which is a typical feature of high power gyrotron windows and which is related to the excitation of C-H contaminants and residues at the diamond surface.

After the positive demonstration of the steering and transmission characteristics of the beam line mock-up for the RS launcher in the configuration of the initial reference model, the coaxial gyrotron is projected for high power / short pulse test of the torus windows adapted to the up-dated mm-wave launcher configurations, in particular the front steering (FS) variant. After registration of the improved coaxial gyrotron beam pattern and related adaptations for the mirrors forming the MOU, the FS torus window will be studied with respect to the beam pattern and arc formation. A comparison will be made to the performance of the RS window prototype [3].

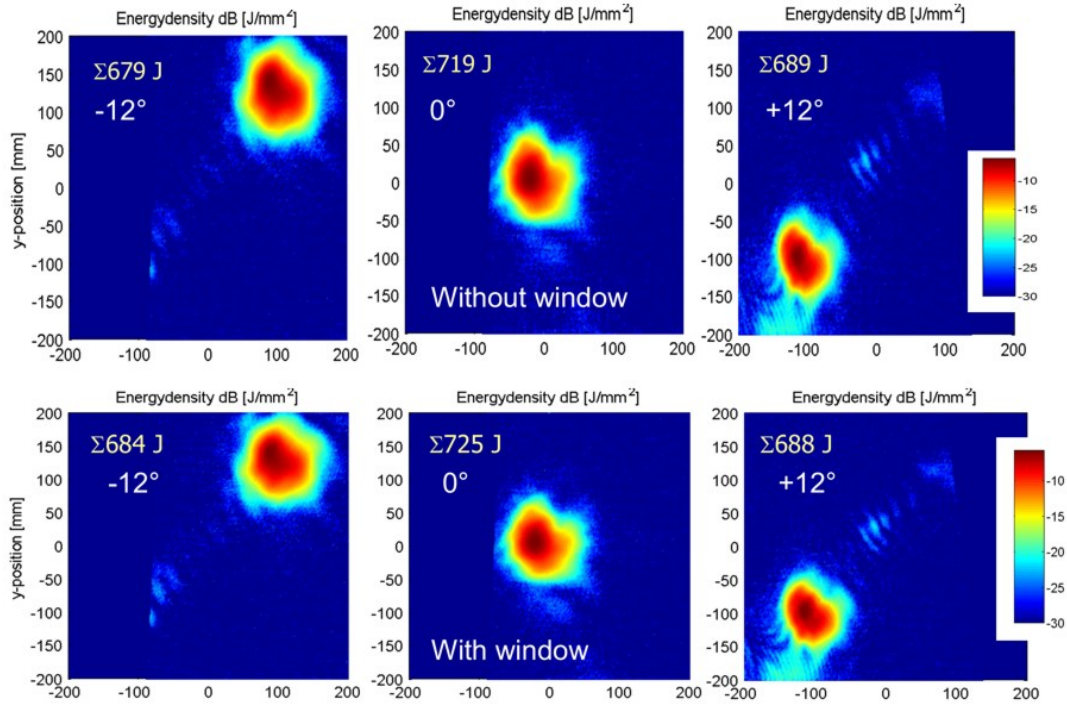


Fig. 9: Beam patterns measured for transmission of a 170 GHz/160 kW/ 7ms pulse through the beam-line mock-up without (top) an with (bottom) the torus window prototype.

Staff:

- I. Danilov
- R. Heidinger
- A. Meer
- B. Piosczyk
- S. Illy
- W. Leonhard
- D.Mellin
- T. Rzesnicki
- M. Schmid
- W. Spiess
- J. Szczesny
- M. Thumm

Literature:

- [1] R. Heidinger, I. Danilov, A. Meier, P. Spaeh, B. Piosczyk, M. Thumm, W.A. Bongers, M. Graswinckel, B. Lamers, A.G.A Verhoeven; Design and performance tests of a high power torus window for a remotely steered EC launcher; IRMMW-THz 2005 :Joint 30th Int. Conference on Infrared and Millimeter Waves and 13th Int. Conference on Terahertz Electronics, Williamsburg (USA), September 19-23, 2005, Proc.Vol.2 S.565-66 Piscataway, N.J. : IEEE, 2005, ISBN 0-7803-9348-1
- [2] R. Heidinger, I. Danilov, A. Meier, P. Spaeh, B. Piosczyk, M. Schmid, M. Thumm, W.A. Bongers, M. Graswinckel, B. Lamers, A.G.A Verhoeven; Transmission and cooling studies of the torus window for a remotely steered EC launcher; 7th Biennial ECH Transmission Line Workshop, Virginia Beach, Va., September 14-16, 2005
- [3] W.A. Bongers, M. Graswinckel, A. Fernandez, A. Bruschi, B.S.Q. Elzendoorn, R. Heidinger, K. Schwörer, O.G. Kruyt, B. Lamers, R. Lammers, B. Piosczyk, D.M.S. Ronden, M.R. Rugebregt, A.G.A Verhoeven; Low- and high-power measurements on a remote steering upper port launcher mock-up for ITER; IRMMW-THz 2005 :Joint 30th Int. Conference on Infrared and Millimeter Waves and 13th Int. Conference on Terahertz Electronics, Williamsburg (USA), September 19-23, 2005, Proc.Vol.2 S.425-26 Piscataway, N.J. : IEEE, 2005, ISBN 0-7803-9348-1

## EFDA/05-1230

### Detailed Design and Analysis of the Upper Launcher for the ITER ECH&CD System: Launcher Structural Design Integration

#### Objectives

A remote participating team to the ITER-IT ("ECHULA group") of EURATOM Associations (ENEA/CNR Milano, CRPP Lausanne, FZK Karlsruhe, FOM Rijnhuizen, IPP/IPF Garching/Stuttgart) is developing, coordinated by FZK, the conceptual design for subsequent procurement of the ECH upper launcher system for the upper ports of ITER. With the aim of establishing an optimum ECH launching system to counteract the formation of neoclassical Tearing Modes (NTM), a new design effort was allocated to the front steering (FS) concept in addition to the initially preferred option of the remote steering (RS) concept. The driving force for this extension of the design effort in the EU was the low NTM stabilisation efficiency achieved by the RS launcher, once a range of ITER reference scenarios were included in the analysis of the launcher performance. In fact, the target plasmas for the design were extended from the originally specified Scenario 2 (Inductive operation II,  $P_{fus}=400$  MW) to include also the hybrid operation Scenario 3a as well as Scenario 5 (high performance inductive operation with  $I_p=17$  MA), including variations of the plasma  $\beta$  and current profile for each scenario. This has adverse consequences for the focussing of the beam, leading to a reduction of the local density of driven current and thus of projected performance of the RS launcher design. As a consequence, the reference design, which was transferred to the ITER design office in 2004, for the launcher configuration named 3-ports/8-beams reference RS model (called RS 3/8 model) underwent several modifications in the mm-wave system concurrent with physics performance assessments, starting from arrangements with 8 beams per launcher and single end mirrors, over 6 beams with single end mirrors, to the presently preferred RS 'dogleg' launcher with 6 beams and pairs of 'dogleg' end mirrors.

The special challenge of the integration engineering was to ensure the feasibility of the advanced 'dogleg RS' and FS microwave system within the boundaries and interfaces at ITER and to develop the basic concepts for the cooling and nuclear shielding design up to a level allowing the assessment of objective criteria for a comparison of the launcher concepts.

#### Basic concepts of the upper launcher design activity (Deliverable c.1)

The present RS launcher design is based on a mm-wave system composed of 6 beam-lines (each compatible with 2 MW power transmission), as shown in Fig. 1. It consists of two sets of front mirrors, arranged in a dog-leg configuration, six corrugated waveguides (SCW), the isolation valve connected to the SCW and the diamond window. These are the mm-wave components

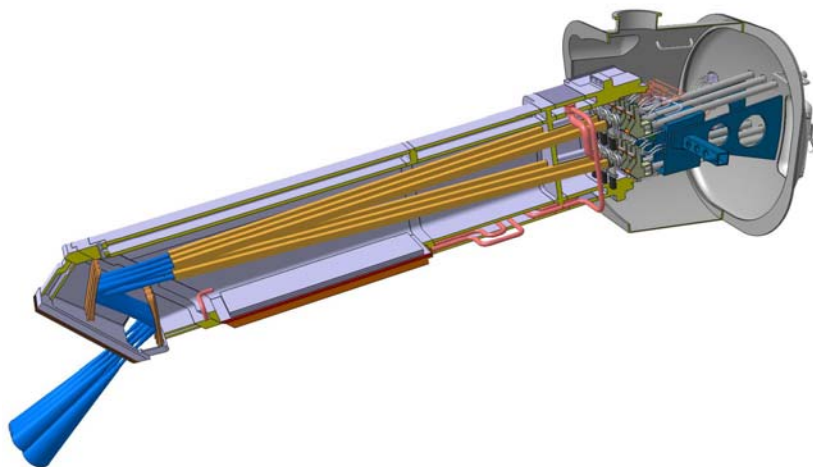


Fig. 1: RS dogleg launcher injecting six 2.0 MW microwave beams into the plasma.

that are connected to or placed in primary vacuum or torus vacuum. All other components from that point on are placed in secondary vacuum or outside the vacuum. The next component is the steering unit connected to the water cooling circuits, the circular tubes are the

HE11 waveguides and the last component is the RF compatible isolation valve which is placed outside the vacuum. The principle of remote steering is that beams steered under an angle through the middle of the square waveguide entrance will exit the waveguide under the same angle but with opposite sign. This scheme has the advantage that the steering mechanisms for the beams are located far from the plasma (~7 meters) and placed in secondary vacuum just outside the first tritium containment.

The present FS launcher design is shown in Fig. 2. The launcher consists of 8 waveguides entering into the port plug. All 8 beams (up to 2.0 MW per beam) are reflected by one single focusing mirror down to two steering mirrors. The design was made to allow a very large beam spot size on both the focusing (65mm) and steering (50mm) mirrors so that the beams can be focused to a small spot size (~20mm) far away in the plasma (~1.6m from the steering mirror). As a result, the related profiles of driven current,  $j_{\text{ECCD}}(r)$  are relatively narrow satisfying the physics NTM requirements ( $\eta_{\text{NTM-FS}} \geq 1.7$  for all surfaces, where  $\eta_{\text{NTM}} = j_{\text{ECCD}}/j_{\text{bs}}$  with  $j_{\text{ECCD}}$  the maximum of  $j_{\text{ECCD}}(r)$  and  $j_{\text{bs}}$  the bootstrap current density). The steering range can be increased beyond the range determined for just NTM stabilisation to cover a wider scope of physics applications such as control of the sawteeth and edge localised modes (ELMs).

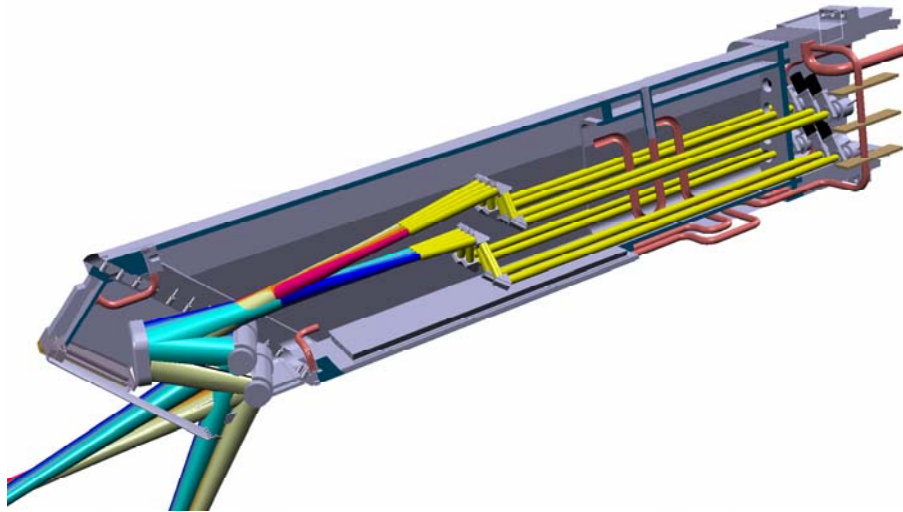


Fig. 2: FS launcher injecting eight 2.0 MW microwave beams into the plasma.

In a design revision meeting with the ITER-IT, it was concluded on the basis of the documentation and analysis of objective performance criteria and critical design issues, that there exist various open issues of major importance with respect to the engineering sufficiency of the upper ECRH launcher. These are the front steering units for the FS launcher that have moving parts close to the plasma and major fatigue issues on these elastically moving parts. For the RS launcher, there are only fixed mirrors close to the plasma. However, they have to stand substantial heat loads ( $\approx 5 \text{ MW/m}^2$ ) and consequently, critical fatigue issues on the mirror itself have to be considered.

As under the physics aspects, only the FS launcher meets the requirements with a comfortable margin for all scenarios, it was recommended that the emphasis on design work has therefore to be shifted towards the front steering design which was prepared to be assigned as the new reference launcher model. Further more, a dedicated engineering and testing phase is being initiated with the target of advancing towards the port-plug/launcher final design and the comprehensive definition of technical specifications to promote the preparatory stage for the launcher procurement.

## Design of the neutron shielding elements for the alternative model of a remote (RS) and a front (FS) steering launcher (Deliverable c.2)

Alternative designs of the mm-wave system for RS dogleg and FS launcher call for specific modifications of the structural components. In particular, the cut-out of the first wall panel, the size and positioning of front shielding elements inside the blanket shield module (BSM), the internal shield and the closure plate must allow the preferred arrangement of the waveguides and the mirrors for the specific mm-wave system. Figure 3 shows cutaways of the BSM area of the three launcher options and the distinct areas available for shielding elements.

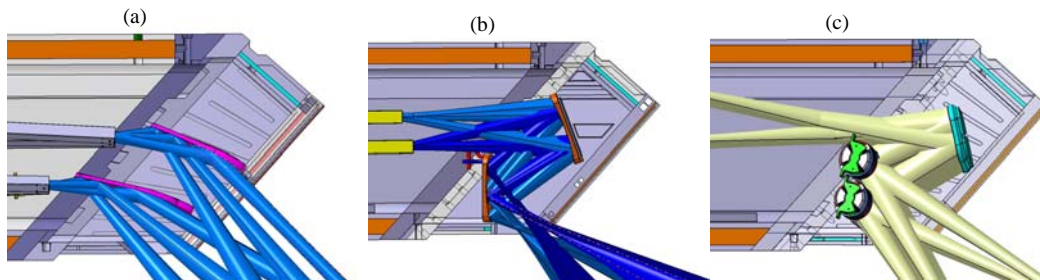


Fig. 3: Blanket shield module (BSM) structure for initial and advanced launcher concepts:  
a) Initial RS 3/8 Reference model,  
b) RS dogleg design,  
c) Front steering launcher

Considering the space conditions inside the BSM, the most important aspect is the clearance between the beams and the top side of the flanges. This area is necessary to house the feed tube for the FWP cooling circuit. The use of this area for beams or mm-wave components was avoided as this would imply a severe revision of the reference cooling concept for the BSM.

For the BSM, a once-through cooling flow is foreseen. Thus the shielding arrangement has to provide access for cooling connections to the FWP. To keep this readily manageable (as achieved for the RS 3/8 reference launcher), the minimum distance between the outer beam contour and the rear flange is set to 150 mm.

For the RS dogleg launcher, the current BSM-shielding design uses up to 3 shielding elements (see. Fig. 4), named according to their position inside the BSM as

- shield block top (1)
- shield block bottom (2)
- shield block wall (3)

All shielding elements are fixed inside the BSM. Disassembly of the BSM requires remote handling (RH) tools for cutting of two cooling tubes. The small shield block behind the FWP is only considered as an optional component. The actual nuclear analysis gives clear indications that this element could be omitted.

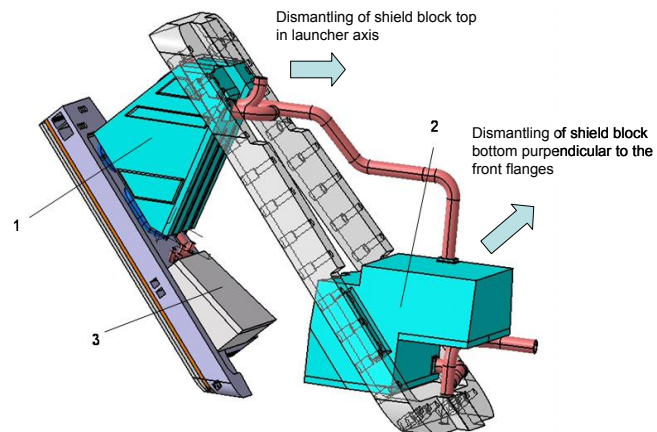


Fig. 4: Shield blocks top (1), bottom (2), wall (3; optional) of the RS dogleg launcher.

For the FS launcher, the shielding elements of the RS concept cannot be used because of the essentially different microwave beam configuration. Therefore, readjusted shielding elements were designed to comply with the available space, once-through-cooling flow concept,



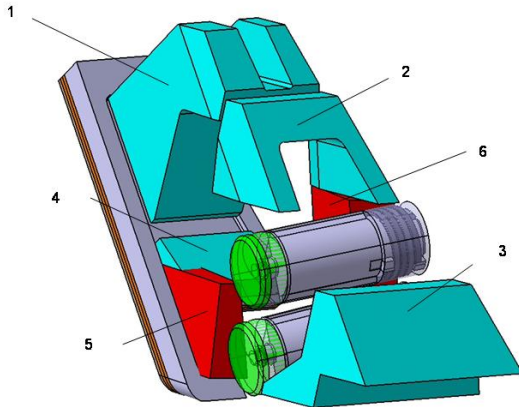


Fig. 5: Preliminary design of shielding elements for the FS launcher: Shield blocks top (1), bottom (2), wall (3), additional blocks required for the steering mechanism of the mirrors)

FS mirror components and shielding capacity. As design and integration of steering mirrors is still ongoing, the design of shielding elements had to left at a preliminary state, confined to outer contours to provide nuclear analysis (Fig. 5). It comprises three removable shielding blocks following the same terminology as for the RS concept. Furthermore, integral shielding elements were set at the rear side of the first wall panel and at the bottom area of the BSM integrated into the lateral walls. These elements provide additional shielding as required by the steering mechanism of the mirrors. Integration of the internal shields into the cooling scheme of the BSM is conceivable but has to await a more specific definition of the microwave beam paths.

The concept of a tank design for the internal shield is straightforward for the RS dogleg launcher, but requires to respect some limitations in terms of waveguide configuration to keep the advantages from the engineering view. Minimum distance between the waveguides and the inner wall of the launcher is 40mm to maintain a proper design with an outer shell and individual pressure tubes, only welded at the front and the rear side of the shield block. For the FS launcher with its essentially different waveguide arrangement at the location of the internal shield, the tank design concept has to be modified by breaking up the integral tank into two individual components in the front and the back of the mitre bend area.

### **Outline design of the neutron shielding elements for the Launcher, including the shielding blanket modules (Deliverable b.3)**

Nuclear analyses were performed for the RS dogleg and FS launcher designs. The results of the analyses proof conformity with all nuclear shielding criteria for both designs. Calculations were performed along the general lines for neutronic analysis using 3D MCNP models which are based on the shield elements designed for the dogleg type of the RS launcher and for the blanket shield module described in detail for the FS design. The selection of nuclear criteria was based on the ITER Nuclear Analysis Report and the particularities of special materials (such as CVD diamond) used in the ECRH launcher under ITER radiation conditions (Table.1).

Shutdown dose rate calculations were performed for the initial reference RS design. From these, it could be extrapolated that the essentially reduced neutron flux both for the RS dogleg and the FS designs results in less activation of rear-side materials and lower values of shutdown dose rates. Analyses of the nuclear responses in the Toroidal Field Coil (TFC) near the ECRH launcher permit to conclude that the radiation design limits for the superconducting magnets are satisfied for all considered ECRH RS and FS models. Thus all radiation design limits can be safely met by the RS, included dog-leg, and FS ECRH launcher design concepts.

The temperature distribution of the blanket shield module housing (BSMH) caused by nuclear heating and plasma radiation has been investigated for the initial RS reference launcher. Based on the resulting temperature field, the mechanical stresses of the BSMH were calculated. The analyses have been done with either the full modelling the BSMH under constant loading, steady state solution or with the slice model which represents a section of the BSMH for studying the case of transient loading. It was proven that during the typical

ITER burn cycles, no critical stresses have to be expected in the BSMH. The stress values occurring for the transient loads are lower in all material zones than the peak values reached in the static analyses with the full model and also significantly lower than the tolerable stress limits.

Table 1: Nuclear sufficiency criteria analysed with the adapted shield elements for the front steering (FS) and the dogleg remote steering (RS) launcher

Criterion	Definition of the nuclear sufficiency criterion	Max. Value in FS design	Max. Value in RS design	Max. Value of general design limit	Depend. on fusion power
1	Dose rate behind the CVD diamond window is below 100 microSv/hr after 10 days of shutdown	Less than 15 microSv/hr	Less than 15 microSv/hr	100 microSv/hr	Non-linear
2	Fast neutron fluence at the CVD diamond window kept below $10^{20} \text{ m}^{-2}$ (0.5 fpy)	$\sim 10^{17} \text{ m}^{-2}$	Less than $2 \cdot 10^{19} \text{ m}^{-2}$	$10^{20} \text{ m}^{-2}$	Linear
3	Helium production in the joining areas of the vacuum vessel is below 1.0 appm (0.5 fpy)	0.12 appm	0.15 appm	1.0 appm	Linear
4	Compatibility with conservative limit for nuclear heating of $10^{-3} \text{ MW/m}^3$ at the outer housing of the vacuum vessel	$2 \cdot 10^{-4} \text{ MW/m}^3$	$3 \cdot 10^{-4} \text{ MW/m}^3$	$10^{-3} \text{ MW/m}^3$	Linear
5	Nuclear response in the structures of superconductive magnets of TFC near the launcher in accordance with ITER requirements, in particular fast neutron fluence in isolator is below $5 \cdot 10^{21} \text{ n/m}^2$ (0.5 fpy)	$1 \cdot 10^{20} \text{ n/m}^2$	$1 \cdot 10^{20} \text{ n/m}^2$	$5 \cdot 10^{21} \text{ n/m}^2$	Linear
6	Nuclear heating density in the vacuum vessel kept below $\sim 0.3 \text{ MW/m}^3$	Near the launcher: $5 \cdot 10^{-2} \text{ MW/m}^3$	Near the launcher: $5 \cdot 10^{-2} \text{ MW/m}^3$	$0.3 \text{ MW/m}^3$	Linear

#### **Adaptation of cooling scheme for the launcher internals to the specific mm-wave configuration for the RS and FS launcher models (Deliverable c.4)**

Coolant routing and channelling were established for the BSM components of the RS dogleg launcher. The main design guide lines for the launcher cooling system are to use regular ITER blanket cooling water supplied by the PHTS-BLK system of 100°C/148°C inlet/outlet temperature at 3 MPa, including baking capability. Remote handling should be possible. Hence, a once-through cooling scheme has been chosen mainly in order to minimise the number of RH cooling connections between the BSM and the main launcher structure and because of narrow space in the BSM to accommodate extra piping to the mirrors. In general, there is a single stream of water flowing through the individual BSM components, i.e., front panel, BSM double wall, shield block top, first set of front mirrors, shield block bottom and the second set of mirrors. In some sections the flow is split into several parallel branches. The thermal-hydraulics performance of these components (except for the mirrors) was evaluated, and it was concluded that the goals in terms of overall temperature rise and pressure loss can be achieved. An separate mirror cooling system alternative to the once-through cooling scheme has been briefly studied but proved to be impractical. So the missing in-vessel temperature and flow control of vulnerable components like mirrors and front panel have to be tolerated with the cooling concept presented. Also the fact that, for instance, a single mirror failure would require launcher replacement/repair is a serious drawback. The problem of contact between copper-alloy and blanket cooling water in the mirrors can be tolerated because of the small surfaces involved. The thermal load on the retracted edge of the beam cut-out in

the BSM housing needs quantification from the physics side. Overall, cooling of the RS dog-leg launcher option is uncritical from the design point of view (when excluding the mirrors), but is delicate with respect to reliability/availability. For the FS launcher the issue appears to be relaxed with respect to flow control and temperature monitoring at the steering mirrors due to the separate cooling loops, while other integration issues remain open until a firm design is available.

### **Conceptual design of the port plug (Boundary conditions and interfaces; maintenance and testing/hot cell) (Deliverable c.5)**

In the preparation of the launcher design review for setting the priority between the RS dog-leg and FS launcher, the critical design issues of structural integration for the ECRH launcher variants were assessed. A total of 10 issues were identified, mainly concerning the blanket shield module design and cooling, and the launcher main structure and internal shield. A key achievement of the integration engineering was the proof that structural design issues are essentially generic for the current variants in the RS and FS launcher systems, under the condition of dedicated design adaptations in specific components, such as the coolant routing, blanket shield module, and internal shield.

The work for this deliverable covered the definition of the boundary conditions towards the neighbouring regular blanket modules, vacuum interfaces, remote handling needs, shielding requirements, and the integration into the ITER primary heat transfer system. A particular focus was in the field of launcher fabrication, assembly, and maintenance in the hot cell. With respect to remote handling needs, a number of issues were identified, based on the partly revised and supplemented design features of the RS dogleg and the FS variant. The launcher main structure with the double-wall is unchanged relative to the reference launcher, thus cooling and baking are kept straightforward. Axial assembly - disassembly of launcher internals could be maintained for both RS dogleg and FS. Also the BSM fixation to the main launcher structure by bolts is unchanged; keys at the interface between the BSM flange and the counter flange provide alignment and take up shear forces. Typical maximum temperature in the flange and bolts is about 200°C. Removal of the BSM in the hot cell requires special tools for cutting/welding of the secure welds, for handling lock caps, and for torque-controlled bolting at limited space conditions. To take off the BSM, two tubes with about 34 mm outer diameter have to be remotely cut from inside the tubes by special tools. Thus for a reassembly, firm alignment and welding must be secured, necessarily from inside the tubes. The required tools are not readily available and the whole technique must be developed in cooperation with RH experts, since a similar concept is envisaged for the ITER blankets. The internal shield is supported and aligned by means of a dovetail profile, to minimise machining of fitting surfaces. Axial fixation at the front side allows thermal expansion. Dedicated devices for handling and installation in the hot cell are required for an expected mass of 4.5 tons.

### **Outlook towards future design activities**

The very recent shift of the emphasis of the design work towards the front steering design could be made on the basis of evidence that the remaining open design issues, which have to be settled to comply with all engineering sufficiency criteria, do not contain any principle feasibility concerns with respect to structural integration. Actually, basic design work is underway with high priority to ensure that sufficient fatigue margins are present in the front steering mechanism. Further more, a dedicated engineering and testing phase is being initiated with the target of advancing towards the port-plug/launcher final design and the comprehensive definition of technical specifications to promote the preparatory stage for the launcher procurement.

The special challenge of the integration engineering is to develop the specific cooling and nuclear shielding design up to the level of detailed drawings for manufacturing. The integration of the front steering unit and its pneumatic driving elements and of the components of

the microwave system which have to handle extreme power levels of 2 MW in continuous wave (CW) operation has to be accomplished. The mechanical and hydraulic integration of the corresponding shield, consisting of blocks in the blanket shield module and the internal shield in the main structure, has to comply with the complex requirements for fixing a detailed design in terms of coolant routing, fixation and alignment of the structural and microwave components and the manufacturing technology fulfilling nuclear quality assurance criteria. A particularly important aspect is the definition, development and testing of remote handling tools for bolting, cutting/welding and gripping of shield components and supplying tubes.

#### Staff:

Y. Chen  
I. Danilov  
U. Fischer  
G. Hailfinger  
R. Heidinger  
K. Kleefeldt  
M. Lux  
A. Meier  
A. Serikov  
P. Späh  
H. Tsige-Tamirat

#### Literature:

- [1] R. Heidinger, M. Henderson, U. Fischer, G. Hailfinger, K. Kleefeldt, G. Saibene, A. Serikov, P. Spaeh, A.G.A. Verhoeven; Structural integration studies for the ITER ECRH Upper Launcher; Journal of Physics: Conference Series **25** (2005), pp. 66 -74
- [2] R. Heidinger, U. Fischer, G. Hailfinger, M. Henderson, K. Kleefeldt, G. Saibene, A. Serikov, P. Spaeh, A.G.A. Verhoeven; Structural integration of the EC wave launcher at the ITER upper port plug; Dig. Joint 30th International Conference on Infrared and Millimeter Waves and 13th International Conference on Terahertz Electronics, September 19-23, 2005, Williamsburg (USA)
- [3] A. Serikov, U. Fischer, Y. Chen, K. Lang, R. Heidinger, Y. Luo, E. Stratmanns, H. Tsige-Tamirat; Neutronics analysis of the ECW launching system in the ITER upper port; Fusion Engineering and Design, **74** (2005), pp. 229-235
- [4] A. Serikov, U. Fischer, R. Heidinger, K. Lang, Y. Luo, H. Tsige-Tamirat; Radiation shielding analyses for the ECRH launcher in the ITER upper port; Journal of Physics: Conference Series **25** (2005), pp. 181 -188
- [5] H. Zohm, R. Heidinger, M. Henderson, E. Poli, G. Ramponi, G. Saibene, A.G.A. Verhoeven; Comparison of the performance of different options for the ITER ECRH Upper Launcher; Journal of Physics: Conference Series **25** (2005), pp. 234 -242
- [6] A.G.A. Verhoeven, W.A. Bongers, A. Bruschi, S. Cirant, I. Danilov, B.S.Q. Elzendoorn, J.W. Genuit, M.F. Graswinckel, R. Heidinger, W. Kasperek, K. Kleefeldt, O.G. Kruijt, S. Nowak, B. Piosczyk, B. Plaum, T.C. Plomp, D.M.S. Ronden, H. Zohm; Design of the mm-wave system of the ECRH upper launcher for ITER; Fusion Engineering and Design, **74** (2005), pp. 431-435
- [7] M.A. Henderson, R. Chavan, R. Heidinger, P. Nikkola, G. Ramponi, G. Saibene, F. Sanchez, O.Sauter, A. Serikov, H. Shidara, H. Zohm; The Front Steering Launcher Design for the ITER ECRH Upper Port; Journal of Physics: Conference Series **25** (2005), pp. 143 -150

## **TW4-TPDC-IRR CER**

### **Irradiation Effects in Ceramics for Heating and Current Drive, and Diagnostics Systems**

#### **Objectives**

The overall objective of this task is to provide the required irradiation testing and screening of small prototype components and the necessary insulator research and database for heating and current drive, and diagnostic systems for ITER. Especially for EC components, work was carried out to assess the effect of tritium on the optical and dielectric (loss) properties of CVD diamond for ECRH applications. To reduce cost, it was decided that deuterium rather than tritium will be employed. An important aspect is the influence of radiation on the permeation effect. Thus, diamond specimens are also considered to be exposed to deuterium under electron irradiation for radiation enhanced diffusion including also specimens with significant structural damage (typically  $10^{-4}$  dpa).

#### **Effects of hydrogen isotopes on the dielectric loss and thermal conductivity for CVD diamond ECRH/ECE applications (Deliverable 13)**

Preceding the present task period, two large area CVD diamond windows of a window size suited for high power Electron Cyclotron (EC) wave transmission lines were exposed to deuterium in a permeation test facility at FZK. The window units differed in the joining of the diamond disks (108 mm dia.) to the metallic structure of the window cuff:

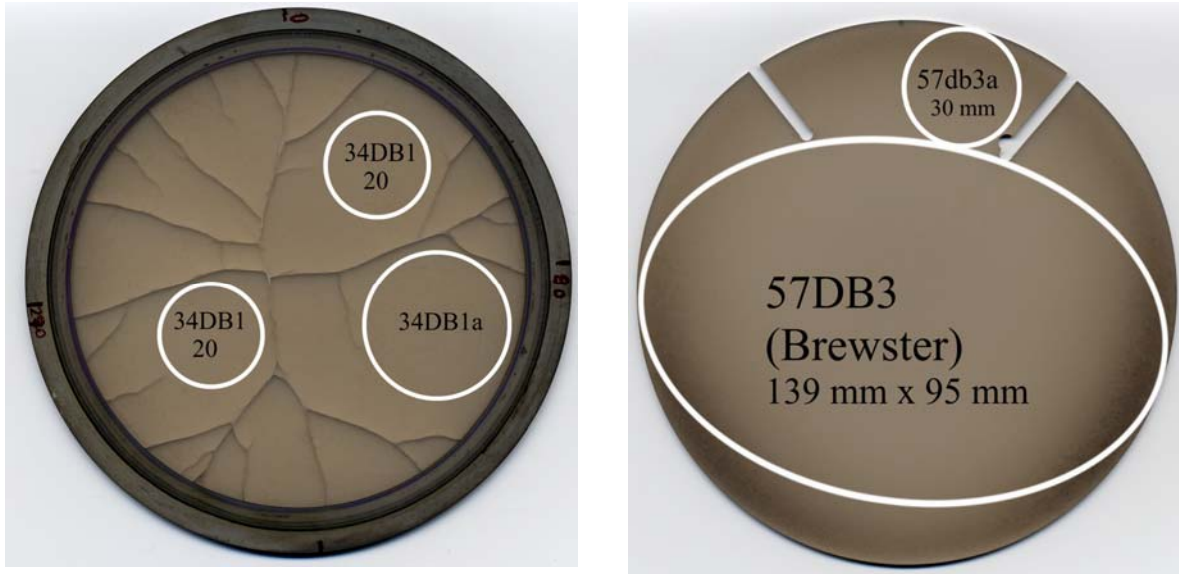
a) 34DB1: Al-braze to Inconel; b) 36DB1: Ag-braze to copper

For both CVD window units, no evidence for  $D_2$  permeation through the diamond disk was found [1]. Dielectric measurements in the disk 34DB1 showed the building-up of a surface loss which was in the order of 5 times the bulk loss. Similar values were observed for this disk during the brazing process, and are typical for surface loss induced by carbon contaminants which become conductive by protonic 'activation'. These states which were believed to be fully removed by an oxidising chemical treatment were apparently re-activated by the exposure to deuterium. The disk 34DB1 failed after a second welding of the inconel cuff to the test flange apparently because of the internal stress formed by the non axially symmetric temperature profile in the cuff.

In the preparatory stage of this deliverable, it was decided that the specimens originally foreseen to investigate the role of ionising and structural radiation damage on deuterium diffusion, and consequently on surface and bulk absorption of CVD diamond, should be reserved for a later stage of the studies to be performed at the deuterium diffusion/permeation test facility at CIEMAT. Instead, specimens for dielectric, thermal conductivity and optical measurements were cut from the fractured disk 34DB1 after removal of the Al-braze by NaOH (see Fig. 1a). Dielectric measurements of the 30 mm disk (34DB1) showed that the NaOH treatment had essentially eliminated the absorptive surface states and therefore the disks were given a final chemical treatment by hot oxidising acid ( $H_2SO_4$  with in situ addition of  $NaNO_3$ ). Indeed, the dielectric was typical for bulk absorption in regular low loss CVD diamond grades (see Table 1). The 20 mm disks are suited for optical and thermal conductivity measurements, but not for dielectric loss measurements, because of substantial mm-wave diffraction loss at edges of the small disks.

It turned out that the operation of the test facility at CIEMAT required substantial modifications. In particular, the deuterium sensing system (leak detector) had to be changed for one with much higher sensitivity. For irradiations of the specimens in the deuterium permeation test chamber, the request for shielding has become far more critical extending the testing procedure of the installation. Given the lack of deuterium exposed specimens, another dielectric test specimen was prepared from an up-scaled CVD diamond grade grown to a diameter of 140 mm. In this grade, two cracks formed at the outer edges in the growth process, which were isolated by two laser cuts to preserve the adequate area for an elliptical disc

to be used as a Brewster window for multifrequency gyrotrons (see Figure. 1 right). Close to one of cracks, a 30 mm disk could be cut which showed essentially higher bulk loss. The effect of deuterium on bulk dielectric loss may potentially vary with the microstructure, for which the two different grades will represent different types.



108 mm disk: 34DB1

140 mm disk: 57DB3

Fig. 1: Cutting scheme of the specimens prepared by laser cutting for the exploratory diffusion studies at the CIEMAT permeation test facilities (view to the growth face):

Left: Diamond specimens prepared out of CVD diamond window 34DB1

Right: Diamond specimen 57DB3a prepared from the edge part of the large area disk 57DB3 (140 mm diameter) after cutting of the elliptical Brewster window for a broadband window in multifrequency gyrotrons

In conclusion, two characteristic CVD diamond grades were prepared to obtain basic indications on the effects of hydrogen isotopes on the dielectric loss for CVD diamond ECRH/ECE applications. The dielectric measurements on this first specimen set will be performed in the first quarter of 2006 according to the present progress at the CIEMAT diffusion/permeation test facility. Thermal conductivity will follow at a second stage while the study of CVD diamond with radiation induced structural damage will need to await the completion of the exploratory study.

Table 1: CVD diamond specimens prepared for the deuterium diffusion/permeation experiments at CIEMAT with dielectric loss determined for the 30 mm disks.

Specimen code	Original disk	Geometry	Measured loss (140 GHz)	Measured loss (90 GHz)
34DB1a	34DB1	30mm dia x 1.81mm	$1.2 (\pm 0.2) \times 10^{-5}$ (effective)	$1.2 (\pm 0.1) \times 10^{-5}$ (GF) $1.5 (\pm 0.2) \times 10^{-5}$ (NF)
34DB1_20b	34DB1	20mm dia x 1.81mm	n/a	n/a
34DB1_20c	34DB1	20mm dia x 1.81mm	n/a	n/a
57DB3a	57DB3	30mm dia x 1.70mm	$3.6 (\pm 0.2) \times 10^{-5}$ (effective)	$2.0 (\pm 0.2) \times 10^{-5}$ (GF) $3.1 (\pm 0.3) \times 10^{-5}$ (NF)

Staff:

I. Danilov  
R. Heidinger  
A. Meier  
M. Rohde  
P. Lukits

Literature:

- [1] R. Heidinger, A. Meier, J. Burbach, Deuterium permeation studies through CVD diamond window structures, Proc. 17th Joint Russian-German STC Workshop on ECRH and Gyrotrons, Greifswald, May 30 - June 4, 2005.





## **Vessel/In-Vessel**



## TW5-TVV-EBWO Demonstration of Overhead E-Beam Welding

Deep penetration electron beam (EB) welding is an advanced welding method for the joining problem of the vacuum vessel (VV) required for the ITER project. This technique can yield fewer passes (compared to TIG welding) and less distortion. On the other hand, one-path welding of stainless steel plates with a thickness of approximately 60 mm in all positions will lead to a drop-out of the melt, at least in overhead position. This can only be avoided with the aid of a melt support system. The objective of this task is the design and test of an adequate electromagnetic system.

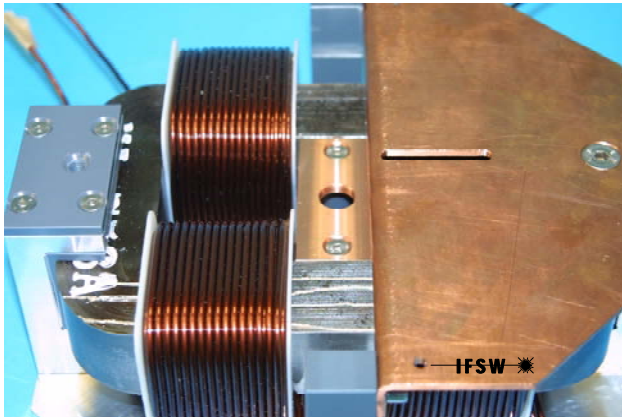


Fig. 1: Electro magnet for overhead welding,  $B \approx 0.74$  T (amplitude) @ 800 Hz, dimensions: 200 x 230 x 90 mm<sup>3</sup>, weight: approx. 20 kg.

The principal functionality of such a system (Fig. 1) was already demonstrated in a previous project<sup>1</sup>. In that project, the system was tested during laser welding of aluminium. During those experiments with a 4 kW Nd:YAG laser, a magnetic field strength of  $B_0 = 0.26$  T and a frequency  $f_0 = 779$  Hz a pressure of  $p_M = 2$  kPa was created.

As a first step towards the demonstration of overhead e-beam welding of 60 mm stainless steel, new experiments with a modified setup were performed within this task. An aluminium container filled with liquid PbSn was welded (Fig. 2). A pressure of 4 kPa, generated by the liquid aluminium melted during welding and

by the liquid PbSn in the container, could be compensated by the applied magnet system. This is exactly the pressure necessary during welding of 60 mm steel in overhead position.

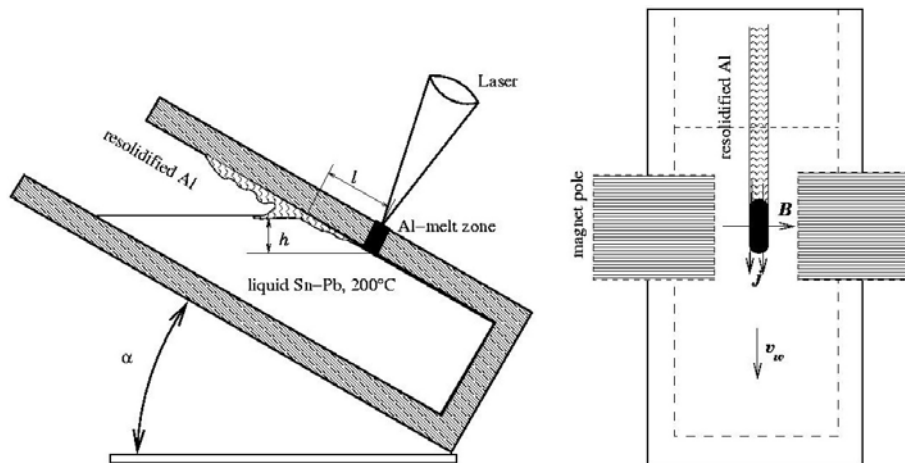


Fig. 2: Scheme of the test welding.

<sup>1</sup> Avilov, V. V.; Berger, P.; Ambrosy, G.: Simulation of weld-pool support system for power beam welding of VV sector welds. January, 29th 2003. Task TW1-TVV/WELDSP (Contract 01584).

In a second step, the system was prepared for welding of steel. Due to the different electrical conductivity of steel compared with aluminium, the frequency of the system had to be changed (Fig. 3). Therefore, new windings had to be manufactured and a new capacitor bank and a new power generator had to be implemented.

The functionality of this system again was tested with laser beam welding. As laser source a 15 kW CO<sub>2</sub> laser of Trumpf company in Ditzingen was used. The welding parameters and the parameters of the weld support system are given in Table 1 and the set-up is shown in Fig. 4. Welding without the support system led to severe undercut (Fig. 5, reference). With the aid of the electromagnetic device located below the specimen the melt could be kept in the gap. A very stable weld bead could be obtained on both sides of the workpiece.

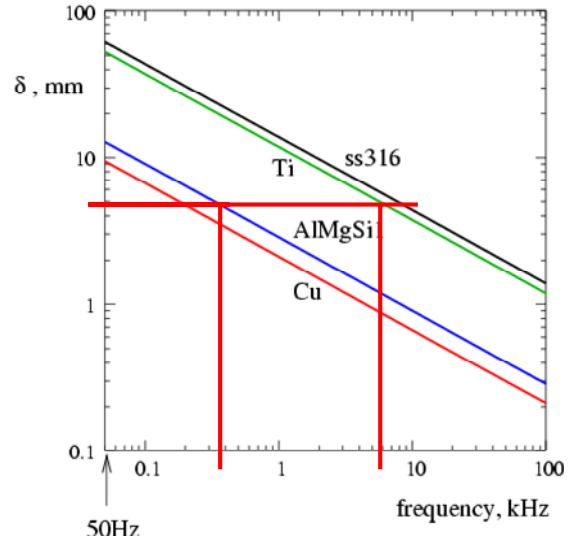


Fig. 3: Penetration depth of a magnetic field in a workpiece in dependence of the workpiece material and the applied frequency of the magnet.

Table 1: Characteristics of the test laser beam welding.

Welded material	Stainless steel 324
Plate thickness	$h_0 = 18 \text{ mm}$
Hydrostatic pressure	$p_h = 1.3 \text{ kPa}$
Laser power	$P_L = 15 \text{ kW}$
Welding speed	$v_w = 0.8 \text{ m/min}$
Basic oscillation frequency	$f_0 = 3.2 \text{ kHz}$
Applied magnetic field (amplitude)	$B_0 = 0.2 \text{ T}$
Width of magnet poles	$z_m = 25 \text{ mm}$
Gap between magnet poles	$d_m = 20 \text{ mm}$
Skin depth in cold metal	$\delta_c = 7.7 \text{ mm}$
Penetration depth for EM forces	$\delta_c/2 = 3.8 \text{ mm}$
EM pressure in the weld pool	$p_{EM} \approx p_h$

Actually, the pulsed operation mode necessary for e-beam welding has been designed. The components are being tested now for compatibility with the e-beam system.

In the time coming the pulsed operation mode has to be established (high current switches have to be used) in order to provide a 100 Hz alternating operation of the e-beam and magnet, a special pulse shape and shielding device has to be developed and tested to guarantee demagnetisation after each pulse

and finally tests with an e-beam will be performed, as already planned.

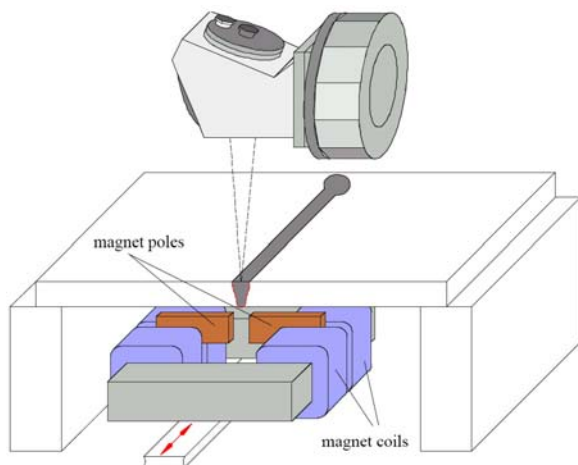


Fig. 4: Schematic view and photo of the CO<sub>2</sub> laser beam welding with EM weld-pool support. Both the magnetic field and the electric current in the welded material are directed parallel to the surface.

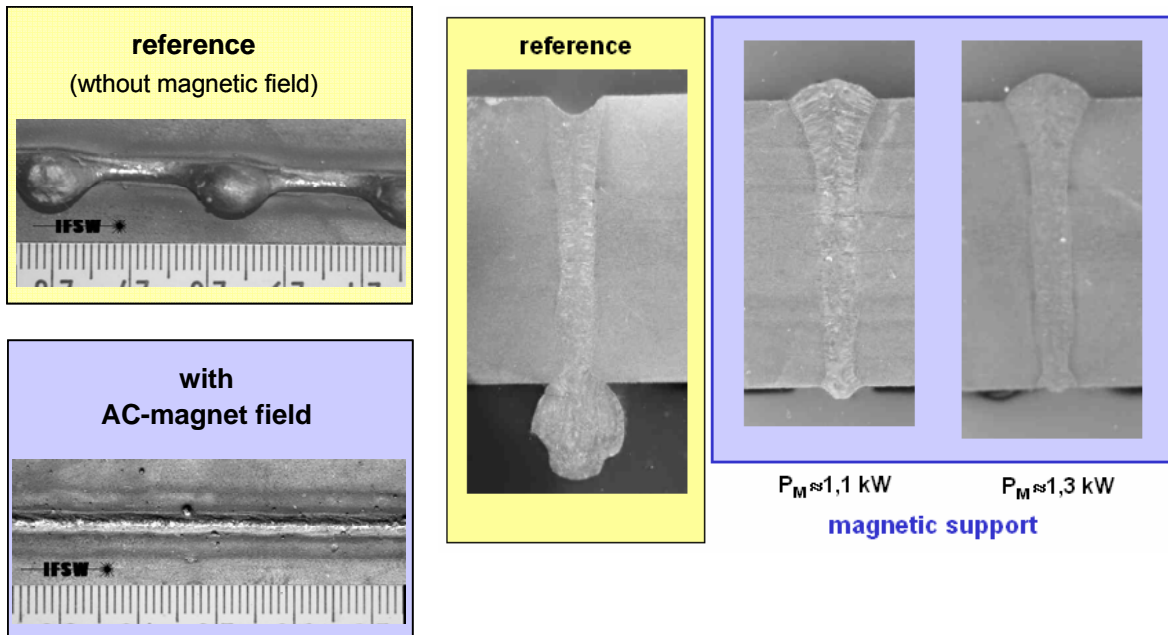


Fig. 5: Left: Photos of the rear side of the welds obtained without and with the EM weld-pool support. Right: Cross-sections of the same welds. The net AC magnet supply power of about 1.3 kW is enough for full compensation of the hydrostatic pressure in the weld pool (for parameters see Table 1).

#### Staff:

V. Avilov  
P. Berger  
G. Ambrosy  
T. Graf

#### Literature:

- [1] Avilov, V. V.; Ambrosy, G.; Berger, P.: MHD melt control systems for high-power beam welding of metals. In: Proc. Joint 15<sup>th</sup> Riga and 6<sup>th</sup> PAMIR International Conference on Fundamental and Applied MHD, June, 27<sup>th</sup> – July, 1<sup>st</sup>, 2005, Riga, Latvia, V. 2, S. 249 – 252.
- [2] Berger, P.; Avilov, V. V.; Ambrosy, G.: EM-supported, power-beam overhead welding. 6th ITER Vacuum Vessel Manufacture Design and Assembly – EU R&D Meeting, Magdeburg, Saxony-Anhalt, Germany, 4-6 October, 2005.



## **Magnet Structure and Integration**





## EFDA/03-1105

### Cryogenic Laboratory Tests for V-I Characterisation of Subcable Samples

#### Objectives

The main objective of this work is to perform measurements of the V-I (voltage versus current) characteristics of Nb<sub>3</sub>Sn sub-size (>30 strands) CICC (cable-in-conduit conductors) under applied longitudinal strain in liquid He (T = 4.2K) and high magnetic fields (up to B = 14T).

Emphasis shall be put on the measurement of the thermal pre-strain of the strands. To this end the experimental set-up shall be capable of performing accurate measurements of specimens having in particular different conduit materials, thickness, cables sizes and void fractions. The strain applied to the strand shall be typically up to  $\approx 1.5\%$ . The instrumentation sensitivity is planned to allow measurements of critical electric fields as low as  $E=10 \mu\text{V/m}$  with a sensitivity better than  $1 \mu\text{V/m}$ .

After the experimental set-up has been completed, instrumented and accurately calibrated, specimen testing shall be started. All specimens (not heat treated) will be made available by EFDA. In total, during the contract period, about 25 specimens shall be tested.

#### Test Facility

In the late 1985's the *FBI*-facility was established at the Forschungszentrum Karlsruhe to investigate the influence of applied longitudinal strain ( $F$ ) and magnetic field ( $B$ ) on the critical current ( $I_c$ ) at liquid helium temperature. The facility contains two separate experimental set-ups to cover tests on single superconducting strands and also on CICC.

With the ongoing development of different strand types (e.g. bronze route, internal tin or powder in tube) and cable layout, the facility could meet the requirements, so far. However, this old experimental setup that was used until the year 2000 was not modern in its art any more and had to be modernized in several aspects.

Within the framework of the European Fusion Technology Program, the facility was upgraded in the past two years and is now under use for performance tests of advanced single strands and CICC developed for ITER.

The measurement method in general used by the *FBI*-facility to examine the critical current  $I_c$  depending on applied tensile strain  $\epsilon_{\text{applied}}$  and magnetic field  $B$  is the same for single strands and CICC differing only in dimension of the sample and mounting procedure.

#### Results

##### *Results on single jacketed Nb<sub>3</sub>Sn composite strands*

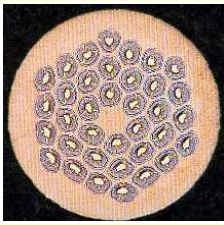
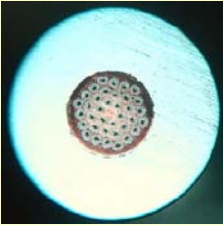
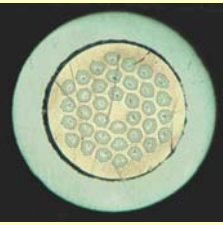
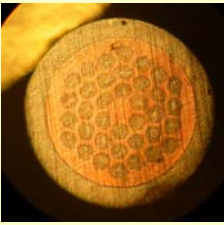
Comparing the critical current density and its strain dependence of a single strand with a larger CICC sample containing the same strand a discrepancy is apparent. This effect was seen in several experiments in the past. The  $I_c(\epsilon_{\text{applied}})$  dependence is shifted to higher strain values to reach the maximum critical current. This effect seems to be mainly influenced by the material's thermal expansion properties and the volume fraction used for the outer conduit. Additionally, the achievable  $I_c$  is well below the expected value scaled with the number of strands. However, the explanation turned out to be very complex and a series of issues have to be taken into account. Starting with the  $I_c(B, \epsilon_{\text{applied}})$  parameters of the single strand the manufacture process alters these parameters of the CICC obviously. At the beginning the strand has to be cabled in packages containing three or more single strands (e.g. several stages of twisted triplets or braids). The packages are then put into a steel tube for mechani-

cal stabilization (e.g. 316LN, Incoloy 908 or titanium) and are compacted to a given void fraction between 20 to 40% inside the conductor. In the last step the conductor has to be heat treated to form the superconducting Nb<sub>3</sub>Sn phase. While cooling down from the highest aging temperature of about 920 K to the operation temperature of 4.2 K the influence of the thermal expansion depending on the used tube material plays an important role. With all this different manufacturing steps it is impossible to distinguish the influence between each step on the parameters from single strand to the final CICC.

To tackle this problem in a systematical way several sub-stage samples are made comparable to the different stages of the manufacturing process. First of all the single strand alone is examined, following the single strand jacketed in a steel tube, giving answer to the effect of the steel tube on the parameters  $I_c(B, \epsilon_{\text{applied}})$ . The next sub-stage samples contain the different stages of the cabling pattern used for the final CICC.

Within this task first tests were accomplished to reach a suitable method for jacketed single strands by ENEA (Frascati / Italy). Single Nb<sub>3</sub>Sn strands coming from Europa-Metali LMI were jacketed into 316LN steel tubes with different jacket thicknesses. In Table 1 the different jacket dimensions of the strands are given. Before starting the heat treatment both ends of the prepared strands were clamped with the outer jacket to avoid a possible slipping of the inner strand. After the heat treatment the steel jacket at both ends was removed partially to allow a good electrical contact while tested in the single strand setup of the FBI-facility. The results of the magnetic field dependence on  $I_c$  can be found in Figure 1a and b.

Table 1: Parameter of jacketed Nb<sub>3</sub>Sn strands

			
Nb <sub>3</sub> Sn Bare EM LMI strand OD: 0.805 mm	$d_{\text{jacket}} \approx 0.6$ mm OD: 2.03 mm ID: 0.80 mm	$d_{\text{jacket}} \approx 0.2$ mm OD: 1.2 mm ID: 0.805 mm	$d_{\text{jacket}} \approx 0.1$ mm OD: 0.98 m ID: 0.78 mm

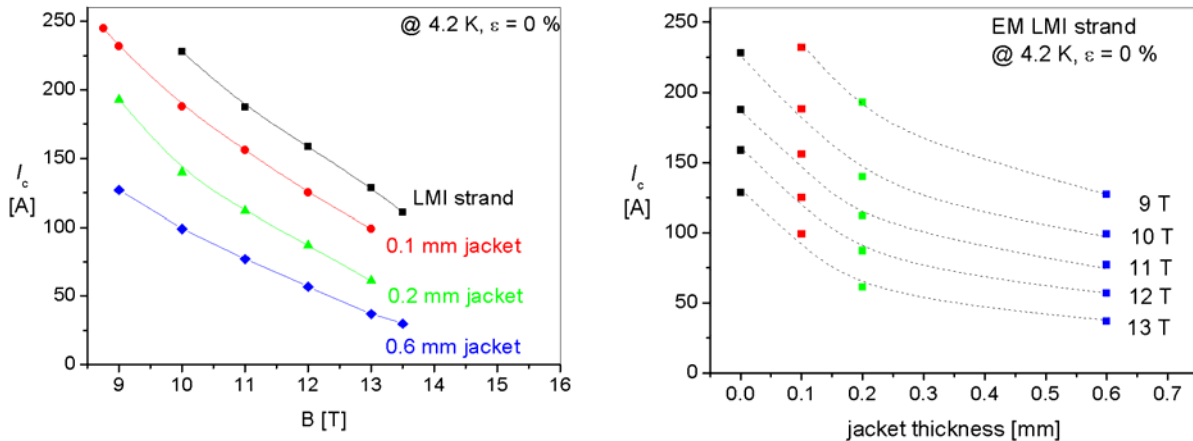


Fig. 1a / b: Magnetic field dependence of the critical current (a) and the effect of the jacket thickness (b).

As can be seen in Figure 1a the jacket thickness influences the  $I_c$  dependence significantly. Figure 1b illustrates this effect with rising jacket thickness. Starting with 0.1 to 0.2 mm thickness the drop of  $I_c$  is very pronounced. Going to higher jacket thickness the decrease of  $I_c$  gets less, because only steel is here the dominant material. This can be very well understood in the light of the compressive pre-strain due to the higher thermal contraction of the outer steel tube compared to the inner strand during cool down. With higher steel fraction the parabolic  $I_c(\epsilon_{\text{applied}})$  curve is shifted to higher strain values, resulting in a drop of  $I_c$  at zero strain. In Figure 2a the stress-strain results are given. The strand with 0.6 mm thick jacket is comparable to 316LN and the mechanical property of the strand inside is quite negligible. On the other side the 0.1 mm thick jacket shows a very small effect on the mechanical properties of the jacketed strand. In Figure 2b the  $I_c$  versus strain dependence at 13 T shows the sensibility of the electrical properties on the steel fraction. The bare strand without jacket gives a maximum  $I_c$  of 133 A ( $261.8 \text{ A/mm}^2$ ) at 0.135%. Adding a 0.1 mm jacket the  $I_c$  curve is shifted to a lower maximum current of 114 A ( $238.5 \text{ A/mm}^2$ ) at higher strain 0.267%. Presumably, the remaining 9% drop of the maximum achievable critical current density can be attributed to the internal radial stress components together with a degradation of the inner  $\text{Nb}_3\text{Sn}$  filaments (e.g. micro-cracks). However, the strain results of the 0.2 mm thick jacket had to be discarded due to a poor bonding of the steel jacket to the strand only the 0% value is shown. For the 0.6 mm thick jacket the maximum of the critical current could not be reached due to the limited maximum load of the setup.

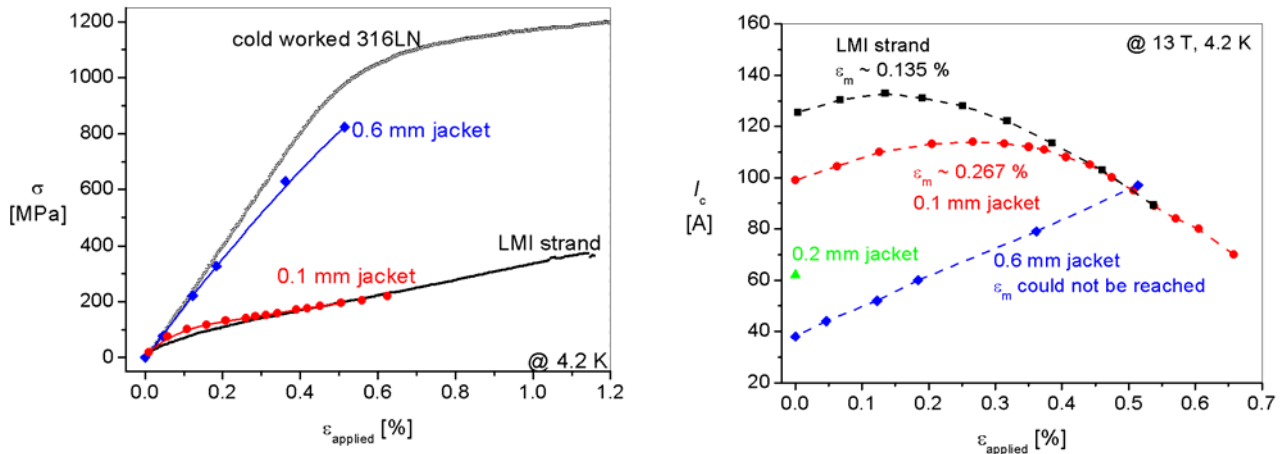


Fig. 2a / b: Stress-strain property of the jacketed strands (a). The strand with 0.2 mm thick jacket is missing because of improper bonding between jacket and strand. Strain dependence of the critical current for the different jacketed strands (b).

With the practice gathered from jacketing single strands, new jacketed single strands and sub-stage samples are prepared by ENEA Frascati/Italy and CEA Cadarache/France using advanced strands from OST in near future.

### $I_c(B)$ measurement of first sub-size 3x3x5 CICC sample

Subsequent to the upgrading of the single strand setup, the improvements were adopted for the CICC setup.

One set of a measurement on a sub-size cable (used in a task in 1997) was performed to proof the functionality of the adopted control and measurement procedure. This is examined successfully and in Figure 3a the stability of the signal versus rising current is shown. Following this, a V-I measurement was done at 12 T, first without applied strain and in a second step with an applied strain of 0.1%. In Figure 3b the V-I characteristic can be seen. At present the system works without any problem and the critical current using a  $0.1 \mu\text{V/cm}$  criterion can be measured.

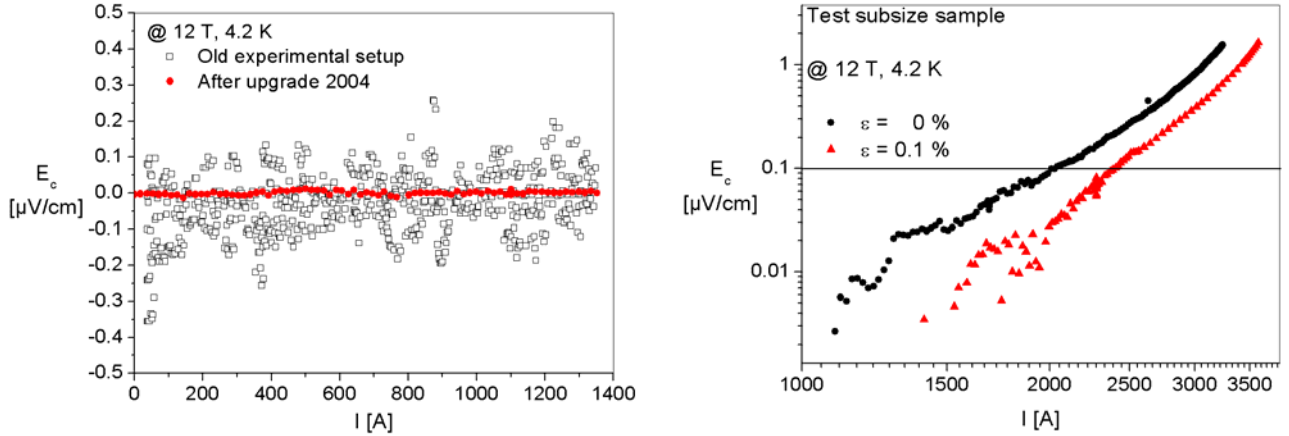


Fig. 3a / b: Scatter of the voltage versus current signal measured at a CICC cable (a). The open boxes indicate the typical level of noise using the old measurement electronics, the dots show the reduced noise due to the new adapted measurement electronic system and procedure. Logarithmic plot of the normalized electrical field (b). The line at 0.1 μV/cm indicates the critical current of the CICC sample at 12 T and 4.2 K. The closed circles gives the measurement at zero applied strain and the triangles with an applied strain of 0.1%.

Two prototype CICC sub-size samples were delivered by CEA-Cadarache, one with a 3x3 cabling pattern and a second with a 3x3x5 pattern (two superconducting strands + one Cu strand in the 1<sup>st</sup> triplet).

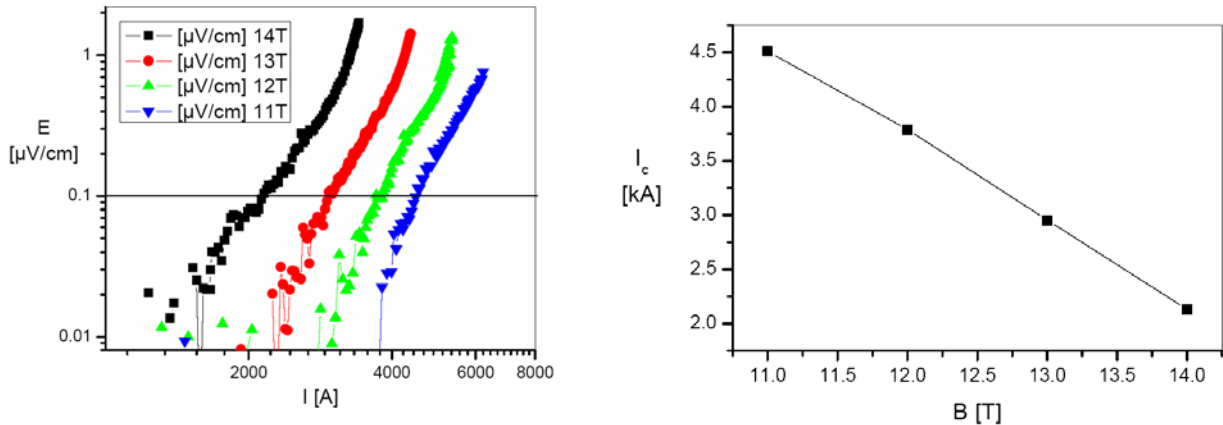


Fig. 4a: Raw data of measurement at various fields at 4.2 K. Fig. 4b: Resulting  $I_c(B)$  dependence from 14 T to 11 T at 4.2 K

Table 2: Summary of results

B [T]	$I_c$ [kA]	$n^*$
14	2.132	4.3
13	2.954	5.9
12	3.79	6.2
11	4.509	6.3

\*The  $n$ -value is the slope of  $E$  vs.  $I$  (fig. 4a) and was determined between 0.03 to 0.3 μV/cm

The larger 3x3x5 sample was used to perform a first set of measurements. After mounting the sample in the test facility and cool down to 4.2 K the V-I(B) dependence was measured starting at 14 T using a voltage tap distance of 5 cm. The current was ramped down to zero after exceeding 5 μV (1 μV/cm). No external force was applied to the sample. The magnetic field was stepwise reduced to 11 T. The raw data of the measurement are shown in Figure 4a. The resulting  $I_c(B)$  are given in Figure 4b and are summarized in Table 2. The measurements were all successful until reaching a magnetic field of 11 T. Here a quench of the sample occurred at an electrical field of 0.76 μV/cm and a maximum current of

6.2 kA. As can be seen in Figure 4a the reached value of the electrical field was still below the values reached during the measurements at higher magnetic fields.

### **Outlook**

After these successful tests a batch of 22 samples will be measured until 2006 varying cabling pattern, void fraction and twist pitch. With the collected data of the samples a systematic study can be done to investigate the effect of these parameters on cable performance.

### Staff:

K.-P. Weiss  
H. Kiesel

### Literature:

K.P. Weiss: "The FBI Facility - Critical Current Measurement of Nb<sub>3</sub>Sn Composite Strands and Cable-in-Conduit Conductors as a Function of Strain", MEM05 Workshop Kyoto, Japan, 18.-20. Juli 2005, to appear in Supercond.Sci.Techn.

## EFDA/05-1250 HTS Current Lead Operation with Liquid Nitrogen

### Introduction

In the frame of the European Fusion Technology Programme, Forschungszentrum Karlsruhe and Centre de Recherches en Physique des Plasmas (CRPP), Villigen/Switzerland have designed and built a 70 kA current lead (CL) for the ITER TF Coils using high temperature superconductors (HTS). At the beginning of 2004 the HTS current lead (Figure 1) was installed in the TOSKA facility of the Forschungszentrum Karlsruhe and thereafter successfully tested in the framework of an EFDA technology task (EFDA contracts 02-1013 and 02-1014) in 2004.

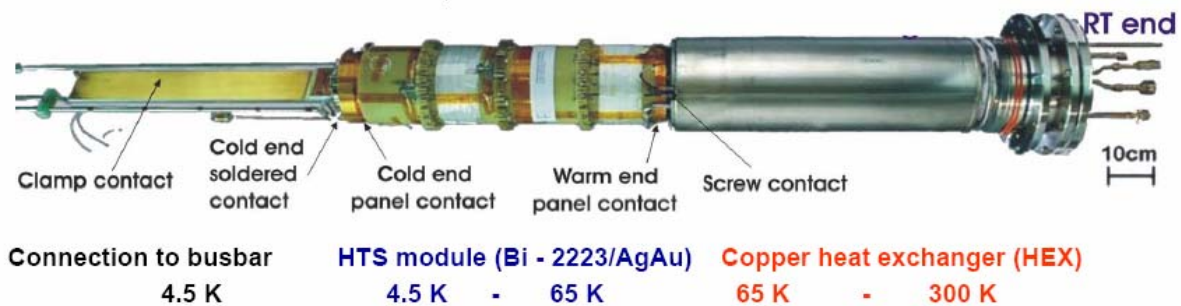


Fig. 1: HTS current lead consisting of three parts; left: connection to busbar; middle: HTS module; right: conventional heat exchanger

Before disassembly from TOSKA facility, Forschungszentrum Karlsruhe decided to perform another short test campaign of the 70 kA HTS CL in December 2004 to demonstrate an operation at a He inlet temperature of 80 K. This test confirmed the possibility of using the 80 K cooling circuit foreseen for the thermal shields of ITER. About 1% of the 80 K cooling power foreseen for ITER would already be sufficient to operate all HTS current leads leading to a significant reduction of the average power consumption for the current lead cooling.

The International Team asked about the possibility of using liquid nitrogen LN<sub>2</sub> as coolant for the HTS CL. Although this would imply modifications of the present ITER cryogenic system, the advantage of using an independent LN<sub>2</sub> cooling circuit for the current leads would be a significant improvement of the ability to tolerate a coolant circulation failure with the consequence of a much longer discharge time for the coils. In addition, it was proposed by Forschungszentrum Karlsruhe to investigate the possibility of an automatic regulation of the current lead operation parameters. In view of the large number of current leads in ITER a quasi-automatic regulation is necessary for an effective control of the ITER magnet system.

### Background

The first experiments from April to June 2004 focused on the operation of the current lead at standard conditions with  $T_{\text{He, in}}=50$  K He at the inlet of the heat exchanger (HEX). Such an operation could be performed without problems and was even extended to 80 kA. The temperature of the HTS module warm end was approx. 65 K during these experiments. After these excellent results the current lead was retested in December 2004 with an inlet temperature  $T_{\text{He, in}}=80$  K, neglecting that the CL was optimized for 50 K and 80 K was never planned. With a temperature of 85 K at the warm end of the HTS module the current lead was really at the edge but a stable operation at 68 kA was possible. The temperature variation along the current lead was as calculated during the design. The necessary He mass flow was 4.7 g/s for 50 K helium and 16 g/s for 80 K helium. The much higher flow rate at 80 K was necessary to keep the warm end temperature of the HTS module at 85 K. At zero current the heat flow of the HTS CL to the low temperature 4.5 K end is composed of 18.5 W background losses plus 13.5 W at 50 K or 20 W at 80 K operation. Loss of flow experiments

showed that at 50 K a current of 68 kA can be operated for more than 5 minutes after the flow was stopped. However, as has to be expected for an 80 K operation the time margin was with only 1.3 minutes not sufficient. These results demonstrate that the margin of the HTS CL is large when it is operated with 50 K helium cooling which was the design value. With 80 K He cooling it is understandable that the time margin especially in case of a loss of flow cannot be sufficient.

### Experimental Results of LN<sub>2</sub> Operation

To check if this time margin can be increased at 80 K, the coolant has been changed to LN<sub>2</sub>. Fig. 2 gives the flow scheme that has been used for that experiment. The LN<sub>2</sub> has been taken from storage with a pressure of 2.6 bar which results in a temperature of 86 K. Using a subcooler that was filled with LN<sub>2</sub> boiling to the atmosphere, the LN<sub>2</sub> from the storage was subcooled via a heat exchanger to 77 K. With this 77 K liquid LN<sub>2</sub> the first segment of the HEX was filled resulting in a LN<sub>2</sub> saturation temperature in that segment of 81 K at 1.6 bar when 11.6 g/s were evaporated to the atmosphere. Under these conditions the HTS current lead could be operated stable at 68 kA for more than half an hour which is shown in Fig. 3. The big advantage of this cooling method is that in case of a loss of flow there is a LN<sub>2</sub> reservoir in the first segment of the HEX. As shown in Fig. 4 with the existing reservoir in the 1st segment of the HTS CL the 68 kA could be operated for more than 5 minutes after stopping the LN<sub>2</sub> supply.

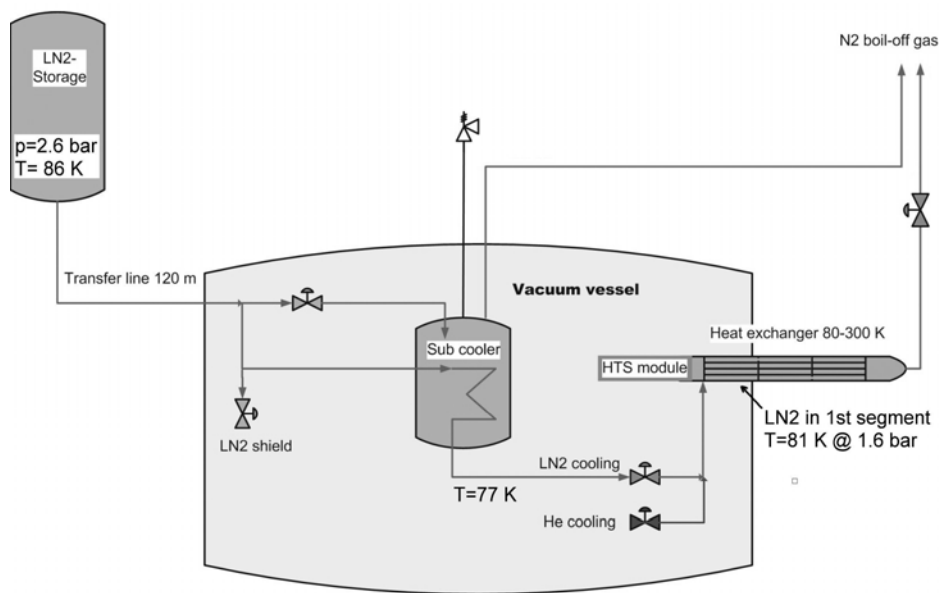


Fig. 2: Flow scheme for HTS CL testing with LN<sub>2</sub> cooling.

The size of the LN<sub>2</sub> reservoir can be optimized to match the needs. In principle an 80 K operation of the HTS CL would be possible with this method, especially when the HEX would be optimized for such a cooling method. On the other hand an operation at 80 K needs a large amount of expensive HTS material. To check the possibility of a LN<sub>2</sub> operation at lower temperature a pump was installed at the LN<sub>2</sub> outlet of the HEX to lower the pressure and demonstrated an operation with zero current at 70 K. Under current operation a higher LN<sub>2</sub> mass flow is necessary and due to the high pressure drop in the HEX (the HEX was of course not optimized for that purpose) the boiling pressure in the first segment of the HEX could be lowered to 1.2 bar which corresponds to a temperature of 78 K. However, this was sufficient to operate a current of 75 kA stably. With an optimization of the HEX a 68 kA operation at 70 K should be possible which would combine savings of HTS material with a cheap cooling with LN<sub>2</sub>. In Table 1, the main results of the HTS CL operation with 50 K and

80 K helium as well as with LN<sub>2</sub> at both atmospheric and subatmospheric pressure are summarized.

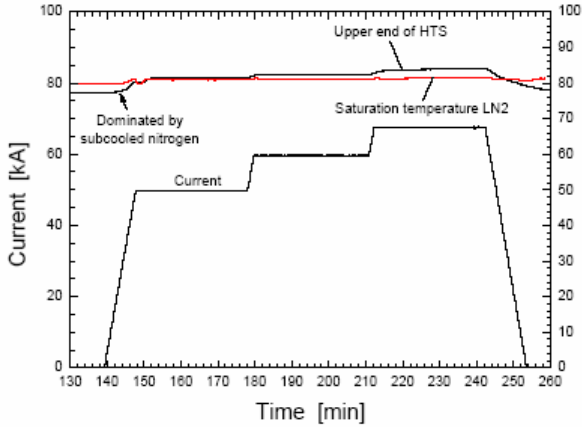


Fig. 3: HTS CL operated at currents up to 68 kA with 80 K LN<sub>2</sub> cooling.

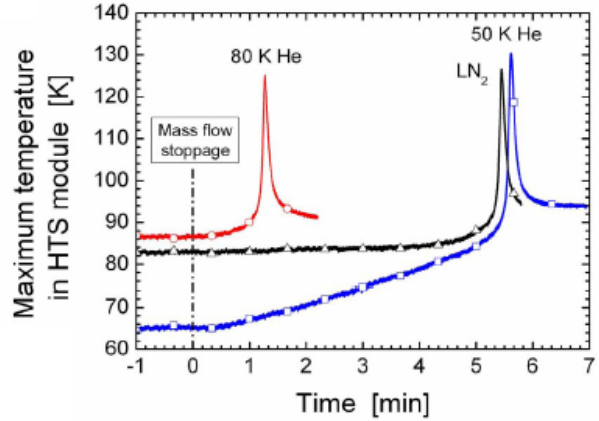


Fig. 4: Loss of flow experiments at 68 kA for cooling with 50 K He, 80 K He and 81 K LN<sub>2</sub>.

Although the attempt of using subcooled LN<sub>2</sub> at temperatures close to 70 K looks really promising there is one drawback. In case of a failure of the pump at the HEX outlet the pressure in the 1st segment of the HEX will increase immediately with the corresponding temperature increase. In this case there would be almost no time margin to discharge the system which is not acceptable. As a consequence an operating mode at subcooled LN<sub>2</sub> temperature is only promising when redundancy is foreseen for that pump at the HEX outlet.

Table 1: Cooling conditions of the HTS and conventional current lead (Conv CL, <sub>D</sub>)

	Operation	$I_{coil}$	$\dot{m}_{HEX}$	$T_{Inlet\ HEX}$	$P_{inlet\ HEX}$	$T_{Warm\ end\ HTS}$	$T_{Outlet\ HEX}$	$\dot{Q}\ at\ 4.5\ K$	P	R	t LOFA
	Unit	kA	g/s	K	bar	K	K	W	kW		min.
He cooling	Standby	-	0.9	50	5.4	102	277	23	10.0	5.7	-
		-	1.9	50	5.4	67	264	14	13.7	4.2	-
		-	1.0	4.5	5.0	75	271	16	22.0	2.6	
	Rated	68	4.7	50	5.4	65	260	26	28.1	3.0	5.5
		68	2.7	4.5	5.0	66	312	26	57.4	1.5	
		68	16.0	80	7.6	85	175	32	65.1	1.3	
LN <sub>2</sub> cooling	Extended	80	5.1	50	3.0	65	260	32	41.1	2.1	1.5
	Standby <sub>at</sub>	-	5.0	77	1.2	77	265	17	14.2	4.0	-
	Standby <sub>sub</sub>	-	3.5	77	0.35	70	285	15	13.1	4.4	-
	Rated <sub>at</sub>	68	11.0	77	1.6	83	265	32	29.4	2.9	5.5
	Rated <sub>sub</sub>	68	13.0	77	1.1	80	288	31	42.4	2.0	-
Conv.C	Extend <sub>sub</sub>	75	13.0	77	1.2	82	288	34	41.9		-
	Standby	-	2.7	4.5		-		6.8	57.4		
	Rated	68	4.1	4.5		-		13.2	85.7		

I=current, T=temperature, p=pressure,  $\dot{m}$  =mass flow rate,  $\dot{Q}$  =heat load at 4.5 K with joint losses, t= time after LOFA, P= Total power consumption, R= Reduction factor compared to the conventional CL, <sub>D</sub> The values for the conventional current lead were taken from the ITER DDD 11, <sub>at</sub> Atmospheric pressure operation, <sub>sub</sub> Sub-atmospheric pressure operation



## Summary

The results can be summarized as follows:

- Stable operation at 68 kA and even up to 80 kA with a He inlet temperature of 50 K.
- Measured temperature profiles and He mass flows agree with calculations.
- Current sharing temperature 77 K at 68 kA (10  $\mu$ V criterion).
- 68 kA operation possible with LN<sub>2</sub> cooling.
- LN<sub>2</sub> at low pressure allows lower temperatures (target: 70 K with optimized HEX).
- Loss of coolant experiment gives good margin for 50 K He and LN<sub>2</sub> at low pressure.
- LN<sub>2</sub> cooling with lowered pressure possible but needs pump redundancy.

The HTS current lead works reliable and an optimized version should be used for ITER.

## Outlook

As a consequence of the results of the HTS CL, ITER IT asked for a more detailed study to assess advantages and problems of helium and LN<sub>2</sub> cooling. So an expression of interest for a new task has been sent to EFDA.

### Staff:

M. Borlein  
M. Darweschad  
G. Dittrich  
W.H. Fietz  
S. Fink  
U. Fuhrmann  
R. Heger  
R. Heller  
W. Herz  
A. Kienzler  
R. Lietzow  
A. Lingor  
I. Meyer  
E. Specht  
M. Süsser  
V.L. Tanna  
D. Weigert  
G. Zahn

### Literature:

- [1] R. Heller, M. Borlein, S.M. Darweschad, G. Dittrich, W.H. Fietz, S. Fink, W. Herz, A. Kienzler, A. Lingor, I. Meyer, M. Süsser, V.L. Tanna, R. Wesche, F. Wüchner, and G. Zahn, "Report of the Phase III Operation of the 70 kA HTS Current Lead", Forschungszentrum Karlsruhe Internal Report, May 2005, unpublished
- [2] R. Heller R. Heller, W.H. Fietz, R. Lietzow, V.L. Tanna, A. Vostner, R. Wesche and G. Zahn, "70 kA High Temperature Superconductor Current Lead Operation at 80 K- the Strategy for ITER "Proceedings of the 19th Internat. Conf. on Magnet Technol. (MT-19), Sept. 18-23, 2005, Genova, Italy, to appear in IEEE Transact. Appl. Supercond.
- [3] G.R. Zahn, W.H. Fietz, R. Heller, R. Lietzow and V.L. Tanna "Cryogenic benefits of a 70 kA High Temperature Superconductor Current Lead " to appear in the Proc. of CEC/ICMC August 29 – September 2, 2005, Keystone Colorado, USA
- [4] W.H. Fietz, R. Heller, R. Lietzow, V.L. Tanna, G. Zahn, R. Wesche, E. Salpietro, A. Vostner, "High Temperature Superconductor Current Leads Proposal for ITER", presented at Symposium on Fusion Engineering SOFE 205, Knoxville, TN, USA, Sept. 26-30, 2005.

## **TW4-TMSF-HTSCOM**

### **Conceptual Design of External HTS Busbars**

#### **Introduction**

High temperature superconductors have successfully demonstrated their considerable advantages over conventional materials and entered the market. Therefore, a R&D programme was launched in Japan and EU in order to design and construct high temperature superconducting (HTS) components for ITER. As a result of this programme a 60 kA HTS current lead was successfully manufactured and tested in Japan in 2002. The EU 70 kA ITER prototype current lead using HTS was tested in 2004. The introduction of HTS current leads between the NbTi bus bar and the resistive heat exchanger significantly reduces the heat load at the 4.5 K level, thereby considerably saving costs of the cryogenic system.

The primary objective of this task was to compare the actual ITER design with and without using HTS current leads. This study did not only elaborate the differences in initial and operating costs but also did point out implications with other ITER components and the required ITER design changes. The performance assessment of the HTS current lead was based on the test results of the EU 70 kA prototype current lead.

Furthermore, the study assessed the possible benefits of a third ITER design option which not only replaces the conventional current leads but also the water-cooled bus bars by HTS materials. The substitution of these aluminium bus bars would not only reduce the electrical power losses but would also require significantly less space for their installation. This option includes a conceptual design of a HTS bus bar suitable for ITER.

The task was a joint work between the Centre de Recherches en Physique des Plasmas, Villigen, Switzerland, and Forschungszentrum Karlsruhe, Germany.

#### **Comparison of ITER Design with and without HTS Current Leads**

After a review of the actual ITER feeder design (including current leads and coil terminal boxes) this design is compared to an improved design where the conventional current leads are replaced by HTS current leads. The overall performances of both options are compared taking into account the operation scenarios of ITER and the safety requirements of the feeder system.

The application of HTS current leads will give a techno-economical solution for future fusion machines. One can considerably reduce the cooling power required for current leads by using HTS binary current leads.

The operational cost analysis has shown the following cooling power per year for an ITER duty cycle:

Conventional current leads	2.164 MW
HTS current leads	
50 K He cooling	0.53 MW
80 K He cooling	0.777 MW
80 K He cooling (only 4.5 K level)	0.217 MW

Using electricity costs of 5 cents/kWh, one gets for the yearly costs

Conventional current leads	0.948 M€
HTS current leads	
50 K He cooling	0.232 M€
80 K He cooling	0.340 M€
80 K He cooling (only 4.5 K level)	0.095 M€

Depending on the cooling mode, the cost reduction is 0.716 M€ (50 K) to 0.853 M€ (80 K).

Concerning the HTS modules required for ITER, about 3.8 M€ are required. To this number, additional design and development costs including the fabrication and cold test of one prototype HTS current lead has to be added.

The higher investment costs for the HTS current leads are more than compensated by the cost saving for the 4.5 K refrigerator plant. If looking to the maximum liquefaction capacity required to cool all ITER leads, 143 g/s would be needed at 4.5 K which is equivalent to about 22 kW refrigeration capacity. A 22 kW cryo plant unit will require higher investment cost than the costs required for the HTS parts of the current leads. Cost estimations for the cryo plant unit give about 10 M€.

A final cost assessment can be made as soon as the parameters of the ITER cryo plant and the ITER operation cycle are finalized.

### Conceptual design of HTS bus bar

In a further step, a third option was considered which is the replacement of the aluminium bus bar system foreseen in the ITER design to connect the coil terminal boxes and the power supplies by a HTS cable. Figure 1 shows a schematic of the layout. The designed HTS bus bars have to fulfill the following requirements:

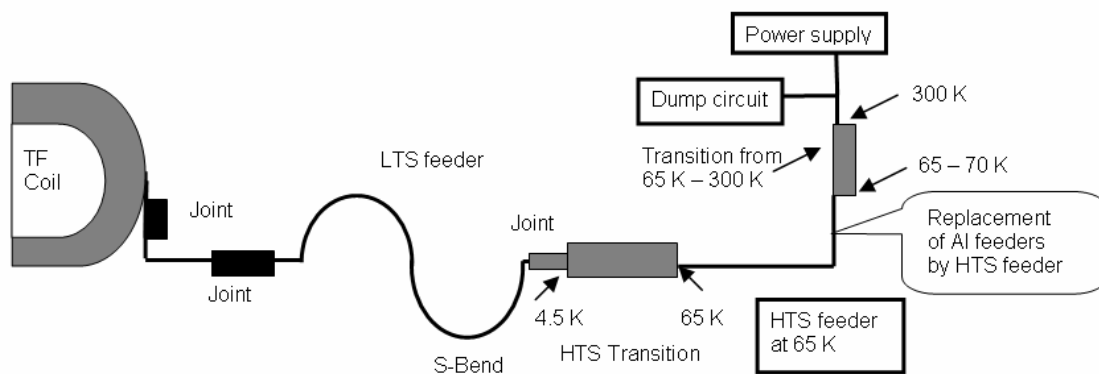


Fig. 1: Schematic layout of current feeder system of the TF coils including the HTS feeder.

1. Maximum allowable steady state heat load of about  $\sim 3\text{-}4$  W/m at 77 K.
2. Use of the warm dielectric insulation scheme.
3. HTS tapes are actively cooled in the cable area.
4. A temperature margin of at least 15 K should be maintained at an operating current of 68 kA.
5. The bus bar and its terminations should be Paschen tight with minimum heat load.
6. Smooth bending and flexibility.

The main parameters of the 68 kA HTS bus bar are given in Table 1.

Table 1: 68 kA HTS bus bar parameters.

Parameter	Value
Rated current	68 kA
Critical current	85 kA
Unit length	12 m
HTS cable design	Power transmission type
HTS materials	Bi-2223/AgMg/Ag
Typical tape dimensions	4.0 mm width x 0.22 mm thick
$I_c$ of tape at 77 K and self field	115 A
Steel flex pipe dimensions	53 mm OD, 50 mm ID
Super insulation	25 layers/cm
Cryostat	Steel flexible pipes
Max. discharge voltage / test voltage	17.5 kV / 36 kV
Coolant	50 K He/ 70 K sub-cooled LN <sub>2</sub>
Final outer diameter of cable	< 140 mm

Many design and development activities for HTS power transmission cables are reported. In this investigation emphasis was put on the warm dielectric design to make the design simpler. The superconducting Bi-2223/Ag/AgMg tapes are arranged in multilayers and wound onto a flexible stainless steel pipe. This sub-assembly is housed in a flexible steel cryostat with vacuum and super insulation in order to minimize the steady state thermal loads. The forced flow active cooling of the HTS tapes bundle as well as the central flexible pipe is considered. The warm dielectric insulation (e.g. Teflon) will be wrapped around the steel cryostat for protection against the high voltage. Finally, a steel sleeve will be wrapped around the warm dielectric for mechanical protection. Figure 2 shows a schematic illustration of such a transmission cable.

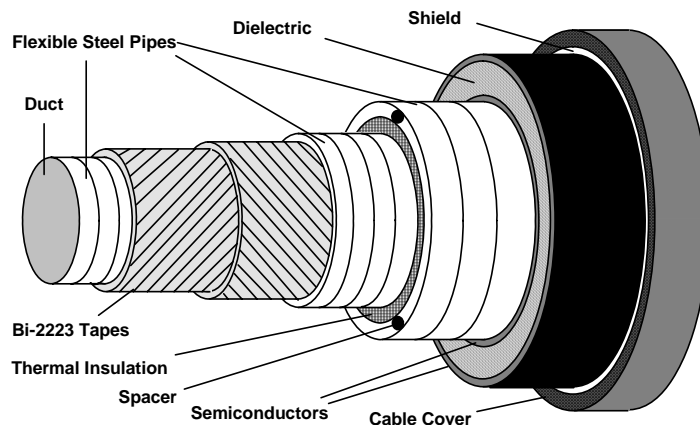


Fig. 2: Schematic illustration of a single phase power transmission cable with warm dielectric.

The forced flow cooling of 1-3 kA class HTS bus bars with sub-cooled liquid nitrogen (LN<sub>2</sub>) at 70-72 K has been discussed in the literature. Particularly for ITER a possibility to cool the HTS bus bar either with 50 K helium or forced flow sub-cooled LN<sub>2</sub> at 70-72 K is recommended. In Figure 3, both the 50 K He cooling scheme and scheme for sub-cooled LN<sub>2</sub> cooling for the HTS bus bar and its termination are shown. It is also not desirable to cool the HTS cable with 80 K He because it requires a huge amount of HTS material and large installation space requirements and nevertheless a lower temperature margin compared to other mentioned cooling options.

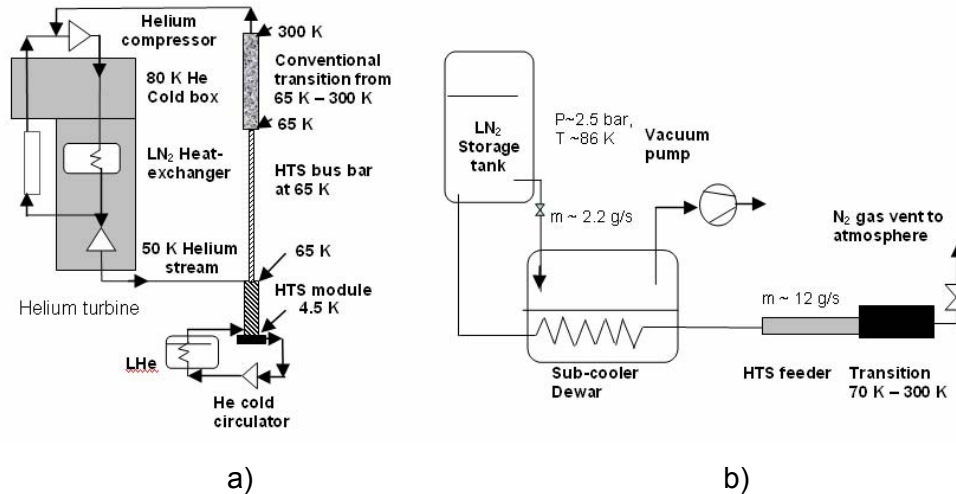


Fig. 3: a) 50 K He cooling scheme. b) Sub-cooled LN<sub>2</sub> cooling scheme.

Different sources of steady state heat loads acting on the HTS bus bar including radiation, conduction and Joule heating in the joints are estimated to be about 45 W at 50 K. In case of the TF bus bars, there is no AC operation (besides the charge and discharge of the coils) but AC losses due to current ripple of the power supply will be generated. Estimations show that in case of ITER, the TF system contributes with only a few mW of ripple loss at 600 Hz with 30 V reactive load voltage. A 1-D thermo-hydraulic model of the HTS bus bar has been developed for optimization of coolant requirement, pressure drop, and coolant inlet/outlet conditions. The analysis has been carried out for both the cooling options i.e. 50 K helium and sub-cooled LN<sub>2</sub> at 70 K and the results are summarized in Table 2.

Table 2: Results of thermo-hydraulic analysis.

Parameters	50 K helium cooling	70 K (LN <sub>2</sub> sub-cooling)
Inlet pressure	6 bar	2.5 bar
Inlet temperature	50 K	70 K
Flow length	12 m	12 m
Total mass flow rate	5 g/s	12 g/s + 2.2 g/s for sub-cooler
Void fraction within the bundle region	~ 50%	~ 40%
Pressure drop within network	0.3 bar	~ 0.7 bar
Available heat transfer coeff.	414 W/m <sup>2</sup> K	300 W/m <sup>2</sup> K
$\Delta T = T_{out} - T_{in}$ in the bus bar	1.75 K	~2.0 K
Refrigeration plant efficiency	0.284	0.30
Power consumption	~26 kW	~27 kW + 5 kW LN <sub>2</sub> for sub-cooler

## Conclusion and Outlook

The design concept, optimization and main parameters of a TF HTS bus bar model for ITER have been studied. The operating temperature is one main parameter for the HTS cable design. The optimization between the amount of superconductors and operating cost of the cryogenic system is essential. 50 K He and 70 K sub-cooled LN<sub>2</sub> options are possible options for an ITER HTS cable. The 50 K He option looks more economic because less superconductor is needed compared to 80 K He cooling. Sub-cooled LN<sub>2</sub> cooling consumes more power and gives less temperature margin compared to 50 K helium cooling but the LN<sub>2</sub> cooling system is much simpler. In a further step, the detailed conceptual design of PF and CS HTS bus bars including termination will be worked out.

Staff:

R. Heller  
V.L. Tanna

Literature:

- [1] R. Heller, W.H. Fietz, R. Lietzow, V.L. Tanna, R. Wesche, and G.Zahn, "Report on the Comparison of ITER Design with and without HTS Current Leads, EFDA No. TW4-TMSF-HTSCOM, Deliverable 1", Forschungszentrum Karlsruhe Internal Report, June 2005, unpublished
- [2] R. Wesche, R. Heller, W.H. Fietz, V.L. Tanna, and G. Zahn, "Report on the conceptual Design of External HTS Bus Bars, EFDA Reference: TW4-TMSF-HTSCOM, Deliverable 2", Centre de Recherches en Physique des Plasmas Internal Report, June 2005, unpublished
- [3] V.L. Tanna, W. H. Fietz, R. Heller, A. Vostner, R. Wesche, and G.R. Zahn, "Conceptual design of a High Temperature Superconductor current feeder system for ITER", presented at European Conference on Applied Superconductivity EUCAS 2005, Vienna, Austria, Sept 12-15, 2005

## EFDA/04-1216

### Cryogenic Testing of Materials and Welds for Magnet Structures

The cryogenic material testing and qualification programme within the framework of the European fusion technology task consists of cyclic loading investigations on TF helium inlets with the target to assess the final test results with respect to required performance of the mock-up. In addition, for dipole magnet design cryogenic mechanical measurements were conducted with respect to high permeability ferritic materials. In a parallel task enforced by EFDA, the cryogenic material testing laboratory of CEA / Air Liquide, Grenoble/France worked with our laboratory with the goal to check the present ability of their site on standard cryogenic mechanical measurements with respect to tensile, fracture toughness, and fatigue crack growth rate tests.

#### Investigations on LHE Inlet Mock-up for TF Cooling

Two samples of the mock-up (TF-IN3 and TF-IN4) provided by CEA were tested using the large 630 kN servo hydraulic machine at 4 K. The first TF-IN3 sample test was foreseen to qualify the structure/machine parameters for the final test of TF-IN4. The primary test parameter requirements were as follows:

A mean strain of  $\varepsilon = 0.11\%$  with a cyclic strain range of  $\pm 0.03\%$  for 600,000 cycles.

Considering the jacket cross section of  $197 \text{ mm}^2$ , the corresponding load was  $F = 43.5 \text{ kN} \pm 11.8 \text{ kN}$  at this envisaged strain or an average stress of  $\sigma = 220 \text{ MPa} \pm 60 \text{ MPa}$ .

All data concerning the load, stroke displacement, and the average strain, determined by extensometry from the base metal section and from the weld metal section could be monitored in real time and saved with 100 Hz sampling rate onto the hard disks. The data acquisition during the cyclic loading was performed using two different systems. Firstly, a PCMCIA small card (8 channels, 16 bit resolution, and 100 kHz sampling rate capacity) from IoTech Company (DAQ/216B) connected to a note book. Secondly, an 18 bit data acquisition board (type Strawberry Tree) for averaging of attached two extensometer signals (strain information) which were separately saved onto the hard disc of a PC for the reason of high resolution low noise data and data safety. Figure 1 shows the inserting of the assembled mock-up structure TF-IN4 into the cryostat of 630 kN capacity test facility.

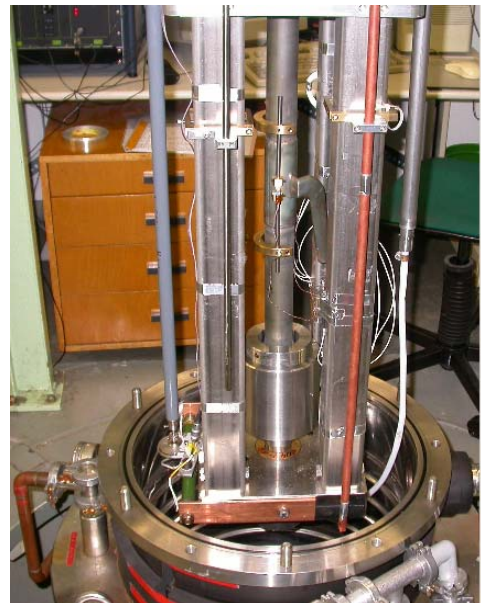


Fig. 1: Photography shows the assembled TF-Mock-up No II inside the 4 K rig during the elevation procedure of the cryostat.

In contrast to the first test the two extensometers of the second test sample were attached to the structure with a collar system, thus ensuring the monitoring of the two weld zones simultaneously as given in Figure 2.

The measurement of the sample TF-IN3 was carried out on June 6, 2005 in a one day campaign. After cooling the structure inside the  $450 \text{ mm } \varnothing$  bore cryostat the structure has been subjected to three static loading (ramp rate =  $1 \text{ mm/min}$ ) steps up to  $270 \text{ MPa}$  stress level. The first two load steps were carried out as stress versus base metal strain by using the double extensometer system clamped on the tube, whereas the 3<sup>rd</sup> loading has been performed under the same condition but using the extensometer system clamped onto the orbital weld section region. The obtained stress versus strain diagram indicated a large bend-

ing behaviour of the structure during the loading and the acquired data resulted in a Young's modulus of 220 GPa, which was around 6 % higher than usual, resulting most probable from the bending effects.

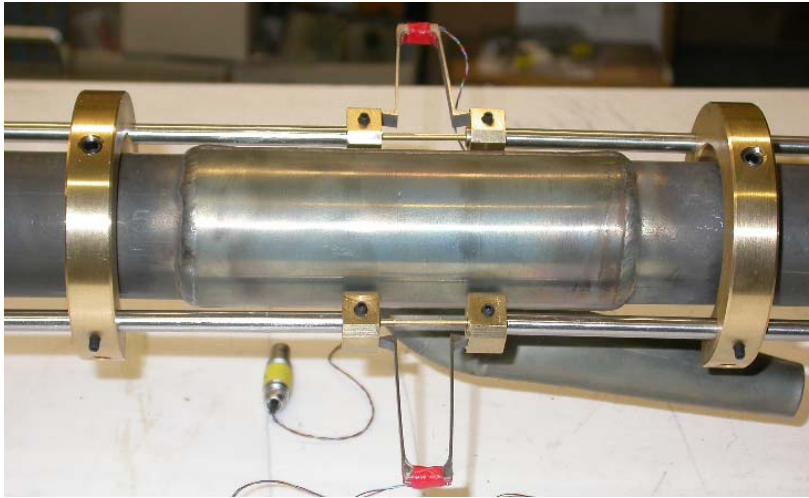


Fig. 2: Photography shows the details of the extensometer attachment using the collar system. The assembly shows the fixed two extensometers between the two collars with a gauge length of 173.93 mm.

A total of 125,000 cycles were conducted within circa 6 hours at 4 K. The LHe consumption was as follows: We started at 80 % LHe level which means all four extensometers were submerged in LHe. At the end of cycling period the LHe level sunk to 5 %. Temperature of the structure was, however, in all cases around 4.2 – 5 K. The frequency of the cyclic load was 7 Hz and the sampling rate of the data acquisition was 100 Hz. For this preliminary test the results were as follows:

- At 4 K it was possible to load the TF mock-up structure under cyclic condition up to a final cycle number of 125,000 cycles.
- The machine and structure interplay was tested and a stable cyclic regime could be attained in this case with 4 Hz frequency achieving the required mean strain of 0.11% with a corresponding mean stress level of ~ 220 MPa.
- Slipping of the tube/attachment could be identified. This slipping, however, had no adverse effect on the envisaged loads.
- The LHe consumption was within the circa 5 hours period 220 litres.
- All data of the first measurement campaign is saved on a CD-ROM and could be handled along with appropriate software capable to open the files, their viewing, and printing of charts for a detailed inspection.

The second sample TF-IN4 was tested on August 10, 2005. The test comprised a total of three days with warm up intermediate periods during night time. A total of 332,797 cycles were conducted at 4 K within the first two days without any detectable adverse effects of the structure. The LHe consumption was considerable lower after the first day owing to the cold situation of the cryostat from the former day. In the morning the temperature was 37 K at the start of LHe filling. The frequency of the cyclic load was again ~ 7 Hz and the sampling rate of the data acquisition was similar as at past with 100 Hz. The test on third day showed after a couple of hours indications of a strain range change as shown in Figure 3. During this final experimental day a total of 476,117 cycles have been achieved at 4 K. The TF-structure, however, did not survive the envisaged 600,000 cycles. The test history was the same as for the recent days and covered the requirements. Figure 4 shows the final failure sequence of cyclic loaded TF Mock-up structure.



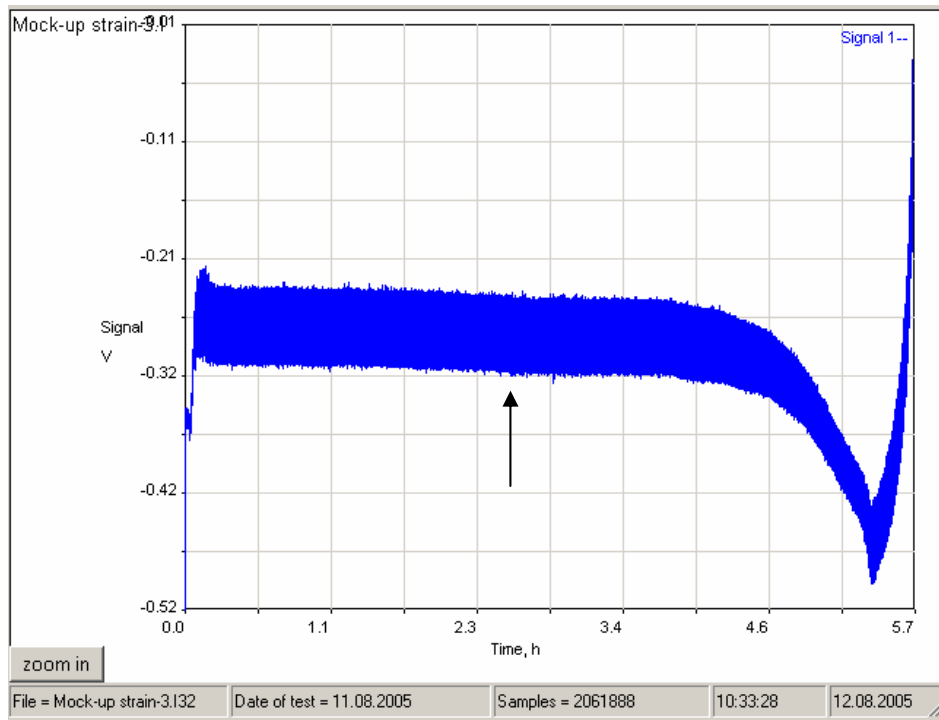


Fig. 3: Diagram shows the view of averaged strain versus time of the third days test. The arrow indicates starting of a crack. The strong strain range variation at the end is the final stage of the failure. The y-axis is the strain values in %.

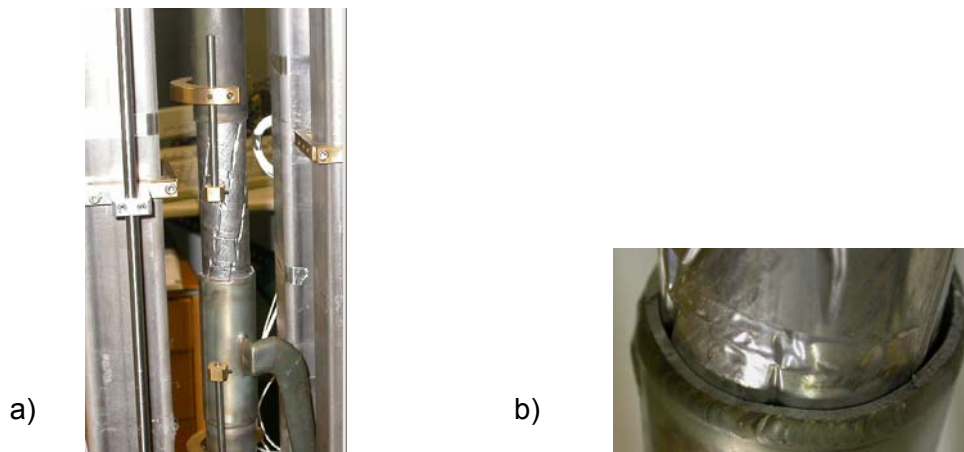


Fig. 4: Image (a) shows the structure after the failure inside the rig. Image b) shows the fatigue failure occurrence at the weld/base fusion boundary of the tube.

### Investigations on Ferritic Material Characterization for Dipole MAG-NET

Table 1 shows the determined mechanical properties of the provided ferritic material by CERN, Geneva. This material was selected as the main structure of the dipole magnet and is a so called low carbon ferritic steel. Obviously the total elongation at fracture of this material is around 0.5% strain at 7 K, which indicates the brittleness of this material. The same mate-

rial was tested also with respect to the fracture toughness in two orientations at 7 K. The determined values according to ASTM E 399 standard are  $\sim 30 \text{ MPa}\sqrt{\text{m}}$  at 7 K, which indicates its brittle characteristics. This behavior must be assessed into design consideration using the fundamentals of fracture mechanics philosophy.

Table 1: Tensile properties of soft magnetic iron at different temperatures and at two different orientations.

File	Temperature K	Young's Modulus GPa	Yield Strength MPa	Ultimate Tensile strength MPa	Uniform elongation %	Total elongation %
Cernx-1	295	205	115	249	32	52
Cernx-2	7	200	-	723	0,5	0,5
Cernx-3	233	196	151	260	$\sim 25$	$\sim 50$
Cerny-1	295	200	123	282	26	44
Cerny-2	7	211	-	926	0,5	0,5
Cerny-3	90	210	642	653	5,9	20

### **CRYOLA, A Collaboration Task between CEA Grenoble and Forschungszentrum Karlsruhe**

The present collaboration efforts deal with the guidelines of measurement techniques with respect to tensile and fracture toughness properties of alloys at 4 K. The close collaboration between Forschungszentrum Karlsruhe and CEA/Air Liquide, Grenoble about this topic has the goal to prepare the French partners for the ITER materials qualification programme, which will be required soon after the very start of the manufacturing phase. The experiences gained during the last two decades of Forschungszentrum Karlsruhe were transferred to CEA/Air Liquide, Grenoble. Special attention has been focused on J-tests carried out with small size specimens at 4 K. A small round robin test procedure between these two institutions deepened the methodology and the knowledge. Sensing systems (extensometers) provided by Forschungszentrum Karlsruhe enabled to carry out sensitive tests resulting in fracture toughness values accepted by the worldwide community.

Following the required work package, several fracture toughness tests were conducted with Model 3 and Al-alloy materials using both ASTM standards E 813 and E 399 after calibration checks of the present Instron machine at Air Liquide site. The machine control poses still problems and for the present status the displacement control could be run only in manual mode. This problem was recognized and Air Liquide is working on this specific issue. Besides, the developed evaluation software at Forschungszentrum Karlsruhe (MatDat) applicable for J-test will be directly used by Air Liquide. The data acquisition system will be also the same (PCMCi cards with DaysLab software) as the presently used one at Forschungszentrum Karlsruhe.

#### Staff:

A. Nylas  
K. Weiss  
H. Kiesel

## EFDA/04-1198 European Dipole Design

### Background

During the construction of the ITER TF- CS- and PF-coils, the superconductor fabrication needs to be qualified by testing full-size short samples of conductor unit lengths under ITER relevant conditions. Such qualification programme has to be consistent with the conductor production rate and shall be completed within about 3 years. The total number of full-size samples to be tested during the QA programme by the EU PT will include both TF and PF conductor samples, joint samples, R&D samples etc. The only existing facility in Europe to test full-size short samples is the SULTAN facility at CRPP. After about 20 years of operation it was now decided by EURATOM to cope with the high number of tests required during ITER construction.

Because such a dipole with a rather large free bore of > 130 mm is a challenge (use of Nb<sub>3</sub>Sn conductors, high electromagnetic forces and stresses), various options were addressed and investigated by different associations. Forschungszentrum Karlsruhe investigated the warm bore option with the necessary space for rectangular samples with the size of 145 x 95 mm because this option is targeting a high sample testing rate. Of course, a larger bore requires a larger magnet and causes higher costs.

### Input parameters and boundary conditions for the dipole design

In detail an advanced strand of 0.81 mm with 2000 A/mm<sup>2</sup> at 4.5 K and 12 T was used to define the layout of the dipole for a guaranteed field of 12.5 Tesla over a length of 1.5 m. The

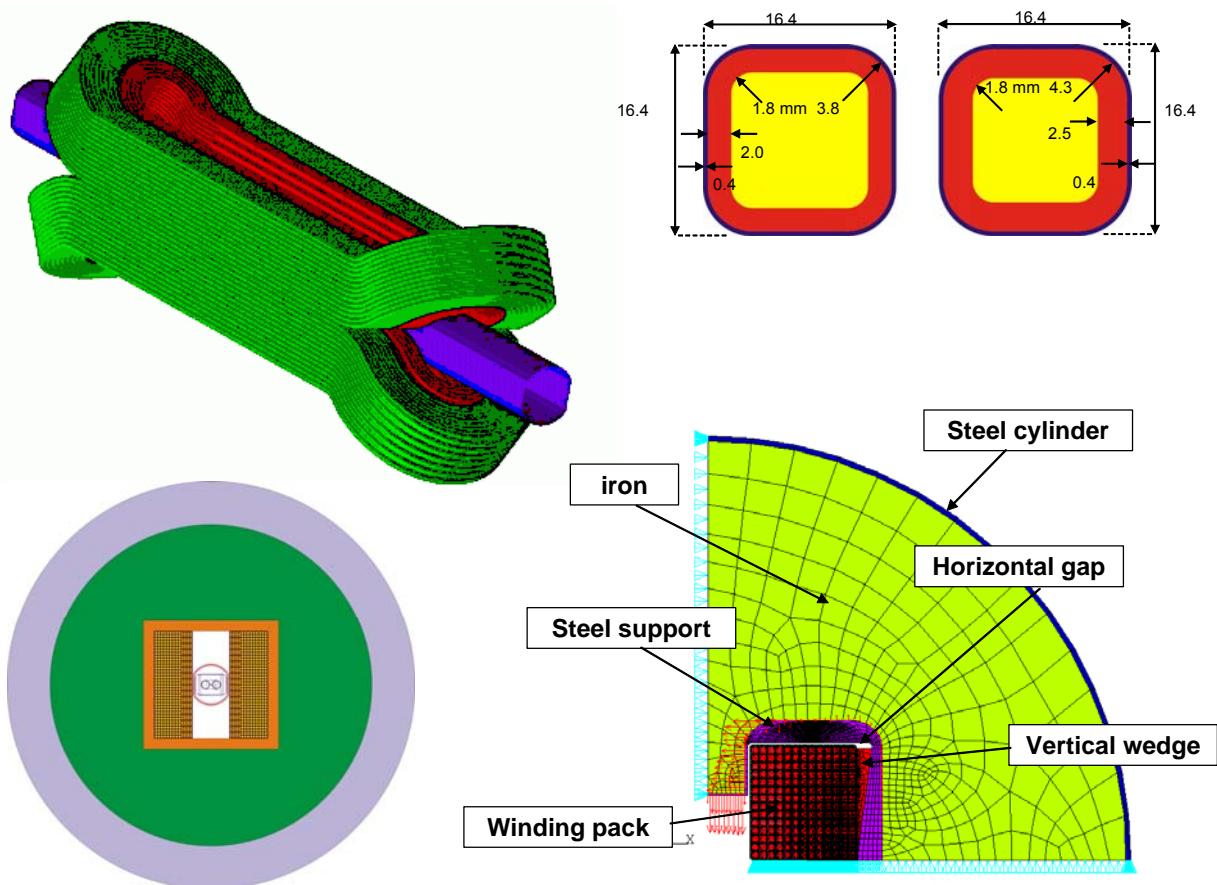


Fig. 1: Sketch of the dipole winding (top left), the HF- and LF-conductors (top right), the dipole cross section (bottom left), and the ANSYS model of 1/4 dipole cross section (bottom right).

so called Summers scaling law for  $j_{c,nc}$  of the strands was used. The cable geometry and the coil geometry were defined and optimised, including winding, power supply rating, jacket dimension. The critical issues for the conductor dimensions were to withstand the maximum pressure during quench and the minimum acceptable bending radius for the coil winding. The operation current density in the conductor was adjusted to get an acceptable hot spot temperature and to minimize the superconductor strand volume.

For that design a cooling concept for 4.5 K supercritical helium has been developed, defining cooling length, heat removal, pressure drop and the connected temperature increase. In the engineering design the mechanical and support structure were performed including stress analysis of the coils mechanical structure in operating condition as well as a thermohydraulic analysis (in nominal condition as well as during quench). For cost reasons, a non-planar racetrack coil design was chosen as it was also studied by EFDA for the cold bore option. In Figure 1, the schematic of the dipole as well as a view of the HF and LF-conductor dimensions are shown.

To optimise the design, magnetic field, structure mechanic and thermal hydraulic calculations were performed. The non copper current density is lower than in the EFDA design leading to less demanding requirements in case of a quench. The detection, discharge initiation and discharge of the magnet is less time critical compared to the EFDA dipole. For the warm bore design a delay time of 0.5 s and a dump time constant of 1.4 s is achievable.

### **Results of the dipole warm bore design**

#### Electromagnetic performance:

The overall current density in the conductor is about  $67 \text{ A/mm}^2$  which is much lower than for the EFDA conductor. The magnetic field homogeneity is about 2% in a box of  $\pm 50 \text{ mm}$  in horizontal,  $\pm 30 \text{ mm}$  in vertical and  $\pm 500 \text{ mm}$  in axial dimension, computed with saddle coil geometry of  $90^\circ$  bending of the coil heads.

#### Thermohydraulics and quench performance:

The dipole winding cooling requires 26 cooling channels for both the HF and LF conductors with a total helium mass flow rate of  $33.5 \text{ g/s}$ . For a delay time of 0.5 s, the resulting dump time constant will be 1.4 s. Both numbers are larger than for the EFDA dipole. So the hot spot temperature is less sensitive to possible additional delays in case of a failure of the switch or of the quench detector.

The maximum quench pressure and temperature are 260 bar and 160 K, respectively. The quench propagates very fast, so a quench detection time of 50 ms should be sufficient.

#### Structure mechanics performance:

The maximum Tresca stress in the iron is limited to values below 170 MPa because a support structure made of stainless steel was introduced to carry the peak stresses. The maximum Tresca stress in the jacket is 880 MPa which is the upper limit of that which could be accepted. The maximum shear stress in the insulation is 65 MPa and the RBS is 41 MPa. The peak Tresca stress in the jacket for a quench pressure of 300 bar is acceptable. The displacement within the winding pack is about  $30 \text{ }\mu\text{m}$ .

A cost comparison was done to evaluate the differences between the cold and warm bore designs. The result is that the costs increase from the cold bore to the warm bore design would be only 20%.

Figures 2 to 5 show the main results of the electromagnetic, hot spot, quench performance and mechanical analysis.

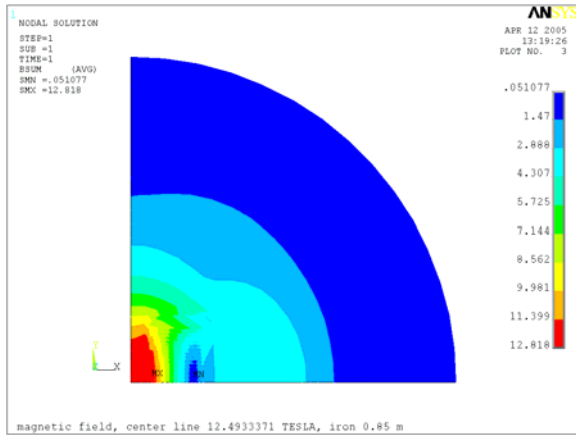


Fig. 2: Magnetic field strength in the dipole calculated with ANSYS.

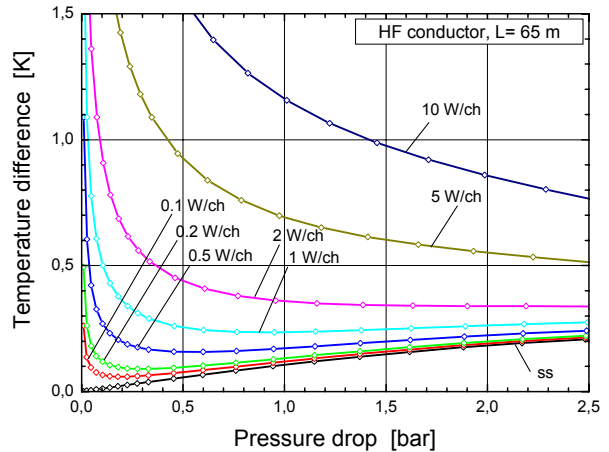


Fig. 3: Thermohydraulic analysis and heat removal.

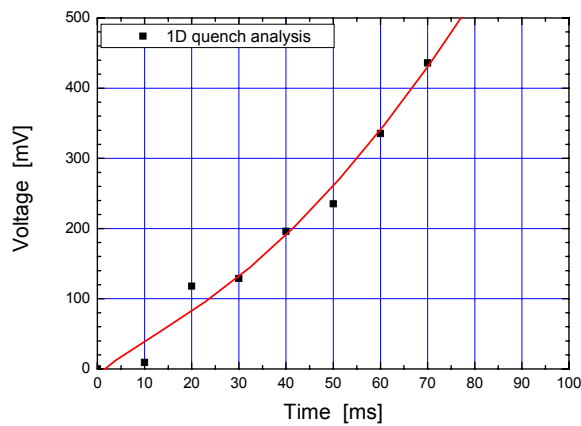


Fig. 4: Voltage evolution during quench.

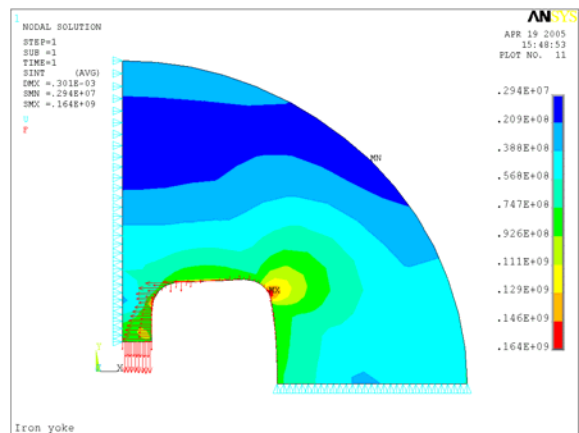


Fig. 5: Tresca stress in iron and steel support.

Staff:

W.H. Fietz  
 R. Heller  
 R. Müller  
 S. Raff  
 M. Sander  
 G. Zahn

Literature:

[1] R. Heller, W.H. Fietz, R. Müller, S. Raff, M. Sander, G. Zahn, "Design of the EFDA Dipole - warm bore option – 1<sup>st</sup> Intermediate Report Contract No. FU06 CT 2004-00154 (EFDA No. 04-1198)", Forschungszentrum Karlsruhe Internal Report FE.5130.0071.0012/A, March 2005, unpublished

[2] R. Heller, W.H. Fietz, S. Raff, and G. Zahn, "Final Design Report of the EFDA Dipole - warm bore option – Contract No. FU06 CT 2004-00154 (EFDA No. 04-1198)", Forschungszentrum Karlsruhe Internal Report FE.5130.0071.0012/B, July 2005, unpublished

[3] A. Portone, E. Salpietro, L. Bottura, P. Bruzzone, A. Della Corte, W.H. Fietz, R. Heller, S. Raff, J.M. Rifflet, P. Testoni, J. Lucas, F. Toral, „The design and optimization of the 12.5 T EFDA Dipole“, presented at the CHATS Workshop, TU Twente, Netherlands, June 26-28, 2005, to appear in Cryogenics

[4] A. Portone, L. Bottura, P. Bruzzone, W.H. Fietz, R. Heller, J. Lucas, S. Raff, J.M. Rifflet, E. Salpietro, P. Testoni, F. Toral, "Conceptual Design of the 12.5 T Superconducting EFDA Dipole", Proceedings of the 19th Internat. Conf. on Magnet Technol. (MT-19), Sept. 18-23, 2005, Genova, Italy, to appear in IEEE Transact. Appl. Supercond.

## **TW5-TMSF-HTSMAG**

### **Scoping Study of HTS Fusion Magnets**

#### **Objectives**

After Forschungszentrum Karlsruhe and CRPP have shown with the 70 kA high temperature superconducting (HTS) current lead that HTS materials can be used for ITER, these materials should be introduced in other components, primarily in fusion magnets. First a scoping study of HTS fusion magnets shall be performed to check the benefits of using high temperature superconducting materials in fusion magnets including the identification of potential problems.

In collaboration with other associations different operating scenarios are assessed:

1. "High field option": Operating temperature at 5 K and high toroidal magnetic fields in the range of 15 to 20 T. In this case a comparison LTS vs. HTS shall be included.
2. "Intermediate temperature": Operating temperatures in the range of 20 to 30 K and ITER-like magnetic fields, i.e., 10 to 15 T.
3. "High temperature": Operating temperatures in the range of 65 K and ITER-like magnetic fields, i.e., 10 to 15 T.

The task will be performed as follows:

- First the three options will be checked using literature data.
- In the second phase the new data from the parallel task HTSPER will be used to assess the usability of HTS materials for future fusion magnets.

The work is divided in manageable parts for each participating Association. The work performed at the Forschungszentrum Karlsruhe focuses on the third operating scenario, i.e., the high temperature option.

#### **Critical issues**

Following the requirements taken from the reactor studies, the HTS material has to be selected according to the

1. engineering current density in the conductor at the specific temperature and magnetic field;
2. mechanical strength, i.e., stress-strain dependence;
3. AC losses originated by the outer poloidal field coils and possibly by the central solenoid coil;
4. hotspot and quench behavior of the HTS conductor;
5. flux jump stability;
6. coolant choice, i.e., nitrogen, helium, neon etc.;
7. current distribution, i.e. interstrand resistance and joints;
8. activation of materials due to neutron flux;
9. conductor electrical insulation.

Some comments to the requirements listed above are given:

- Due to the anisotropic behavior of the superconductor material, both directions of the magnetic field acting on the conductor have to be considered.
- Since YBCO is a brittle material, the performance of the tape under axial and transverse stress has to be known. Especially the presence of a high strength substrate as well as a low resistive cap layer material will lead to pre stresses originated from different thermal contractions from reaction temperature down to operation temperature.
- Although the quench initiation process might be different in HTS conductors compared with LTS due to the much larger heat capacity of the material at higher temperatures, the hot spot in case of a quench will be an issue. Since the quench propagation velocity in YBCO is very small (low thermal conductivity) and in contradiction the normal state Joule heating is very large (high electrical resistivity), a high performance stabilizing material is mandatory. The large magnetic energy stored in the magnet system determines the discharge time constant and not the thermal evolution of the quench in the coated conductor.
- Due to the geometry of the coated conductors, i.e., large (mono) filament tapes with high aspect ratio, the occurrence of flux jumps as well as large hysteresis losses have to be investigated.
- The electromagnetic stability is not an issue because of the much higher enthalpy of the material at 20 K or even more at 65 – 70 K. Cooling is also not required for thermal stabilization, i.e., the transient heat transfer coefficient is of no importance. An open question is the effect of a possible plasma disruption.
- Conductor insulation is an issue because of the high heat treatment temperature which could require the insulation process to apply afterwards – it is like wind-react-and transfer process.
- Conductor joint may be an issue because of the unsymmetrical layout of the tape – steel on one side, copper on the other side.

### **YBCO material properties**

A literature survey was done to collect the material properties of the YBCO coated conductors structured in superconductor properties, electrical and thermal properties, AC losses, mechanical properties and nuclear activation.

### **Outlook**

The aim of the study is the development of a conductor concept which could be applied in a fusion reactor. For this, the ITER magnet system will be used as reference and the physical parameters relevant for the conductor design will be taken. The most critical issues, beside the manufacturing of the conductors, will be AC losses and quench performance (hot spot).

### Staff:

W.H. Fietz  
R. Heller

## **TW5-TMSC-HTSPER HTS Materials for Fusion Magnets**

### **Introduction**

Mainly 3 kinds of HTS materials can be considered in principle for the use in future HTS coils for fusion reactors: BSCCO-2223 tapes, BSCCO-2212 tapes and wires and YBCO coated conductors. The stage of development is quite different, BSCCO systems are since years an industrial product and are still under improvement, while YBCO coated conductors actually become an industrial product with still limited quantity and quality. From the viewpoint of the possible application temperature in high fields of >15 T, BSCCO needs to be applied at 20-30 K and YBCO is expected being applicable at a temperature of 40-50 K. Therefore BSCCO materials should be investigated as an intermediate solution and YBCO – CC as the final choice. For the BSCCO system, BSCCO(2223) with a critical temperature of 110 K is available as an industrial product in lengths up to 2 km (EAS) with different sheath compositions specified for mechanical reinforcement (dispersion hardened AgMg sheath) or low thermal conductivity (AgAu-alloy) or combining both properties (AgAuMg-alloy sheath). YBCO coated conductors are actually coming into the market with lengths of 10 – 100 m.

### **Task strategy and work program**

- 1) In the first year, the main efforts are necessary in the procurement of the industrial HTS materials and the first test of selected basic properties as handling, transport current at 77 K, self field and stability of the composite with respect to mechanical and thermal events.
- 2) In the second year, the superconducting properties will be investigated with respect to the current carrying capability as function of temperature and background field and field orientation and different kinds of strain application as bending strains and axial tensile strains.

### **Results**

#### **1. Transport critical current measurements**

As summarized in table 1, 8 different BSCCO(2223)-tapes from the leading 4 suppliers were received in lengths of 10 m each. Among these 2 tapes were current lead samples with Au-alloyed sheaths. All samples have mechanically reinforced sheaths applying Mg alloyed Ag or adding a stainless steel lamination by soldering (AMSC). As YBCO coated conductor sample, a 10 m length of DyBCO-CC could be ordered from THEVA and a 10 cm YBCO-CC test piece was achieved from AMSC. Both materials were supplied with a stabilisation coating from Ag or copper. BSCCO(2212) conductors could not be ordered from any supplier. The selection of samples was finished at the status as given in the table.

Transport critical current densities were measured by a standard 4 point method, the criterion for the determination of the critical current was  $1 \mu\text{V}/\text{cm}$ , the measured section of the sample was 8 cm. All samples showed smooth similar transitions, but significant differences in the achieved critical currents as given in figure 1. Due to the different tape cross sections (see table 1), a comparison of the samples requires to calculate the engineering critical current density, referred to the whole tape cross section. These values are also listed in table 1.

Excluding the older version of the EAS current lead tape due to the non actual performance for the comparison, the current densities range from  $8.3 \text{ kAcm}^{-2}$  for the AMSC and Innost material up to  $11.7 \text{ kAcm}^{-2}$  for the Sumitomo high current BSCCO tape. The lower AMSC value is mainly caused through the applied stainless steel clad which leads to a thicker tape. Quite surprisingly high was the current density for the EAS-V388B current lead tape, reach-



ing 9.6 kAcm<sup>-2</sup>. The U-I-transition at the critical currents are quite similar for all materials indicating a throughout good performance (see Figure 1).

Table 1: Acquired BSCCO and YBCO samples and transport current measurements.

Company	Sample	Measurement	I <sub>c</sub> (77 K, self field)	J (engineering) J <sub>e</sub> (77 K, self field)
EAS	BSCCO 2223 /AgMg state-of-the-art (V375B4)		99 A	11.06 kA/cm <sup>2</sup>
EAS	BSCCO 2223 AgMg/AgAu14 current lead cond.		64 A	
AMSC	BSCCO 2223/Ag/SS 4.8 x 0.3 mm cross.sect.		121 A	8.17 kA/cm <sup>2</sup>
Sumitomo	BSCCO 2223/AgMg high strength version (HIP)		110 A	11.39 kA/cm <sup>2</sup>
Sumitomo	BSSCO 2223/AgMg High current version !		130 A	11.66 kA/cm <sup>2</sup>
Innost	BSCCO 2223/AgMg Standard		84 A	9.09 kA/cm <sup>2</sup>
Innost	BSCCO 2223/AgMg Standard + Sn coating		88 A	8.32 kA/cm <sup>2</sup>
Innost	BSCCO 2223/AgMg Standard + Insulation			
AMSC	YBCO-CC PLD/CSD 10 cm neutral axis cond.			
THEVA	DyBCO-CC ISD/TCE		255 A	28.3 kA/cm <sup>2</sup>

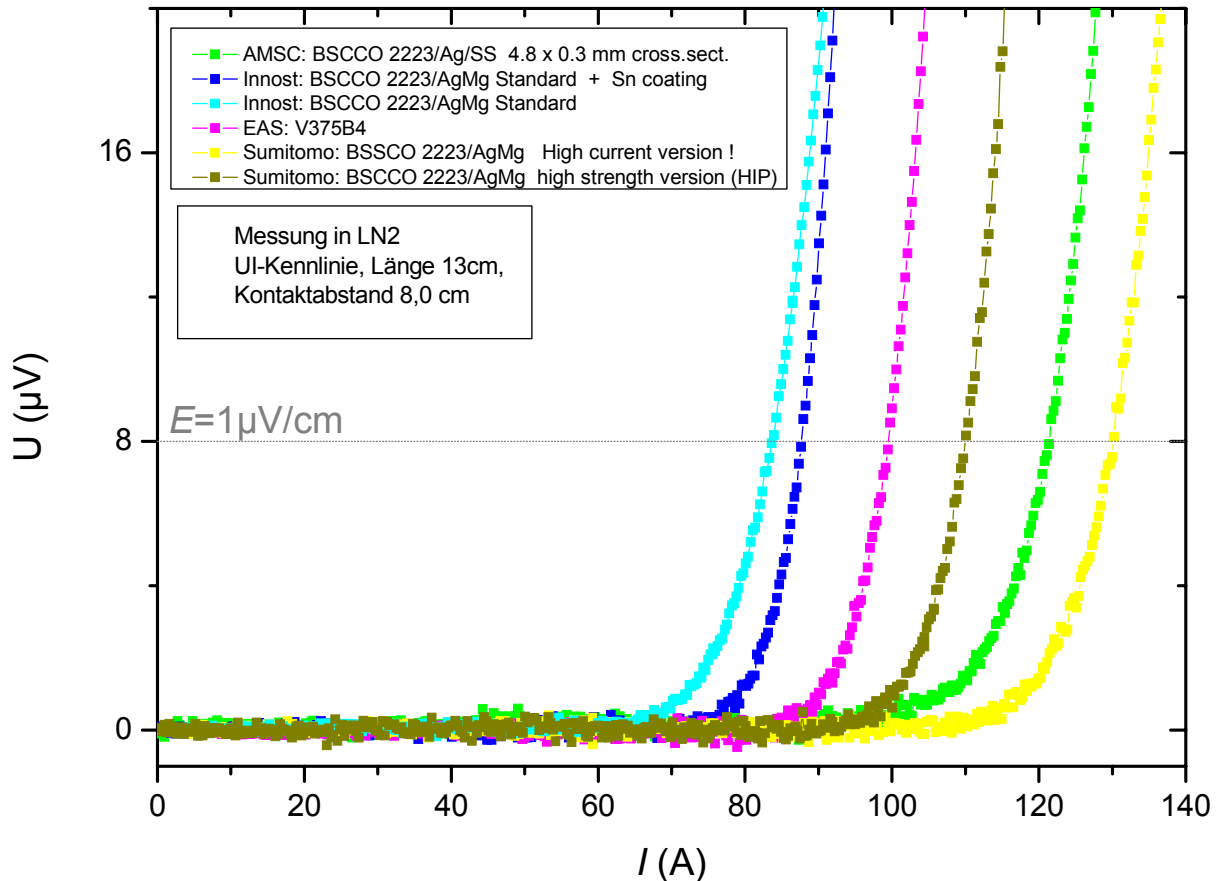


Fig. 1: Transport critical current transitions of BSCCO(2223) tapes at 77 K and in self field.

The DyBCO coated conductor sample with 5 cm length and 10 mm width showed transport currents of typically 250 A (77 K, self field) which increase to 275 A with soldered 0.5 mm copper stabilisation (see figure 2). The cap layer thickness of 400 nm tends to be sufficient for stabilisation for a voltage criterion of about 10-20 μV/cm. For technical application this value has to be improved.

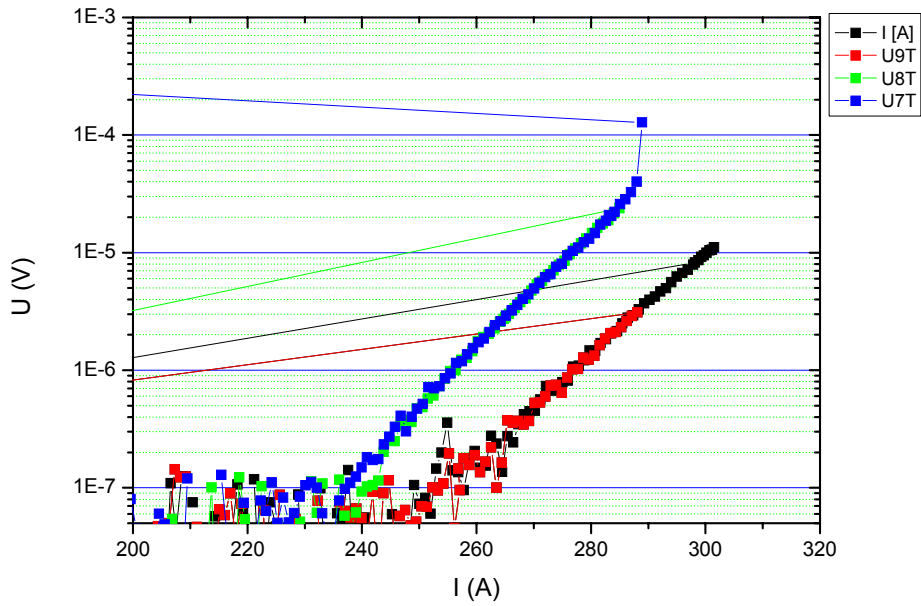


Fig. 2: Transport critical current transition of a DyBCO-tape (10x0.09 mm cross section) with 400 nm Ag cap layer (blue curve) and soldered copper stabilisation (red curve).

## 2. AC loss measurements on DyBCO conductors

Stacks of YBCO and BSCCO(2223) tapes, of 6 mm and 4.3 mm width, respectively, were measured in perpendicular field. The YBCO tapes, supplied by THEVA, Germany, had critical currents between 120 and 160 A for a tape width of 6 mm. The BSCCO tape as reference, supplied by American Superconductor, had 55 untwisted filaments and critical currents of typically 105 A. Since the filaments were strongly coupled by interfilament bridging, they behave like a single thick filament.

The Figure 3 shows AC losses per unit conductor length and cycle, divided by the square of the field amplitude. Parameter is the number of tapes, or

the height  $h$  of the stack, measured between the outer superconductor layers. The losses are hysteretic, coupling losses don't play a role for these samples. As it is expected, the losses increase with decreasing height of the stack. The maximum which is a measure for full penetration is shifted to higher field amplitudes with increasing number of tapes.

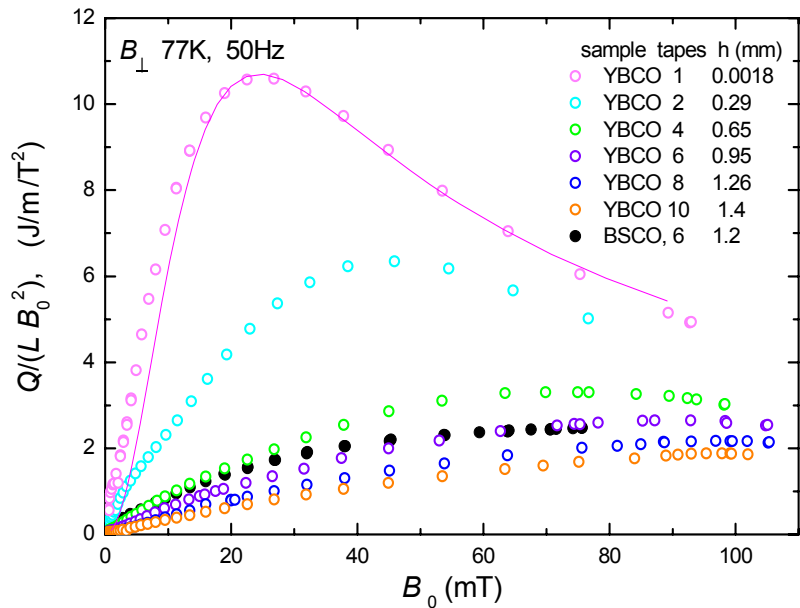


Fig. 3: Losses per unit tape length of stacks of DyBCO and BSCCO tapes

**DyBCO:** tape width 6 mm, sc layer 1.8 $\mu$ m,  $I_c = 120 - 160$  A (THEVA, Germany)

**BSCCO:** 4.3 mm  $\times$  0.24 mm, 55 filaments (untwisted), behaves like a single filament,  $I_c = 105$  A, (American Superconductor - AMSC)

Nomenclature:

$h$ : height of stack,  $Q$ : energy loss per cycle,  $B_0$ : field amplitude: Solid line for 1 tape: fit with Brandt-model, (E. Brandt, Phys. Rev. B 48 (1993) 12893 ;  $c=144$  A (resistively measured: 124 A)

The Brandt model for one tape gives a good fit for the losses. The loss measurement allows determination of the critical current from the position of the maximum,  $B_{\max}$ , of the loss function  $\Gamma \propto Q/B_0^2$  (the function plotted in the Figure 3 is proportional to  $\Gamma$ ).

$\Gamma$  has its maximum at  $B_0/B_c = 2.464$ , with  $B_c = \mu_0 J_c$ , where  $J_c = I_c/d$  is the critical current divided by the tape width. This gives  $I_c = (\pi/2.464 \mu_0) B_{\max} d = 1.015 \times 10^6 \text{ (Vs/Am)} B_{\max} d$ . It is worth to note that the absolute value of losses must not be known.

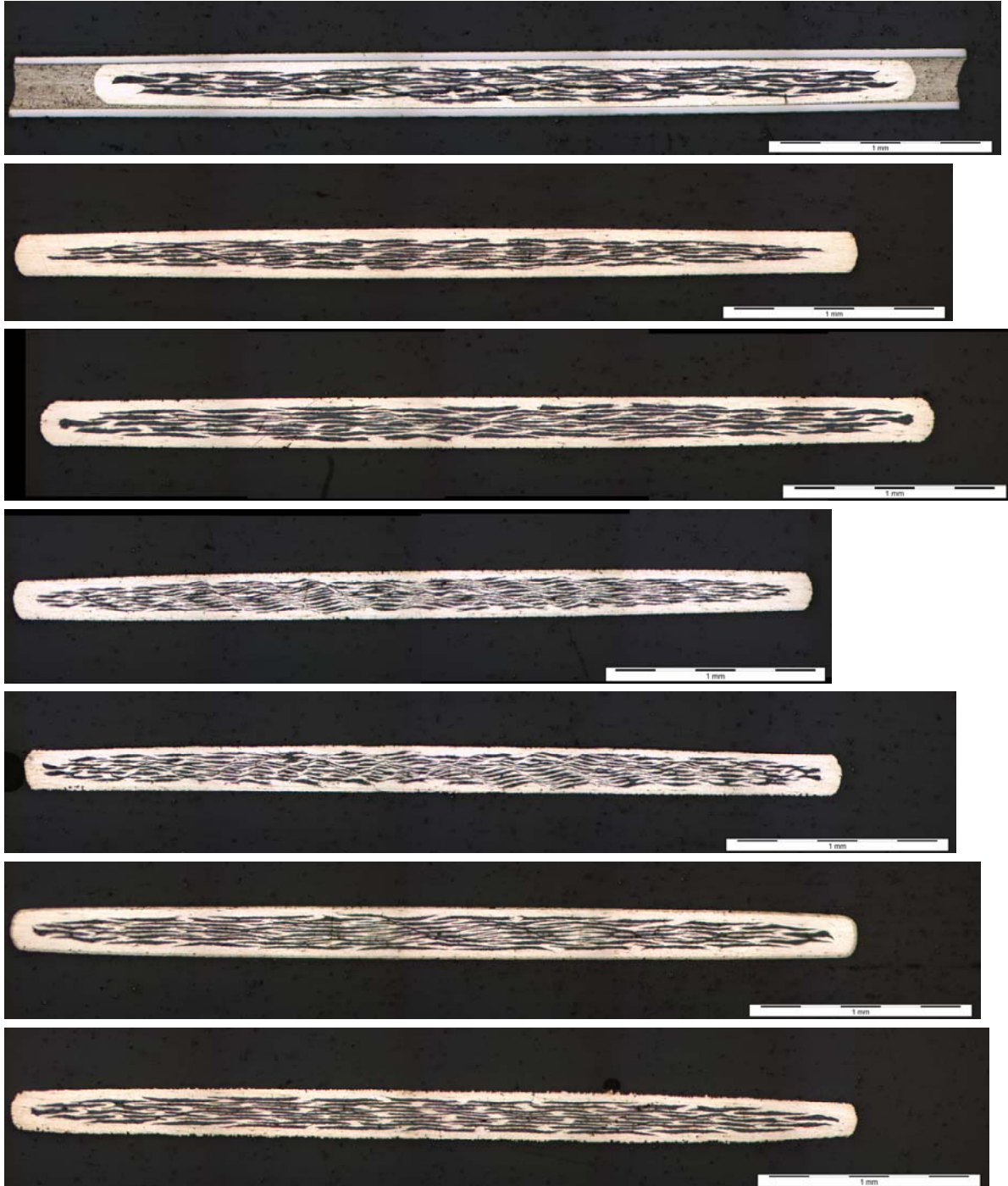


Fig. 4: Sample cross section views from top to bottom.

**AMSC** Steel reinforced ~ 4.78 mm x 0.31 mm, **Sumitomo** High Strength ~ 4.20 mm x 0.23 mm, Bi2223 **Sumitomo** High Ic, ~ 4.46 mm x 0.25 mm, Bi2223 **EAS** CL HTS Tape V388D ~ 4.00 mm x 0.22 mm, Bi2223 **EAS** Standard V375B4 ~ 4.07 mm x 0.22 mm, Bi2223 **Innost** + Sn ~ 4.23 mm x 0.25 mm, Bi2223 **Innost** Standard ~ 4.20 mm x 0.25 mm.

## **Summary**

The procurement of the samples for the task is nearly completed, basic measurements are performed and the goals for the first task period are so far fulfilled.

## **Outlook**

The experimental equipment is actually modified for investigation of the temperature dependent properties of the samples in magnetic fields up to 13 T. AC loss measurement of the YBCO coated conductors are under preparation. A modified version of the DyBCO-CC was ordered from the supplier THEVA to insure an enhanced thermal stability for the current tests at lower temperatures.

## **Staff:**

W. Goldacker  
S.I. Schlachter  
G. Kotzyba  
C. Schmidt  
A. Will  
R. Nast  
B. Ringsdorf  
A. Frank

# **Breeding Blanket HCPB Blanket Concept**



## TTBB-001 Helium Cooled: TBM Design, Integration and Analysis

### TW3-TTBB-001 D1 HCPB TBM System Safety and Licensing

The helium coolant circuit analyses have been continued. The most recent design of the TBM and its associated cooling circuit are modelled. For safety analysis Loss Of Coolant Accidents (LOCA) are the most important ones. Three types, i.e. 'in vessel'-, 'in TBM box'- and 'ex vessel'- LOCA's were investigated. The blow down time now is longer compared to the analyses reported in 2001. This is due to the increased mass in the helium circuit. The consequence is a higher ultimate pressure in the vacuum vessel rising from about 10000 Pa to 26000 Pa which is 1/10 of the maximum allowable pressure for the vacuum vessel.

More interesting is the temperature history of the TBM in case of an ex vessel LOCA. Because in this scenario there is no intrinsic shut down of the plasma the TBM may heat up until evaporation temperature of the beryllium layer on the first wall surface is reached. The time to reach this is typically 250 s for the reference plasma heat load of 270 kW/m<sup>2</sup>. Fig. 1 shows temperature traces in the first wall during such an event. The temperatures in the first wall are high and reach after about 350 s an average value of 900 °C. Therefore it was concluded that even though the mechanical load on the first wall is low, about 0.2 to 0.3 MPa including EM forces, that a rupture of the TBM box can not clearly be excluded. As a consequence after an ex vessel LOCA the plasma must be actively shut down in a time span of 100 s after LOCA. A shut down within 100 s prevents failure also for the hot spot where the local power is 500 kW/m<sup>2</sup>.

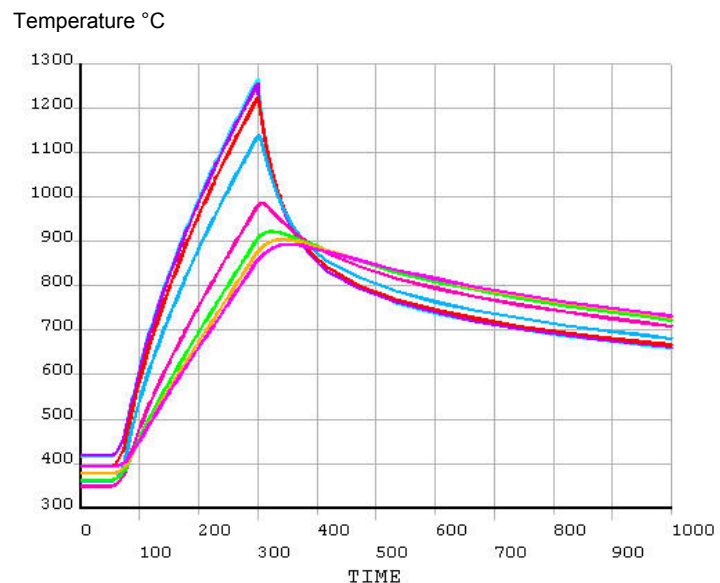


Fig. 1: Temperature traces at different radial positions in the first wall for a heat flux from the plasma of 270 kW/m<sup>2</sup> for 250 s. The cooling is lost at 50 s.

#### Staff:

L. Boccaccini  
B. Dolensky  
M. Ilic  
X. Jin  
R. Meyder  
H. Neuberger  
V. Pereslavitsev  
S. Polixa  
S. Raff  
M. Roccella  
P. Schanz

## **TW3-TTBB-001 D 2**

### **Review of HCPB Blanket Design**

#### **Introduction**

The Helium Cooled Pebble Bed (HCPB) blanket has been a European DEMO reference concept for nearly a decade. While the recent European Power Plant Conceptual Study (PPCS) confirmed that the HCPB built from the reduced-activation ferritic-martensitic steel Eurofer is an acceptable choice of a blanket relying only on limited technological extrapolation, it became clear that the HCPB needs a major review to adapt it to the PPCS plant layout: (i) the selection of an ITER-like modular blanket segmentation required significant changes to the sector (“banana”) segmentation of the previous DEMO regarding blanket box pressurisation and front side access; (ii) the drive to higher blanket efficiency required a review of the thermal layout; (iii) further integration of all in-vessel components within a reactor concept, using modern CAD tools, would be needed for the technological credibility of the plant. In addition, the review was an opportunity to (iv) simplify the blanket by introducing modularity for the breeding zone; and, (v) introduce results from recent breeding blanket R&D.

#### **Results**

A revised design was developed involving new solutions for the First Wall, stiffening of the blanket box by a grid of plates, new design of the back plate and a modular HCPB breeding insert. Furthermore, analysis results were obtained (j) on the neutronic behaviour of the blanket concept, using the plant layout of the PPCS; (jj) on the thermal-hydraulic layout; (jjj) on the structural-mechanical behaviour of the blanket under pressurisation. The new design is an important prerequisite for defining DEMO relevant test blanket modules for ITER, and for future studies on DEMO and power reactors.

#### **Blanket basic configuration**

The basic configuration of the blanket is a sequence of radial layers, i.e. (i) the First Wall, protected by tiles, that removes the substantial surface heat flux; (ii) the breeding zone for Tritium generation; (iii) a shield zone that uses structural and neutron moderator material to achieve the shielding goal set out for the blanket; and, (iv) the in-vessel main piping that supplies the blanket with coolant. As to the poloidal-toroidal segmentation of the blanket, the PPCS selected as reference a modular segmentation similar to ITER.

The coolant used for the blanket is Helium at 8 MPa pressure. The main materials used for the blanket are the Reduced Activation Ferritic-Martensitic (RAFM) reference steel Eurofer for the entire structure. The ceramic breeder material is  $\text{Li}_4\text{SiO}_4$  pebbles and the neutron multiplier is Beryllium pebbles.

#### **Design description**

The modularity of the blanket obtained by the segmentation reduces the characterisation of the breeding blanket to one generic module. The developed blanket module has a rectangular shape and a size of 2000 x 2000 x 800 mm<sup>3</sup>. The blanket module consists of the blanket box and a number of breeder units, which are paced near the plasma at the inside of the box. The blanket box is the primary containment to the blanket functional materials and to the Helium coolant. The actual Tritium breeding takes place in breeder units (BUs) that contain Lithium ceramic and Beryllium pebbles.



## Blanket box

The plasma facing First Wall (FW) of the blanket box and the two neighbouring side walls are formed as a single U-shaped component that is complemented by two caps, and closed by sandwich plates at the radial back. The most significant novelty is a grid of internal stiffening plates (Fig. 2) welded into the box frame that cuts the breeding region into cells and leads to a system of repeating small breeder units of about 20 litres volume. FW, side walls and caps are internally cooled plates, with their cooling channel topology determined by considerations of heat removal – in particular from the First Wall – and of mechanical strength.

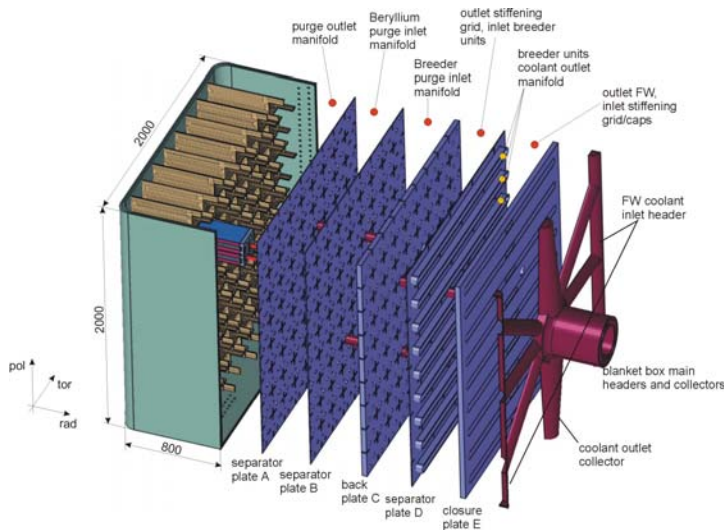


Fig. 1: Blanket box.

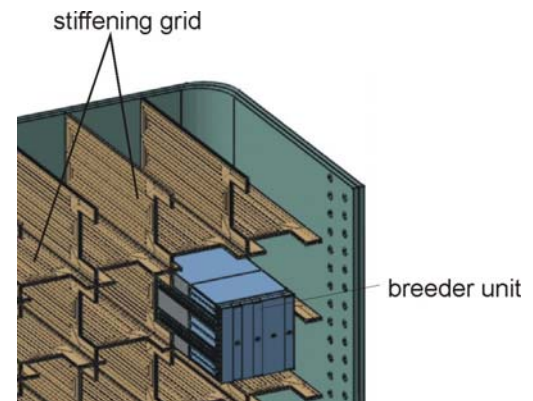


Fig. 2: Detailed view of module box, stiffening grid and breeder unit.

## Stiffening grid

The main justification for using the stiffening grid is a potential internal leak with successive pressurisation of the blanket module. The radial-toroidal and radial-polooidal plates, welded into the box at distances of 216 mm, provide sufficient strength while creating an array of cells for breeder units containing breeder/multiplier materials.

The grid plates have an internal array of meandering cooling channels, fed from the radial back, to remove the heat generated in the steel and the heat transferred from the breeder units. Stiffening grid plates are foreseen to be manufactured by diffusion welding two halves with half channels machined into them.

## HCPB breeder unit

The use of a module stiffening grid creates a cellular structure of the breeding region, with each cell filled by a breeder unit of about 20 litres volume. For the HCPB concept, this breeder unit is based on the principle of pebble beds of Lithium ceramic breeder material and Beryllium neutron multiplier cooled by RAFM steel plates that separate the beds.

The reference design of the breeder unit, see Fig 3, has two double breeder and four multiplier beds separated by cooling plates, with radial orientation of the cooling channels and coolant headers at the radial back of the

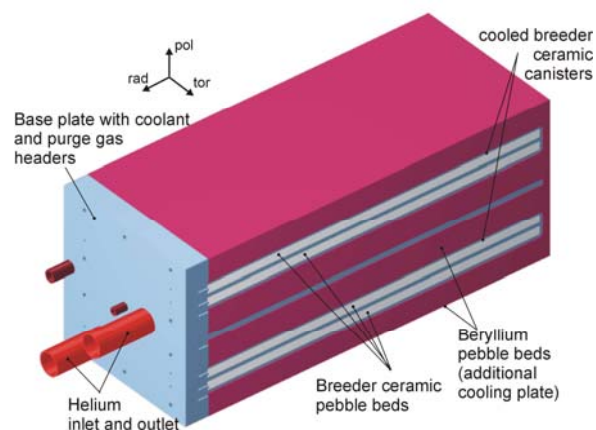


Fig. 3: HCPB breeder unit for PPCS mid-plane neutron wall load.

plates. The calculated temperature distribution under neutron irradiation is shown in Fig. 4.

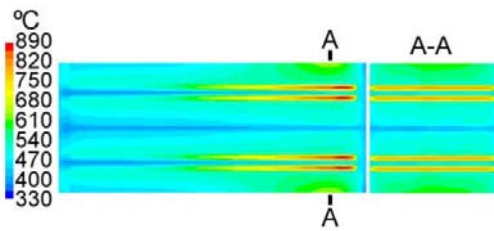


Fig. 4: Temperature distribution in HCPB breeding zone.

### Blanket module cooling lay-out

All manifolds of the blanket boxes are concentrated at the radial back to provide maximum space in the region of high neutron flux to breeder and multiplier materials. This goal is also supported by largely employing short, parallel, radial channels that reach the acceptable pressure drop at a smaller cross section, i.e. less space consumption.

The blanket box cooling is arranged as a three-pass system, see Fig. 5, with the Helium cooling First Wall and side walls in a **first pass**, with alternating flow direction to produce a symmetric temperature pattern in the First Wall; being split up between stiffening grid (75%) and caps (25%) in the **second pass**; and, removing the heat from the breeder units through their cooling plates in the **third pass**.

Using the full mass flow of incoming Helium for the First Wall offers the best chance to keep structural temperatures there below the given limits. For the second pass, the parallel arrangement allows the cap with its FW-like geometry to be used as a by-pass for the stiffening grid, to balance heat removal and pressure drop in the grid.

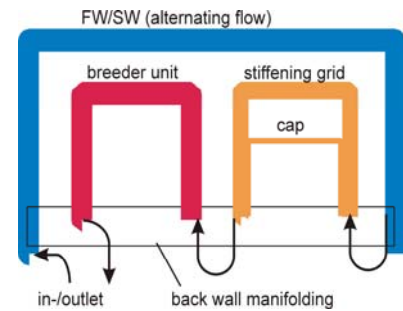


Fig. 5: Three-pass flow scheme of a module's Helium cooling system.

### Blanket module purge system

It is a characteristic of the HCPB concept that the Tritium produced in the ceramic breeder pebble bed is purged by a Helium gas stream and taken to the Tritium plant of the reactor site. In this way, the Tritium partial pressure inside the blanket can be controlled, and Tritium permeation through the hot steel structures and into the coolant gas stream is kept low.

The Beryllium pebble bed is purged, too, to avoid its material from collecting permeated Tritium and building up an inventory. Also, the small amount of Tritium produced by neutronic reactions in the Beryllium needs to be removed when it is released from the pebbles.

### Neutronic performance

The neutronic design analyses are based on three-dimensional Monte Carlo calculations using the MCNP code [2] and nuclear cross-section data from the Fusion Evaluated Nuclear Data Library FENDL-2.

Table 1: Load/power data for model B in the PPCS, and applied to the present study.

Plant fusion power	3300 MW
Mid-plane neutron wall load	2.24 MW/m <sup>2</sup>
Surface heat flux	0.5 MW/m <sup>2</sup>
Local blanket energy multiplication	1.25
Generic HCPB module power	13.2 MW

With a total radial thickness of 46 cm, a neutron multiplication of  $M=1.70$  is achieved for the reference breeder unit. This is sufficient to obtain a TBR of 1.10, 1.12 and 1.14 at a <sup>6</sup>Li enrichment of 30, 35 and 40 at%. The corresponding mass inventories for the entire blanket of the reactor amount to 412 and 147 tons for the Beryllium and the Li<sub>4</sub>SiO<sub>4</sub> breeder, respectively.

With regard to the shielding performance, it was found that the reference BU is superior to the variant with rear breeder canisters. This is due to the fact that Beryllium is a very efficient neutron moderator (high elastic cross-section, low mass) resulting in a better attenuation of the fast neutron flux density than that of variant B ( $3.81 \cdot 10^{13}$  vs.  $4.37 \cdot 10^{13} \text{ cm}^{-2}\text{s}^{-1}$  at the level of the backplate).

### **Conclusions and further work**

A new HCPB blanket box design was developed in a generic way and a lay-out of the Helium cooling system as well as the neutronic analysis and lay-out were done. More detailed analyses will be necessary in almost all areas including design integration to a detailed reactor model, more detailed analyses of the complex cooling system with its manifolds and collectors, the detailed development of the tritium system and an efficient pebble bed filling strategy. Also thermal mechanical analyses have indicated the need for some design modifications to reduce peak stresses. No detailed thermo-mechanical model was applied to determine the behaviour of the pebble beds in a breeder unit yet, whereby also transient conditions have to be studied in the future. The structural integrity of the blanket will have to be analyzed also in case of high electromagnetic forces due to plasma disruption events.

### Staff:

U. Fischer  
S. Hermsmeyer  
C. Koehly  
J. Rey  
Z. Xu

### Literature:

- [1] Z. Xu and S. Hermsmeyer, Thermal-hydraulic analysis and optimization of breeder unit for EU helium cooled pebble bed blanket, Fusion Engineering and Design, Volumes 75-79, November 2005, Pages 785-788
- [2] U. Fischer, P. Pereslvtsev and S. Hermsmeyer, Neutronic design optimisation of modular HCPB blankets for fusion power reactors, Fusion Engineering and Design, Volumes 75-79, November 2005, Pages 751-757

## TW4-TTBB-001 D 1 Detailed Design of the First ITER EM-TBM-Module

### First wall

The first wall of the ITER EM-TBM is exposed to a heat load of 100 kW/m<sup>2</sup> on the average and 300 kW/m<sup>2</sup> peak; while the subsequent modules e.g. the Plant-Integration (PI) module must withstand an average heat load of 270 kW/m<sup>2</sup> and a peak of 500 kW/m<sup>2</sup>. Even though the difference is significant it was decided that there will be no special design of the first wall for the EM module. In 2004 the FW design has been developed, however, the analyses for this design did not show in all respects the desired safety margins. Therefore a further more detailed analysis was initiated for the first wall cooling.

### Achievements

For the thermal analysis of the first wall we use a Heat Transfer Coefficient (HTC) depending on the distance from the inlet and a bulk temperature, this method we call Averaged Heat Transfer Model (AHTM). The transfer coefficient can either be found using a classical formula as proposed in Kakac [1] or can be calculated from the results of a 3 dimensional simulation using a k-e turbulence models of computer codes like STAR-CD or CFX. For extraction of the coefficient a the following formulas are to be used:

$$\alpha = \frac{\langle q_w \rangle}{\langle T_w \rangle - \langle T_B \rangle} \quad (1)$$

where:

$$\langle q_w \rangle = \frac{1}{a_w} \int q_w da$$

denotes heat flux averaged over the wall surface, ( $a_w$ ),

$$\langle T_w \rangle = \frac{1}{a_w} \int T_w da$$

represents averaged wall temperature and

$$\langle T_B \rangle = \frac{\int \rho u T_f da}{\int \rho u da}$$

stands for the so-called bulk fluid temperature, i.e. the fluid temperature averaged over the fluid cross section  $a_c$  assuming constant specific heat. Local fluid density, velocity and temperature are denoted by  $\rho$ ,  $u$  and  $T_f$ , respectively. To obtain the distribution of HTC along the channel the averaging procedure is done for entities of mesh cells contained within one numerical grid step in the direction along the channel.

Three dimensional numerical simulations have been performed for one first wall channel using the STAR-CD code. Parameter was the distribution of the heat load. Three cases have been considered i) modelling of the fluid only, heat load homogeneous on the perimeter, ii) modelling of the fluid only, heat load on one side, i.e. from the plasma and iii) modelling coolant channel steel wall and fluid, heat load on the plasma side of the steel structure. The resulting temperatures in the fluid are shown in Fig. 1, taken at 1.6 m from the inlet. It is clear from these temperature fields that there must be also some effect on the HTC's if they are evaluated using equation (1). This is shown in Fig. 2, left. We see that the homogeneous heating case i) gives the best coefficients followed by cases iii) and ii). I.e. the longer the pe-

rimeter participating on the heat transfer the higher the coefficient. The green line indicates the HTC that would be found using the classical formulas as proposed in [1]. On the right hand side in Fig. 2 the effect of surface roughness of the coolant channel is given. The blue box symbols are corresponding curves in both diagrams. The slight difference is due to a change in channel corner radius from 2 mm left to 4 mm on the right.

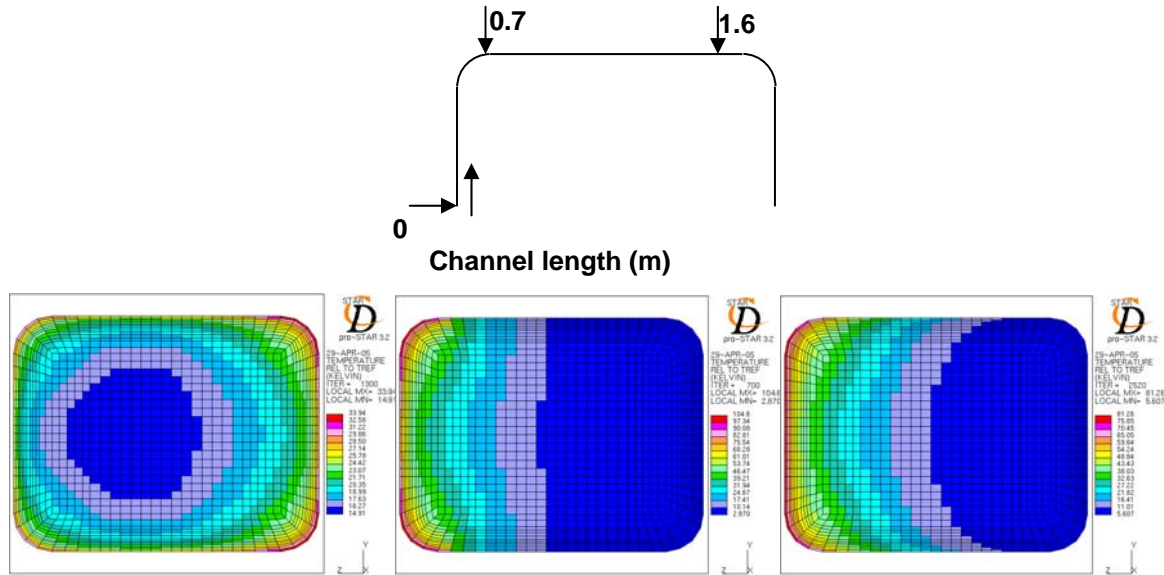


Fig. 1: Fluid temperatures in a first wall channel for different heat flux distribution on the wetted perimeter.

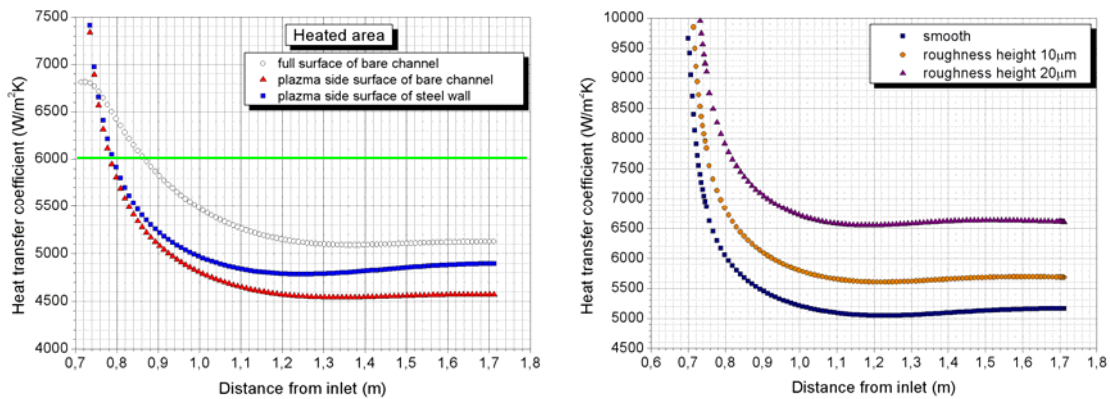


Fig. 2: HTC along the plasma facing portion of a first wall channel, left: Smooth channel, different heat loads; right: Different surface roughness.

These results show that the distribution of the heat flux on the perimeter and the roughness of the channel surface are important for the averaged HTC, moreover for a smooth channel lower HTC's are found in the simulation compared to classical HTC formulas.

Having determined the HTC from the numerical flow simulation the question arises whether the coefficient found leads in the AHTM to the same temperature field in the structure as in the STAR-CD simulation. This question was investigated with a separate 2D model where in one case the local heat transfer conditions were prescribed along the wetted perimeter and in the other only a bulk temperature and a HTC. It turned out that there are differences and therefore corrections are needed. To recover the temperature gradient across the channel a factor was determined; to meet the temperature level a term of sum was determined. Both data are shown in Fig. 3. We see there that the factor around 0.7m channel length, is 1.1 and

at 1.6 m 0.75. This can be interpreted as the effect of a developing flow being initiated by the bend. While the correction of the HTC can easily be applied, correction of the bulk temperature can only be done at the inlet, leading to some inevitable error along the channel, but this must be tolerated and taken into account while evaluating the material properties of the steel.

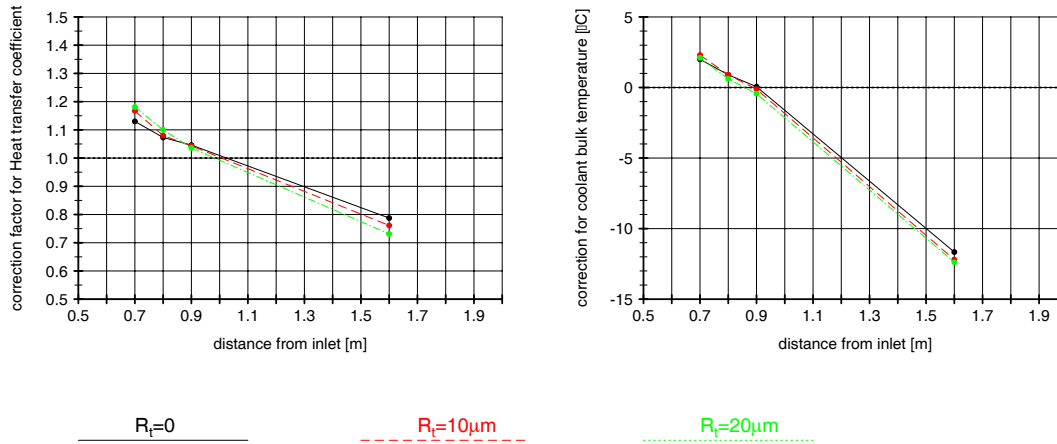


Fig. 3: Corrections for HTC (left) and bulk temperature (right) to achieve in the channel walls the temperature field of the direct simulation.

### Conclusions

Application of the results outlined above to the analysis of the FW gives almost the same as have been achieved in earlier investigations, but the assumptions are now on a sound basis.

### Breeding units

The design of the TBM breeding unit (BU) has been updated in 2005 corresponding to the new design in DEMO. Because the neutron power in ITER is lower than in DEMO only two breeding canisters will be installed in the breeding units for the EM and PI modules. This leads to higher beds and finally in the PI module to the desired temperatures in the pebble beds. Instead of beryllium or ceramic pebbles the fill is made from glass pebbles. This decision allows performing a heat treatment of the TBM even with installed pebble beds. Using glass pebbles is no disadvantage because of the lack of neutrons for the EM module only the inertia of the bed is important to be simulated. As there are no neutrons also the breeding canisters will be simplified. Only one or two breeding units will be equipped with canisters having cooling plates with internal channels, the others will be made by simple dummy steel plates having the same mass and volume as a regular cooling plate.

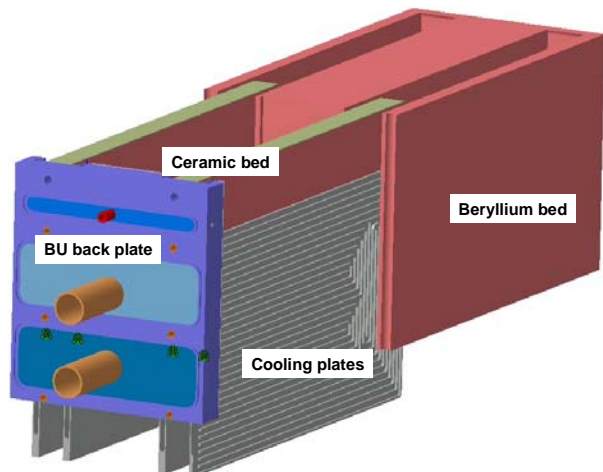
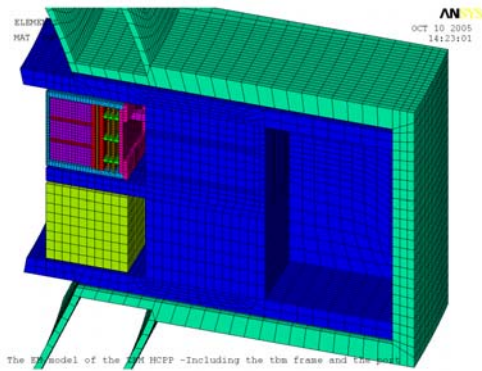


Fig. 4: Breeding unit for the PI module.



### Attachment of the TBM to the port plug

Loads on the TBM caused by plasma disruptions will be determined based on a method developed by Roccella [2] an ANSYS model of the TBM, of the port plug and of the adjacent vacuum vessel has been set up, see Fig. 5. This model will be used to determine the forces in the TBM, especially at the attachment and the pipes connecting the TBM and the ITER systems.

Fig. 5: Meshed model of the TBM environment to perform electro magnetic analyses.

### Staff :

L. Boccaccini  
B. Dolensky  
M. Ilic  
X. Jin  
R. Meyder  
H. Neuberger  
V. Pereslavitsev  
S. Polixa  
S. Raff  
M. Roccella  
P. Schanz

### Literature:

- [1] Kakac, S., Shah, R.K. and Aung, W., Handbook of single-phase heat transfer, John Wiley & Sons, 1987
- [2] Roccella: private communication

## **TW4-TTBB-001 D 2**

### **Review of the Material Data Base and Assessment Reports for the Breeder and Multiplier Materials for the HCLL and HCPB Concept**

#### **1. Objectives**

In the Material Data Base Report (MDBR) and the Material Assessment Report (MAR) all available irradiated and non-irradiated material properties including the physical and chemical properties of the breeders and multipliers used in the HCPB and HCLL blanket concepts are to be compiled in order to provide an up-to-date database for design purposes and the evaluation of the material grade. The revision of these documents is necessary to take into account the new results of the current R&D.

#### **2. Work performed**

The previous versions of the MDBR and the MAR date from the year 2001. In the mean-time significant progress has been achieved in several areas.

The MDBR contains material data, at present recommended to be used for design purposes. It consists of a collection of independent chapters, which are provided by individual specialists in the EU in their fields of expertise. For the revision of the MAR, these data should be available as a basis. These data and those where the database at present is not equally validated are compared in order to indicate where future R&D work is required and/or to give support for future selections of reference materials.

A new version of the MDBR has been compiled for

- $\text{Li}_4\text{SiO}_4$  pebbles/pebble beds,
- $\text{Li}_2\text{TiO}_3$  pebbles/pebble beds, and
- beryllium pebbles/pebble beds.

Because some of the contributions from the EU specialists were not available in time, some sections do not contain updated data.

The MAR has been reviewed substantially, new data have been taken into account also in most of those cases where new MDBR contributions were not available. The new MAR versions reflect the present status on

- beryllium pebbles/pebble beds,
- ceramic breeder pebbles/pebble beds

for the EU HCPB Test Blanket Module,

and on

- Pb-17Li

for the EU HCLL Test Blanket Module.

The work has been documented in the Final Report [1]; for easier use, the data are also available as separated documents [2-5]. These documents have been sent to EFDA.



### 3. Conclusions

With the delivery of the Final Report, the Subtask TW5-TTBB-001-D2 has been terminated. However, especially, the MDBR should be considered as a data base which has to be updated whenever new data become available. This task should be performed within a new subtask within the EU blanket activities.

#### Staff:

R. Knitter  
G. Piazza  
J. Reimann

#### Literature:

- [1] J. Reimann, R. Knitter, G. Piazza, Final Report on "New Compilation of the Material Data Base and Material Assessment Report", EFDA reference: TW5-TTBB-006 D3, Nov. 2005, FZK Internal Report, Nov. 05.
- [2] J. Reimann, R. Knitter, G. Piazza, Material Assessment Report on Ceramic Breeder Pebble Beds for EU HCPB Test Blanket Module, Internal FZK Report, Oct. 05.
- [3] J. Reimann, Material Assessment Report on Beryllium Pebble Beds for EU HCPB Test Blanket Module, Internal FZK Report, Oct. 05.
- [4] J. Reimann, Material Assessment Report on Pb-17Li for EU HCLL Test Blanket Module, Internal FZK Report, Oct. 05.
- [5] J. Reimann, Compilation of Material Data Base Report on Ceramic Breeder and Beryllium Pebble Beds for EU HCPB Test Blanket Modules, Internal FZK Report, Oct. 05.

## **TW5-TTBB-001 D 1**

### **Design and Analysis for the HCPB TBM including Design of Supporting System, Connections and Instrumentation Integration**

In the frame of this task, the structural integration of the TBM in the ITER systems, as well as the integration of the basic instrumentation into the TBM have been investigated. Additionally the requirements for the integration of the TBM auxiliary systems were adapted to the integration needs.

#### **1. Structural integration of the TBM in the ITER systems**

The structural TBM integration sequence can be subdivided into the following three independent main steps:

- Hot cell operations / TBM integration step 1  
TBM integration step 1 comprises the integration of the TBM into the port plug inside the hot cell and includes the following steps operations:
  - Mechanical attachment of the TBM to the port plug
  - Connection of the TBM supply pipes to their extension through the port plug
  - Connection of the TBM instrumentation lines to the interface plug
- ITER standard procedures / integration step 2  
The TBM integration step 2 comprises all the standard operations which are used for all port plugs in ITER in a similar way. These operations combine the following:
  - Connection of the port plug to the hot cell mounting port before TBM installation
  - Removal of the port plug from the hot cell mounting port after TBM installation
  - Transfer of the port plug from the hot cell to the port cell and back
  - Connection of the port plug to the vacuum vessel before the TBM- campaign starts
  - Removal of the port plug from the vacuum vessel after the testing campaign is complete
- Port cell operations / integration step 3  
TBM integration step 3 is the installation of the TBM integration equipment inside the port cell and the connection of the TBM to its sub systems.

All working steps for TBM integration and exchange are executed as remote handling operations without human access. The TBM removal comprises the same operations used for TBM integration but in inversed order.

#### **1.1 Starting situation of this task**

At the beginning of this task the operations for the integration of the TBM into the port plug inside the hot cell of the ITER building were based on a port plug concept designed by FZK. This concept was designed under the assumption that exclusive rear access is used for the tools which are required to connect the TBM to the port plug.

End of 2004 a concept for the TBM integration in the port cell was introduced which allows limiting the number of interfaces for the TBM supply lines inside the port cell to two. This is possible by combining all port cell equipment into one assembly which is called Port Cell Integration Cask (PIC). The PIC has the same outer dimensions like the ITER transfer cask and is located inside the port cell during reactor operation only. But further investigations were required to check whether the systems are compatible to the ITER environment.

## 1.2 Achievements

### Hot cell operations / Integration step 1

In the course of discussions with ITER it turned out that the design of the port plug is the responsibility of ITER. Currently two different concepts of port plugs are discussed. One concept is similar to the FZK design suggestion of the port plug (see figure 1) while the other foresees the removal of the TBM including the shield of the port plug as hot cell operation, which gives more flexibility for operations during TBM exchange. Therefore the design of the port plug influences the operations for TBM integration inside the hot cell significantly. Especially the welding operations for the connection the TBM to its supply lines are dependent on the port plug design. Therefore the impact of the integration of the TBM instrumentation to the hot cell operations was investigated. Further hot cell operations will be further developed after it is decided which port plug concept is chosen.

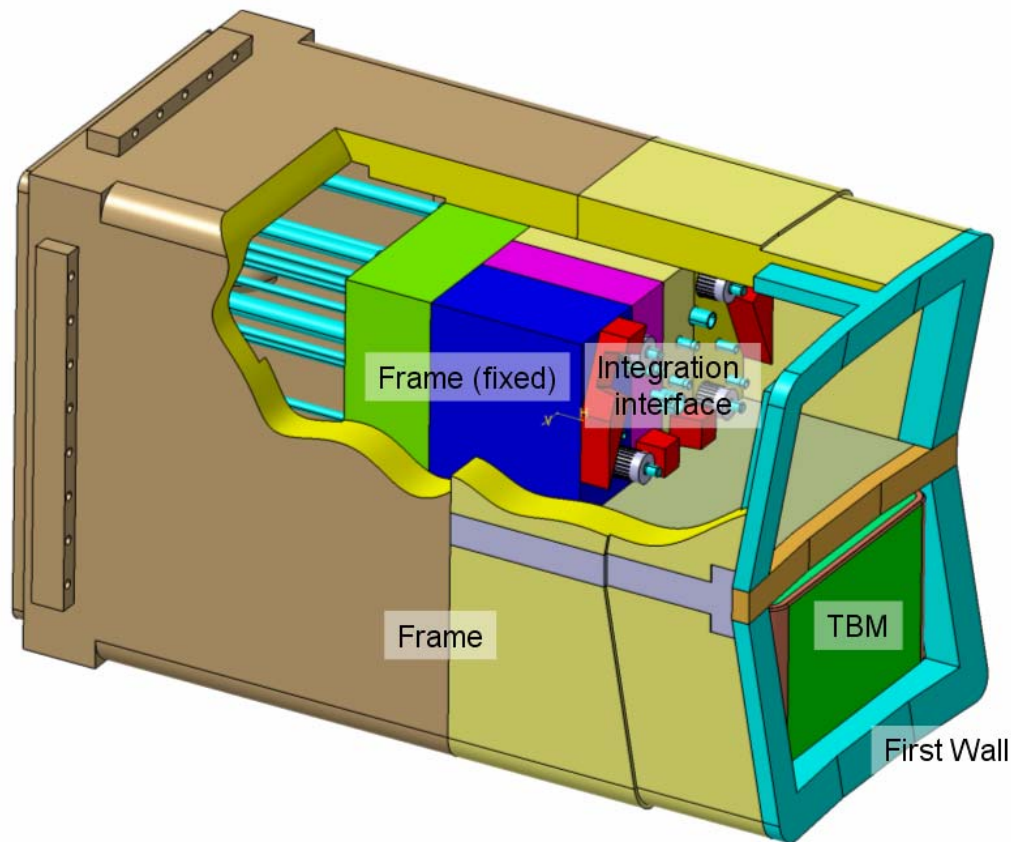


Fig. 1: FZK design suggestion of port plug.

Figure 2 shows the concept for the integration of the TBM instrumentation lines. The sensing lines penetrate the port plug shield inside of an instrumentation pipe which is part of the TBM. After the TBM is connected to the port plug the gap between the instrumentation pipe and the port plug shield is sealed by a bellow. Subsequently the sensing lines protruding the instrumentation pipe of the TBM are connected separately to a multi pin plug at the rear side of the port plug flange. This plug is compatible to another multi pin plug mounted on the PIC at interface 2 to allow a quick and simple connection of the TBM sensors to the DAS.

### Port cell operations / integration step 3

The system for the TBM integration inside the port cell using the PIC was further detailed and investigated with regard to its compatibility with the ITER environment. Figure 3 shows the TBM installed inside the port plug which is connected to the vacuum vessel while the TBM cooling and purge system is completely integrated into the ITER circuits. The interface 2 in front of the PIC and interface 3 behind the PIC are indicated, as well as the TBM supply lines

at the side wall and the ceiling of the port cell which lead to the TBM sub systems outside the cryostat. Figure 4 shows the PIC in detail indicating the main components of the PIC.

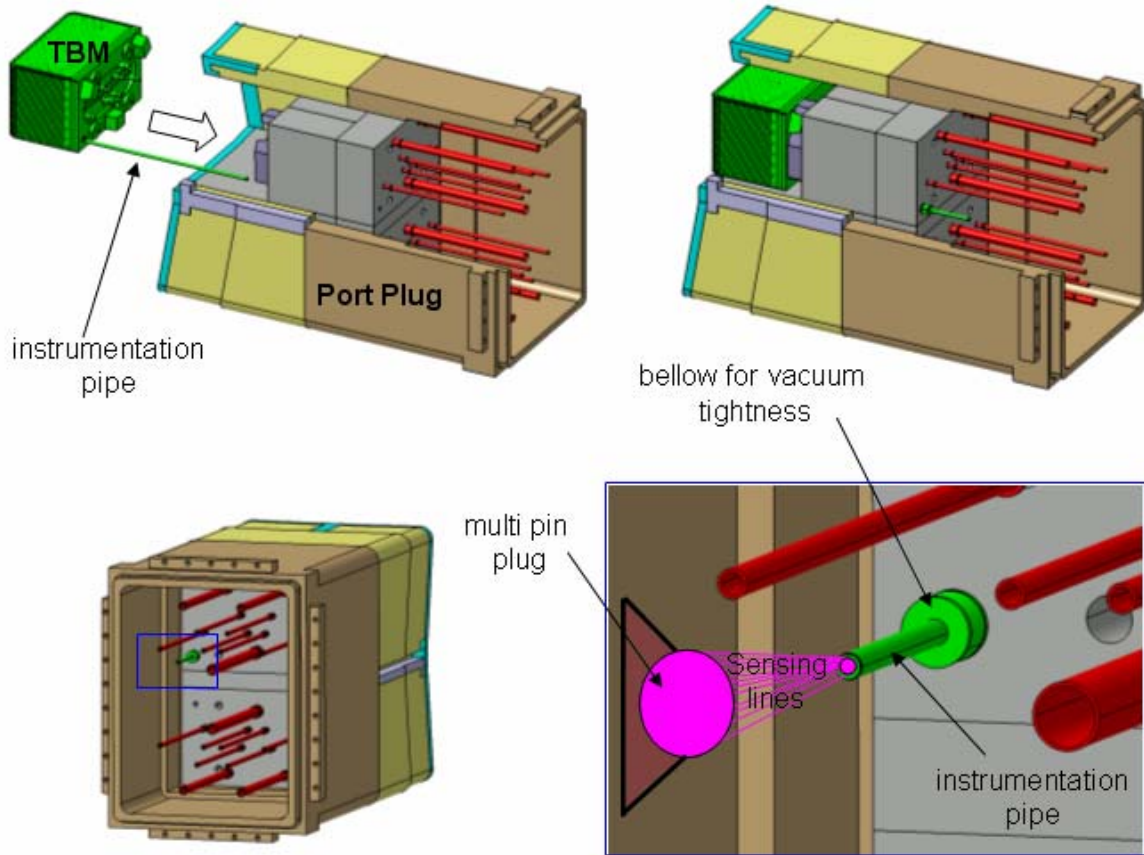


Fig. 2: Integration of TBM instrumentation into port plug.

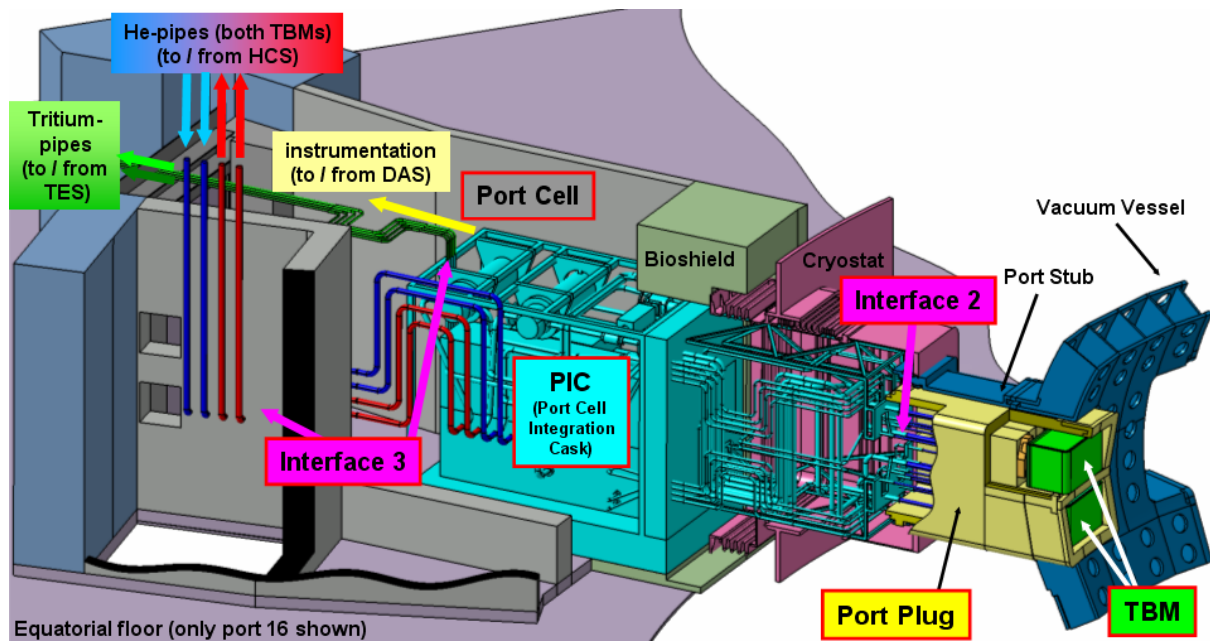


Fig. 3: Port cell with TBM integrated into ITER systems.

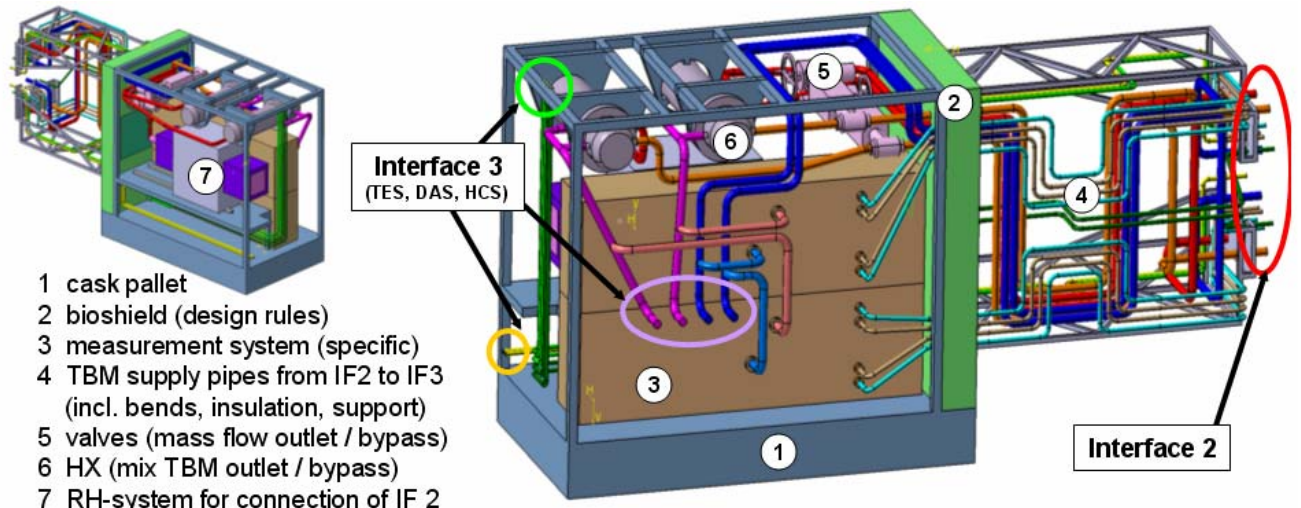


Fig. 4: Port Cell Integration Cask.

### 1.3 Conclusions

In order to design the hot cell operations for the integration of the TBM into the port plug a decision is required whether the port plug design allows rear access only, or if side access is an option.

To give a reliable statement about the space situation inside the port cell, further investigation concerning the PIC is needed. Therefore the following points require detailed investigation:

- Space requirements of measurement systems inside the port cell must be detailed
- Requirements for gas mixer inside the port cell have to be clarified
- The piping of PIC has to be detailed with regard to flexibility and thermal insulation
- Bio shield design has to be improved according to shielding requirements
- Compatibility of interface 2 pipe arrangement to orbital tools has to be checked

It can be concluded that the concept using the PIC is the most simple and quick way for TBM integration. Discussion with ITER revealed that the system of the PIC shown here is compatible with the port cell environment in general.

## 2. Integration of basic instrumentation into EM-TBM

The mechanical integration of the basic instrumentation in the EM-TBM design has been carried out. Thermocouples, pressure and velocity transducers, as well the specific instrumentation for the EM-TBM (e.g. B-flux coils and Rogowski coils) will be integrated in the system. Modifications of the design will be accomplished according to the measurement needs.

### 2.1 Starting situation

At the beginning of 2005 the mechanical design of the EM-TBM was already advanced while the instrumentation has not been taken into account in detail at this stage of development. Neither the requirements on EM-TBM instrumentation for the performance of required measurements have been investigated nor the mechanical integration of sensors during the TBM manufacturing process has been considered.

Consequently the development based on the inclusion of an instrumentation pipe for the routing out of all sensing lines from the TBM. This instrumentation pipe is located at a corner of the TBM and the inner diameter of the pipe is supposed to be 30 mm.

## 2.2 Achievements

In the frame of this task the instrumentation of the EM-TBM has been subdivided into two different groups:

- TBM basic instrumentation
- Sensors for objectives of EM-campaign

The TBM basic instrumentation consists of sensors for system monitoring which are used for checking if the system parameters (temperatures, pressures etc) are within prescribed values. Additionally instrumentation for signaling acceptability to operate or to shut down including a connection to an ITER supervision system will be required. The TBM basic instrumentation will be designed to be suitable for all TBM campaigns which are foreseen in the ITER schedule. Contrary to the basic instrumentation the sensors which are used exclusively for objectives of the EM- campaign (such as devices for current and strain measurement) are designed for the respective environmental conditions (absence of neutrons during H-H-phase plasma).

Additionally the concept of integrating the instrumentation pipes into the port plug has been detailed while it has been estimated how many sensing lines can be integrated into one pipe with an inner diameter of 30 mm. Figure 5 shows a cross section through the port plug while the TBM including its measurement systems is already installed.

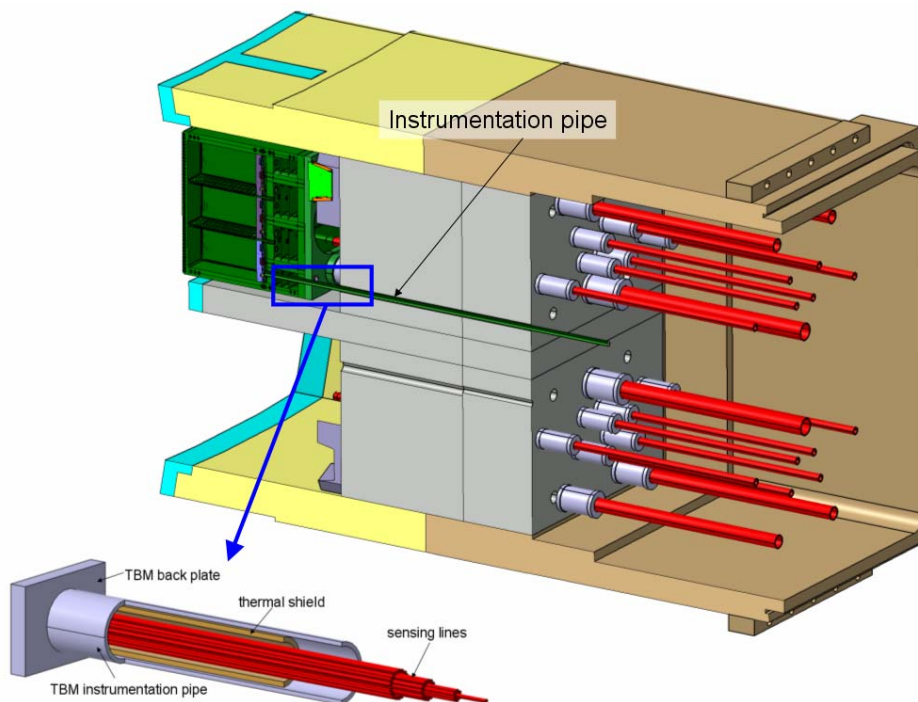


Fig. 5: TBM including instrumentation installed into port plug.

Furthermore principles of measurement were investigated which could be used for the acquisition of the different magnitudes. Additionally possibilities for location of sensors inside the TBM were investigated.

The strategy for the integration of the sensors during the manufacturing of the TBM is an additional achievement of this task. Thereby a concept was worked out which describes the

integration of the instrumentation step by step. Figure 6 shows different steps of the TBM manufacturing process where sensors are integrated.

Finally additional equipment for the integration of the measurement systems such as feedthroughs, measurement cables and data acquisition components were investigated.

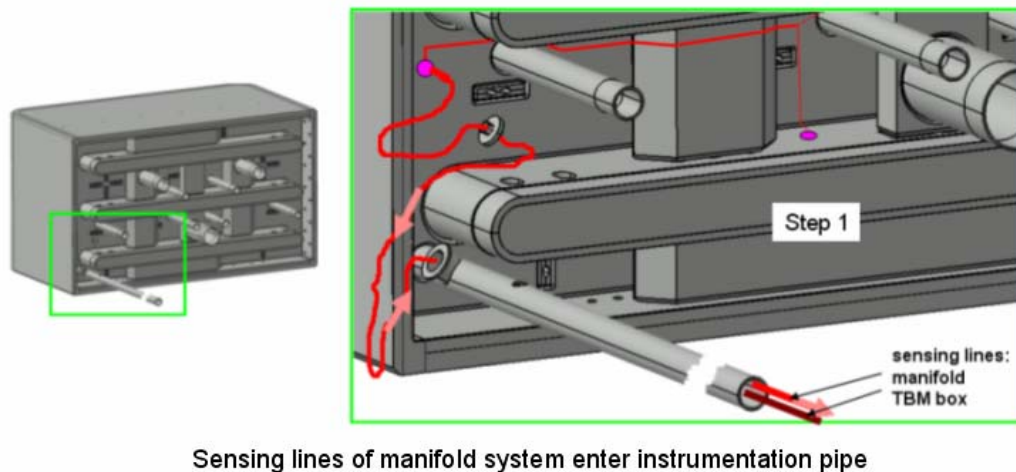
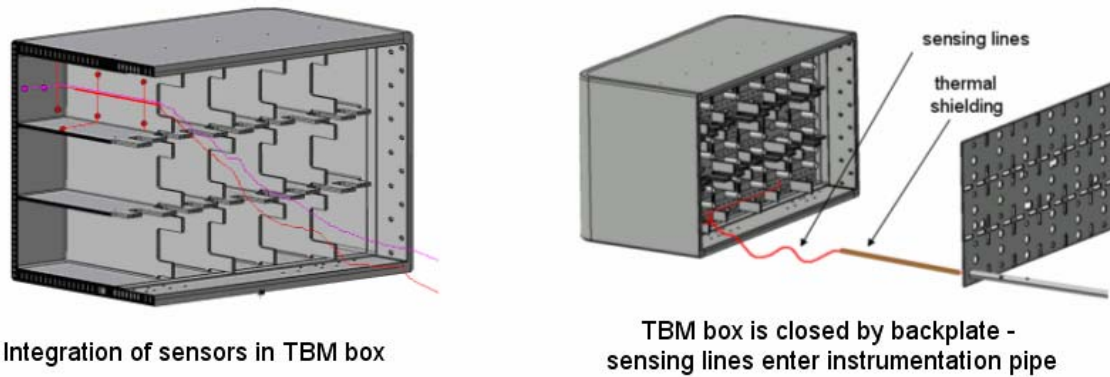


Fig. 6: Steps in sensor integration during TBM manufacturing.

## 2.3 Conclusions

In order to meet the requirements during the EM campaign the TBM instrumentation has to be designed in detail with regard to sensor quantity and location.

However the mechanical integration of the sensors including their sensing lines is quite complicated. It has to be checked if it is possible to increase the number of sensing lines for the EM-TBM by using an instrumentation pipe with a bigger diameter. Another possibility to increase the quantity of sensing lines is to use more pipes for the accommodation of instrumentation lines.

Additionally requirements have to be defined regarding the shielding of the sensors and sensing lines from effects like transient magnetic fields which might affect the measurement results. Therefore experiments at a suitable test facility may be useful.

### 3. Integration of the TBM Helium Coolant System in ITER

The auxiliary systems belonging to the HCPB TBM Concept have been verified according to the ITER requirements. The design of these systems has been verified and updated according to space limitations, piping layout and operating conditions of ITER and TBM. In particular the Helium Coolant System (HCS) the general layout has been validated while taking into account the component technology (cold compressor).

#### 3.1 Starting situation

This task bases on the assumption that primary heat removal Helium loop is arranged in an 8-shaped loop because of the very limited temperature which is allowed at the Helium circulator due to design restrictions. Figure 7 is a schematic drawing of the Helium loop.

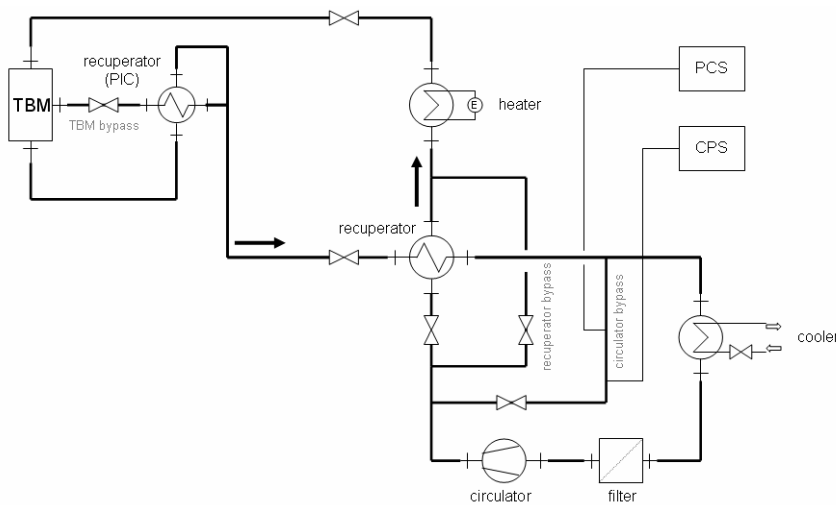


Fig. 8: Helium cooling loop.

The space which has been provided for the components of the HCS by ITER is shown in figure 8 where the location of the HCS may be changed. The reason therefore is that meanwhile port 16 is used for accommodation of the HCPB-TBMs. The space which will be provided for the HCS inside the vault is pointed out as 7.4m x 2.5m x 5m (height).

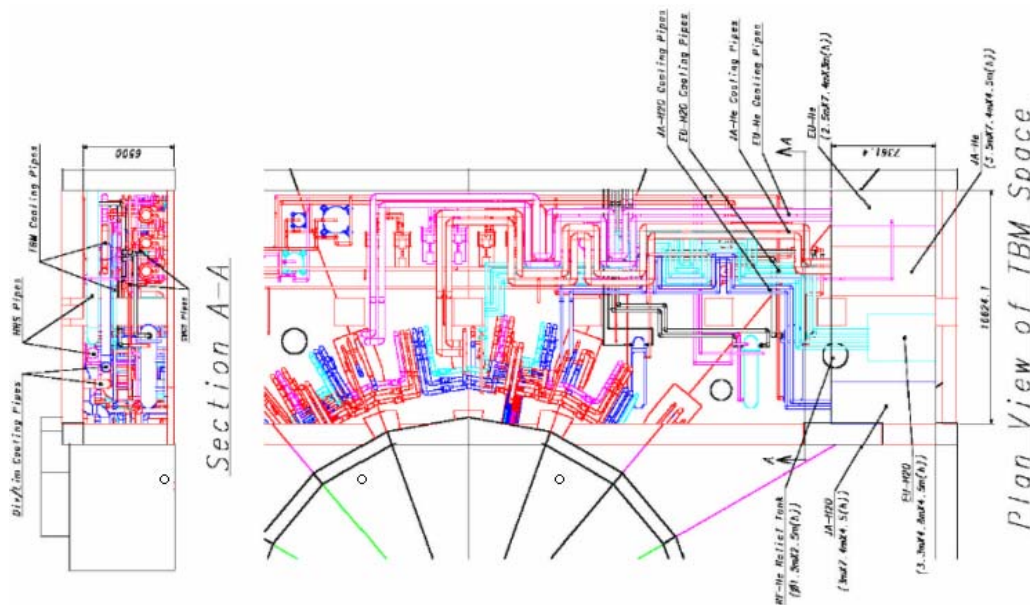


Fig. 8: Layout of the vault.



### 3.2 Achievements

In the course of the discussions about the space which is foreseen for the HCS in the TCWS-vault of ITER, the space requirements of the primary cooling loop were investigated in detail. To get a first impression about the real space situation inside the vault, a CATIA-model of the HCS was made based on the assumption that the HCS for ITER uses the same components than HELOKA (figure 9). But the model does not include the following equipment and components which are essentially:

- Thermal insulation of pipes
- Coolant Purification System (CPS)
- Tritium Extraction System (TES)
- Pressure Control System (PCS)
- Helium storage tank (required during maintenance of loop)
- Space for maintenance/replacement operations (components)
- Electrical control cabinets

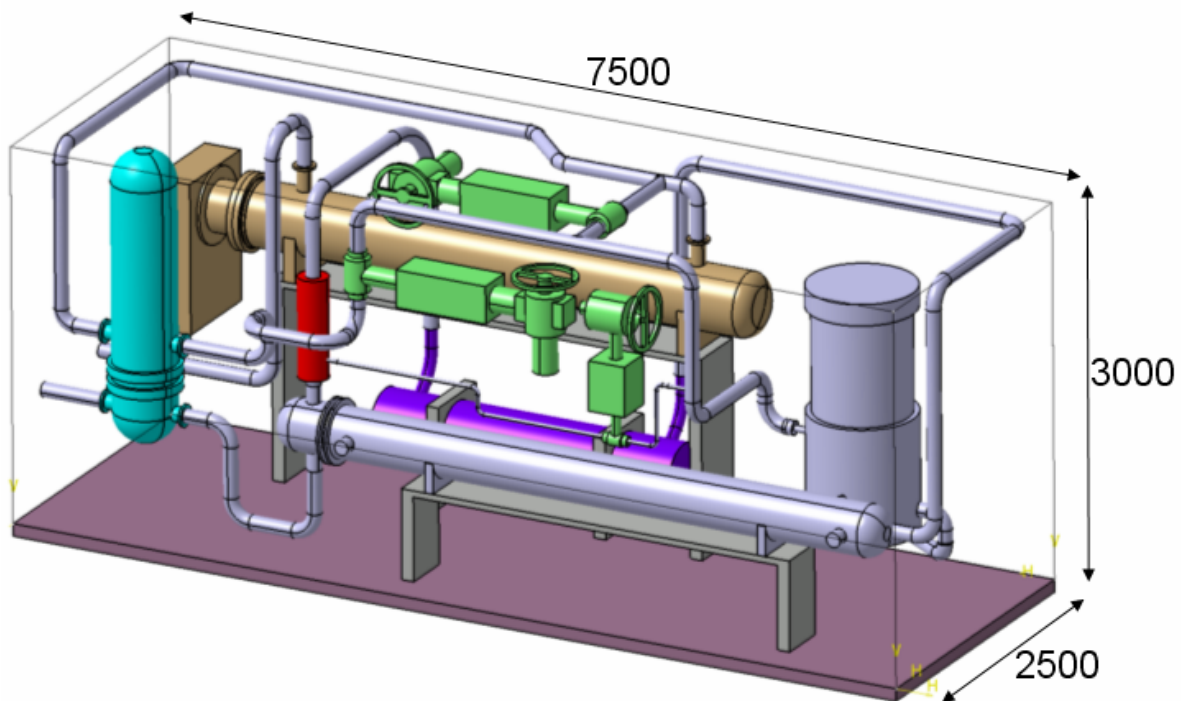


Fig. 9: CATIA-model of the HCS (PCS not included).

The TBM Helium Cooling System in ITER has to provide different operational states according to the requirements of the respective TBM campaign. Additionally some states are required exclusively for TBM exchange and preparation of a new TBM for plasma operation. All of these operational states have been investigated regarding the system behaviour. Figure 10 shows the Helium loop during plasma operation with TBM inlet temperature of 300°C.

Additionally the space requirements for the Pressure Control System (PCS) were investigated.

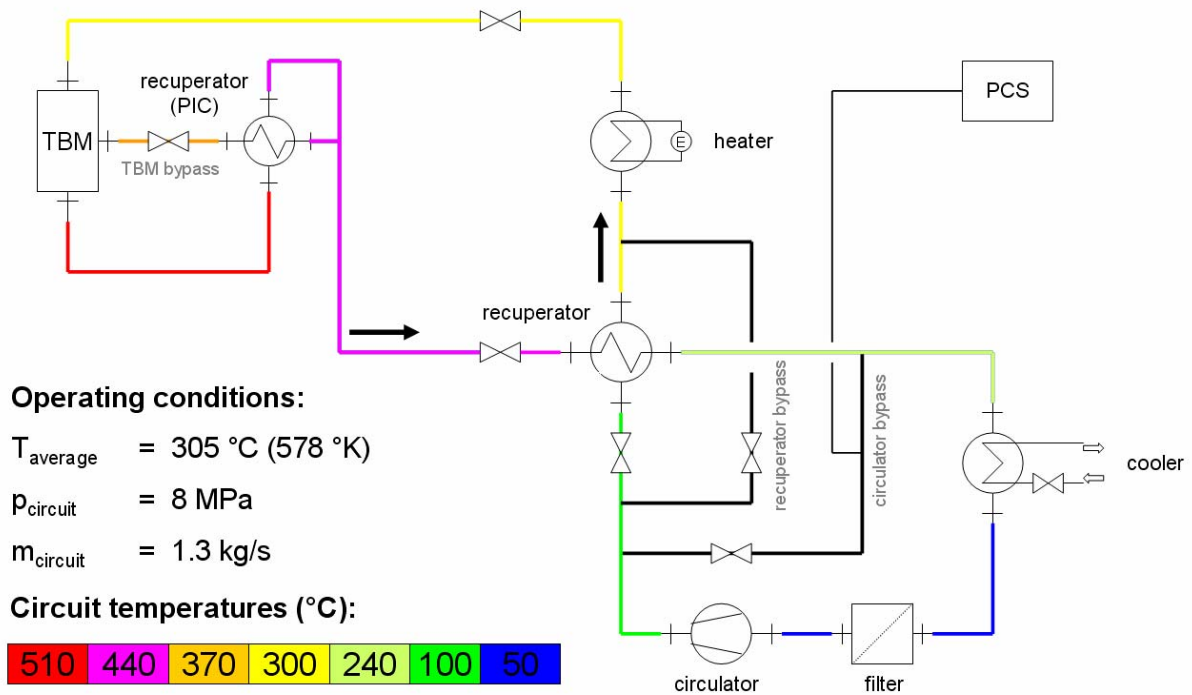


Fig. 10: Plasma operation during TM-campaign.

### 3.3 Conclusions

Currently the allocated space for the HCS inside the TCWS-vault is very limited. A possible alternative is to design one common cooling loop which provides cooling capacity to all helium cooled TBMs. This option requires, however, a detailed analysis in co-operation with concerned partners.

Regarding the PCS it can be concluded that it should be checked if the impacts on the HCS are tolerable when the PCS is neglected. Therefore an additional analysis using RELAP will be required.

#### Staff:

R. Meyder  
H. Neuberger

#### Literature:

- [1] Integration of the EU-HCPB TBM system in ITER, Presentation, JKT, Nürnberg
- [2] Integration of the EU-HCPB-TBM in ITER, Poster, ISFNT7, Tokyo

## TW5-TTBB-001 D 2 Detailed Design of Sub-components and Prototypical Mock-ups for the HCPB TBM Qualification

The progress in the design of the TBM requires starting to test the design with some experiments. A series of tests mock up's have been considered:

- a) In order to investigate the heat transfer in the first wall the HETRA (Heat TRANSfer) experiment will be performed simulating one cooling channel of the first wall. To simulate the plasma heat flux a ceramic heater will be placed on the surface of the first wall and to cope with the heat losses a highly insulating material will be used to enclose the test tube. Most emphasis will be put on the measurement of structural temperatures, in addition the coolant state and mass flow rate will be determined.

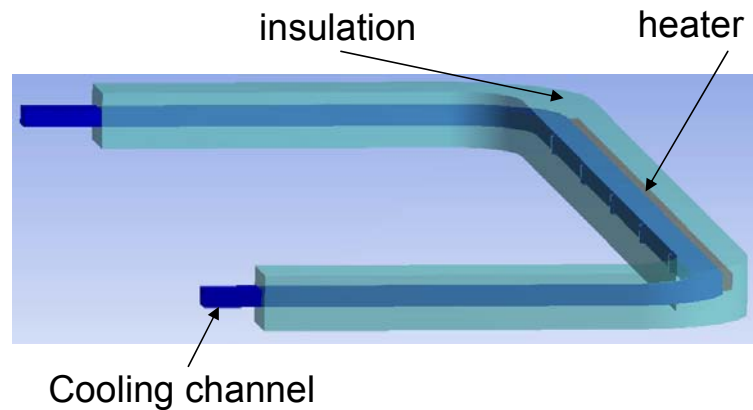


Fig. 1: HETRA test section to investigate the heat transfer in the first wall.

- b) In order to investigate the mass flow distribution in the parallel channels of the stiffening grid and the caps between manifold 2 and manifold 3 the GRICAMAN experiment (GRId Cap MANifold) will be performed. In principle there are two large volumes (manifolds) connected by about 45 individual complicated shaped channels. To get access to the flow in the manifolds the flow in the channels must be simulated. While the correct channel geometry can

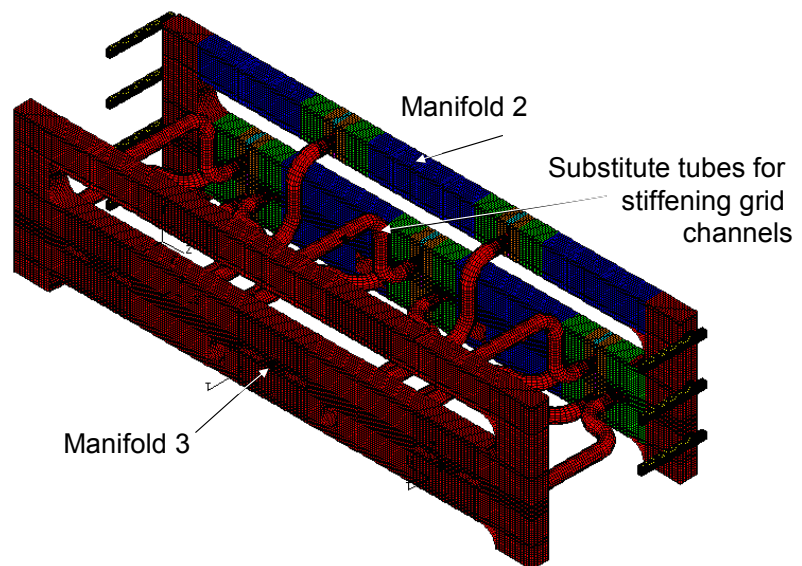


Fig. 2: Model for the GRICAMAN experiment, including the substitute channels for the stiffening grid. Similar substitutes will be defined for the cap channels.

not be applied substitutes for these channels have to be defined. Therefore first the channel mass flow – friction loss characteristics have to be determined analytically and will be done also in a separate experiment. This will allow replacing the real channels by simple but carefully designed tubes. Using such tubes will allow simulating the pressure field in the manifolds and so in turn the simulation of the mass flow rate to be expected for the replaced flow paths. A sketch of the manifold test stand including the tubes for the stiffening grid is shown in Fig. 2.

- c) Several aspects of the fabrication sequence and also the coolant flow distribution under realistic conditions are being investigated. Using a 1/3 mock up of the TBM. Because it offers space for six breeding units it is named 'Six Cell MOck up' (SICEMO). The mock up has all characteristics of the coolant flow sequence and is well suited as test for mass flow distribution. As it is difficult to measure the mass flow for each channel individually a heating plates are foreseen in the space of the ceramic bed. This heating has the task to impose a temperature field in the structure from which we can back out hints on the mass flow distribution. Only three of the six possible BU positions will be used, to give an easy access with sensors to the cooling plate and stiffening grid. The missing BU's will be replaced by a substitute U-bend.

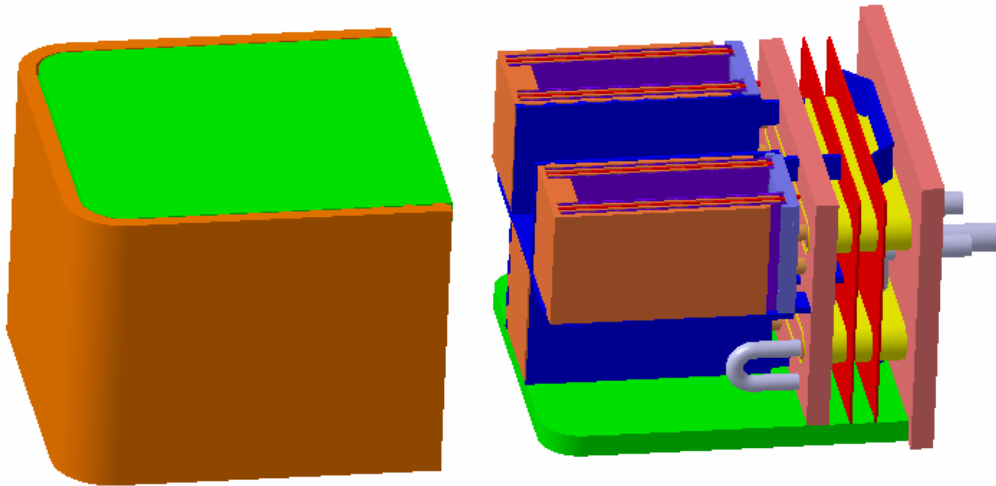


Fig. 3: Sketch of the SICEMO test mock up.

Staff:

L. Boccaccini  
B. Dolensky  
M. Ilic  
X. Jin  
R. Meyder  
H. Neuberger  
V. Pereslavitsev  
S. Polixa  
S. Raff  
M. Roccella  
P. Schanz

## **TW5-TTBB-001 D 8**

### **Detailed HCPB TBM Development Work Plan and First Technical Specification Document**

The objective of this task is to contribute together with the EFDA management to the preparation of the task breakdown, the work plan and the technical specification document for the HCPB TBM.

The conceptual design of the HCPB TBM for the testing in ITER has been completed in 2004; fabrication processes and fabrication route are under definition. In the next years a qualification programme has to be carried out based on the manufacturing and testing of medium/large scale mock-ups. These will be used for the testing of fabrication technologies and for functional tests in large experimental helium loops. These activities will allow the completion of the final design of the TBM system in 2010 with the subsequent start of the procurement and construction of the system for ITER foreseen for the starting of the plasma H-H operation. The work plan should define the milestones that are foreseen in the next years, identify all tasks that are necessary to achieve them and define the dependencies among the different tasks and milestones. In addition to the TBM development, the plan will consider the development of the necessary ancillary systems (helium coolant, tritium extraction, coolant purification), as the related measurement systems (e.g. Neutronic and Tritium) and diagnostic.

The activity started in September and a final report will be issued at the beginning of 2006.

#### Staff:

L.V. Boccaccini  
R. Meyder  
H. Neuberger

## TW5-TTBB-001 D 9 Study with Experimental Verification of the Pebbles Filling in the HCPB TBM

In the fabrication of the HCPB solid breeder blanket, the pebble beds of beryllium and ceramic should be filled at a certain stage of the manufacturing sequences. At the same time the manufacturing of the TBM would require thermal treatment at different temperature levels from a simple stresses reduction to a complete heat treatment. These operations could be incompatible with the presence of ceramic and beryllium in the TBM. The objective of the study is to define different strategies to fill the beds at different stages of the fabrication process and to investigate their impact on the design.

For filling the ceramic beds the purge gas collector plenum, which is located directly behind the back plate of the BU will be used. The back plate has several holes through which the purge gas leaves the ceramic bed. These beds are closed with a fine mesh screen such that the ceramic pebbles cannot leave the beds. The idea for bed filling is to replace the upper most screen by a labyrinth and fill the beds through this labyrinth. The access to the purge gas collector plenum is through a hole in the gap. The hole must be wide enough to have the possibility to remove excessive pebbles from this plenum via a vacuum cleaner nozzle. The hole then must be closed.

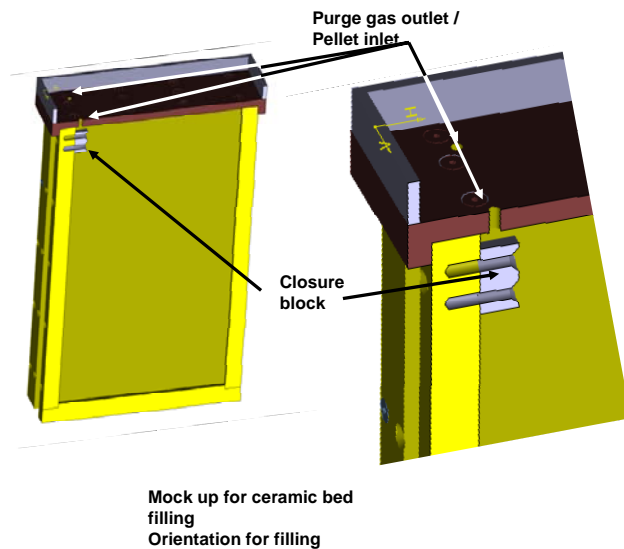


Fig. 1: Schematic for the principle of ceramic bed filling.

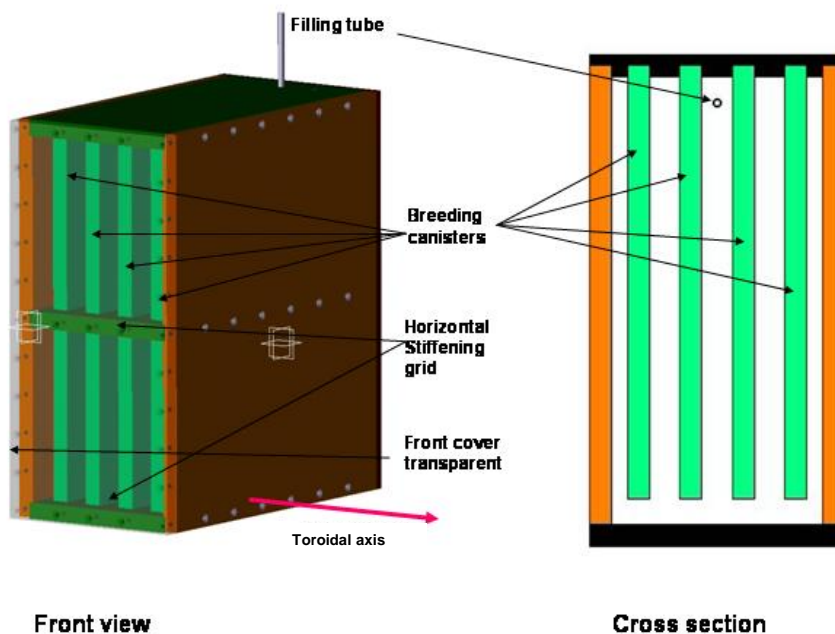


Fig. 2: Schematic for the principle to fill the beryllium beds.

For filling of the beryllium beds access is planned also through the cap. While all the ceramic beds will be filled in parallel, for the beryllium only those BU's are treated which are stacked on top of each other. The connection will be made through holes in the stiffening grid plates. The filling starts with the lowest BU. Vibration and twisting of the module will be needed to fill the beds. After filling the lowest BU the filling tube is withdrawn and the hole in the stiffening grid will be closed. This is to fix the status achieved bed. Then the next BU will be filled.

the stiffening grid will be closed. This is to fix the status achieved bed. Then the next BU will be filled.

Staff:

L. Boccaccini  
B. Dolensky  
M. Ilic  
X. Jin  
R. Meyder  
H. Neuberger  
V. Pereslvtsev  
S. Polixa  
S. Raff  
M. Roccella  
P. Schanz

Literature:

[1] R. Meyder et al: Tritium analysis for the european HCPB TBM in ITER, SOFE 2005 Knoxville

## TTBB-002b

### Helium Cooled: Blanket Manufacturing Technologies

#### TW2-TTBB-002b D 4

### Procurements of Beryllium Materials and Quality Control of Produced Material

#### Introduction

A key issue of beryllium pebble beds in HCPB blankets is its behaviour under fast neutron irradiation: since a large production of gases (helium and, in a much smaller amount, tritium) occurs in-pile, material swelling can cause mechanical interaction with the box walls and material break-up. Also tritium retention is a safety issue. This task is primarily dedicated to the quality control of procured Be pebbles. Beryllium pebbles have been produced since the beginning of the 90's by Rotating Electrode Process (REP), a method developed by the NGK company: a high-purity beryllium electrode melts in an arc ejecting drops which solidify in a helium atmosphere. In 2001 the reference material was fixed as REP 1-mm diameter pebbles, with an optimised composition to avoid the formation of low temperature melting impurity phases at grain boundaries which might enhance swelling. Within the present task, two major procurements of Be pebbles from NGK company took place:

- Be pebbles for the HIDOBE irradiation programme at HFR Petten
- Be pebbles for HEXCALIBER mock-up tests in Brasimone.

#### 1. Quality control of Be pebbles for HIDOBE irradiation programme

Mid 2005 the reference irradiation programme HIDOBE has started at the HFR Petten reactor on a variety of different beryllium qualities. With HIDOBE it is the first time that a benchmark up to high gas concentrations ( $\leq 6000$  appm He,  $\leq 680$  appm T) and displacement levels ( $\sim 36$  dpa) with an international test matrix (Be pebbles, grain size dependence, beryllides, Be with open porosity) will be performed in a fission reactor at blanket relevant temperatures. Although due to the nature of the neutron spectrum the gas and damage production rates in the mixed spectrum reactor HFR Petten differ from that ones of a HCPB blanket in a fusion DEMO reactor within a factor 2-2.5, the HIDOBE experiment is most relevant, as for the first time the achieved helium concentration and damage level will be comparable with about 30-35% of the blanket lifetime of a DEMO reactor. Three different pebble diameters are being irradiated to characterize the pebble size dependency of the tritium release: 0.5 mm, 1.0 mm and 2.0 mm

The optical microscopy (Figure 1) of the as-fabricated pebbles show an almost fully dense metallographic structure characterized by the presence of large grains. However, a quite large number of pebbles exhibit a big pore (up to 0.1 - 0.2 mm) at their centre together with a fully dense region near the external surface.

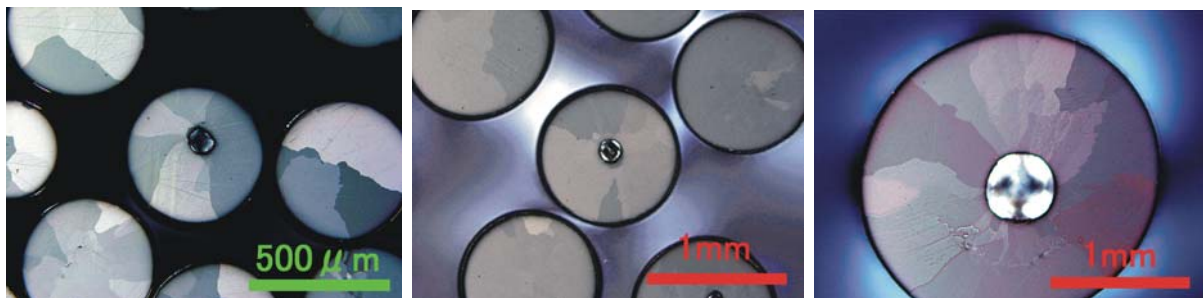


Fig. 1: Pebbles with diameters of 0.5 mm left hand side), 1.0 mm (middle), and 2mm (right hand side).

This kind of pebble structure is typical for a fabrication process with a rapid cooling in the gas atmosphere. Main features of the coolant process include: (i) Rapid condensation of the liq-



uid drop from the outer surface to the center, (ii) frequent appearance of a big cavity in the center as a result of the rapid solidification process, and (iii) grain boundaries in radial direction and, as a consequence, grain diameters that strongly correlates with the pebble radius.

From the observation that the typical grain diameter correlates roughly with the radius of the Be pebbles it can preliminary concluded, that small pebbles are much more favourable with respect to T-release. The chemical composition shown in Table 1 confirms the relatively high purity of all Be Pebble diameters.

Table 1: Impurity concentrations of the Be pebbles delivered to NRG for HIDOBE irradiation.

Element	Diameter: 0.42 - 0.60 mm			Diameter: 0.42 - 0.60 mm			Diameter: 0.42 - 0.60 mm		
	Specified value		Actual value	Specified value		Actual value	Specified value		Actual value
	Min (wt%)	Max (wt %)	(wt%)	Min (wt%)	Max (wt %)	(wt%)	Min (wt%)	Max (wt %)	(wt%)
Be	99.0		99.5	99.0		99.5	99.0		99.5
BeO		0.50	0.36		0.50	0.36		0.50	0.36
Fe		0.10	0.088		0.10	0.094		0.10	0.085
Al		0.09	0.047		0.09	0.048		0.09	0.046
Si			0.027			0.029			0.029
Mg			0.018			0.024			0.030
Co			<0.001			<0.001			<0.001
Sc			<0.005			<0.005			<0.005
U			<0.01			<0.01			<0.01

Obviously, the actual impurity concentrations of the Be pebbles are within the specified ones. Nevertheless, these specified impurity concentrations are not the limit of what is presently achievable: A parallel report (TW5-TTBB-006, D1) discusses the maximum impurity concentrations that are tolerable in pebbles.

## 2. Quality control of Be pebbles for HEXCALIBER mock-up tests in Brasimone

In order to minimize the nuclear inventory to the lowest possible amount, the beryllium pebbles to be used in ITER experiments must have very low impurity levels (nuclear grade material). For an out-of pile test to be performed in ENEA-Brasimone, more than 13 kg of Be pebbles have been procured at NGK and delivered in September 2005. In order to afford the relatively large production, it was accepted in the procurement specification that the impurity level might be somewhat below the mentioned ones in table 1. A detailed chemical analysis, including the radiologically critical elements, has been performed at FZK (table 2).

As accepted in the procurement specifications, Fe, Al and Mg are about a factor of two above "Higher purity" pebbles. However, of outstanding importance is that for the first time Co and U are no longer specified by upper impurity concentrations, but have been resolved analytically in a reliable manner in the ppm range. Obviously, both the Co and U impurity concentrations are even in this "medium grade material" only 3.2 ppm and 8.02 ppm, respectively. This is much cleaner than originally expected.

Table 2: Chemical analysis of 1mm Be pebbles.

Element	Fe	Al	Si	Mg	Cr	Co	U
wt %	0.172	0.101	0.034	0.057	0.0102	0.00032	0.000802

Staff:

U. Jäntschi  
M. Klimiankou  
P. Kurinskiy  
A. Möslang  
J. Reimann

Literature:

- [1] P. Kurinskiy, A. Cardella, M. Klimiankou, A. Möslang, A. A. Goraieb, "Production and Thermal Stability of Beryllium with Fine Grain Structure to Improve Tritium Release During Neutron Irradiation", presented at 23rd Symposium on Fusion Technology (SOFT-23), Venice, September 20-24, 2004, Proceedings
- [2] P. Kurinskiy, M. Klimiankou, G. Bürkle and A. Möslang, "Fabrication and Analysis of New Beryllium Alloys", Final report on the EFDA Task TW4-TTBB-005 D3 (Sept. 2005)
- [3] A. Möslang, E. Alves, L.V. Boccaccini, J. B. J. Hegeman, P. Kurinskiy, J. van der Laan, J. Reimann, L. Sannen, M. Scibetta, F. Druyts, J. Tiliks; „Beryllium for breeder blankets – status of the European R&D“; 7<sup>th</sup> IEA Workshop on Beryllium, 29. Nov-2. Dez 2005, Santa Barbara, USA
- [4] J. Reimann, Material Assessment Report on Beryllium Pebble Beds for EU HCPB Test Blanket Module, Internal Report Forschungszentrum Karlsruhe, Oct. 2005.

## TW2-TTBB-002b D 5 FW Manufacturing by HIPing

**Introduction:** This task is a follow-up activity of the task TW2-TTMS-D1 which was an investigation of the uni-axial diffusion weld (U-DW) process in a more general way. The current task has achieved parameters which should be transferred to a semi-industrial production of cooling plates (CP). These are the basic components of the blanket. The current task is split into two parts:

The first part is dealing with the transfer from laboratory scale U-DW samples to samples with additional features. A series of functional samples have been tested and increased knowledge on leak tightness and material properties has been gained. The second part consists of the production of a full scale CP of a breeding unit (BU).

In addition some investigations have been performed regarding the tensile strength depending on various parameters.

**Improved analysis of U-DW process:** An improved model of visco plastic creep enables the detection of non typical compression results during U-DW process. It turned out that reference compression experiments are required. Results obtained so far lead to a new judgement of U-DW experiments: It is possible to generate perfect U-DW welds by a one step **and** a two step U-DW process which, in contrast to the one step method, uses two different temperatures and two vice versa varying bonding pressures. The two step process has the fundamental advantage of a reduced work piece compression of 4 to 6 % (comparable one step process 10 to 14% compression).

**Tensile strength:** The comparison between tensile strength of earlier U-DW samples and structural material samples indicates a reduced tensile strength. This could be caused by a non fitting post weld heat treatment (PWHT) or a non-optimal U-DW process. But results of Charpy impact tests lead to the conclusion the U-DW process was not the reason for the problem. The base material of U-DW samples has been investigated by tensile tests too demonstrating that the tensile properties of base material and welds agree completely.

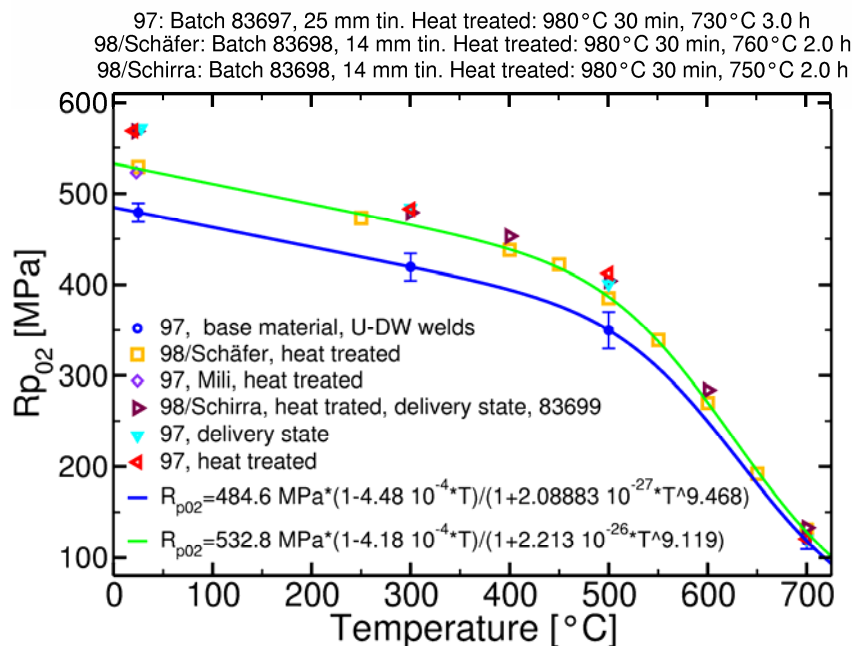


Fig. 1: Tensile results (yield strength) of different EUROFER batches, authors and heat treatments.

A literature survey has been carried out in order to compare achieved experimental results with literature data. The findings are summarized in Table 1.

The batch 83697 shows the same tensile properties as delivered and after the heat treatment. These properties agree to those of other EUROFER 97 batches. A really significant decrease in tensile yield strength caused by a different heat treatment (or PWHT) could not be observed see **green** line in Fig 1!

The observed decrease of yield strength in U-DW samples - see **blue** line in Fig. 1 – can be proved as phenomenon of the additional heat treatment during U-DW process.

**Transfer to functional samples:** The transfer from laboratory non structured U-DW samples to functional samples (Fig. 2) has been performed by different samples: Fig. 2 A shows a typical non structured U-DW sample with an weld area dimensions of 25 x 30 mm. Sample B, C, and D are so called Cat Walk Samples (CWS) with different rib width (8 mm, 4 mm and 2 mm). These serial gives a transfer to a small model of centre part of a CP. A Compact Mock Up (CMU, 60 x 70 mm, Fig. 3) contains cooling channels like CP, manifolds and regions generating destructive mechanical samples like CWS B and C.

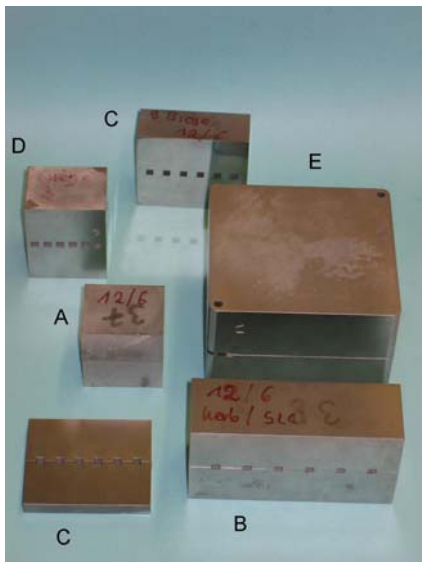


Fig. 2: Functional samples for the technological transfer.



Fig. 3: Half piece of a CMU with manifold in the foreground.

It is desirable to reduce the weld pressure of the first step with respect to a full scale CP production so the first step weld pressure has been changed to 18 MPa regarding to a bond force of 40 kN in case of a compact mock-up (CMU). The process time has been decreased aiming to reduce the decrease of tensile strength.

All of the CMU, CWS and U-DW reference samples have been welded by the same method.

The cooling channels of CMU and CWS fulfill to requested dimensions, less than 0.1 mm deviation. The tensile properties of all CWS welds agree to those tensile properties of the base material or the not structured U-DW reference sample (**green** dashed Line in Fig. 4). But the tensile results (welds and base material, **red**) of CMU disagree with the above CWS-results. This is due to an additional PWHT caused by the manufacturing of a connecting tube for the leak tight test. Two of the tensile results deviate considerably from the red line, the reason being a deviation of the strain-stress curve. Scaled reference experiments have been performed indicating that these two values are not typical and can be disregarded. The decrease of yield strength is observed by 7 of 9 samples of this serial.

Both CMUs have been tested successfully by leak tightness test and pressure test (145 bar@ RT). It has to be noted that the first step weld time of the first CMU has been ten minutes too short because of the large heat capacity of a CMU. But tensile results of both CMU have been identical. This indicates a stable working process.

The Charpy impact tests of CWS yield the following results:

Centre pins are necessary for geometrical adjustment of the half pieces. The centre pin placed in the outer ribs will not weld the structural material. The wholes of these pins cause a weakening of the structure. The CMU experiment shows a trapezoidal forming of the CMU weld area during U-DW caused by different geometrical dimensions of cooling channels and manifolds. Both of these disadvantages of the U-DW process can be avoided by a design change: The width of the margin weld area has to be increased from 2 to 4 mm. The additional area can be used for the wholes of the centre pin. The additional margin can milled away vanishing the trapezoidal forming.

The weld quality of the reference sample has been found to be not sufficient, so this process variant will not be used in future. It is caused by a too low bonding pressure during U-DW.

Both investigated CWS samples are showing the same results: The weld quality (green lines and symbols in Fig. 5) in inner ribs is nearly sufficient. It is very close to that quality of the U-DW reference sample which could be reached in an ideal case. The reduced quality is a matter of non-fitting weld parameters.

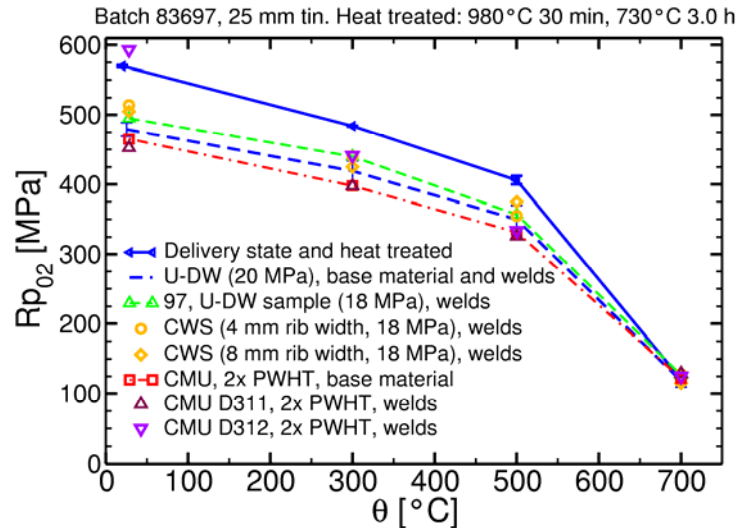
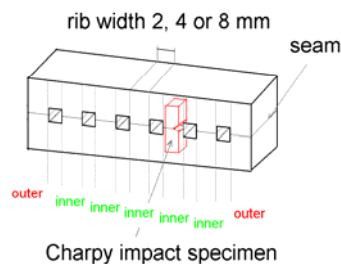


Fig. 4: Tensile results of all functional samples.

CWS as a model CP



"18 MPa prozess", EUROFER 97, 980°C 30', 730°C 3.0 h

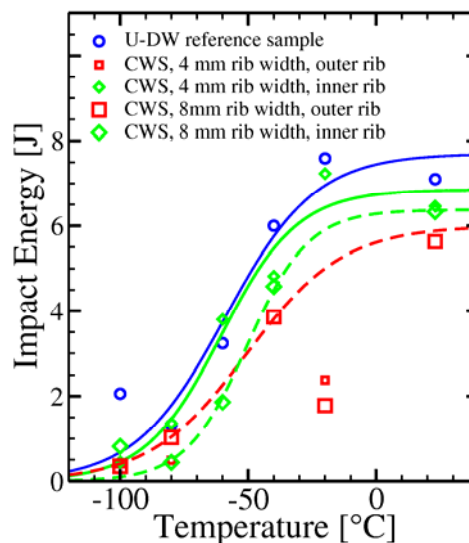


Fig. 5: Charpy impact test results of CWS

The weld quality in the outer ribs has been reduced: The fractional areas of two specimens – both tested at -20°C – show a not fully welded area. Such a phenomenon is typical for a small applied weld pressure. This proves a non equal weld pressure distribution between inner and out ribs. The problem of non welded areas in outer ribs can be solved by an increase of the first step weld pressure corresponding mean pressure larger than 20 MPa. Other specimens taken from outer ribs have been tested but unfortunately at lower temperatures than DBTT observing only brittle fracture. The Charpy impact specimens of the 8 mm rib CWS allow the information of a reduced weld quality in the outer rib omitting the former mentioned samples:

Table 1: Charpy impact results of functional sample serial.

Sample serial	USE [j]	DBTT [°C]
Base material EUROFER 97	9.2	-98
U-DW reference sample "18 MPa"	7.7	-58
CWS inner ribs	7.0	-61
CWS outer ribs (8 mm rib widths)	6.85	-61

**Status of full scale CP manufacturing:** The important challenge of manufacturing a full scale CP has been started: The half pieces of a full scale CP has been produced during this year (Fig 6). The boxing technology is ready for the first weld attempt under industrial condition after some improvements: A CMU has been welded at the end of this year. Results are expected for the following year.

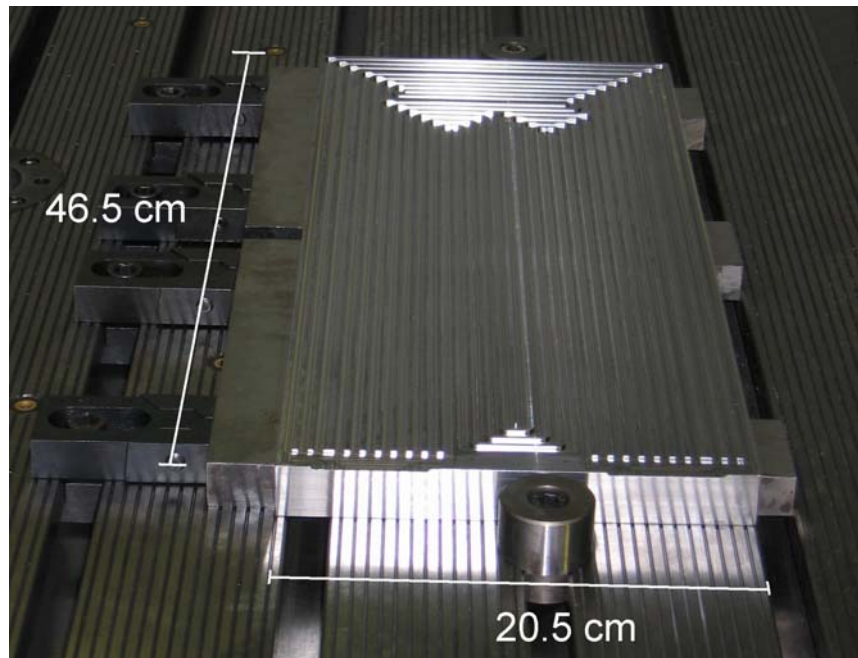


Fig. 6: Picture of a half CP piece.

**Conclusion:** The advantage of a two step U-DW process in comparison to a one step process has been proved by reduced work piece compression.

The reduced yield strength and increased failure tensile strain in U-DW weld and base material samples is clarified as additional improvement of tensile properties caused by the heat treatment during U-DW. The additional PWHT of CMU generates an additional decrease of e. g. yield strength –grain coarsening-. These two facts require an investigation of the number of maximum possible PWHTs.

The design of CP has to be changed according to results of CMU.

The weld parameters for the industrial transfer have been determined by a series of functional samples. The results of these samples direct to a non uniform weld pressure distribution in cooling channel based structures.

The boxing technology has been developed for the first industrial U-DW attempt, which will have been performed during December 2005.

Staff:

J. Aktaa  
U. Bürkle  
B. Dafferner  
H. Kempe  
J. Rey  
A. von der Weth

## **TTBB-006**

### **Helium Cooled: Breeder and Neutron Multiplier Materials**

#### **TW5-TTBB-006 D 3**

#### **Procurements and Quality Control of Orthosilicate Ceramic Pebbles**

$\text{Li}_4\text{SiO}_4$  pebbles are fabricated in a semi-industrial scale facility by a melt-spraying technique for experiments with pebbles and pebble beds. As the fabrication parameters are difficult to monitor, a close and continuous quality control of every batch of pebbles received from the industrial producer will be performed. The deliverable describes the results of this activity.

#### **Quality control of conditioned material for HICU**

A high dose irradiation in the High Flux Reactor of lithium ceramics is performed at Petten to study the impact of neutron spectrum and the influence of constraint conditions on the thermomechanical behaviour of the pebble beds as a part of the European programme for the development of the Helium Cooled Pebble Bed. The results will be used to support a selection between different materials for a HCPB based fusion power plant. Three conditioned batches of lithium orthosilicate pebbles delivered to Petten were characterised.

Three batches of lithium orthosilicate pebbles were heat treated at 970°C for 1 week and fully characterised at FZKa (OSi 00/2-3-c, 02/1-2-c, and 03/2-9-c). These batches had been produced using different raw materials to obtain different  $^6\text{Li}$  enrichments. The microscopic investigation showed the usual amount of cracks and pores in the pebbles (fig. 1). This was also confirmed by Hg-porosimetry, where densities in the range of 94-96 %TD were determined for the three batches (table 1). Only the closed porosity is slightly higher (2.3 %) in batch OSi 00/2-3-c compared to the values of  $\leq 1$  % measured for the other two batches. As a consequence, the crush load of single pebbles of the first batch of 7 N is also slightly lower than in the other two batches with 8 N.

#### **Investigation of amorphous pebbles**

The majority of the pebbles fabricated by the melt-spraying process at Schott is crystallised and appears pearly white, but a small amount of glassy pebbles can also be observed. The ratio between amorphously solidified and crystallised pebbles increases with decreasing pebble size. While the crystallised pebbles always exhibit some cracks and pores, the amorphous pebbles are mostly free of any defects (fig. 2). As cracks and pores affect the mechanical properties of the breeder material, a well controlled crystallisation of amorphous material could lead to an improvement of the thermomechanical behaviour of the pebble bed. The crystallisation behaviour of the predominately amorphous pebbles in the pebbles fraction  $< 50 \mu\text{m}$  was therefore investigated by thermoanalysis and X-ray diffraction. The crystallisation takes place in three steps. At about 300-350°C an unidentified, intermediate phase is nucleated (fig. 3). In a second step the formation of  $\text{Li}_4\text{SiO}_4$  takes place at about 500°C, while Lithium metasilicate ( $\text{Li}_2\text{SiO}_3$ ) is the last phase to appear at temperatures above 600°C. The investigation of the crystallisation of the amorphous material enabled a heat treatment to induce the formation of phases without introducing the usual amount of cracks and pores (fig. 4). To apply this procedure and to verify the improvement of the mechanical behaviour of the breeder material, the fabrication process has yet to be modified to gain a higher yield of amorphous pebbles in the diameter range of 250-630  $\mu\text{m}$ .



Table 1: Properties of conditioned lithium orthosilicate pebbles.

Batch	OSi 00/2-3cond.	OSi 02/1-2cond.	OSi 03/2-9cond.
<b>Raw Materials</b>	Li <sub>4</sub> SiO <sub>4</sub> Li <sub>2</sub> CO <sub>3</sub> SiO <sub>2</sub>	Li <sub>4</sub> SiO <sub>4</sub> Li <sub>2</sub> CO <sub>3</sub> SiO <sub>2</sub>	LiOH SiO <sub>2</sub>
<b>Enrichment of <sup>6</sup>Li</b>	20% enriched	0.06% depleted	natural enrichment
<b>Chemical Analysis of Principal Constituents (Schott)</b>			
Li <sub>2</sub> O / wt%	48.50 ± 0.01	47.65 ± 0.07	48.27 ± 0.02
SiO <sub>2</sub> / wt%	50.83 ± 0.10	51.15 ± 0.16	51.38 ± 0.11
excess SiO <sub>2</sub> / wt%	2.1	3.3	2.8
<b>Size Distribution</b>			
d <sub>50</sub> / μm	350	515	380
<b>He-Pycnometry</b>			
inner density / % TD	97.7 ± 0.1	99.5 ± 0.1	98.9 ± 0.1
closed porosity (calc.) / %	2.3 ± 0.1	0.5 ± 0.1	1.1 ± 0.1
<b>Hg- porosimetry</b>			
density / g cm <sup>-3</sup>	2.25 ± 0.03	2.31 ± 0.04	2.26 ± 0.03
density / % TD	93.7 ± 1.3	96.2 ± 1.7	94.3 ± 1.1
open porosity / %	2.1 ± 0.6	1.8 ± 0.1	3.0 ± 0.4
closed porosity (calc.) / %	4.3 ± 1.7	2.0 ± 1.7	2.8 ± 1.4
<b>Pebble Bed Density</b>			
tap density / g cm <sup>-3</sup>	1.43	1.45	1.47
tap density / % TD	59.6	60.4	61.3
<b>Crush Load Tests (IMF II)</b>			
mean crush load / N	6.7 ± 1.6	7.9 ± 2.0	8.2 ± 1.4
<b>Specific Surface Area</b>			
specific surface area / m <sup>2</sup> g <sup>-1</sup>	0.04	0.08	0.08

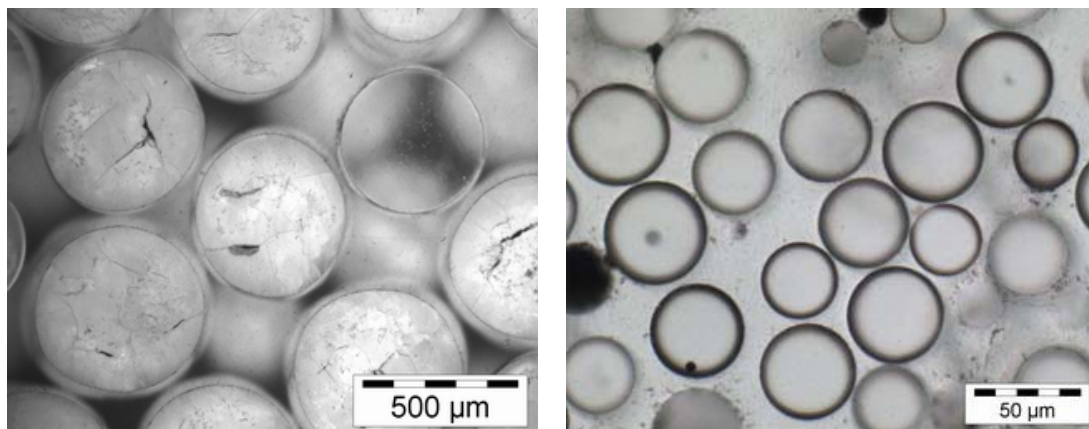


Fig. 2: Optical micrographs of large pebbles (left) and of glassy pebbles with diameters < 50 μm (right).

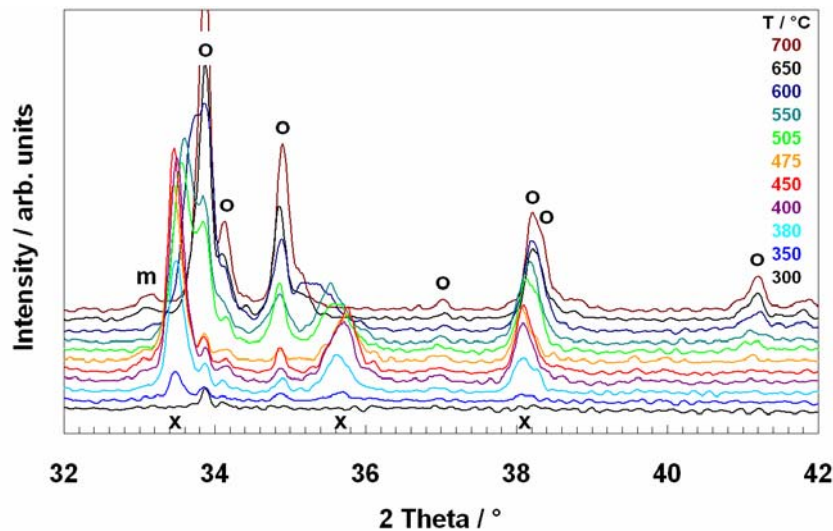


Fig. 3: Details of XRD pattern of initially amorphous pebbles quenched from various temperatures (x = unidentified phase, o = orthosilicate, m = metasilicate).

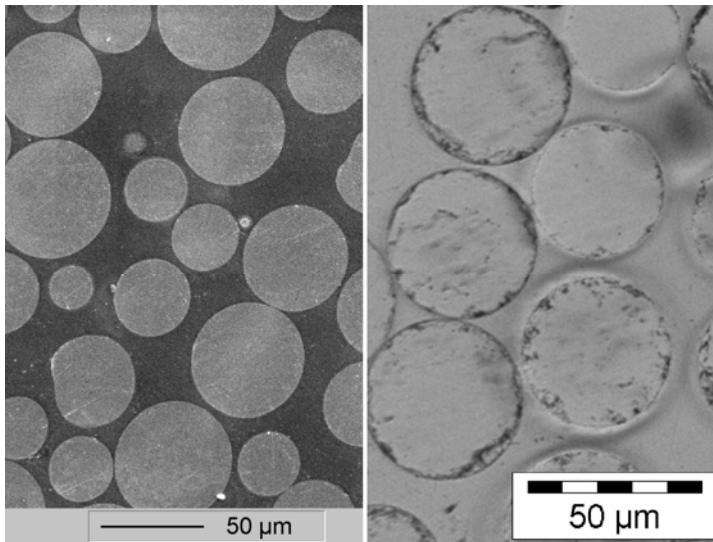


Fig. 4: Cross-sections of initially amorphous pebbles after a heat treatment at 800°C display no pores and only very few defects at the surface of the pebbles (SEM + OM).

## Outlook

In a new fabrication campaign the recycling of OSi pebbles is to be demonstrated. For this purpose, at first OSi pebbles with a Li-content according to DEMO end of life relevant burn-ups will be fabricated. These pebbles will then be remelted with additions of LiOH to gain the initial composition of the usual reference material with an excess of 2.5 wt% SiO<sub>2</sub>. To save costs, this fabrication will be carried out with natural enriched Li components. The isotope ratio is not supposed to have any influence on the fabrication process.

## Staff:

B. Alm  
A. Erbe  
R. Knitter  
C. Odemer  
R. Rolli

## Literature:

- [1] Wondraczek, L.; Deubener, J.; Mixture, S.; Knitter, R.; Keimbildung und Kristallisation von Lithiumorthosilikatglaskeramiken. Symposium Hochleistungskeramiken, 12.-13. Okt. 2005, Selb.
- [2] Knitter, R.; Alm, B.; Odemer, C., Thermal Investigations of Glassy Lithium Orthosilicate Pebbles. CBBI-13, 13th Int. Workshop on Ceramic Breeder Blanket Interactions. 30. Nov.-2. Dec. 2005, Santa Barbara, CA, USA.

- [3] Knitter, R.; Alm, B.; Roth, G., Crystallisation and Microstructure of Lithium Orthosilicate Pebbles. 12th Int. Conf. on Fusion Reactor Materials (ICFRM 12), December 4-9, 2005, Santa Barbara, CA, USA, to be published in J. Nucl. Mater.
- [4] Wondraczek, L.; Misture, S.T.; Deubener, J.; Knitter, R., Crystallization kinetics of lithium orthosilicate glasses. Accepted for publication in J. Am. Ceram. Soc..
- [5] Knitter, R.; Alm, B., Crystallisation of Amorphous Lithium Orthosilicate and Quality Control of Conditioned Pebble Batches. Final report on the EFDA Task TW5-TTBB-006-D3, Forschungszentrum Karlsruhe, Interner Bericht, December 2005.

## TW5-TTBB-006 D 5 Development of Beryllium Alloy Pebbles with Improved Tritium Release Characteristics

### 1. Introduction

The reliable and efficient operation of helium cooled ceramic breeder blankets requires the timely availability of beryllium as appropriate neutron multiplier. In order to overcome some of the disadvantages of existing Be pebbles like tritium release and He embrittlement at blanket operating temperatures, an attempt has been started to systematically investigate relevant properties by producing beryllium and Be-alloys on laboratory scale at Forschungszentrum Karlsruhe. In the present EU concept, the main strategy for the reduction of the tritium release temperature is (i) to reduce the grain size of Be pebbles and/or tablets, or (ii) to use a suitable Be-alloy.

Since a couple of years JAERI and Japanese Universities have been investigating Be-Ti, Be-V and Be-Mo intermetallic compounds (beryllides) in the view of their use for the Japanese pebble bed blanket concept. Presently,  $\text{Be}_{12}\text{Ti}$  seems the most promising beryllide. According to the available test results,  $\text{Be}_{12}\text{Ti}$  shows, in comparison with metallic beryllium, faster tritium release, much smaller swelling, smaller reactivity with stainless steel, steam and water, therefore, it is becoming interesting also in view of its use in the EU-HCPB blanket.

Based on a systematic screening of various fabrication technologies, this report summarizes the fabrication of  $\text{Be}_{12}\text{Ti}$  samples with a combination of powder metallurgical and arc-melting methods. The subsequent characterization included X-Ray diffractometry, Scanning Electron Microscopy (SEM) and Transmission Electron Microscopy (TEM). The perspectives and limitations of the fabrication technology are discussed.

### 2. Experimental equipment and apparatus

For the production of beryllides the glove-box named BETINA (Fig. 1) has been fabricated and assembled which is besides some auxiliary systems equipped with (i) an arc furnace for ingot production of Be-alloys under controlled atmospheres, and (ii) a 20-ton hydraulic press for compacting of metal powders at temperatures of several hundred degrees to a pellet-shaped form.

The Glove-box ANABELL in Fig. 2 was used for the preparation of samples for subsequent analyses with optical microscopy, SEM, X-Ray and TEM. This glove-box system is supplied with a grinding machine for surface preparation of solid samples (etching, polishing, etc.). ANABELL is also equipped with a fully automatic annealing furnace for heat treatment of fabricated specimens in vacuum or in an inert-gas atmosphere.

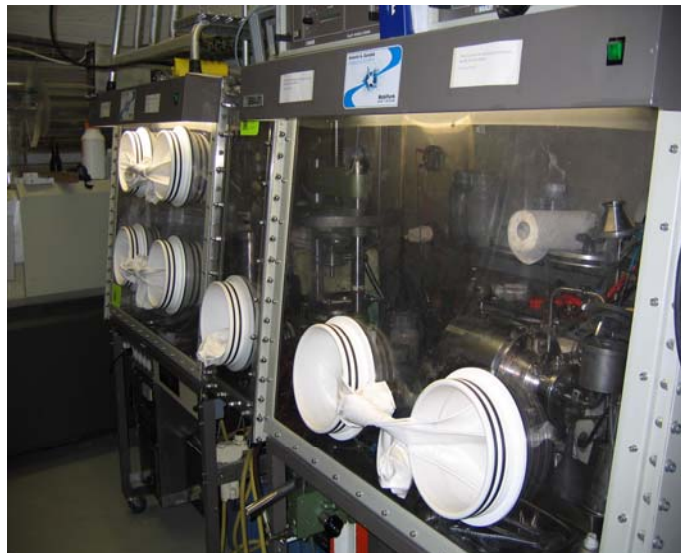


Fig. 1: General view of BETINA glove-box. The assemblies include (i) the milling machine to produce wet micro-crystalline powders, (ii) a high temperature uniaxial press, (iii) an arc melting furnace, and (iv) a microwave facility.

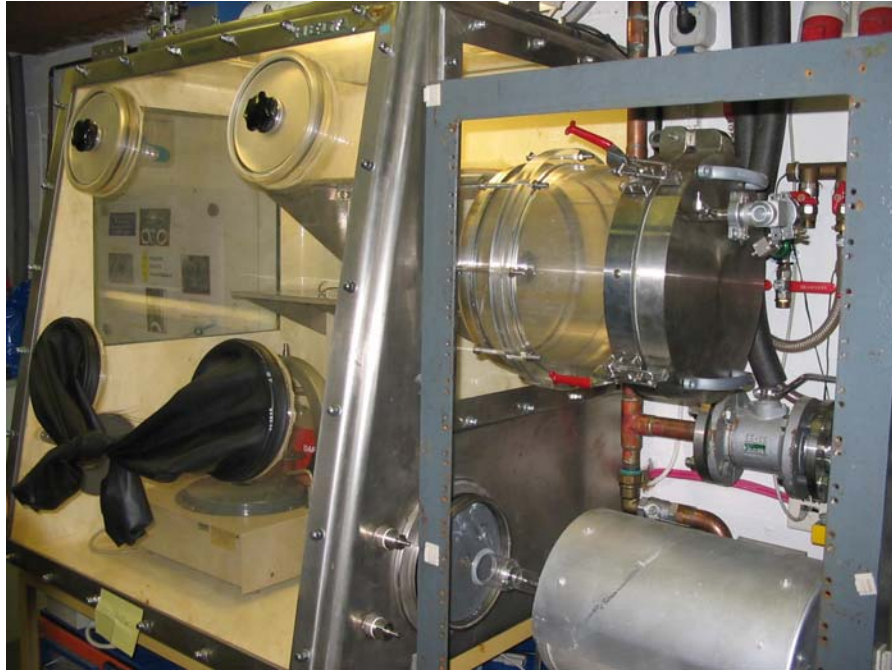


Fig. 2: ANABELL glove-box system. It contains among others a precision balance, tools for etching and polishing and a high temperature vacuum furnace.

### 3. Process of fabrication

The technological process described here is based on the use of an arc-melting facility to obtain Be-alloys from the melt. In this case, tablet-shaped sample pressed out of Be-Ti compositional mixture (Be – 30.8 wt.% Ti corresponding to  $\text{Be}_{12}\text{Ti}$  chemical composition) has been used as a target to be melted by electrode. Afterwards, samples for HIDOBE have been cut with appropriate tools out of melted ingots. The initial powders used for the production of  $\text{Be}_{12}\text{Ti}$  samples were beryllium powder (150-200  $\mu\text{m}$ , Brush Wellman) and titanium powder (less than 44  $\mu\text{m}$ , Alfa Aesar).

#### 3.1 Cold pressing

Pressing is necessary to compact a powder mixture to a tablet-shaped form. With a variation of pressing time and pressing temperature, the density of the pressed sample can be adjusted. A specific pressing tool has been designed and fabricated for the compaction of standard and microcrystalline powders, that is able to produce tablets with 15 mm diameter and 3 mm high at temperatures of up to 600 °C with an integrated ohmic heating system. The experience showed that a uniaxial powder compaction at 400-450 °C and 450-500 MPa for 120 min is sufficient to achieve densities of up to 90 % theoretical density.

#### 3.2 Arc melting process

Typical for arc-melting is the relatively high speed of material alloying during melting. As the first step, the chamber of an arc-melting facility was filled with argon (0,1 bar pressure). Then the pressed Be-Ti tablet has been melted by electrode on a water-cooled copper plate. The main disadvantage of this process is that electrode and plate can be sources of some additional impurities in melted samples. In addition, the experience during the fabrication of many BeTi ingots has shown that it is quite difficult to control the temperature within a narrow window. As a consequence, the amount of Beryllium evaporated during arc melting is not always constant, resulting in slightly different alloy compositions. However, main advantages of this method include: the fast majority of the sample is beryllide of type  $\text{Be}_{12}\text{Ti}$  with a theoretical density of practically 100%. Only some voids occur accidentally due to the quick solidification process.

## 4. Characterization of fabricated $\text{Be}_{12}\text{Ti}$ samples

### 4.1 X-Ray analysis

The analysis of the characteristic X-radiation yields quantitative elemental information from the surface of the sample. In the frame of the present investigations, X-Ray diffraction analysis was performed by means of a D500 X-Ray Diffractometer. Fig. 3 shows X-Ray data of one of the Be-Ti probes in as-pressed condition, and Fig. 4 reflects structural changes in this sample caused after arc-melting of the same tablet. Obviously, the cold pressing at 400 °C range of Ti and Be powders with grains larger than 40  $\mu\text{m}$  does not produce any measurable intermetallides (Fig. 3). However, a completely different X-ray analysis shows up when the Be-Ti tablet is arc melted: the arc melted ingot (Fig. 4) reveals in the fast majority single phase  $\text{Be}_{12}\text{Ti}$ , only with small inclusions of Be and some other impurities.

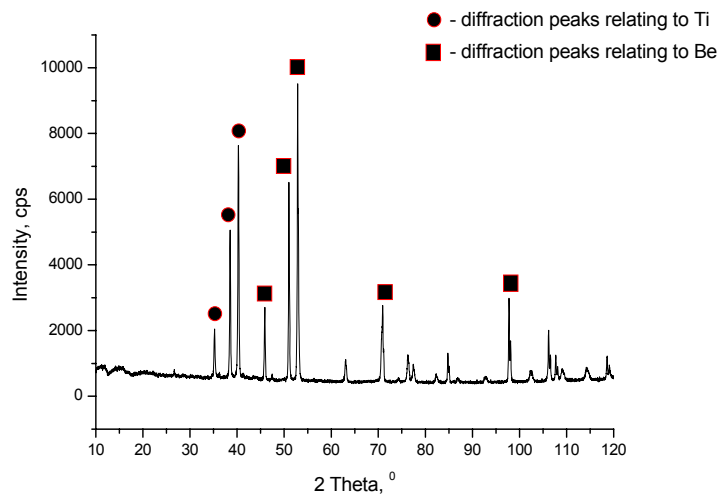


Fig. 3: X-ray diffractometry of  $\text{BeTi}$  powder uniaxial pressed at 400°C.

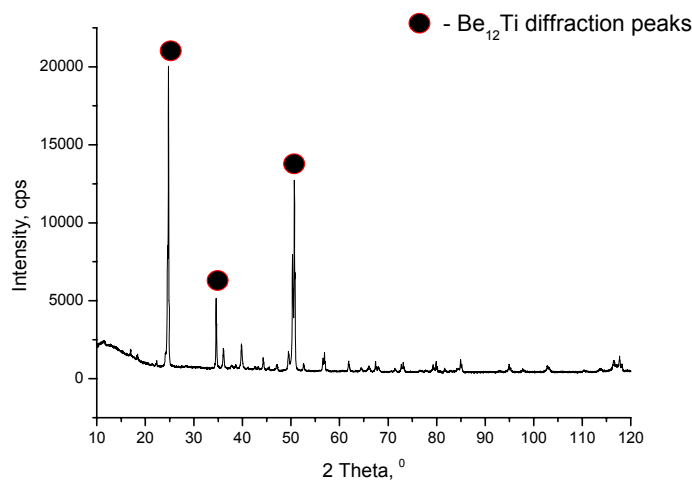


Fig. 4: X-ray diffractometry after pressing at 400°C and arc melting.

### 4.2 SEM observation

Fig. 5 shows the surface structure of the arc-melted Be-Ti sample, revealing a flat and dense structure almost without any visible voids and porosities. The black, “needle type” inclusions

are Be-rich, and the small white inclusions that sometimes show up in the vicinity of black inclusions are Ti-rich. The fast majority, however, is uniformly grey, indicating a single phase intermetallic alloy.

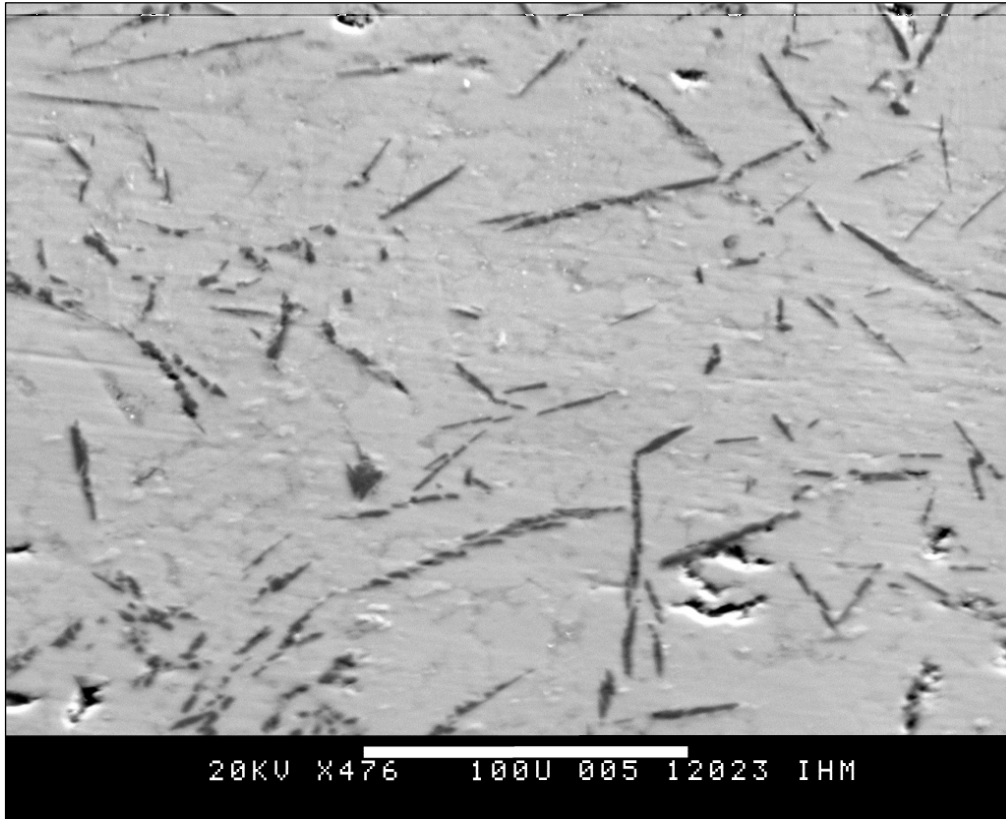


Fig. 5: Micrograph of titanium beryllide. The dark and white areas are rich in Be and Ti, respectively (1/4 of the page).

#### 4.3 TEM analysis of $\text{Be}_{12}\text{Ti}$ probes

Several  $\text{Be}_{12}\text{Ti}$  samples for Transmission Electron Microscopy (TEM) investigations were prepared in the form of disks having 200  $\mu\text{m}$  thickness and 3 mm diameter. The TENUPO device using  $\text{H}_2\text{SO}_4 + 80\%\text{CH}_3\text{OH}$  electrolyte was used for the electro-chemical polishing of the sample. The samples were polished until a small hole has been formed in the middle of the disk.

An accurate determination of Be-Ti phase was performed by a High Resolution TEM (HRTEM) analysis. Fig. 6a shows a HRTEM micrograph of Be-Ti material. The Fast Fourier Transformation (FFT) image of this HRTEM micrograph presented in the Fig. 6b shows three different atomic planes with 0.526nm, 0.37nm and 0.37nm distances. This corresponds to [111] orientation of  $\text{Be}_{12}\text{Ti}$  (tetragonal structure with  $a=0.7278\text{nm}$  and  $c=0.424\text{nm}$ ) perpendicular to the sample surface. All circles and crystallographic indexes were calculated for  $\text{Be}_{12}\text{Ti}$  tetragonal structure by the program Carine Crystallography 3.1. As it can be seen in the FFT image (Fig. 6b), the calculated and measured structures are in the excellent correlation. The differences in the calculated and experimental positions of the diffraction spots were found in the range of 1-2%.

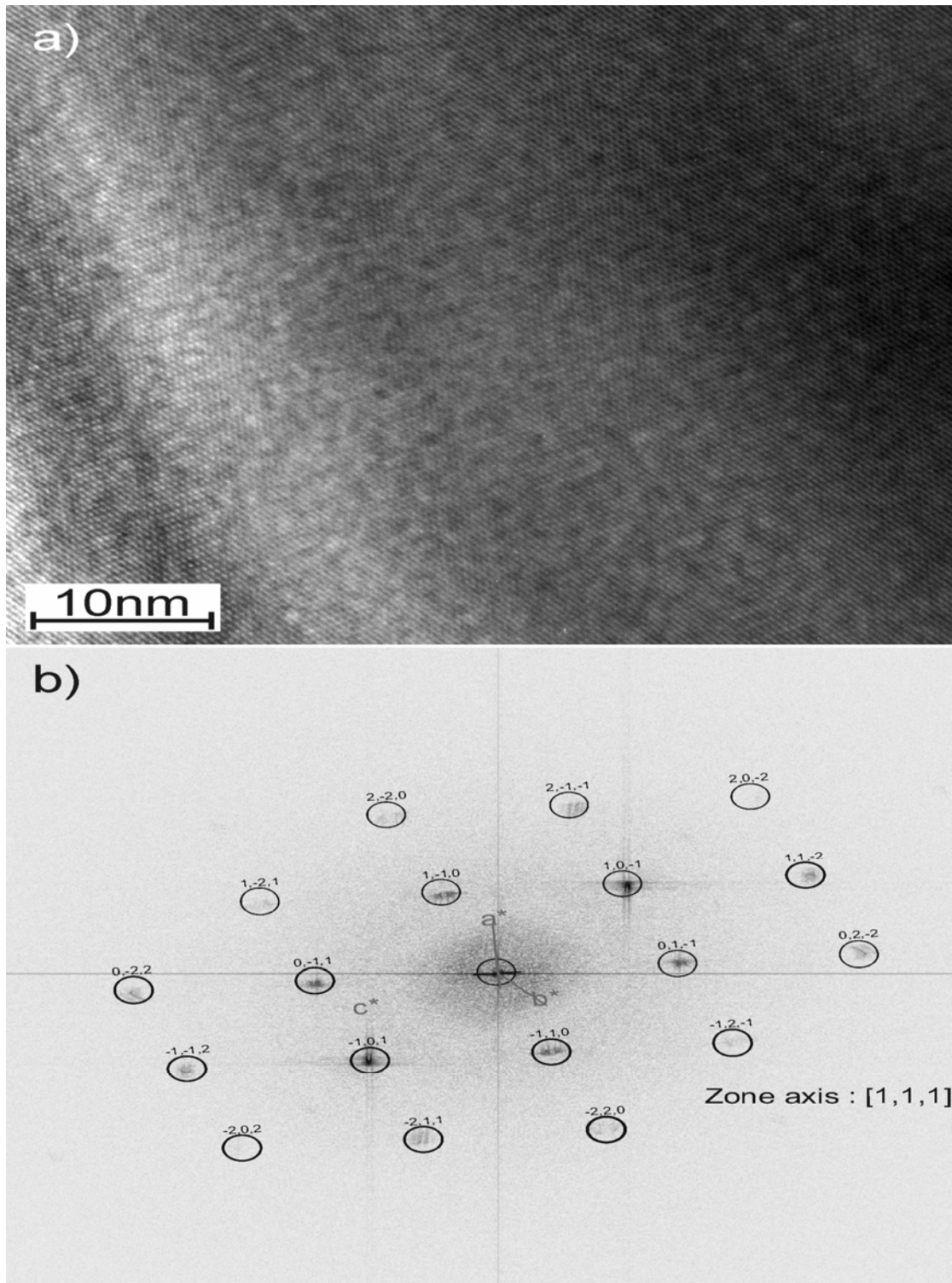


Fig. 6: HRTEM micrograph of a  $\text{Be}_{12}\text{Ti}$  grain oriented with  $[111]$  zone axis (Fig. 6a) and FFT image of this micrograph with calculated reciprocal lattice pattern of  $\text{Be}_{12}\text{Ti}$  tetragonal structure (b) (1/4 of the page for both images).

## 5. Fabrication of $\text{Be}_{12}\text{Ti}$ specimens for HIDOBE Program

The high dose irradiation program HIDOBE has been started in June 2005 in the High Flux Reactor in Petten within the frame of the European Program for the development of the Helium Cooled Pebble Bed (HCPB) to study at blanket relevant irradiation temperatures the irradiation behavior and tritium release properties of various international beryllium products. Long irradiation campaigns of 2 and 4 years are foreseen, providing a helium gas concentration of 3000 and 6000 appm He, respectively, corresponding to about one third of the lifetime



of a DEMO reactor blanket. 19 Be<sub>12</sub>Ti specimens with 3 mm diameter and 3 mm height have been cut out of intermetallic ingots. These ingots were produced by combining powder metallurgy and arc-melting technology:

- cold uniaxial pressing of Be-Ti powder mixture (Be – 30.8 wt.% Ti);
- arc-melting in inert gas atmosphere of cold-pressed Be-Ti tablets.

Before the shipping to the HFR Reactor in Petten, porosities and weight of the fabricated samples have been measured. X-Ray analysis have been also performed in order to make qualitative and quantitative analysis of the obtained Be-Ti phases (mainly Be<sub>12</sub>Ti).

#### Staff:

U. Jäntsch  
M. Klimiankou  
P. Kurinskiy  
A. Möslang

#### Literature:

- [1] P. Kurinskiy, A. Cardella, M. Klimiankou, A. Möslang, A. A. Goraieb, "Production and Thermal Stability of Beryllium with Fine Grain Structure to Improve Tritium Release During Neutron Irradiation", presented at 23rd Symposium on Fusion Technology (SOFT-23), Venice, September 20-24, 2004, Proceedings
- [2] P. Kurinskiy, M. Klimiankou, G. Bürkle and A. Möslang, "Fabrication and Analysis of New Beryllium Alloys", Final report on the EFDA Task TW4-TTBB-005 D3 (Sept. 2005)
- [3] A. Möslang, E. Alves, L.V. Boccaccini, J. B. J. Hegeman, P. Kurinskiy, J. van der Laan, J. Reimann, L. Sannen, M. Scibetta, F. Druyts, J. Tiliks; „Beryllium for breeder blankets – status of the European R&D“; 7<sup>th</sup> IEA Workshop on Beryllium, 29. Nov-2. Dez 2005, Santa Barbara, USA
- [4] P. Kurinskiy, A. Möslang, H. Harsch and A.A. Goraieb; "Production and Characterization of Titanium Beryllides"; 7<sup>th</sup> IEA Workshop on Beryllium, 29. Nov-2. Dez 2005, Santa Barbara, USA
- [5] P. Kurinskiy, M. Klimiankou, A. Möslang and A.A. Goraieb; "Production and Characterization of Titanium Beryllides for HIDOBE Irradiation"; 12<sup>th</sup> Internat.

EFDA/04-1176

## Helium Cooled Pebble Bed: Production and Characterization of Breeder and Neutron Multiplier Materials in Support of the HELICA and HEXCALIBER Experiments

### Part 1

#### 1. Objectives

In the reference HCPB blanket design, orthosilicate (OSi) pebbles with diameters between 0.25-0.63 mm (OSi<sub>Ref</sub>) and 1mm diameter beryllium pebbles are used as breeder and multiplier materials, respectively. In next step experiments, HCPB-mock-ups and HCPB –test blanket modules (TBMs) will be tested out-of pile in different test facilities.

In the HCPB mock-up tests to be performed at ENEA-Brasimone (HELICA and HEXCALIBER-experiments), the OSi pebble bed heights are 5mm compared to about 10mm in the blanket. In order not to change significantly the ratio of bed height to pebble diameter, OSi pebbles with diameters between 0.2 and 0.4 mm will be used (OSi-04). It must be known how these pebbles/pebble beds differ in respect to microstructure and characteristic pebble bed properties compared with the reference material OSi<sub>Ref</sub>.

#### 2. Characterisation of OSi-04 Pebble/Pebble Bed

##### 2.1 Characterisation of OSi-04 pebbles

Procurement, processing and characterisation of lithium orthosilicate (Li<sub>4</sub>SiO<sub>4</sub>) (OSi) pebbles were carried out for the out-of-pile experiments HELICA and HEXCALIBER at ENEA in Brasimone. A quantity of 7 kg OSi pebbles with diameters of 0.2 - 0.4 mm was produced, an amount of 6 kg was delivered to Brasimone in November 2004, 1 kg was delivered to FZK for quality control. The objective of the task is to perform the quality control of the delivered material.

The OSi-04 pebbles with diameters ranging from 200 to 400 µm were characterised in the initial state as they were delivered to ENEA. Only the compressive crush load tests were carried out at 500 µm pebbles of the same production run to obtain results, which are comparable to previously characterised pebble batches.

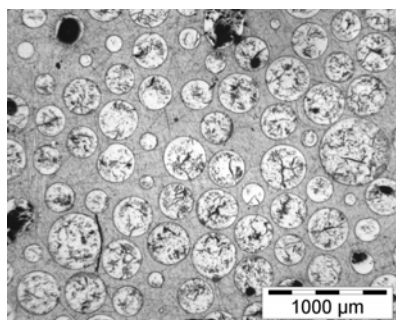


Fig. 1: Cross section of orthosilicate batch OSi 04.

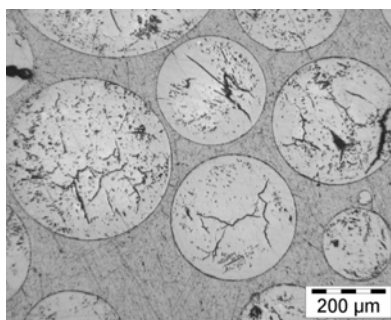


Fig. 2: Detailed view of pebble cross sections showing cracks and pores in the pebbles.

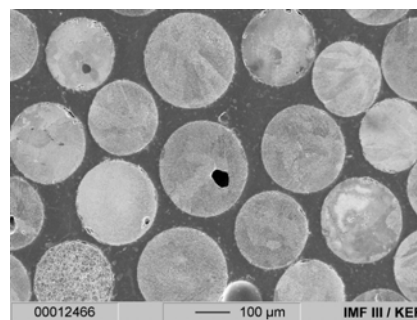


Fig. 3: Cross sections of OSi 04 pebbles.

The microscopic investigation revealed the usual amount of cracks and pores in the pebbles (figs. 1-3). By Hg-porosimetry a density of approx. 93 %TD and an open porosity of nearly 4 % were measured (table 1). A closed porosity of 1.4 % was determined by He-pycnometry. While the density is slightly lower than the usually observed density for reference material of 94 – 95 %TD, the closed porosity is marginally higher. A tap density of 1.41 g/cm<sup>3</sup> was determined for OSi-04 that is smaller than tap densities previously measured for the reference

OSi pebbles. Considering the material density of about 93 %, this value indicates that in this batch with a more narrow pebble size distribution (200 – 400  $\mu\text{m}$ ) a packing volume fraction of only 0.63 is achieved.

The mean crush load of single pebbles amounts to 6.4 N. This value is a little lower than recently reported values of 8 - 9 N for good reference batches, but not outside the usually observed variation. It may be caused by the slightly lower density of this batch.

In addition some pebbles (200 - 400  $\mu\text{m}$ ) were heat treated at 970°C for 1 week. During heat treatment, the coarsening of the microstructure took place, and the usually observed post-sintering led to a slight increase of the density (table 1).

Table 1: Properties of lithium orthosilicate pebbles OSi 04 and OSi 04-c

Batch	OSi 04	OSi 04-c
<b>Size Distribution</b>		
$d_{50} / \mu\text{m}$	225	n/a
<b>He-Pycnometry</b>		
inner density / % TD	98.6 $\pm$ 0.0	99.4 $\pm$ 0.0
closed porosity (calc.) / %	1.4 $\pm$ 0.0	0.6 $\pm$ 0.0
<b>Hg-Posimetry</b>		
density / $\text{g cm}^{-3}$	2.23 $\pm$ 0.03	2.28 $\pm$ 0.03
density / % TD	92.8 $\pm$ 1.2	95.0 $\pm$ 1.1
open porosity / %	3.6 $\pm$ 0.8	3.1 $\pm$ 0.9
closed porosity (calc.) / %	3.7 $\pm$ 0.8	2.0 $\pm$ 0.3
<b>Pebble Bed Density</b>		
tap density / $\text{g cm}^{-3}$	1.41	1.42
tap density / % TD	58.8	59.2
<b>Specific Surface Area</b>		
specific surface area / $\text{m}^2 \text{g}^{-1}$	0.13	0.08
<b>Crush Load Tests (IMF II)</b>		
mean crush load / N	6.4 $\pm$ 1.7	n/a
<b>Chemical Analysis of Principal Constituents (Schott)</b>		
$\text{Li}_2\text{O} / \text{wt}\%$	47.98 $\pm$ 0.05	n/a
$\text{SiO}_2 / \text{wt}\%$	51.53 $\pm$ 0.02	n/a

## 2.2 Characterisation of OSi pebble beds

Uniaxial compression tests (UCTs) were performed in order to determine the relation between uniaxial stress and uniaxial strain both for the first stress increase period (fig.4, curve a)) and the first stress decrease period (fig. 4, curve b)). The Youngs pebble bed modulus  $E = \sigma(\text{MPa})/\varepsilon(1)$  is determined for curves a) and b) and expressed by an potential function  $E = C \sigma^m$ . Figure 4 shows a good agreement of the curves for the two materials. Therefore, the correlation proposed previously [3] for  $\text{OSi}_{\text{Ref}}$ , see table 2, is recommended to be used also for OSi-04.

Table 2: Correlations for Youngs pebble bed modulus, E, for ambient temperature T.

Granular material	$E(\text{MPa}) = C \sigma(\text{MPa})^m$			
	1st stress increase		1st stress decrease	
	C	m	C	m
OSi ex hydroxide	125*	0.50	176	0,66

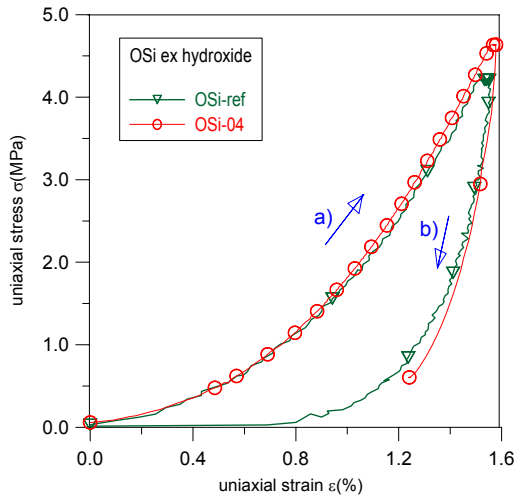


Fig. 4: Uniaxial stress as a function of uniaxial strain.

Furthermore, experiments were carried out to determine pebble bed thermal creep strain as a function of creep time  $t$ , temperature  $T$ , and stress level  $\sigma$ . Figure 5 shows creep strain data as a function of time for both OSi<sub>ref</sub> pebble beds (no symbols) and OSi-04 pebble beds. The data agree quite well in respect to strain level and slope. Therefore, again the correlation developed for the standard material (table 3, from [3]) is recommended.

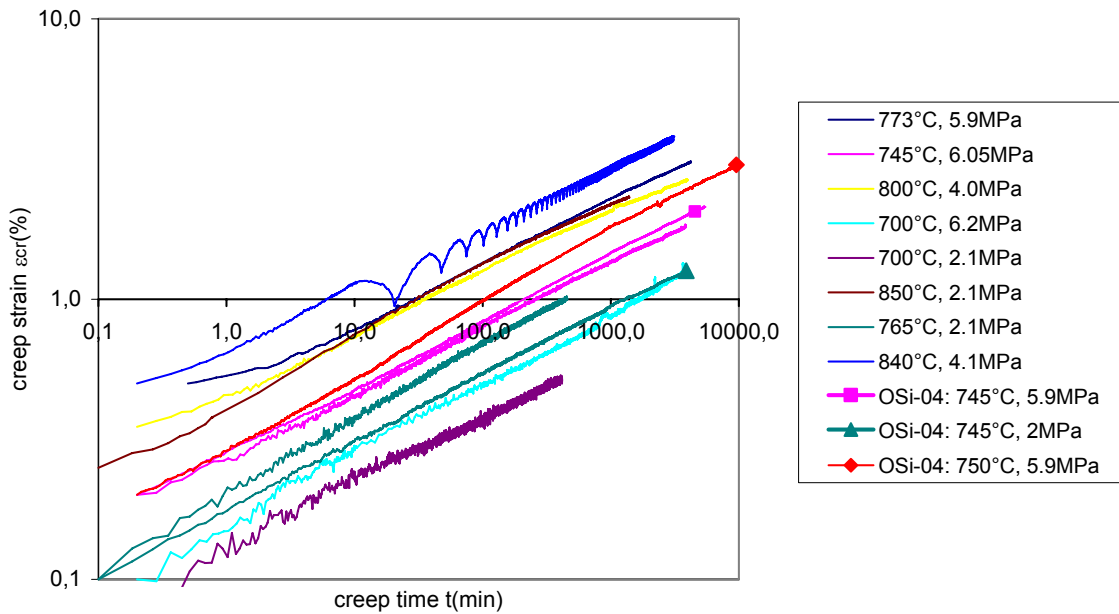


Fig. 5: Thermal creep strain as a function of creep time.

Table 3: Correlation for thermal creep strain,  $\epsilon_{cr}$ .

Granular material	$\epsilon_{cr}(1) = A \exp(-B/T(K)) \sigma(\text{MPa})^p t(\text{s})^n$			
	A	B	p	n
OSi ex hydroxide	20.1	11005	0.65	0.23

### 3. Conclusions

The chemical analysis revealed a slightly high excess of 3.3 wt% SiO<sub>2</sub>, the important material properties like crush load, density, and the content of impurities, however, are well within the range of the usually produced OSi reference material. During annealing at 970°C for 1 week, the decomposition of the high-temperature phase and the usual coarsening of the microstructure took place without any significant changes of the properties.

From the results of quality control and characterisation there is no indication that the material will not behave well in the out-of-pile experiments HELICA and HEXCALIBER.

The measurement of characteristic pebble bed data for the pebble beds consisting of smaller pebbles revealed that there are no remarkable differences to the reference material. Therefore, previous correlations can be directly applied.

#### Staff:

C. Adelhelm

B. Alm

A. Erbe

R. Knitter

C. Odemer

J. Reimann

R. Rolli

#### Literature:

- [1] Knitter, R.; Alm, B., Production and Characterisation of Lithium Orthosilicate Pebbles in Support of the HELICA and HEXCALIBER Experiments. Final Report on the EFDA Task TW5-TTBB-006-D1, Forschungszentrum Karlsruhe, Interner Bericht, FUSION Nr. 248, April 2005.
- [2] Alm, B.; Knitter, R., Characterization of Lithium Orthosilicate Pebbles for HELICA and HEXCALIBER Experiments. CBBI-13, 13th Int. Workshop on Ceramic Breeder Blanket Interactions. 30. Nov.-2. Dec. 2005, Santa Barbara, CA, USA.
- [3] J. Reimann, H. Harsch, Characterisation of orthosilicate ex hdroxide pebble beds and mechanical cycling of different types of ceramic breeder materials, Proc. of the CBBI-12, Report FZKA 7078, Dec. 2004.

## **Part 2:**

### **Procurement and Quality Control for Be in HEXCALIBUR**

#### **1. Objectives**

In the reference HCPB blanket design, orthosilicate pebbles and 1mm diameter beryllium pebbles are used as breeder and multiplier materials, respectively. In follow-up experiments, HCPB-mock-ups and HCPB –test blanket modules (TBMs) will be tested out-of pile in different test facilities.

The beryllium pebbles to be used in ITER experiments must have very low impurity levels in order to minimise activation (nuclear grade material). In future out-of pile tests (e.g. HEXCALIBER mock-up tests in Brasimone and first TBM tests), for economical reasons, non-nuclear quality beryllium material will be used. This material is characterised by a larger impurity level which might change the thermal-physical and thermal-mechanical properties of the pebbles/pebble beds.

In order to be able to extrapolate the results of out-of pile tests to TBM tests in ITER, the pebble/pebble bed properties must be known for both the reference beryllium ( $Be_{ref}$ ) and the beryllium with higher impurity levels ( $Be_{hil}$ ). The  $Be_{ref}$  pebbles/pebble beds have been intensively characterised, see e.g. [4]. This report describes work on the characterisation of  $Be_{hil}$  pebble/pebble beds. This experimental work could not start before September 2005 because of the delayed delivery of the 1mm NGK beryllium pebbles.

#### **2. Characterisation of Beryllium Pebble/Pebble Beds**

##### **2.1 Characterisation of beryllium pebbles**

Table 4 shows the chemical composition of the reference beryllium pebbles [5], acceptable for the use in ITER. The ductility of these pebbles might depend on Al and Mg impurities.

They tend to segregate at grain boundaries as low-melting phases (Al-Mg phases melt at about 450°C). Thus, it is important, if the impurity amounts are higher than the solubility limit, that Al and Mg are tied up by impurities such as Fe and Si, to form solid intermetallic phases stable at high temperatures ( $Al_5Fe_2$  with  $T_{melt} = 1169$  °C and  $Mg_2Si$  with  $T_{melt} = 1085$  °C) [6]. This is possible if the mass ratios Al/Fe and Mg/Si are:

$$\begin{aligned} Al(\text{wt } \%) / Fe(\text{wt } \%) &< 0.5 && (\text{atomic ratio } Al/Fe < 1) \\ Mg(\text{wt } \%) / Si(\text{wt } \%) &< 1.7 && (\text{atomic ratio } Mg/Si < 2) \end{aligned}$$

Table 4: Chemical composition of 1mm NGK Beryllium pebbles (wt%).

Element	reference beryllium, $Be_{ref}$ [2].	higher impurity level beryllium, $Be_{hil}$	
		specified	actual*
Be	99.5	99	99.5
BeO	0.23	0.5	0.27
Al	< 0.04	0.1	0.056
Fe	0.09	0.18	0.12
Mg	<0.03	0.11	0.014
Si	>0.02	0.06	0.032
U	<0.01		
Co	0.001		
Sc	< 0.005		
Mn	0.01	0.04	0.006
Others	~ 0.065		

\* NGK analyses

Table 4 shows that, compared to the specified values for  $Be_{hil}$  pebbles, the actual values are significantly lower and – as far as specified - are not too far from the required values.

The present investigations include various metallographic analyses like REM, optical microscopy, X-ray diffractometry, EDX and QMS to characterise the microstructure as well as an independent analysis of the elemental composition. Detailed results will be available in the near future.

### 3.2 Characterisation of Beryllium pebble beds

#### Youngs modulus of deformation

Uniaxial compression tests (UCTs) were performed in order to determine the relation between uniaxial stress and uniaxial strain both for the first stress increase period (Fig. 6, curve a) and the first stress decrease period (Fig. 6, curve b)). The Youngs pebble bed modulus  $E = \sigma(\text{MPa})/\epsilon(1)$  is determined for curves a) and b) and expressed by a potential function  $E = C$

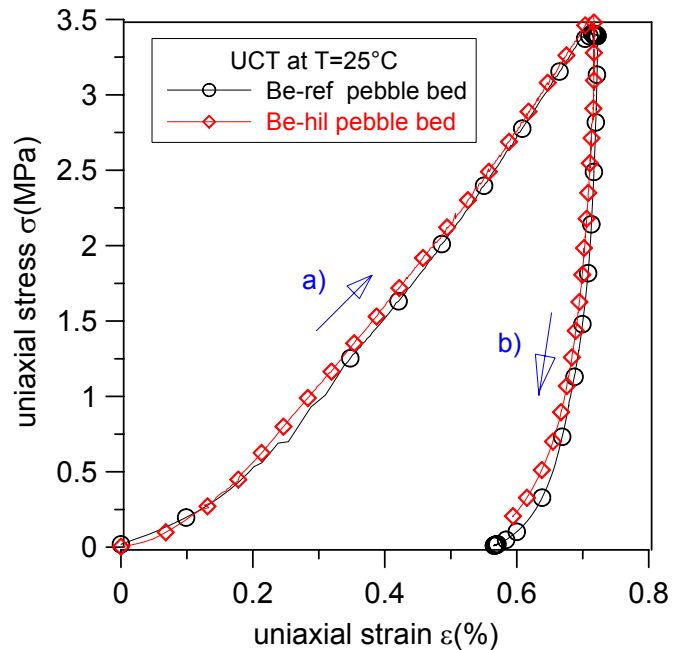


Fig. 6: . Stress-strain relationships for stress increase and decrease (standard beryllium pebbles and non nuclear grade beryllium pebbles).

$\sigma^m$ . Figure 6 shows a good agreement of the curves for  $B_{ref}$  and  $B_{hil}$  pebble beds. Therefore, the correlation proposed previously [4] for  $B_{ref}$ , see Table 5, is recommended to be used also for  $B_{hil}$  pebble beds.

Table 5: Correlation for Youngs pebble bed modulus E for pebble beds, from [4].

Granular material	E(MPa)=C $\sigma^m$ MPa $^m$			
	1 <sup>st</sup> stress increase		1 <sup>st</sup> stress decrease	
	C	m	C	m
1mm NGK beryllium pebbles	313	0.33	1074	0,60

### Thermal creep strain

Figure 7 show thermal creep strains as a function of creep time. Taking into account the thermal creep which occurred during the stress increase period, constant slopes for almost the total creep period are observed. In agreement with results for  $Be_{ref}$  pebble beds [7], creep strain  $\epsilon_{cr}$  is proportional to  $t^{0.35}$ . The temperature and stress dependence of the new  $Be_{hil}$  pebble beds is also in very good agreement with data for  $B_{ref}$ , see Figure 8.

Therefore, again, the correlation established for  $Be_{ref}$ , Table 6, can be directly applied for  $Be_{hil}$  pebble beds.

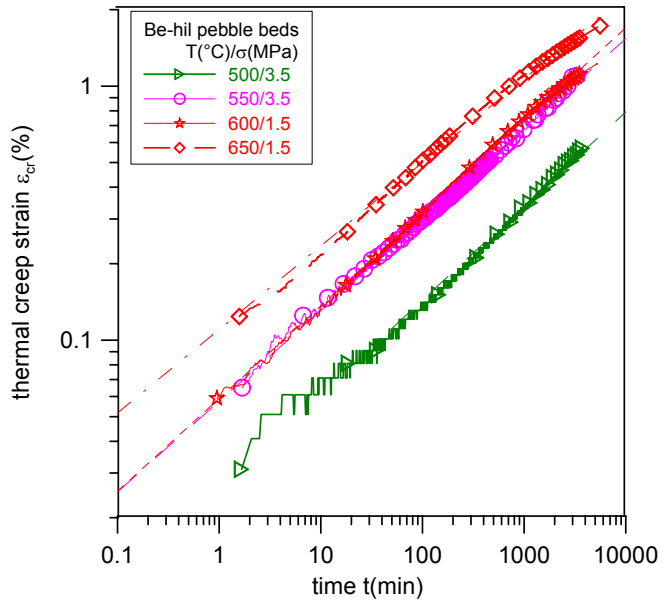


Fig. 7: Thermal creep strain of  $Be_{hil}$  pebble beds.

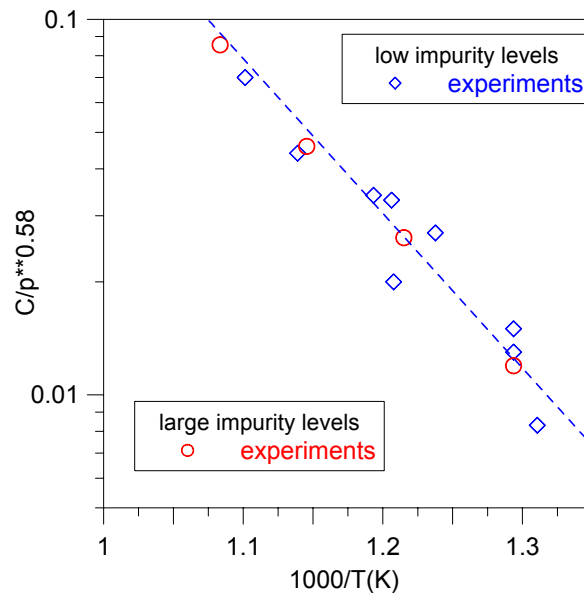


Fig. 8: Temperature dependence of  $Be_{ref}$  and  $Be_{hil}$  pebble beds.

Table 6: Thermal creep correlation for 1mm beryllium pebble beds, from [7].

Granular material	$\epsilon_{cr}(\%) = A \exp(-B/T(K)) \sigma(\text{MPa})^p t(\text{min})^n$			
	A	B	p	n
1mm NGK pebbles	1614	9124	0.62	0.35

### Thermal conductivity

The influence of pebble bed compression on the thermal conductivity  $k$  of  $\text{Be}_{ref}$  pebble beds was investigated in detail recently [8, 9]. The following correlation was proposed:

$$k(\text{W}/(\text{mK})) = 1.81 + 0.0012T(^{\circ}\text{C}) - 5 \cdot 10^{-7} T(^{\circ}\text{C})^2 + (9.03 - 1.386 \cdot 10^{-3} T(^{\circ}\text{C}) - 7.6 \cdot 10^{-6} T(^{\circ}\text{C})^2 + 2.1 \cdot 10^{-9} T(^{\circ}\text{C})^3) \epsilon(\%) \quad (1).$$

Experiments with  $\text{Be}_{hil}$  pebble beds were performed in the temperature range between 300 and 650°C, using the HECOP-facility. Some test section components were replaced prior to the measurements. Therefore, an experiment with a  $\text{Be}_{ref}$  pebble bed was also performed. Figure 9 shows a comparison of the new experimental data with the correlation (1). The agreement is good, the data scatter is within the range observed previously, see [8, 9].

### 3. Conclusions

The new 1mm beryllium pebbles with higher impurity levels ( $\text{Be}_{hil}$ ) compared with the reference granular material ( $\text{Be}_{ref}$ ) to be used in ITER has not been characterised completely yet. Big differences are not expected because the actual impurity levels are not very far from the impurity levels of the reference material.

The corresponding pebble bed investigations show that the pebble bed data established for  $\text{Be}_{ref}$  can be directly applied. These data can be considered as a valuable complement of the previous pebble bed data base.

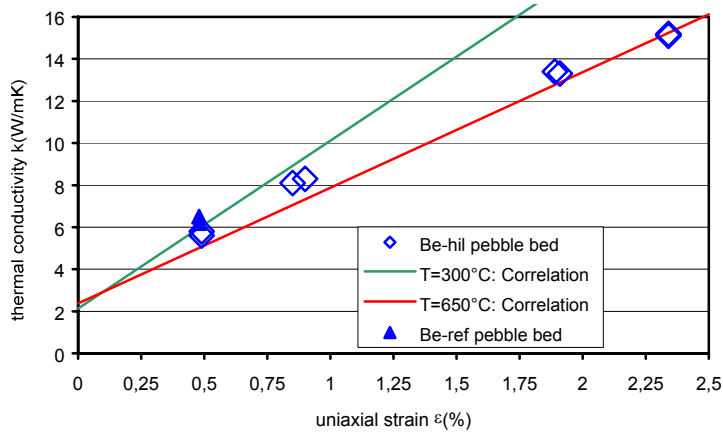
#### Staff:

P. Kurinski  
A. Möslang  
J. Reimann  
H. Harsch

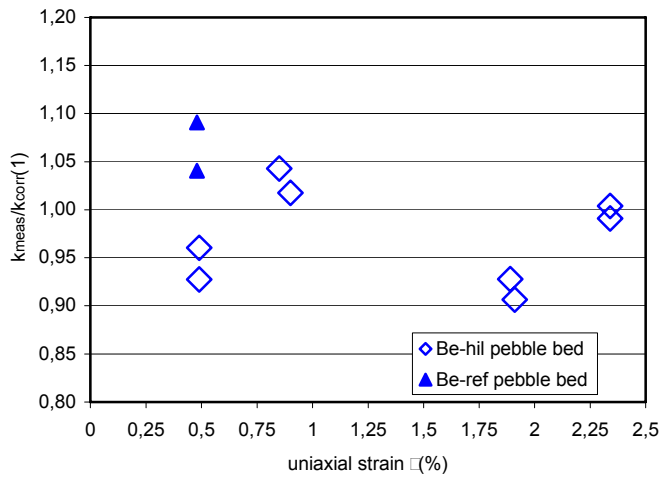
#### Literature:

- [4] J. Reimann, Material Assessment Report on Beryllium Pebble Beds for EU HCPB Test Blanket Module, Internal FZK Report IKET 10/05, FUSION 256, Oct. 05.
- [5] G. Piazza, Report on the characterisation of beryllium pebbles activity, EFDA reference: TW2-TTBB-007a Deliverable Nr. 1, March, 2003.
- [6] H. Kleykamp, Selected thermal properties of beryllium and phase equilibria in beryllium systems relevant for nuclear fusion reactor blankets, J. Nucl. Materials 294 (2001), 88-93.
- [7] J. Reimann, H. Harsch, Thermal creep of beryllium pebble beds, 23<sup>rd</sup> Symp. Fusion Techn., 20-24 Sept., Venice, Italy, 2004.
- [8] J. Reimann, G. Piazza, Z. Xu, A. Goraieb, H. Harsch, Measurements of the Thermal Conductivity of Compressed Beryllium Pebble Beds, FZKA 7096, May 2005.
- [9] J. Reimann, G. Piazza, H. Harsch; Thermal conductivity of compressed beryllium pebble beds, ISFNT-7, Tokyo, Japan, May 22-27, 2005.

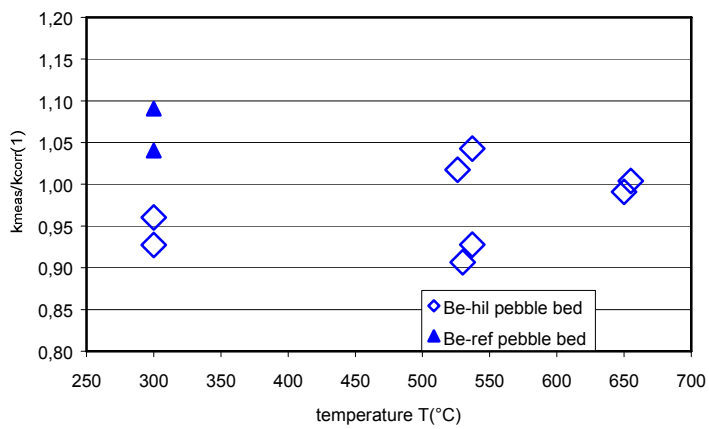




a)  $k = f(T)$



b)  $k_{meas} = k_{corr} = f(\epsilon)$



c)  $k_{meas} = k_{corr} = f(T)$

Fig. 9: Experimental data on thermal conductivity  $k$  of beryllium pebble beds as a function of bed strain  $\epsilon$ .

## TTBB-006b

### Helium Cooled: Thermo-mechanical Modelling of Pebble Bed Assembly

#### TW2-TTBB-006b D 2

#### Development of Pebble Beds Models

A thermo-mechanical model for pebble beds is developed based on earlier experiments. The framework of the present material model is composed of a non-linear elastic law (Coube, 1998), the Drucker-Prager Cap theory (ABAQUS), a modified creep law (Hofer and Kamlah, 2005), and volumetric plastic strain dependent thermal conductivity of beryllium pebble beds (Reimann *et al.*, 2005).

By analyzing the deformation mechanism of the oedometric experiments, a new method was developed to determine the set of material parameters from the empirical curves, including the temperature dependent hardening law. With the new method, the empirical equations (Reimann fits for pebble beds) can be used directly and also the thermo-plastic behavior of pebble beds is predicted. All these thermo-mechanical constitutive laws are implemented in ABAQUS with a subroutine USDFLD (user defined field) and CREEP. The oedometric compression tests and creep tests under different temperatures are simulated by the present model, and the results show that the model gives a good description of experimental results.

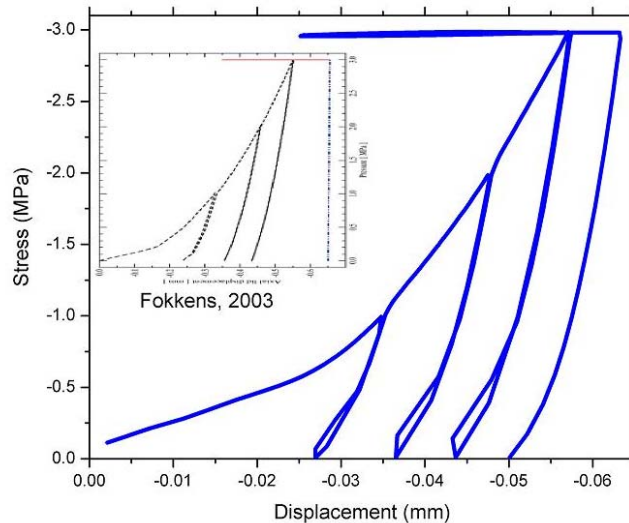


Fig. 1: Stress-displacement curve of pressure lid.

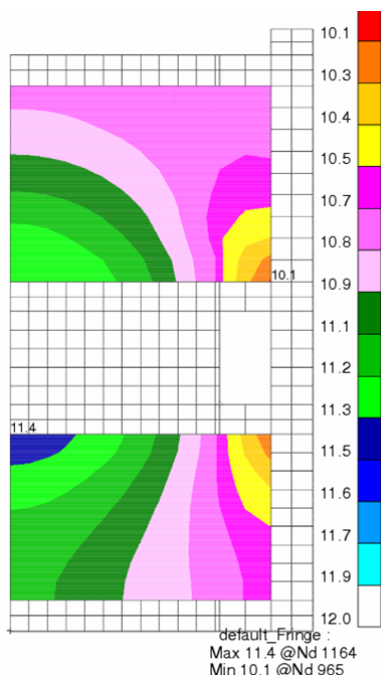


Fig. 2: The profile of thermal conductivity of the beryllium pebble beds after the precompaction procedure.

Furthermore, the precompaction procedure of the pebble bed assembly experiment (NRG Petten, see Fokkens, 2003) is simulated for validation purposes. With the present thermo-mechanical pebble bed model, the displacement of the lid, and the thermal conductivity of beryllium pebble beds are computed (see Fig. 1 and Fig. 2)..

#### Staff:

Y. Gan  
M. Kamlah

Literature:

- [1] Coube, O. (1998). Modelling and numerical simulation of powder die compaction with consideration of cracking. PhD Thesis.
- [2] ABAQUS User Manual.
- [3] Fokkens, J. H. (2003). Thermo-mechanical finite element analysis of the HCPB in-pile test element. TW0-TTBB-004-D1.
- [4] Hofer, D. and Kamlah, M. (2005). Drucker–Prager–Cap creep modelling of pebble beds in fusion blankets. *Fusion Engineering and Design* **73**, 105 - 117
- [5] Reimann, J. *et al.* (2005). Measurements of the thermal conductivity of compressed beryllium pebble beds. FZKA 7096.



# **Breeding Blanket HCLL Blanket Concept**



## TTBA-006b Water-Cooled: Magneto-Hydrodynamics

### TW2-TTBA-006b D 1 Test and Modeling of Forced Convection MHD

The objective of the subtask is the investigation of liquid metal magneto-hydrodynamic (MHD) flows in expansions or contractions which are major components of the currently considered HCLL concept. Abrupt changes of flow direction in feeding and draining lines as well as expansions and contractions cause flow redistributions and additional pressure drops. Experiments on MHD flows in a sudden expansion of conducting rectangular ducts have been performed in the MEKKA laboratory of the Forschungszentrum Karlsruhe. The measured quantities presented here are the pressure variation along the axis of the duct and the surface potential for different values of flow rate and magnetic field. These values are compared with results of an inertialess asymptotic analysis and with complete numerical simulations.

#### Experimental setup

The test section for a sudden expansion has been fabricated from stainless steel with walls of 3mm thickness. A number of 16 pressure taps positioned along the upper wall are connected to a pressure measurement system. This consists of an array of valves that switch the pressure measuring tubes to a line of pressure transducers of different sensitivity. The test section has been covered by fiberglass plates on which more than 300 potential probes are mounted for detection of the distribution of electric potential values from the surface of the duct (Fig. 1). Electrical surface signals are connected to a multiplexer that switches the large number of signals in packages of 20 individuals to a digital nano-voltmeter that measures the mean values. The multiplexer and the nano-voltmeter are controlled by a PC.



Fig. 1: Test section.

Velocities at different axial cross sections are measured using traversable potential probes. Fig. 2 shows the traversing mechanism used to travel the probe through a cross section close to the expansion.

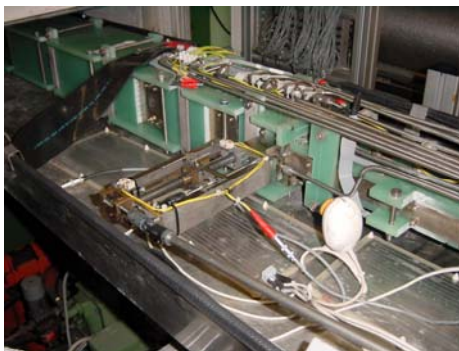


Fig. 2: Drive for velocity probe.

As working fluid the eutectic alloy NaK is used which allows (in the available magnetic field of 2T) to reach flow parameters close to those expected in fusion applications. The Hartmann number whose square measures the ratio of electromagnetic forces to viscous forces may reach values close to  $Ha=6000$ . Inertia effects are characterized by the interaction parameter  $N$  which denotes the ratio of electromagnetic to inertia forces. In the experiments  $N$  varies between 50 and  $10^5$  so that one gets a complete view of the whole range of inertial flows.

The pressure distribution along the upper wall has been measured at different axial positions. Fig. 3 shows results for a high magnetic field with  $Ha=5000$  for different interaction parameters. The experimental data are compared with the results of an inertialess asymptotic theory valid for infinite  $N$ . The results show that the measured values for pressure (symbols) converge monotonically towards the theoretical line with increasing values of  $N$ . Nevertheless, even at such high values as  $N=39151$  the flow is still weakly inertial. It is possible to identify an irreversible pressure drop  $\Delta p_{3D}$  due to three dimensional effects near the expansion. Careful evaluation of this property shows that the pressure drop at an expansion is composed mainly by two contributions as  $\Delta p_{3D} = \Delta p_{3D,v} + \Delta p_{3D,i}$ , where  $\Delta p_{3D,v}$  and  $\Delta p_{3D,i}$  stand for the viscous and inertial contribution, respectively. As shown in Figs. 4, 5 these contributions scale as  $\Delta p_{3D,v} \sim Ha^{-1/2}$  and  $\Delta p_{3D,i} \sim N^{-1/3}$ .

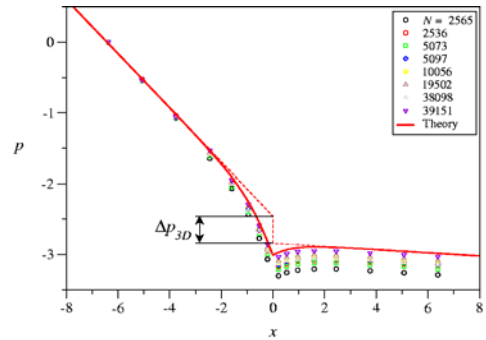


Fig. 3: Pressure along the axis for  $Ha=5000$  and different values of  $N$ .

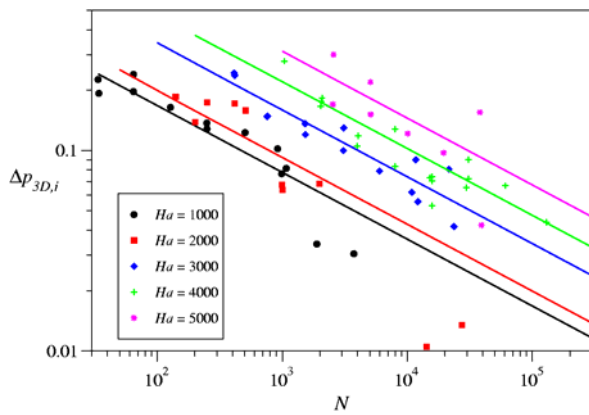


Fig. 4: Inertial fraction of pressure drop.

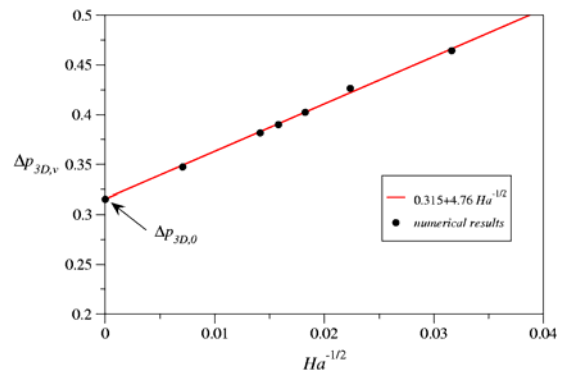


Fig. 5: Viscous fraction of pressure drop.

The electric potential measured on the surface of the duct wall agrees also quite well with those obtained by an asymptotic theory and by numerical simulations with an extended version of the commercial software CFX. Therefore one can conclude that the validity of both types of analyses can be confirmed by the present experiments.

With these experiments the subtask task TW2-TTBA-006b-D1 is completed. The final report is expected in January 2006.

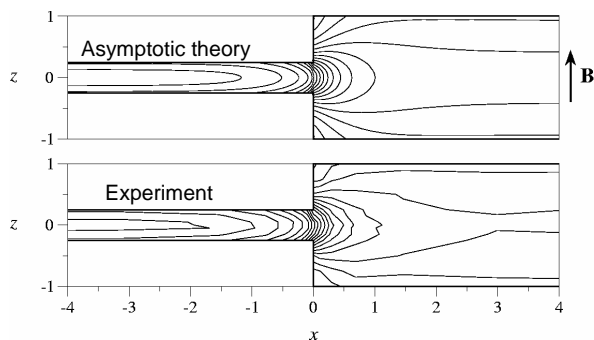


Fig. 7: Isolines of potential on the side wall of the expansion  $Ha=4000$ ,  $N=2000$ .

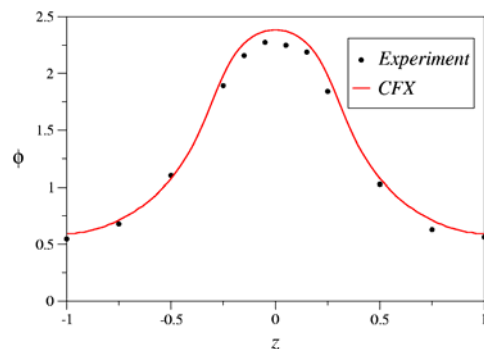


Fig. 8: Potential at the side wall at  $x=0$  along magnetic field lines,  $Ha=500$ ,  $N=50$ .



## Conclusions

Experiments for MHD flows in a sudden expansion have been performed in the MEKKA laboratory of the Forschungszentrum Karlsruhe for Hartmann numbers up to  $Ha=5500$ . Approaching the expansion the magnitude of pressure gradient increases considerably due to a 3D electric current loop. Some fraction of this extra pressure drop is recovered behind the expansion. The irreversibly lost part of pressure drop scales proportional to  $Ha^{-1/2}$  and  $N^{-1/3}$ . The results are compared with theoretical predictions on the basis of an inertialess, asymptotic-numeric approach which is valid at high Hartmann numbers. For the high interaction parameters considered so far the agreement between theory and experiment is quite good. Similar quality of agreement was also found in comparisons with theoretical predictions using the commercial software CFX in the range of lower Hartmann numbers.

### Staff:

E. Arbogast  
L. Bühler  
S. Horanyi  
C. Mistrangelo

### Literature:

- [1] Bühler, L.: 2003, Magnetohydrodynamic flows in sudden expansions in strong magnetic fields, 4th International Conference on Electromagnetic Processing of Materials, Proceedings on CD-Rom, Lyon, 14-17 October 2003.
- [2] Bühler, L.: 2003, Inertialess magnetohydrodynamic flows in expansions and contractions, *Forschungszentrum Karlsruhe*, Technical report, FZKA 6904.
- [3] Bühler, L., Arbogast, E., Gnieser, S., Horanyi, S., Stieglitz, R.: 2004, Design and construction of an expansion test section and first experiments, *Forschungszentrum Karlsruhe*, Internal report.
- [4] Horanyi, S.; Bühler, L.; Arbogast, E. 2005, Experiments on magnetohydrodynamic flows in a sudden expansion of rectangular ducts at high Hartmann numbers. *Fundamental and Applied MHD : Joint 15th Riga and 6th PAMIR Internat.Conf.*, Riga Jurmala, LV, June 27 - July 1, 2005 Proc.Vol.1 S.243-46.
- [5] Mistrangelo, C.; Bühler, L. 2005, Three-dimensional magnetohydrodynamic flows in rectangular channels under a non-uniform magnetic field. *Jahrestagung Kerntechnik 2005*, Nürnberg, 10.-12.Mai 2005 Berlin : IN-FORUM GmbH, 2005 S.483-86.
- [6] Mistrangelo, C.; Bühler, L. 2005 Three-dimensional magnetohydrodynamic flows in sudden expansions. *Fundamental and Applied MHD : Joint 15th Riga and 6th PAMIR Internat.Conf.*, Riga Jurmala, LV, June 27 - July 1, 2005 Proc.Vol.1 S.239-42.

## TTBC-006

### Helium-Cooled Lithium Lead: Magneto-Hydrodynamics and Liquid Metal Material

#### TW5-TTBC-006 D 1

#### MHD Experiments on a 3D Relevant Mock-up of the HCLL TBM

The objective of the subtask is to investigate experimentally the magnetohydrodynamic (MHD) flow in a TBM-relevant test section for a Helium Cooled Lead Lithium (HCLL) blanket, in which a number of breeder units arranged in columns, are fed with liquid metal through poloidal manifolds. Most breeder units have common, electrically conducting walls, through which an electrical coupling of neighboring flow regions is possible. A full theoretical description of such electrical coupling is difficult so that major conclusions about MHD flows in a TBM should be drawn from an experiment.

In 2004 a test section for experimental investigations of fusion relevant MHD flows in HCLL breeder units and their poloidal manifolds has been designed. For various reasons it was decided to manufacture the central part of the mock-up from a solid piece of material by spark erosion technique. The thin walls which remain at the end of this process require that the raw material is of high quality. This is realized by using a forging part to avoid danger of lamination. The front part with the poloidal manifold and the rear cover (the first wall in the HCLL) are also made from the same material. The fabrication of all parts is finished. All parts have been checked for correct dimensions, oxides on all surfaces have been removed by chemical cleaning, and the test section has been welded. The new test section has been completed during 2005 so that it can be inserted into the liquid metal NaK-loop of the MEKKA laboratory of the Forschungszentrum.

For safety reasons the completed test section has been pressure tested at a pressure level of 6.2 bar in order to ensure a safe operational pressure range up to 5.6 bar. The pressure test has been performed using argon inert gas to avoid local wetting with water at the internal walls. This reduces the formation of oxide layers and keeps all gaps free from moisture which could become a problem for the future operation of the test section when it is filled with alkali metals. The pressure test was performed submerged in an "aquarium" which allowed the observation of the whole surface for leak detection.

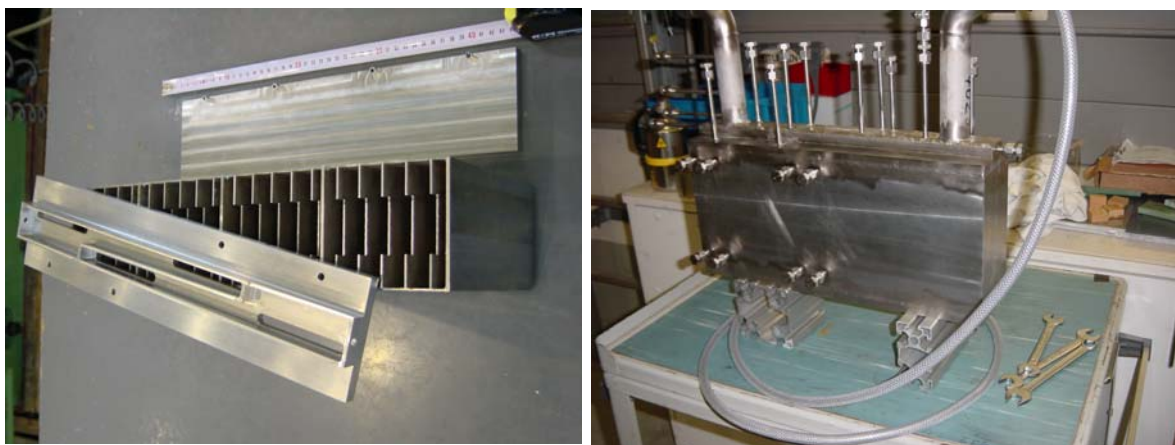


Fig. 1: HCLL test section before welding and finally prepared for pressure test.

Staff:

L. Bühler  
S. Horanyi  
C. Polixa  
J. Rey  
K. Starke

Literature:

- [1] L. Bühler, S. Horanyi, C. Polixa, J. Rey; 2005, Interim Report 2005-1 Design and fabrication of a MHD mock-up for a HCLL TBM, Internal report, Forschungszentrum Karlsruhe..
- [2] Bühler, L. 2005 Magnetohydrodynamic pressure-driven flows in the HCLL blanket Fusion Engineering and Design, Volumes 75-79, November 2005, 923-926.
- [3] Bühler L. Horanyi S., Polixa C. Rey J. 2005, Design and fabrication of a MHD mock-up for a HCLL TBM, Internal report, Forschungszentrum Karlsruhe..
- [4] Reimann, J.; Bühler, L.; Molokov, S. 2005, Magnetohydrodynamic issues of the HCLL blanket. 7th Internat.Symp.on Fusion Nuclear Technology (ISFNT-7), Tokyo, J, May 22-27, 2005.
- [5] Bühler, L.; Wetzel, C. 2005, Asymptotic analysis of 3D buoyant magnetohydrodynamic flows in strong magnetic fields. Fundamental and Applied MHD : Joint 15th Riga and 6th PAMIR Internat.Conf., Riga Jurmala, LV, June 27 - July 1, 2005 Proc.Vol.1 S.235-38.
- [6] Bühler, L.; Giancarli, L. 2005, Magnetohydrodynamic flow in the European HCLL blanket concept. Wissenschaftliche Berichte, FZKA-7069.



## **High Pressure He-Loop – HELOKA**



## TW5-TTB-001

# Construction of the High Pressure He Loop (HELOKA-HP/TBM) for Testing of TBMs

### Objectives

In the EU TBM qualification program it was recently decided to test 1:1 TBM scale mock-ups in an experimental helium loop simulating realistic temperature and pressure profiles in order to validate design calculations and fabrication technologies prior to their installation in ITER. For the performance of such experimental investigations a suitable experimental helium loop must be made available. Therefore a detailed conceptual design of the helium loop HELOKA-HP/TBM has been elaborated which enables testing all He cooling related aspects of TBM mock-ups up to full size and featuring the main following design parameters: 10 MPa, 550°C and helium mass flow rate 1.8 kg/s.

The objective of this task is to construct the HELOKA-HP/TBM loop as presented and agreed in the “EFDA HELOKA Assessment Report” in a renovated building of FZK comprising the purchase of loop components and supply systems, acceptance tests at the manufacturer’s site, installation, commissioning and acceptance tests.

### Design of the auxiliary systems

The construction started in 2005 by installing/upgrading the auxiliary systems: the water cooling system and the power supply system in the HELOKA experimental hall.

### Water Cooling System (WCS)

The water cooling system (WCS) already existing in the HELOKA experimental hall has a cooling capability of 7 MW. The TBM thermal load is estimated to be between 2.5 and 3.5 MW, which is well below the maximum cooling capability of the system.

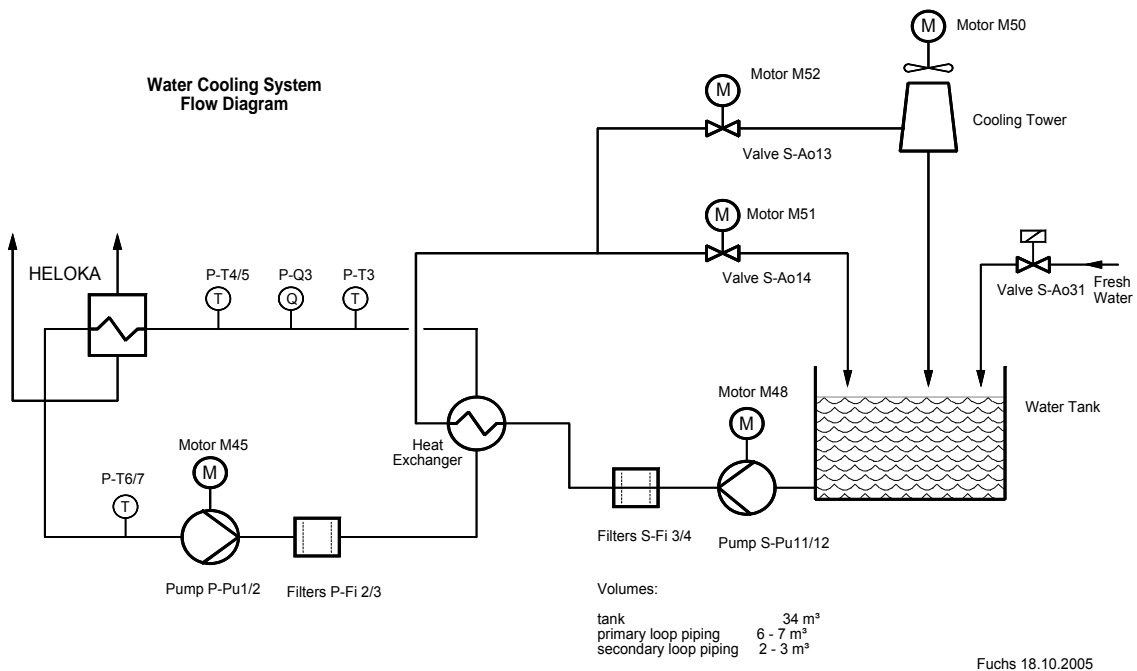


Fig. 1: Water Cooling System – Flow Diagram.

The water cooling system (WCS) consists of two loops connected by a heat exchanger (see Fig. 1):

- The primary loop, which feeds to the water distribution system (WDS) with a flow rate of 450 m<sup>3</sup>/h, and
- the secondary loop, with a flow rate of 470 m<sup>3</sup>/h, which uses a cooling tower, installed on the roof, and a large indoor tank capable to store up to 34 m<sup>3</sup> of tap water.

The initial number of signals to and from the control room was relatively small due to the facts that many WCS components were manually controlled, many measuring positions had local displays and/or settings (information is not further sent to either the local control cabinet or the control room) and most of the control loops were locally implemented (in the local control cabinet), only alarm information being sent to the control room.

The system has been upgraded for the HELOKA requirements defined in order to test the ITER Test Blanket Modules (TBM) starting from 2008, as follows:

- The control has been modified.
- The instrumentation has been analyzed, in order to decide which additional measurements are necessary and which should be replaced. All the instruments for which the signal cables are gathered on the terminal block in LCC have been kept, while most of the instruments that can be read only locally have been replaced by new sensors. New measuring positions have been also added.
- The existing water distribution system (WDS) has to be dismantled and to be replaced by a new water distribution system for the HELOKA experiment.

Initially, the WCS worked at constant flow rates both in the primary and in the secondary loop. For energy saving purposes, the control of the flow rate as a function of the heat required to be removed from the experiment, has been implemented.

## **Power Supply System**

In 2005 the engineering support for HELOKA in the fields of control, instrumentation and power supply systems has been concentrated mainly in the following activities:

1. Infrastructures and electric installations.
2. Analysis of switching transients on the 20 kV supply grid.
3. He loop circulator.
4. Upgrade of the existing 7 MW Water Cooling System.
5. Sequential control of resistive heaters.

**Infrastructures and electric installations.** In 2005 two existing buildings for the housing of HELOKA were investigated and an experimental hall was selected which requires relatively low refurbishment costs and fully meets the HELOKA requirements. After an analysis of the existing electric installations and infrastructure, the activities included the preparation of AutoCAD drawings of possible layouts and preliminary cost estimates.

**Analysis of switching transients on the 20 kV supply grid.** The analysis has been performed with a computer code for the modelling and simulation of electric circuits, called “Sim Power Systems”, running under SIMULINK. The analysis was focussed mostly on TBM loads in the test section and on the He loop main loads (He heater and circulator). The 20 kV external network was simulated with an equivalent generator of a given short circuit power and X/R. Two step-down transformers of 2.5 MVA each will be used to bring the voltage to the required level of 700 and 400V. The short circuit power of the existing substation is quite high (i.e., 309 MVA in the normal configuration). The simulations have shown that an expected maximum pulsed load of 5 MVA there is no need of reactive power compensation.



**He loop circulator.** This concerns the engineering support for the preparation of the Technical Specification for the supply of the circulator for the He loop, launched by EFDA, in collaboration with ENEA Brasimone. The activity was concentrated mainly on control, interlock, instrumentation, definition of the electric drive and power supply.

**Upgrade of the existing 7 MW Water Cooling System.** A status of the art control and data acquisition system is being proposed for control, monitoring and energy management of the existing water cooling system. The control and monitoring of the system designed and installed in 1981 for the BETA experiment, need to be modernised if, as planned, the system is going to be used for the next 10-15 years (at least). In addition, the cooling system runs at constant flow (450 m<sup>3</sup>/h in the primary and 500m<sup>3</sup>/h in the secondary) and therefore a substantial energy saving can be obtained if variable speed drives are used (e.g., since the torque of the pumps is proportional to the square of the speed at 1/2 of the rated speed the power is 1/8 of the rated power). The new control system includes also the control and monitoring of the auxiliary power system feed from the 20 kV grid through a 1.6 MVA transformer.

**Sequential control of resistive heaters.** Resistive heaters, feed by single phase or three phase ac, are normally controlled with power semiconductors (e.g., thyristors) connected back-to-back, as shown in Fig. 2.

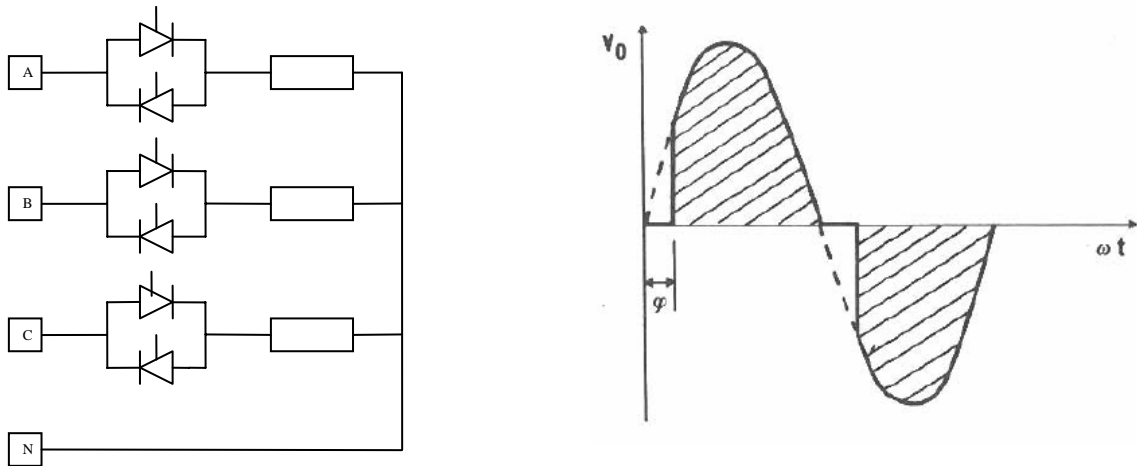


Fig. 2: Three phase resistive load controlled by thyristors connected back

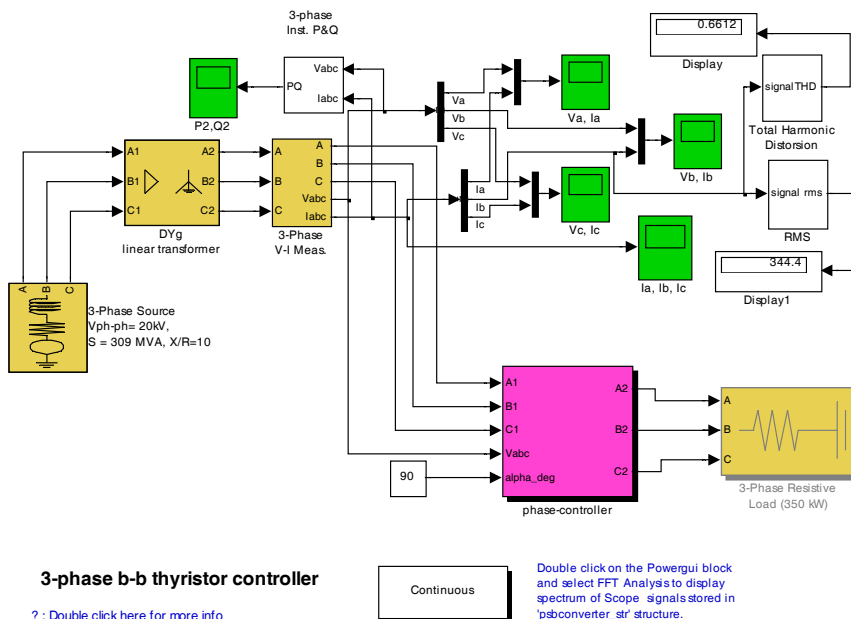


Fig. 3: "Sim Power Systems" model for the control of a 3-phase resistive load.

Figure 3 shows a “Sim Power Systems” model for the control of a 3-phase resistive load through the firing angle  $\phi$ .

The active power dissipated in the resistors is a function of the thyristor firing angle. For example, with  $\phi = 90^\circ$  the rms (root mean square) current is 50% of the nominal current and the active power 25% of the maximum power (see Fig. 4).

The condition  $\phi = 90^\circ$  is most disadvantageous regarding both the Total Harmonic Distortion (THD) and the voltage drop at the supply points (i.e., computed THD = 64.52%). A method to avoid harmonic distortion at the supply point of connection, in alternative to the installation of expensive harmonic filters, is proposed in [1]. For example, a resistive load is split in 4 subunits of each connected to the same power line, shown in Fig. 5. A subunit is operated always in full wave ( $\phi=0^\circ$ ) also during power ramp up, ramp down and during operation at reduced power. All subunit are powered sequentially as shown in Fig. 6 to achieve four discrete power levels:  $\frac{1}{4}$ ,  $\frac{1}{2}$ ,  $\frac{3}{4}$  and 1 p.u. of the rated power. Intermediate power level is also possible controlling the firing angle of one subunit at the time.

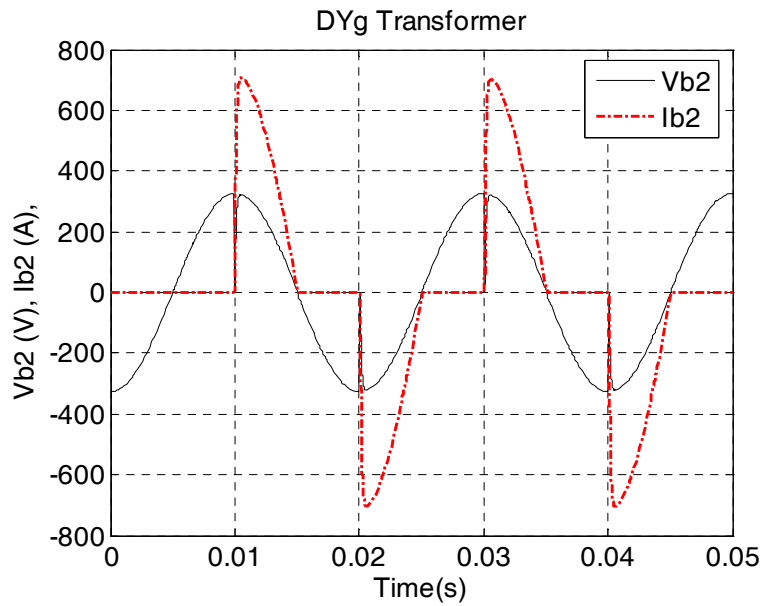


Fig. 4: Computed phase voltage and current ( $\alpha=90^\circ$ ).

This method, proposed for HELOKA resistive heaters, will reduce the voltage drop and the harmonic distortion at the supply point at 20 kV.

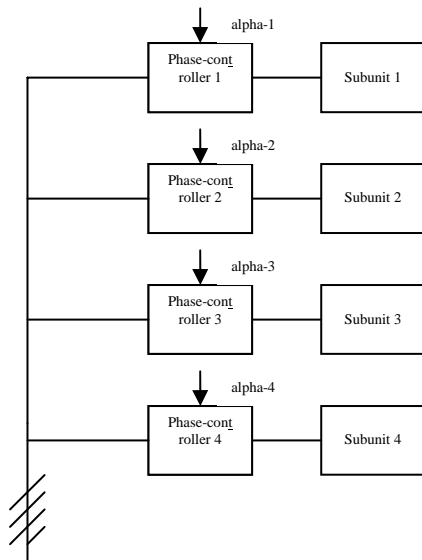


Fig. 5: Sequential control of 4 subunits.

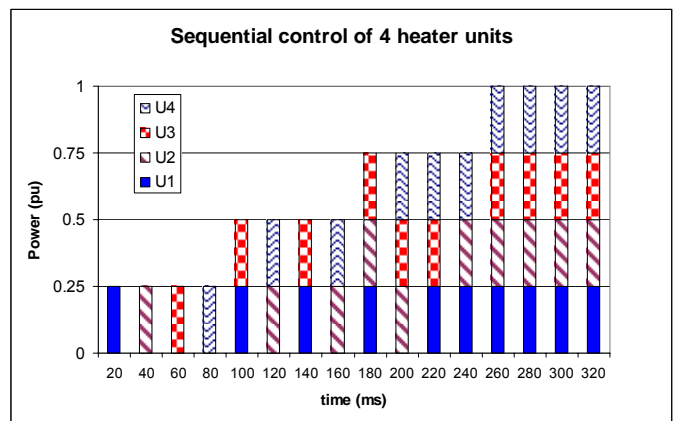


Fig. 6: Control sequence of 4 subunits each operating in full wave mode.

Staff:

B.-E. Ghidersa  
M. Ionescu-Bujor  
X. Jin  
A. Jianu  
V. Marchese  
W. Sengpiel

Literature:

- [1] B.E. Ghidersa, M. Ionescu-Bujor, G. Janeschitz: Helium Loop Karlsruhe (HELOKA): A Valuable Tool for Testing and Qualifying ITER Components and their He Cooling Circuits, Contribution to ISFNT-7 in Tokyo 2005.
- [2] B.E. Ghidersa, M. Ionescu-Bujor, G. Janeschitz, X. Jin: Experimental Helium Loop for Testing ITER-Test Blanket Module and its Cooling System, Contribution to KTG in Nürnberg 2005.
- [3] V. Marchese, Sequential control of TBM resistive heaters, HELOKA-HP/TBM Power System Design Document, PS-0101, Issue 2, 07/07/2005



# **Materials Development Structural Materials**



## **TTMS-001 Irradiation Performance**

### **TW2-TTMS-001b D 5 Tensile, Charpy and Fatigue Specimen Testing after Neutron Irradiation up to 15 dpa in the Range of 250°C-450°C, Completion of the Irradiation and PIE**

#### **Objectives**

Mechanical properties of modified commercial (MANET) steels and newly developed RAFM (OPTIFER, F82H) steels have been thoroughly studied within former irradiation programmes (SIENA, MANITU, HFR Ia, HFR Ib) up to 2.4 dpa (MANET: 15 dpa) at different irradiation temperatures (250/300/350/400/450 °C). Although the reduced activation ferritic martensitic (RAFM) 10%CrWVTa steels (OPTIFER, F82H) exhibit clearly better irradiation performance compared to the modified commercial 10-11%-Cr-NiMoVNb alloys (MANET), the hardening induced by neutron irradiation accompanied by the embrittlement and by reduction of toughness still remains a main concern indicating a further need of material improvement. The objectives of the HFR Phase IIB – SPICE irradiation experiment are to evaluate the mechanical properties of material samples after irradiation at a nominal dose of 15 dpa and at different irradiation target temperatures (250/300/350/400/450 °C). The aim is the development of structure materials for future fusion reactors.

In the SPICE irradiation programme the emphasis is put on the investigation of irradiation induced embrittlement and hardening in the newly developed reduced activation steel EUROFER 97 for different heat treatment conditions (EUROFER97 ANL: 980 °C/0.5 h + 760 °C/1.5 h and EUROFER97 WB: 1040 °C/0.5 h + 760 °C/1.5 h) and for HIP powder steels. The alloy is a result of the development from OPTIFER I to OPTIFER VII intensively studied in previous irradiation programmes (MANITU, HFR Ia, HFR Ib) that already showed promising embrittlement behaviour after neutron irradiation up to doses of 2.4 dpa. The embrittlement behaviour of EUROFER 97 is compared with the results on international reference steel F82H-mod included in the SPICE project. A role of He in a process of non hardening embrittlement is investigated in EUROFER 97 based steels, that are doped with different contents of natural boron and the separated <sup>10</sup>B-isotope (0.008-0.112 wt.%).

#### **Work Performed in Previous Reporting Periods**

The SPICE experiments included three simultaneously performed irradiation campaigns placed in a TRIO capsule located in the in-core position (C3) of the High Flux Reactor (HFR), Petten. Three specimen types: Charpy V specimens of KLST type, tensile specimens and fatigue specimens have been loaded into three sodium filled specimen holders coded as 329-01 (SPICE-C), 330-01 (SPICE-T) and 331-01 (SPICE-F), respectively. A total of 130 Charpy, 91 tensile and 160 fatigue specimens were involved. Irradiation at five different target temperatures (i.e. 250,300,350,400 and 450 °C) has started on August 10, 2001 and ended after 771 full power days (31 reactor cycles) on May 24, 2004. An average dose level of 16.3 dpa in steel has been reached according to HFR-TEDDI calculations. The NRG contribution to the SPICE project was limited to the instrumentation and consequently the neutron metrology evaluation of six activation monitor sets in the SPICE-T assembly. The specimens have been transported into the hot cells of the Fusion Materials Laboratory of FZK in December 2004.

#### **Post Irradiation Examination of Specimens**

The second decontamination of the specimens has been performed in the hot cells of the Fusion Materials Laboratory. The instrumented impact tests on irradiated KLST specimens (L-T orientation) have been carried out with a newly built facility installed in the hot cells. The

facility is identical in construction with the one used for testing on unirradiated specimens. The test and evaluation procedures are identical with those employed in previous investigation programmes: 25 J pendulum impact hammer of a striker radius of 2 mm; distance between supports 22 mm; impact velocity 3.85 m/s; strain gauges applied in striker; PC controlled test execution and recording, sampling rate 1 MHz; semi-automatic specimen cooling, heating and transporting system; test temperature range between -180 °C and 600 °C.

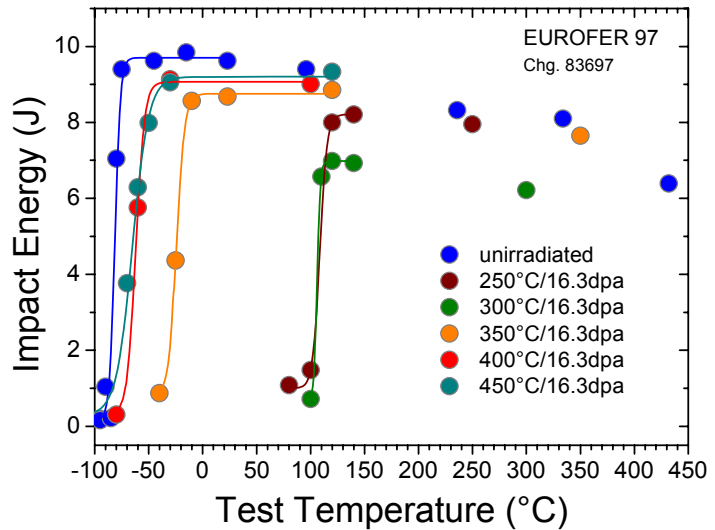


Fig. 1: Charpy impact energy vs. test temperature curves for unirradiated and irradiated EUROFER97 ANL (irradiation conditions are indicated in figure legend). The solid lines are fits according to Eq. (1).

For each experiment, the force vs. deflection curve was recorded. The impact energy (E) was then determined by the integration of force vs. deflection curve. The impact energies have been plotted vs. test temperature (T), see Fig. 1, and analyzed with respect to the characteristic values of the charpy upper shelf energy (USE, i.e. maximum in the energy vs. temperature diagram) and the ductile-to-brittle transition temperature (DBTT). The latter was obtained by fitting the ductile-to-brittle transition region by a hyperbolic tangent function:

$$E(T) = (LSE+USE)/2 + ((USE-LSE)/2) \tanh((T - DBTT)/r) \tag{Eq. (1)}$$

with LSE being the impact energy in the lower shelf, and r the fitting parameter related to the slope of the curve in the ductile-to-brittle transition region.

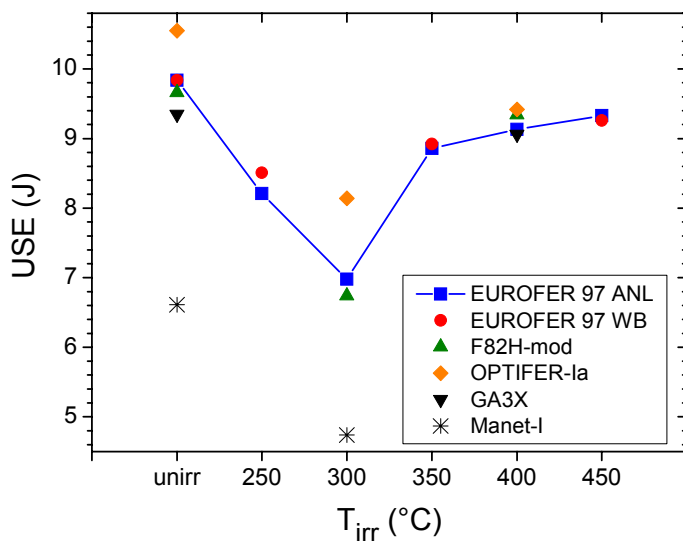


Fig. 2: Upper shelf energies for unirradiated and irradiated conditions (materials are indicated in figure legend).

The dynamic yield stress ( $\sigma_{Dy}$ ) was derived from the force vs. deflection curves at the onset of plastic deformation.

Fig. 2 shows the USE as a function of irradiation temperature ( $T_{irr}$ ), for comparison the results in the unirradiated condition are also included. At low irradiation temperatures ( $T_{irr} \leq 300$  °C) the USE of EUROFER 97 ANL is strongly affected by neutron irradiation mostly pronounced at 300 °C. At higher irradiation temperatures ( $T_{irr} \geq 350$  °C) the USE recovers though it still remains below the USE in the unirradiated



condition of 9.8 J. The impact toughness properties of EUROFER 97 WB are influenced by 250, 350 and 450 °C neutron irradiation in a quite similar way. The 300 °C irradiated reference steel OPTIFER-1a shows the highest USE of 8.1 J, while the USE of 300 °C irradiated F82H-mod is comparable to that of EUROFER 97 ANL. Comparatively, MANET-I showed the worst impact toughness at  $T_{irr}=300$  °C. The 400 °C irradiated OPTIFER-1a, F82H-mod and GA3X show the USE comparable to that of EUROFER 97 ANL.

Fig. 3 shows the DBTT as a function of irradiation temperature, for comparison the results in the unirradiated condition are also included. For all investigated materials the DBTT is mostly influenced at low irradiation temperatures ( $T_{irr} \leq 300$  °C). Remarkably, at  $T_{irr}=250$  °C the DBTT of EUROFER 97 WB is by 50 °C lower than the DBTT of EUROFER 97 ANL. The difference in the DBTT between EUROFER 97 materials austenitized at different temperatures decreases with increasing  $T_{irr}$  completely vanishing at 450 °C. The DBTT of reference F82H-mod and OPTIFER-1a materials compares to that of EUROFER 97 ANL at  $T_{irr}=300$  °C. However, for F82H-mod the slope of the Charpy impact energy curve in transition region is smaller than the corresponding slopes for EUROFER 97 ANL and OPTIFER-1a samples. DBTT of the materials irradiated above 400 °C remain below -30 °C and therewith well below the material application temperature.

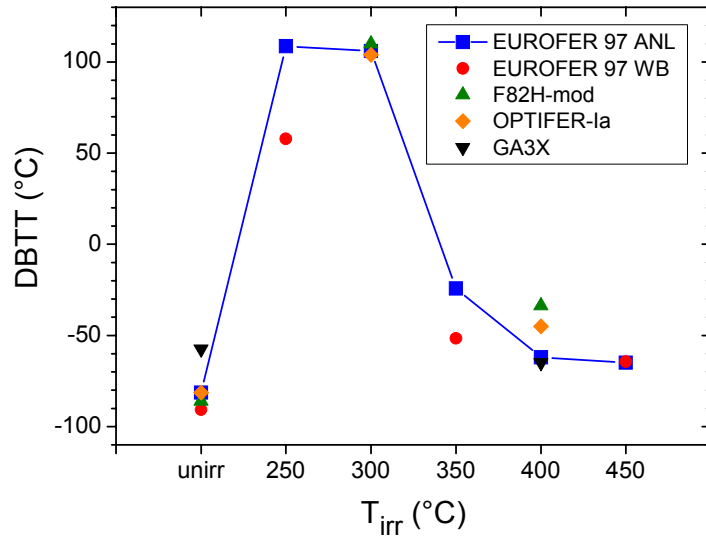


Fig. 3: DBTT for unirradiated and irradiated conditions (materials are indicated in figure legend).

The hardening behaviour of the irradiated materials is shown in Fig. 4 where the dynamic yield stress is plotted as a function of the irradiation temperature. The unirradiated values of the  $\sigma_{Dy}$  are also included for comparison. Two test temperature bins have been defined for the yield stress analysis: a) RT and b) 100-120 °C (nominal 100 °C). At low irradiation temperatures ( $T_{irr} \leq 300$  °C) EUROFER 97 ANL shows strong hardening ( $\Delta\sigma_{Dy}$ ) mostly pronounced at 300 °C/16.3 dpa irradiation. At higher irradiation temperatures ( $T_{irr} \geq 350$  °C) the hardening of EUROFER 97 ANL is substantially reduced in clear agreement with our previous observation on RAFM steels at lower irradiation doses up to 2.4 dpa (HFR Ib). EUROFER 97 WB and reference

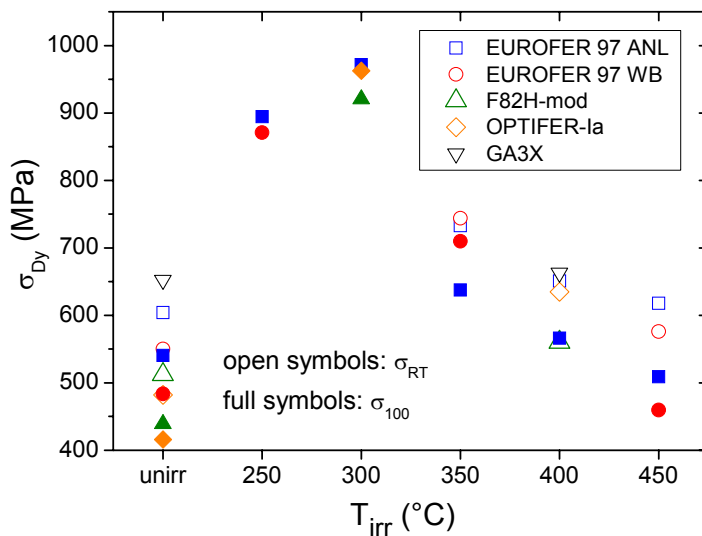


Fig. 4: Dynamic yield stress vs. irradiation temperature (materials are indicated in figure legend); open symbols:  $\sigma_{RT}$ , full symbols  $\sigma_{100}$ .

RAFM steels show basically the same hardening behaviour with irradiation temperature. Remarkably, at  $T_{irr}=300$  °C the dynamic yield stress is comparable for all RAFM steels, though OPTIFER-1a shows the most pronounced  $\Delta\sigma_{Dy}$ .

### **Conclusion and Outlook**

European reference RAFM steel EUROFER 97 irradiated at 16.3 dpa at 250-450 °C showed embrittlement behaviour and hardening comparable to that of best reference RAFM steels. At  $T_{irr}=300$  °C the DBTT and the dynamic yield stress of EUROFER 97 is comparable to those of OPTIFER-1a. The latter showed the best impact toughness at  $T_{irr}=300$  °C. The embrittlement behaviour of reference material F82H-mod at  $T_{irr}=300$  °C is somewhat worse than that of EUROFER 97 ANL showing large impact energy scattering in the ductile-to-brittle transition region. At  $T_{irr}=400$  °C the embrittlement behaviour of EUROFER 97 is superior to that of OPTIFER-1a and F82H-mod, though the DBTTs of these materials remain below -30 °C. Heat treatment of the as-delivered EUROFER97 plate led to the reduction of the embrittlement at low irradiation temperatures.

Charpy impact testing of EUROFER ODS HIP steels as well as EUROFER based steels doped with different contents of natural boron and the separated  $^{10}\text{B}$ -isotope (0.008-0.112 wt.%) will be completed and analyzed with respect to the irradiation performance.

#### Staff:

J. Aktaa  
B. Dafferner  
E. Gaganidze  
S. Lautensack  
E. Materna-Morris  
H. Ries  
R. Rolli  
H.-C. Schneider

#### Literature:

- [1] E. Gaganidze, H.-C. Schneider, B. Dafferner, J. Aktaa, Embrittlement Behaviour of Neutron Irradiated RAFM Steels, submitted for publication in the proceedings of the Twelfth International Conference on Fusion Reactor Materials (ICFRM-12), December 4-10, 2005 Santa Barbara, USA.

## TW2-TTMS-001b D 9

### Fast Reactor Irradiation up to 30 dpa, at 340°C of Tensile, Charpy and LCF RAF/M Specimens, Completion of the PIE

#### Objectives

In an energy generating fusion reactor structural materials will be exposed to very high levels of irradiation damage of about 100 dpa. Due to the fact, that fast reactor irradiation facilities in Europe are not available anymore, a cooperation with the Russian institution SSC RF RIAR has been implemented. The irradiation project is named "ARBOR-1" (Latin for tree). Impact, tensile and low cycle fatigue specimens of Reduced Activation Ferritic/Martensitic steels, e.g. EUROFER 97, F82H mod., OPTIFER IVc, EUROFER 97 with different boron contents and ODS-EUROFER 97 have been irradiated in a fast neutron flux ( $> 0.1$  MeV) of  $1.8 \times 10^{15}$  n/cm<sup>2</sup>s at a temperature less than 340°C up to ~ 30 dpa. Mechanical PIE is under way at SSC RF RIAR

#### Status end of 2004

The modernized LCF-testing facility and the instrumented Charpy testing facility for KLST specimens under remote handling conditions are installed, calibrated and operating in the hot cells of SSC RF RIAR.

#### PIE of ARBOR-1

The mechanical PIE of ARBOR-1 specimens is performed at material science laboratory of SSC RF RIAR. The impact testing results reported here are the first part of the mechanical PIE that includes also tensile and fatigue testing. Due to the fact that tensile test results are still uncompleted and low cycle fatigue tests will start in December 2005, we concentrate here on impact data. The impact tests are performed with a modern instrumented impact testing facility of Zwick 5113-HKE type, equipped with a pendulum hammer of 15 J impact energy and installed in the VK-39 hot cell of the SSC RF RIAR. The primary "force to time" curves are used to determine the impact energy for each specimen. These values are plotted vs. testing temperature and the DBTT is derived as the temperature at which the energy corresponds to USE/2 that is one of the characteristic values for ductile-brittle transition.

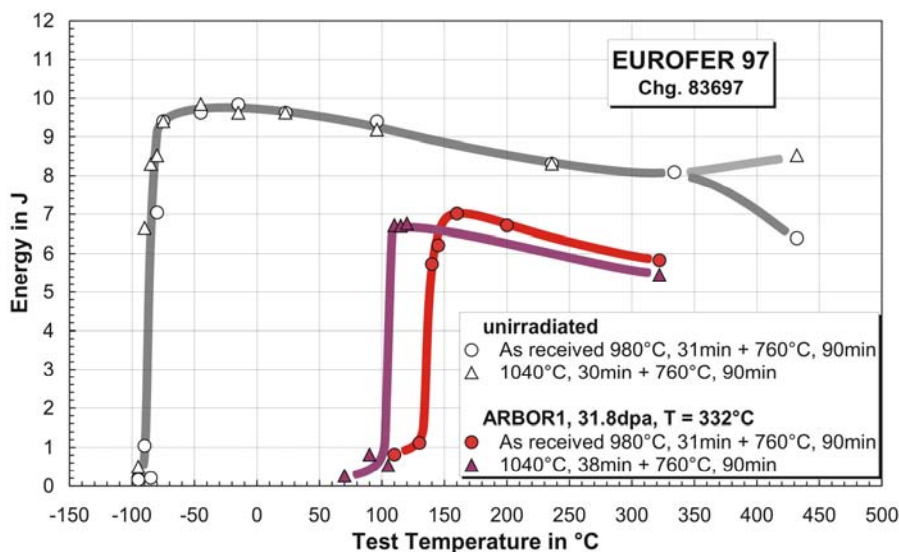


Fig. 1: KLST impact transition curves for unirradiated and irradiated EUROFER 97 of 25 mm plate for two heat treatment conditions.

Results of the technically relevant materials as EUROFER 97, F82H mod. and for comparison also OPTIFER IVc are plotted in the following graphs.

In figure 1 the impact curves for EUROFER 1 and EUROFER 2 are shown in the unirradiated condition and irradiated at 332°C up to 31.8 dpa as an average value. The DBTT-values for unirradiated

ated materials lie very close together (EUROF 1: - 81°C and EUROF 2: - 90°C), the USE-values are for both materials 9.84 J. The DBTT are found for 31.8 dpa damaged EUROF 1 to be 137°C and for EUROF 2 to be 107°C. The irradiation induced shift in DBTT ( $\Delta$ DBTT) has been for EUROF 1 218 K and for EUROF 2 197 K. The USE is reduced in the irradiated state to lower values, as 7.01 J for EUROF 1 and 6.76 J for EUROF 2. The earlier finding was confirmed that the higher austenizing temperature of EUROF 2 with 1040°C reduces the irradiation damage with respect to impact properties, mainly DBTT.

Figure 2 gives the impact curves for F82H mod. in the unirradiated condition and irradiated at 332°C up to 32.3 dpa as an average value. The DBTT for unirradiated condition was - 72°C, the USE-value 9.41 J. The DBTT are found for 32.3 dpa damaged F82H mod. to 148°C. The irradiation induced  $\Delta$ DBTT has been for F82H mod. 220 K. The USE is reduced in the irradiated state to lower values, as 5.03 J for F82H mod.. The reduction in USE after irradiation is much higher for F82H mod. than for EUROFER 97 in both modifications.

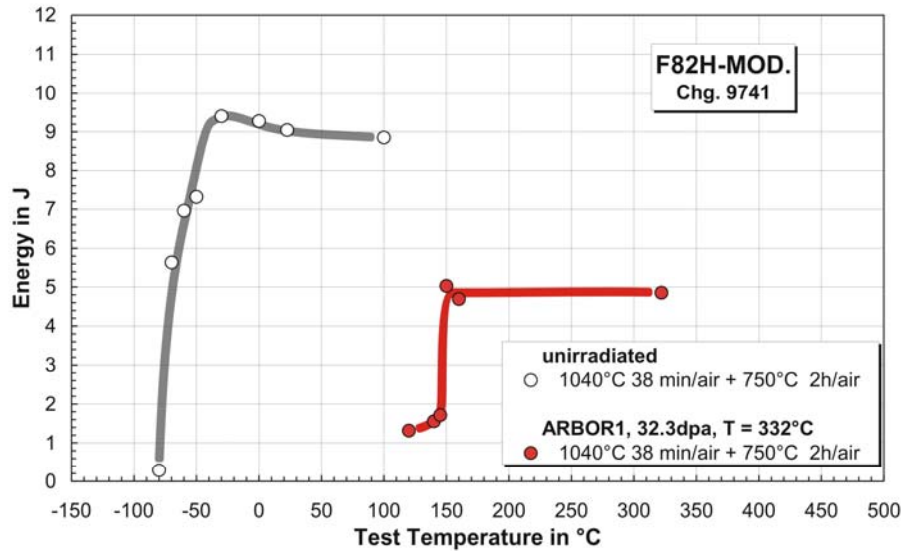


Fig. 2: KLST impact transition curves for unirradiator and irradiated F82H mod. of 25 mm plate for as received condition.

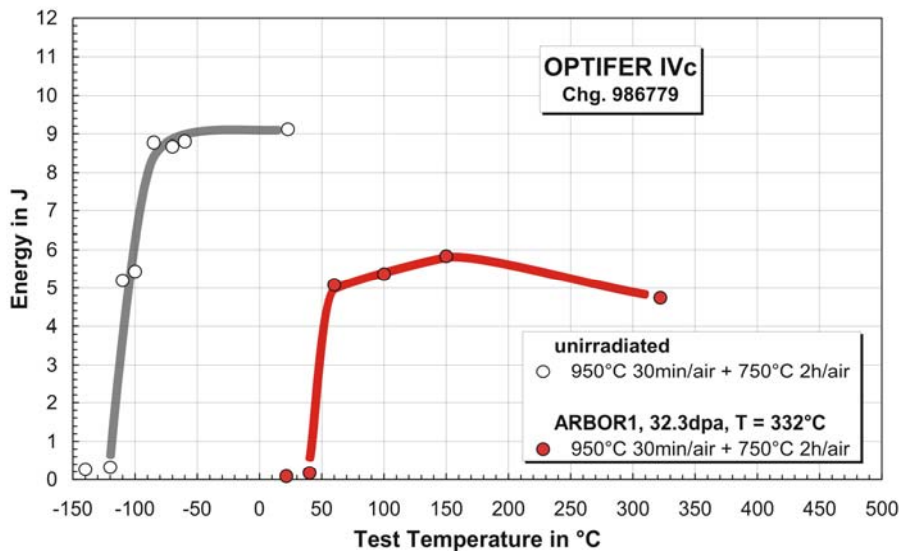


Fig. 3: KLST impact transition curves for unirradiator and irradiated OPTIFER IVc of 25 mm rectangular bar.

The impact behaviour of OPTIFER IVc can be depicted from figure 3. The general tendency is very similar to the above reported materials, but OPTIFER IVc shows the lowest DBTT of 48°C after the ARBOR-1 irradiation conditions of 332°C up to 32.3 dpa. The reduction of USE after irradiation is very similar to F82H mod..

To demonstrate the state of the art of the impact behaviour of RAF/M steels, in figure 4 a comparison of irradiation damage dependence on DBTT of EUROFER 97, F82H mod. and OPTIFER heats is plotted in respect to the conventional steel MANET-I.

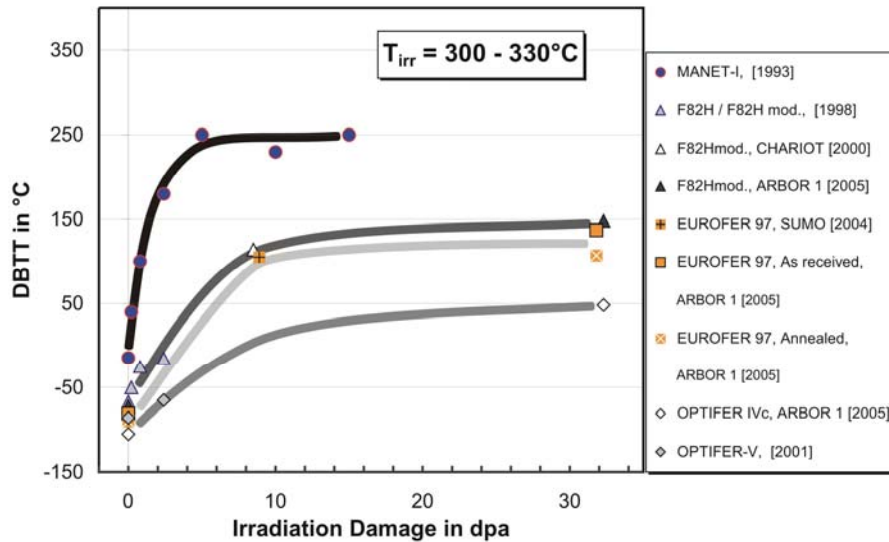


Fig. 4 : Comparison of irradiation dependence on the DBTT behavior for different technically relevant RAF/M steels in respect to conventional 12%Cr steel MANET-I.

The increase of DBTT with increasing irradiation damage is actually half of that of MANET-I, but the hope to have already a saturation state is not confirmed. This answer will be given by the joint ARBOR-2 irradiation with specimens from FZK and CEA irradiated up to a damage of 70 to 80 dpa, respectively.

is a considerable shift in DBTT to higher temperatures for all materials after damage doses of about 30 dpa at 330°C in the ARBOR-1 irradiation.

The general result of the impact tests

The PIE will be continued with tensile and LCF tests in 2006.

Staff:

- B. Dafferner
- M. Klotz
- C. Petersen
- D. Rodrian
- M. Walter
- M. Lerch

Literature:

C. Petersen, A. Povstyanko, V. Prokhorov, A. Fedoseev, O. Makarov and B. Dafferner: "MECHANICAL PROPERTY DEGRADATION OF FERRITIC/MARTENSITIC STEELS AFTER THE FAST REACTOR IRRADIATION "ARBOR 1"", abstract submitted to the ICFRM-12 Conference, accepted as oral presentation, Ref-Nr.: ICFRMA-6ADSQA-26246

## TW4-TTMS-001 D 1

## TW5-TTMS-001 D 2

# Fabrication and Irradiation of Fe-54 enriched Samples to Study the Influence of He/dpa Ratio on Materials Degradation up to Medium Dose Level

### Overview

The structure components of future fusion reactors will suffer from specific irradiation damage, i.e. the ratio of helium production (in appm) to displacement rate (in dpa) varies around 10 appm He/dpa. Due to the lack of appropriate high energy neutron sources there seems to be only one promising way to generate such irradiation damages in a RAFM steel with common in-pile fission reactor irradiation experiments: If the content of natural iron would be replaced by the stable isotope Fe-54, helium production would be stimulated by the according (n, alpha) reactions. A significant advantage over the alternative boron-10 helium production technique would be a uniform helium distribution through the whole matrix as outlined in Fig. 1.

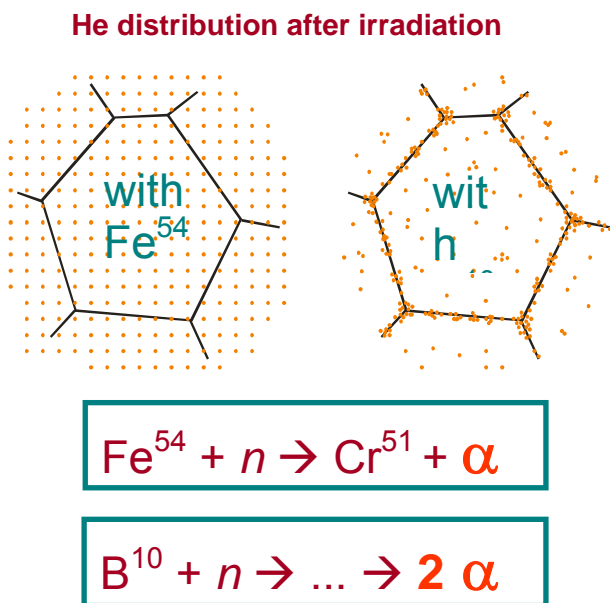


Fig. 1: Boron precipitates mainly at grain boundaries. Therefore, irradiation induced helium production is concentrated on the grain boundaries, too. Compared to the boron-10 helium production technique Fe-54 leads to a uniform helium distribution.

The goal of the task is to produce a heat similar to EUROFER using Fe-54 instead of natural iron. Then miniaturized Charpy and tensile specimens with cores of Fe-54 substituted EUROFER steel have to be fabricated. Finally some of the specimens will be used to perform instrumented Charpy and tensile tests, the remaining specimens will be provided for an according irradiation programme which has to be planned and managed. The whole production, processing and testing procedures have to be accompanied by chemical and micro-structural examinations.

Furthermore, an assessment report on irradiation performance of 8-10%CrWVTa ferritic-martensitic steels (EUROFER, OP-TIFER, and F82H) has to be prepared. Material properties that are taken into account are tensile, Charpy, hardening, isothermal fatigue, and microstructural evolution.

### Initial Status

A number of different pre-tests finally led to a more simplified production of the desired EUROFER plate as was planned initially. Casting the heat into a suitable mould spared further forging or rolling. In a first step all alloy components were molten to pellets in an arc melting furnace. Natural iron was included as powder comparable to the final Fe-54 isotope. The other components were available in form of foliages, small pieces, or powder. Applying this first melting step separates oxide layers and other impurities from the initial alloying components. After that the pellets were molten in a conduction furnace within a ceramic crucible in argon environment. The resulting heat was then cast into a copper mould. Thickness and width were adapted to the desired plate dimensions. As can be seen from Fig. 2, the casting procedure led to a plate with even surfaces free of oxides. In this way only a small amount of the valuable heat got lost.

After that the focus was laid on the investigation of the microstructure of the plate. Before heat treatment it looked inhomogeneous as expected. Further there were relatively large areas of  $\delta$ -ferrite recognizable. But austenitization at 1040 °C recovered a fine grained homogeneous structure. And after annealing at 750 °C the hardness values were at about the same level as with the EUROFER steel. A direct comparison with the EUROFER alloy after austenitization for 1 h at 1100 °C is given in Fig. 3. Both heats show fully martensitic microstructure with about equal grain size. With this it was demonstrated that a plate production is possible without further forging and/or rolling.



Fig. 2: The opened copper mould with the solidified heat.

To reduce the amount of the valuable Fe-54 isotope, needed for the production of a small batch of EUROFER-Fe54, the specimen fabrication was planned as shown in Fig. 4. The final plate (about 6 mm thick) consists of a core of EUROFER-Fe54. Two additional stripes of standard EUROFER will be welded on both sides. Then specimens may be fabricated as indicated in Fig. 4 for the case of a Charpy specimen, i.e. the critical parts (for Charpy specimens this is the notch and for tensile specimens it is the gauge length) consist of EUROFER-Fe54 while the ends are made of standard EUROFER.

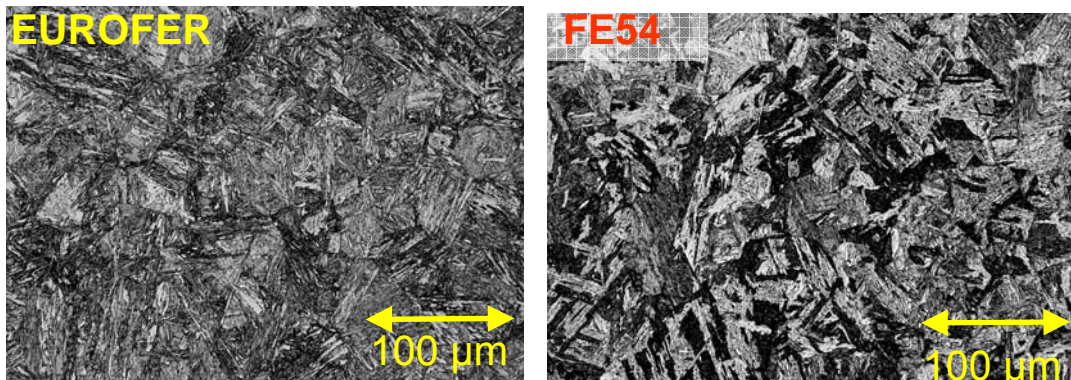


Fig. 3: After annealing at 1100 °C for 1h the EUROFER as well as the test heat of EUROFER FE54 show similar fully martensitic microstructures with about the same grain sizes.

## Progress

In order to find the most suitable joining of the stripes three different welding procedures (TIG with EUROFER filler wire, Electron Beam, and Laser) were applied to EUROFER plates (further details are given in the report TW4-TTMS-004-D1 in this volume). First mechanical tests already showed that Electron Beam welding seems to be the best joining technique for the final EUROFER and EUROFER-FE54 stripes. But completion of the welding investigations has shown that TIG welding is probably more appropriate for this task.

A chemical analysis has been made of the first two experimental Fe-54 melts. The results are depicted in Table 1 together with the Eurofer 97 specification and analysis. As can be seen, content of Cr is too high while C and N are too low in the experimental heats. Some other elements are slightly out of the specification limits but their level is still tolerable.

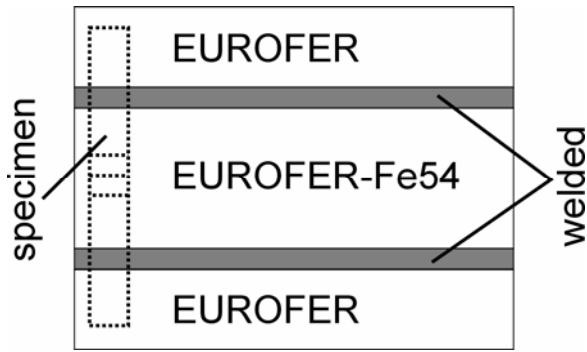


Fig. 4: Specimen fabrication. To reduce the amount of the Fe54 isotope, only critical parts of the specimens consist of EUROFER-Fe54.

The isotope should have been available in April 2005 but finally it was delivered only in October and in addition, the conduction furnace was out of order until recently. Currently a further experimental Fe-54 heat is produced with an improved chemical composition. All further task activities have to be postponed to 2006.

The irradiation is foreseen to take place in the HFIR reactor of ORNL and, if possible, in the Petten HFR. A detailed irradiation program will be elaborated after the specimen fabrication is completed.

Table 1: Chemical analysis of Eurofer 97 and the first two experimental FE54 heats.

	Specification (wt.-%)	EUROFER 97 FZK-Analysis (wt.-%)	1. Experimental Heat FZK-Analysis (wt.-%)	2. Experimental Heat FZK-Analysis (wt.-%)
<b>Cr</b>	8,5-9,5	9,2	9,5	10,5
<b>C</b>	0,09-0,12	0,1	0,041	0,046
<b>Mn</b>	0,2-0,6	0,5	0,4	0,6
<b>V</b>	0,15-0,25	0,2	0,3	0,4
<b>W</b>	1,0-1,2	1,15	1,3	1,1
<b>Ta</b>	0,05-0,09	0,14	0,16	0,14
<b>N<sub>2</sub></b>	0,015-0,045	0,023	0,007	0,002
<b>O<sub>2</sub></b>	<0,01	<0,001	0,006	0,022
<b>S</b>	<0,005	0,004	<0,01	<0,01
<b>Si</b>	<0,05	0,043	0,03	0,01
<b>Al</b>	<0,01	0,0051	0,06	0,02
<b>P</b>	<0,005	<0,04	<0,01	<0,01
<b>Cu</b>	<0,005	0,0035		0,01-0,02

## Conclusions and Outlook

In principle, it has been shown that it is possible to fabricate plates in the proper dimensions by premelting, remelting, and casting which reduces the amount of waste significantly. After optimization of the chemical composition the specimens will be fabricated and planning for irradiation campaigns may be completed.

### Staff:

C. Adelhelm  
 P. Graf  
 A. Falkenstein  
 S. Heger  
 U. Jäntschi  
 A. Möslang  
M. Rieth  
 P. Vladimirov  
 H. Zimmermann



## **TW5-TTMS-001 D 10**

### **Mechanical Post Irradiation Examinations of FZK-Specimens Irradiated in the ARBOR-2 Experiment in the BOR 60 Reactor**

#### **Objectives**

In an energy generating fusion reactor structural materials will be exposed to very high levels of irradiation damage of about 100 dpa. Due to the fact, that fast reactor irradiation facilities in Europe are not available anymore, a cooperation with the Russian institution: SSC RF RIAR, has been implemented. "ARBOR-2" is the succeeding experiment after ARBOR-1 from FZK and ALTAIR from CEA, to reach irradiation damages up to 70 till 80 dpa.

#### **Status end of 2004**

The ARBOR-2 irradiation in BOR 60 of SSC RF RIAR, Dimitrovgrad, with pre-irradiated RAF/M specimens of FZK from the ARBOR-1 irradiation (30 dpa), of CEA from the ALTAIR irradiation (40 dpa) and new RAF/M specimens of FZK and CEA, running up to a damage of 40 to 80 dpa, had been started on February 11, 2003 and accumulated up to the end of 2004 another 30 dpa of damage, i.e. 30.1 und 48.8 dpa for the new specimens and 60.1 dpa for the specimens pre-irradiated in ARBOR-1. The specimens exchanged in June 2004 reached 6 dpa.

#### **The Irradiation project ARBOR-2**

The ARBOR-2 irradiation was running in the 10<sup>th</sup> and 11<sup>th</sup> cycle of irradiation as planned. The maximum damage dose has been reached in May 2005, already, half a year earlier as initially planned. The rig was dismantled. The specimens are identified and stored in the hot cells of SSC RF RIAR.

Negotiations for the contract of mechanical PIE of the FZK part of specimens from the ARBOR 2 irradiation are under way. The aim is to perform these experiments starting September 2006 again at the hot laboratory of SSC RF RIAR under an ISTC partner contract.

#### **Staff:**

B. Dafferner  
M. Klotz  
M. Lerch  
C. Petersen  
D. Rodrian  
M. Walter

## TW5-TTMS-001 D 11

### Assessment of Irradiations Performed on EUROFER 97

#### Objectives

The structure materials of future fusion reactors will be exposed to high neutron flux. Although the reduced activation ferritic martensitic (RAFM) 10%CrWVTa steels (EUROFER, OPTIFER, F82H) exhibits clearly better irradiation performance compared to the modified commercial 10-11%-Cr-NiMoVNb alloys (MANET), the hardening induced by neutron irradiation accompanied by the embrittlement and by reduction of toughness still remain a main concern. The assessment of impact performance of irradiated RAFM steels (EUROFER, OPTIFER, F82H) will support material database generation and specification of new EUROFER-2.

#### Data Collection and Assessment

The collection of irradiated Charpy impact data has been started. The impact data on low and medium dose irradiated EUROFER and F82H steels from SUMO-02÷SUMO-07 irradiation experiments carried out by NRG have been analyzed and prepared for comparison with the low dose irradiation FZK data from MANITU, HFR Phase-Ia, HFR Phase-Ib as well as with the 15 dpa FZK data (SPICE experiment). 15 dpa WTZ data as well as 32 dpa FZK data (ARBOR 1 experiment) have been used for the analysis of the high dose irradiation induced embrittlement trend.

Fig. 1 shows impact data on unirradiated EUROFER 97. The impact testing was performed with KLST type Charpy specimens of  $3 \times 4 \times 27 \text{ mm}^3$  dimensions. The specimens have been machined in L-T orientations from plates of different thicknesses of 8, 14 and 25 mm.

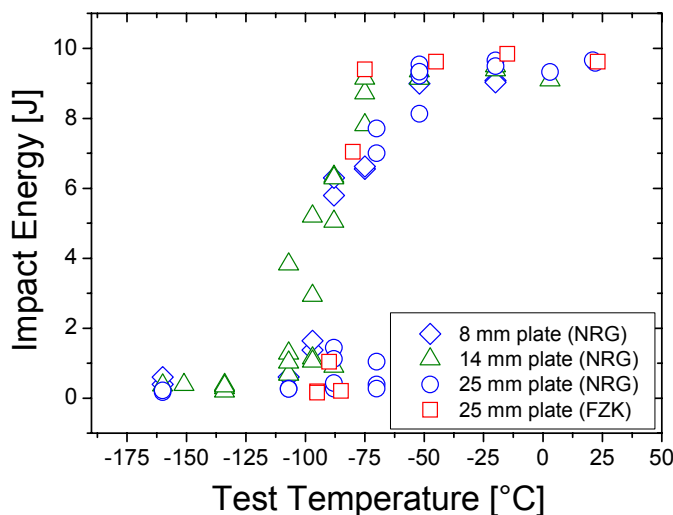


Fig. 1: KLST impact energy vs. test temperature curves on unirradiated EUROFER 97. The thicknesses of plates of base materials along with data sources are indicated in figure legend.

There is a considerable scattering in the ductile-to-brittle transition temperature (DBTT) between  $-90$  and  $-68$  °C. Even the specimens machined from the 25 mm thick plate of the same heat (83697) show remarkably different DBTTs of  $-68$  °C and  $-81$  °C for NRG and FZK experiments, respectively. The DBTT from latter experiment is closer to the DBTT of NRG experiment for specimens machined from 8 mm plate.

Fig. 2 shows KLST impact data on unirradiated and irradiated 25 mm thick EUROFER 97 plate. NRG data show progressive embrittlement with irradiation dose accom-

panied by decrease of the upper shelf energy (USE) – behaviour typical for RAFM steels (OPTIFER, F82H). The data scattering increases for 2.4 dpa/300 °C and 8.9 dpa/300 °C irradiation condition partly due to different doses received by individual specimens. Remarkably, 16.3 dpa/300 °C FZK data show lower embrittlement and the narrower ductile-to-brittle transition region than 8.9 dpa/300 °C NRG data, though the USEs are comparable. 15 dpa/330 °C WTZ data show impact properties that resemble to those of 16.3 dpa/300 °C FZK

data in the transition region. The lower DBTT for 15 dpa/330 °C WTZ data (95 °C) compared to 16.3 dpa/300 °C FZK data (106 °C) is prescribed to the lower irradiation dose and higher irradiation temperature in the former case. 31.8 dpa/332 °C FZK data show further embrittlement, though the USE is comparable to those of 15 dpa/300 °C FZK and 15 dpa/330 °C WTZ data.

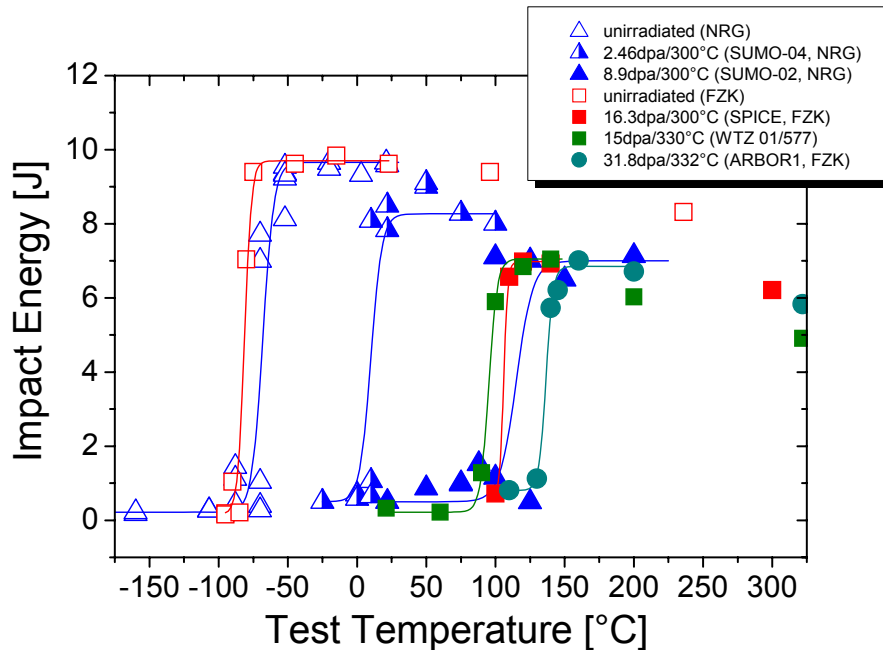


Fig. 2: KLST impact energy vs. test temperature curves on unirradiated and irradiated EUROFER 97. The specimens have been independently machined by NRG and FZK from the as-delivered 25 mm thick plate with the heat number of 83697.

## Conclusion and Outlook

Collection and assessment of the Charpy impact data on RAFM steels (EUROFER, OP-TIFER, F82H) have been started. Although FZK data for 16.3 dpa/300 °C irradiation condition supports the irradiation induced embrittlement trend observed in NRG experiments, large data scattering in the latter case prevents precise quantitative description of the DBTT shift. No embrittlement saturation can be observed by comparison of 15 dpa/330 °C WTZ and 31.8 dpa/332 °C ARBOR 1 experiments. The ARBOR 2 (~330 °C/70 dpa) irradiation experiments will shed more light on the high dose embrittlement behaviour.

### Staff:

B. Dafferner  
E. Gaganidze

### Literature:

- [1] E. Gaganidze, H.-C. Schneider, B. Dafferner, J. Aktaa, Embrittlement Behaviour of Neutron Irradiated RAFM Steels, submitted for publication in the proceedings of the Twelfth International Conference on Fusion Reactor Materials (ICFRM-12), Decemver 4-10, 2005 Santa Barbara, USA.

## TW5-TTMS-001 D 14

### Assessment of Irradiated Fracture Mechanic Samples on EUROFER, F82H (and OPTIFER) to Study the Size Effect

#### Objectives

Various fracture mechanics (FM) experiments have been performed on EUROFER 97 and other reduced activation ferritic-martensitic (RAFM) steels. Different specimen types and testing methods were used for specimens irradiated at different conditions. The assessment aims comparison of DBTT and DBTT shift calculated from different specimen geometries to study the size effects. Comparison of DBTT from FM against Charpy will be also discussed.

#### Data Collection and Assessment

The collection of irradiated FM data on EUROFER and other RAFM steels has been started. In the framework of different irradiation programmes (SUMO-02÷SUMO-07, SIWAS-09, SINAS-80/6, SINAS-80/7) NRG investigated fracture mechanical and impact properties on unirradiated and 2.13, 2.5, 10 dpa irradiated EUROFER and F82H mod. steels. Compact tension specimens of  $W=22.5$  mm (width),  $H=27$  mm (height),  $a_0/W\approx 0.5$  (relative fatigue crack length) and of 5 and 10 mm thicknesses (labelled by CT5 and CT10, respectively) have been chosen for fracture toughness determination. Impact properties have been quantified by Charpy impact testing on KLST specimens of  $3\times 4\times 27$  mm<sup>3</sup>. SCK studied fracture toughness and impact properties on EUROFER 97 irradiated within IRFUMA I, II and III campaigns up to 0.25, 1 and 2.25 dpa nominal doses. Fracture toughness tests have been performed on pre-cracked Charpy v (PCCv) specimens of  $10\times 10\times 55$  mm<sup>3</sup> dimensions,  $a_0/W\approx 0.46-0.53$ . Impact testing has been performed on the standard Charpy specimens of the same dimensions.

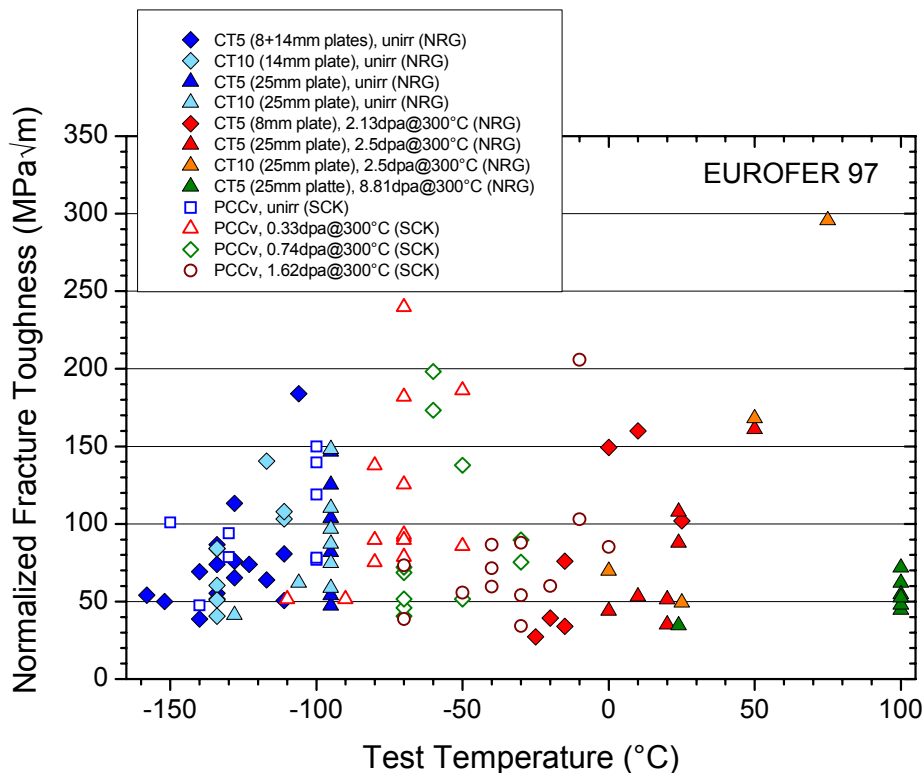


Fig. 1: Fracture toughness data normalized to reference geometry. Specimen type (base material), irradiation condition and data sources are indicated in the legend. Specimens have been machined from 8, 14 and 25 mm EUROFER 97 plates.

Fig. 1 shows uncensored fracture toughness data on EUROFER 97 for unirradiated and irradiated conditions. For comparison of different specimen data, measured fracture toughness data have been thickness adjusted to the reference  $B_0=25.4\text{mm}$  thickness according to statistical weakest link model by the relation

$$K_{25.4\text{mm}} = K_{\min} + [K_{Jc} - K_{\min}] \left( \frac{B}{B_0} \right)^{1/4}.$$

Here,  $K_{Jc}$  is the fracture toughness as measured on a specimen of a thickness  $B$ ,  $K_{\min}$  is the lower bound fracture toughness fixed at  $20 \text{ MPa}\cdot\text{m}^{0.5}$  in ASTM E 1921-02 and  $K_{25.4\text{mm}}$  is the normalized fracture toughness. The NRG data show considerable scattering in the unirradiated condition. Whereas, the 8 mm and 14 mm plates fall in the same scattering band for both specimen thicknesses, the 25 mm plate specimens show lower toughness at a given temperature, or equivalently, a higher transition temperature. The unirradiated SCK data agree well with the unirradiated NRG data, remaining in the same scattering band. The NRG data show progressive embrittlement with irradiation dose from 2.13 to 8.81 dpa. Data scattering is increased for irradiated condition partly due to different damage doses received by individual specimens. The SCK data irradiated between 0.33 and 1.62 dpa confirm qualitatively the irradiation induced embrittlement trend observed for the irradiated NRG data.

No unambiguous correlation is observed between the impact DBTT and the FTTT. For NRG experiments KLST impact DBTT and estimated FTTT show nearly one to one relationship for EUROFER 97 irradiated in similar conditions. For SCK experiments in contrast no clear relationship was found between the irradiation induced standard Charpy impact DBTT and fracture toughness reference temperature shifts. The latter ones were consistently and significantly larger.

## Conclusion and Outlook

Collection and assessment of the fracture toughness and Charpy impact data on RAFM steels (EUROFER, F82H) have been started. Thickness adjusted unirradiated fracture toughness data fall in the same scattering band for CT and PCCv specimens showing no remarkable size and geometry effects. Different fracture toughness results observed for different base materials (different plate thicknesses) indicate toughness dependence on steel fabrication details. Progressive material embrittlement observed for the discussed experiments indicate no saturation for the achieved damage doses. Application of Master Curve (MC) methodology will be tested for the collected data if not done so far. Additional data will be obtained by retrieving the databases and literature.

### Staff:

B. Dafferner  
E. Gaganidze

## TTMS-002 Metallurgical and Mechanical Characterisation

### TW2-TTMS-002a D 19

### Creep-Fatigue Testing at 550°C on EUROFER, Continuation to Longer Times Preferably under Controlled Atmosphere

#### Objectives

A structural component like a Test Blanket Module is subjected during service to alternating thermal and mechanical stresses as a consequence of the pulsed reactor operation. Since the operating temperatures of a future nuclear fusion reactor increase due to economic considerations, the knowledge of the reasons of the creep fatigue endurance of Reduced Activation Ferritic/Martensitic (RAF/M) steels like F82H mod. and EUROFER 97 becomes more important.

#### Status end of 2004

Thermal mechanical fatigue (TMF) experiments with hold times of 1000 s on EUROFER 97 with temperature changes between 100 °C and 450 to 600 °C have been finished. With the modified TMF-test facility for post-irradiation TMF experiments, installed in the hot cell area of CRISM, St. Petersburg, (under binational WTZ-contract) the reference experiment on unirradiated specimens under hot cell conditions has been performed successfully.

#### TMF-experiments

Data of about 500 TMF experiments, with and without hold times, performed in the last 15 years have been transferred to modern data storage media like CD and/or DVD. For these data sets reduction programmes have been developed to implement qualified results of TMF tests on austenitic steels like AISI 316L and on Ferritic/Martensitic steels, including RAF/M modifications, like EUROFER 97, into the CEA data bank as well as in the Mat-DB, the data bank system of JRC, Petten.

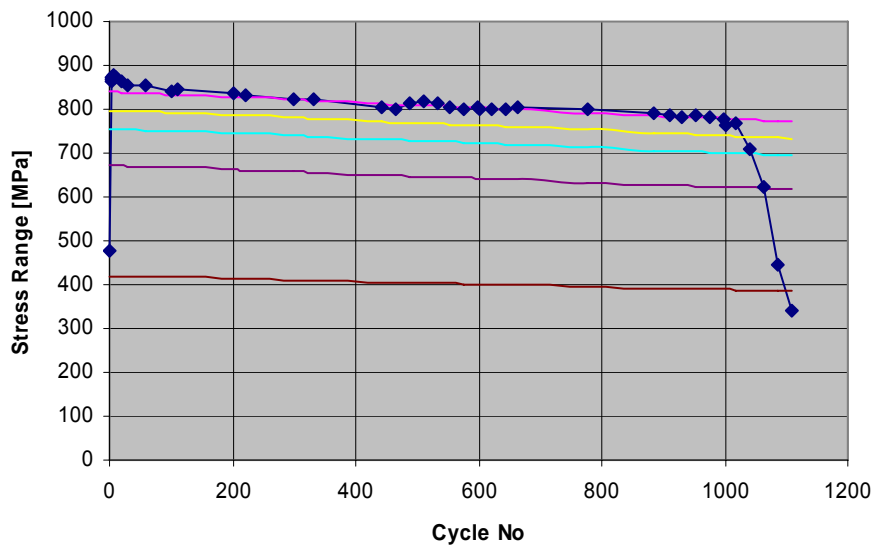


Fig. 1: Cyclic softening behaviour of stress range of NIMONIC 90 in TMF tests between 400 and 850°C, end of life criteria from 5% to 50% of  $N_f$ .

As a basis for this implementation serves the code of practice for TMF experiments on NIMONIC 90 that had been proposed under the European Contract N° G6RD-CT-2001-00526 with the title "Thermo-mechanical fatigue – the route to standardisation" by 21 leading European laboratories, including Forschungszentrum Karlsruhe, in the last 48 months, ending 30 November 2005.

## TMF-experiments on preirradiated specimens

The irradiation at CRISM in 1999 had been performed into two ampoules under the following conditions: low irradiation temperature of 30 to 400 K; low flux density of fast neutrons  $10^{13}$  n/(cm<sup>2</sup>s); that gives about  $10^{21}$  n/cm<sup>2</sup> or an irradiation damage of 1 dpa per year. The irradiation lasted around half a year resulting in about 0.5 dpa.

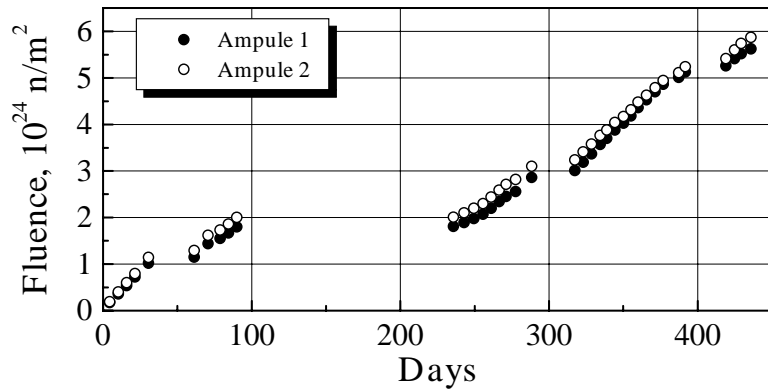


Fig. 2: Irradiation campaign of MANET II and F82H mod. TMF-specimens in the WWW-R reactor of CRISM.

After having performed cold reference tests at the TMF-facility in the hot cells of CRISM on cylindrical hollow specimens of MANET II in the temperature range 100 °C – 550 °C laying in the scatter of our experiments ( $N_f = 69,090$  cycles and  $N_f = 30,256$  cycles) two irradiated cylindrical hollow specimens of MANET II had been tested. The  $N_f$  values in the same temperature range of 100 °C – 550 °C have been reduced to 2,100 and 2,150 cycles, respectively. A similar finding we received with the F82H mod. material. Our cold reference TMF data in the temperature range 100 °C – 550 °C were  $N_f = 5,005$ , 3,261 and 1,725 cycles, whereas after the above irradiation conditions we found  $N_f = 700$  cycles only.

Implementation of qualified results of TMF tests on AISI 316L and on Ferritic/Martensitic steels, including RAF/M modifications into the CEA data bank as well as in the Mat-DB, the data bank system of JRC, Petten is planned for the first half of 2006.

### Staff:

C. Petersen  
D. Rodrian

### Literature:

C. Petersen and D. Rodrian: "Thermo-Mechanical Fatigue Behavior of Reduced Activation Ferrite/Martensite Stainless Steels", to be published in Int. Journal of Fatigue.

## **TTMS-003 Compatibility with Hydrogen and Liquids**

### **TW4-TTMS-003 D 1 Development of Modeling Tools to Describe the Corrosion Behavior of Uncoated EUROFER in Flowing Pb-17Li and their Validation by Performing of Corrosion Tests at T up to 550°C**

#### **Objectives**

Reduced activation ferritic-martensitic steels (e.g. EUROFER) are considered for application in future fusion technology as structural material, which is in contact with the breeding material Pb-17Li. Various corrosion experiments have been made in the past, however, evaluation of these tests, which were mostly conducted up to moderate temperatures of up to 480 °C, was performed with respect to determine corrosion rates and mechanisms e.g. dissolution of some elements out of the steels and comparison of the results with earlier tested RAFM-steels of type F82H-mod., OPTIFER, and MANET. In the mean time the envisaged operation limits e.g. in temperature increased to roughly 550 °C and flow regimes may change. Thus extrapolations of the RAFM-steel corrosion behavior determined in the past to the new working conditions may be problematic due to large uncertainties and, additionally, only poor knowledge on transport of dissolved components in the Pb-17Li flow is present. In contrast to earlier investigations, these changes in requirements need the going over from (only) mechanism-based corrosion tests to model supported tests. Furthermore, the whole loop (system) has to be considered in the evaluation of the corrosion tests together with other occurring phenomena and mechanisms as transport effects and precipitations.

Therefore, under this task the development of modeling tools for describing Pb-17Li corrosion (dissolution, material transport and precipitations) will be performed besides updating the corrosion loop PICOLO and performing corrosion tests at the new relevant temperature of 550 °C. The modular structured tools are based on physical, chemical and thermo-hydraulic parameters and, in the first stage, the development will be focused on the dissolution of EUROFER (as iron-based alloy) and validation with older test results obtained at 480 °C in our PICOLO loop. In the second stage the new gained 550 °C test results will be used for validation and transport phenomena will be included. This report will give first results concerning corrosion testing at 550 °C and modeling of 480 °C tests.

#### **Corrosion testing**

The alloy EUROFER 97, a 9 Cr W V Ta alloy, which was developed on base of the experience with RAFM alloys of e.g. Optifer type, is at the moment the favored FM-steel for application in a future fusion system. During the last years the thermal and mechanical behavior of EUROFER 97 was examined [1] and first corrosion testing in the Pb-17Li loop PICOLO [2, 3] at moderate temperature (480 °C) was performed. However, the corrosion tests were only evaluated regarding corrosion rates and occurring mechanisms e.g. dissolution of alloy components neglecting the impact of the whole loop. Additionally, envisaged new operation conditions have to be considered in the corrosion analyses e.g. service temperature in a fusion reactor were increased to about 550 °C. Reliable extrapolations to the new operation regimes and considering the loop behavior (e.g. temperature profiles, flow rates) need model support and some specific corrosion tests for validating the model.



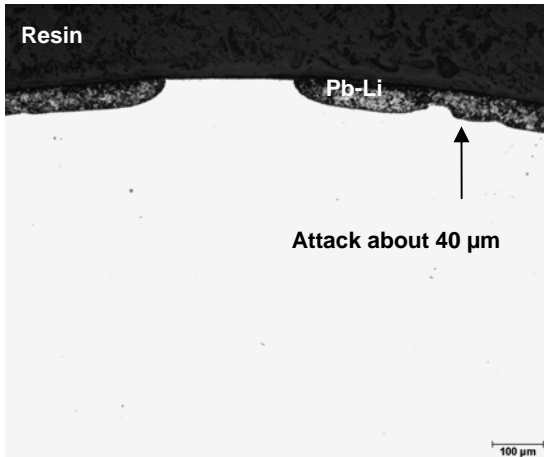


Fig. 1: EUROFER sample exposed to Pb-17Li at 550 °C with attacked and unattacked surface.

Due to the new test conditions (test temperature 550 °C) in the actual task a re-layout and updating of the PICOLO loop was performed. Most affected components were the electric heating and control system (required additional power was about 50%), upgrade of the air cooling device for permanent working, changing several tube sections to Cr-steels, and inserting a new test section made from a Si containing 10% Cr-steel (1.4713). A first commissioning test with working at 550 °C was successfully performed in early 2005. Since that time PICOLO loop is running with small interrupts for maintenance (e.g. changing the magnetic trap, removal of samples) at a flow rate of 0.3 m/s. The envisaged testing time of EUROFER of 5000 h exposure time in this task was reached short time ago. Met-

allographic investigations including EDX analyses are under way and will be finished in early 2006 in total. First results are available for the short term exposure. Fig. 1 shows the microstructure of the EUROFER exposed for 500 h to the flowing Pb-17Li at 550 °C. The selected picture shows an unattacked area in the centre and well wetted and corroded sections to the right and left. The visible step height in corrosion attack is about 40 µm. This value delivers a corrosion rate of about 700 µm/a in comparison to a rate of about 90 µm/a for the 480 °C tests. The performed EDX line scans exhibit a structure well known from the 480 °C tests for the first analyzed test times of 500 and 1025 h. The performed EDX and metallographic analyses underline that the corrosion mechanism is dissolution of the steel components. The corrosion attack is uniform also at 550 °C. However, in contrast to the 480 °C tests incubation times are reduced to below 500 h at 550 °C compared to values below 1500 h.

The first evaluated test samples indicate that corrosion attack at 550 °C is heavily increased (roughly by a factor of 10) compared to the 480 °C tests. The observed strong corrosion attack at 550 °C may be valued as dramatically increased and, additionally, the large amount of corrosion products in the loop may cause serious problems in handling such an advanced system. The precipitated Fe particles collected in the magnetic trap of PICOLO loop required a loop shut off after 2500 h due to dramatically reduced Pb-17Li flow (loop blockage) and underline this serious problem. An application of EUROFER for longer times under these conditions will require corrosion resistant coatings to keep corrosion and precipitation effects at a manageable level.

## Modeling

The Pb-17Li alloy is considered as coolant and breeding medium in future fusion reactors which is in contact with the structural components. Under liquid metal flow in a non-isothermal loop system (e.g. also PICOLO loop) beside corrosion in the hot part additional effects as e.g. transport of corrosion products and precipitation of them in cooler parts will take place. In Pb-17Li oxide phases can not be formed on the steel components due to the low O<sub>2</sub> activity of the coolant medium and existing oxide scales will be dissolved. The corrosive attack of the structural alloys, a dissolution process, will be determined mainly by the temperature dependency of the solubility of the steel components in Pb-17Li and by the flow characteristics of the melt. It is clear, that the smaller solubility at lower temperatures leads to precipitations in the cold legs of the system. PICOLO tests performed in the past were looking only at the corrosion attack and the mechanisms but neglected the influence of transport and precipitation phenomena. At 480 °C and a flow velocity of 0.3 m/s a linear correlation between corrosion rate and exposure time was detected. In the mean time boundary conditions in a fusion reactor changed and reliable extrapolations to these new conditions inclu-

sively the behavior of the Pb-17Li in the cold parts are required. Due to this facts and under keeping experimental work at an acceptable level considering the new test requirements (e.g. 550 °C test temperature or varied flow rates) modeling work has to be integrated into this corrosion subject. Under this task model development was started to calculate in the first step the mass transfer and the geometrical changes of structural components (corrosive attack) in PICOLO loop. The validation of these tools will be performed by the corrosion data for EUROFER provided in this task for 550 °C and by older PICOLO-data. These modeling tools are designed for implementing into a computer code named MATLIM.

The theoretical background in this modeling is that, in general, one has forced convection flow conditions in a Pb-17Li loop, either laminar or turbulent flow. If one wants to calculate the transport of ions, atoms, or molecules present in the liquid metal in a certain concentration  $c_i$  (with  $i$  denoting the solute), one can use the convective diffusion equation (cp. ref. [4]):

$$\frac{\partial c_i}{\partial t} + (\vec{v}\nabla)c_i = \nabla(D_i\nabla c_i) \quad (1)$$

where  $\vec{v}$  is the velocity of the liquid metal and  $D_i$  the diffusivity of solute  $i$  in the liquid metal.

It is possible to use this equation (1) for solving the problem, however, a different route is here chosen for the development of the modeling tools. Namely, one can take profit of the principles of convective mass transfer, which stipulate that under forced convection flow conditions the mass flux is determined by a dimensionless characteristic flow parameter, the so-called Sherwood number; and we can take profit (if needed) of the analogy between heat and mass transfer. Going ahead this way the calculation of dissolution (corrosion attack) and precipitation rates can be managed.

However, it has to be noted that the calculated rates depend strongly on the used solubility data e.g. of Fe in Pb-17Li. An extensive literature review was performed [4, 5, 6, 7, 8] and for first calculations (480 °C rates) values of Feuerstein [8] will be used, which were valued as the most realistic ones. The reliability of the calculated values will increase automatically by using the 550°C test results and (if available) other flow rates due to reductions of uncertainties in used physico-chemical data (e.g. solubility).

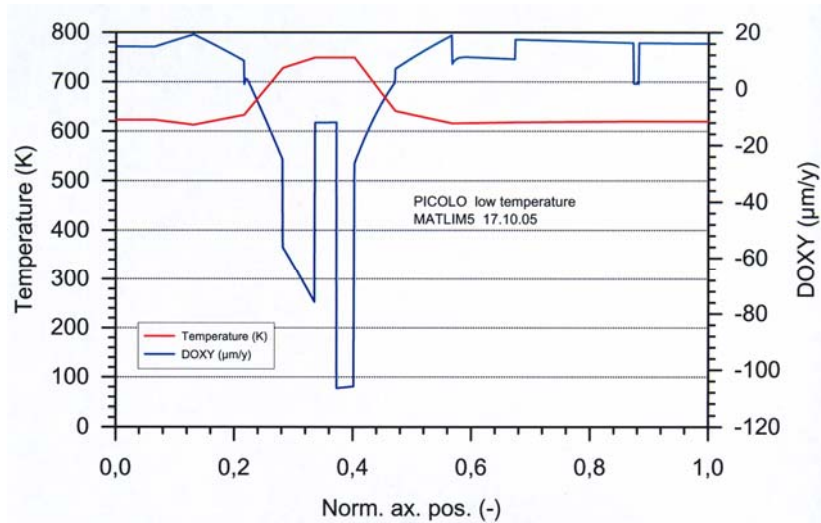


Fig. 2: Calculated dissolution rates for PICOLO loop with test section heated to 480 °C.

After parameterization of PICOLO loop (e.g. temperatures, flow velocities, diameters etc. in dependence of loop position) calculations were performed on corrosion rates and precipitation rates. Fig. 2 shows the dissolution / precipitation rate for 480 °C tests in dependence of loop position and corresponding temperature. It can be seen, that the highest dissolution rate (about 110 µm/a) is present in the test section. All positive values of the (blue colored) dissolution curve indicate that precipitation takes place. This is the fact for all positions with a loop temperature below about 400 °C. This first calculated values (dissolution = 110 µm/a) is a rather encouraging result that indicates the chosen path / modeling tools are correct due to the good conformity with the measured value of 90 µm/a. However, as mentioned and illus-

trated above, validation of the tools with other measured values is absolutely necessary and transport and precipitation effects have to be analyzed in more detail and included into the modular structured modeling part.

## Conclusions

The technological work of upgrading PICOLO-loop for corrosion testing of EUROFER at 550 °C was conducted as planned in the first quarter of 2005 and first samples were exposed. The first inspection of removed samples indicate, that incubation times as observed in earlier campaigns (480 °C testing) are reduced. First corrosion attack was observed after 500 h with a depth of about 40 µm. Evaluation of the first short term exposure tests indicate corrosion rates of about 700 µm/a. Corrosion attack at 480 °C is near 90 µm/a. These values show that corrosion at 550 °C is in the 'dramatically' corrosive range under PICOLO test conditions. A more precise valuation (corrosion rates and determination of precipitations) needs additional analyzes work, which is under preparation for corrosion attack up to about 5000 h. However, these first results give hints that special measures (e.g. corrosion barriers) have to be developed to reduce corrosion attack or bring back to acceptable level at high temperatures.

A kinetic model for the calculation of mass transfer in liquid metal systems (Pb-17Li e.g. PICOLO loop) under forced convection flow conditions has been set up. It is based on the use of the relevant characteristic thermo-hydraulic numbers, which determine the mass flux from the wall into the fluid. The modeling work started is assuming oxygen free surface and underlying a mechanism of dissolving components (Fe) out of the steel, however the dissolution (or formation) of oxide scales can be integrated which may be present on fresh surfaces and may be responsible for observed incubation times. The tools developed were integrated into the code MATLIM to simulate the behavior of the Pb-17Li PICOLO-loop. First modeling of the 480 °C conditions of PICOLO loop was performed and corrosion rates were calculated using most reliable diffusivity data. The calculated corrosion rates of about 110 µm/a are in good agreement with the measured values near 90 µm/a. However, it should be noted that the tools have to be validated with other rates measured at 550 °C and , if available, with other flow conditions to increase reliability of the modeling work. At the moment the tools set up can describe dissolution, however, in the next steps the effects of precipitations, transport effects and magnetic fields have to be integrated and validated.

## Staff:

J. Konys  
W. Krauss  
H. Steiner  
J. Novotny  
Z. Voss  
O. Wedemeyer

## Literature:

- [1] R. Lindau, A. Möslang, M. Schirra; Thermal and mechanical behaviour of the reduced-activation-ferritic-martensitic steel EUROFER, Fusion Eng. Design., 61-62, 2002, 659
- [2] W. Krauss, J. Konys, Z. Voss, J. Novotny, Corrosion behaviour of EUROFER 97 in flowing Pb-17Li, Corrosion testing in Picolo loop (480°C), TW1-TTMS-003
- [3] J. Konys, W. Krauss, Z. Voss, O. Wedemeyer, Corrosion behaviour of EUROFER steel in flowing eutectic Pb-17Li alloy, J. Nucl. Mat., 329-33 (2004) P.1379-1383
- [4] F. Balbaud-Celerier, F. Barbier, J. Nucl. Mater. 289 (2001) 227-242
- [5] M.G. Barker, V. Coen, H. Kolbe, J.A. Lees, L. Orecchia and T. Sample, J. Nucl. Mater. 155-157(1988) 732-735

- [6] M.G. Barker, T. Sample, Fus. Eng. Des. 14 (1991) 219
- [7] H.U. Borgstedt, H.D. Röhrig, J. Nucl. Mater. 179-181 (1991) 596
- [8] H.U. Borgstedt, H. Feuerstein, J. Nucl. Mater. 191-194 (1992) 988-991

## **TTMS-004 Qualification Fabrication Processes**

### **TW4-TTMS-004 D 1 Improve Design Limits of Welded Components through Improved Post Weld Heat Treatments**

#### **Overview**

In contrast to austenitic steels untreated welded joints of ferritic-martensitic steels like EUROFER suffer from hardening and embrittlement due to uncontrolled martensite formation in the vicinity of the heat affecting zones. To improve the joint performance usually two-step post welding heat treatments are applied where the temperature of the first step varies around 1050 °C and the second between 700 °C and 780 °C. With respect to specific Test Blanket Module (TBM) design and assembly requirements there is a significant discrepancy between the optimum post heat treatment and its applicability. Therefore, the main objective is the qualification of sub-components consisting of EUROFER welded joints. The investigation of suitable and applicable post heat treatments for different available (and also applicable) welding technologies takes place in close co-operation with the TBM design teams.

The limiting factors for the post welding heat treatment result from the following considerations: If future blanket modules will be assembled including beryllium pebble beds, annealing temperatures for these structures have to be (significantly) below 750 °C. Otherwise the beryllium pebbles would interact with their surrounding. That is, two-step post welding heat treatments can not be applied to welded joints in the near vicinity of Be pebble-beds. For the other parts, however, annealing temperatures above 1050 °C could be applied in principle. But of course, the larger the joint structures, the more extensive and inapplicable the annealing efforts. Therefore, in these cases annealing temperatures as low as possible would also be desirable.

#### **Initial Status**

Tungsten-Inert-Gas (TIG) with EUROFER filler wire, Electron Beam (EB), and Laser welding were applied to EUROFER plates in the condition as received. For the beam welds beam stoppers (0.5 mm x 0.5 mm) were milled at the joining parts. The TIG weld geometry was ½ V joint with a root height of 1 mm and a distance of 2 mm. All welds were fabricated parallel to the last rolling step direction (applied during the EUROFER plate production).

Spark eroded EUROFER surfaces show severe oxidation. Welding such surfaces would neither allow for reproducible nor for optimum joints. Therefore, a standard industrial applicable pickling treatment was applied to the EUROFER filler wire and to the plates. Even though the result was recognizable, it was not possible to avoid a remaining thin surface film. Therefore, immediately before welding the joining plate surfaces have been dry milled by 0.1 mm and the filler wire has been emeryed blank.

Prior to final welding, pre-tests were performed to adjust the EB and Laser beam intensity to the 5 mm plates. TIG welds on 5 mm and 10 mm plates were manually fabricated in a vacuum box flooded with inert-gas. All relevant parameters like current, voltage, feed rate, etc. were recorded. After that, the microstructure in the vicinity of the joints was examined and specimens (Charpy and tensile) were fabricated perpendicular to the weld line (and therefore also to rolling direction). In the case of Charpy specimens, the notch was positioned at the weld center as well as at the heat affecting zone (HAZ).

Prior to specimen fabrication the microstructure of the different welds were investigated. Both TIG welds showed coarse grain formation which is typical for solidification micro structures

that form during the welding cycles. Both beam welds didn't show this severe grain coarsening.

Also typical for TIG welds was the observation of soft regions in the HAZ. While the lateral extensions of the beam welds were significantly smaller, softening in the HAZ could not be observed here by hardness tests.

From these microstructural examinations it was feared that TIG welds would need a full two-step heat treatment (austenitization plus annealing) in order to recover a uniform distributed fine grain. Without that, the weld would suffer from embrittlement which has been confirmed by Charpy tests. But Charpy tests on beam welded specimens have shown surprisingly good results, even without post-weld heat treatment. Therefore, the first post-weld heat treatment applied to the welds was pure annealing at 700 °C for 2 hours. Compared to the EUROFER base material, the Ductile-to-Brittle-Transition-Temperature (DBTT) of Laser and EB welds was almost comparable: There was only a shift by 10-20 K.

Charpy testing the HAZs showed about the same results for the embrittlement behaviour of the beam welds. It is obvious that the results for TIG welds are better in the HAZ compared to the welding zone, since here – as previously mentioned – the microstructure consists of an extended fine grained softened area.

### Progress

The investigations have been continued first by producing TIG and EB welds of 12 mm plates under the same conditions and with the same parameters that have been used for fabricating the 5 mm plates. On both of these welds different heat treatments were applied and the resulting hardness was measured and compared to the base material (see Fig.1).

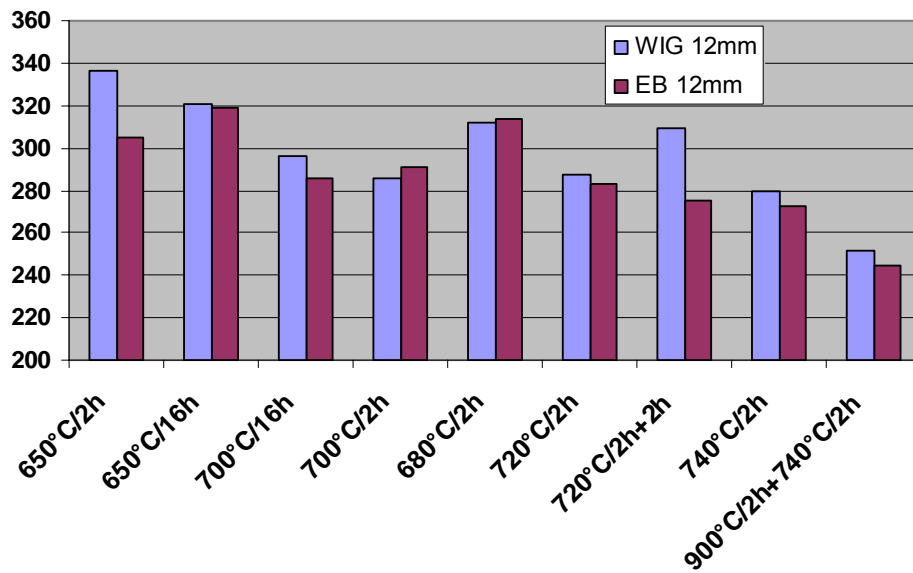


Fig. 1: Hardness (HV1) of EB and TIG weld zones after heat treatment. The hardness level of the base material varies between 210 and 220. The influence of annealing time on softening is negligible as can be seen for the example of 650 °C and 700 °C (2 and 16 hours). Also repeated tempering and cooling doesn't drop the hardness recognizable (see 720 °C results with one and two-fold heat treatment, each for 2 hours). The most significant hardness reduction was observed after austenitization at 900 °C for 2 hours. The heat treatments indicated with red arrows have been applied to Charpy specimens.

From the results it can be seen that neither an increase of the annealing time from 2 h up to 16 h nor a repetition of the annealing have a recognizable effect on hardness release. With respect to temperature sensitive Be pebble beds we applied heat treatments of 680 °C, 700 °C, and 740 °C on Charpy specimens to examine the ductility. Additionally, we applied also a

full heat treatment with the lowest possible austenitization temperature of 900 °C and annealing at 740 °C. This resulted in the lowest post welding hardness values of about 245 HV1 (base material has 210-220 HV1).

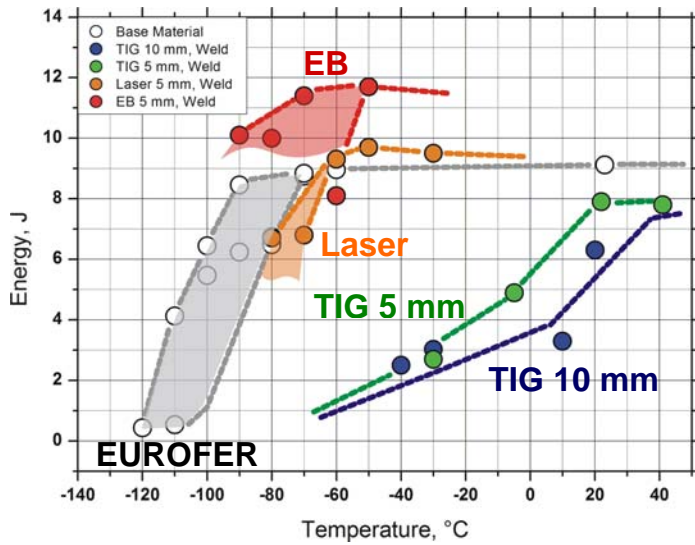


Fig. 2: Charpy test results of the different welded 5 and 10 mm plates after annealing at 700 °C for 2 hours. The notch of the Charpy specimens was fabricated in the center of the welds.

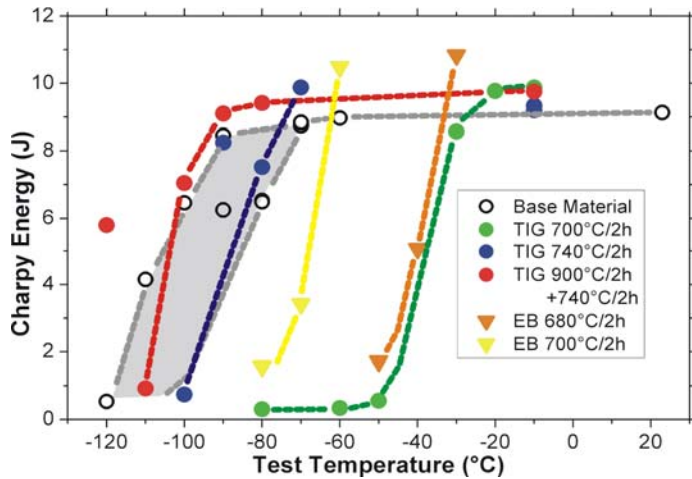


Fig. 3: Charpy test results of 12 mm EB and TIG welds after different heat treatments. The notch of the Charpy specimens was fabricated in the center of the welds.

bubbles emerge. Their size and distribution depend primarily on the beam intensity and purity of the weld surfaces. Another problem is the adjustment of the beam intensity. If chosen too high, material leaves the opposite side, and if chosen too low, the weld goes not through the whole component. Also, if welding parts are not perfectly aligned, extended unbonded areas may appear, as can be seen in Fig. 4.

Beside embrittlement due to grain coarsening during the weld process, also degradation of creep strength is a known weak point of ferritic-martensitic alloys. The loss in strength results from fine grain formation in the vicinity of the HAZs. Figure 5 gives an overview of creep test results with TIG and EB welded 12 mm plates compared to the base material. At 500 °C

The Charpy test results of all plates (5 mm, 10 mm, and 12 mm) and welds (EB, Laser, TIG) are plotted in Figs. 2 and 3. While all specimens of Fig. 2 were post-welding heat treated at 700 °C for 2 h, different treatments were applied to the specimens of Fig. 3. One can see that there is not much difference between DBTT of 5 mm and 12 mm EB welds tempered at 700 °C. When the annealing temperature is decreased by only 20 °C down to 680 °C, DBTT of the 12 mm EB welded plate increases by nearly 40 °C. On the other hand, the 5 mm EB welded plate without heat treatment showed already DBTT values nearly as good as with 700 °C treatment. With this, one can draw the conclusion that beam welds with thinner plates (5 mm) are less prone to embrittlement compared to thicker plates (12 mm).

With TIG welds, however, it looks the other way round. While DBTT of the 5 mm and 10 mm plates after heat treatment at 700 °C varies between -20 °C and +10 °C, the 12 mm TIG welded plates shows DBTT of -40 °C. After annealing at 740 °C DBTT is already comparable to that of the base material, and after the complete heat treatment of 900 °C and 740 °C it is even better.

But besides the encouraging Charpy test results of the beam welded plates one has also to mention their typical downsides which are illustrated in Fig. 4: During the welding process more or less extended bubbles emerge.

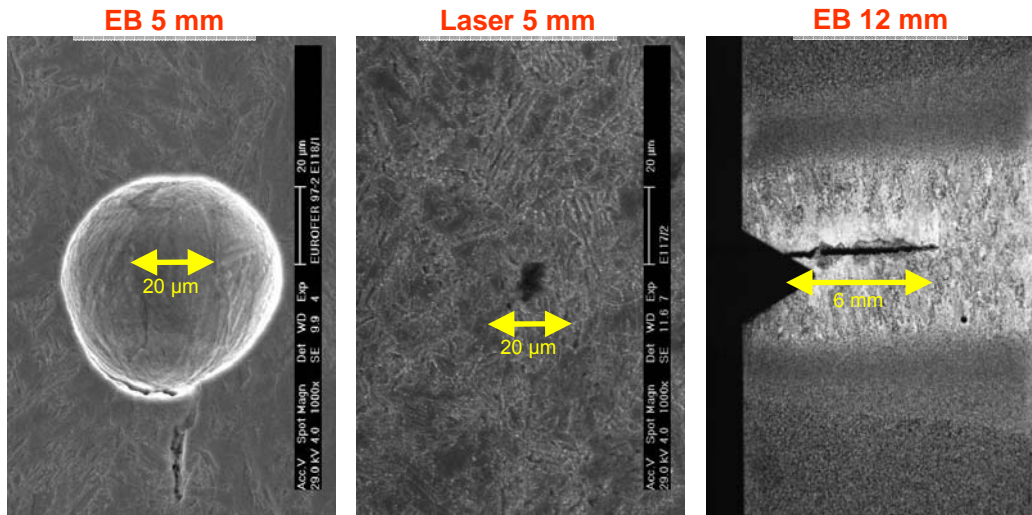


Fig. 4: Microstructure of the different welds. Typical drawbacks of beam welds – especially with EB welding – are pores (left and middle image). In thicker plates even large unbonded areas have been observed (right image).

there is nearly no difference. But at 600 °C creep strength of the welded plates is significantly lower. The reason for this is illustrated in Fig. 6. Up to temperatures of 500 °C the welded creep specimens deform uniformly and show distinct necking like the specimens of the base material. At 600 °C, however, the deformation mechanism changes to gliding which leads to shorter rupture times. Micrographs of the fractured specimens confirm that this glide process takes place in the fine grained HAZ of the weld.

### Conclusions

The most important result of these investigations is that EUROFER may be welded by TIG, EB or Laser techniques with the necessity of just a one-step post-welding heat treatment below 750 °C, i.e., without preceding austenitization.

The restrictions for beam welding are the known difficulties connected to the selection of the beam characteristic, the formation of pores, and the surface preparation. Our results might be interpreted to that effect that thinner plates (5 mm) are better suited for beam welding than thicker plates (12 mm) while for TIG welds it seems to be the other way around.

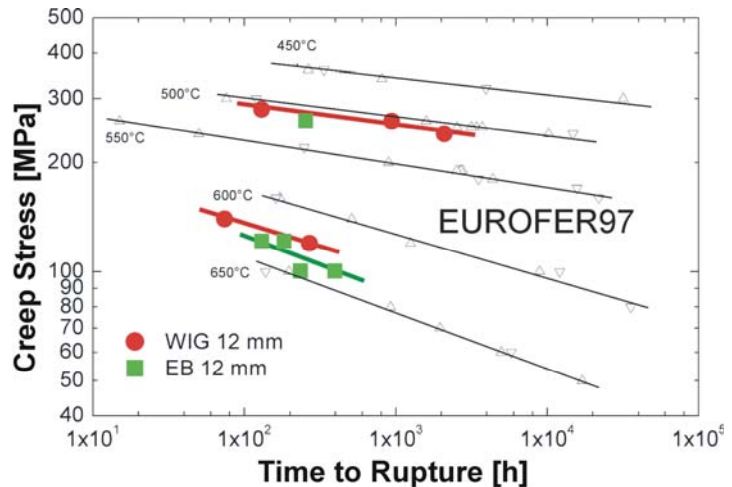


Fig. 5: Results of creep tests at 500 °C and 600 °C of the EB and TIG welded 12 mm plates after annealing at 700 °C for 2 hours compared to the base material. At 500 °C EB and TIG welds have about the same strength as the base material. But at 600 °C the rupture times of the welded specimens are significantly lower, that is, creep strength of the welded plates decreases at temperatures above 500 °C.

Both welding types (EB and TIG) loose creep strength of about 40 MPa at 600 °C. Since the maximum operation temperature for EUROFER is 550 °C, the reduction in creep strength might still be tolerable.

The ongoing investigations focus on a more detailed characterization of creep and tensile strength.



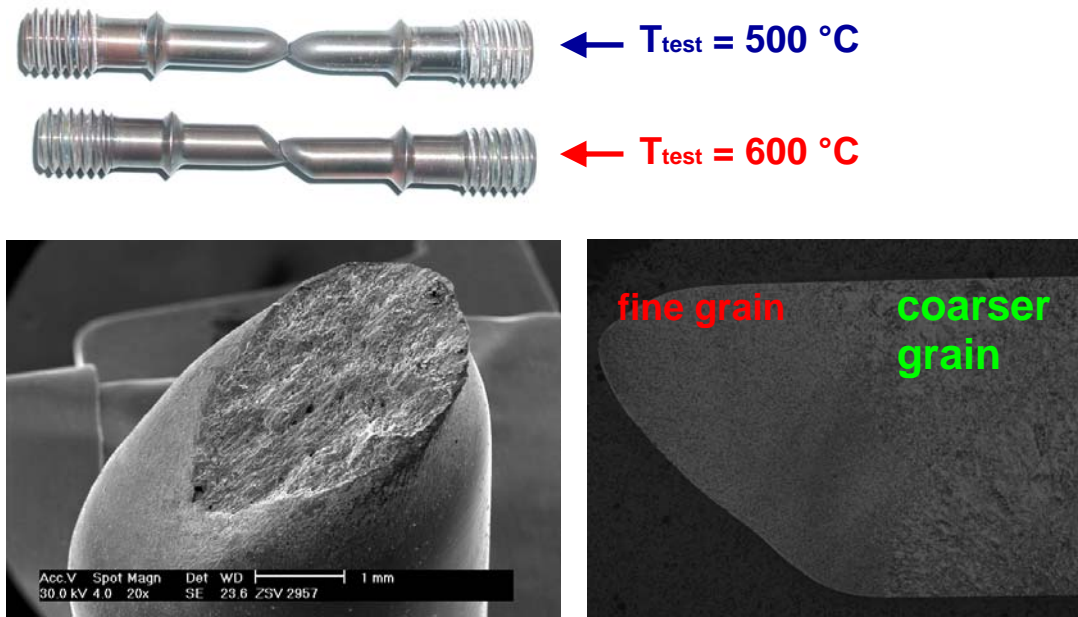


Fig. 6: Upper image: At 500 °C creep testing the welded specimens deform in the usual way, that is, they show distinct necking like the specimens of the base material. At 600 °C, however, creep strength goes down due to gliding of both specimen halves. Lower left image: Fracture surface of a welded creep specimen after testing at 600 °C. The deformation mechanism was gliding as can be clearly seen. Lower right image: The micrograph of the fractured creep specimen shows that gliding at 600 °C takes place in the fine grained HAZ of the weld.

### Staff:

A. Baumgärtner  
B. Dafferner  
P. Graf  
A. Falkenstein  
S. Heger  
U. Jäntschi  
M. Klimiankou  
A. Möslang  
M. Rieth  
R. Ziegler  
H. Zimmermann

### Literature:

- [1] Rieth, M.; Weldments of ferritic-martensitic EUROFER steel for fusion applications. Jahrestagung Kerntechnik 2005, Nürnberg, 10.-12.Mai 2005, INFORUM GmbH, S.455-58, CD-ROM.
- [2] Rieth, M.; Microstructure and Mechanical Properties of Different EUROFER Welds; EUROMAT, Prague, 5-9 September 2005.
- [3] Rieth, M.; Assessment of different welding techniques for joining EUROFER blanket components, ICFRM-12, Santa Barbara, 4-9 December 2005.

## TW5-TTMS-004 D 1 Diffusion Welding Techniques - One Step HIP

### Introduction

The objective of this task is to investigate possible influences of variations in the base material on the quality of the weld after a uniaxial diffusion welding (U-DW) process depending on the welding parameters (temperature, pressure, time) applied. For example, it is well known that rolled plates can exhibit a local varying hardening behaviour which causes a different visco-plastic creep performance that can largely influence the weld quality. The results of these investigations will support future large scale industrial diffusion welding by setting up a matrix of tolerable process parameters. The experimental programme will be performed using the recently produced batch of EUROFER 97-2.

### Base Material Characterisation

Samples were taken from the edge (margin) as well as the centre region of a EUROFER 97-2 plate. The tensile experiments performed show no significant difference between samples taken from the margin region or middle (centre) region in terms of tensile properties. A prior heat treatment corresponding to a post welding heat treatment (PWHT) does not change the results. Fig. 1 depicts the results in comparison with former investigations by other authors. The measured tensile properties agree within the limits of typical material deviation and measurement errors. The differing yield strength for former generated U-DW samples (-97) is caused by the additional heat treatment applied during the U-DW process.

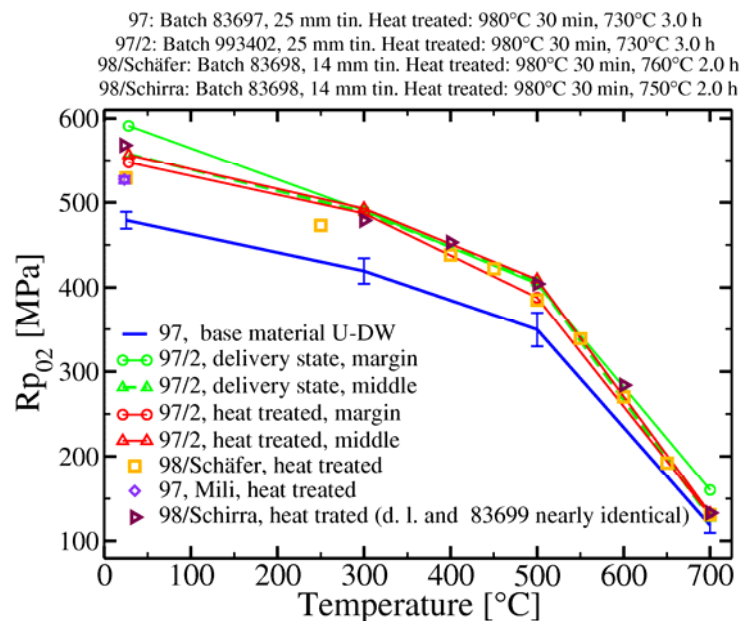


Fig. 1: Comparison of yield strength of EUROFER 97/2 with results of other authors.

Results from Charpy impact investigations are showing a different behaviour (Fig. 2). Firstly, the DBTT of EUROFER 97-2 is about 20 °C decreased in comparison to EUROFER 97. The DBTT differs about 10 °C between samples taken from the middle and samples taken from the edge (margin) region of the plate. This might be an indication for locally varying hardening. The increased DBTT is an additional hint to this supposition. Such a material behaviour would generate a very complicated analysis of the weld quality because it has to be considered from which position the sample has been taken. Therefore, this investigation has been repeated with heat treated samples. The red symbols and lines in Fig. 2 indicate only a partial success: The fracture toughness far above the DBTT and the USE are equalised, but the DBTT is still differing.

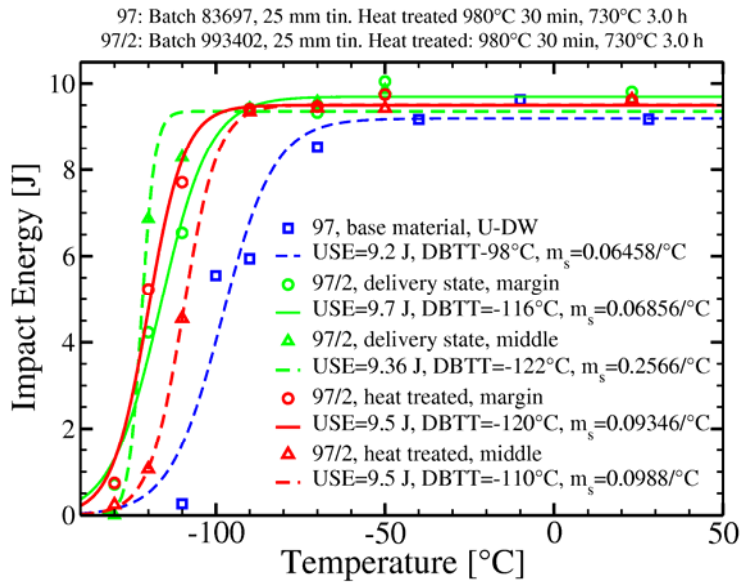


Fig 2: Results of Charpy impact tests with specimens taken from the new batch EUROFER 97-2:

## U-DW Experiment

Up to now one U-DW experiment using EUROFER 97-2 has been performed. The welding pressure was chosen to 18 MPa instead of 20 MPa as for the former experiments with EUROFER 97. When producing a full scale cooling plate (CP) it is desirable to reduce the weld pressure of the first HIP step. The EUROFER 97-2 U-DW sample has been compressed by only 4% in comparison to 6% of the old batch EUROFER 97. The time dependency of the compression creep behaviour also differs by a missing primary creep phase mostly. This will influence the weld quality largely as depicted

in Fig. 3 by Charpy impact experiments. The blue dashed line represents the properties of a perfect U-DW weld of EUROFER 97. The reduced weld pressure lowers the weld quality displayed by the green symbols and line. The reduced compression speed of EUROFER 97-2 will decrease the weld quality further (red dashed line).

These results also support the necessity of performing compression creep behaviour experiments to estimate the fitting U-DW parameters.

## Outlook

The compression creep samples taken from the margin and the middle region are produced and the measurements will be performed in 2006. The analysis of the experimental results will yield the test matrix of U-DW parameters applied to samples taken in the same manner. The results will be used to evaluate the range of allowable weld parameters and will be applied to an empirical U-DW simulation model.

## Staff:

J. Aktaa  
 U. Bürkle  
 B. Dafferner  
 H. Kempe  
 A. von der Weth

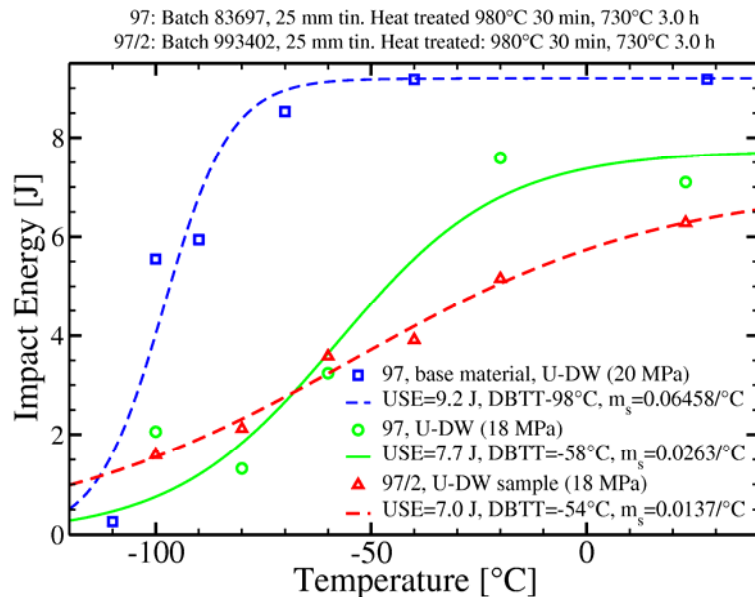


Fig 3: Comparison of fracture toughness between samples taken from different EUROFER batches.

**TTMS-005**  
**Rules for Design, Fabrication and Inspection**

**TW2-TTMS-005b D 1**  
**TBM Design Rules**

The objective of this task is the development of design rules for ITER test blanket modules (TBM) built from RAFM steels. The TBM has to be dimensioned against different kinds of failure: ductile, creep and fatigue failure taking into account the influence of irradiation. The design rules will be built up on existing codes for nuclear applications considering the life time prediction approaches developed within TTMS-005 for RAFM steels and their specific mechanical behaviour. The assessment of the design rules formulated is also a part of this task. Therefore the performance and evaluation of suitable verification experiments among others isothermal multi-axial fatigue tests at room temperature as well as at elevated temperature, close to the operating temperature, on the reduced activation alloy EUROFER 97 are foreseen.

The isothermal multi-axial fatigue tests with fixed principal axis under purely alternating strain controlled loading were completed. All these tests were performed at room temperature. To compare the results of experiments with different phase shift the equivalent plastic strain range  $\Delta\varepsilon_{pl}^{eq}$  was used.

The nominal amplitude was thereby the same for both directions (axial and circumferential). In Fig. 1 the equivalent plastic strain range  $\Delta\varepsilon_{pl}^{eq}$  is plotted over the nominal amplitude.

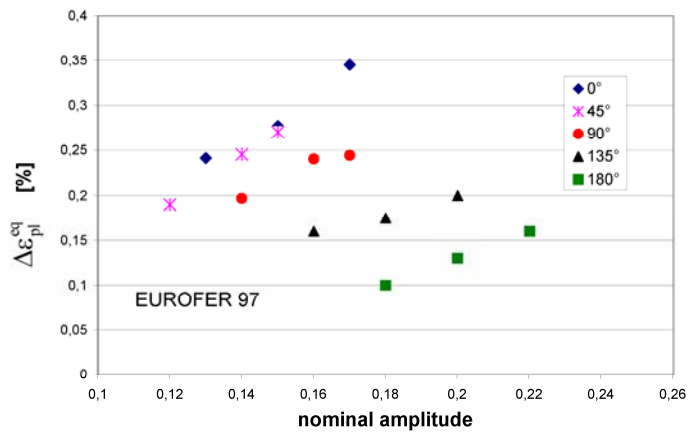


Fig. 1  $\Delta\varepsilon_{pl}^{eq}$  as a function of the nominal amplitude.

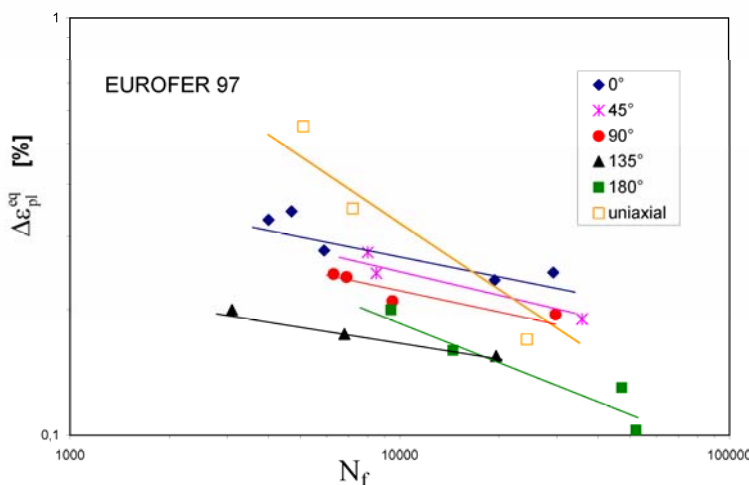


Fig. 2:  $\Delta\varepsilon_{pl}^{eq}$  as a function of lifetime.

At the same nominal amplitude the resulting equivalent plastic strain range varies for the different phase shifts very clearly. This indicates the strong effect of the phase shift on the loading. For an increasing phase shift the equivalent plastic strain range decreases at the same nominal amplitude value. For a lifetime prediction the correlation between  $\Delta\varepsilon_{pl}^{eq}$  and the number of cycles is of interest. In Fig. 2 the experimental determined  $\Delta\varepsilon_{pl}^{eq}$  are plotted

over the experimental observed lifetimes. A clearly dependence of the lifetime on the load, represented by  $\Delta\varepsilon_{pl}^{eq}$ , as well as on the phase shift can be noticed. A decreasing phase shift tends to result in a higher life at the same equivalent load.

After completion of the experiments with fixed principal axis, the setup of the facility was modified to perform tension/torsion experiments at room temperature as well as at elevated temperature. For this purpose the pressure vessel was replaced by a resistance furnace. Furthermore the extensometers were replaced and cooling sleeves were mounted on the modified bolts, which are welded with the specimen.

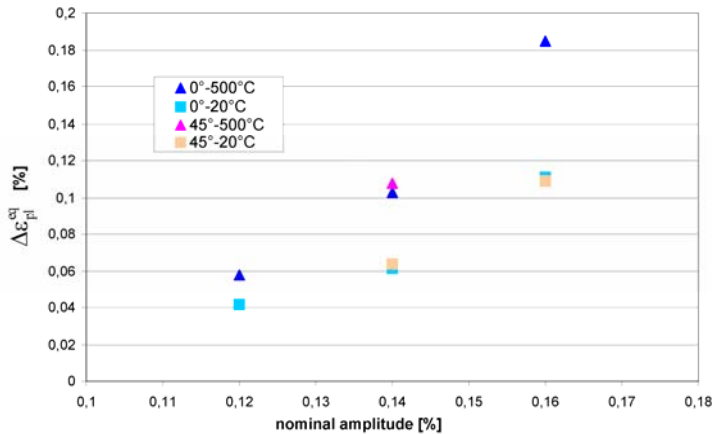


Fig. 3:  $\Delta\varepsilon_{pl}^{eq}$  as a function of the nominal amplitude.

The correlation between the adjusted nominal amplitudes and the obtained  $\Delta\varepsilon_{pl}^{eq}$  for those two phase shifts is shown in Figure 3.

So it was able to perform tension/torsion tests at room temperature as well as at elevated temperature. So far we performed tests with 0° and 45° phase shift, whereas the tests with the 45° phase shift are not finished now, at room temperature as well as at elevated temperature. The results obtained so far show nearly no difference

between the two phase shifts, but a big difference concerning the temperature. For elevated temperature the resulting equivalent plastic strain ranges are higher as for room temperature, at the same adjusted nominal strain amplitudes.

The number of cycles to failure against  $\Delta\varepsilon_{pl}^{eq}$  is plotted in Figure 4. The equivalent plastic strain range was determined for the cycle after half number of cycles to failure.

A big difference between room temperature and elevated temperature, concerning the lifetime, at the same equivalent strain is observed. Surprisingly the experiments with the highest strain ranges (for room temperature as well as for elevated temperature) have not the lowest lifetime. This leads to the assumption, that for these processes the plastic strain is not the only critical parameter. So we calculated the equivalent stress range  $\Delta\sigma^{eq}$  also for the cycle at half number of cycles to rupture, for each test and listed the results in figure 5. The stresses show expected results. Higher lifetimes correlate to lower stresses. But the most interesting result is that higher nominal strain amplitudes and thus higher plastic strain ranges lead not necessarily to higher stress ranges. The cyclic softening of this material is, at least for this setup, apparently so strong pronounced, that higher nominal strains could lead to lower stress and therewith to higher lifetimes. The outstanding experiments with rotating principal axes (180°,

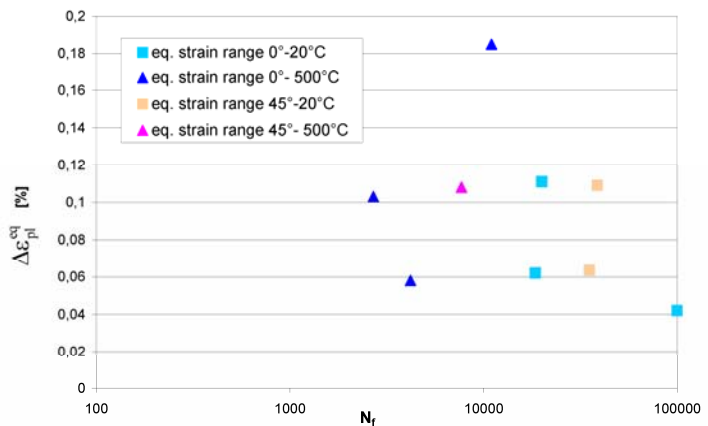


Fig. 4: Correlation of lifetime with  $\Delta\varepsilon_{pl}^{eq}$ .

135°, 90° and the rest of 45° phase shift,) will bring more clarity to this behavior. So it will be able to clarify whether the equivalent plastic strain range is the only characteristic value determining failure.

The experimental results will be used to verify the lifetime prediction models developed so far as well as their implementation in the design code.

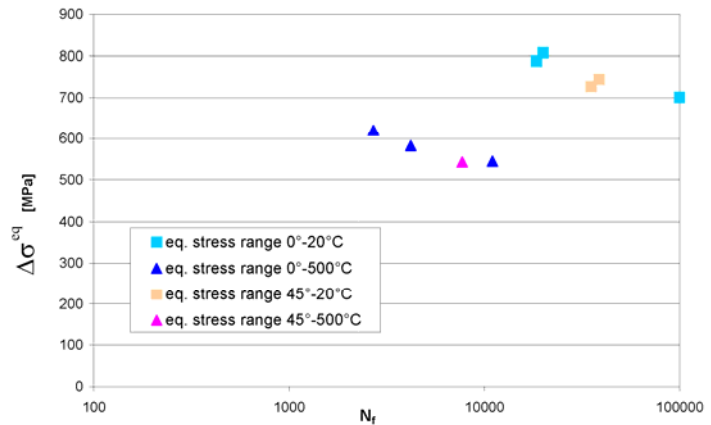


Fig. 5: Correlation of lifetime with  $\Delta\sigma^{eq}$ .

Staff:

J. Aktaa  
M. Weick  
S. Knaak

Literature:

- [1] Aktaa, J.:  
Oral presentation: "Design code for components built from RAFM steels", EFDA Review and Strategy Meeting on Task TTMS-005, Garching, 13. Januar 2005
- [2] Aktaa, J.:  
Oral presentation: "Design code for components built from RAFM steels", EFDA Review and Strategy Meeting on Task TTMS-005, FZK, Karlsruhe, 11. December 2005

## **TW2-TTMS 005b D 2**

### **Evaluation of the Material Design Limits for TBM's Application**

#### **1 Objectives**

The range of working temperature and loads on the basis of the mechanical properties including irradiation, the hydrogen effect and corrosion effect by the coolant will be defined.

Life time assessment of TBM sub-components and modules is based on finite element calculations of temperature fields and stress fields under ITER conditions and includes:

- Assessment and evaluation of stress and strain fields in so-called "stress-reports";
- Application of the SDC design rules;
- Comparison to material (property) limits as a function of temperature and environmental conditions.

#### **2 Activity status at the beginning of 2005**

An activity within the subtask has been started first in the 2<sup>nd</sup> half of 2004. Up to the end of 2004, the following steps have been done:

- Revision of the experimental, design and simulation data available at IRS/IKET (FZK) and related to the TBM. Thereby, a special attention has been directed to a current TBM design, normal and accidental ITER operating conditions as well as typical problems connected with the TBM development.
- Adjustment of material parameters required for the ABAQUS-own non-linear kinematic/isotropic hardening material model (see ABAQUS/Standard User's Manual, Vol. II, Ch. 11.2.2) on the basis of the data stemming from a life time study of EUROFER 97 at 450, 550 and 650° C performed by J. Aktaa & R. Schmitt (see FZKA 6931).
- Creation of a 2D finite element (FE) model of a ¼ of the test blanket module (TBM) according to current propositions of designers.
- Execution of a simplified thermal simulation to obtain a temperature distribution in the TBM model.
- Verification of the material model by simulation of 5 cycles under a heat flux of 500 kW/m<sup>2</sup> ("MARFE") on the plasma-facing side as well as a heat flux of 60 kW/m<sup>2</sup> and of 35 kW/m<sup>2</sup> on the vertical and horizontal interior respectively due to breeder units as well as a pressure of 80 MPa in cooling channels.

#### **3 Results achieved in 2005**

The activity in 2004 has established a good basis for further investigations. The results achieved in 2005 are discussed more detailed below.

##### **3.1 Enhancement of material parameters**

Material parameters required for the ABAQUS-own hardening model and determined in the end of 2004 were not correct since the data concerning the accumulated plastic strain used for the determination of the isotropic hardening behaviour at 450° C and 550° C have been computed incorrectly. It seemed also to be necessary to determine the material parameters for the test temperature of 650° C. Furthermore, results of the cyclic experiments at RT be-

come available only after the annual report 2004 was finished. For these reasons, material parameters have been adjusted to the new, enhanced data.

Details of the determination of material parameters are described in the ABAQUS / Standard user's manual as well as in the annual report 2004 so that only the enhanced parameters are collected in Table 1. Experimental curves depicted in fig. 1 are required to adjust material parameters.

Table 1: The fitted hardening parameters for different temperatures; the parameter  $\gamma = 1150$  for all T

T, K	293	723	823	923
C, MPa	147200.00	153922.00	180590.00	194900.00
Q, MPa	-104.00	-133.00	-145.00	-108.77
b	0.89	1.05	1.80	3.70

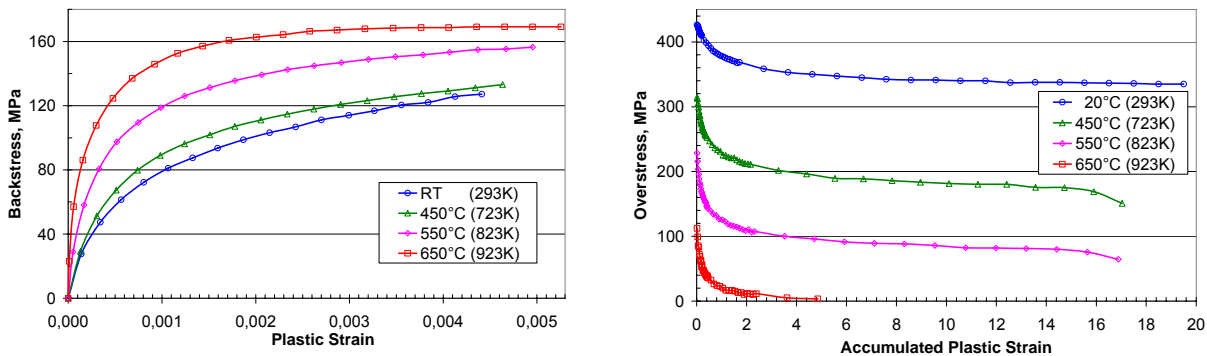


Fig. 1: Backstress curves for the 1/4 of the 1<sup>st</sup> cycle (on the left) and overstress curves as functions of the accumulated plastic strain (on the right) at RT, 450° C, 550° C & 650° C.

### 3.2 Computation of the temperature distribution

During the operating mode, it should be accounted for a heat flux of 250 up to 500 kW/m<sup>2</sup> (peak) on the plasma-facing side as well as a heat flux of 60 kW/m<sup>2</sup> and of 35 kW/m<sup>2</sup> on the vertical and horizontal interior, respectively, due to breeder units as shown in fig. 2. For the reason of simplicity, temperature boundary conditions depicted in fig. 2 have been considered in the simulations.

In order to determine admissible loads, the behaviour of the TBM should be simulated under consideration of different temperature distributions. To obtain such distributions, thermal simulations have been performed for four values of the plasma heating: 250 kW/m<sup>2</sup> (the usual operating mode), 500 kW/m<sup>2</sup>, 750 kW/m<sup>2</sup> and 1000 kW/m<sup>2</sup> as well as for three different temperatures in the cooling channels ( $T^{cc}$ ): 673 K, 773 K and 873 K. The heating due to the breeder unit remains thereby constant. As an example of the typical temperature distribution, results of a thermal computation for the peak operating mode and  $T^{cc} = 773$  K are also shown in fig. 2.

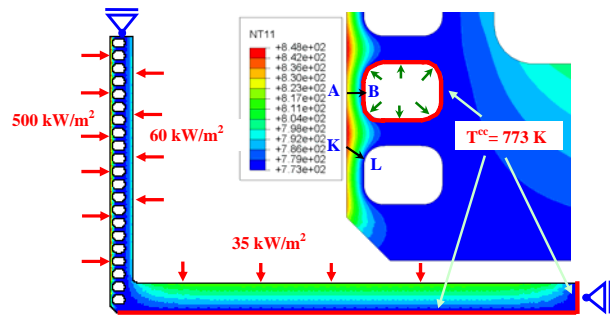


Fig. 2: The FE model with both mechanical and thermal constraints and loadings. The temperature distribution shown corresponds to the depicted thermal loadings. AB and KL are the support lines used for the stress categorization.



### 3.3 Comparison of the usual and generalized formulation of the plain strain elements

First simulations using plain strain elements CPE8 have exhibited non-physically high out-of-plane stresses, which have a numerical source. For those simulations where thermal stresses occur, ABAQUS promotes a so called generalized plane strain element formulation, which accounts for an elongation in the out-of-plane direction. The influence of the generalized element formulation on simulation results has been investigated by comparison of the results obtained using CPE8 and CPEG8 elements. It turned out that the application of the generalized formulation leads to a remarkable reduction only of the out-of-plane stresses, whereas all other stress components remain unchanged. This statement is illustrated in fig. 3, where only the vertical ( $yy$ ) stress component is representative also for other in-plane stress components.

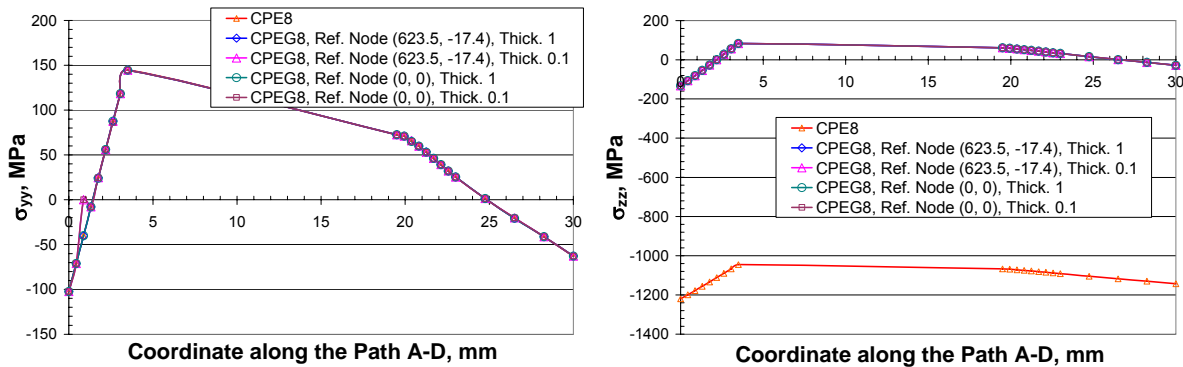


Fig. 3: Comparison of results obtained using usual CPE8 and generalized CPEG8 plain strain elements: vertical (on the left) and out-of-plane strain components across the 1st wall in the mid of the 5th channel (as if the path AB in fig. 2 is drawn for the 5th channel and continued across the wall).

According to results of the study, the generalized plane strain element formulation has been used in the simulations performed in 2005 contrary to the simulations of 2004.

### 3.4 Determination of the elastic limit

By variation of both the temperature in cooling channels and the plasma heating, a critical pressure has been determined. The critical pressure is defined as the minimum pressure causing any inelastic deformation after the 1<sup>st</sup> heating i.e. after the ½ of the 1<sup>st</sup> cycle.

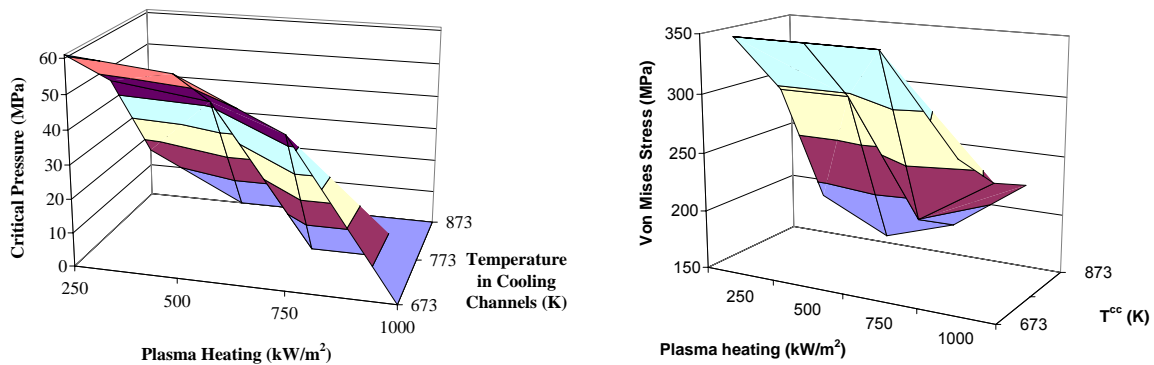


Fig. 4: Critical pressure and the corresponding maximum of the von Mises stress (on the right) as a function of the plasma heating and the temperature in the cooling channels.

The critical pressure and the corresponding von-Mises stress are shown in fig. 4 in dependency on the plasma heating and  $T^{cc}$ . Evidently, the critical pressure is strongly dependent on the temperature in the cooling channels and relatively slightly on the plasma heating up to 450 - 500  $\text{kW/m}^2$  approximately. Increasing plasma heating takes however a leading influence on the critical pressure whereas the temperature in the cooling channels plays a decreasing role and, finally, a plastic deformation occurs without pressure due to the tempera-

ture gradient alone for all  $T^{cc}$  if the plasma heating reaches  $1000 \text{ kW/m}^2$ . The maximum of the von-Mises stress is almost independent of the plasma heating up to  $500 \text{ kW/m}^2$  approximately (up to  $750 \text{ kW/m}^2$  for  $T^{cc} = 673 \text{ K}$ ). Then the influence of the temperature in cooling channels becomes smaller.

Simulations show that plastic deformation occurs without pressure firstly for the plasma heating higher than  $750 \text{ kW/m}^2$  as well as for  $T^{cc}$  higher than  $773 \text{ K}$ . Only the plasma heating of  $1000 \text{ kW/m}^2$  causes plastic deformation independent on  $T^{cc}$ . For this value, the plastic deformation is located in a narrow band along the plasma-facing side, see fig. 5 on the left. A high pressure causes an additional plastic deformation located in a left bottom or left top corners of the 1<sup>st</sup> or 2<sup>nd</sup> cooling channels if the pressure in the channels reaches a critical value discussed above, see fig. 5 on the right. The magnitude of the deformation is thereby higher than the magnitude of the thermal plastic strain.

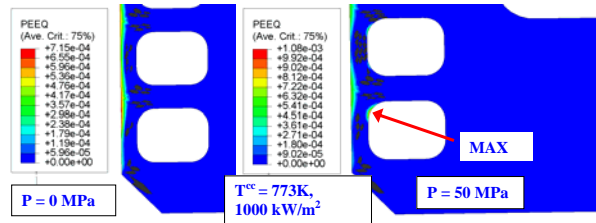


Fig. 5: Distribution of the equivalent plastic strain in the most loaded region of the TBM for the plasma heating of  $1000 \text{ kW/m}^2$  at  $T^{cc} = 773 \text{ K}$  in the absence of pressure (on the left) and at the pressure of  $50 \text{ MPa}$ .

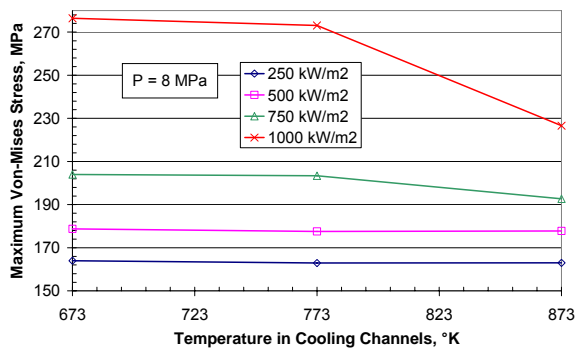


Fig. 6: The maximum von-Mises stress as a function of the temperature in cooling channels for different values of the plasma heating at the constant pressure of  $8 \text{ MPa}$ .

$600^\circ \text{ C} = 873 \text{ K}$ ; the plasma heating  $750 \text{ kW/m}^2$  and the coolant pressure  $P = 50 \text{ MPa} = 500 \text{ bar}$ . It was assumed on the basis of the study reported in the previous section that an essential plastic deformation should occur affected by such loads.

Each cycle consists of four steps: (1) a heating and application of the pressure,  $30 \text{ sec}$ ; (2) a holding at the HT,  $400 \text{ sec}$ , (3) a cooling,  $100 \text{ sec}$  and, finally (4) a holding at the RT,  $1400 \text{ sec}$ . Note that the steps (2) and (4) are not relevant for the ABAQUS-own material model.

The results have been generated in a table format along the paths AB and KL depicted in fig. 2. The follow-up examination has shown that the highest plastic strain in the model occurs near the point L of the path KL as in fig. 2. A change of the maximum equivalent plastic strain near the point L within the first 300 cycles is depicted in fig. 7 on the left. A detailed investigation shows a negligible linear increase of the equivalent plastic strain during the first 300 cycles. It can be assumed that the accumulated plastic strain remains constant. The diagram on the right-hand side of fig. 7 shows the evolution of the von Mises stress near the point L. The stress decreases cycle by cycle according to the assumptions of the material model.

The maximum von Mises stress as a function of  $T^{cc}$  is shown in fig. 6 at the constant pressure of  $8 \text{ MPa}$  corresponding to the usual operating mode and for different values of the plasma heating. Except for  $750 \text{ kW/m}^2$  and  $1000 \text{ kW/m}^2$  if  $T^{cc} > 773 \text{ K}$ , the maximum von Mises stress depends rather only on the plasma heating and is almost non-sensitive to the variation of  $T^{cc}$  at this pressure.

### 3.5 Simulation of the cyclic behaviour of TBM

The cyclic behaviour of the TBM model has been studied within the first 300 cycles under consideration of the following loadings:  $T^{cc} =$

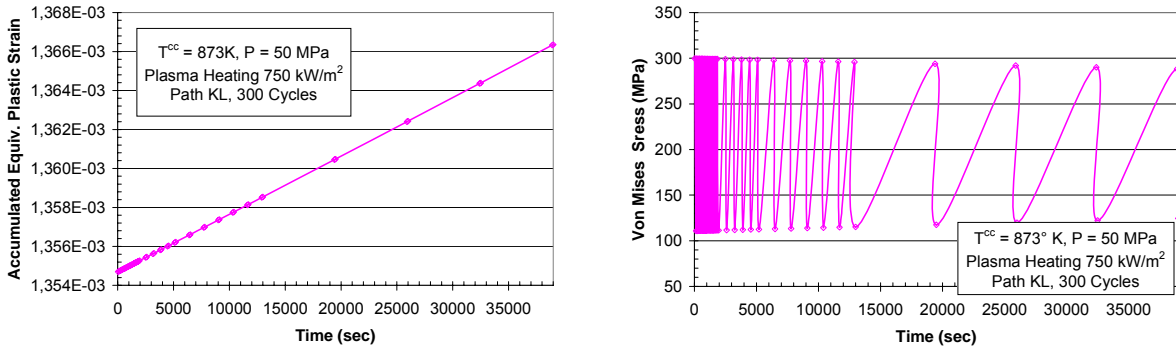


Fig. 7: The evolution of the maximum accumulated equivalent plastic strain (on the left) and the maximum von Mises stress during the first 300 cycles.

#### 4 Outlook

The work within the sub task seems to be completed. It should be remarked that this activity is inseparable from the activity within the sub task TW5-TTMS-005-Del. 8. It turned out that the material model describing time-dependent phenomena and used for the deliverable is more adequate for the simulation of the cyclic behaviour of the TBM at high temperatures (HT) including a HT stand by. For this reason, only results of the simulations using this model have been used for the verification of design rules. Because of the length limitation, all features concerning an application of design rules are placed in the annual report to the sub task mentioned above.

#### Staff:

R. Sunyk

#### Literature:

- [1] R. Sunyk, J. Aktaa, "Evaluation of Material Design Limits for TBM Applications", 2005 in IEEE/SOFE05 proceedings; <http://216.228.1.34/Conf/sofe05/versions/64291/PID131414.pdf>
- [2] R. Sunyk, J. Aktaa, "Verification of Design Rules for EUROFER under TBM Operating Conditions ", Submitted to J. Nuc. Mat. (special issue)

## **TW2-TTMS-005b D 4**

### **Creep-fatigue Lifetime Prediction Rules for Irradiated EUROFER**

The objectives of this task are the modification of the lifetime prediction model developed in TTMS-005a D4 [1] for RAFM steels under creep fatigue conditions taking into account the irradiation influence and the verification of the modified model by applying it to EUROFER 97 in the post-irradiated state.

At the beginning of the reporting time period and according to the outcome of the literature study performed within the year before an irradiation dose driven terms in the evolution equations of hardening was proposed taking into account the irradiation induced hardening and its influence on damage. This modification was found to describe qualitatively the observed behaviour of F82H in irradiated states.

Within the reporting time period the irradiation dose driven terms in the evolution equations of hardening has been modified taking into account saturation effects of irradiation induced hardening. The modification is based on the physical model by Dimelfi et al. developed to describe the post-yield flow behaviour of iron-base alloys after neutron irradiation. The post irradiation investigations of EUROFER 97 have been already started but no data are yet available for application on EUROFER 97. However, the coupled deformation damage model, which was implemented in the finite element code ABAQUS, has been used to simulate thermo-mechanical tests performed on EUROFER 97 in the reference (unirradiated) state. Thereby it has been found that the cyclic softening of EUROFER 97 yields to serious strain localisation which results in higher local mechanical loads determining lifetime under creep/fatigue.

#### Staff:

J. Aktaa

#### Literature:

- [1] Aktaa, J.  
Oral presentation: "Creep-fatigue lifetime prediction for irradiated EUROFER. Design Rules and Fracture Mechanics", EFDA Review and Strategy Meeting on Task TTMS-005, Garching, 13 .Januar 2005

## **TW2-TTMS-005b D 7**

### **Small-scale Fracture Mechanics Specimens**

#### **1 Objectives**

The aim of the work is to find a convenient model for a fracture mechanical experiment, in particular for the Three-Point-Bending (3PB) experiment performed for variously sized samples. Such a model should yield correct results (e.g. crack tip fields and J-integrals) independent of the sample size i.e. should be based on micromechanics.

This approach includes

- FE analysis of specimen for determination of global fracture mechanics parameters;
- Micromechanical based material modelling (Gurson and Lemaitre-type coupled plasticity-damage models );
- Adjustment of fracture mechanics model parameters. (experiments under Del.8);
- Adjustment of model parameters. (underlying deformation and damage model);
- Design and optimization of sub-sized bend-bar specimens;
- Mechanical experiments (tensile-hold-unloading) for determination of parameter of the deformation an damage model.

#### **2 Activity status at the beginning of 2005**

The following steps have been performed during 2004:

- Determination of some material parameters of EUROFER 97 required for the conventional plasticity model on the basis of tensile experiments.
- Determination of the optimum mesh in the crack tip vicinity.
- FE simulations of the FM experiments performed at 3PB specimens (standard- and sub-sized) using conventional plasticity models, estimation of J-integral.
- Verification of some damage parameters required by a standard ABAQUS GTN damage model.

#### **3 Achieved results**

It was planned to use a micromechanics-based GTN material model implemented as a UMAT by F. Reusch (University of Dortmund) to be able to simulate a crack growth and to calculate the crack resistance curve. Unfortunately, the model became available only by the mid of 2005. Diverse problems connected with the software requirements as well as with the activity concerning the TW2-TTMS-005b, Del. 2 and TW5-TTMS-005, Del. 8 lead to a delay in the present deliverable. At the moment, the software problems are solved, first test simulations should be performed up to the end of 2005.

#### **4 Outlook**

- Further cooperation with University of Dortmund (Prof. B. Svendsen).
- Further adjustment of unknown firstly local and possibly (if needed) non-local damage parameters for EUROFER 97 based on corresponding verification tests and fractographical studies, which should be performed within another deliverable. Thereby, the damage parameters determined by M. Walter for F82H and reported in his PhD work should be firstly used instead of the unknown parameters for EUROFER 97.

- Modelling of the 3PB FM experiments using firstly the local GTN model and comparison of the results obtained for standard as well as subsized specimens.

Staff:

R. Sunyk

## TW4-TTMS-005 D 2 Mechanical and Structural Characterization of EUROFER97-2 Acceptance Tests of the 2003 Procured EUROFER Batch

EUROFER97-2 is the most recently produced batch of RAFM-steels and was delivered as round forgings and sheets or plates, Tab. 1. This material is needed for technological tests and further fabrication trials, particularly to build the Test Blanket Modules (TBM) mock-ups. The technical specification of the batch was based on the experience gained with various RAFM 9CrWtAV-alloys. The use of carefully selected raw materials was essential to achieve high cleanness and low contents of undesired elements or impurities as Nb, Mo, Ni, Cu, Al, Co, and others, which produce long-living radio-active isotopes under neutron irradiation. One important aim of the procurement was to achieve a good reproducibility of the satisfying properties of the former EUROFER 97 alloy. To check the reproducibility different investigations on EUROFER97-2 in the conditions as delivered and after two heat-treatments is being performed including the following items:

Table 1: Delivery forms of the EUROFER97-2 batch.

Heat number	Delivery form	Dimension
993378	round forging	Ø100 mm
993394	round forging	Ø100 mm
993394	plate	8 mm
993393	plate	14 mm
993391	plate	25 mm
993402	plate	25 mm

- Tensile tests at RT, 300, 400, 500, 600, 700 °C;
- Creep rupture tests at temperatures of 550 and 600 °C and for times to rupture in the range of up to 8000 h;
- Charpy tests on ISO size specimens and KLST specimens to define DBTT;
- Analysis of microstructure;
- Chemical analysis of the alloying elements and impurities.

### Round Forging

Investigations of the first two heats began with structure analysis in the beginning of 2004. The last step of the heat-treatment in the as received condition was normalizing 960 °C 1.5 h/oil and annealing 750 °C 4 h/air. An influence due to the forging direction could not be determined. The hardness was between 216 and 229 HV30 in both heats, and the grain size was in the range of ASTM 10 and 11. Material characterization was accomplished in the as received state and after the heat-treatments 980 °C 0.5 h + 750 °C 2h and 1040 °C 0.5 h + 750 °C 2 h. After the heat-treatments the materials were set to grain-size ASTM 8 – 10 with a hardness between 208 and 212 HV30. As reported last year, the hardening and annealing behavior is in the same range as the former EUROFER97, the first batch E 83669 [1].

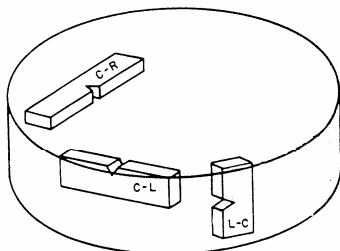


FIG. 3 Crack Plane Orientation Code for Bar and Hollow Cylinder

Fig. 1: Orientation of the notch.

Specimens for tensile, creep, and Charpy-tests were fabricated, and the mechanical tests were carried out. Creep samples were tested only in the as received condition. Tensile, creep, and Charpy samples ISO-V were taken parallel to the forging direction. Only KLST-specimens were fabricated in the three directions of the round bars; Fig. 1.

**Tensile tests** were carried out at RT, 300, 400, 500, 600, 700 °C. The specimen geometry was 38 mm x M5, gauge length 18 mm x Ø3 mm. In the graphs of  $R_m$  and  $R_{p0.2}$ , the data are in a narrow distribution range; Fig. 2 and 3. By closer attention, there is a small tendency to higher strength at lower test-temperatures in Heat 993394. But with higher test-temperature the scatter becomes more closely and no differences can be observed. The parameters of  $A_g$  and  $A$ , in Fig. 4 and 5, the

highest values are available of heat 993378 after austinitization of 1040 °C 0.5 h and annealing 750 °C 2 h. Parameters of Z show a wide distribution range at lower test-temperatures, which contracts at higher test-temperature up to 700 °C.

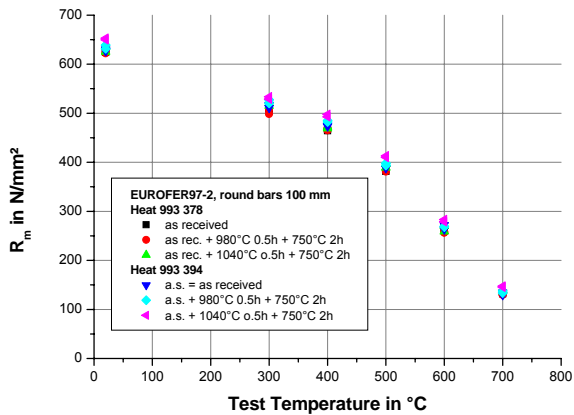


Fig. 2: Tensile strength,  $R_m$ .

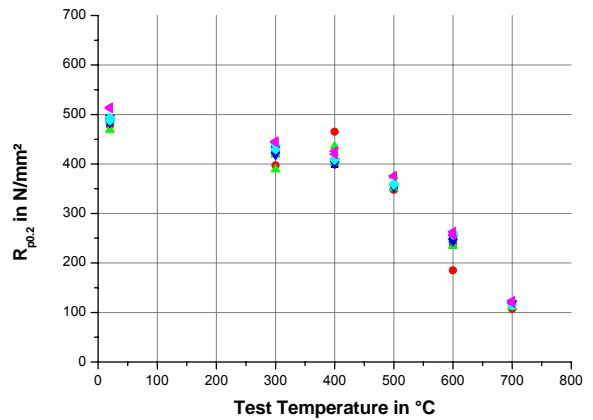


Fig. 3: 0,2%-Yield strength,  $R_{p0.2}$ .

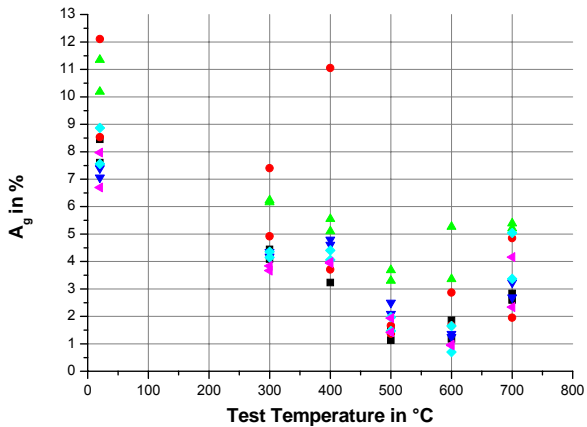


Fig. 4: Elongation before reduction,  $A_g$ .

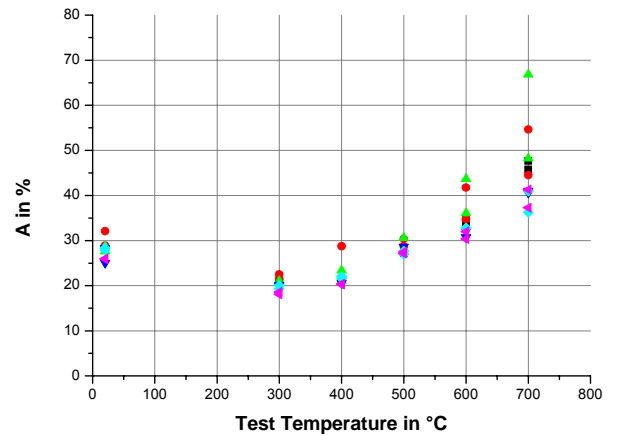


Fig. 5: Elongation after fracture,  $A$ .

Most **creep-tests** (56xM8 and 94xM12) are completed and cover the test-time up to 5000 h. Fig. 6 represents the data of heat 993378 and 993394 together with former heats of EUROFER. Test-temperatures were between 450 and 650 °C. The good congruence between the different heats is recognizable.

**ISO-V-Charpy specimens** (55x8x10) were fabricated longitudinal (L-C), parallel to the forging direction. First, the impact properties of the as received conditions were determined; Fig. 8. There is a better transition from upper-shelf to lower-shelf in heat 993378 compared to 993394.

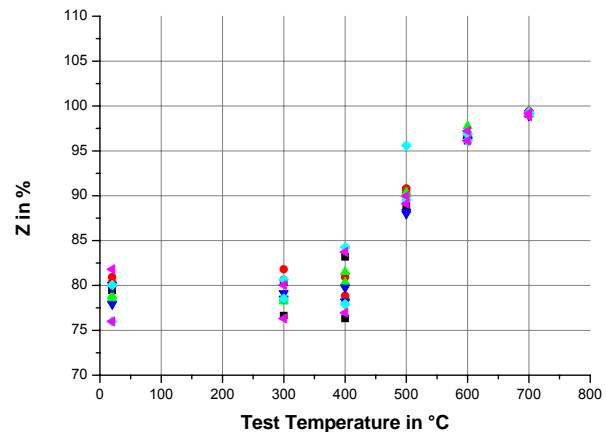


Fig. 6: Reduction of area after fracture,  $Z$ .



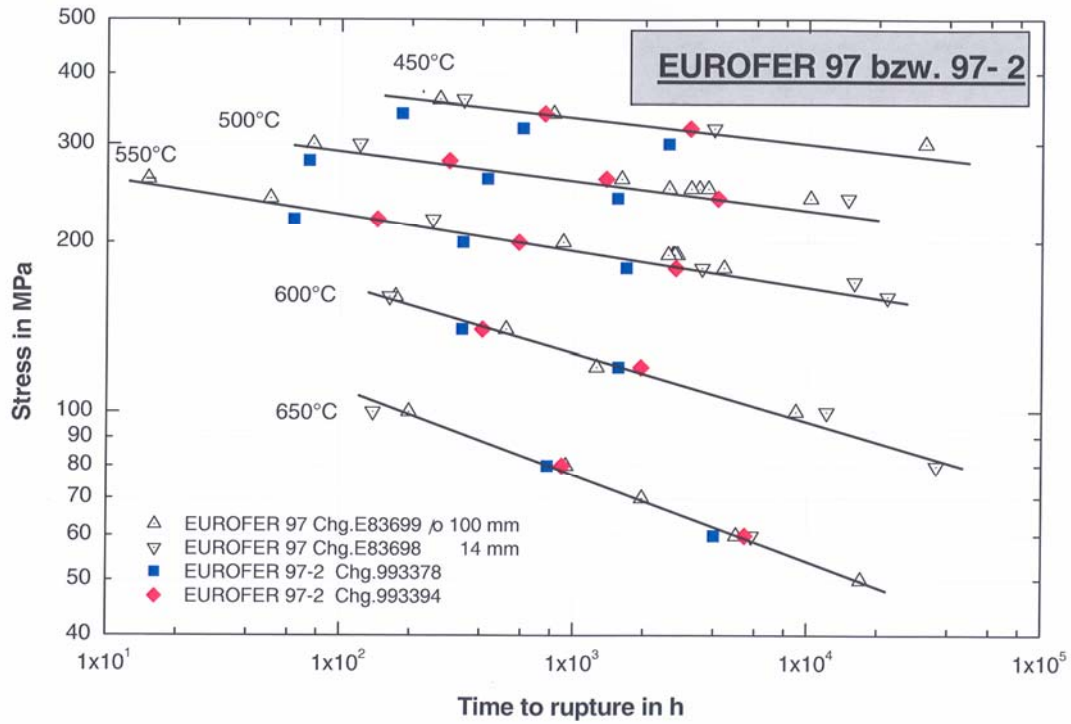


Fig. 7: Influence of heats on time to creep-rupture.

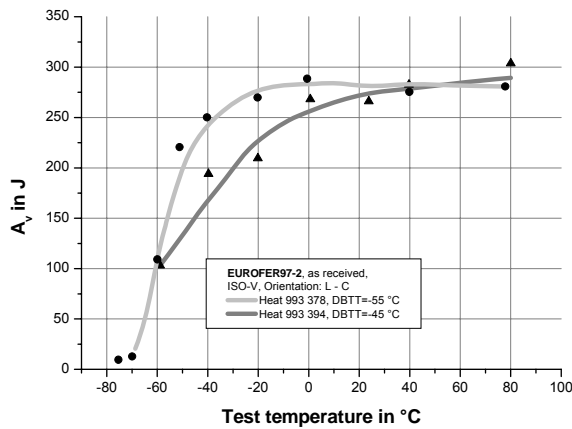


Fig. 8: Charpy properties of EUROFER97-2; heat 993378 and 993394.

Graphs of Fig. 9 and 10 show the properties of the recent two heats in the as received condition and after the heat-treatments with 980 and 1040 °C 0.5 h, and the annealing 750 °C 2 h. Heat 993378 yields again a better DBTT=-55 °C than heat 993394 with DBTT=-45 °C. The observed difference remains after the heat-treatments, too. In heat 993378 after the heat-treatments, the upper shelf could be improved up to about 20 ° higher than in heat 993394.

**KLST-specimens** (27x4x3) were made in three orientations out of the round forging. From a lot of possibilities of comparisons, like heat material, orientations, and different heat-treatments, two

graphs are shown here, Fig. 11 and 12. All DBTTs of heat 993378 are -100 °C, independent of the condition. The data of heat 993394 have in DBTT a scatter between -50 and -100 °C, but this material is also applicable for the technical use.

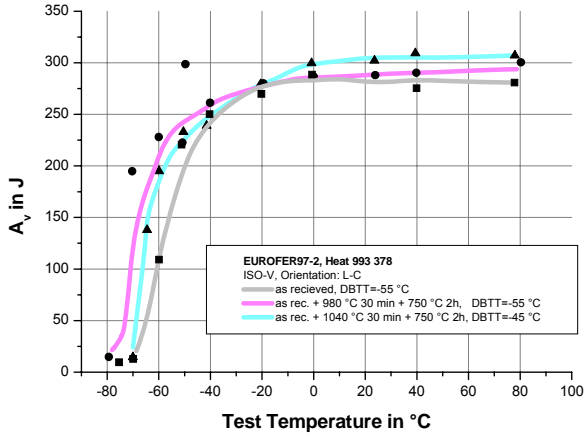


Fig. 9: Heat 993 378 with heat-treatments.

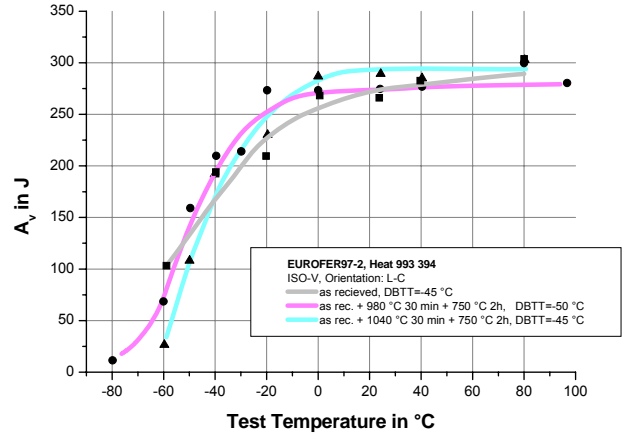


Fig. 10: Heat 993 394 with heat-treatments.

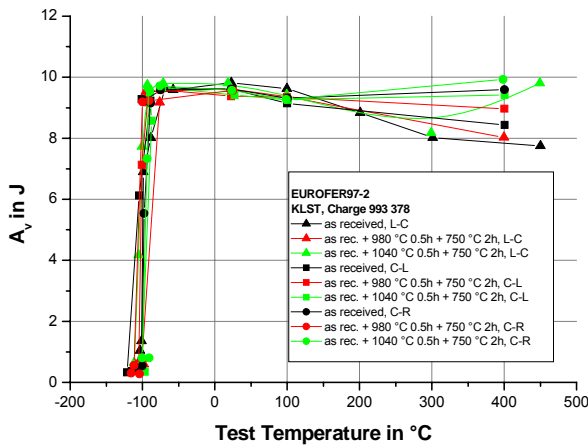


Fig. 11: Charpy properties of heat 993 378.

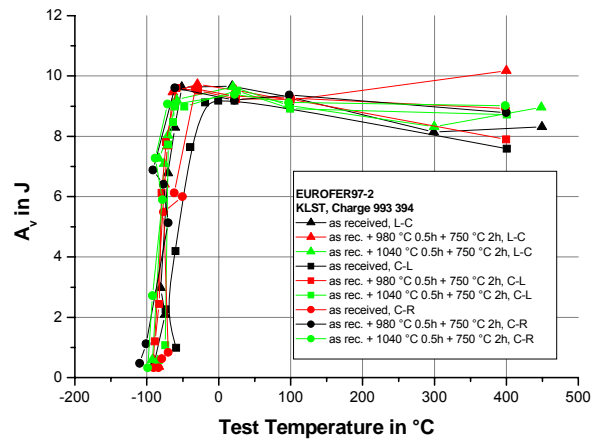


Fig. 12: Charpy properties of heat 993 394.

## Plate Material

The remaining part of the 8 t batch was converted to plates in different thickness, see Tab. 1. The first metallographic investigations showed a similar structure as seen in the first two heats. This material qualification will be continued by mechanical tests in the as received state 960 °C 1.5 h/oil + 750 °C 4 h/air and the two heat treatments 980 °C 0.5 h + 750 °C 2 h and 1040 °C 0.5 h + 750 °C 2 h. The anticipated results will give the range of the technological machining and application.

## Conclusion and Outlook

Up to now the characterization of the heats of EUROFER97-2 reveals good accordance to the former EUROFER-alloys. These new RAFM-steels are a further step of optimization of material properties targeted on the development of components for fusion reactors [2]. The results obtained form the basis for design and construction of fusion reactor components and will serve for comparing results from future irradiation tests.

Staff:

B. Dafferner  
M. Klimiankou, Dr.  
P. Graf  
A. Falkenstein  
U. Jäntschi  
R. Lindau  
E. Materna-Morris  
C. Petersen  
D. Preininger, Dr.  
H. Zimmermann

Literature:

- [1] Materna-Morris E.; et.al.: TW4-TTMS-005D2 Mechanical and structural characterization of EUROFER97-2. FZKA 7117, EUR 21526 EN, Nuclear Fusion Programme Annual Report of the Association Forschungszentrum Karlsruhe / EURATOM, January 2004 – December 2004.
- [2] Möslang, A.; Diegele, E.; Klimiankou, M.; Lässer, R.; Lindau, R.; Lucon, E.; Materna-Morris, E.; Petersen, C.; Pippan, R.; Rensman, J.W.; Rieth, M.; van der Schaaf, B.; Schneider, H.C.; Tavassoli, F.: Towards reduced activation structural materials database for fusion DEMO reactors. Nuclear Fusion, 45(2005) S.649-55.

## TW5-TTMS-005 D 4 Experiments in Support of Modelling Activities on Size Effects

### Objectives

The development of a convenient model for fracture mechanics (FM) experiments on structure materials is a huge challenge. To support modelling work on size effects in the ductile and ductile-to-brittle transition region of structure materials several fracture mechanics experiments are needed.

### Fracture Mechanics Experiments on Sub-size Specimens

The Three-Point-Bending (3PB) experiments have been performed on MANET II and EUROFER 97 steels. Mini-bar specimens of KLST type (3x4x27 mm<sup>3</sup>) fatigue pre-cracked to relative crack lengths of ~0.25 have been chosen for quasi-static fracture toughness testing with a servohydraulic testing machine.

965°C/2h+1075°C/0.5h+700°C/2h heat treated MANET II exhibited failure in the ductile-to-brittle transition region at room temperature. Following a multi-specimen procedure for fracture toughness measurement the specimens have been subjected to different deformation levels. After each experiment the specimen was heat tinted in order to estimate fatigue pre-crack and actual crack lengths by nine point average. Crack resistance *J-R* curve shown in Fig. 1 has been constructed from the recorded load load-line-displacement curves. The analysis of *J-R* curves resulted  $J_{IC}=250$  N/mm ( $K_{IC}=240$  MPam<sup>0.5</sup>) and  $J_{0.2}=339$  N/mm for the critical J integral and J integral at 0.2mm crack growth, respectively.

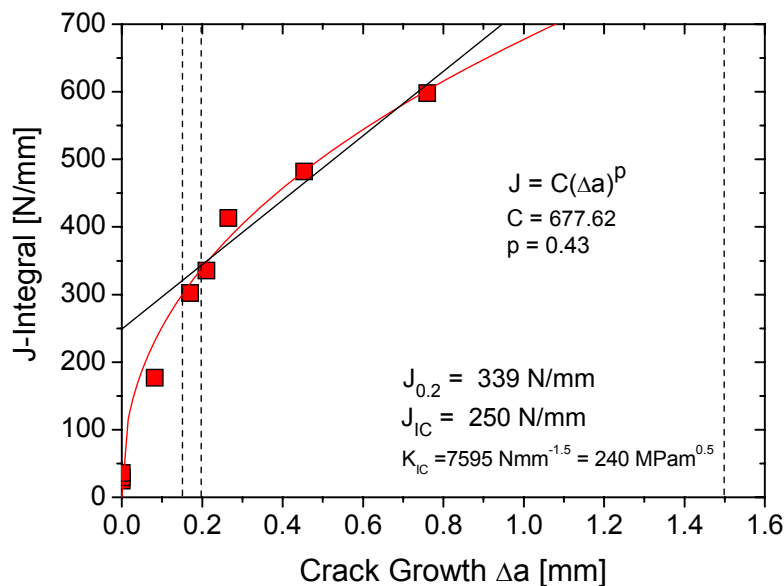


Fig. 1: J-integral as a function of crack growth  $\Delta a$  for MANET II. Red line is the least square fit according to  $J=C(\Delta a)^p$  for the data between  $0.15 \text{ mm} \leq \Delta a \leq 1.5 \text{ mm}$ . Best fit is obtained with  $C=677.62$  and  $p=0.43$ . Black line gives the estimation of critical J-integral  $J_{IC}$ . J-integral at 0.2 mm crack growth  $J_{0.2}=339$  N/mm.

At room temperature EUROFER 97 (980°C/0.5h +760°C/1.5h) exhibited failure in the upper shelf region. The specimens have been loaded to different deformation levels in order to find a critical load ( $F_c$ ) leading to the onset of stable crack growth. Fig. 2a shows the recorded load vs. load-line displacement curve for the sample loaded up to the critical load  $F_c$ . Fig. 2b shows the corresponding ruptured cross section. The onset of stable crack growth is identified.

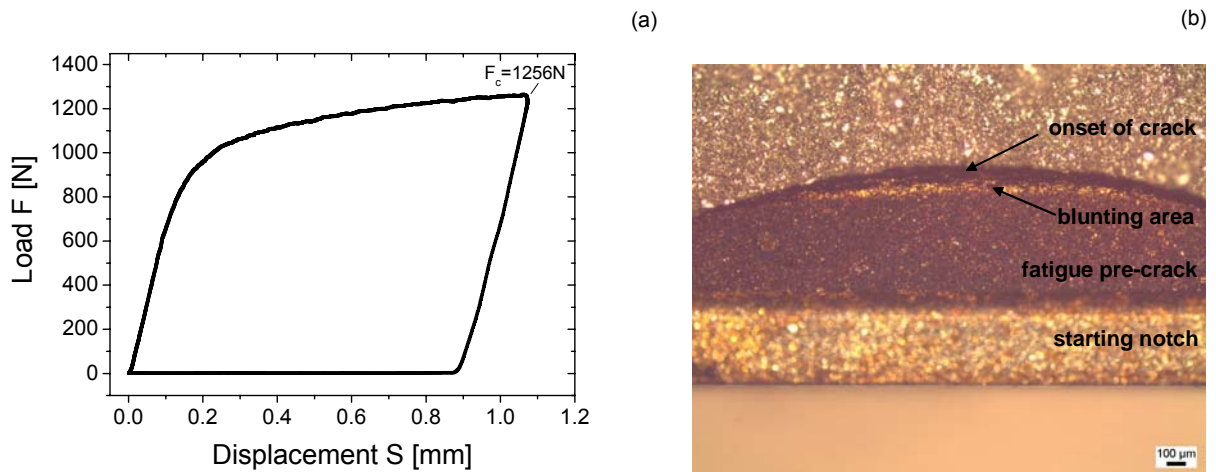


Fig. 2. a) Load vs. load-line-displacement for EUROFER 97. Estimated critical load for the onset of stable crack growth  $F_c=1256$  N. b) ruptured cross-section of EUROFER 97 loaded up to  $F_c$ .

## Conclusion and Outlook

Critical J integral and fracture toughness has been determined for MANET II showing failure in ductile-to-brittle transition region. The critical load leading to the onset of stable crack growth has been found for EUROFER 97 showing ductile tearing at room temperature. For Fracture toughness estimation additional 3PB experiments will be performed on EUROFER 97.

### Staff:

J. Aktaa  
B. Dafferner  
E. Gaganidze  
R. Sunyk

## **TW5-TTMS-005 D 5**

### **High Temperature Fracture Mechanical (Creep-fatigue) Rules: Formulation and Implementation**

The objectives are the development of the high temperature part of a design code for fusion reactor components built from EUROFER which includes reliable fracture mechanical rules for the assessment of detected defects under creep and creep-fatigue conditions.

This task was started in March, 2005. Within the reporting time period the high temperature fracture mechanical approaches compiled under TW2-TTMS-005b, which are based on R6 and PD6493 (British Standards) and R5 and PD6539, have been evaluated by an extensive literature study on their published applications. For applying them for the assessment of detected defects in EUROFER components it is necessary to verify the validity of appropriate relations estimating crack loading parameter  $C^*$ . Therefore finite element simulations have been started, with which the crack loading parameter is calculated using the appropriate algorithm provided by the finite element code and then compared with that estimated by the R5 rules. In addition the determination of the parameters of the creep crack growth relation for EUROFER needs the accompanying fracture mechanical tests to be performed on EUROFER under deliverable 6, which are now however in progress.

#### Staff:

J. Aktaa  
H. Riesch-Oppermann

#### Literature:

- [1] Aktaa, J.: Oral presentation: "Design code for components built from RAFM steels," EFDA Review and Strategy Meeting on Task TTMS005, FZK, Karlsruhe, 11. December 2005
- [2] Riesch-Oppermann, H.: "A fracture mechanics concept for the high temperature part of the structure design criteria for ITER in-vessel components," Final report on sub-topic of the EFDA task TW2-TTMS-005b D1, Internal Report Forschungszentrum Karlsruhe, 2005

## TW5-TTMS-005 D 6

### Accompanying Experiments for the Formulation of High Temperature Fracture Mechanical Rules

#### Background and Objectives

For TBM's licensing, in order to establish design rules for the materials, joints and specific sub-components, a broad set of R&D activities have been launched within the WP 2002. These activities will continue with emphasis on implementation in DSCD (Demo structural design code) and verification and validation experiments. Additional rules for HT (high temperature) fatigue-creep interaction need to be formulated, in particular for fracture mechanics.

The low ductility of EUROFER (in particular after irradiation ) gives very conservative limits for design against fast fracture and local flow localization. Some experiments are required in support of special design code activities that could lower very conservative assumptions in existing frameworks.

Development of small scale test techniques in fracture mechanics will continue including transferability of the small size specimens tests to the behaviour of the TBM's sub-components.

The objective of this subtask is to perform creep crack growth experiments from EUROFER to determine the  $da/dt$  (crack velocity) -  $C^*$  ( $C^*$ -integral)- behaviour at the temperatures 500°C and 550°. The results are needed to fit material parameters in HT fracture mechanical rules. Therefore long time tests must be done.

#### Status

The individual parts (holder etc.) for the modification of the long period creep testing machines have been designed. Most of the pieces have been fabricated, only the clip gages to measure the crack opening displacement during the experiments are missing. They should be made from a HT creep resistant alloy named RGT 15. Because Röchling, the company which produced this material in the past no longer exists, a new producer had to be found.

For measuring the crack growth during the experiment, we decided to use the Direct Current (DC) potential method. Therefore, the experimental set-up has been prepared.

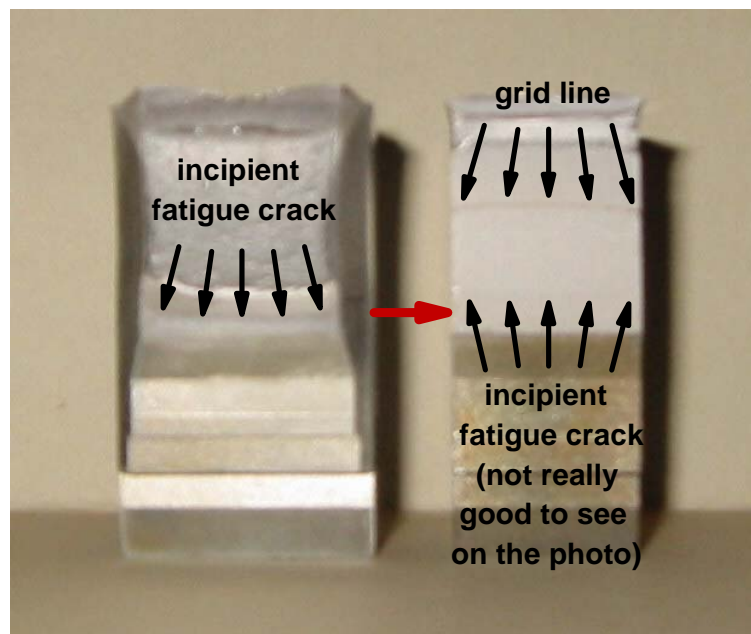


Fig. 1: Left hand side: surface of a ruptured CT-specimen with side notches after creating a incipient fatigue crack. Right hand side: surface of a ruptured CT-specimen (made out of a pre-cracked side-notched specimen) with a continued fatigue crack propagation.

Compact Tensile (CT) specimens have been designed (their size depends on the space in the furnace) and fabricated. Since the average grain size of the latest delivered charge of EUROFER is oversized, the material has been cut into pieces a little larger than the CT-specimens to do a new heat treatment. After that a 2-step fabrication of the specimens started. In the first step the specimens have been fabricated (a little larger width) with side-notches to get a nearly straight crack front during creation of the incipient fatigue crack. Afterwards the side-notches will be removed for the main experiments (so that the geometry of the specimen is in agreement with the ASTM-norm). In preliminary tests, one can clearly see that this method leads to a nearly straight crack front during the incipient crack creation, also after removing the notches and continuing the fatigue crack propagation (Fig. 1).

At the moment preliminary tests with the set-up for the DC potential method are running in order to determine the correct correlation between voltage and crack length. Also, preliminary tests to determine the suitable load cases for the long term experiments are under way.

### **Conclusion and Outlook**

The design and fabrication of specimens and the assembling of the experimental set-up has nearly been finished. Preliminary tests are running. As soon as the fabrication of the clip gages is finished, the whole experimental set-up will be implemented into the long period creep testing machines. After finishing the pre-tests, the main experiments will start.

#### Staff:

M. Walter  
M. Lerch

#### Literature:

- [1] M. Walter, J. Aktaa: Talk: 'Experimental programme for verification of HT creep-fatigue rules from uniaxial experiments and on creep-crack-growth experiments'; EFDA Review and Strategy Meeting on Task TTMS-005, 11.11.05, FZK



## **TW5-TTMS-005 D 7**

### **General Implementation of HT Rules (Including Creep Fatigue Interaction Rules)**

The objectives are the development of the high temperature part of a design code for fusion reactor components built from EUROFER which includes reliable simplified rules for the assessment of creep, fatigue and creep-fatigue interaction.

This task was started in March, 2005. Within the reporting time period and on the base of the rules provided by well established design codes for nuclear applications (ASME BPVC and RCC-M) as well as the advanced deformation and damage models developed under TW2-TTMS-005 for RAFM steels simplified rules for life assessment taking into account creep, fatigue and creep-fatigue interaction have been derived. Thereby two different analysis routes, the elastic and the inelastic analysis route will be considered. Instructions including criteria for the applicability of both routes have been formulated. Documentation in a design code like form is in progress.

#### Staff:

J. Aktaa

#### Literature:

- [1] Aktaa, J.: Oral presentation: "Design code for components built from RAFM steels", EFDA Review and Strategy Meeting on Task TTMS-005, FZK, Karlsruhe, 11. December 2005

## TW5-TTMS-005 D 8

### Definition of an Experimental Programme for Validation of HT Creep-fatigue Rules at Fusion Relevant Conditions

#### 1 Objectives

The deliverable is closely connected to the activity under TW2-TTMS-005b, Del. 2. The aim of the present deliverable is to define an experimental programme for validation of HT creep-fatigue rules at fusion relevant conditions (multiaxial thermo-mechanical loadings, temperature gradients, interaction of primary -secondary stresses) by analysis of the FE-based evaluation of the material design limits for TBM application.

The main part of the work consists of the FE-based thermal and mechanical analysis of the TBM under cyclic thermo-mechanical loadings using the coupled deformation damage model developed and implemented as a user material (UMAT) in ABAQUS within the TW2-TTMS-005a, Del. 4 (s. FZKA 6931), which considers the creep fatigue as well as material damage.

On the basis of such an analysis, the loading and boundary conditions should be formulated for verification experiments. The already performed work concerning verification experiments deals solely with the material properties independent of any special shape of the probes. Firstly within the foreseen activity, testing of TBM subcomponents manufactured from the previously studied material (EUROFER 97) should be considered. A determination of a mock-up experiment is thus the global aim of such an activity.

#### 2 Results achieved in 2005

The activities within present subtask as well as the subtask TW2-TTMS-005b, Del. 2 have been performed simultaneously. For this reason, a part of the common steps performed in 2005 are described in the annual report to the subtask mentioned above. Note that the methodological difference to TW2-TTMS-005b, Del. 2 lies only in another material model accounting for time-dependent phenomena. This difference is however essential.

##### 2.1 Computation of the temperature distribution

A typical distribution is shown in fig. 1. For details see the annual report to TW2-TTMS-005b-Del. 2.

##### 2.2 Determination of the elastic limit

The minimum coolant pressure causing an inelastic response after the 1<sup>st</sup> cycle has been computed as a function of the plasma heating and the temperature of cooling channels  $T^{cc}$ . by the same method as in TW2-TTMS-005b, Del. 2 (see the corresponding annual report). The critical pressure and the corresponding maximum von Mises stress are shown in fig. 2. An application of the UMAT leads to considerably lower critical pressures than the application of the ABAQUS-own material model. The results obtained using the UMAT should be probably more correct due to taking into account a high-temperature creep.

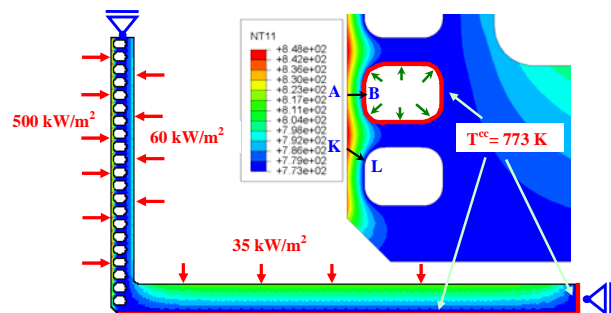


Fig. 1: The FE model with both mechanical and thermal constraints and loadings. The temperature distribution shown corresponds to the depicted thermal loadings. AB and KL are the support lines used for the stress categorization.

The maximum von Mises stress as a function of  $T^{cc}$  is shown in fig. 3 for different values of the plasma heating at the constant pressure of 8 MPa corresponding to the usual operating

mode. The UMAT and the ABAQUS-own model yield quantitatively and qualitatively similar results for this pressure level.

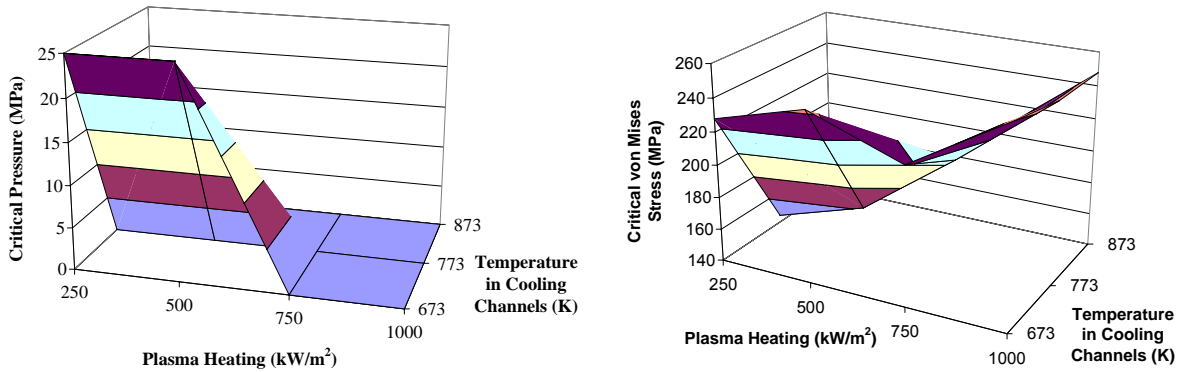


Fig 2: Critical pressure and the corresponding maximum of the von Mises stress (on the right) as a function of the plasma heating and the temperature in the cooling channels.

### 2.3 Simulation of the cyclic behaviour of TBM

The cyclic behaviour of the TBM has been simulated using the UMAT for the first 600 cycles under consideration of the same loadings as in the TW2-TTMS-005b, del. 2 (see the corresponding annual report). The application of the UMAT leads evidently to considerably higher plastic strains due to the creep and damage of the material. Note that the values of the variable PEMAG (the magnitude of the plastic strain) after the 1<sup>st</sup> heating are quite similar for both models, see fig. 4. As follows from the curve depicted in fig. 4, the magnitude of the plastic strain seems to reach a saturated value. Furthermore, the equivalent stress represented in fig. 5 as a function of the accumulated plastic strain corresponds rather to a non-ratcheting behaviour. However, to obtain a definite answer, the TBM should be simulated up to the failure. It is however possible only using the extrapolation method discussed below. Only more conservative results obtained under an application of the UMAT are used below for the verification of some design rules.

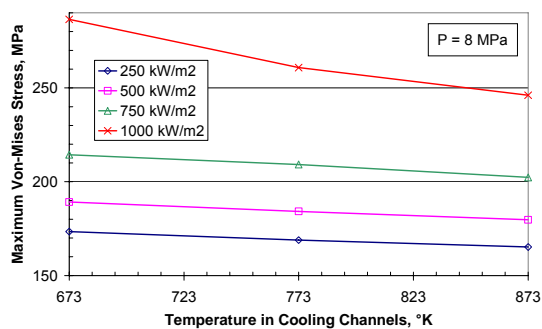


Fig. 3: The maximum von-Mises stress as a function of the temperature in cooling channels for different values of the plasma heating at the constant pressure of 8 MPa.

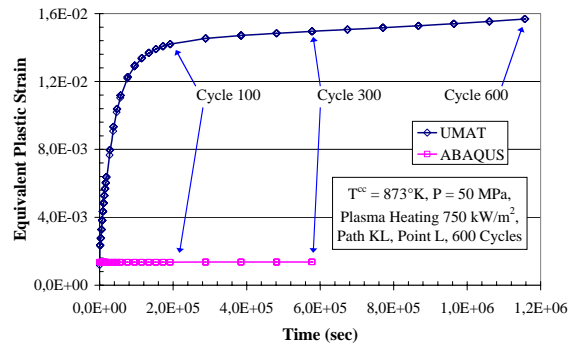


Fig. 4: The change of the maximum equivalent plastic strain among all values along the path KL cycle by cycle during the first 100 cycles computed using the ABAQUS-own material and the UMAT.

### 2.4 Calculation of the allowable membrane stress intensity $S_m$

The available  $S_m$  and  $S_{mt}$  values do not consider a change of the tensile strength and yield stress cycle by cycle. This change can be however taken into account if  $S_m$  is calculated on the basis of the experimental data discussed in the section 3.1 of the annual report to TW2-TTMS-005b, del. 2. Thereby, the maximum achieved tensile stress has been used here for calculations instead of the ultimate tensile strength. To obtain the needed tensile strengths, tensile tests should be performed after e.g. 10, 20 etc. cycles.

The new-calculated in such manner value is represented in fig. 6 together with the  $S_m$  values from the DEMO SDC. It was assumed that each cycle is 1930 sec = 0,54 h long. To avoid a misunderstanding, the value has been labelled as  $S_m^*$ . Note that any stress should lead to a plastic collapse e.g. already after 200 cycles at 650 °C (923 K). As follows from the diagrams in fig. 6, the DEMO SDC provides too high values of  $S_m/S_{mt}$ . For instance, values proposed for 650 °C (923 K) are valid for 550 °C (823 K). On the other hand, the cycles in the mechanical tests differ from the operating cycles of the TBM with respect to the material damage, whereby the mechanical tension-compression cycling causes considerably higher material damage. It means that the new introduced values yield rather conservative estimations and should be used by designers with a factor, which should be firstly determined.

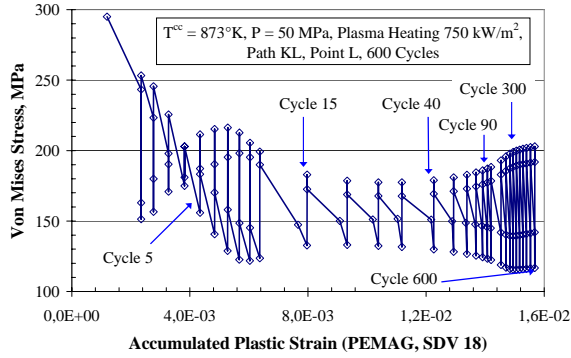


Fig. 5: Equivalent stress as a function of the accumulated plastic strain computed using the UMAT for the first 600 cycles.

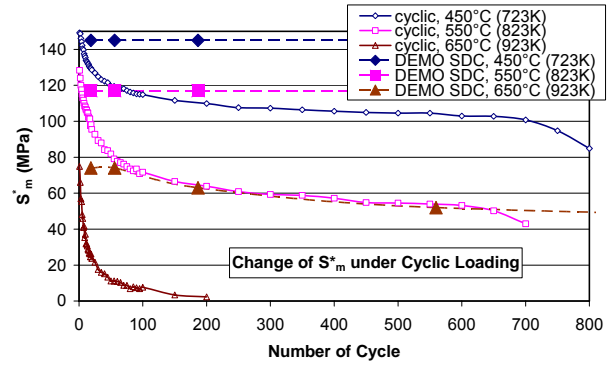


Fig. 6: Change of  $S_m^*$  under cyclic loading at 450 °C (723 K), 550 °C (823 K) and 650 °C (923 K); available data for these temperatures are also given for comparison.

## 2.5 Stress categorization

To separate primary and secondary stresses, linear-elastic simulations have been performed for three load cases: thermal and mechanical loads acting together and separated. A comparison of the results obtained allows to recognize that the coolant pressure partially compensates the influence of the plasma heating. Results of these simulations have been then linearized automatically along the two paths discussed above using the corresponding option of the ABAQUS VIEWER.

## 2.6 Application and verification of design rules

Within the frame of the work presented, the following low-temperature design criteria have been checked:

- rules for prevention of an immediate plastic collapse and a plastic instability (M-type damage)

$$\begin{aligned} \overline{P}_m &\leq S_m \\ \overline{P}_m + \overline{P}_b &\leq K S_m \end{aligned} \quad (1)$$

- the rule for prevention of a progressive deformation or a ratcheting (C-type damage)

$$\overline{P}_m + \overline{P}_b + \left[ \overline{\Delta P}_{\max} + \overline{\Delta Q}_{\max} \right] \leq 3 S_m \quad (2)$$

Thereby,  $K$  is the bending shape factor, which ranges in general between 1.0 and 2.0. Here,  $K = 1.5$ . The more conservative rule accounting for a possible embrittlement caused by irradiation is not considered here since the material tested is unirradiated. Besides this factor, the following conventional notations are used here:  $\overline{P}_m$  and  $\overline{P}_m + \overline{P}_b$  denote the primary membrane stress intensity and the primary membrane and bending stress intensity

excluding plasma disruption loadings respectively;  $\overline{\Delta Q}_{\max}$  and  $\overline{\Delta P}_{\max}$  are the maximum in the thickness secondary (thermal) stress intensity range and the stress intensity range due to disruption loadings (here is not considered). Furthermore, the low-temperature Bree-diagram rule has been also evaluated:

$$Y \leq \frac{1}{X} \text{ if } 0 \leq X \leq 0.5 \text{ or } Y \leq 4[1 - X] \text{ if } 0.5 \leq X \leq 1.0 \quad (3)$$

Here,  $X = \overline{P}_m / S_y$ ,  $Y = [\overline{\Delta P}_{\max} + \overline{\Delta Q}_{\max}] / S_y$ ;  $S_y$  is the average of the minimum yield strength evaluated at the minimum and maximum thickness-averaged temperatures and fluences during the cycle calculated along the supporting line segments.

The maximum values required for an evaluation of (1) and (2) are collected in tab. 1. An easy comparison allows to see that none of the three criteria is fulfilled even for the  $S_{mt}$  value stemming from DEMO SDC at  $T^{cc} = 600 \text{ }^\circ\text{C}$  (873 K). If the  $S_{mt}$  value at the average temperature along the path (approx.  $625 \text{ }^\circ\text{C}$  or 899 K) is considered, the difference becomes more essential. The  $S_m^*$  value for this temperature is however out of any competition.

Table 1: Maximum absolute values of the categorized stress components and their combinations among all values for the chosen paths together with the corresp. values of  $S_{mt}$

$\overline{P}_m$	$S_{mt}^{898 \text{ K}}$	$S_m^{*898 \text{ K}}$	$S_{mt}^{873 \text{ K}}$	$S_m^{*873 \text{ K}}$
<b>117.0</b>	82.0	<b>23.7</b>	98.0	39.7
$\overline{P}_m + \overline{P}_b$	$K * S_{mt}^{898 \text{ K}}$	$K * S_m^{*898 \text{ K}}$	$K * S_{mt}^{873 \text{ K}}$	$K * S_m^{*873 \text{ K}}$
<b>179.7</b>	123.0	<b>35.5</b>	147.0	59.5
$\overline{P}_m + \overline{P}_b + \overline{\Delta Q}_{\max}$	$3 * S_{mt}^{898 \text{ K}}$	$3 * S_m^{*898 \text{ K}}$	$3 * S_{mt}^{873 \text{ K}}$	$3 * S_m^{*873 \text{ K}}$
<b>395.5</b>	246.0	<b>71.0</b>	294.0	119

An application of (3) shows that the less conservative Bree-diagram rule is fulfilled for three different temperatures from 873 K to 923 K. Nevertheless, the criterion (2) should also be satisfied to apply the high-temperature  $3S_{mt}$ -rule, see ITER SDC for in-vessel components, IC3541.3.

Thus, the chosen design rules predict (a) the plastic collapse and plastic instability as well as (b) probably the accumulation of the plastic deformation. Results of the simulation performed under the application of the UMAT considering damage seems to show rather a shakedown after the first 600 cycles. To obtain a definite answer, the simulation should be performed until the material fails. A distribution of the damage variable after the first 600 cycles is shown in fig. 7, on the right. The maximum value reaches thereby only 0.0017 whereas the value corresponding to the material failure is approximately equal to 0.08. If the trend in the evolution of the damage variable shown in fig. 7 on the left remains valid, this recent value corresponds to approximately 5000 cycles. It is absolutely impossible to perform such a simulation.

### 3 Outlook

One of possible solutions is an extrapolation method reported by H. Kiewel, J. Aktaa and D. Munz in Comput. Methods Appl. Mech. Engrg. 182 (2000) 55-71 („Application of an extrapolation method in thermocyclic failure analysis“), which should be applied during further activity.

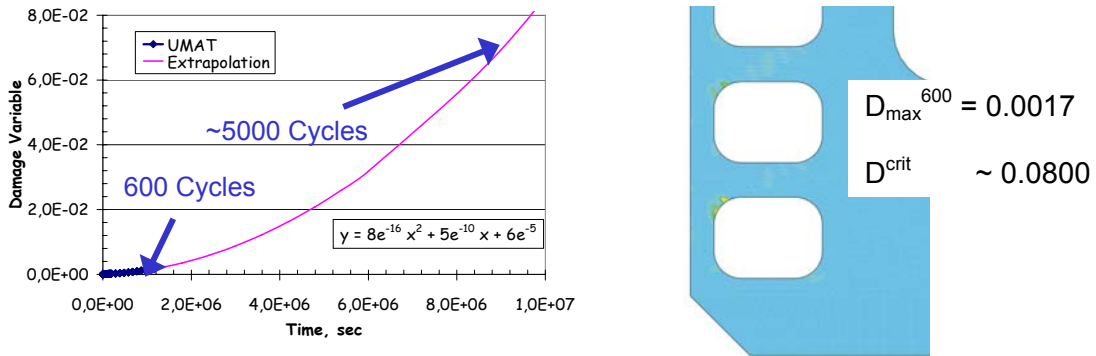


Fig. 7: The trend in the evolution of the damage variable (on the left); the computed distribution of the damage variable in the most loaded model region.

On the other hand, all design criteria should be checked according to the scheme given in ITER SDC for in-vessel components, IC3030 to decide whether the design proposed is suitable. It means that the evaluation of the existing design rules should be continued possibly within a separated EFDA-subtask.

The performed simulations are however sufficient to define boundary conditions for verifications experiments to close the current subtask.

Staff:

R. Sunyk

Literature:

- [1] R. Sunyk, J. Aktaa, "Evaluation of Material Design Limits for TBM Applications", 2005 in IEEE/SOFE05 proceedings; <http://216.228.1.34/Conf/sofe05/versions/64291/PID131414.pdf>
- [2] R. Sunyk, J. Aktaa, "Verification of Design Rules for EUROFER under TBM Operating Conditions ", Submitted to J. Nuc. Mat. (special issue)

## **TW5-TTMS-005 D 9**

### **Experimental Programme for Verification of HT Creep-fatigue Rules from Uniaxial Experiments (e.g. LCF tests with long dwell time) and/or Multi-step LCF Tests**

#### **Background and Objectives**

For TBM's licensing, in order to establish design rules for the materials, joints and specific sub-components, a broad set of R&D activities have been launched within the WP 2002. These activities will continue with emphasis on implementation in DSCD (Demo structural design code) and verification and validation experiments. Additional rules for HT (high temperature) fatigue-creep interaction need to be formulated, in particular for fracture mechanics.

The low ductility of EUROFER (in particular after irradiation ) gives very conservative limits for design against fast fracture and local flow localization. Some experiments are required in support of special design code activities that could lower very conservative assumptions in existing frameworks.

Development of small scale test techniques in fracture mechanics will continue including transferability of the small size specimens tests to the behaviour of the TBM's sub-components.

The objectives of this subtask are to evaluate the mechanical properties of EUROFER in the region of creep-fatigue. Therefore suitable uniaxial Low Cycle Fatigue experiments in the temperature range  $550^{\circ}\text{C} \pm 50^{\circ}$  must be done (multi-step experiments, experiments with higher dwell times). The results are needed for the verification of High Temperature creep-fatigue lifetime rules.

#### **Status January 2005**

2-step experiments - high/low and low/high with different total strain amplitudes by variation of the ratio of number of cycles ( $n_x$ ) to the number of cycles to failure ( $N_{xf}$ ) in the first step - were started in 2004. In principle the two steps have been realized with a total strain amplitude ( $\Delta\varepsilon_{tot}$ ) of 0.6% (low) and 1.0% (high). The experiments were performed at  $450^{\circ}\text{C}$  and  $550^{\circ}\text{C}$ .

#### **Status**

The 2-step experiments have been finished. As shown in the Palmgren-Minor-Diagram (Fig. 1), a non linear damage accumulation was found in our tests. Beginning with a high  $\Delta\varepsilon_{tot}$  (1.0%) leads to lower lifetimes in comparison to linear behaviour (especially with decreasing  $n_1/N_{1f}$  ratio). In contrast, starting with low  $\Delta\varepsilon_{tot}$  (0.6%) leads to clearly higher lifetimes, in some cases even higher than in single 1-step experiments with low total strain amplitude.

The 3-step experiments - high/low/high and low/high/low with different total strain amplitudes by variation of the ratio of number of cycles ( $n_x$ ) to the number of cycles to damage ( $N_{xd}$ ) in the first step and the second step - have been nearly finished (some experiments at  $450^{\circ}\text{C}$  are missing). In principle, the 3-step experiments have also been realized with total strain amplitudes ( $\Delta\varepsilon_{tot}$ ) of 0.6% (low) and 1.0% (high) at  $450^{\circ}\text{C}$  and  $550^{\circ}\text{C}$ , respectively. Up to now one can observe that beginning with a value  $n_1 = 0.2 - 0.5 N_{1d}$  in the first step leads to nearly the same lifetimes in comparison to a linear behaviour and beginning with a  $n_1$  out of this range leads to lower lifetimes (especially with decreasing  $n_1^*/N_{1d}$  ratio –  $n_1^*$  is the number of cycles in the first step plus the number of cycles in the third step up to the initiation of a macro-crack – in this case it is also nearly impossible to perform a real 3-step test). The re-

sults of these experiments are also plotted in a Palmgren-Minor-Diagramm (Fig. 2). Fig. 3 shows a comparison of the 2-step experiments (only the 'worse case' results) and the 3-step experiments with respect to the fracture values ( $n_1^*/N_{1f} - n_2^*/N_{2f}$ ).

The LCF experiments with dwell time have been started. In principle, they will be done at 450 °C and 550 °C with a total strain amplitude of 1.0% and a dwell time of 60 minutes for 3 different cases – dwell time only under tension, dwell time only under compression and dwell time under tension and compression. Because of the long dwell time, the individual experiments take up to months. So presently the third experiment is running.

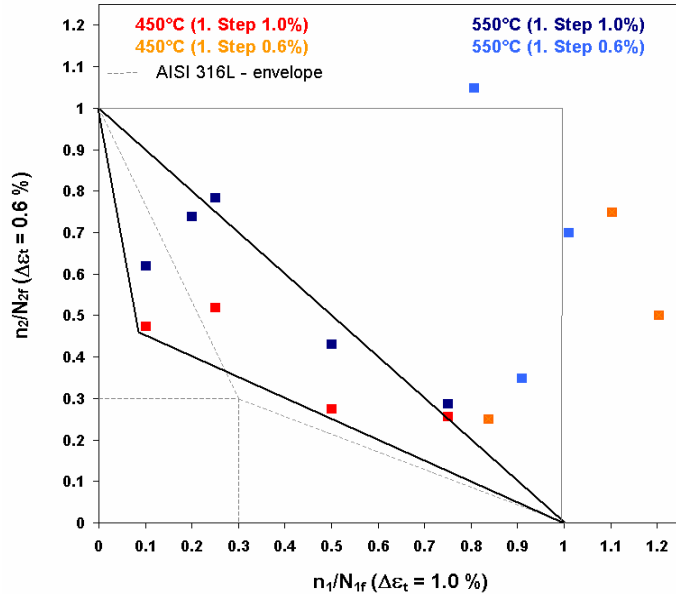


Fig. 1: Results of the 2-step experiments, plotted in a Palmgren-Minor-Diagram.

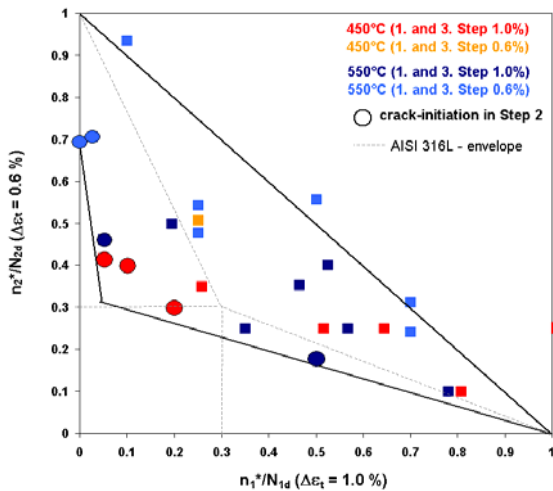


Fig. 2: Results of the 3-step experiments, plotted in a Palmgren-Minor-Diagram.

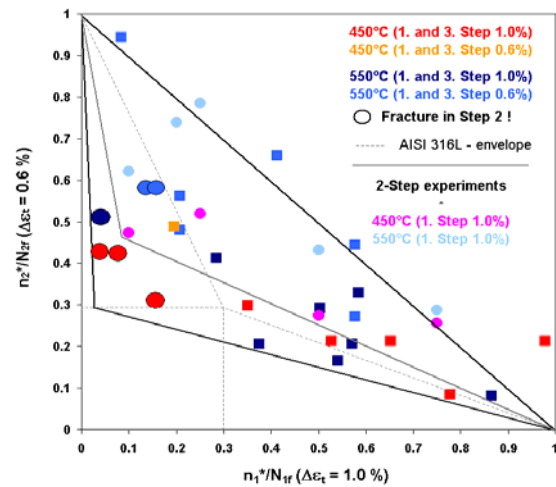


Fig. 3: Comparison of the 2-step and 3-step experimental results, plotted in a Palmgren-Minor-Diagram.

## Conclusion and Outlook

The results of the multi-step experiments generally show that beginning the tests with a high total strain amplitude leads to lower lifetimes in comparison to a linear behaviour, even more so with a decreasing  $n_1/N_{1f}$  ratio. In comparison to the AISI 316L envelope, the design space for EUROFER becomes clearly smaller, especially in the area with a low  $n_1/N_{1f}$  ratio.

In the dwell time experiments, one can observe that creep processes under compression obviously lead to more damage in the material (lower lifetimes, lower stress levels). In comparison to experiments with lower dwell times one can see, that the lifetime is decreasing with increasing dwell time, even more with an increasing fraction of dwell time under compression.



The next steps will be finishing the 3-step experiments and to continuing the dwell time tests.

Staff:

M. Walter  
M. Lerch

Literature:

- [1] M. Walter, J. Aktaa: Talk: 'Experimental programme for verification of HT creep-fatigue rules from uniaxial experiments and on creep-crack-growth experiments', EFDA Review and Strategy Meeting on Task TTMS-005, 11.11.05, FZK

## TTMS-006 High Performance Steels

### TW3-TTMS-006 D 1 EU ODS Steel Specification and Production

#### D1a) EU ODS production (about 50 kg) according to the selected manufacturing route

The replacement of presently considered conventionally produced reduced-activation ferritic-martensitic (RAFM) steels for structural applications in future fusion reactors by suitable ODS alloys would allow to increase the operating temperature by about 100 °C to approximately 650 °C or more. ODS RAFM steels with varying yttria contents were developed in close co-operation of FZK and Plansee AG. First attempts to produce only hiped ODS steels, following the idea of producing Near-Net-Shape blanket parts, were successful. Yield strength and ultimate tensile strength between RT and 750 °C were increased by 35% and more, compared to non-ODS RAFM steels. Creep tests between 600 and 700 °C confirmed the good behaviour. The major drawback of hiped ODS-EUROFER were the poor impact properties with 40% lower upper shelf energy (USE) and a ductile-to-brittle-transition-temperature (DBTT) at around 100 °C compared to -100°C for non-ODS EUROFER. Optimisation trials performed by CEA and CRPP to develop “improved” ODS alloys applying different production routes (TW2-TTMS-006 D1 and D10) were not successful. The mechanical properties of these two “improved” alloys were not satisfying (TW3-TTMS-006 D3, D5, D6).

Following a new blanket concept an ODS-EUROFER plate was produced according to FZK specifications. Applying special thermo-mechanical treatments improved DBTT considerably to values at about -50 °C without lowering tensile and creep strength.



Fig. 1: Different product forms of ODS-EUROFER.

Independently, FZK developed together with Plansee a production route for ODS-EUROFER, which included a thermo-mechanical treatment which finally, after some optimisation work (TW4-TTMS-006 D1), led to a material with much higher ductility and improved impact properties without considerable losses in tensile and creep strength. This production

route was chosen for the production of a 50 kg ODS-EUROFER batch in different product forms (6 and 17 mm rolled plates, and 12.5 and 20 mm extruded bars).

**D1b) Assessment of the influence of Carbon and Oxygen content during the production on the mechanical and microstructural properties.**

It is believed that the content of carbon and oxygen and other gases could have an effect on the mechanical and microstructural properties. It was therefore decided to investigate the development of the C-, and O-content during the different production steps including the initial steel powder production, the mechanical alloying process and the consolidation process by hot isostatic pressing.

In former steel powder productions (Starck) it was observed, that the carbon content decreased during the inert gas atomisation of the EUROFER steel while it remained nearly constant during the following mechanical alloying and hipping process. It can be assumed that this decrease is due to irregularly high oxygen content of the argon, which has been used as protective gas for the atomisation process. This decrease of the C-content was not observed in other productions (Studsvik, Nanoval). A certain minimum carbon content is necessary to achieve an air-hardening material. The oxygen content, which is suspected to have a negative effect on the mechanical properties, especially on the ductility, was measured after the different production steps. The oxygen content of the atomised powder is increased compared to the solid ingot, which is melted and sprayed into the inert gas that contains also a small amount of oxygen.

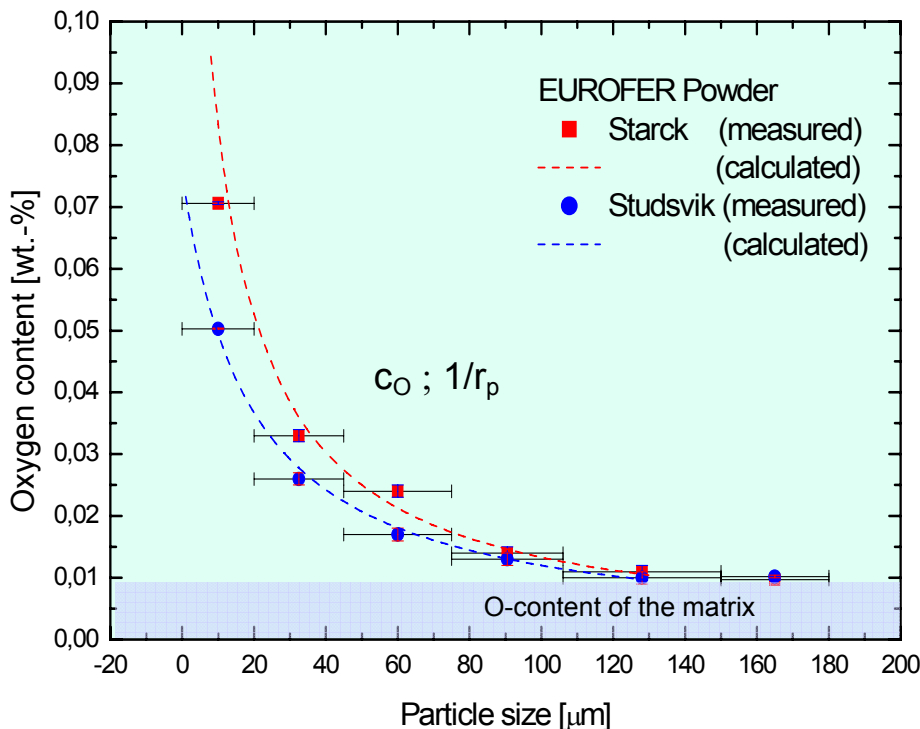


Fig. 2: Oxygen content of EUROFER steel powders in dependency of the particle size.

As shown in Fig. 2 the oxygen content of the steel powder depends on the powder particle size. It correlates very well with the surface to volume ratio ( $S/V=3/r_p$ ) of the particles, i.e. that the particles are mainly oxidised at the surface while the matrix content remains constant. During mechanical alloying process the O-content is further increased. For the mechanical alloyed materials, the excessive oxygen, which is the difference between the total oxygen content and the oxygen chemically bound in the yttrium oxide, is the most important value.

### Staff:

Ch. Adelhelm  
S. Baumgärtner  
A. Falkenstein  
P. Graf  
M. Klimiankou  
T. Kaiser  
R. Lindau  
A. Möslang  
D. Preininger  
U. Jäntschi  
R. Ziegler  
H. Zimmermann

### Literature:

- [1] Klimiankou, M.; Lindau, R.; Möslang, A.; Energy-filtered TEM Imaging and EELS Study of ODS Particles and Argon-filled Cavities in Ferritic-martensitic Steels, *Micron*, 36 (2005) p.1-8.
- [2] Klimiankou, M.; Lindau, R.; Möslang, A.; Schröder, J.; "TEM study of PM 2000 steel" *Powder Metallurgy* (2005) Vol. 48 (3) p. 277-288
- [3] Lindau, R.; Möslang, A.; Rieth, M.; Norajitra, P.; ODS-Eurofer - A Reduced Activation Ferritic Martensitic (RAFM) ODS-steel for Application in Advanced Blanket Concepts. EUROMAT 2005, European Congress on Advanced Materials and Processes, 5.-8. September 2005, Prag, Keynote lecture in Symposium C32 "Materials for Fusion Applications", Abstract in <http://www.euromat2005.fems.org/>
- [4] Paul, A.; Alves, E.; Marques, C.; Lindau, R.; Odriozola, J.A., Microstructural characterization of Eurofer-ODS RAFM Steel in the normalized and tempered condition after aging in simulated fusion conditions, 23rd Symposium on Fusion Technology, 20.-24. September 2004, Venice, Italy, *Fusion Engineering and Design*, 75-79 (2005) p.1061-1065

## TW4-TTMS-006 D 1 Optimisation of Fabrication Parameters of Current EUROFER ODS Plate Material

The aim of this study is to improve the high temperature tensile ductility and impact properties, in particular the very low fracture toughness in the upper shelf region and the relatively high ductile to brittle transition temperature (DBTT). At the same time the good high temperature properties should be maintained. The aim is here to reach comparable tensile and creep strength at 600-700 °C as EUROFER at 100 K lower. In particular any development of ODS material should not contravene the goal to produce a low activation steel.

Optimisation trials performed by CEA and CRPP to develop “improved” ODS-EUROFER alloys applying different production routes were not successful and the mechanical properties of these two alloys were not satisfying. Independently, FZK developed together with Plansee AG a production route for ODS-EUROFER, which included a thermo-mechanical treatment. This thermo-mechanical treatment led finally, after some optimisation work, to a material with much higher ductility and improved impact properties without considerable losses in tensile and creep strength. Fig. 1 shows the results of tests on sub-size KLST specimens of rolled and heat-treated ODS-EUROFER (plate) compared to only hipped ODS-EUROFER of the first generation and standard EUROFER steel. DBTT could be shifted from values between +60 and +100 °C for hipped ODS-Eurofer of the first generation to values between -40 and -80 °C. The upper shelf energy (USE) was increased by about 40%.

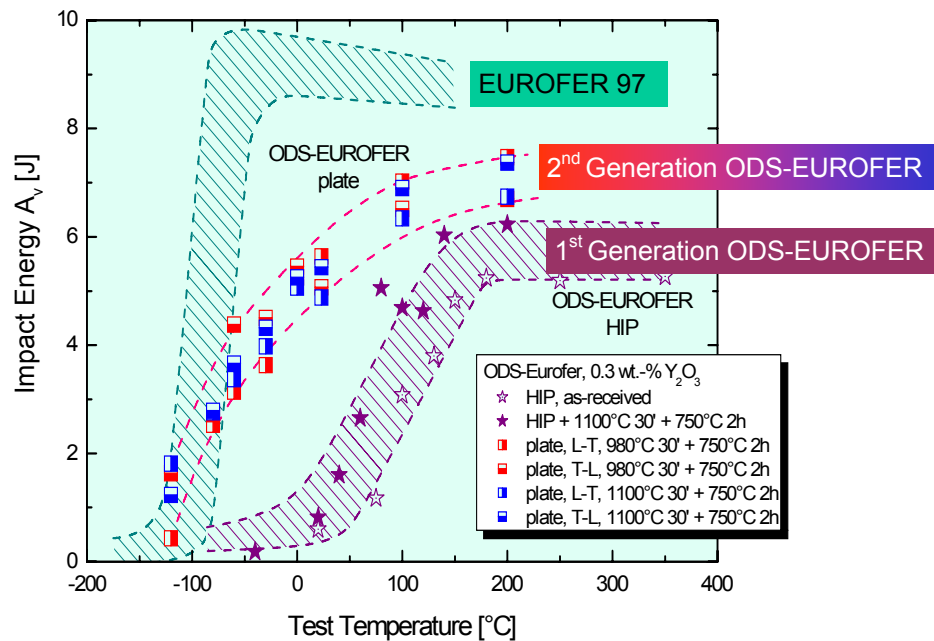
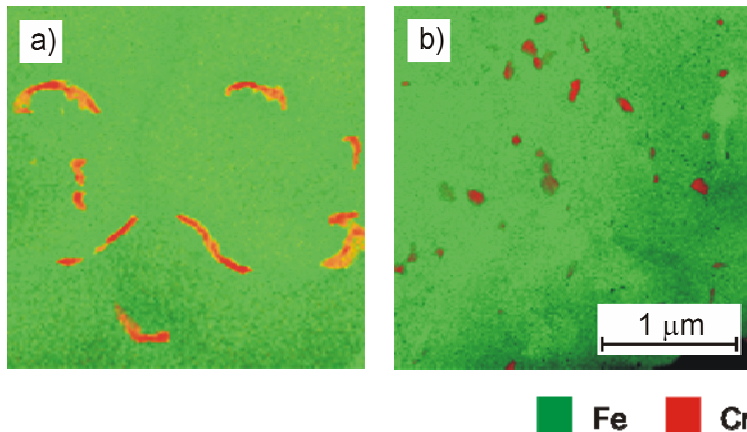


Fig. 1: Test temperature dependence of total absorbed energy of different ODS-EUROFER steels in comparison with EUROFER 97 (KLST specimens).

In order to understand the impact of hipping conditions, heat treatments and thermo-mechanical treatment on the mechanical behaviour, an extensive microstructural characterisation programme was launched. The differences in ductility, especially the high DBTT and low USE in the impact test, can be attributed to microstructural changes occurring during the different steps in the manufacturing process. After consolidation in a hot-isostatic-pressing (HIP) process with subsequent furnace cooling, the formation of a massive precipitation of long-shaped  $(Fe,Cr)_{23}C_6$  precipitates on the grain boundaries, which may act as crack initiators, can be observed (Fig. 2a). This appearance correlates with the poor impact energy values in Fig. 1 (1<sup>st</sup> Generation ODS-EUROFER, aubergine coloured hatched area). A normalising treatment at 1100 °C 30 min with water quenching and a subsequent tempering at 750 °C

for 2 h with air-cooling applied to the hiped samples led to a slight improvement in DBTT and USE (full stars in Fig. 1). The heat treatment was not sufficient to dissolve the massive precipitates and to reprecipitate the  $M_{23}C_6$  in a less harmful form. A solution treatment above 1100 °C for 3 hours was necessary to dissolve the carbides. Applying a thermo-mechanical treatment, i.e. a hot roll plus a subsequent normalising and tempering treatment (2<sup>nd</sup> Generation ODS-EUROFER, red and blue squares in Fig. 1) leads to more globular shaped  $(Fe,Cr)_{23}C_6$  precipitates (Fig. 2b) which are less deleterious. As a side effect of the hot rolling, the grain size decreases from 2-8 microns for the hiped samples to 0.6-2 microns, which is also beneficial for the impact properties. It could be clearly shown that the mechanical properties of ODS-EUROFER can be directly correlated to the microstructural development during different fabrication steps.



Staff:

C. Adelhelm  
S. Baumgärtner  
B. Dafferner  
A. Falkenstein  
P. Graf  
S. Heger  
T. Kaiser  
M. Klimiankou  
R. Lindau  
A. Möslang  
D. Preininger  
U. Jäntsch  
M. Rieth  
H. Zimmermann

Fig. 2: Analytical TEM-analysis of precipitates in a) hiped sample and b) thermo-mechanically treated sample. EDX-mapping in FEI Tecnai 20 FEG microscope.

Literature:

- [1] Grant, G.J.; Gelles, D.S.; Lindau, R.; Friction Stir Welding of Oxide Dispersion Strengthened EUROFER Steel. Fusion Materials Semi-annual Report for the Period Ending June 30, 2005; DOE-ER-0313/38; p. 47-53. <http://www.ms.ornl.gov/programs/fusionmatls/pubs/semiannual.htm>
- [2] Grant, G. J.; Lindau, R.; Packer, S.; Gelles, D. S., Friction Stir Welding of Oxide Dispersion Strengthened Steels, 12th Internat.Conf.on Fusion Reactor Materials (ICFRM-12), Santa Barbara, Calif., December 4-9, 2005, Book of Abstracts p. 9
- [3] Klimiankou, M.; Lindau, R.; Möslang, A.; "Direct Correlation Between Chromium Phases And Impact Behavior Of ODS Steels" 12th Internat.Conf.on Fusion Reactor Materials (ICFRM-12), Santa Barbara, December 1-5, 2005, Book of Abstracts p. 305
- [4] Lindau, R.; Klimiankou, M.; Möslang, A.; Rieth, M.; Schedler, B.; Schröder, J.; Schwaiger, A.; ODS-EUROFER - a reduced activation ferritic martensitic ODS-steel for structural applications in future nuclear fusion reactors. Powder Metallurgical High Performance Materials : Proc.of the 16th Internat. Plansee Seminar, Reutte, A, May 30 - June 3, 2005 Vol.1: High Performance P/M Materials p.545-57 Reutte : Plansee AG, 2005
- [5] Lindau, R.; Möslang, A.; Rieth, M.; Norajitra, P.; ODS-Eurofer - A Reduced Activation Ferritic Martensitic (RAFM) ODS-steel for Application in Advanced Blanket Concepts. EUROMAT 2005, European Congress on Advanced Materials and Processes, 5.-8. September 2005, Prag, Keynote lecture in Symposium C32 "Materials for Fusion Applications", Abstract in <http://www.euromat2005.fems.org/>
- [6] Preininger, D.; Correlation between ductility and impact properties of oxide dispersion-hardened ODS-Ta-W alloys. EUROMAT 2005, European Congress on Advanced Materials and Processes, 5.-8. September 2005, Prag, Abstract in <http://www.euromat2005.fems.org>.
- [7] Preininger, D.; Grain refinement effects on tensile ductility and impact properties of oxide dispersion-hardened ODS-Ta-W alloys. submitted to Journal of steels and related materials (2005)

## TW5-TTMS-006 D 6

### Characterisation of Reference EU ODS-EUROFER Batch (Tensile, Creep and Charpy)

Several developmental ODS-alloys on the basis of the RAFM steel EUROFER have been produced in the past by different associations, i.e. FZK, CEA and CRPP. Results of mechanical tests revealed good tensile, creep and LCF properties of the hipped ODS but poor DBTT ( $\sim 100$  °C) compared to EUROFER. Applying special thermo-mechanical treatments i.e. mechanical deformation plus subsequent heat treatment lead to a substantial shift of DBTT to temperatures well below 0 °C without negative effect on the tensile properties. Moreover the total elongation was increased at higher temperatures compared to only hipped ODS. This fabrication route was chosen (TW-3-TTMS006 D1) for the fabrication of 50 kg EU-ODS-EUROFER reference alloy in 4 different product forms, i.e. 2 rolled plates ( $t = 6$  and 17 mm) and 2 extruded rods ( $\varnothing 12.5$  and 20 mm).

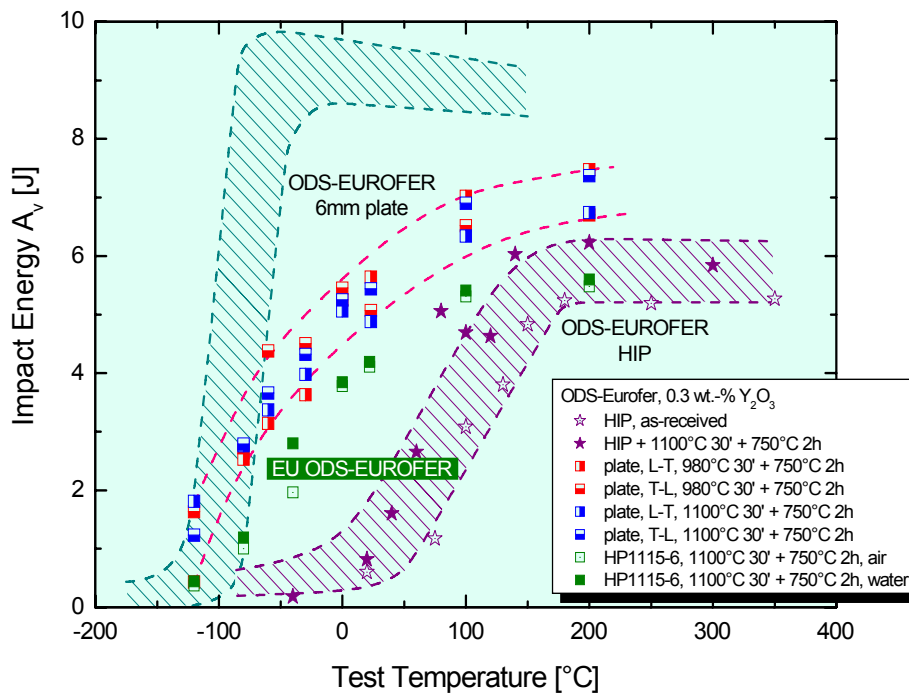


Fig. 1: Test temperature dependence of total absorbed energy of EU ODS-EUROFER in comparison with former ODS-EUROFER and EUROFER 97 (KLST specimens).

After first heat treatment trials (TW5-TTMS-006 D10) a reference heat treatment (normalising + tempering) of 1100 °C 30 min air-/water-quenching + 750 °C 2 h air-cooling was chosen. Due to a higher C-content (0.13 wt.-%) of the EU-batch compared to the precursor alloys, the material was air-hardening. Since the impact properties are most sensitive, impact tests on KLST specimen, applying these two different heat treatments, were performed. Fig. 1 shows the results of these tests in comparison to the precursor alloys and standard EUROFER. It turned out, that the new EU-reference batch (green squares) did not reach the good values of the thermo-mechanically treated plate material produced earlier (red and blue squares). Independent from the cooling procedure applied after normalising, the different samples show nearly the same impact behaviour. The ductile to brittle transition temperature (DBTT) of the EU-batch is about  $-30$  °C which is not much worse than DBTT of the former plate material. The most critical changes occurred in the decrease of the upper shelf energy (USE) which did not exceed the values of the first only hipped ODS-EUROFER alloys. The reason for these deviations might be found in the microstructural evolution. Due to the higher carbon and nitrogen content the samples show a quite high density of precipitates (see TW5-

TTMS006 D10). Further heat treatment trials are necessary to examine whether it is possible to improve the impact properties. Tensile and creep tests are under way, to assess the short term and long term tensile behaviour.

Staff:

S. Baumgärtner  
B. Dafferner  
A. Falkenstein  
S. Heger  
M. Klimiankou  
R. Lindau  
A. Möslang  
U. Jäntschi  
M. Rieth  
H. Zimmermann

Literature:

- [1] Lindau, R.; Klimiankou, M.; Möslang, A.; Rieth, M.; First Results On The Characterization Of The Advanced EU Reference RAFM ODS-EUROFER Steel, 12th International Conference on Fusion Reactor Materials, ICFRM 12, Dec. 4-9, 2005, Santa Barbara, CA, USA, Book of Abstracts p. 305
- [2] Lindau, R.; Möslang, A.; Rieth, M.; Klimiankou, M.; Materna-Morris M.; Present Development Status of EUROFER and ODS-EUROFER for Application in Blanket Concepts. Materials Seminar, Metals & Ceramics Division, ORNL, Oak Ridge TS, USA, April 22, 2005



## TW5-TTMS-006 D 10

### Characterisation of Reference EU-ODS-EUROFER Batch: Optimisation of Heat Treatment, Ageing Behaviour and Microstructural Characterisation

The efficiency of future fusion reactors will strongly depend on the operating temperature allowed by selected structural materials. With this respect, ODS steels are attractive candidates since they would allow to increase the operating temperature by approximately 100 °C. The reduced activation martensitic steel EUROFER-97 (8.9Cr, 1.1W, 0.14 Ta, 0.42 Mn 0.11 C wt%), which is currently considered as a European reference for structural application, has been selected as a base material. Based on the experience with a precursor a 50 kg EU-ODS-EUROFER batch has been specified and produced (TW3-TTMS-006 D1a). Within this task an optimum heat treatment should be determined. The influence of different heat treatments on microstructure was also investigated.

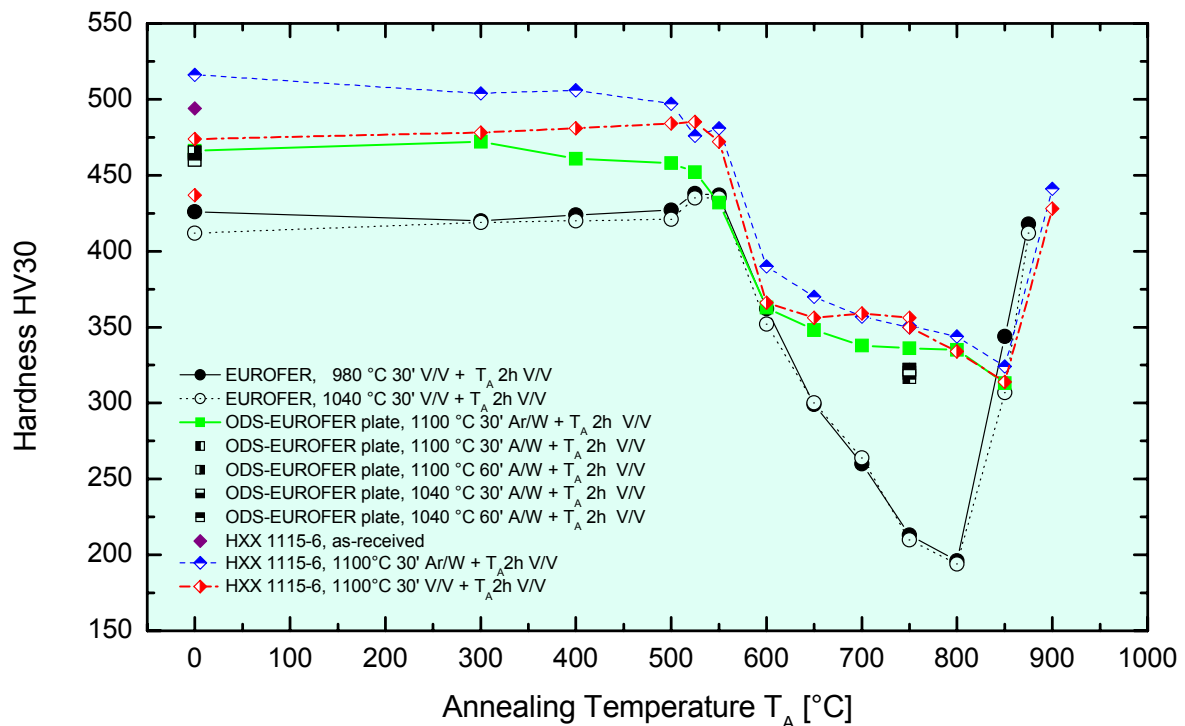


Fig. 1: Vickers hardness HV30 in dependence of the annealing temperature.

First heat treatment trials on the EU-ODS-EUROFER material were performed. The samples were normalized at 1100 °C for 30 min following a tempering treatment at temperatures between 300 and 850 °C for 2 hours. The cooling to room temperature after austenitisation was performed either by air- or water- quenching. Fig. 1 gives the development of hardness HV30 in dependence of the annealing temperature. The tempering treatment was performed in a tubular 3-zone furnace. The cooling was performed by withdrawal of the furnace from the vacuum quartz recipient. Due to the small specimen size the cooling rate is equivalent to air-cooling. The tempering behaviour of the EU-batch (HXX 1115-6, blue and red diamonds) is compared to the precursor alloy (green and black squares) and standard non-ODS EUROFER steel (full and open black circles). The Vickers hardness of all ODS alloys in the interesting temperature range between 550 and 850 °C is very similar. According to the good mechanical behaviour of the precursor ODS-EUROFER steel, 1100 °C 30 min air-/ water-quenching + 750 °C 2 h air-cooling was chosen as reference heat treatment. Due to a higher C-content (0.13 wt.-%) of the EU-batch compared to the pre-cursor alloys, the material was air-hardening.

The microstructural examinations included OM, SEM, and TEM methods.

The optical micrograph of the HXX 1115-6 in the normalised and tempered (NT) condition (1100 °C 30 min V/V + 750 °C 2 h V/V) (Fig. 2) shows a very homogeneous grain structure with grain sizes of about 1 µm. Fig. 3 presents two SEM images of normalised and tempered samples, either air- or water-quenched, that show a very similar precipitate distribution.

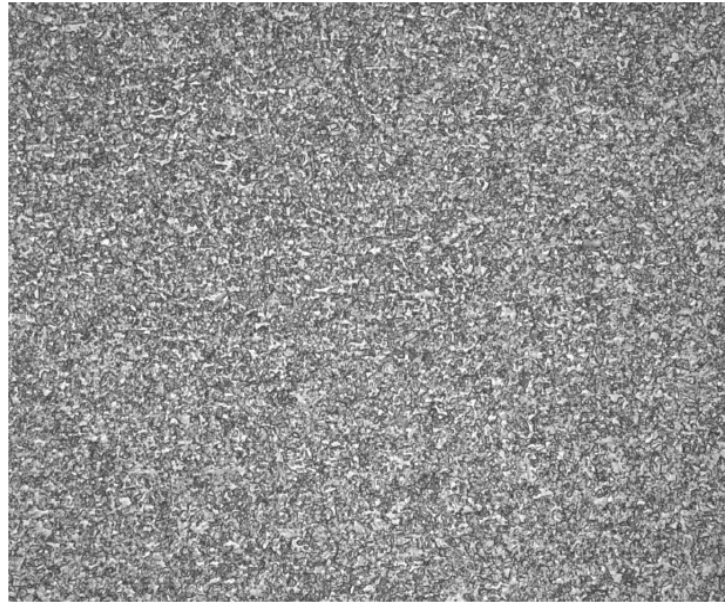


Fig. 2: Grain structure of EU-ODS-EUROFER.

The character of the different precipitates was determined by TEM analysis using an analytical FEI Tecnai 20 FEG microscope equipped with a high-angle annular dark field detector for scanning TEM.

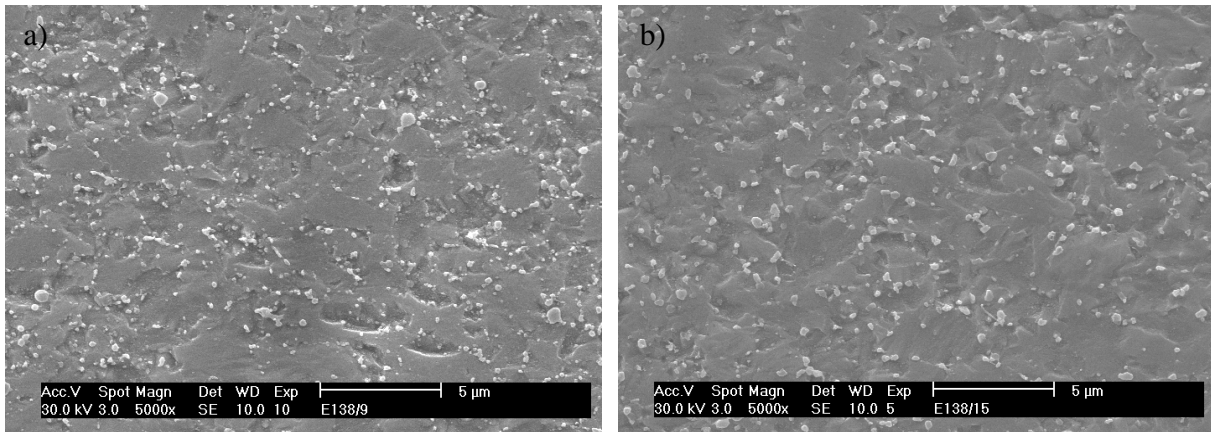


Fig. 3: SEM images taken from air-hardened (a) and water-quenched (b) samples.

The STEM investigations show, that the precipitates in the air-hardened sample (1100 °C V/V) without any tempering, which appear in a more globular shape have a composition of 45% Cr, 26% Fe, 26% Mn and 3% V (wt. %) (Fig. 4). The precipitate size varied from 50 to 500 nm. The EDX spectrum presented in the Fig. 4b was acquired when the electron beam was focussed on the imaged precipitate. The question, whether these precipitates are carbides, nitrides or carbo-nitrides will be answered by later experiments. The typical  $M_{23}C_6$  carbides have not been detected in the air-/water-quenched samples.

The formation of carbide precipitates was observed in the water-quenched sample (1100 °C Ar/W) after annealing at 750 °C for 2 h (Fig. 5). Their size varied from 60 to 300 nm. The precipitates are imaged in the Cr EDX map with the brighter contrast and in Fe EDX map with the darker contrast. This darker contrast indicates the Fe deficiency in the carbides compared to the average matrix value.

The microstructural investigations will be continued.

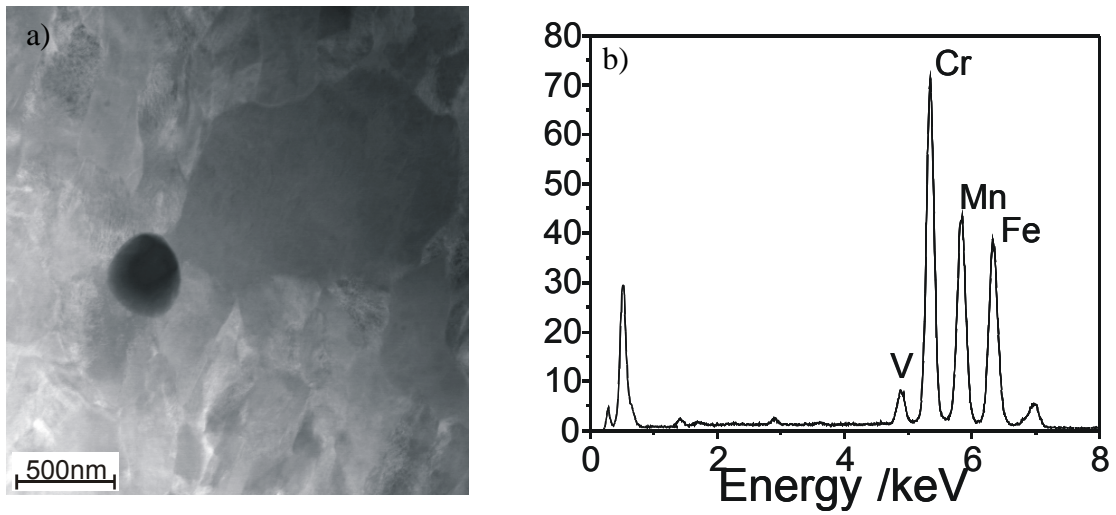


Fig. 4: HAADF images of a precipitate taken in air-hardened sample (a) and EDX spectrum of the precipitate (b).

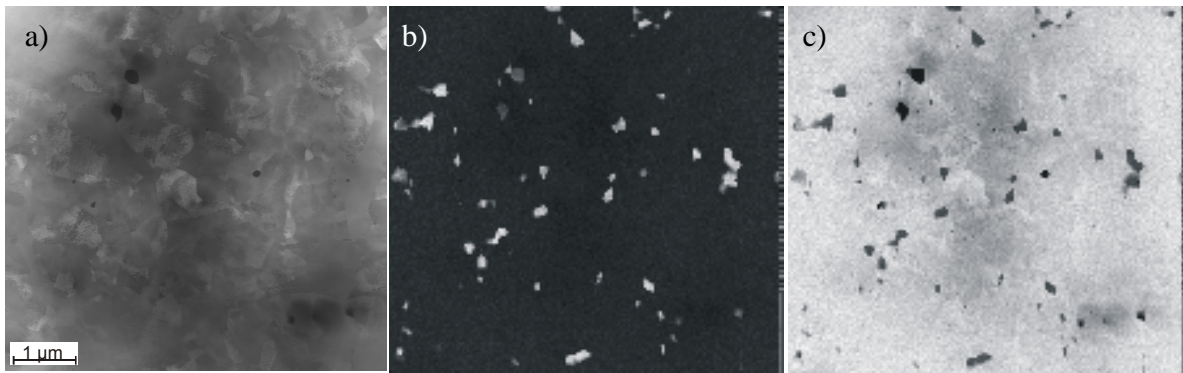


Fig. 5: HAADF images of a NT sample (1100 °C Ar/W + 750 °C/2 h V/V) (a) and Fe (b) and Cr (c) EDX maps of the area respectively.

Staff:

P. Graf  
U. Jäntsch  
M. Klimiankou  
R. Lindau  
H. Zimmermann

## TW5-TTMS-006 D 5

### Nano Composites Ferritic Steels for HT Application: Identification of Promising Candidate Alloy Compositions and Respective Fabrication Routes According to the outcome of the 2004 Study. Production of Different Laboratory Batches (14%Cr)

The operation temperature of RAFM ODS steels like ODS-Eurofer for application as structural material in advanced blanket concepts like the Dual-Coolant Concept is limited to about 650°C. More advanced blanket concepts like the Advanced HCPB (Model C) or the use as backbone material in gas cooled divertors, require allowable operational temperatures of 700 to 750 °C or even more. Reduced activation ferritic (RAF) ODS-steels could fulfil these requirements but are not commercially available at the moment and must be developed. Fe-(12-14)Cr-(2-3)W-(0.2-0.5)Ti-(0.2-0.5)Y<sub>2</sub>O<sub>3</sub> being developed in USA and Japan for fission and fusion application seem to be promising and is presently also considered to form the basis for EU efforts.

Within this task, two master alloys containing 13-14% Cr and 1.0-1.2% W and varying Ti contents will be ordered and inert gas atomised. This steel powders will be the basis for the production of different ODS steels with varying Y<sub>2</sub>O<sub>3</sub> and Ti contents by mechanical alloying in a high-energy attritor mill. Hot-Isostatic-Pressing will be applied to solidify the MA powder. Powders and hipped samples of the different alloys will be screened by appropriate methods like metallography, SEM, XRD, HRTEM, and chemical analyses. Tensile and Charpy tests on miniaturised specimens will be used for the mechanical testing of these alloys. The main goal of this task is the screening of composition, production parameters and heat treatments on microstructure and mechanical properties of RAF 13-14Cr1.1W(Ti, Y<sub>2</sub>O<sub>3</sub>) ODS steels. In a further (future) developmental step the influence of thermo-mechanical treatment and recrystallisation will be determined.

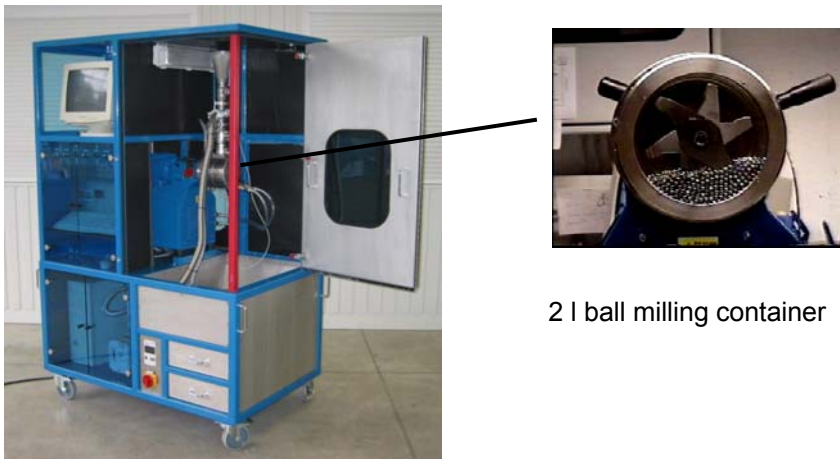


Fig. 1: PC-controlled attritor ZOZ Simoloyer CM01-2l with noise insulation box.

A ferritic master alloy containing 13.5 wt.-% Cr and 1.1wt.-% W was specified and ordered. The 15 kg ingot was melted by SaarSchmiede in a vacuum induction furnace and remelted in a vacuum arc furnace. Special emphasis was laid on low contents of radiologically undesired elements like Nb, Mo, Ni and Co to achieve reduced activation properties. The remelted ingot was inert gas atomised by Nanoval to a steel powder with an average particle diameter of about 46 microns. First mechanical alloying experiments in a high-energy horizontal attritor ZOZ Simoloyer CM01-2l (Fig. 1) under protective gas have been performed to optimise the milling procedure. Since the oxygen content is of great importance for the mechanical properties of the ODS alloy, it was monitored during the different production steps. The oxygen content increases during the gas atomisation process by about 200 ppm and is further increased during the mechanical alloying process by the same order of magnitude. The mini-

misation of oxygen uptake is one of the future goals for process improvement. The work will be continued with the consolidation of the produced powders by hot isostatic pressing and mechanical characterisation.

Staff:

C. Adelhelm  
S. Baumgärtner  
C. Eiselt  
P. Graf  
M. Klimiankou  
T. Kaiser  
R. Lindau  
A. Möslang  
U. Jäntsch  
R. Ziegler  
H. Zimmermann

Literature:

- [1] Lindau, R.; Hoelzer, D.; Kimura, A.; Ukai, S.; Current Status and Future Prospects of ODS Steel Development for Fusion. Invited oral presentation on the 12th International Conference on Fusion Reactor Materials, ICFRM 12, Dec. 4-9, 2005, Santa Barbara, CA, USA, Book of Abstracts p. 114

## TTMS-007 Modelisation of Irradiation Effect

### TW5-TTMS-007 D 5, D 7, D 10 and D 22

Design and perform well controlled ion irradiation experiments in Fe and Fe-Cr to validate modeling results performed in other deliverables, production and characterization of single Fe-Cr crystals, neutron irradiation and TEM analysis of Fe-Cr single crystals, and definition of a programme for verification and validation of the tools developed using multi-ion beam sources

#### Overview

So far, a lot of different tools for modeling irradiation effects on Fe-Cr materials were developed within this task. In the next future the focus will be laid on verification and validation of these tools by means of multi-ion beam experiments with available and future facilities. Therefore, strategies have to be developed and future needs for analyses have to be discussed for a detailed planning of this experimental programme.

Until today there is also still a lack of physical and mechanical data for Fe-Cr single crystals (SC) with a low Cr content. But it would be most desirable for the development of Fe-Cr potentials to know the real elastic constants and thermal expansion coefficients. These data could be directly used to adjust the according fits. Therefore, Fe-Cr single crystals will be produced containing 15 % chromium. Provided the crystal production succeeds, elastic constants and thermal expansion and/or thermal conductivity data could be produced on two different orientations each.

Within collaboration between FZK and SCK.CEN (Mol, Belgium) an irradiation program will be performed to verify present modeling results and to provide further input to the ongoing Fe-Cr potential development activities. FZK will produce and provide 24 Fe-Cr specimens (diameter 3 mm, thickness 0.1 mm) for post irradiation TEM investigations. After irradiation these specimens will be transported to the FZK hot cell facilities for preparation and following examinations. The transport will be planned and performed by FZK. Further, FZK will provide SCK.CEN with single crystals for their needs.

Within collaboration between FZK and Hahn-Meitner-Institute (HMI) Berlin an ion irradiation program will be performed to validate present modeling results and to provide further information about the microstructural evolution of irradiation induced defects. Direct input will be delivered to the Fe-Cr potential development groups. FZK will produce and provide pure Fe and Fe-15%Cr specimens (diameter 3 mm, thickness 0.1 mm) for irradiation. After irradiation parts of the specimens

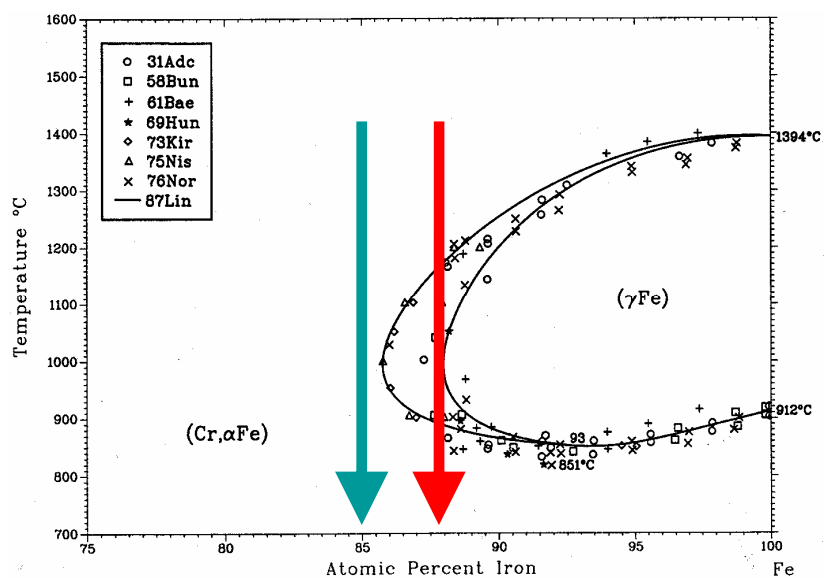


Fig. 1: Fe-Cr binary phase diagram. The difficulty with drawing single crystals from the melt is to avoid the  $\gamma$ -nose during cooling. With Cr contents of 12% (red arrow) it was not possible to get a SC. Only at higher contents (green arrow for 15% Cr) the SC production succeeded.

will be transported to the FZK for preparation and following TEM examinations. If feasible, additional atomic probe tomography investigations will be performed at HMI.

**Progress**

First the production of Fe-Cr SCs with low chromium content has been tested. But the production failed for Cr contents lower than 15 %. The difficulty with drawing single crystals from the melt is to avoid the  $\gamma$ -nose during cooling (see Fig. 1). Therefore, the current task had to be restricted to examinations of pure iron SCs and Fe-15%Cr SCs. From these SCs TEM specimens with [100], [110], and [111] oriented surfaces were fabricated. In addition, multi purpose specimens (6 mm x 4 mm x 4 mm) with [100], [110], [111], and [211] surfaces were produced. In all cases the quality of the specimens has been controlled by x-ray (see Fig. 2) and chemical analysis (see Table 1). Both, purity and degree of orientation are well within the acceptable tolerances.

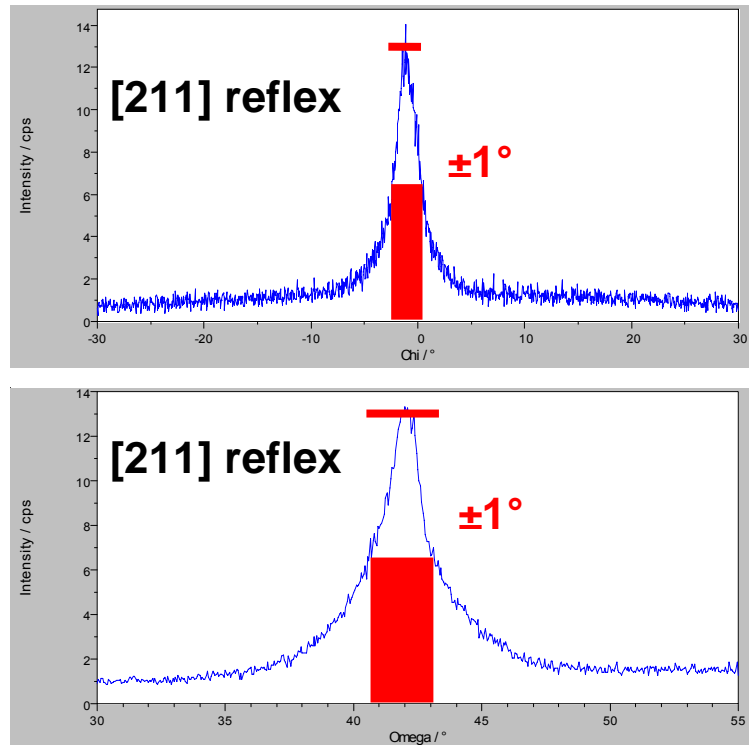


Fig. 2: X-ray measurements of the Fe and Fe-15%Cr SCs have been performed for quality control. Here is an example for the orientation of the two directions of a [211] surface. The half-width of the peaks (indicated with red bars) is a measure for the quality. Here we have deviations of approximately  $\pm 1^\circ$  in both cases which is acceptable.

Table 1: Chemical analysis of the pure Fe single crystals (values are given in ppm from an external lab). The most critical impurities are indicated by red arrows.

Ag < 0.1	Mo < 0.1
Al < 0.1	→ <b>N 10.0</b>
As < 0.1	Na 1.6
→ <b>C 12</b>	Ni < 0.1
Ca 0.8	→ <b>O 30.0</b>
Cl 0.8	P 0.7
Co 2.6	S 2.6
Cu 0.6	Si 2.9
Cr 1.6	Ti 1.4
K 1.8	V 0.1
Mg 0.87	Zn 1.9

TEM specimens have been provided to HMI for irradiation at 300 °C to damage levels of 2.5 dpa and 15 dpa. After the irradiation the specimens will be sent back for preparation in FZK prior to TEM examination. Figures 3 and 4 illustrate the usable layer and difficulties connected with the future preparation.

Another load of TEM specimens has been delivered to SCK.CEN Mol for neutron irradiation in the BR2 reactor at 300 °C for about 6 month. After that the accumulated damage will be about 0.5 dpa. Other than the ion irradiated specimens they will be activated and therefore, preparation and TEM examination has to take place in hot cell facilities.

The examinations of irradiated SC specimens may provide specific information on size and density distribution/mobility of loops/clusters, the chemical composition at the border of loops, hints on Cr-loop interaction, and morphology of He bubbles and their interaction with Cr and dislocations.

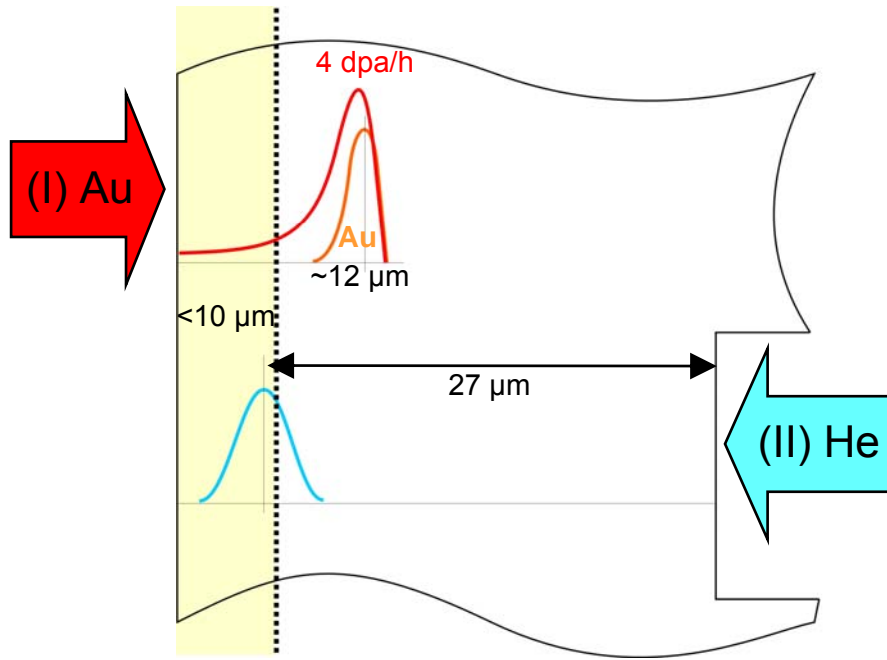


Fig. 3: In principle, irradiations at HMI could be performed in two steps. During the first stage, significant damage can be produced by a gold ion beam (peak damage rate in Fe-15%Cr is approximately 4 dpa/hour at 350 MeV). The usable layer in which gold concentration is negligible has a depth of about 10  $\mu\text{m}$  (see also Fig. 4). In a second step helium could be implanted to the desired depth. It is evident that the success of consequent TEM examinations strongly depends on rather precise specimen preparations.

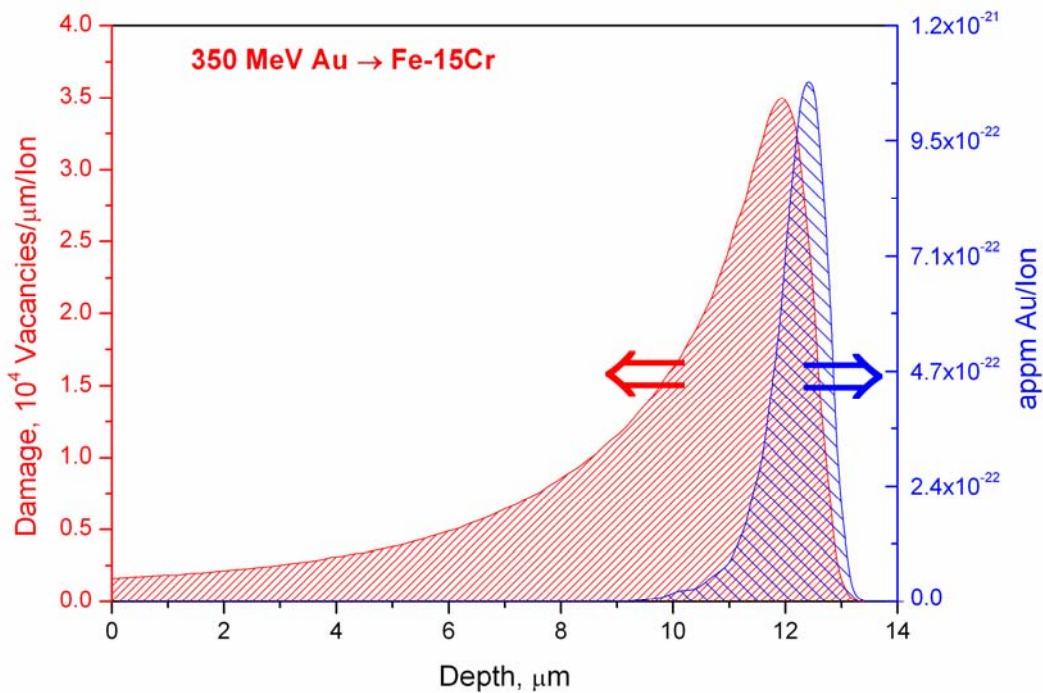


Fig. 4: Damage (red) and gold deposition (blue) during ion irradiation (350 MeV Au on Fe-15%Cr) at HMI. Maximum damage is at a depth of 12  $\mu\text{m}$ . At 10  $\mu\text{m}$  distance damage decreases to half of the peak level while concentration of gold atoms is negligible.

Finally, the preparation of a strategy paper including proposals for specific experiments and analyses for the future multi-ion beam facilities was supported by some contributions. It contains a brief critical assessment of available computational tools, a discussion about parameters, properties, and phenomena that may be observed by multi-ion beam facilities, and a proposal (strategy for 2006/2007) for verification and validation experiments.



## Conclusions and Outlook

Unfortunately, it was not possible to prepare larger Fe-Cr single crystal parts with less than 15% Cr. But at least Fe-15%Cr SCs could be fabricated with a rather good quality which can be used (together with pure Fe SCs) for irradiations and TEM examinations. The irradiation programs will be finished in the near future and therefore, PIE can take place in 2006.

The multi purpose SC specimens have been prepared for nanoindentation. With this non-destructive testing method the elastic constants will be determined. If this method fails, standard ultrasonic measurement technique has to be applied. Thereafter, thermal expansion will be measured and then destructive measurements like thermal conductivity tests might be applied. Most of this work has to be completed in 2006.

### Staff:

C. Adelhelm  
P. Graf  
A. Falkenstein  
S. Heger  
U. Jäntschi  
M. Klimiankou  
A. Möslang  
M. Rieth  
P. Vladimirov  
H. Zimmermann

## **EFDA/01-622**

### **Order of EUROFER Heats**

The European programme related to fusion reactor relevant structural materials aims to develop a low activation material, which can withstand high neutron loads under temperature and coolant conditions required in a fusion reactor based on magnetic confinement plasma. For that purpose the 8-12 Cr reduced activation ferritic/martensitic (RAFM) steel was selected as reference structural material and the present R&D aims to:

- Develop, characterise and implement a RAFM steel to be used for the fabrication of the Test Blanket Modules (TBMs) to be installed in ITER,
- Optimise such a RAFM steel for the utilisation in a Fusion reactor (DEMO and Power Plant).

Based on the substantial experience gained from various RAFM alloys developed in JA and EU and in order to reduce the long-term activation and improve the mechanical properties of such a steel prior and after irradiation, an industrial 3.5 tons batch of 9 CrWVTa RAFM steel, named EUROFER 97 was specified, ordered, and produced.

Additional EUROFER 97 material is needed for further fabrication trials, particularly to build TBM mock-ups. This new procurement has also as major objective to check the reproducibility of properties compared to batches available from the previous fabrication, to assess the achievable limits of reduction of detrimental impurities like Nb, Mo, Ni, Cu, Al, Co and others and to improve the quality of the tubing production.

Under operation the material will be exposed to temperatures up to 550 °C, cyclic loading and neutron irradiation. The limitation of the undesired elements like Nb, Mo, Ni, Cu, Al, Co and others, that produce long-lived radio-active isotopes under neutron irradiation, makes this steel a so-called reduced activation steel. Components made of such a steel can be handled and stored within a manageable period of time after reactor shut down. This steel will be used for components with high reliability requirements.

The scope of this task was to provide a normalised and tempered martensitic steel type 9 CrWVTaV designated EUROFER 97-2, under different product forms. Therefore a technical specification had been elaborated considering all the experiences with the procurement of the first heats of EUROFER 97. Since reproducibility of the good properties of EUROFER 97 was an important goal of the procurement, the technical specification leaned close to that of the first heats produced by Böhler in Austria. After evaluation of the offers, SaarSchmiede, an experienced German manufacturer of special and super clean steels and producer of the OPTIFER RAFM steels, was selected for the production of about 8 tons of different product forms (forgings, plates and tubes). The use of carefully selected raw materials was essential to achieve high cleanliness and low contents of undesired elements. Table 1 gives the required chemical analysis as specified in the technical specification, and the achieved results according to the manufacturer's analyses given in the inspection certificates.

The production of EUROFER 97-2 is finished and the material was delivered end of 2004 to the different associations. Small amounts were delivered in 2005 mainly for irradiation programs to EU associations as well as US National Laboratories. The rest is stockpiled for future use.

#### Staff:

R. Lindau  
C. Adelhelm  
T. Kaiser

Table 1

Comparison of specified and achieved chemical composition of Eurofer 97-2.

A) main alloying elements in mass%

B) radiologically undesired elements in µg/g = ppm

		Radiologically de- sired (ppm)	Eurofer 97-2 specified (mass-%)	Eurofer 97-2 achieved <sup>*)</sup> (mass-%)
A)	C		0.09 - 0.12 [ 0.11 ]	0.10 - 0.12
	Cr		8.5 - 9.5 [ 9.0 ]	8.95 - 9.11
	W		1.0 - 1.2 [ 1.1 ]	1.04 - 1.14 (1.33)
	Mn		0.20 - 0.60 [ 0.40 ]	0.50 - 0.56
	V		0.15 - 0.25	0.20 - 0.24
	Ta		0.10 - 0.14 [0.12]	0.12 - 0.14 (0.011) <sup>1)</sup>
	N <sub>2</sub>		0.015 - 0.045 [ 0.030 ]	0.022 - 0.040
	P		< 0.005	0.001 - 0.003
	S		< 0.005	0.001
	B		< 0.002	0.0007 - 0.0009
	O <sub>2</sub>		< 0.01	0.0007 - 0.0011
B)	Nb	< 0.01 ppm	[ < 50 ppm ]	1 - 50 ppm
	Mo	< 1 ppm	[ < 50 ppm ]	50 (100) ppm
	Ni	< 10 ppm	[ <100 ppm ]	100 (130) ppm
	Cu	< 10 ppm	[ < 100 ppm ]	50 ppm
	Al	< 1 ppm	[ < 100 ppm ]	90 - 130 ppm
	Ti	< 200 ppm	< 100 ppm	10 - 20 ppm
	Si	< 400 ppm	< 500 ppm	160 - 310 ppm
	Co	< 10 ppm	[ < 100 ppm ]	40 - 100 ppm
			target values [ ]	

\*) all analyses by manufacturer

Eurofer 97-2: range of 5 heats, 8 tons of 8 different product forms (forged bar, plates, tubes)

<sup>1)</sup> reasons identified

### Literature:

- [1] Fernandez, P.; Lancha, A.M.; Lapena, J.; Lindau, R.; Rieth, M.; Schirra, M.; Creep strength of reduced activation ferritic/martensitic steel Eurofer 97, Fusion Engineering and Design, 75-79 (2005) p.1003-1008
- [2] Lindau, R.; Möslang, A.; Rieth, M.; Klimiankou, M.; Materna-Morris, E.; Alamo, A.; Tavassoli, A.-A. F.; Cayron, C.; Lancha, A.-M.; Fernandez, P.; Baluc, N.; Schäublin, R.; Diegele, E.; Filacchioni, E.; G.Rensman, J.-W.; v.d. Schaaf, B.; Lucon, E.; Dietz, W.; Present Development Status of EUROFER and ODS-EUROFER for Application in Blanket Concepts, Fusion Engineering and Design, 75-79 (2005) p.989-996
- [3] Möslang, A.; Diegele, E.; Klimiankou, M.; Lässer, R.; Lindau, R.; Lucon, E.; Materna-Morris, E.; Petersen, C.; Pippan, R.; Rensman, J.W.; Rieth, M.; van der Schaaf, B.; Schneider, H.C.; Tavassoli, F. Towards reduced activation structural materials database for fusion DEMO reactors. Nuclear Fusion, 45(2005) p. 649-55 DOI:10.1088/0029-5515/45/7/013

## **EFDA/05-1244**

### **Investigation of Options to Reduce Critical Elements in Low Activation Ferritic/Martensitic Steels**

In the last few years considerable improvement has been made in the definition and fabrication of 'reduced activation' ferritic-martensitic steels (RAFM). Two batches of a 9CrWVTa-steel called EUROFER 97 and EUROFER 97-2, respectively, and including 10 heats were produced by Böhler in 1999 and by SaarSchmiede in 2003. The production has demonstrated that RAFM steels can successfully be produced at industrial scale. The steels, nominally according to the same specification, actually differ in the detailed contents of minor alloying elements and of impurities. All met the goal of an overall low content of those detrimental elements with respect to the long-term activation behaviour. Thereby, a remarkable step is achieved towards the final goal of the production of 'low activation' steels for the use in a DEMO (demonstration reactor).

Studies for further reduction of impurities need to be launched as a generic property of RAFM steels. The objectives of this task are

- To identify a number of critical elements that should be further reduced for the EUROFER 97 technical specification and to which level.
- To assess in cooperation with steel producers the technical feasibility.
- To define the specifications of a new heat (or a series of heats) to be produced.
- To determine in cooperation with the steel producers the uncertainty range in the concentrations of the various elements (alloying elements and impurities) in the heat.
- To determine the different and likely increasing costs of the heats with reduced impurity levels.
- To produce this material by industry at the smallest amount that is acceptable.
- To analyse by different laboratories (i.e. the steel producers and qualified EU/EFDA associations) and different methods, the chemical composition of the material produced up to now and from the new melts.

In order to qualify laboratories well in advance a Round Robin should be organized where a 'blind test' of a laboratory heat is going to be analysed for a list of critical elements to specified in advance.

#### **Status of work:**

An organisation chart for the work, indicating the interfaces with EFDA and with subcontractors has been drafted. A comparison of the chemical composition as specified in the technical specification for EUROFER 97-1 and EUROFER 97-2 and the results achieved in the industrial production of the different products has been performed and the reasons for occurring deviations from the specifications have been analysed. Table 1 gives a summary of these evaluations. Currently, calculations are being performed to assess the impact of these deviations on the activation behaviour.

#### Staff:

R. Lindau  
C. Adelhelm  
T. Kaiser

Table 1

Comparison of specified and achieved chemical composition of EUROFER 97 and 97-2

A) main alloying elements in mass-%

B) radiologically undesired elements in  $\mu\text{g/g} = \text{ppm}$

	Radiologically desired (ppm)	EUROFER 97 / (97-2) <sup>1)</sup> specified (mass-%)	EUROFER 97 achieved <sup>*)</sup> (mass-%)	Eurofer 97-2 achieved <sup>*)</sup> (mass-%)	
A)	C	0.09 - 0.12 [ 0.11 ]	0.10 - 0.12	0.10 - 0.12	
	Cr	8.5 - 9.5 [ 9.0 ]	8.82 - 8.96	8.95 - 9.11	
	W	1.0 - 1.2 [ 1.1 ]	1.07 - 1.15	1.04 - 1.14 (1.33)	
	Mn	0.20 - 0.60 [ 0.40 ]	0.38 - 0.49	0.50 - 0.56	
	V	0.15 - 0.25	0.18 - 0.20	0.20 - 0.24	
	Ta	0.10 - 0.14 [ 0.12 ]	0.13 - 0.15	0.12 - 0.14	
	N <sub>2</sub>	0.015 - 0.045 [ 0.030 ]	0.018 - 0.034	(0.011) <sup>2)</sup> 0.022 - 0.040	
	P	< 0.005	0.004 - 0.005	0.001 - 0.003	
	S	< 0.005	0.003 - 0.004	0.001	
	B	< 0.001 (0.002) <sup>1)</sup>	0.0005 - 0.0009	0.0007 - 0.0009	
	O <sub>2</sub>	< 0.01	0.0009 - 0.0018	0.0007 - 0.0011	
B)	Nb	< 0.01 ppm	[ < 10 ppm ] (50 ppm) <sup>1)</sup>	2 - 7 (25) <sup>2)</sup> ppm	1 - 50 ppm
	Mo	< 1 ppm	[ < 50 ppm ]	10 - 34 ppm	50 (100) ppm
	Ni	< 10 ppm	[ < 50 ppm ] (100 ppm) <sup>1)</sup>	75 - (280) <sup>2)</sup> ppm	100 (130) ppm
	Cu	< 10 ppm	[ < 50 ppm ] (100 ppm) <sup>1)</sup>	15 - (210) <sup>2)</sup> ppm	50 ppm
	Al	< 1 ppm	[ < 100 ppm ]	50 - 90 ppm	90 - 130 ppm
	Ti	< 200 ppm	< 100 ppm	30 - 90 ppm	10 - 20 ppm
	Si	< 400 ppm	< 500 ppm	400 - 600 ppm	160 - 310 ppm
	Co	< 10 ppm	[ < 50 ppm ] (100 ppm) <sup>1)</sup>	30 - 70 ppm	40 - 100 ppm
target values [ ]					

<sup>\*)</sup> analyses by manufacturers and Ch. Adelhelm FZK

EUROFER 97: range over 4 heats, 3.5 tons of 9 different product forms (forged bar, plates, tubes, wire)

Eurofer 97-2: range over 5 heats, 8 tons of 8 different product forms (forged bar, plates, tubes)

<sup>1)</sup> higher values for EUROFER 97-2

<sup>2)</sup> reasons identified

### Literature:

- [1] Lindau, R.; Möslang, A.; Rieth, M.; Klimiankou, M.; Materna-Morris, E.; Alamo, A.; Tavassoli, A.; Cayron, C.; Lancha, A.-M.; Fernandez, P.; Baluc, N.; Schäublin, R.; Diegele, E.; Filacchioni, E.; G.Rensman, J.-W.; v.d. Schaaf, B.; Lucon, E.; Dietz, W.; Present Development Status of EUROFER and ODS-EUROFER for Application in Blanket Concepts, Fusion Engineering and Design, 75-79 (2005) p.989-996
- [2] Möslang, A.; Diegele, E.; Klimiankou, M.; Lässer, R.; Lindau, R.; Lucon, E.; Materna-Morris, E.; Petersen, C.; Pippan, R.; Rensman, J.W.; Rieth, M.; van der Schaaf, B.; Schneider, H.C.; Tavassoli, F. Towards reduced activation structural materials database for fusion DEMO reactors. Nuclear Fusion, 45(2005) p. 649-55 DOI:10.1088/0029-5515/45/7/013



# **Materials Development Advanced Materials**





## TTMA-002 Divertor and Plasma Facing Materials

### TW3-TTMA-002 D 3 Mechanical Testing of Improved W Alloys: Tensile and Fracture Toughness Testing

#### Objectives

A structural component like the divertor is subjected during service to very high heat loads and also to alternating thermal and mechanical stresses as a consequence of the pulsed reactor operation. For helium cooled ITER divertor concepts tungsten alloys are considered as structural material. The aim of the task is to perform tensile and fracture toughness tests at high temperatures on pure tungsten and tungsten alloys.

#### Status end of 2004

The delivery of the high temperature specimen gripping and strain measurement system was end of September 2004. Since the one existing high temperature high vacuum furnace, necessary for testing, was occupied by diffusion welding activities of EUROFER 97 the beginning of the experiments was delayed until January 2005.

#### Reference tensile testing

For the installation of the high temperature pull rods, an adjustment step is necessary by loading a special designed installation specimen at room temperature up to 8 kN. During this step a half shell of the gripping system made of W La<sub>2</sub>O<sub>3</sub> broke down and had to be replaced by a self-manufactured part out of quickly available TZM. Therefore, maximum temperatures had to be limited to 1250 °C until November 2005. Another problem was the temperature calibration. Due to the fact that the Pt-RhPt-TC could not be spot



Fig. 1: High temperature pull rods for tensile- and LCF-testing with Pt-PtRh-TC application by intermediate tantalum foils welded on holder rings.

welded directly onto the specimen and holder rings, tantalum foils were welded on one side of the specimen and the gripping rings whereupon the Pt-RhPt-TC was welded.

After having performed these installation and calibration procedures, tensile tests on both reference materials, which was pure tungsten and W La<sub>2</sub>O<sub>3</sub> were performed in the high temperature range between 700 °C and 1200 °C. The strain rate was selected to  $3 \times 10^{-3} \text{ s}^{-1}$  for all tensile tests. Pure tungsten has shown until 1100 °C the typical behaviour of very low uniform elongation and temperature dependence of high ultimate tensile stress followed by a longer temperature dependent strain softening period generating total strains above 20%.

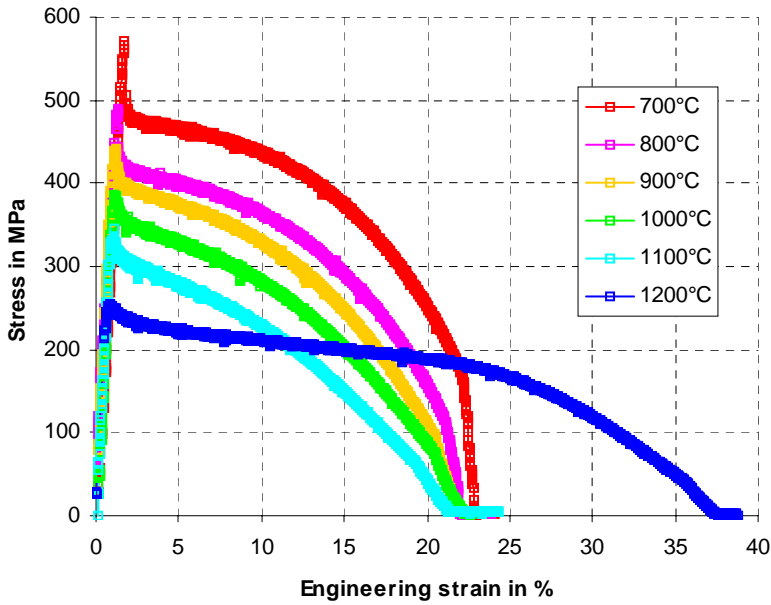


Fig. 2: High temperature tensile-testing of pure tungsten.

But at 1200 °C the softening period was extended to a very high total strain of around 37%. This dramatic change in tensile behaviour leads to the conclusion of a considerable dynamic recrystallization of pure tungsten in this temperature range.

W La<sub>2</sub>O<sub>3</sub> has also shown until 1200 °C the typical behaviour of very low uniform elongation and temperature dependence of high ultimate tensile stress, but followed by a slower temperature dependent strain softening period generating total strains of 14 to 18%. Dynamic recrystallization did not occur in this temperature range.

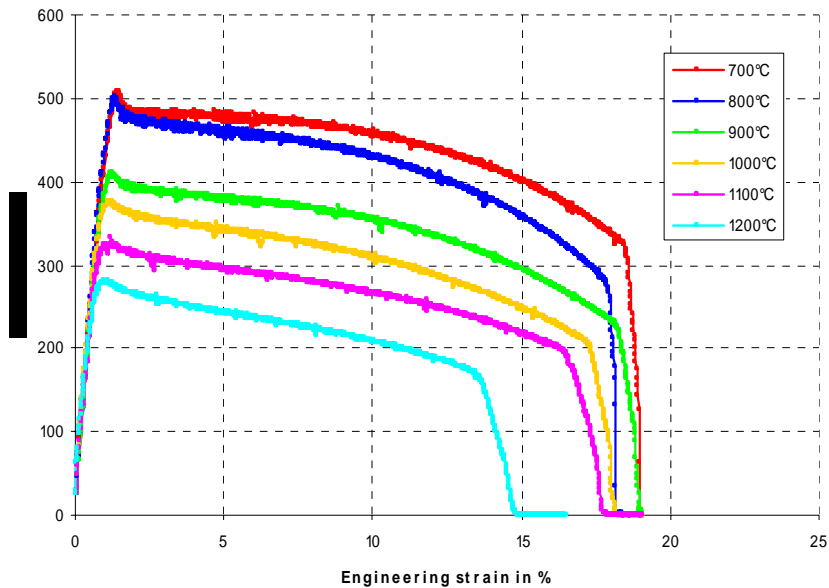


Fig. 3: High temperature tensile-testing of W La<sub>2</sub>O<sub>3</sub>

The new high temperature high vacuum furnace, necessary for tensile- and fracture toughness-testing, independent of the diffusion welding activities of EUROFER 97, has been set into operation in October 2005 and tests will start in 2006.

Staff:

- U. Bürkle
- M. Klotz
- C. Petersen

## TW3-TTMA-002 D 7

# Screening of Promising Tungsten Candidate Alloys by Creep Testing and Microstructural Characterization

### Overview and Objectives

Since the recrystallization temperature of W and its alloys decreases significantly with aging time, even dispersion strengthened W alloys can re-crystallize during DEMO relevant exposure times in the temperature range where the structural material of advanced divertors must operate. Tungsten and selected W-alloys are considered to be the primary candidates for armour and structural materials of ITER and of even more ambitious DEMO divertor designs. For the later, present design outlines are based on a structural material with temperatures up to about 1300 °C. A critical issue is the recrystallization of W-alloys and its interaction with aging time and elastic-plastic deformation during mechanical loading.

Therefore, the goal of this task is to perform instrumented creep rupture tests on selected reference refractory alloys – pure W and W-La<sub>2</sub>O<sub>3</sub> (WL10) – in high vacuum up to about 5000 h at 1100 °C and 1300 °C, in order to provide the designers with data on relevant creep and creep rupture properties.

### Initial Situation

In the previous year a special creep testing facility has been developed and implemented successfully for the present task. It allows for performing fully instrumented creep and creep rupture tests at typical temperatures of the divertor structural material. From Plansee pure tungsten and W-La<sub>2</sub>O<sub>3</sub> rods (D8 mm x 1000 mm) were purchased. From these, standard size creep specimens (M8 x 56 mm) have been fabricated and 6 specimens were already tested at 1100 °C and 1300 °C.

In addition, microstructural investigations on the materials have shown that the grain size is inhomogeneous and varies between 2 and 6 µm. Further, the grains are oriented along the rod axis which results from forging during rod production. As a consequence, the formerly spherically shaped La<sub>2</sub>O<sub>3</sub> particles have been deformed to needles – also aligned parallel to rod direction – with diameters of about 0.5-1 µm and lengths between 10 and 20 µm.

From creep tests it could be seen that tungsten in not recrystallized condition shows a very high plasticity at 1100 °C which leads to necking of more than 90%. Under the same conditions WL10 shows less ductility (necking of only 20%) but has increased creep strength by about 10-20%. At 1300 °C, creep strength of pure tungsten drops significantly, recrystallization starts immediately, pores develop at grain triple points, and then cracks propagate along grain boundaries which finally lead to inter-granular fractures.

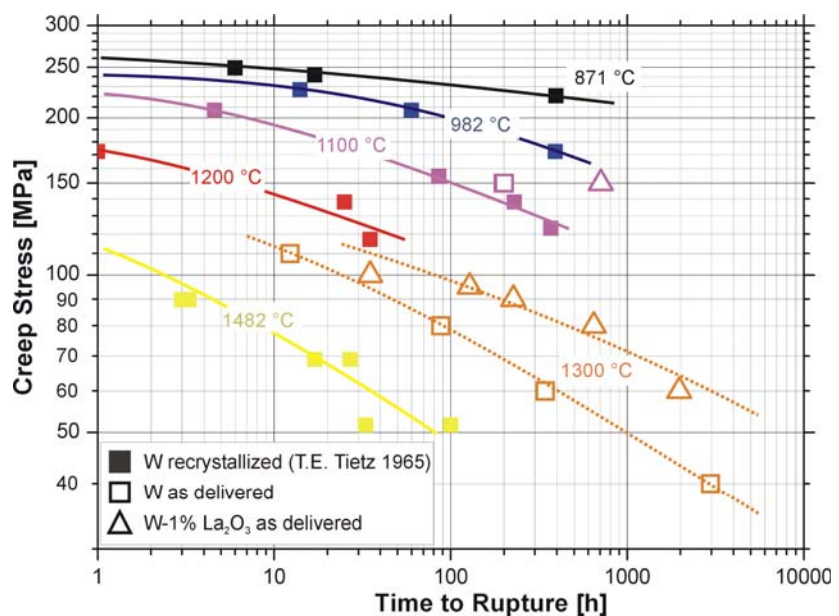


Fig. 1: Own creep rupture test results (open symbols) compared to those available from literature (filled quadratic symbols).

## Progress

The following investigations were aimed to determine reliable design limits. Therefore, both materials have been tested at 1300 °C. The results are shown in Fig. 1 together with experiments on recrystallized tungsten known from literature. As can be seen, a direct extrapolation up to 5000 h of times-to-rupture should be possible without much deviation for pure tungsten while a direct extrapolation for WL10 leads to some uncertainties due to scattering (the load fluctuated during the tests at 100 MPa and 60 MPa and therefore the rupture times are probably too small).

Figure 2 shows the Larson-Miller plot of all creep test results. From this plot extrapolations are possible in a more accurate way. However, obviously the test results from literature (grey triangles) lead to a significant overestimation of the lifetime which is mainly due to their short testing period. Present divertor designs are based on a structure material with creep strength of more than 55 MPa for a time-to-rupture of 20000 hours at 1200 °C. According to our tests, pure tungsten shows only about 45 MPa under such conditions, but WL10 exceeds this design criterion with a creep strength of more than 60 MPa.

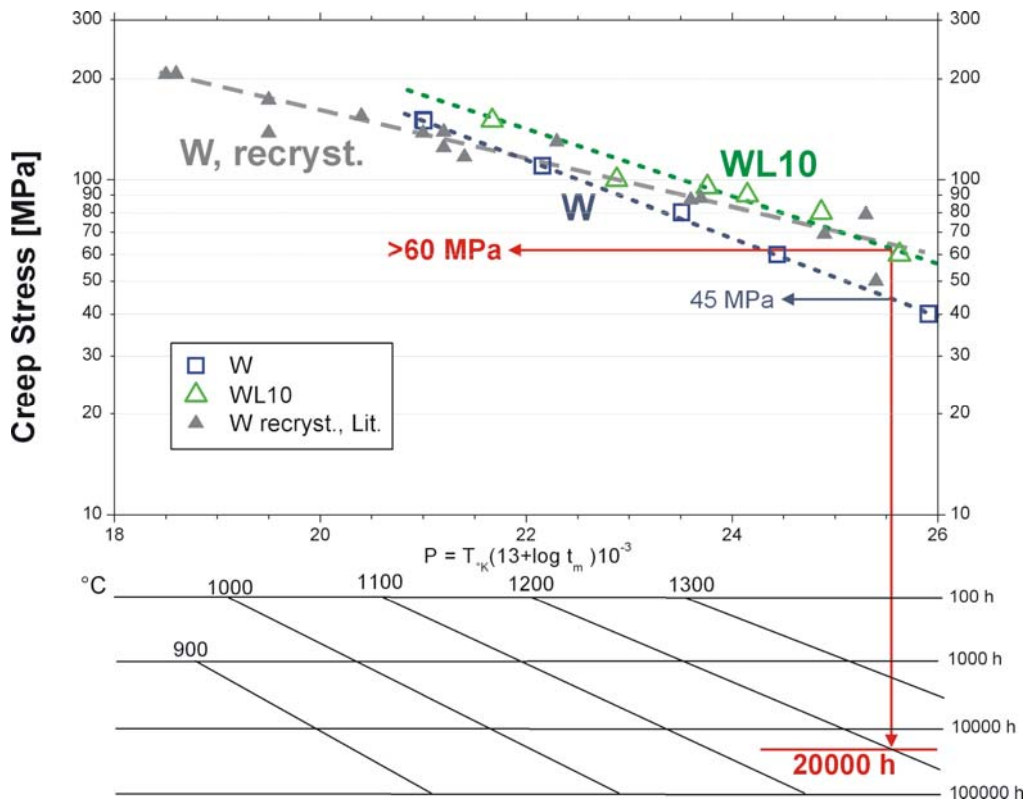


Fig. 2: Larson-Miller diagram of the creep test results from Fig. 1. It can be seen quite clearly that the short time creep test results from literature (grey triangles) lead to a significant overestimation of the lifetime. In present divertor designs, the structure material should show creep strength of more than 55 MPa for a time to rupture of 20,000 hours at 1200 °C. According to our tests, pure tungsten shows only about 45 MPa, but WL10 exceeds this design criterion with a creep strength of more than 60 MPa.

Microstructural examinations of the undeformed specimen threads enable a determination of recrystallization behaviour (see Fig. 3). In pure tungsten recrystallization takes place rather soon at 1300 °C and after 3000 hours the grain size varies around 50 µm (see Fig. 3c). With WL10 specimens, however, recrystallization could not be observed even after aging at 1300 °C for 2000 hours (see Fig. 3a and b).

Since WL10 showed acceptable results with respect to creep and recrystallization design criteria we had a closer look on another criterion which is ductile-to-brittle transition temperature (DBTT). According to the divertor design, the structural material should have maximum DBTT values of about 300 °C in the unirradiated condition. So sub-size charpy specimens

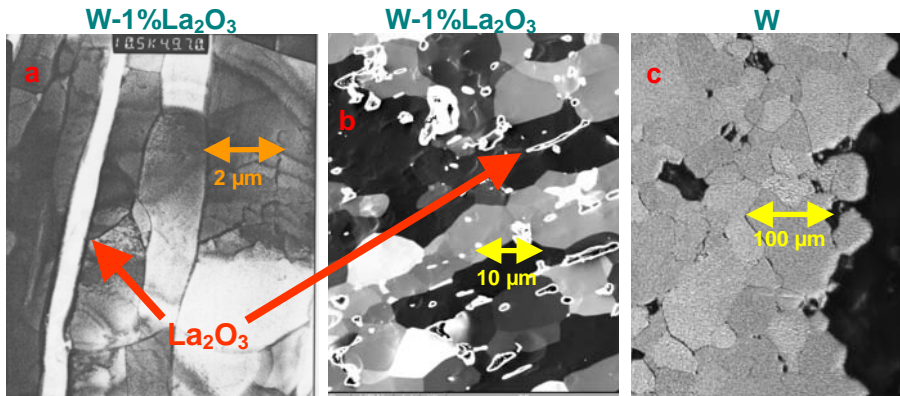


Fig. 3: Microstructure of WL10 as delivered (a) and after 2000 h at 1300 °C (b) by TEM examination. Both images show about the same grain size. That is, recrystallization does not take place. For comparison, pure W shows severe recrystallization after aging at 1300 °C for 3000 hours (c).

(3 mm x 4 mm x 27 mm) have been fabricated from the W and WL10 rods with L-R orientation (notch root perpendicular to the rod axis) and tested up to about 1050 °C using gas burners. The results are plotted in Fig. 4. DBTT measured at 1/2 upper shelf energy (USE) is about 800 °C for W and 950 °C for

WL10. This is far more than specified by the design criterion.

Another problem of refractory alloys is the strong dependency of mechanical properties from the forging direction during the material production. In the case of TZM DBTT varies about between 400 and 600 °C for specimens in L-R orientation. But in R-C orientation (notch root parallel to rod axis) DBTT increases to more than 900 °C which has been examined by further charpy tests (see Fig. 4).

It is clear that the most critical divertor design criterion is that for low DBTT values. To verify a proposal for a more ductile refractory material additional tests have been performed with DENSIMET D180. This alloy is produced by sintering tungsten with 3.5 wt.% nickel and 1.5 wt.% iron. The resulting microstructure is given in Fig. 5 which demonstrates that the W particles are just embedded in the Ni-Fe matrix. The according charpy test results (see Fig. 4) show only a slightly improved DBTT but a rather low USE, that is, impact toughness is far too low.

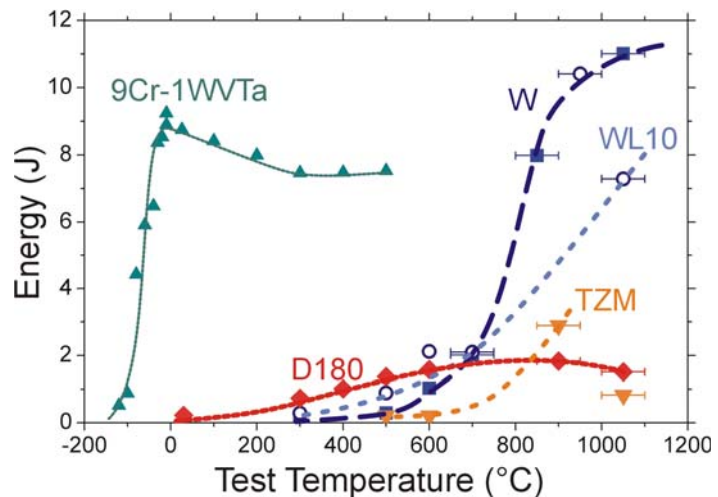


Fig. 4: Brittle-to-ductile transition of tungsten and WL10. Determination of DBTT at 0.5 USE leads to 800±50 °C for tungsten while a conservative estimate for WL10 leads to DBTT of 950±50 °C. The DENSIMET D180 alloy (microstructure is given in Fig. 5) shows only a slightly improved DBTT value. But the toughness (given by the upper shelf energy) is far too low. The anisotropic behaviour of refractory alloys is demonstrated by Charpy test results with TZM specimens which were fabricated perpendicular to the rod axis, that is, notches are parallel to the forging direction. In this case DBTT is higher than 900 °C while with notches perpendicular to forging direction TZM usually shows DBTT values between 400 and 600 °C. For comparison, the transition of a 9Cr-1WVTa steel is also illustrated which clearly demonstrates the extraordinary brittleness of the different refractory materials.

## Conclusions

Oxide dispersion strengthening tungsten with La<sub>2</sub>O<sub>3</sub> increases the possible operation temperature by approximately 70-90 °C with the material at hand for a given life-time and load. For a given temperature WL10 compared to pure tungsten may be stressed more by at least 15 MPa to reach the same life-time. That is, WL10 meets the current divertor creep design criterion for time-to-rupture at 1200 °C.

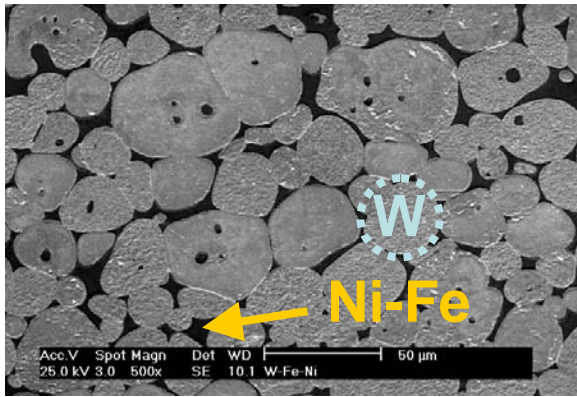


Fig. 5: Microstructure of DENSIMET D180 (W-3.5wt.%Ni-1.5wt.%Fe). Tungsten particles are simply embedded in a more ductile Ni-Fe matrix.

During all creep tests – even at 1300°C up to 2000 hours – recrystallization of WL10 has not been observed. This demonstrates a further well-known benefit of the oxide particles which suppress recrystallization significantly. At 1300 °C recrystallization does not influence the creep behaviour recognizable but it is accompanied by severe embrittlement which would raise DBTT additionally.

The charpy tests have shown that WL10 seems to be even more brittle than pure tungsten and therefore, it seems to be rather unlikely to meet the divertor DBTT design criterion with current commercially available tungsten alloys. So additional tasks have been initiated to try to develop ductile refractory materials which might be applicable for divertor applications.

The ongoing investigations within this task will be restricted to the completion of the creep behaviour of W and WL10 with times-to-rupture in the range of 1000-5000 hours which allow for more precise extrapolations as well as for creep-stress vs. time-to-1% strain plots.

#### Staff:

B. Dafferner  
P. Graf  
A. Falkenstein  
S. Heger  
U. Jäntsch  
M. Klimiankou  
A. Möslang  
M. Rieth  
R. Ziegler  
H. Zimmermann

#### Literature:

- [1] Rieth, M.; High-temperature creep of pure and dispersion-strengthened tungsten. Jahrestagung Kerntechnik 2005, Nürnberg, 10.-12.Mai 2005, INFORUM GmbH, S.455-58, CD-ROM.
- [2] Rieth, M.; Dafferner, B.; Limitations of W and W 1%La<sub>2</sub>O<sub>3</sub> for use as structural materials. Journal of Nuclear Materials, 342 (2005).
- [3] Rieth, M.; Creep and Recrystallization of Pure and Dispersion Strengthened Tungsten; EUROMAT, Prague, 5-9 September 2005.
- [4] Rieth, M.; Evaluation of the mechanical properties of W and W-1%La<sub>2</sub>O<sub>3</sub> in view of divertor applications; ICFRM-12, Santa Barbara, 4-9 December 2005.

## **TW4-TTMA-002 D 2**

## **TW5-TTMA-002 D 2**

### **Developing of Improved W-Alloys for Application in a Power Plant with He Cooled Divertor**

#### **Objectives:**

Within the framework of Fusion Power Plant Design Studies, intense R&D work has been made in the recent past on the development of materials issues for a helium-cooled divertor. The success of this design is strongly correlated to the availability of special tungsten alloys, their effective and economic shaping due to extremely high heat transfer loads, the development of assembling technologies to overcome mismatches in expansion coefficients and the joining of W-components with special functions to avoid embrittlement by brazing alloys and zones. Additional features are low impact of fast neutrons on mechanical properties, low-activation and application in the service temperature range of RT to 1500°C. However, commercially available qualities cannot fulfill these requirements. All these facts lead to challenging work packages in the fields of microstructural processing, joining technologies and development of new improved tungsten alloys with resistance to environment conditions in fusion power plants. Under the task TW4-TTMA 002 and TW5-TTMA 003 the development of tungsten alloys with improved properties will be executed. Based on our experience on the behaviour of refractory alloys and their processing we selected for performing this work programme the method of mechanical alloying to synthesize improved ODS-W precursors with nano-scale features. During the subsequent adopted compaction steps (e.g. HIP) the powders will be consolidated to compacts with interlinked grains and controlled morphology. The properties of the improved W-alloys will be compared to standard, commercially available WL10 grade.

#### **Actual status:**

Determination of tungsten alloy properties (tensile properties, microstructure) were continued applying raw materials (rods) fabricated by the state of the art. The tested alloys, pure W and WL10 (W-1%La<sub>2</sub>O<sub>3</sub>), exhibit due to the processing large longitudinally elongated grains partially with a rather big diameter of approx. 20 µm for W grains and the ODS particles are not homogeneously dispersed in the WL10 quality. The detected microstructure implies that the grain structure and the ODS distribution is not optimized to a structural material and affects properties. Thus finer grains and a more homogeneous ODS distribution should improve mechanical and physical properties.

For synthesising improved W powders with a homogeneous distribution of ODS particles an attritor ball milling system was build up and successfully tested with EUROFER steel powder. During processing of W powders the grain size was milled down as expected. However, strong abrasion effects inside the milling vessel appeared. They lead to an overheating and destroyed the feedthrough of the milling rotor. Evaluation of the tests indicated that vessel filling ratio and ball to powder ratios have to be reduced to keep these effects in tolerable limits in future milling tests. Meanwhile a redesign was performed of the critical components which are under manufacturing by the subcontractor. Due to this system defect and the unexpected behaviour of W powder compared to EUROFER the tasks TW4 and TW5-TTMA-002 are delayed and the originally set up time schedule has to be adapted. The mechanical alloying tasks applying the attritor mill will be continued in 2006 with powder processing, powder characterization and thermal treatment of the homogenized powders as planned earlier.

### **Cooperation:**

With Plansee AG, Reutte, Austria a cooperation agreement for a joint development of improved W-alloys is under settlement. Plansee corporation will deliver first improved W alloys by industrial standards in 2006 for testing mechanical and physical properties.

### **Staff:**

W. Krauss

J. Konys

A. Möslang

M. Rieth

R. Lindau

S. Baumgärtner

### **Literature:**

- [1] M. Rieth, B. Dafferner, Limitations of W and W-1%La<sub>2</sub>O<sub>3</sub> for use as structural materials, J. Nucl. Mat. 342 (2005) 20-25
- [2] W. Krauss, N. Holstein, J. Konys, Development and fabrication aspects regarding tungsten components for a He-cooled divertor, Fus. Eng. Design 75-79 (2005) 775-778



## TW5-TTMA-002 D 6 Mechanical Testing of Irradiated W Tungsten Samples

High temperature alloys (such as tungsten) are assumed to be primary materials candidates for divertor structural application. However, these materials suffer from embrittlement at “low temperature” after irradiation. The DBTT strongly depends on the irradiation dose and could also depend strongly on the material processing. Tungsten is also considered as plasma facing material, i.e. as a first wall coating for Demo-related blankets and as armour material for gas-cooled divertors. Appropriate techniques for mechanical characterisation are to be investigated.

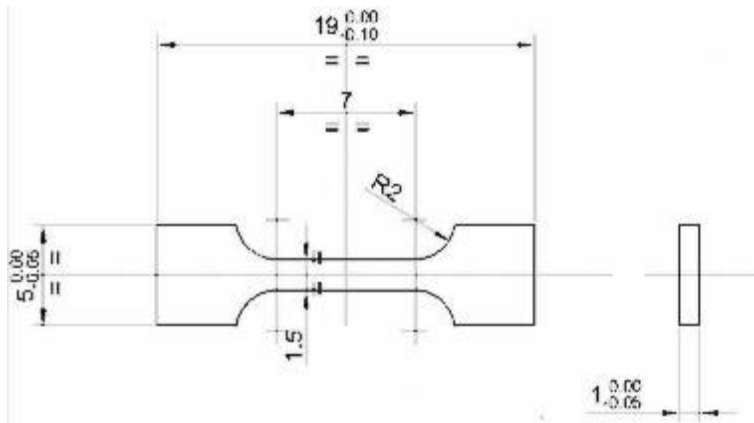


Fig. 1: Tensile specimen (T 19-type), drawing by CEA.

Specimens of WL10 (Tungsten and 1% of  $\text{La}_2\text{O}_3$ ) are included in an irradiation experiment in the OSIRIS reactor. KLST-type bend bar specimens and mini tensile specimens (flat bar, T19-type) are to be irradiated at temperatures of 600 and 1000 °C up to 5 dpa - equivalent in steel - in 2005 (TW5-TTMA-002 Del. 3). Specimens are 3 x 4 x 27 mm<sup>3</sup> Charpy-specimens [KLST] and 5 x 1 x 19 mm<sup>3</sup> flat bar mini tensile specimens [T19] with a centre area of 1.5 mm (number to be defined), cf. Fig. 1.

Tensile and KLST-specimens are foreseen for PIE in Karlsruhe after end of irradiation. 56 KLST- and a to be defined number of tensile specimens will be transported to the Karlsruhe Fusion Materials Laboratory. They will be tested at different elevated temperatures to define the ductile-to-brittle-transition and the irradiation's effect on it. Fractographic analysis of the tested specimens will be done by light microscopy and by SEM. If available, unirradiated reference tests will be performed during the irradiation in addition. The PIE will be finished 12 months after availability of specimens.

The Charpy specimens will be tested with an instrumented pendulum to define the transition region, the transition temperature, the upper- and lower shelf energy for every irradiation parameter. For every specimen, force-versus-deflection-curve is recorded, impact energy and dynamic yield stress are derived. The pendulum's energy and impact speed can be varied if necessary. As WL10's properties depend strongly on the material deformation ratio, additional quasi-static tests in a new testing device on the KLST-specimens are offered.

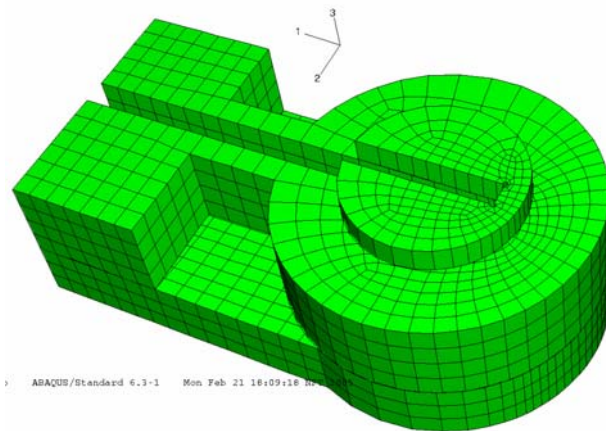


Fig. 2: Mounting device for specimen (lower part).

Tensile tests will be performed accompanying to the impact tests as well as at irradiation temperature to give a full dataset of tensile results. A universal testing machine with vacuum-furnace (1200 °C) for force- and strain-

controlled tensile tests is used. For the T19-type tensile specimens, modifications of the assembling and mounting devices are done.

A special mounting device adapted for the thin foil specimens ( $5 \times 1 \times 19 \text{ mm}^3$ ) has been developed (Fig. 2). It serves for clamping of the specimen and for centring of the package in the testing machine's standard fixations.

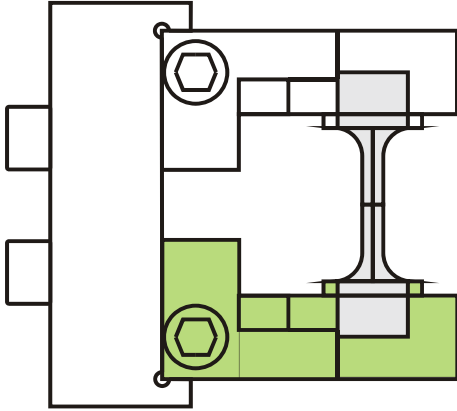


Fig. 3: Mounting device for specimen (assembled, simplified representation).

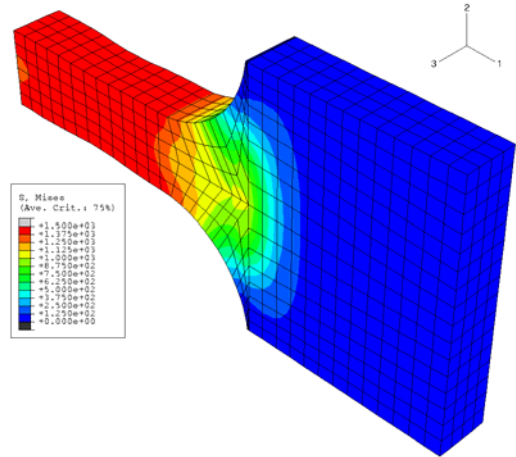


Fig. 4: Stress distribution in clamped specimen (von Mises stress).

The device serves as well for the transport of the fragile specimens by fixing an additional bracket as shown in Fig. 3 on the left side. The design of the mounting device, based on Finite-Element-calculations, ensures the maximum stresses taking place in the reduced area of the specimen and not in or near the clamping jaw. Von Mises stress distributions for simulated clamping and tensile test are shown in Fig. 4.

Staff:

H.-C. Schneider

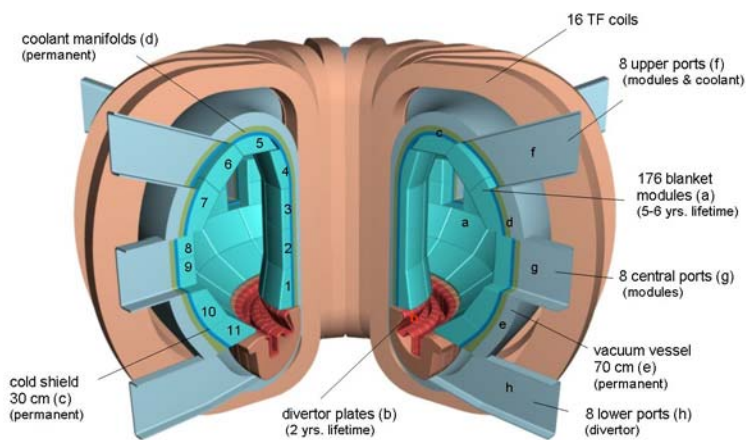
## TW5-TTMA-002 D 7

### Investigate Joint Techniques Appropriate for W to EUROFER ODS for Divertor Application (Cyclic Operation between RT and 650 °C)

The objective is a mechanical characterization and lifetime evaluation of brazing as a possible joining technique for W-1%La<sub>2</sub>O<sub>3</sub> to EUROFER in view of divertor application. Brazed joints of dissimilar materials suffer from a mismatch in coefficients of thermal expansion. The components of the joint are exposed to mechanical and cyclic thermal loads which give rise to development of high stresses and could lead to failure. Mechanical characterization experiments are performed in order to collect sufficient knowledge about the failure behavior of the joints particularly under thermal fatigue conditions. The experiments are accompanied by finite element computations which can provide additional information for the reasons of failure.

#### Introduction

In the course of the European power plant conceptual study, a concept for a He-cooled divertor for DEMO (Fig. 1) has been investigated [1, 2]. The great heat flux from the plasma causes thermal loads of about 10-15 MW/m<sup>2</sup> in the divertor which corresponds to about 15% of the total thermal power of the reactor. The high heat flux on the divertor target plates requires the use of refractory alloys, e.g. tungsten based alloys, for the plasma facing components. This is a protective shield for the structural parts behind, which are made of the high temperature resistant and low-activating ferritic-martensitic steel EUROFER 97. The shielding components should connect to the structural body leak-free in order to separate the cooling system behind the plates from possible penetration of plasma impurities and particle wastes.



Tungsten and EUROFER steel have different Young's moduli and thermal expansion coefficients. This gives rise to development of high stresses and stress gradients in the transition joint under mechanical and thermal loadings. In addition, cyclic changes of the mechanical and thermal loads, e.g. caused by shutting down the reactor, can result in fatigue and creep of the materials.

Fig. 1: Fusion tokamak reactor with dual-coolant blanket and He-cooled divertor.

#### Finite element simulation of a model

The brazed joint in the divertor transition zone has complicated geometry, which can be investigated with a discrete finite element model shown on Fig. 2. The axial symmetry with respect to the y-direction allows reduction to a 2D model.

The analysis considers plastic deformation as a result of thermal and mechanical loading. The calculated stress distribution, occurring in the joint due to the combined loading situation, identifies the locations with highest loads. This allows to assess the reliability of the joint and to support further design optimization. Previously, it was shown that pure mechanical loading does not lead to plastic deformation [2]. An extension of the FE calculations has been made by simulating the brazing process with heating to the brazing temperature of 1120 °C, cooling to room temperature, followed by heating to work temperature of 700 °C. The detailed elastic-plastic finite element analyses have been used to investigate the stress distribution for the described geometry and to determine the role of the mismatch of the materials due to their different thermal expansion coefficients. For all three materials, the tungsten alloy, EUROFER 97, and the braze, elastic-plastic behavior without hardening using temperature dependent material properties, including thermal expansion coefficient, elastic moduli and yield strength are assumed. As an initial stress free condition, a uniform nodal brazing temperature field of 1120 °C was applied. Figs. 3 and 4 show the von Mises-stress and the plastic strain, respectively, along the AB path indicated in Fig. 2. For both plots, each single curve represents a certain joint temperature.

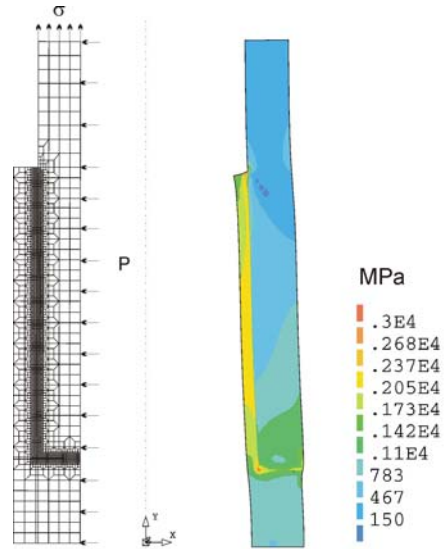


Fig. 2: FE model and von Mises stress distribution in the divertor transition zone.

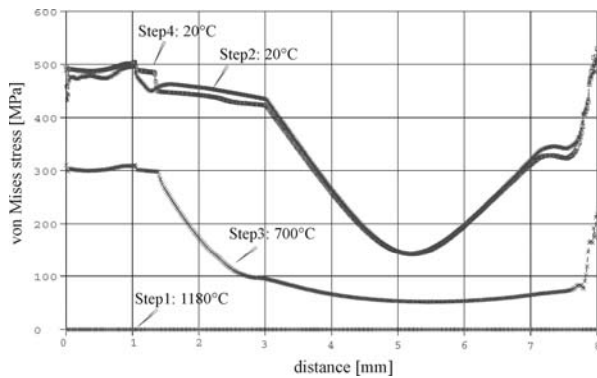


Fig. 3: Von Mises stress curves along the path AB on Fig. 2.

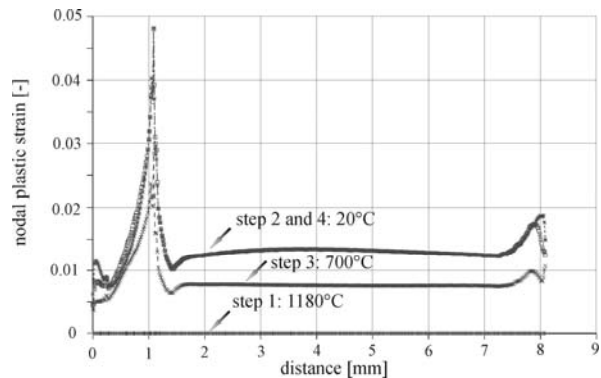


Fig. 4: Plastic strain distribution along the selected path AB in Fig. 2. The curves represent temperatures between RT and 700 °C.

The highest stresses are concentrated mainly in the braze region. However, at high temperatures the braze material can be deformed and, as a result, large plastic deformation in the braze material occurs. This indicates that in particular under cyclic loading conditions the brazed joints may be subject to fatigue and ratcheting. Therefore, the finite element analysis will be extended by simulating the material behavior under cyclic thermal loading with a number of cycles in the temperature range of interest in order to understand the role of ratcheting.

### Brazing process and microstructural analysis of the joints

Different processes of brazing [3] are introduced to join specimens of W-1%La<sub>2</sub>O<sub>3</sub> and EUROFER steel to determine the optimal brazing parameters for those materials. Brazing was performed in vacuum and under pressure in order to avoid oxidation of the tungsten alloy, and to center the specimen and filler metal, respectively. A similar temperature profile of the brazing process is applied for brazing with an amorphous Ni-based brazing foil STEMET 1309 and a commercial brazing paste BrazeTec 1135 (Fig. 5) of the firm BrazeTec. Brazing temperature is set to 1180 °C in the case of the paste and 1150 °C in the case of the foils. At

400 °C, the temperature is set constant for about 600 s to allow the filler material to degas without harming the braze strength. After the brazing, a heat-treatment at 900 °C is needed to reduce the initial stresses in the joint.

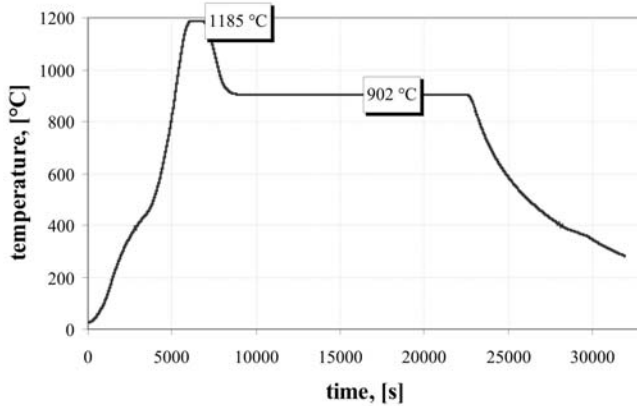


Fig. 5: Typical temperature profile of the high temperature brazing process, as measured for the brazing paste.

analysis. Comparisons of specimens with different brazing history show, that the diffusion process is very important for the strength of the joint. Large and gradual diffusion zones provide better mechanical strength and reliability.

### Experimental results and discussion

The joint strength was determined under mechanical, thermal and combined type of loading, with a set of mechanical characterization experiments. Results of 4-point-bending test and Charpy impact test on specimens of brazed EUROFER 97 - W-1%La<sub>2</sub>O<sub>3</sub> joints are shown in Fig. 7-8. All the brazed joints have standard geometry - 3x3x27 mm samples for the 4-point-bending test and 3x4x27 mm with notched bar of 60° for the Charpy samples [4]. With increasing the temperature, the bending strength of the joint increases almost linear. At room temperature the strength of the brazed materials is very low. Reasons for that is the brittleness of the braze material and the residual stresses in the braze zone.

By Charpy impact test the highest values of the absorbed energy are achieved at temperatures of 550-600 °C. With further heating, the Charpy energy slightly decreases. Compared to specimens of pure tungsten or EUROFER 97, the brazed joints show much smaller impact energy values. This is most likely related to the reduced mechanical toughness of the materials in the zone near the brazed joint [5, 6]. More detailed investigation of fractured samples will clarify the exact crack path in order to identify the weakest link in the joint. By comparing the measured bending strength with the stresses calculated in the FE simulation, it is obvious that spontaneous joint fracture is a possible issue since the calculated stresses are much higher than the measured strength. However, such a comparison is not straightforward since in Fig. 4 von Mises stresses are reported while in a bending experiment the joint is loaded with a tensile stress perpendicular to the joint.

A detailed microstructural study has been performed to determine joint characteristics at the micro-scale. Fig. 6 exemplifies of brazed joint of the tungsten alloy to EUROFER 97 steel. The joint region forms three zones indicating that diffusion takes place between the brazing metal and the tungsten alloy and the steel takes, respectively. In the middle the brazing metal remains the same whereas the composition in the diffusion zones varies and includes elements from the base materials, mainly tungsten and chromium, as confirmed by energy dispersive x-ray

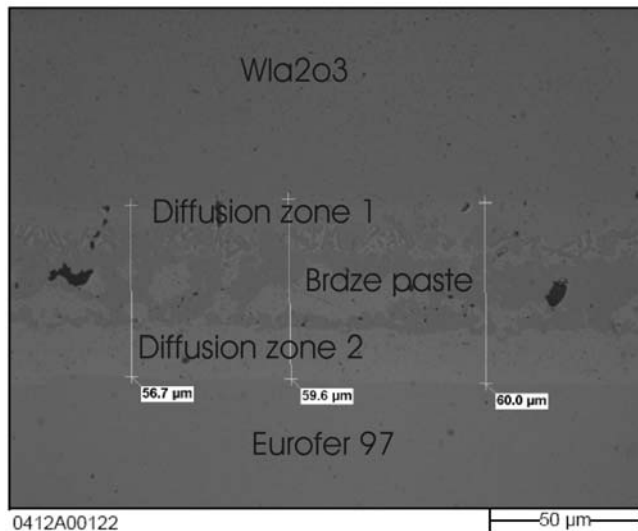


Fig. 6: SEM micrograph of the diffusion zones between the braze material and EUROFER (bottom) and the tungsten alloy (top).

The quality of the joints can be improved by further optimization of the brazing parameters. This will include a variation in the brazing pressure, and brazing and annealing time in order to achieve an optimized diffusion zone. Furthermore, tensile test and thermal fatigue test experiments are in progress for a more complete assessment of joint reliability.

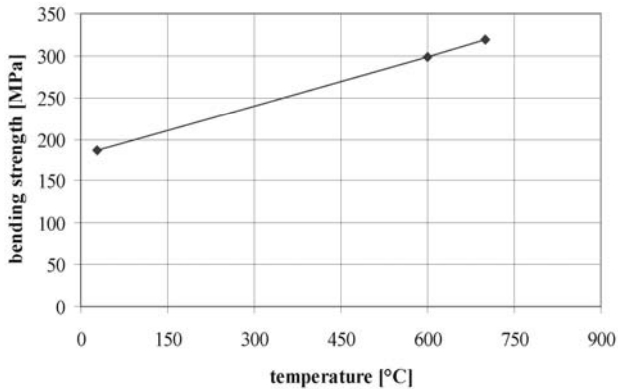


Fig. 7: Bending strength as a function of the test temperature on a specimen brazed with BrazeTec. Sample dimensions were 3x3x27 mm.

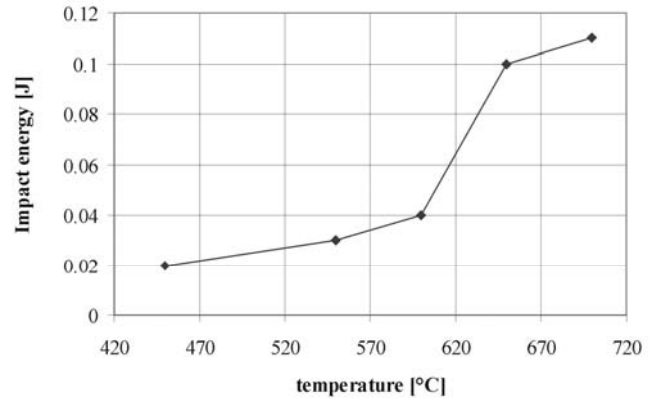


Fig. 8: Charpy-impact energy as a function of the test temperature on brazed specimen with BrazeTec. Sample dimensions were 3x3x27 mm.

## Conclusions

Brazing as a possible technique of joining W-alloy ( $W-1\%La_2O_3$ ) to Eurofer was investigated with respect to a divertor application. Therefore, a set of finite-element computations has been performed in order to characterize the mechanical loading situation of the joints at different temperature levels.

Experimental data of 4-point-bending test and Charpy test were presented. As a next step mechanical characterization experiments including tensile test and isothermal fatigue test in the temperature range of 100-650 °C will be carried out for a more complete mechanical characterization. In addition, thermal cycling experiments between 150 °C and 650 °C with brazed W-alloy ( $W-1\%La_2O_3$ ) / EUROFER 97 joints are in progress. All these experiments will provide a deeper understanding of the failure mechanisms and quantitative data, which are needed for a lifetime assessment of brazed divertor component.

## Staff:

T. Chehtov  
U. Bürkle  
H. Kempe  
M. Klotz  
A. von der Weth

## Literature:

- [1] T. Chehtov, A. Gervash, R. Giniyatulin, T. Ihli, R. Kruessmann, V. Kuznetsov, A. Makhankov, I. Mazul, P. Norajitra, I. Ovchinnikov, J. Weggen, B. Zeep, *Status of He-cooled divertor development (PPCS Subtask TW4-TRP-001-D2)*, FZKA 7100, 2005.
- [2] R. Kruessmann, P. Norajitra, L. V. Boccaccini, T. Chehtov, R. Giniyatulin, S. Gordeev, T. Ihli, G. Janeschitz, A.O. Komarov, W. Krauss, V. Kuznetsov, R. Lindau, I. Ovchinnikov, V. Piötter, M. Rieth, R. Ruprecht, *Conceptual Design of a He-cooled Divertor with integrated Flow and Heat Transfer Promoters (PPCS Subtask TW3-TRP-001-D2)*, Part I (Summary) and Part II (Detailed Version), FZKA 6974 & 6975, 2004.
- [3] B.A. Kalin, V.T. Fedotov, O.N. Sevryukov, A. Moeslang, M. Rohde, *Development of rapidly quenched brazing foils to join tungsten alloys with ferritic steel*, Journal of Nuclear Materials 329-333 (2004) 1544-1548

- [4] H.-C. Schneider, B. Dafferner, H. Ries, S. Lautensack, O. Romer, *Bestrahlungsprogramm HFR Phase Ib Ergebnisse der Kerbschlagbiegeversuche mit den bis 2,4 dpa bestrahlten Werkstoffen*, Tech. Report Nr. FZKA 6976, Forschungszentrum Karlsruhe GmbH, Karlsruhe, 2004
- [5] H. Nishi, K. Kikuchi, Influence of brazing conditions on the strength of brazed joints of alumina dispersion-strengthened copper to 316 stainless steel, *Journal of Nuclear Materials* 258-263 (1998) 281-288
- [6] H. Nishi, Y. Muto, M. Eto, *Trans. SMIRT-14* 4 (1997) 455.

## TW4-TTMA-002 D 3

# Development of Testing Procedures for Mechanical Characterisation of Plasma Sprayed or CVD Coated W Layers on EUROFER Steel before and after Irradiation

## Introduction

Tungsten coatings of several millimetres in thickness can be produced by plasma spraying or CVD. Such coatings are of interest as a protection material for plasma facing first wall components made of EUROFER steel. The mechanical behaviour of such tungsten coatings and its behaviour after irradiation is totally unknown.

Because only small volumes can be produced and irradiated a method is required with which the mechanical properties, such as yield strength and hardening behaviour of small volumes can be tested. In addition, tungsten is very brittle and it is practically impossible to perform standard tensile tests at temperatures below about 600 °C. One possible alternative to tensile testing is the use of depth-sensing indentation, which supplies information on the viscoplastic deformation properties of a small volume under simple experimental conditions. The capabilities for testing W-coatings on EUROFER steel will be investigated. The goal of this deliverable is to install an indentation testing device in the Fusion Materials Lab (FML) at the Forschungszentrum Karlsruhe and use it for mechanical characterisation of materials before and after irradiation.

## State of the Art

A new analysis method for the identification of the material parameters of a viscoplastic material from spherical indentation experiments was developed on the basis of finite element simulations and neural networks. The identification software was validated by simulations and experiments in cooperation with Bundesanstalt für Materialforschung und -prüfung (BAM) Berlin. The practical applicability was shown and the measurement uncertainty of the analysis software was examined for a variety of materials. On the basis of this work the purchase of a custom tailored ZWICK indentation system for installation in the FML at the Forschungszentrum Karlsruhe has been initiated.

## Results

### Purchase and installation of an indentation testing device in FML (Hot Cells)

The Zwick machine with maximum application force of 200 N and a depth resolution of 20 nm has been purchased and installed (Fig. 1). As an indenter tip a commercial Rockwell indenter has been selected that has a tip radius of 200 µm. Indentation depths will be 10% of the tip radius so that typical indents achieve a penetration depth of 20 µm. With such small indents, small volumes down to a few millimetres can be tested. The ma-



Fig. 1: Zwick system with depth and force reading hardness measurement, xy-stage, and microscope (left) and Box 4 in FML in which the machine will be installed (right).



chine is equipped with a xy-stage, microscope and a special testing software that allows for cyclic loading with creep phases of different duration, which is a requirement for application of a loading history as presented in Fig. 2. This specific loading history enables the developed analysis software to identify plastic hardening and viscous overstress of the material uniquely.

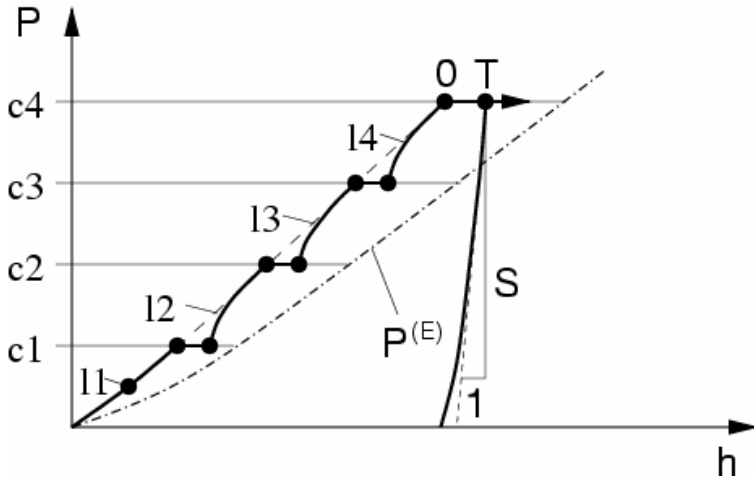


Fig. 2: Loading history required for the identification of the viscoplasticity model.

A series of indentation tests have been performed before starting the necessary modifications in the mock-up, where the performance of remote controlled experiments is tested. The measured data for EUROFER 97 and titanium are plotted in Figs. 3 and 4. EUROFER 97 has been chosen as a reference material and it can be seen from the small scatter in this plot that (i) this material is very homogeneous and (ii) that the indentation device has a very high repeatability. The deviation of

Eurofer-3 from the other experiments is due to thermal drift that may cause an artificial negative creep and vanishes as soon as the specimen reaches the temperature of the machine. From experiment Eurofer-5 and higher, there is almost no deviation visible in the experiments. The results for titanium in Fig. 4 show the change of local properties depending on the position of a material that is not so homogenous as the reference material. The difference in the loading response indicates a significant change of hardness and consequently also of the stress-strain behaviour from one location to the next.

Currently, the installation of mock-up is under way while the Hot Cell is prepared for the transfer of the indentation device until end of 2005.

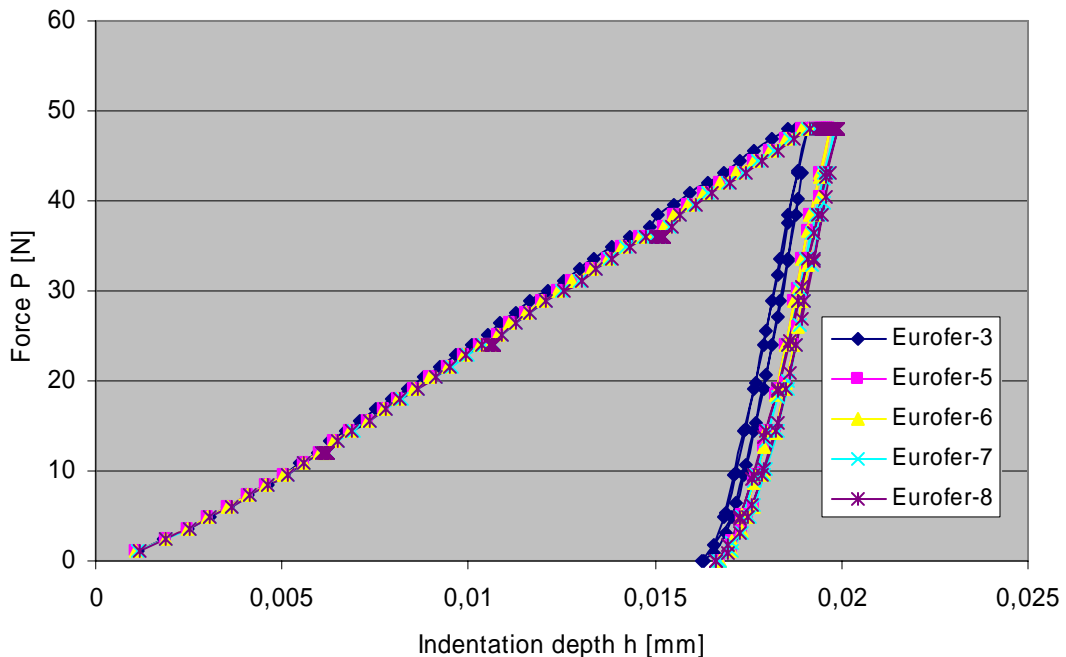


Fig. 3: Indentation experiments with Zwick-Indenter for EUROFER 97 (EA33).

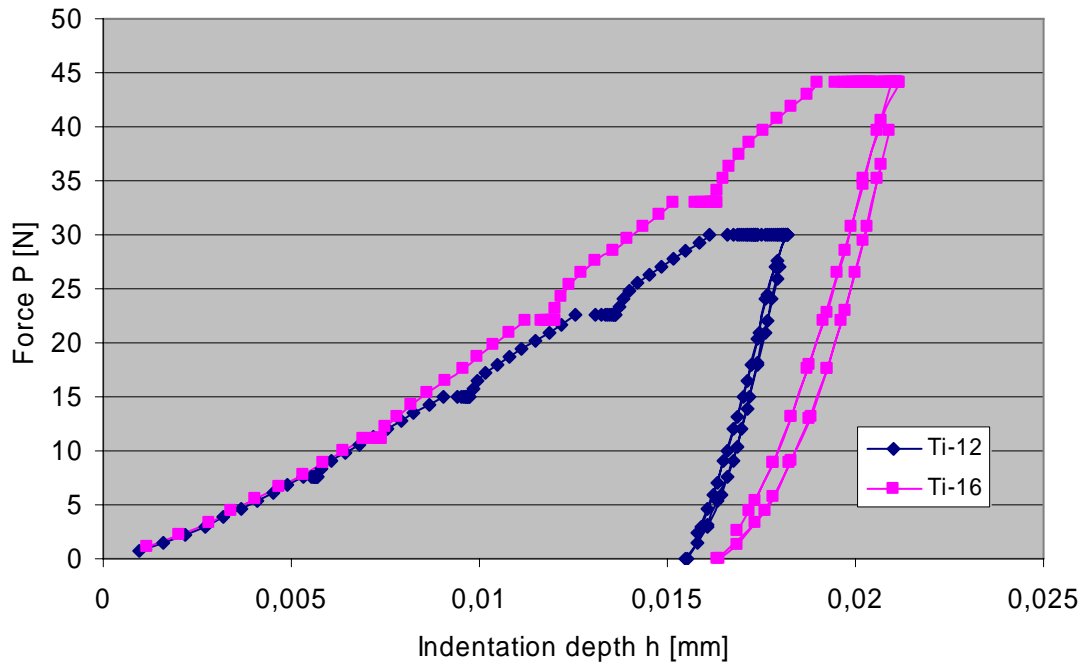


Fig. 4: Indentation experiments with Zwick-Indenter for Titanium.

Development of indentation testing procedure and application to unirradiated W-layers at room-temperature for measurement of Young's modulus, stress-strain behaviour and creep properties

The neural network software developed for the analysis of the load-depth curves has been applied to the data shown in Fig. 3 and 4. The determined material parameters represent a viscoplastic constitutive model with elasticity, nonlinear isotropic and kinematic hardening of Armstrong-Frederick type as well as a viscous overstress. Altogether eight material parameters (Young's modulus and yield strength, two hardening parameters for each hardening rule as well as two viscosity parameters) can be identified within a few milliseconds. These material parameters can be used to compute the stress-strain behaviour of the tested material for any loading history as well as for dimensioning of parts using finite element simulations. Since the parameters describing kinematic hardening are determined in the last step, they are afflicted with the highest identification uncertainties. Depending on the quality of the specimen and the experiment, it can happen that it is possible to determine only the total hardening behaviour that is then assumed to be purely isotropic.

For the high quality reference material both options have been applied so that a slightly different identification was obtained from the same experiments. The results are presented in Fig. 5 and 6 in comparison with data from a tensile experiment. Both cases show a very good agreement between tensile and indentation data. It can be seen that by including kinematic hardening the nonlinearity of the stress-strain behaviour at the onset of plastic deformation and at ultimate tensile strength is described slightly better, but the results show a larger scatter for small plastic strains. The contribution of kinematic hardening, which is important for cyclic loading of a material, is significant as shown in Fig. 7. The observed scatter can be attributed to the initial slope of the identified kinematic hardening rule while the asymptotic value is very stable for all experiments.

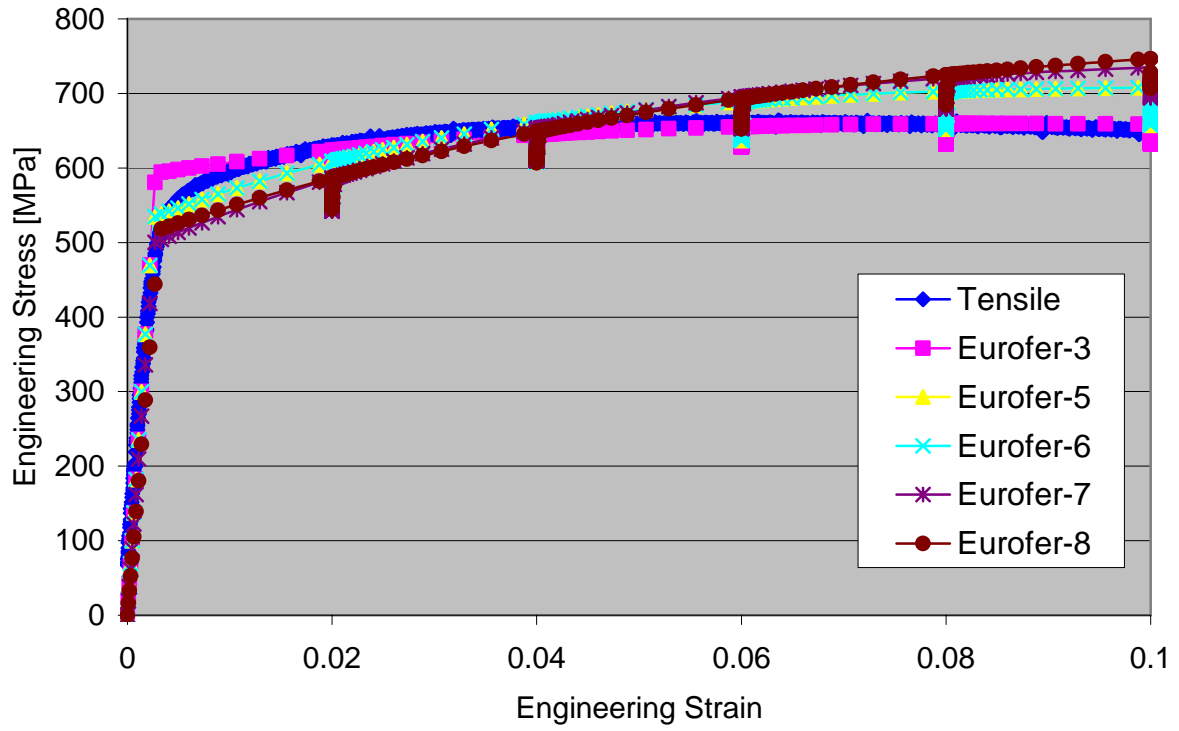


Fig. 5: Identification of stress-strain behaviour for EUROFER 97 under the assumption of pure isotropic hardening.

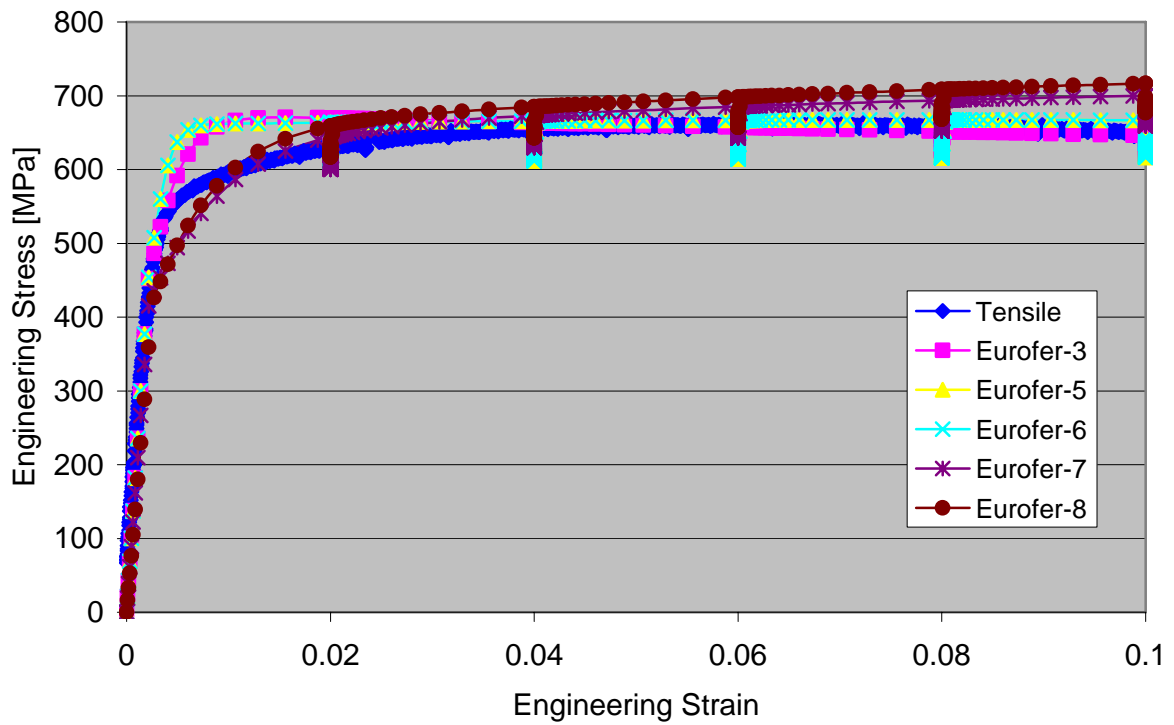


Fig. 6: Identification of stress-strain behaviour for EUROFER 97 under the assumption of isotropic hardening and kinematic hardening.

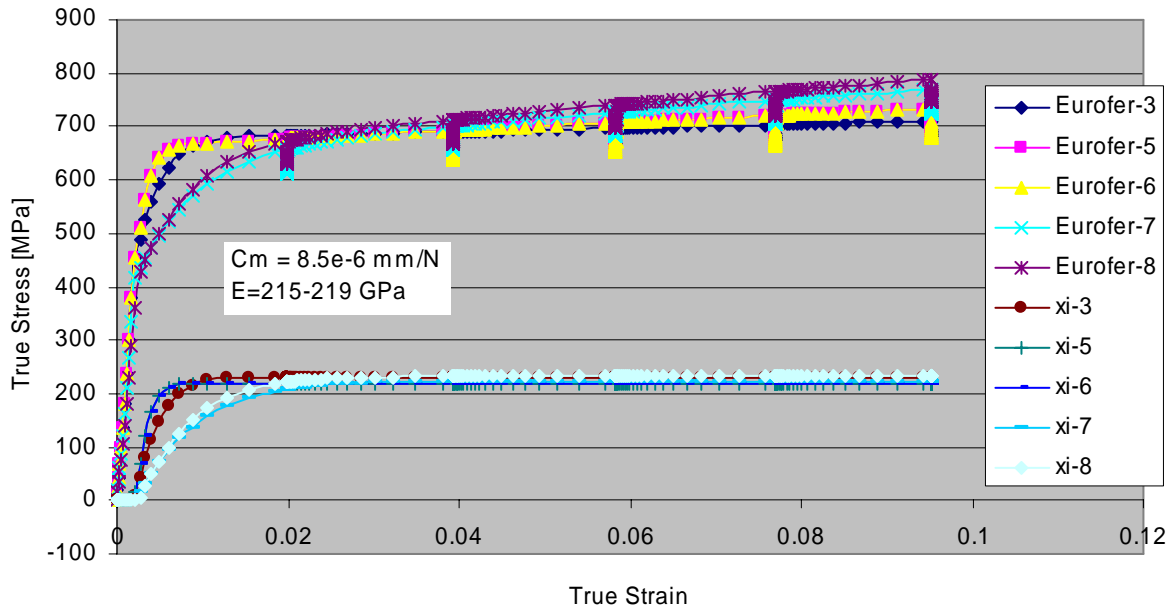


Fig. 7: Contribution of kinematic hardening to the total hardening response of EUROFER 97 in a true stress-true strain diagram.

The machine compliance of  $C_m = 8.5 \cdot 10^{-6} \text{ mm/N}$  has been adjusted to obtain the correct Young's modulus  $E$  for EUROFER. The scatter of all determined values of  $E$  is within 4 GPa, which is less than 2%. Using this compliance the modulus identification is validated using the titanium experiments. The determined modulus for titanium is between 105 GPa and 110 GPa, and shows very good agreement with the literature value, which is 108 GPa. In contrast to EUROFER the titanium shows a significant viscous overstress that is visible in the pronounced relaxation phases inserted in the tensile simulations in Fig. 8. It makes almost 30% of the total stress and would therefore produce significant creep in high loaded part.

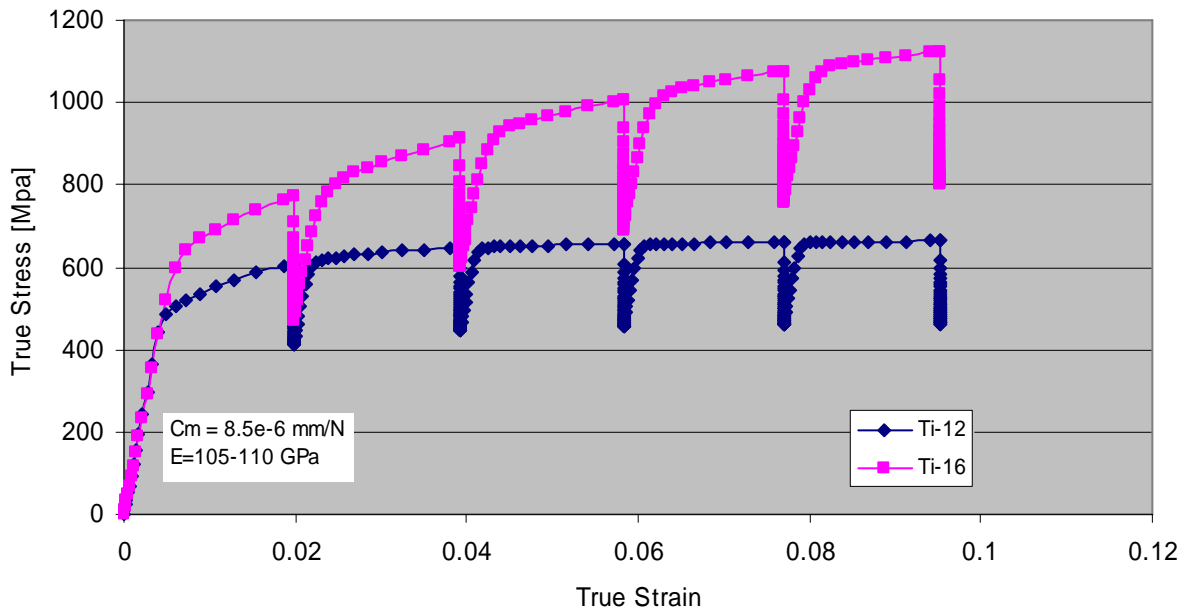


Fig. 8: Identified stress-strain behaviour with inserted relaxation phases of 3600 s.

The applicability of the whole method for tungsten coatings is demonstrated with indents made in a cross-section of a polished W-coating deposited on an EUROFER substrate. The micrographs in Fig. 9 indicate several difficulties when indenting the W-coating, which can be avoided using the positioning system. The indent should have sufficient distance to the interface (left micrograph) as well as to big pores (right micrograph) in the plasma deposited coating. The height of the coating is about 2 mm and therefore sufficient material is available for the about 100  $\mu\text{m}$  wide imprints. The middle micrograph shows an indent in a typical area for which good results have been obtained.

The corresponding stress-strain behaviour identified by the analysis software is presented in Fig. 10. Here wrong positioning of the indent leads to significant misinterpretation by the neural networks. However, wrong identified parameter sets can be easily sorted out by quality inspection of the indent position and measured load-depth behaviour as indicated by the links to the micrographs.

The measured stress-strain behaviour of the tungsten coating is much softer than that of bulk tungsten. Also a significant viscous overstress of about 200 MPa can be observed. The yield strength lies between 270 MPa and 450 MPa, the maximum equilibrium strength of the coating material is 600 MPa. At a strain rate of  $\dot{\epsilon} = 10^{-3} \text{ s}^{-1}$ , the estimated ultimate tensile strength is 1000 MPa.

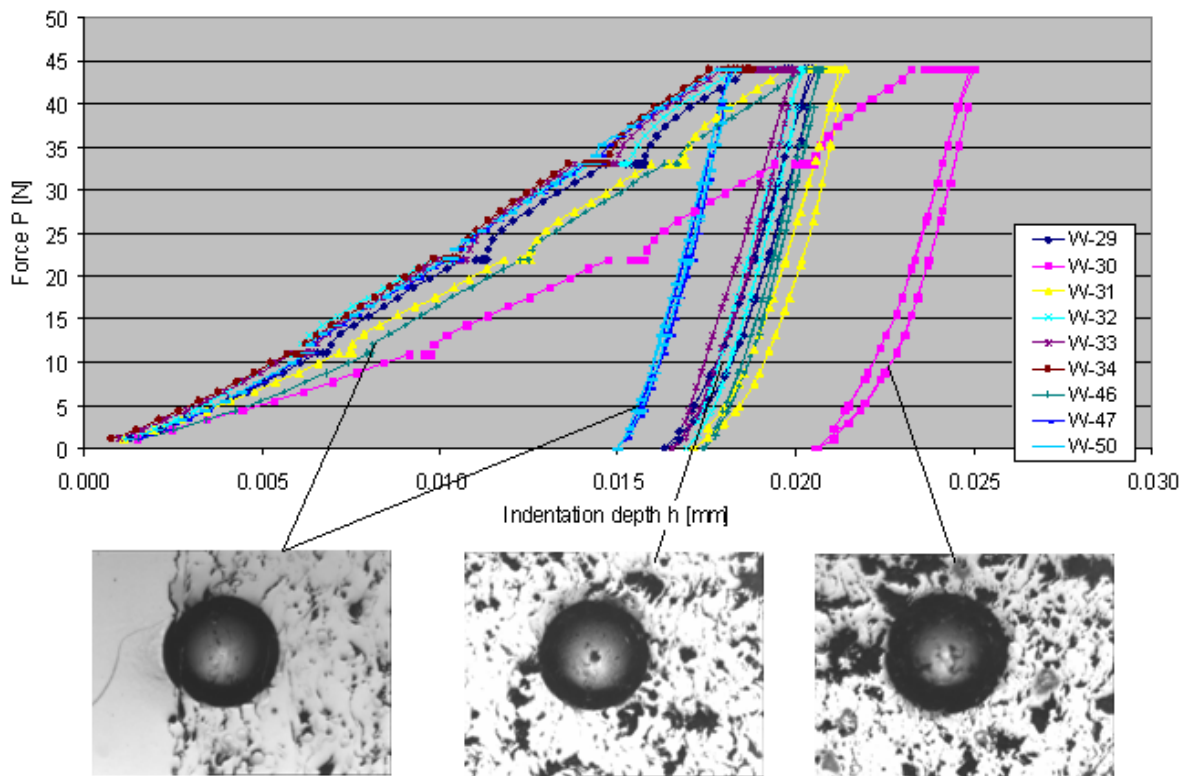


Fig. 9: Load-depth curves for a W-coating deposited on EUROFER. The interface between tungsten and EUROFER can be seen in the lower left micrograph.

## Conclusions and Outlook

The results show the feasibility and potential of an indentation device in the Fusion Materials Lab (FML). Brittle materials like bulk W and W-Coatings can be tested easily with indentation methods. In addition rich information on the mechanical properties, like e.g. Young's modulus, true stress-strain curve, and creep properties can be obtained before and after irradiation. However, due to the measurement principle experiments will be restricted to room temperature.

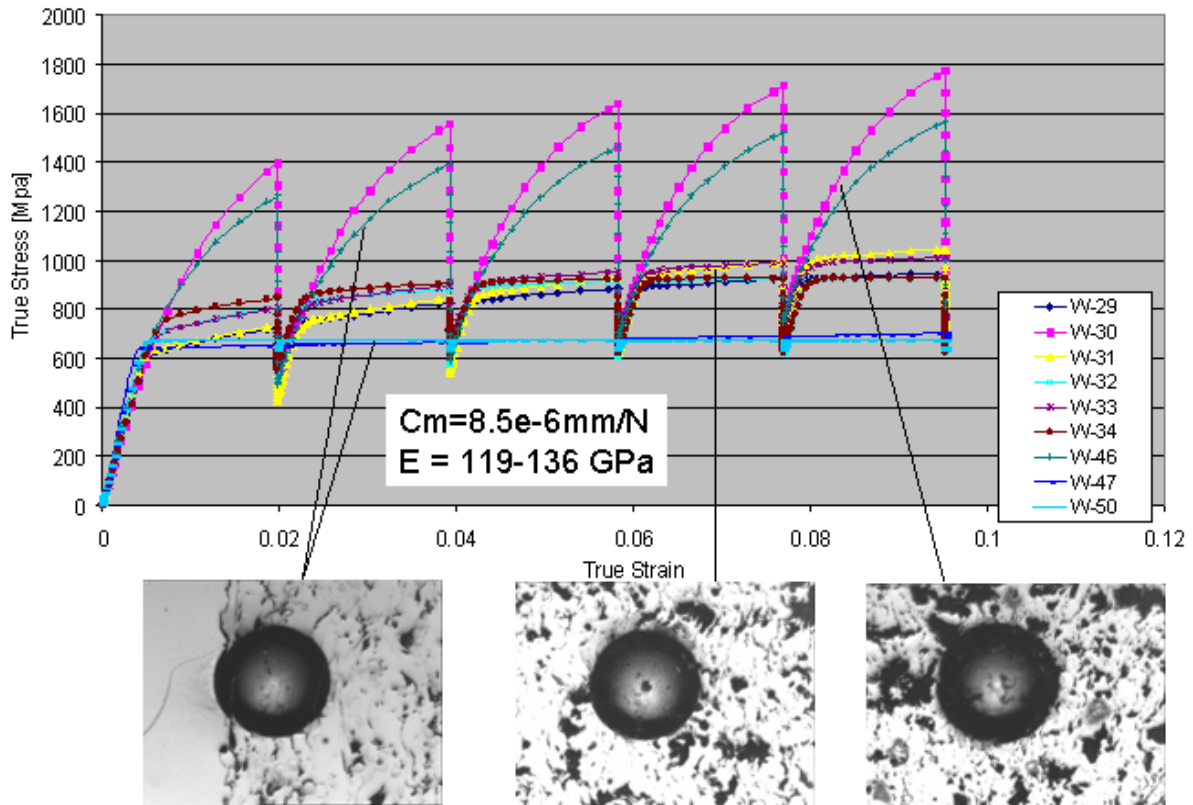


Fig. 10: Stress-strain behaviour with inserted relaxation phases of 3600 s for a W-coating on EUROFER.

Regarding the thickness of W-coatings under consideration and due to the reduction of the indenter size below 250  $\mu\text{m}$ , the analysis can be restricted to consider the W-coating as a bulk material what is in advantage with respect to the robustness of the method. The radiation shielded installation of the indentation test setup within a Hot Cell of the FML will be completed within 2005 so that from 2006 on experiments with irradiated specimens can be conducted.

#### Staff:

N. Huber	D. Klötzer, BAM-Berlin
R. Rolli	Ch. Ullner, BAM-Berlin
H.-Ch. Schneider	E. Tyulyukovskiy, IZBS/Universität Karlsruhe

#### Literature:

- [1] E. Tyulyukovskiy, N. Huber: Identification of viscoplastic material parameters from spherical indentation data. Part I: Neural networks, Journal of Materials Research, accepted for publication, 2005.
- [2] D. Klötzer, Ch. Ullner, E. Tyulyukovskiy, N. Huber: Identification of viscoplastic material parameters from spherical indentation data. Part II: Experimental validation of the method, Journal of Materials Research, accepted for publication, 2005.
- [3] E. Tyulyukovskiy: Identifikation von mechanischen Eigenschaften metallischer Werkstoffe mit dem Eindruckversuch, Wissenschaftliche Berichte, FZKA-7103 (März 2005), Forschungszentrum Karlsruhe, zugleich, Dissertation, Universität Karlsruhe, 2005.
- [4] N. Huber, T. Dietz, E. Tyulyukovskiy: An Investigation of Non-linear Stress-Strain Behavior of Thin Metal Films, Mater. Res. Soc. Symp. Proc. Vol. 841, R12.2.1, 2005
- [5] D. Klötzer, Ch. Ullner, N. Huber, A. Richter: Validation of a procedure for estimating tensile properties from the instrumented indentation test, Poster number AKFH 1.18, DPG-Tagung Berlin, 04.03 - 09.03.2005.

# **Materials Development Nuclear Data**





## **TTMN-001**

### **Nuclear Data: EFF/EAF Data File Upgrade, Processing and Benchmark Analyses**

The European Fusion File (EFF) and Activation File (EAF) projects aim at developing a qualified nuclear data base and validated computational tools for nuclear calculations of fusion reactors. The related Task TTMN-001 of the EFDA technology work programme is devoted to the evaluation, processing, application, and benchmarking of required nuclear cross section and uncertainty data as well as the development of computational tools for uncertainty calculations. The FZK contribution to Task TTMN-001 is on the evaluation of EFF-3 data, the qualification of new and updated EFF data evaluations through computational benchmark analyses including sensitivity/uncertainty analyses and the development of advanced computational schemes for sensitivity calculations based on the Monte Carlo technique.

## **TW5-TTMN-001 D 2**

### **Estimation of Uncertainties in Neutronics Calculation: Testing of MCSEN Code for Track Length Detectors for the TBM Mock-up Neutronics Experiment**

The overall objective is to develop the computational tools that allow the calculation of sensitivities and uncertainties of neutron fluxes and nuclear responses in the ITER Test Blanket Module (TBM) on the basis of the Monte Carlo technique. To this end algorithms were developed (TW3-TTMN-001, Deliverable 4) and implemented (TW4-TTMN-001, Deliverable 3) into the MCSEN code to allow the efficient calculation of sensitivities with the track length estimator (MCNP tally F4). The objective of the 2005 task deliverable was to test and validate the new feature of the MCSEN code through the application to the TBM mock-up neutronics experiment at the Frascati neutron generator (FNG).

A full 3D MCNP model of the experimental set-up with HCPB (Helium Cooled Pebble Bed) TBM mock-up assembly and supporting structure, neutron generator and experimental hall was employed in the MCSEN test calculations.

Using the new track length estimator feature of the MCSEN code, sensitivities of the neutron flux and the Tritium production rate were calculated for the two detector positions in the back of the HCPB TBM mock-up where the flux spectra will be measured by the experimental team of the Technical University of Dresden (TUD). Neutron flux spectra and sensitivities were calculated with the track length method in a small volume (average flux/reaction-rate in cell) and with the point detector estimator at the two detector positions. The calculated fluxes and the reaction rates calculated with the two methods agree at both positions except for the lowest energy (<1eV) where they differ by a few percent. The energy range below 1 eV, however, is populated by very few neutrons and therefore does not contribute at any significant level to the neutron flux and the Tritium production.

The integrated sensitivities calculated with the point detector and the track length estimators agree very well in the whole energy range above 1 eV. The same is true for the calculated sensitivity profiles. It was thus concluded that the sensitivities calculated with the point detector and the track length estimator agree provided the calculated responses (flux, reaction rate) do also agree [1].

The calculation of sensitivities based on the track length estimator approach with the MCSEN code thus has been qualified for assessing nuclear data related sensitivities and uncertainties of nuclear responses in the neutronics TBM mock-up experiment. In a first real application, the newly developed MCSEN feature is being applied to the uncertainty analysis of the tritium production rate measurements conducted as part of TW5-TTMN-002, Deliverable 3 [2].

## TW5-TTMN-001 D 5 Evaluation of Ta-181 Cross-Sections up to 150 MeV for the EFF-3 Library

The overall objective is to develop during FP6 a general-purpose nuclear data library up to 150 MeV neutron energy by adopting existing high-energy evaluations, up-grading and adapting them to the EFF/JEFF data and performing new evaluations as required. According to the priority list elaborated in 2003 to satisfy, in particular, the data needs of the IFMIF project, the objective of the 2005 work programme was to provide a complete 150 MeV data evaluation for Ta-181 [3].

In the evaluation process use was made of the codes ECIS96 for optical model calculations and GNASH for nuclear reaction cross section calculations. Recent high energy experimental data were taken into account for evaluating the total cross section. Global optical potentials for neutrons, protons, deuterons and  $\alpha$ -particles were used. Optical model potentials for tritons and He-3 were constructed on the basis of proton and neutron potentials. To improve the neutron emission spectra, collective excitations were included in the GNASH calculations. Double-differential cross sections of the emitted particles were calculated on the basis of the Kalbach systematics. A complete ENDF data file was finally prepared for  $^{181}\text{Ta}$  covering the full energy range data up to 150 MeV. JENDL-3.3 data were adopted to some extent at low energies (below 1 MeV). ENDF/B-VI data were not used due to a very poor quality of the  $^{181}\text{Ta}$  evaluation which was taken over from the earlier ENDF/B-IV version of 1972.

Fig. 1 shows the flowchart of the evaluation process. Total, reaction, elastic and inelastic scattering cross sections were calculated with ECIS96 applying a spherical optical model potential. Nuclear model calculations were performed with the GNASH code utilizing the Hauser-Feshbach theory for multiple particle equilibrium and the exciton model for pre-equilibrium particle emissions up to 150 MeV.

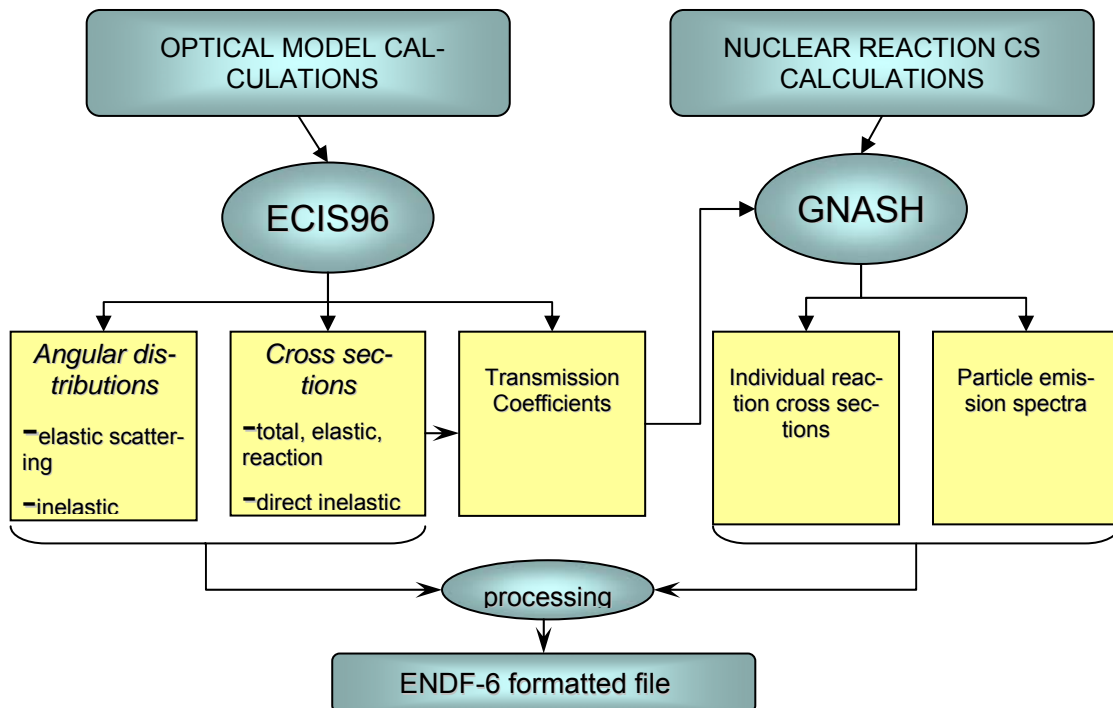


Fig. 1: Flowchart for the evaluation of neutron cross section data of the  $^{181}\text{Ta}$  isotope up to 150 MeV neutron energy.

Measurements of the total cross-sections performed at Los Alamos for the tantalum isotope were used to validate the high energy neutron optical model potential. The global potential of Koning & Delaroche appeared to be the most accurate one over the entire energy range from 1 to 150 MeV. It was also used for the proton exit channel. For the deuterons and  $\alpha$ -particles

the global potentials by Bojowald and Avrighianu & Hodgson, respectively, were applied. For tritons and He-3 the folding approach by Watanabe was used because for these particles there exist neither local nor global potentials covering the full energy range from 1 to 150 MeV. Figs. 2 a,b compare evaluated and measured total cross-sections and elastic scattering angular distributions for  $^{181}\text{Ta}$ . Note the perfect agreement of the new evaluations (red curves) with the measured cross-sections over the entire energy range.

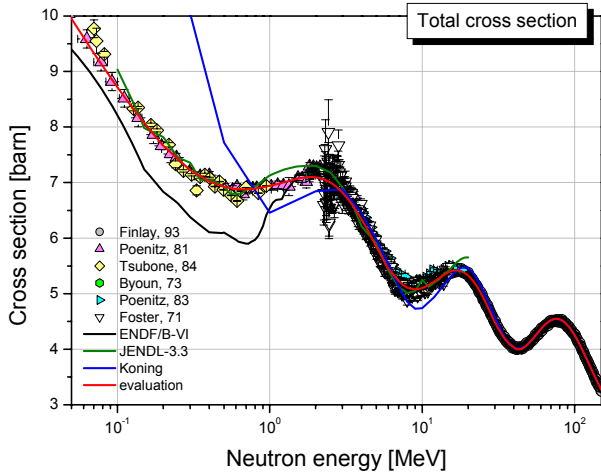


Fig. 2a: Total cross-section for  $n + ^{181}\text{Ta}$

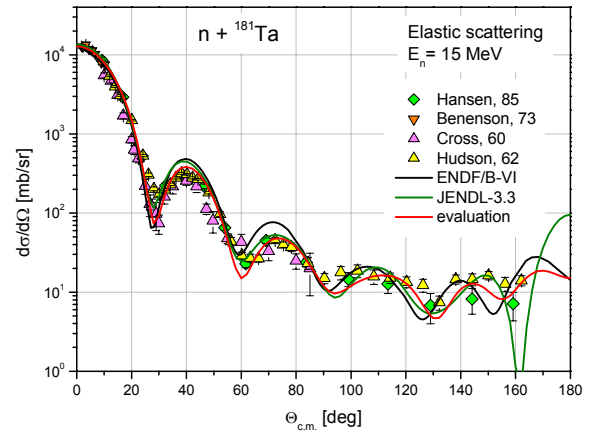


Fig. 2b: Elastic scattering angular distribution for 15 MeV  $n + ^{181}\text{Ta}$

Examples of neutron emission spectra calculated with GNASH are shown in Fig. 3. The good agreement of the new evaluation with the measured emission spectra at higher secondary energies is due to the fact that collective excitations and direct reactions have been taken into account. These have not been included in the ENDF/B-VI and JENDL-3.3 evaluations.

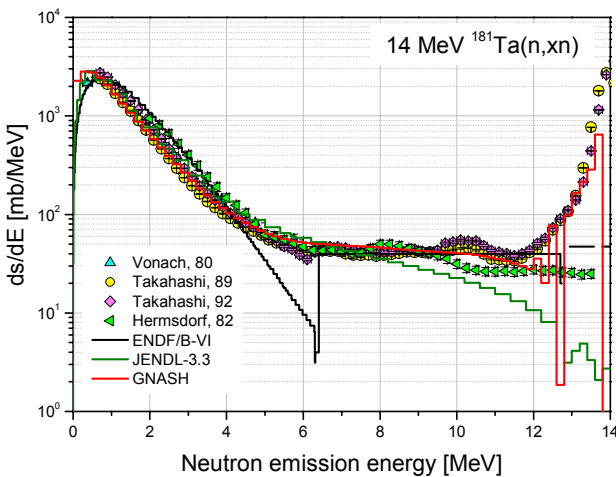


Fig. 3a: Neutron emission spectrum for 14 MeV neutron incidence energy.

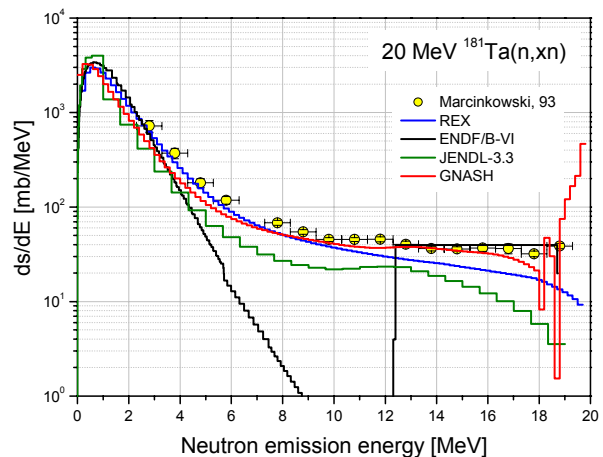


Fig. 3b: Neutron emission spectrum for 20 MeV neutron incidence energy.

The final ENDF data file includes entire new evaluations in the MF=3 file section for the total and elastic scattering cross sections (MT=1,2), the (n,2n), (n,3n), (n,np), (n,nα), (n,p), (n,d), (n,t), (n,He3), (n,α) activation cross sections (MT=16,17,22,28,103,104,105,106,107) and the inelastic scattering cross sections (MT=51-91). Differential neutron emission data were newly evaluated for the reactions MT=2, 51-61 in MF=4 (angle distributions). Neutron emission spectra as well as angular distributions were evaluated with GNASH for MT=16,17,22,28,91 and stored in the MF=6 file section. Above 20 MeV, the files contain complete new evaluations. The high energy data are stored in file sections MF=3 (MT=2, MT=5), MF=4 (MT=2)

and MF=6 (MT=5). The MT=5 cross-section accounts for all reactions with the emission of secondary particles. MF=6 contains particle emission spectra in the center of mass frame and photon and recoil spectra in the laboratory system.

## **TW5-TTMN-001 D 6**

### **Benchmark Analyses Based on Monte Carlo Calculations with MCNP for Revised/updated EFF-3 Data Evaluations (including W and Ta)**

The objective of this sub-task is to check and validate the new EFF-3 data evaluations for a reliable use in design calculations and provide feed-back to the evaluators

A series of benchmark analyses has been performed as part of the 2005 work programme to test and qualify the new and updated fusion data evaluations for Be, Pb, Ti and W which enter into the JEFF-3.1 general purpose data library.

The JEFF-3.1 Ti evaluation was shown to agree essentially with the NRG-2003 evaluation analysed previously. There is still an unphysical jump in the neutron emission spectrum at 14 MeV neutron incidence energy which could not be removed. The neutron leakage spectrum measured in the OKTAVIAN spherical shell experiment can be better reproduced with JEFF-3.1 than with other available Ti data evaluations although the agreement is considered not satisfactory [4].

The new W isotopic data evaluation, provided by FZK in the frame of TW4-TTMN-001, Deliverable 1, was tested against the FNG tungsten benchmark experiment with measurements of the neutron and photon spectra [5]. A good reproduction of the measured photon spectra was achieved. Underestimations of the neutron flux spectra were obtained, however, in the high energy ( $E > 12$  MeV) and low energy (1 -5 MeV) range indicating too high (n,2n) and inelastic (MT=91) neutron cross-sections. The new W data evaluation also provides a very good reproduction of the secondary neutron energy distribution at 14 MeV neutron incidence energy.

The new JEFF-3.1 isotopic lead evaluation was benchmarked against fusion relevant integral experiments and compared to FENDL-2.1 which is identical to ENDF/B-VI.8 for lead [6]. The neutron multiplication was found to agree between these two data evaluations. Measured multiplication factors are underestimated, however, by up to 15%. The neutron leakage spectra are underestimated by typically 10 -20 % (FNS time-of-flight measurements of angular neutron leakage fluxes). A significant underestimation was obtained for the photon leakage spectra above 5 MeV. As for the secondary energy and angle distributions, there is good agreement with the available measured data.

The newly assembled Be JEFF-3.1 data evaluation, based on the EFF-3 data of Tagesen and Vonach, was benchmarked against the various Be EFF-3 evaluations making use of the FNS time-of-flight experiment on Be slabs [7]. Inconsistent results were obtained for JEFF-3.1 and EFF-3.05 which actually should agree. The discrepancies are most probably due to the processing of the data with different version of the NJOY code. The standard NJOY-99.90 code was used for the processing of the Be JEFF-3.1 data. The LAW=7 data representation (angle-energy distribution) thereby is automatically converted to LAW=1 (energy-angle distribution) which may cause problems with some special features of the Be data evaluation. At FZK, NJOY-99.50 with local patches was applied to maintain the proper LAW=7 distribution data.

First benchmark analyses have been done for Ta as preparatory step for the forthcoming qualification of the new data evaluation underway at FZK [8]. Currently, only two independent Ta evaluations (up to 20 MeV) do exist which are included in the American ENDF/B-VI and the Japanese JENDL-3.3 data library, respectively. The ENDF/B-VI Ta evaluation is an obso-

lete evaluation performed in 1972 for ENDF/B-IV. With regard to experimental data, an integral benchmark experiment was performed at the Lawrence Livermore National Laboratory (LLNL) in 1986 on two Ta spherical shells with a central 14 MeV neutron source. The shell thicknesses amounted to 3.4 and 10.2 cm corresponding to 1 and 3 mean free paths for 14 MeV neutrons, respectively. Time-of-flight spectra were recorded at a distance of 10 m from the centre of the Ta shell. A full 3D model of the experimental setup was devised for the benchmark calculations with the MCNP code for calculating the neutron leakage spectra. The comparisons to the measured spectra show severe discrepancies in the order of  $\pm 50\%$  in the energy range between 1 and 12 MeV and overestimations of up to 25% for 14 MeV neutrons, see Figs. 4a,b below. Severe inconsistencies were also obtained for the neutron emission spectra as compared to the measured differential energy spectra for neutron incidence energies between 5 and 20 MeV. Thus, a clear need is indicated for updating the Ta data evaluations with special focus on the energy spectra of neutrons emitted through the Ta(n,xn) reactions. Such an evaluation is being conducted at FZK in the frame of the EFDA fusion technology work programme 2005, sub-task TTMN-001, Deliverable 6 (see above).

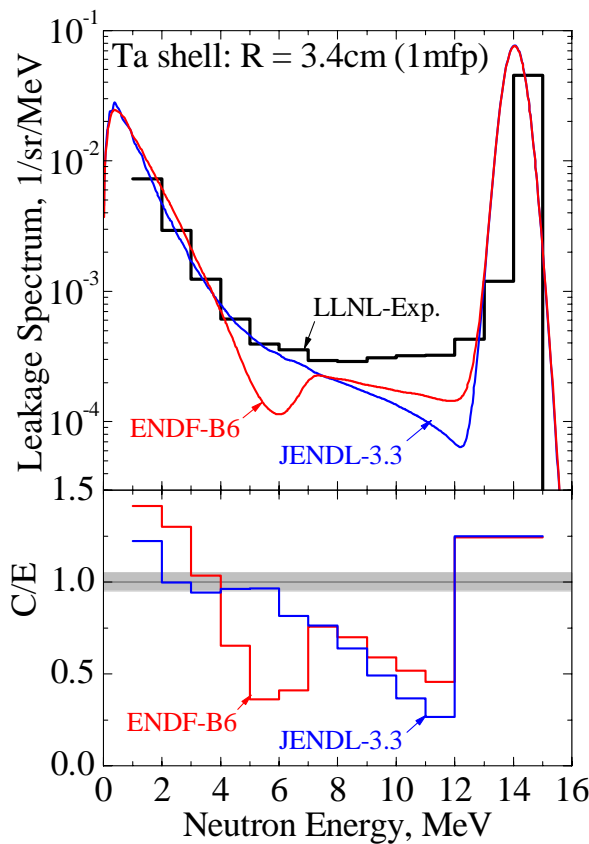


Fig. 4a: Ta shell with 3.4 cm radial thickness.

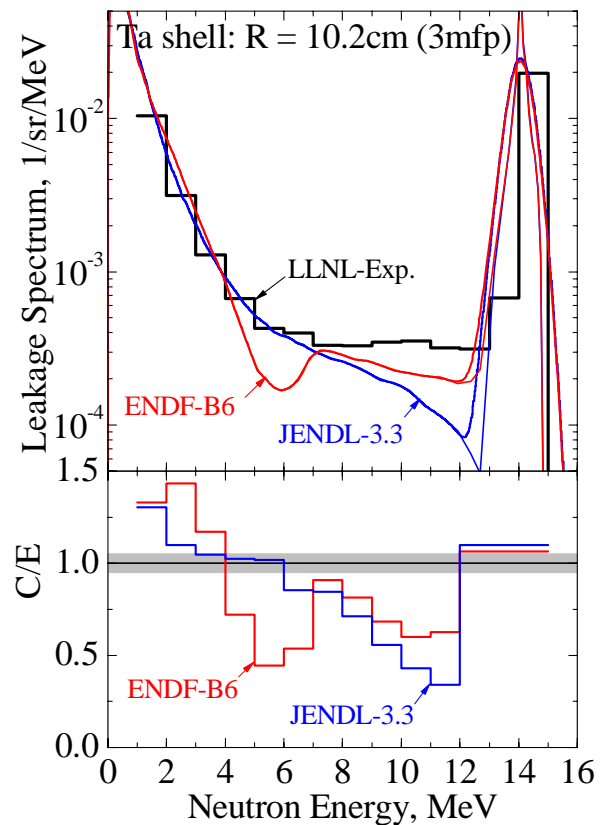


Fig. 4b: Ta shell with 10.2 cm radial thickness.

Fig. 4: Comparison of measured and calculated neutron leakage spectra for Ta spherical shells with central 14 MeV neutron source.

**Staff:**

- U. Fischer
- D. Leichtle
- R. Perel (Hebrew University of Jerusalem)
- P. Pereslavtsev
- S. P. Simakov
- I. Schmuck

Literature:

- [1] R. L. Perel, Testing MCSEN track-length sensitivity calculations for the TBM mock-up experiment, EFF-DOC-926, NEA Data Bank, Paris, May 2005.
- [2] U. Fischer, D. Leichtle, R. Perel, Monte Carlo based transport and sensitivity/uncertainty analyses of the Tritium production in the HCPB breeder blanket mock-up experiment, EFF-DOC- 954, NEA Data Bank, Paris, November 2005.
- [3] P. Pereslavytsev, U. Fischer, Evaluation of Ta-181 cross-sections for the EFF data library up to 150 MeV, EFF-DOC-953, NEA Data Bank, Paris, November 2005.
- [4] U. Fischer, I. Schmuck, S. P. Simakov, Benchmark analyses of Ti JEFF-3.1T data for fusion applications, EFF-DOC-930, NEA Data Bank, Paris, May 2005
- [5] U. Fischer, P. Pereslavytsev, S. P. Simakov, Testing of new W data evaluations for EFF-3, EFF-DOC-931, NEA Data Bank, Paris, May 2005
- [6] S. P. Simakov, U. Fischer, Benchmark analyses of Pb JEFF-3.1T data for fusion applications, EFF-DOC-929, NEA Data Bank, Paris, May 2005
- [7] D. Leichtle, Benchmark analyses of Be-9 JEFF-3.1T data for fusion applications, EFF-DOC-932, NEA Data Bank, Paris, May 2005
- [8] S. P. Simakov, U. Fischer, First benchmark analyses of Ta evaluated data for fusion neutron transport calculations, EFF-DOC-952, NEA Data Bank, Paris, November 2005.

## TTMN-002

### Nuclear Data: Benchmark Experiments to Validate EFF/EAF Data

The objective of Task TTMN-002 is to provide the experimental data base required for the validation of the nuclear data libraries EFF (European Fusion File) and EAF (European Activation File) developed in the frame of Task TTMN-001 of the EU Fusion Technology Programme. According to the FP6 programme orientation on ITER (TBM) and IFMIF, the focus is on the experimental validation of TBM design calculations by means of a neutronics mock-up experiment and cross-section validation experiments relevant for IFMIF.

#### TW5-TTMN-002 D 2

### Measurement of Tritium Production Rates and of Neutron and Gamma-ray Flux Spectra in the TBM Mock-up (TU Dresden)

#### Objectives

A neutronics experiment with a mock-up of the Helium Cooled Pebble Bed (HCPB) Test Blanket Module (TBM) for ITER was carried out with the objective to validate the nuclear design parameters of the TBM. The mock-up was irradiated with 14 MeV neutrons and the main nuclear responses were measured and compared with the calculated values using the design tools of the TBM, i. e. nuclear data of the European Fusion File (EFF) and the Monte Carlo code MCNP. In collaboration with groups of FZ Karlsruhe, ENEA Frascati, IJS Slovenia, the TU Dresden contributes with measurements of tritium production rates and of neutron and  $\gamma$ -ray flux spectra in the mock-up.

#### Measurement of tritium production rates

Tritium self-sufficiency of a fusion reactor is a key issue of the breeding blanket development. In order to meet the required uncertainty margins of the tritium production measurement in the mock-up, a benchmark of experimental techniques was carried out in 2004 by groups of ENEA Frascati, JAERI Tokai-mura and TU Dresden. The results showed that experimental techniques are available for the measurements in the mock-up [1] to be carried out in 2005.

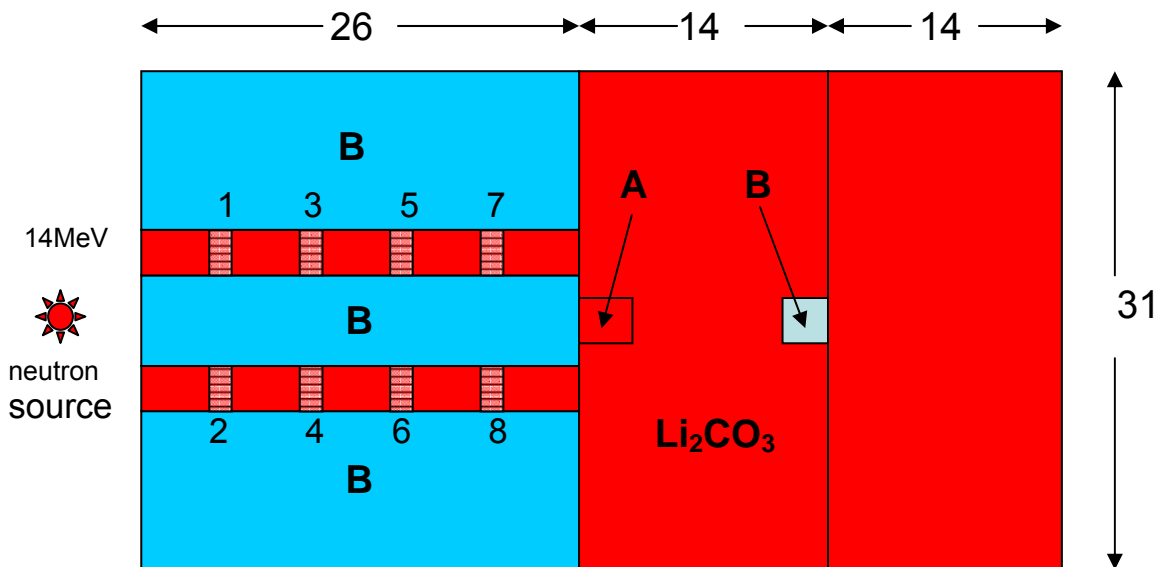


Fig. 1: Vertical cross section of the mock-up. Steel boxes are filled with metallic Be (blue) and with Li<sub>2</sub>CO<sub>3</sub> powder (red) of natural isotopic abundance. Dimensions are given in mm.

A schematic view of the experimental assembly is given in Fig.1. The block close to the neutron source consists of two layers of Li<sub>2</sub>CO<sub>3</sub> (thickness of 24 mm) in which stacks of Li<sub>2</sub>CO<sub>3</sub> pellets are inserted at 8 positions. Each stack has 12 pellets with a diameter of 13 mm. Three

layers of metallic Be act as neutron multiplier. The assembly was irradiated at the Frascati Neutron Generator in April this year with a total of  $5.8 \cdot 10^{15}$  source neutrons.

After the irradiation the pellet stacks 1, 3, 5 and 7 were sent to Dresden. Their tritium activity was measured by  $\beta$ -counting in a liquid scintillator, after solution in  $\text{CH}_3\text{COOH}$  and precipitation of the  $\text{LiF}$  obtained by adding  $\text{HF}$  [1]. For the normalization of the count rates,  $\text{Li}_2\text{CO}_3$  not irradiated, but with  $\text{HTO}$  standard added, was counted. The background rate was measured with blank samples ( $\text{Li}_2\text{CO}_3$  not irradiated and tritium-free water). As the pellets had different quenching behaviour, the counting efficiency was measured with  $^{152}\text{Eu}$  and taken individually into account for each of the pellets.

The results are shown in Fig. 2. The uncertainties of the measured values ( $2 \cdot \sigma$  interval) represent the total uncertainties. They include those of the  $\beta$ -counting of the sample cocktail, the chemical procedure and the normalization.

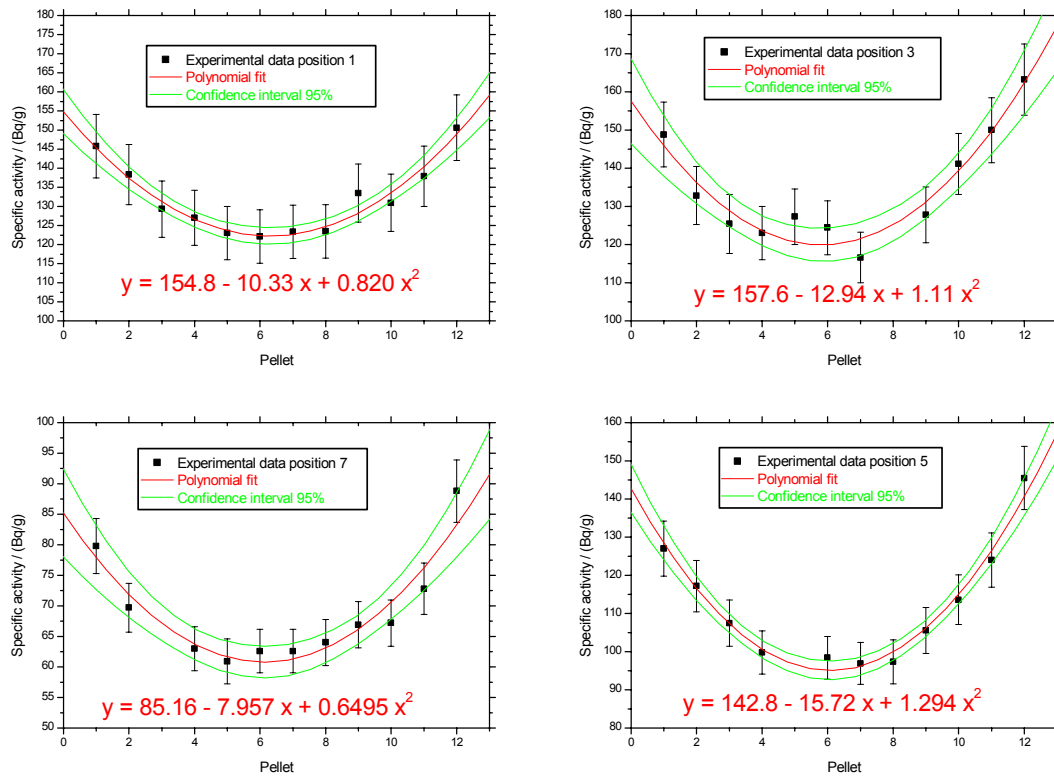


Fig. 2: Specific tritium activity for the four pellet stacks versus pellet number (No 1 is the lowest in the stack, the nearest to the central axis of the mock-up; No 12 is the highest and has the largest distance to the central axis). The polynomials that fit the experimental data are inserted.

The highest tritium activity is found for the pellets that are located close to Be blocks. This tendency is expected, and also a smooth behaviour with a minimum in between. Therefore, the measured values for each position (stack) were fitted with polynomials of second order. They should be used for comparisons with calculated values. The 95% confidence interval obtained is sufficiently small for analysing the tritium production rate of the TBM mock-up with MCNP/EFF.



### Measurement of neutron and gamma-ray flux spectra

Flux spectra are the key for calculating nuclear parameters such nuclear heating, shielding, activation, breeding and radiation damage. In the present TBM mock-up experiment, the flux spectra are measured in the positions A and B of Fig. 1, mainly in order to test the shielding capability of the  $\text{Li}_2\text{CO}_3\text{-Be}$  block and to obtain information on the tritium breeding in the block in which the flux detectors are inserted.

In the Final Report on TW4-TTMN-002, D2, [2] it was concluded, that the flux spectra of the fast neutrons and of the  $\gamma$ -rays, which determine the tritium breeding on  $^7\text{Li}$  (and Be) and indicate the shielding performance, shall be measured with an NE213 spectrometer already used in previous neutronics experiments. The flux spectra of the slow neutrons, which determine the tritium breeding on  $^6\text{Li}$ , shall be measured with a pulsed neutron source and time-of-arrival (TOA) spectroscopy with a  $^3\text{He}$ - detector. This new method was demonstrated for a LiAl-Pb assembly [2], Fig. 3.

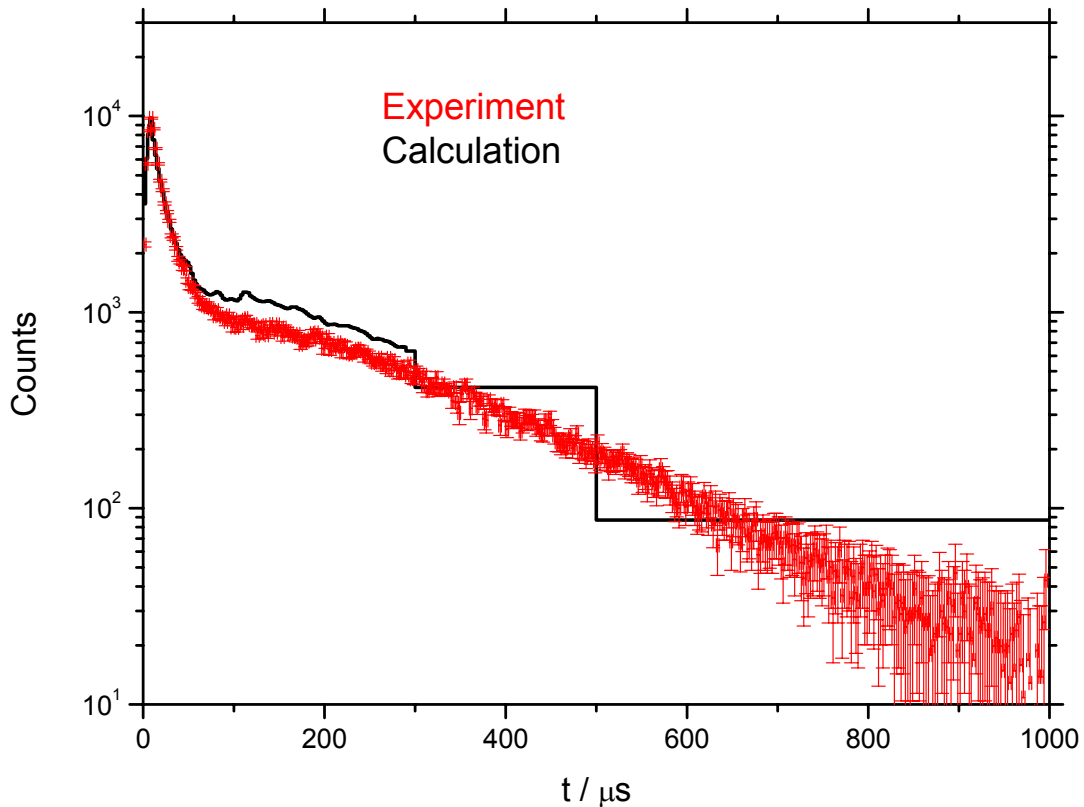


Fig. 3: Counts of the multi-channel scaler (channel width 2.5  $\mu\text{s}$ ), started with the neutron source pulse, at detector position A in the LiAl-Pb assembly in comparison to the expected distribution calculated with MCNP/FENDL.

The neutron generator of TUD can be operated in pulsed mode. Therefore, the mock-up was transferred from Frascati to Dresden in autumn this year. For the spectra measurements, an additional shielding block (right hand in Fig.1) filled with  $\text{Li}_2\text{CO}_3$ , was installed. In November, the measurement of the TOA spectra in the positions A and B was completed; the measurements with the NE213 spectrometer were just started.

### Staff:

H. Freiesleben  
A. Klix  
E. Pönitz  
I. Schäfer  
K. Seidel  
S. Unholzer

### Literature:

- [1] P. Batistoni, M. Angelone, P. Carconi, K. Ochiai, M. Pillon, I. Schäfer, K. Seidel, G. Zappa, International comparison of measuring techniques of tritium production for fusion neutronics experiments, Symposium on Fusion Technology, SOFT-23, September 20-24, 2004, Venice.
- [2] K. Seidel, H. Freiesleben, E. Pönitz and S. Unholzer, Preparation of measurement of neutron and gamma-ray flux spectra, Report TUD-IKTP/02-05, TU Dresden, May 2005.

## **TW5-TTMN-002 D 3**

### **Monte Carlo Based Transport and Sensitivity/Uncertainty Analysis of Neutron Flux Spectra and TPR Measured in the Ceramic Breeder of the TBM Mock-up**

The TBM mock-up neutronics experiment aims at validating the capability of the neutronics codes and nuclear data to predict the nuclear performance of the HCPB (Helium-Cooled Pebble Bed) test blanket module (TBM) in ITER in terms of important nuclear responses such as the tritium production. Measurements of the tritium generated during irradiation of the mock-up at the Frascati Neutron Generator (FNG) were performed by experimental teams of the Technical University Dresden (TUD) and ENEA Frasacti applying different measuring techniques. The objective of sub-task TW5-TTMN-002, D3, was to analyse the tritium production rate (TPR) measurements conducted by TUD (TTMN-002, Deliverable 2) and provide C/E (calculation/experiment) data and related uncertainty assessments using the same Monte Carlo codes (MCNP and MCSEN) and nuclear data that will be later used for the nuclear analysis of the TBM in ITER.

The HCPB TBM mock-up assembly consists of a box of SS-316 steel box with external dimensions of 31.0 cm (x) x 29.0 cm (y) x 31.0 cm (z). The box is filled with metallic beryllium and contains two double layers of breeder materials. The breeder layers have a height of 12 mm and are filled with  $\text{Li}_2\text{CO}_3$  at 7.5 at%  $^6\text{Li}$ . The mock-up is backed by a another box with external dimensions of 31.0 cm (x) x 14.8 cm (y) x 31.0 cm (z) filled with  $\text{Li}_2\text{CO}_3$ . A total of 8 stacks, including 12  $\text{Li}_2\text{CO}_3$  pellets each, were inserted in the front part of the mock-up for measuring the tritium generation in the breeder layers. The pellet stacks were placed at 4.2, 10.5, 16.8 and 23.1 cm from the front surface of the assembly, see Fig. 1. The TUD measurements of the tritium generation were performed for the upper row of  $\text{Li}_2\text{CO}_3$  pellets stacks labelled 1, 3, 5 and 7.

A detailed three-dimensional geometry model of the experimental set-up including neutron generator, HCPB mock-up with measurements equipments, assembly support and experimental hall was provided by ENEA Frasacti. Monte Carlo calculations were performed with the MCNP code for this model using nuclear data form the European Fusion File (EFF-3) and, for comparison, the Fusion Evaluated Nuclear Data Library (FENDL), versions 2.0 and 2.1 [1].

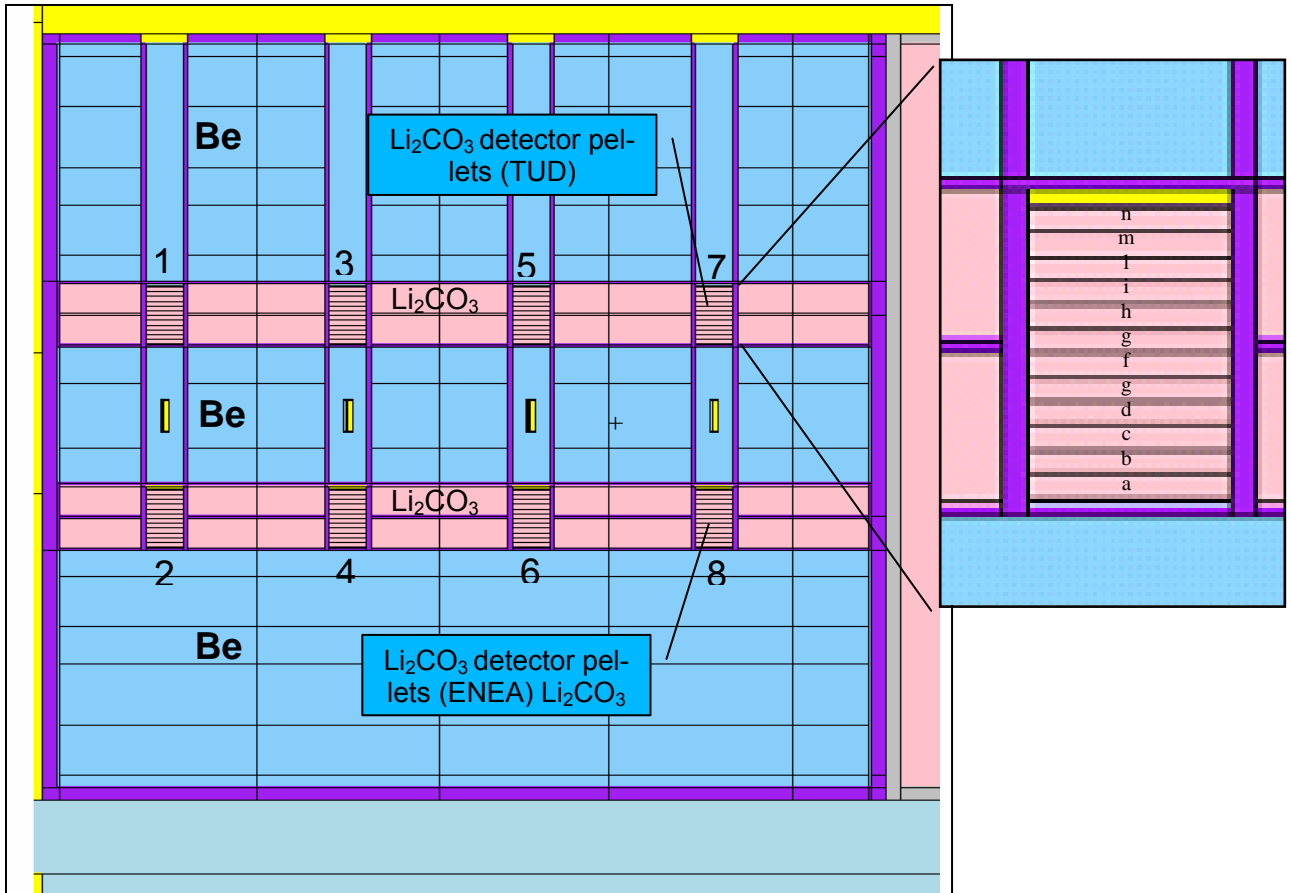


Fig. 1: HCPB TBM mock-up assembly with  $\text{Li}_2\text{CO}_3$  detector stack numbers indicated (vertical cross section of MCNP model). The insert on the right side of the figure shows an enlarged view of a pellet stack with pellet labels assigned.

The tritium production rates and the resulting specific activities were calculated for the pellets in the stacks # 1, 3, 5 and 7 after an irradiation by  $5.834 \cdot 10^{15}$  neutrons. Fig. 2 compares the calculated and measured tritium activities in terms of C/E (calculation/experiment) ratios. There is a trend for underestimating the measured tritium activities by 5 to 10% on average. The C/E ratios vary, however, to some extent across the pellet stack height and the radial depth of the stacks. In particular, higher C/E ratios are obtained for the pellets close to the surfaces of the breeder layers (i. e. near to the beryllium layers) where the contribution to the tritium production by  ${}^7\text{Li}$  is higher. Furthermore, the C/E ratios for stacks # 3, 5 in the central part of the mock-up are higher (and closer to unity) than those for stacks # 1, 7 at the front and rear side of the mock-up, respectively. No significantly different results were obtained when replacing the EFF-3 data by cross-sections from the FENDL-2.0 and 2.1 libraries.

These results indicate that design calculations for the tritium breeding ratio (TBR) of fusion power reactors employing a HCPB type breeder blanket are conservative. Thus an additional TBR margin is provided which allows compensating for potential other uncertainties.

Monte Carlo sensitivity calculations were performed with the MCSSEN code using the track length estimator for the pellet stacks #1, 3, 5 and 7 in the TBM mock-up. The sensitivities of the tritium production to the cross-sections of Be,  ${}^6\text{Li}$ , C and O were calculated. The tritium production from  ${}^6\text{Li}$  was shown to be mainly sensitive to the Be cross-sections for the elastic scattering (2% change per % change of cross-section) and the (n,2n) reaction (0.5-0.7 %/%). The tritium production from  ${}^7\text{Li}$ , which actually has minor importance for the tritium production in the HCPB blanket, is most sensitive to the  ${}^7\text{Li}(n,n't)$  reaction (about 1%/%). Reactions on the other involved nuclides (O, C) do not contribute at a significant level to the sensitivity.

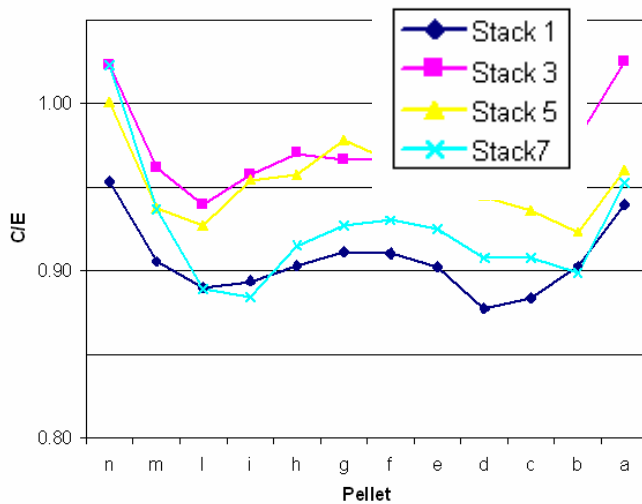


Fig. 2: Ratio of calculated (C) and experimental (E) tritium activities measured in the pellets of stack numbers 1, 3, 5, and 7 (TUD measurements) using EFF-3 cross-section data.

Sensitivity profiles were calculated with MCSEN in the VITAMIN-J 175 group structure to enable the calculation of data related uncertainties by making use of the covariance data provided in the same group structure. The co-variance data were taken from EFF ( $^9\text{Be}$ ,  $^6\text{Li}$ ,  $^{12}\text{C}$ ), FENDL-2 ( $^7\text{Li}$ ) and JENDL-3.3 ( $^{16}\text{O}$ ). The uncertainties calculated for the tritium generation due to the underlying cross-section uncertainties amount to about 2%. The total uncertainties including the data uncertainties, the statistical uncertainties of the Monte Carlo calculation and the experimental uncertainties are at a level of 6.5%.

#### Staff:

U. Fischer  
 D. Leichtle  
 R. Perel (Hebrew University of Jerusalem)  
 P. Pereslavitsev  
 S. P. Simakov

#### Literature:

- [1] U. Fischer, D. Leichtle, R. Perel, Monte Carlo based transport and sensitivity/uncertainty analyses of the Tritium production in the HCPB breeder blanket mock-up experiment, EFF-DOC- 954, NEA Data Bank, Paris, November 2005

### **TW5-TTMN-002 D 5 Pre- and Post-Analysis of the Validation Experiments for Ta Activation Cross Sections up to 55 MeV in an IFMIF – Like Neutron Spectrum**

In the frame of Task TW5-TMN-002, Deliverable 6, an activation experiment on Tantalum was performed at the cyclotron of the Nuclear Physics Institute (NPI), Řež, with the objective to provide the experimental data base for validating the activation cross-section data in the energy range relevant to the International Fusion Material Irradiation Facility (IFMIF) [1]. The objective of Task TTMN-002, Deliverable 5, conducted by FZK, was to perform the computational pre-analysis required for optimizing the experimental set-up and the measurements and to conduct the post-analysis to check and validate the high-energy cross-section data for neutron activation calculations. The computational analyses comprised transport calculations with the MCNPX Monte Carlo and SAND-II unfolding codes for the neutron source characterization and activation calculations with the ALARA inventory code [2] and cross-section from the Intermediate Energy Activation File IEAF-2001 [3] as well as with European Activation System EASY-2005 (FISPACT/EAF-2005) [4, 5]. Previous efforts to check and validate IEAF-2001 activation cross-section were performed for Eurofer-97, SS-316, F82H steels [6, 7] and Tungsten [8].

## Neutron source spectrum characterization

A 37 MeV proton beam impinging on a heavy water target has been used to produce a neutron spectrum up to 35 MeV similar to that of the IFMIF neutron source which employs the d-Li reaction. The objective of the present task was to reproduce the experimental neutron spectrum at the position where the Ta foil was irradiated. The MCNPX Monte Carlo code with the Los Alamos proton library LA-150h and in-built Bertini model was used to model the experimental set-up (Fig. 1) and calculate the differential neutron yield at the points of interest. These calculations were checked against measurements of the neutron spectrum at a large distance from the D<sub>2</sub>O target using a scintillation detector. As shown in Fig. 2, MCNPX calculations with LA-150h data fail to reproduce both the absolute yield and the energy distribution of the source neutrons. By investigating the reason for the observed large discrepancy, it was shown that the LA-150h library does not properly reproduce the double differential cross sections for the D(p,n)2p reaction.

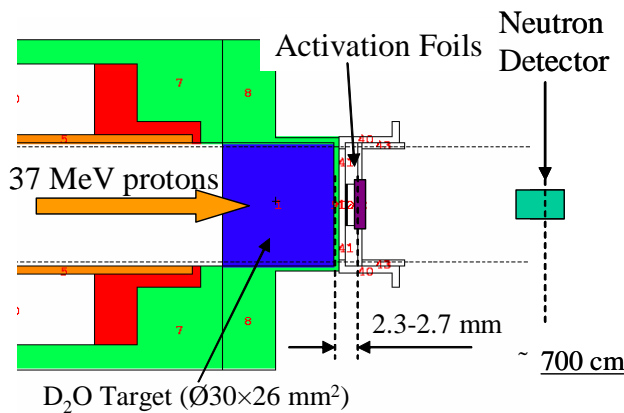


Fig. 1: MCNPX model of the experimental configuration with proton beam indicated.

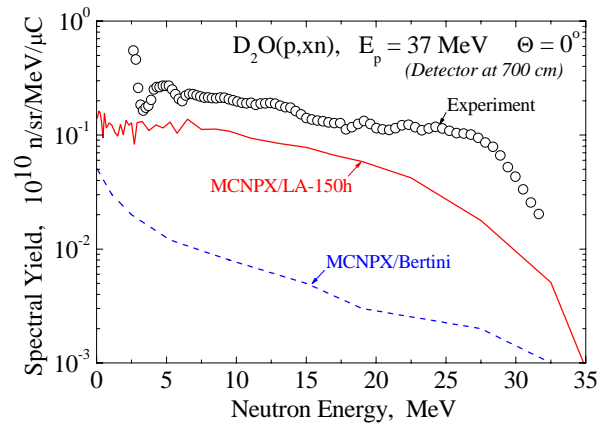


Fig. 2: p-D<sub>2</sub>O neutron spectrum at large distance from the heavy water target as measured and calculated by MCNPX.

To determine the neutron flux spectrum at the positions of the Ta sample the dosimetry foil activation method was applied. For this purpose a stack of pure metallic foils (Al, Au, Co, Fe, Lu, Nb, Rh, Y, Ti and Zr) was located behind the Ta sample and was simultaneously irradiated. The  $\gamma$ -ray activities detected in the dosimetry foils were used for the determination of the neutron flux spectrum by a modified version of the SAND-II code. To accomplish this procedure, the cross sections for the relevant dosimetry reactions need to be extended above 20 MeV.

The status of the neutron induced activation cross sections for elements selected for dosimetry has been analyzed by comparing available evaluations (EAF-2005, IRDF-2002, ENDF-B6.8, IAEA-2001) and experimental data paying special attention to the neutron energy range 20 to 35 MeV. The following reactions were finally selected for the unfolding of the measured neutron energy differential flux:  $^{27}\text{Al}(n,\alpha)^{24}\text{Na}$ ,  $^{197}\text{Au}(n,2n)^{196}\text{Au}$ ,  $^{197}\text{Au}(n,2n)^{196\text{m}}\text{Au}$ ,  $^{197}\text{Au}(n,3n)^{195}\text{Au}$ ,  $^{197}\text{Au}(n,4n)^{194}\text{Au}$ ,  $^{197}\text{Au}(n,\gamma)^{198}\text{Au}$ ,  $^{93}\text{Nb}(n,2n)^{92\text{m}}\text{Nb}$ ,  $^{93}\text{Nb}(n,\alpha)^{90\text{m}}\text{Y}$ ,  $^{59}\text{Co}(n,2n)^{58}\text{Co}$ ,  $^{59}\text{Co}(n,3n)^{57}\text{Co}$ ,  $^{59}\text{Co}(n,p)^{59}\text{Fe}$ ,  $^{59}\text{Co}(n,\alpha)^{56}\text{Mn}$ ,  $\text{Ti}(n,x)^{46}\text{Sc}$ ,  $\text{Ti}(n,x)^{48}\text{Sc}$ ,  $\text{Ti}(n,x)^{47}\text{Ca}$ ,  $\text{Ni}(n,x)^{57}\text{Co}$ ,  $\text{Ni}(n,x)^{58}\text{Co}$ ,  $\text{Ni}(n,x)^{60}\text{Co}$ ,  $\text{Fe}(n,x)^{54}\text{Mn}$ ,  $\text{Fe}(n,x)^{56}\text{Mn}$ ,  $\text{Fe}(n,x)^{51}\text{Cr}$ ,  $\text{Lu}(n,x)^{173}\text{Lu}$ ,  $\text{Lu}(n,x)^{174}\text{Lu}$ ,  $\text{Lu}(n,\gamma)^{177}\text{Lu}$ . The cross sections were found to be most reasonably represented in the EAF-2005 activation library. Fig. 3 shows the resulting neutron spectrum as obtained by the SAND-II unfolding code.

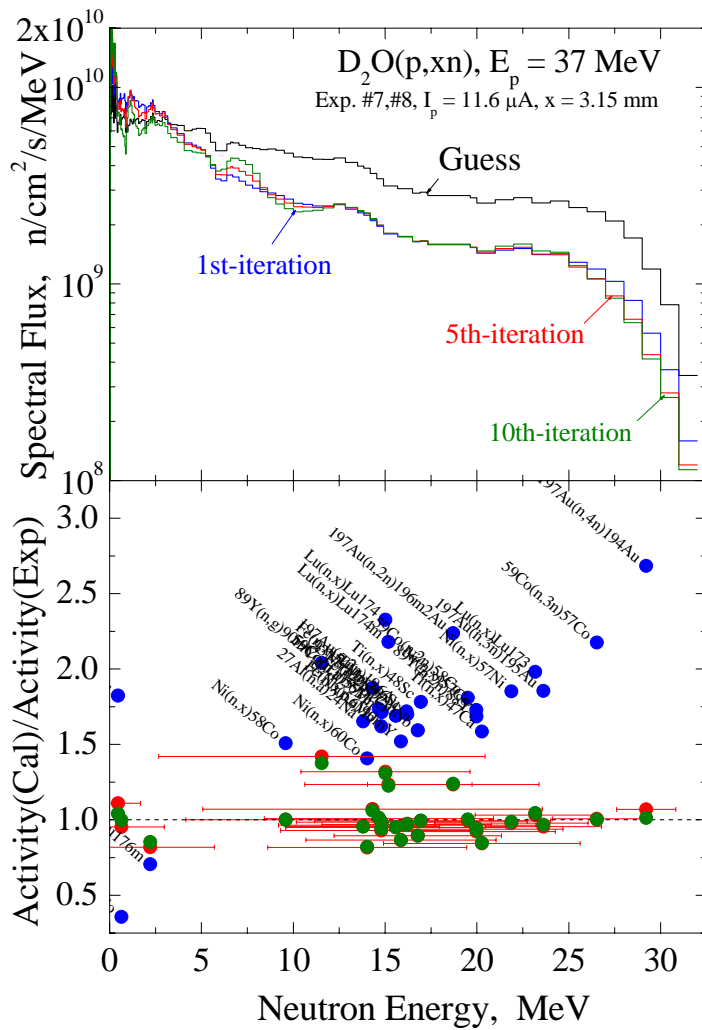


Fig. 3: Neutron flux and C/E ratios obtained from the  $\gamma$ -activities of dosimetry foils by the SAND-II code: black curve guess (input) spectrum used for de-convolution, coloured curves - after corresponding iterations.

In the experiment, the Ta foil (99.9%) has been irradiated for 12 hours at distances of 2.15 mm from the D<sub>2</sub>O target bottom. The irradiation history was derived from the proton beam current recorded as a function of time during the irradiations and was represented in the activation calculations by a five pulses approximation (Fig. 4). Re-normalization of the neutron flux from the dosimetry foils to the Ta spot has been performed by using the measured yield of <sup>24</sup>Na generated in the Al monitoring foils (Fig. 5).

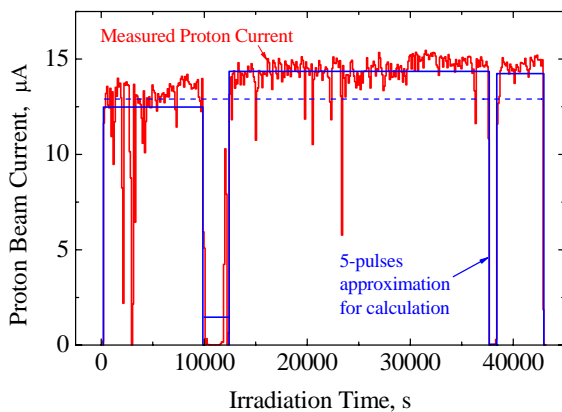


Fig. 4: The Ta irradiation time profile as measured and approximated for activation calculations.

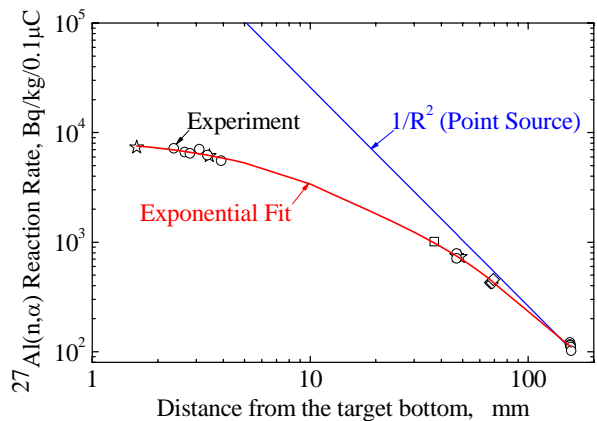


Fig. 5: <sup>27</sup>Al(n,α)<sup>24</sup>Na reaction rate as a function of distance from the D<sub>2</sub>O target bottom.

**Validation of the IEF-2001 and EAF-2005 activation cross-section data.**

The activation calculations have been performed with ALARA/IEAF-2001 and FISPACT/EAF-2005. Fig. 6 and Table 1 compare calculated and measured activities (in terms of C/E ratios) for the 8 radio-isotopes detected in the irradiated Ta sample.

It is seen that both activation libraries satisfactorily predict (within 20%) the yield of  $^{180}\text{Ta}$ , EAF-2005 additionally  $^{179}\text{nHf}$  and  $^{181}\text{Hf}$ , but both fail to reproduce the other radioactive inventories. Pathway analyses for the production of the specific radio-nuclides have been performed to identify the dominant reactions and the reasons of the observed discrepancies. The results are displayed in Table 1 showing that the generation of the radio-active products in each case is dominated by one single reaction.

Several examples of the relevant cross sections from IEF-2001 and EAF-2005 libraries are displayed in Figs. 7 to 9. It is noted that they essentially disagree. The cross sections have a maximum above 20 MeV where no measurements with mono energetic neutron sources are available.

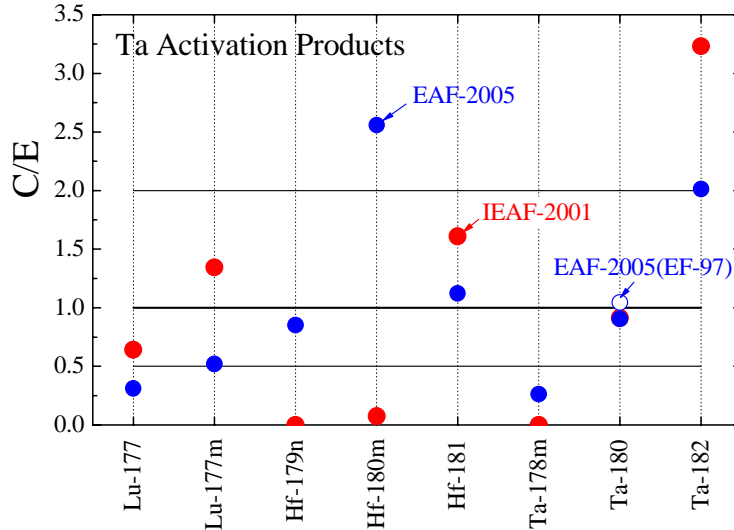


Fig. 6: C/E ratios for specific  $\gamma$ -activities induced in Tantalum calculated with EAF-2005 and IEF-2001 activation libraries.

Table 1: C/E ratios for Ta (weighted mean at several decay times) and dominant reactions.

Nuc- lide	$T_{1/2}$	Reaction Pathway	C/E	
			FISPACT/EAF-2005	ALARA/IEAF-2001
$^{177}\text{Lu}$	6.734 d	$^{181}\text{Ta}(n,n\alpha) - 99.94\%$	0.31	0.64
$^{177\text{m}}\text{Lu}$	160.4 d	$^{181}\text{Ta}(n,n\alpha) - 100\%$	0.52	1.34
$^{179\text{n}}\text{Hf}$	25.05 d	$^{181}\text{Ta}(n,t+) - 99.95\%$	0.85	6.7 E-6
$^{180\text{m}}\text{Hf}$	5.5 h	$^{181}\text{Ta}(n,d+) - 100\%$	2.56	0.07
$^{181}\text{Hf}$	42.39 d	$^{181}\text{Ta}(n,p) - 100\%$	1.12	1.61
$^{178\text{m}}\text{Ta}$	2.36 h	$^{181}\text{Ta}(n,4n) - 100\%$	0.26	3.6 E-7
$^{180}\text{Ta}$	8.152 h	$^{181}\text{Ta}(n,2n) - 99.97\%$	0.91	0.91
$^{182}\text{Ta}$	114.4 d	$^{181}\text{Ta}(n,\gamma) - 100\%$	2.01	3.23

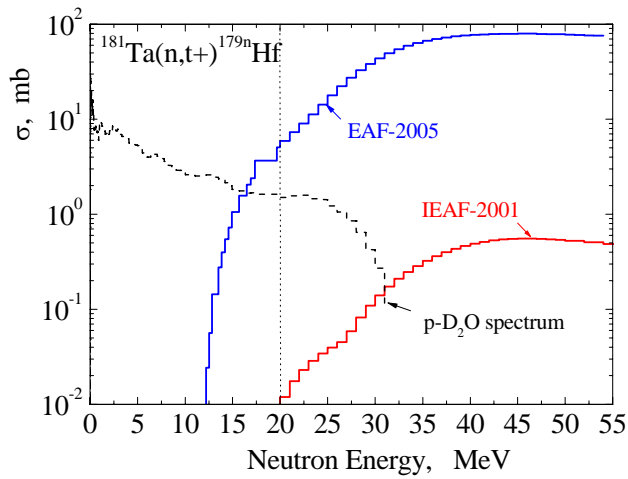


Fig. 7:  $^{181}\text{Ta}(n,t)^{179n}\text{Hf}$  reaction cross section as evaluated in IEAFF-2001 (red) and EAF-2005 (blue).

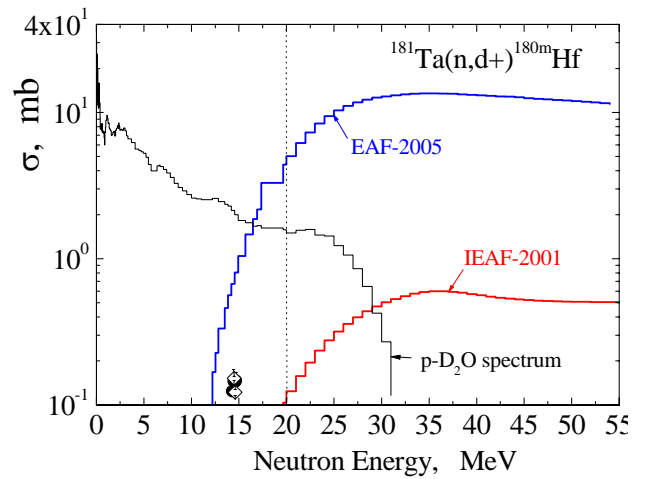


Fig. 8:  $^{181}\text{Ta}(n,d)^{180m}\text{Hf}$  reaction cross section as evaluated in IEAFF-2001 (red) and EAF-2005 (blue).

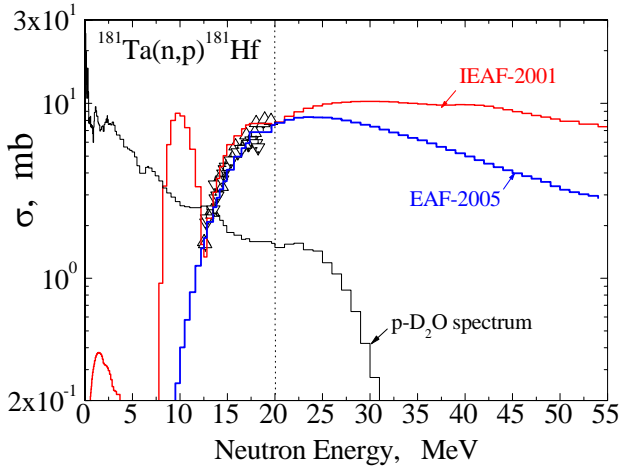


Fig. 9:  $^{181}\text{Ta}(n,p)^{181}\text{Hf}$  reaction cross section as evaluated in IEAFF-2001 (red) and EAF-2005 (blue).

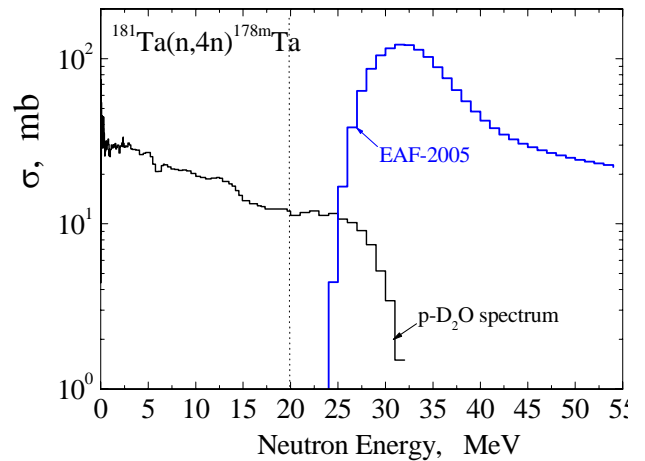


Fig. 10:  $^{181}\text{Ta}(n,4n)^{178m}\text{Ta}$  reaction cross section as evaluated in IEAFF-2001 (red) and EAF-2005 (blue).

Staff:

U. Fischer  
S. Simakov

NPI / Řež: P. Bém  
V. Burjan  
M. Götz  
M. Honusek  
V. Kroha  
J. Novák  
E. Šimečková

Literature:

- [1] P. Bém, V. Burjan, M. Götz, M. Honusek, U. Fischer, V. Kroha, J. Novák, S. Simakov and E. Šimečková., Activation experiment on tantalum in the NPI p-D2O neutron field, Report NPI ASCR Řež EXP(EFDA)-01/2005, November 2005.



- [2] P.P.H. Wilson, D.L. Henderson, "ALARA: Analytical and Laplacian Adaptive Radioactivity Analysis, Volume I, Technical Manual", University of Wisconsin, Report UWFD 1080, January 1998.
- [3] U. Fischer, D. Leichtle, U. v. Möllendorff et al., Intermediate Energy Activation File IEAF-2001, NEA data bank Programme Library Package NEA-1656/01 (2001), RSICC Oak Ridge, DLC-217/IEAF-2001 (2002).
- [4] R.A. Forrest, "The European Activation System: EASY-2005 Overview", Report UKAEA FUS 513 (January 2005).
- [5] R.A. Forrest, J. Kopecky and J-Ch.Sublet, "The European Activation File: EAF-2005 cross section library", Report UKAEA FUS 515 (January 2005).
- [6] P. Bém, V. Burjan, M. Götz, M. Honusek, U. Fischer, V. Kroha, U. von Möllendorff, J. Novák, S. Simakov and E. Šimečková, Activation of Eurofer in an IFMIF-like neutron field, Fusion Eng. and Des, 2005, in press.
- [7] S.P. Simakov, U. Fischer, U. v. Möllendorff, I. Schmuck, H. Tsige-Tamirat, P.P.H. Wilson, Validation Analyses of IEAF-2001 Activation Cross-Section Data for SS-316 and F82H Steels Irradiated in a White d-Li Neutron Field, Int. Conf. on Nuclear Data for Science and Technology, Santa Fe (2004), AIP Conference Proceedings, 769 (2005), p. 117; see also: EFF-DOC-922, NEA Data Bank, Paris, November 2004.
- [8] S.P. Simakov, U. Fischer, Bém, V. Burjan, M. Götz, M. Honusek, V. Kroha, J. Novák, E. Šimečková, Analysis of the NPI irradiation experiment for Tungsten activation cross-sections up to 35 MeV, Report EFF-DOC-913, NEA Data Bank, Paris, November 2004.

## **TW5-TTMN-002 D 7**

### **Validation Experiment of Gamma Activities of Tantalum Irradiated in Fusion Peak Neutron Field (TU Dresden)**

#### **Objectives**

The activation induced by neutrons in the materials of fusion power plant projects represents a central safety related topic. Reduced activation structural materials, such as EUROFER, with acceptable radiological safety performance and low long-term radiation level have been developed for first wall and breeding blankets [1].

The activity of the materials is mainly produced by neutrons of the fusion peak energy range, where the number of reaction channels is at maximum, and by thermal neutrons because for some reactions; the cross section is large in this energy region. EUROFER was already previously irradiated with 14 MeV neutrons, and the activation originating from reactions on the main constituents (Fe, Cr, Mn, V) and on some impurities have been investigated [2]. Contributions from Ta, that is an alloying constituent of EUROFER, could not be observed. Therefore, samples of pure Ta were irradiated with D-T neutrons in the present work, and the measured  $\gamma$ -activities were analysed with the European Activation System EASY [3].

#### **Experiment**

In order to determine the time region during which measurements of the neutron induced activities should be done after irradiation, a calculation with EASY was carried out. Tantalum was assumed to be irradiated at power plant conditions; this means at a flux of the 14 MeV neutrons corresponding to a power density of 1.0 MW/m<sup>2</sup>, for a period of one year. The results obtained for the contact dose rate as a function of the decay time after irradiation, are shown in Fig.1.

The dose rate is dominated up to the recycling limit of the material by the activities of <sup>182</sup>Ta, <sup>181</sup>Hf, <sup>180</sup>Ta, <sup>178</sup>Lu and <sup>178m</sup>Lu. <sup>179</sup>Ta shows a significant contribution only for the decay time range where the recycling limit is reached. The hands-on limit is determined by <sup>178m</sup>Hf and <sup>178n</sup>Hf.

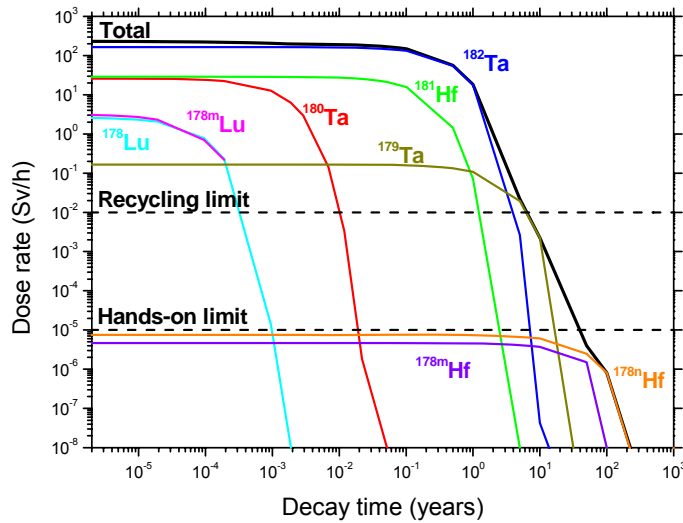


Fig. 1: Calculated total contact dose rate and contribution of the different nuclides after irradiation of Ta with fusion peak neutrons of 1.0 MW/m<sup>2</sup> power density for one year as a function of the decay time.

In order to investigate the major activities up to the recycling limit, two irradiations were performed. A short irradiation with  $\gamma$ -spectra taken at decay times in the range of minutes up to two hours and a longer irradiation with spectra taken at decay times from 4 hours up to 2 days. The irradiations of the samples were performed at a neutron generator of TUD. In the long irradiation, a total neutron fluence of  $7.86 \cdot 10^{11} \text{ cm}^{-2}$  was applied, and in the short one a fluence of  $1.96 \cdot 10^{11} \text{ cm}^{-2}$ . The fluence was determined by simultaneous activation of niobium foils and evaluating the activity induced by the  $^{93}\text{Nb}(n,2n)^{92\text{m}}\text{Nb}$  reaction.

The Ta samples had a purity of 99.95%, a diameter of 25 mm and thicknesses of 0.25 mm and 0.75 mm, respectively.

$\gamma$ -ray spectra were taken with an HPGe-spectrometer at a distance of 50 mm from the irradiated sample. The  $\gamma$ -activities identified by energy and half-life were used to determine the nuclide activities, using  $\gamma$ -yield data from EASY. The attenuation of the neutron and of the  $\gamma$ -ray fluxes in the sample as well as the geometry factors (neutron source – sample and sample –  $\gamma$ -ray detector) were determined by 3D Monte Carlo calculations.

## Results

The experimental data were analysed with the versions EASY-2003 and EASY-2005 of the European Activation System. Results of the EASY-2005 analyses are presented in Table 1 (those of the EASY-2003 analysis in Ref.[4]).

The uncertainty of the calculated activities ( $\Delta C/C$ ) includes both cross section and half-life errors as estimated by EASY. The uncertainties of the experimental values ( $\Delta E/E$ ) take into account possible errors of the  $\gamma$ -activity measurements (statistical uncertainty of the  $\gamma$ -ray counting, the uncertainty of the efficiency of the spectrometer, including the geometry factors), of the sample mass, of the  $\gamma$ -yield data and of the neutron flux monitoring.

The results have been discussed in detail, including recent cross section measurements for the neutron reactions of Table 1 and evaluated data of other libraries, in the final report of the subtask, where also the experiment is described more in detail [4].

Table 1: Results obtained for the activity of nuclides; nuclide identified, its half-life and  $\gamma$ -rays with yield data used to determine the activity, the neutron reaction producing the activity, the ratio of calculated-to-experimental activity (C/E) and the uncertainty of both calculated and experimental activity.

Nuclide	Half-life	E (keV)	Y (%)	Reaction	Contr. (%)	C/E	$\Delta C/C$ (%)	$\Delta E/E$ (%)
$^{178m}\text{Lu}$	23 min	325.5 426.4	94.1 96.9	$^{181}\text{Ta}(n,\gamma)$	100	0.92	20.0	10.3
$^{180m}\text{Hf}$	5.5 h	332.3 443.1	96.4 82.1	$^{181}\text{Ta}(n,d)$ + $^{181}\text{Ta}(n,np)$	99.9	4.82	191.	11.8
$^{181}\text{Hf}$	42.4 d	133 482	41.9 83.0	$^{181}\text{Ta}(n,p)$	99.9	1.01	20.0	13.1
$^{180}\text{Ta}$	8.08 h	103.6	0.78	$^{181}\text{Ta}(n,2n)$	100	1.19	15.0	25.7
$^{182}\text{Ta}$	114.7 d	1112 1189	0.349 0.164	$^{181}\text{Ta}(n,\gamma)$ $^{181}\text{Ta}(n,\gamma)\text{IT}$	93.7 6.3	1.18	43.6	10.0
$^{182n}\text{Ta}$	16 min	147 171.7	34.8 45.9	$^{181}\text{Ta}(n,\gamma)$	100	0.16	47.0	14.8

## Conclusions

For four of the dominant activities in the decay time range up to the recycling limit of Ta irradiated with fusion peak neutrons, the EASY-2005 data have a good quality. As the experimental uncertainties ( $\Delta E/E$  in Table 1) are for most of the activities smaller than the  $\Delta C/C$ , the measurements can contribute further to improve the EASY data base [5].

The  $^{182}\text{Ta}$  activities are in fusion reactors mainly produced by thermal neutrons (not by fusion peak neutrons) and should be validated in an appropriate neutron field.

From the present experiment it may be concluded that the recycling limit of Ta irradiated with fusion peak neutrons at power station conditions will be reached at decay times smaller than 10 years.

### Staff:

R. Eichin  
H. Freiesleben  
K. Seidel  
S. Unholzer

### Literature:

- [1] R. Andreani, E. Diegele, R. Laesser, B. van der Schaaf, The European integrated materials and technology programme in fusion, J. Nucl. Mater. 329-333 (2004) 20.

- [2] K. Seidel, R.A. Forrest, H. Freiesleben, V.D. Kovalchuk, D.V. Markovskij, D.V. Maximov, S. Unholzer, Experimental investigation of radioactivity induced in the fusion power plant structural material Eurofer and in other steels by D-T neutrons, *J. Nucl. Mater.* 307-311(2002) 1037.
- [3] R. A. Forrest, The European Activation File: EASY-2005 overview, Report Culham Science Centre, UKAEA FUS 513, 2005.
- [4] R. Eichin, R.A. Forrest, H. Freiesleben, K. Seidel, S. Unholzer, Validation experiment of  $\gamma$ -activities of Ta irradiated in fusion peak neutron field, Report TUD-IKTP/01-05, TU Dresden, May 2005.
- [5] R. A. Forrest, M. Pillon, U. von Möllendorff, K. Seidel, J. Kopecky, J-Ch. Sublet, Validation of EASY-2003 using integral measurements, Report UKAEA FUS 500, EURATOM/UKAEA Fusion Association, Culham, December 2003.

## **TW5-TTMN-002 D 9a**

### **Prepare for the Design of a HCLL Mock-up for Neutronics Studies: Pre-analysis on a Mock-up of the Test Blanket Module based on the HCLL Concept**

The neutronics mock-up experiment on the HCLL (Helium-Cooled Lithium Lead) blanket concept aims at validating the capability of the neutronics codes and nuclear data to predict the nuclear performance of the HCLL TBM in ITER in terms of important nuclear responses such as the neutron flux spectra, the tritium production and the nuclear heating. It is thus required to demonstrate that the essential nuclear features of the HCLL TBM can be replicated by the experiment. This can be achieved by analysing the TBM in ITER and using the results as reference for designing and optimising the TBM mock-up configuration.

Along this guideline, the objective of TW5-TTMN-002, D9a, was to provide the data, by means of pre-calculations, required for preparing the design of the HCLL TBM mock-up experiment. To this end, MCNP Monte Carlo calculations of the flux spectra and the tritium production were performed for the HCLL TBM in ITER. A suitable TBM model of the new modular HCLL breeder blanket was developed with the MCNP code and integrated into the (horizontal) test blanket port of the standard ITER 20° torus sector model (Fig. 1).

Calculations were performed with the MCNP5 Monte Carlo code [4] and nuclear cross-section data from the Fusion Evaluated Nuclear Data Library FENDL-2. Neutron flux spectra and tritium production rates were calculated in lithium lead as a function of the radial blanket depth. Two different Lithium enrichment levels were considered in the TBM calculations: 90 at%  $^6\text{Li}$  as assumed for the HCLL Demo blanket and 7.5 at%  $^6\text{Li}$  as will be used in the neutronics experiment. For enriched lithium, the tritium production is about 3.5 times higher than for natural lithium (7.5 %  $^6\text{Li}$ ). This results in a lower total neutron flux due to the enhanced neutron absorptions in  $^6\text{Li}$ .

In addition to the preparatory calculations of the HCLL TBM in ITER, first assessments were performed for the tritium production anticipated for the neutronics mock-up experiment at the Frascati Neutron Generator (FNG). To this end, a HCLL assembly was integrated into the 3d MCNP model of the FNG mock-up experiment. The dimensions of the HCLL mock-up were 34.5 cm (depth) x 45 cm (height) x 45 cm (width). Lithium lead with natural lithium isotope abundance was used in the calculations. Assuming an irradiation by  $5.834 \cdot 10^{15}$  neutrons resulted in a calculated total tritium activity of  $1.02 \cdot 10^5$  Bq for the HCLL mock-up. This activity is comparable to that of the HCPB mock-up under the same irradiation conditions. The local tritium production rates, however, will be significantly lower since tritium is produced over the entire assembly filled with lithium lead. Local tritium production rates were calculated for small  $\text{Li}_2\text{CO}_3$  probes placed at 5, 13, 21 and 29 cm from the front surface of the HCLL mock-up. They were shown to be lower than for the HCPB mock-up experiment by the factor 6, 17, 38 and 67, respectively. Thus, suitable measures must be provided (such as increased pellet sizes, increased neutron budget and improved measuring techniques) to allow the tritium measurement with sufficient accuracy.

**Specification of material composition for the model:**

- TBM FW: EUROFER with beryllium coating** ①
- TBM HCLL breeding unit: eutectic Pb-15.8 at.% Li** ②
- TBM case: EUROFER (68%) He-cooling** ③
- Manifold: EUROFER (60%), He-cooling** ④
- TBM frame: SS316(80 vol.%), H<sub>2</sub>O(20 vol.%)** ⑤
- Shield blanket: SS316(84v.%), H<sub>2</sub>O(16 vol.%)** ⑥
- SS-borated-2% ASTM-A887-89 (60 v. %), H<sub>2</sub>O(40v.%)** ⑦

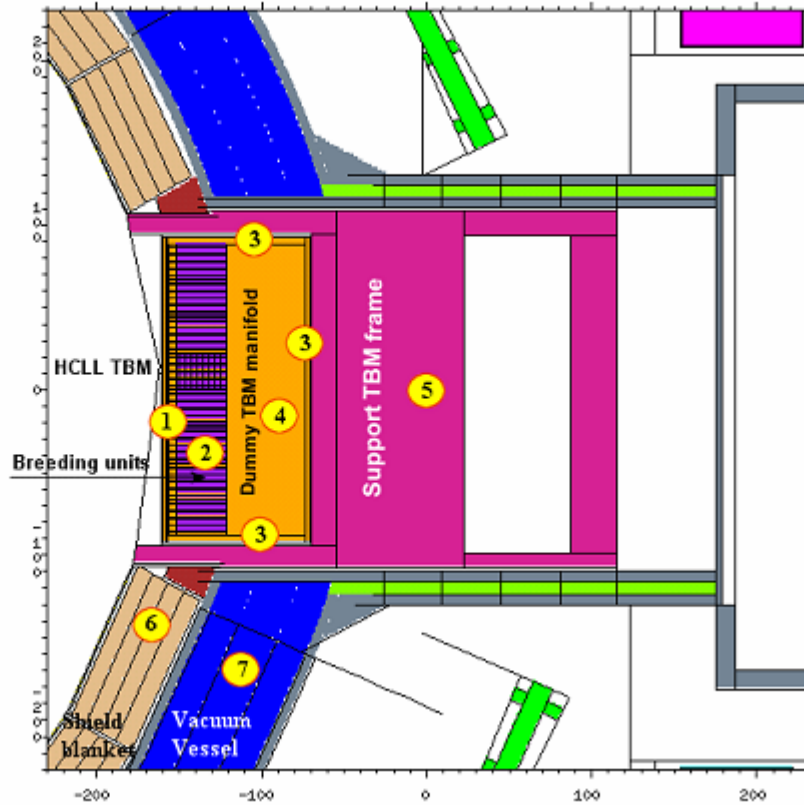


Fig. 1: MCNP model of ITER with HCLL TBM integrated in the equatorial port (vertical cut).

Staff:

U. Fischer  
A. Serikov



**Materials Development  
IFMIF**





**TTMI-001**  
**IFMIF – Accelerator Facilities**

**TW3-TTMI-001 D 4**  
**Numerical and Design Evaluation of the Potentiality of a novel Superconducting CH-Drift-Tube Linac. Test of Superconducting Prototype**

**Objectives**

The IFMIF linac must be capable to accelerate a cw beam of deuterons to a total energy of 40 MeV. Within the r.t. reference design, a 4-vane RFQ and a conventional drift tube linac (Alvarez-type) are foreseen. The rf frequency is 175 MHz. In general, it is advantageous to use superconducting linacs for cw operation. Therefore an alternative design has been developed consisting of an RFQ, one r.t. IH-structure and a chain of several s.c. CH-structures. The main part of the H-linac is superconducting, offering large aperture diameters up to 80 mm. This is especially important with respect to beam losses which must be extremely low to guarantee a hands-on maintenance system. Beam dynamics simulations showed that these requirements can be fulfilled by a superconducting CH-DTL.

The transverse focusing is provided by quadrupole triplet lenses between the superconducting cavities. Their alignment is easy and quite robust against any distortions. The coils will be mounted on magnetic steel yokes. The RF losses are about 120 kW in the r.t. IH-structure and below 200 W for the superconducting part. With an assumed RF amplifier efficiency of 60% and an efficiency of the cryo system of 0.3% a total plug power of about 260 kW per linac can be estimated (without RFQ and beam). The estimated plug power for the Alvarez solution (without RFQ and beam) is about 2 MW per linac which is about eight times higher than for the H-type linac.

Whereas many IH-structures have been built and operated, the CH-structure is a new type of drift tube structure which has been developed at the IAP in Frankfurt. Due to its mechanical rigidity at room temperature as well as superconducting cavities can be realised. A superconducting prototype has been designed, built and tested successfully. The tuning of the structure and the rf coupling has been investigated numerically and experimentally. A numerical mechanical analysis of the superconducting CH-prototype has been performed which showed the expected stiffness of the cavity.

**Status of the work before the time Period**

Different methods to couple the rf power to the CH-cavity have been investigated numerically and experimentally. For the experimental validation of the simulations a room temperature CH-copper model has been used. It has been shown that enough coupling strength can be provided with magnetic as well as with electric coupling. It has been decided to use an electric coupler for the first cryogenic tests of the CH-prototype with an external Q-value of  $2e8$ .

The superconducting CH-prototype has been built by the company ACCEL. A new tuning concept for superconducting multi-cell cavities has been demonstrated and it has been possible to obtain a flat field distribution which is required by the beam dynamics.

## Results and achievements obtained during the time period

After the delivery to Frankfurt the prototype has been conditioned at room temperature with our new 2 kW rf amplifier. An rf power of up to 300 W cw has been coupled into the cavity. In pulsed operation, rf pulses of up to 2 kW have been used. After the conditioning the pressure went down from  $6e-8$  mbar to  $2e-8$  mbar. Fig. 1 shows the experimental setup for the room temperature conditioning.

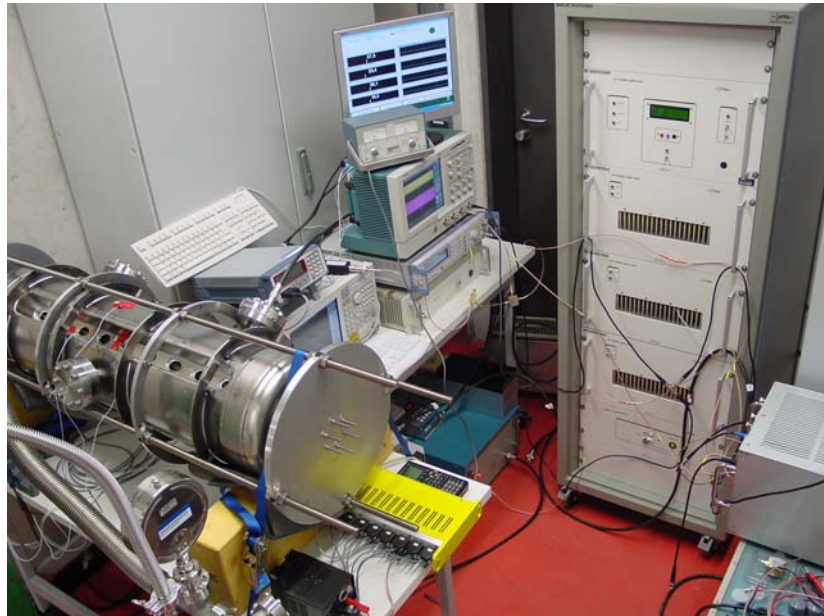


Fig.1: Experimental setup for the room temperature conditioning.

After the successful room temperature test the cavity has been prepared for the first cryogenic test at helium temperature. For this reason a new cryogenic RF laboratory has been established in Frankfurt.

It is equipped with:

- Class 10000 clean room
- Class 100 laminar flow box
- 3 m vertical bath cryostat
- Magnetic shielding
- 2 transport dewars for liquid helium
- 2 kW RF amplifier
- 50 W amplifier
- Helium recovery system
- RF control system
- Temperature measurement system



Fig. 2: View in the cryogenic RF laboratory in Frankfurt.

Figure 2 shows a view of the cryogenic laboratory with the rf system and figure 3 shows the CH-prototype with the position of 8 temperature sensors before inserting into the cryostat. The cavity has been pre-cooled with liquid nitrogen und than cooled down with liquid helium.

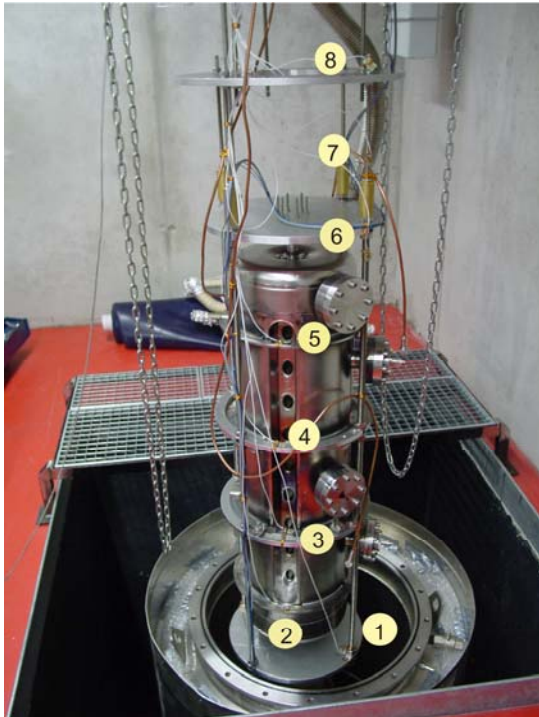


Fig. 3: The superconducting CH-prototype with 8 temperature sensors ready for the first cold test.

At a field level of about 40 kV/m, a multipacting barrier occurred. But this barrier could be processed within one hour without problems. Our experience with a large number of existing H-type structures showed that there is in general no problem with multipacting. As expected, multipacting is not a severe problem for superconducting CH-structures.

The control system which has been developed in Frankfurt worked very well. During the second day of the first cold test a maximum accelerating voltage (including the transit time factor) of about 3.54 MV has been reached in cw operation. The limitation in the test was field emission at electric surface peak fields of more than 20 MV/m. The maximum voltage corresponds to an electric surface peak field of 24 MV/m and a maximum magnetic peak field of 26 mT. The design gradient of the prototype cavity (3.2 MV/m) has been exceeded. The reached gradient with respect to the full cavity length was 3.4 MV/m and with respect to a length of  $n\beta\lambda/2=9.5\beta l$  was 4.45 MV/m. In pulsed operation these fields have been exceeded.

Figure 4 shows typical RF signals of the CH-prototype cavity and figure 5 shows the measured Q versus E curves.

The Q-value decreases typically for superconducting structures due to non Ohmic losses like field emission. The Q-value at low field was  $5e8$  which corresponds to a total surface resistance of 110 nW. The BSC value at 4.2K and the design frequency is 41 nW. Together with an additional resistance due to trapped magnetic flux of 4 nW, the surface residual resistance is 65 nW. The dissipated power at the design gradient was approximately 15W.

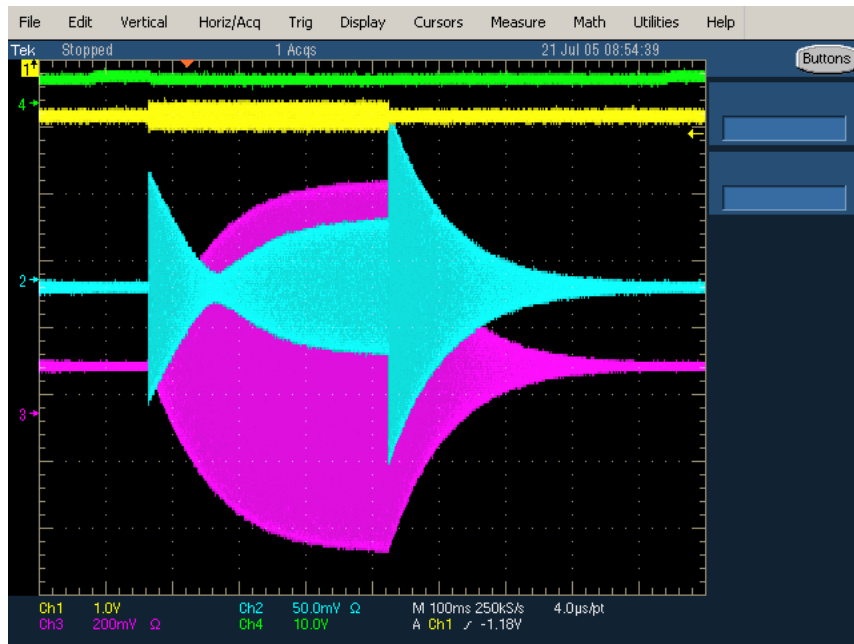


Fig. 4: RF signals during the first cryo test of the superconducting CH-prototype. Yellow=forwarded power, green=reflected power, purple=transmitted power.

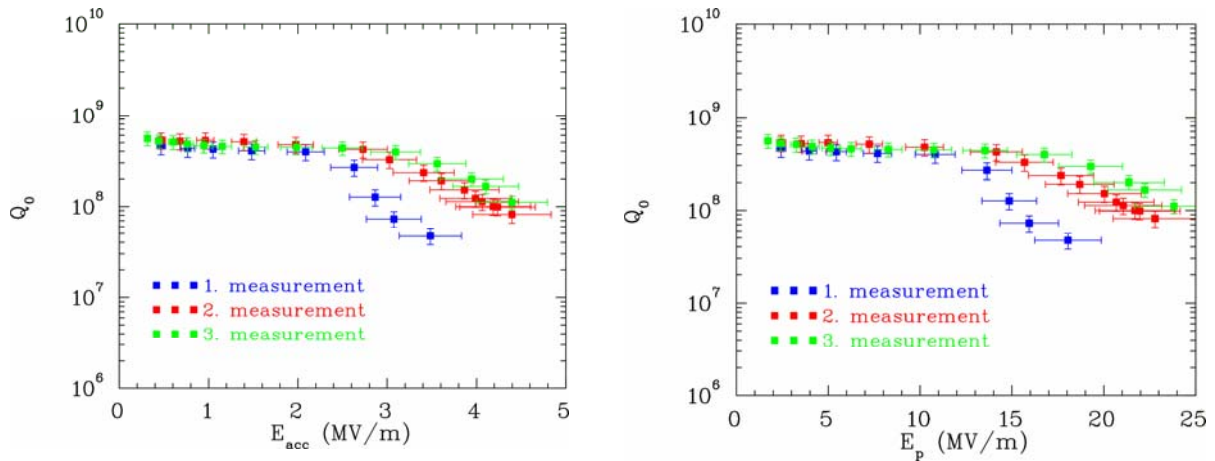


Fig. 5: Left: Q-value as function of the accelerating gradient based on an accelerating length of  $l=9.5\beta\lambda$ . Right: Q-value as a function of the corresponding maximum electric surface field. The operation mode was cw.

## Conclusion

A design layout for the IFMIF linac has been investigated which consists of a r.t. IH-DTL and several s.c. CH-structures. This H-mode linac fulfils the IFMIF requirements of very small losses to keep the hand-on maintainability. The main part of the linac is superconducting. This allows to use large aperture diameters und avoids thermal problems due to the cw operation. Additionally it reduces the operational costs significantly. A superconducting CH-prototype cavity has been designed, built and tested successfully to prove the excellent mechanical and electrical properties. Tuning and RF coupling have been demonstrated successfully. A cryogenic laboratory has been established to test the superconducting cavities. The first prototype has reached superconductivity without any problems. Multipacting was no problem. The Q-value at low field is  $5e8$ . The maximum voltage which has been reached in the first tests was 3.6 MV which exceeded the design value of 3.3 MV.

More tests are foreseen to test all rf properties and the reliability of the cavity. Depending on these results an additional surface preparation could be performed. The cavity will be prepared for cryogenic tests in a horizontal cryostat.

The successful test of the first superconducting CH-prototype is a solid base for the development of a 175 MHz superconducting CH-drift tube linac for IFMIF. Based on the experience of the design, production and test of the superconducting prototype the engineering for a CH-DTL could start immediately.

## Staff:

H. Klein  
 U. Ratzinger  
 H. Podlech  
 H. Deitinghoff  
 H. Liebermann  
 C. Commenda  
 S. Sauer  
 D. Bänsch  
 I. Müller

Johann Wolfgang Goethe-Universität  
 Institut für Angewandte Physik (IAP)  
 Robert-Mayer-Strasse 2-4  
 60486 Frankfurt am Main

Literature:

- [1] H. Podlech, H. Deitinghoff, H. Klein, H. Liebermann, U. Ratzinger, A. Sauer: Test of the Superconducting CH-Structure, Proceedings of the PAC2005, Knoxville, TN, USA, May 16-20 2005
- [2] H. Liebermann, H. Podlech, U. Ratzinger, A. Sauer: Coupling Methods for Superconducting CH-Cavities, Proceedings of the PAC2005, Knoxville, TN, USA, May 16-20 2005
- [3] H. Podlech, H. Liebermann, A. Sauer, U. Ratzinger: Development of Superconducting CH-Structures for Low and Medium Beta Beams, Proceedings of the ICFA-HB04, Bensheim, Germany, AIP Proceedings 773(2005)107-109

## **TTMI-003 IFMIF – Test Facility**

### **TW4-TTMI-003 D 2**

## **HFTM: Implementation of a Suitable Software Package to Link Thermal Hydraulics with Stress Analysis Codes; Exemplary Application of HFTM Reference Design**

### **Background and Objectives**

The design of the test facilities has been advanced significantly, comprising neutronics, thermal and mechanical analyses.

The objective of the subtask was to study the fluid-structure interaction by coupling a thermo-hydraulic code with a stress analysis code and to validate the procedures for temperature and heat transfer changes in connection with thermal deformations and stresses.

### **Implementation of the MPCCI for the coupling of the CFD code Star-CD with the stress analysis code Abaqus**

The operation conditions of the IFMIF/HFTM are very severe because significant mechanical and thermal loads can result in the deformation of the rig walls and, hence, result in the deformation of the cooling channels. The cooling channels of the IFMIF/HFTM have a rectangular cross section, being 0.5 mm wide on the short side of the rig and 1 mm wide on the long side of the rig. So, even a small deformation of the cooling channels results in a significant change in the channel cross section area, which, in its turn, would change the thermo-hydraulic characteristics of the HFTM.

The simulation of the thermal hydraulic process in the He coolant is provided by the CFD Code Star-CD. The calculated temperature field in the structure is used for the thermal stress analyses in the FEM Code Abaqus. Abaqus calculates stresses and deformations taking into account pressure forces on the channel surface and thermal loads in the structure. This 'one way' method cannot take into account the influence of the cooling channel deformation on the hydraulic properties. For the simulation of the interaction between the rig structure and He flow a tool, which allows the exchange of heat transfer data, forces and deformations, is required.

The Mpcci (Mesh-based parallel Code Coupling Interface) code has been developed at the Fraunhofer Institute SCAI in order to provide an application independent interface for the coupling of different simulation codes. Mpcci enables the exchange of data between meshes of two simulation codes in the coupling region. Additionally Mpcci needs code adapters, which establish a direct connection between the Mpcci and the codes themselves.

The Implementation of Mpcci is divided in two main parts:

1. Installation of Mpcci and adapters on the two OS platforms: Linux (Mpcci - Star-CD) and Aix (Mpcci - Abaqus).
2. Testing of the suitability of Mpcci for the analyses of the fluid structure interaction in the HFTM.

The Mpcci code is a new software and includes some parts, which are still under development. In spite of the vendor's support this fact makes the full implementation of the Mpcci very difficult. The Mpcci version 3.0 with adaptors for Star-CD and Abaqus has been available since January 2005. Problems with supporting of OS platforms and elimination of deficiencies in the Abaqus adaptor and in the Guide Interface Mpcci has changed the date of

Mpcci applicability to end of August 2005. Since then the code implementation went on rather successful till finally first data exchange and proper execution could be proved.

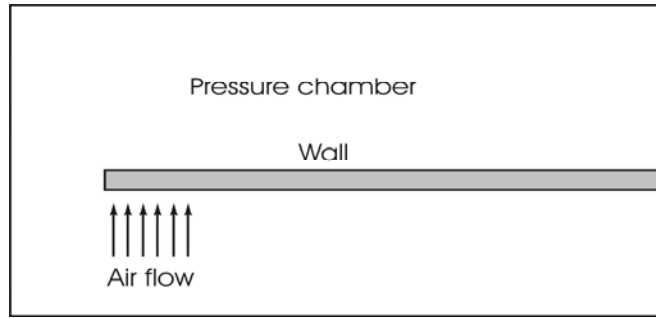


Fig 1a): Geometry of test case 1.

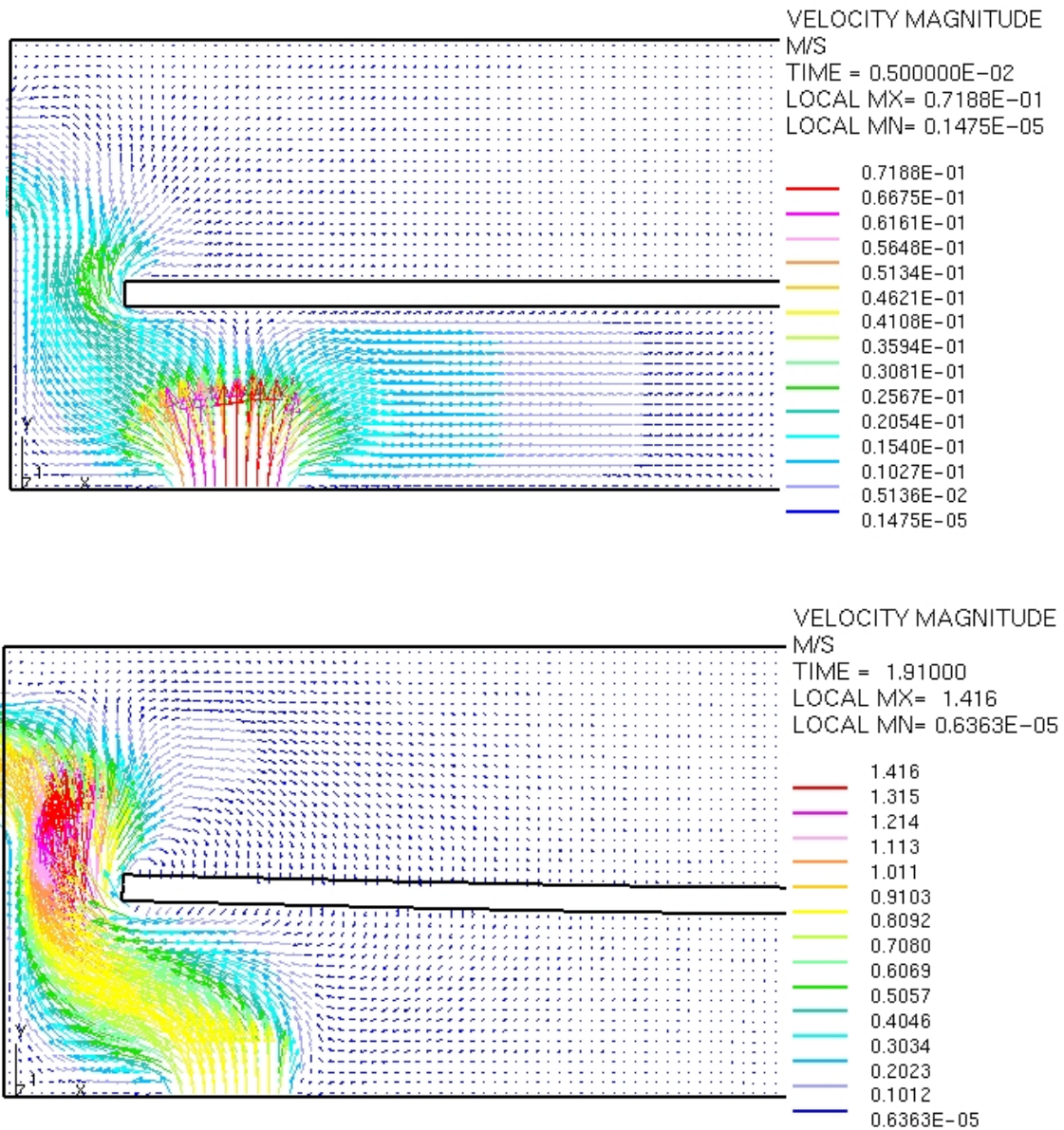


Fig. 1b): Local velocities at and 1.91s after onset of air flow in test case 1.

Because of its complexity Part 2 is divided into three test analyses, which will be completed by the end of 2005:

1. Testing the exchange of mechanical quantities (wall forces and deformations)
2. Testing the exchange of heat transfer quantities (wall temperature, heat flux, heat transfer coefficient)
3. Testing the exchange of mechanical and thermal quantities.

In the test case 1 (Fig. 1) the thin wall with one fixed edge deforms because of the air flow. Star CD sends via Mpcci calculated forces on the wall surface to the Abaqus. In the next step Abaqus sends calculated nodal positions on the coupling surface to the Star CD. The data are transferred after each iteration.

In the test case 2 the structure of the HFTM rig (container wall and capsule) has been modelled. The container wall and the rig outer surface form the cooling channel. The internal He cooling flow was modelled in Star-CD while the structural heating is simulated using Abaqus. Boundary conditions were set as follows: constant inner heat source in the structure  $10 \text{ W/cm}^3$ , temperature  $20^\circ\text{C}$  on inlet boundaries. For Star-CD the set of boundary conditions are: cooling gas – He (ideal gas), inlet velocity  $50 \text{ m/s}$ , inlet pressure  $2 \text{ bar}$ , inlet temperature  $20^\circ\text{C}$ . The exchanged quantities are the wall temperature and heat flux. Figures 3 and 4 show results of the coupled steady state calculation.

For test case 3 the boundary conditions for both codes are the same as in the test case 2. Additional exchange parameters are the wall forces calculated by Star-CD and deformation of the wall calculated by Abaqus. In the first step Star-CD sends the start values of the heat flux and forces on the channel wall to Abaqus. In the fully coupled thermal-stress analysis Abaqus calculates the temperature distribution, thermal deformations and stresses (Fig. 5). Calculated nodal displacements are transferred by Mpcci to Star-CD as new nodal coordinates. Star-CD calculates new thermal-hydraulic condition and sends the heat flux and wall forces to Abaqus.

First test runs show that in contrast to the case 2 calculations performed as steady state analysis are not stable and have a poor convergence. Non realistic temperature distribution at the beginning of calculation can lead to wrong thermal stresses and deformations in the channel structure, which makes unstable or break the calculation processes. The transient solution is more time consuming and needs an accurate time coordination between the codes.

The strategy for the transient analyses which can accelerate the calculation and improve the results accuracy is under development.

In spite of the installation problems with the performed test calculations indicate that Mpcci is in principle suitable for the coupled thermal hydraulic and stress analyses of the HFTM. In 2006 the coupled thermal hydraulic and stress analyses of the HFTM container with rigs and lateral reflectors will be performed.



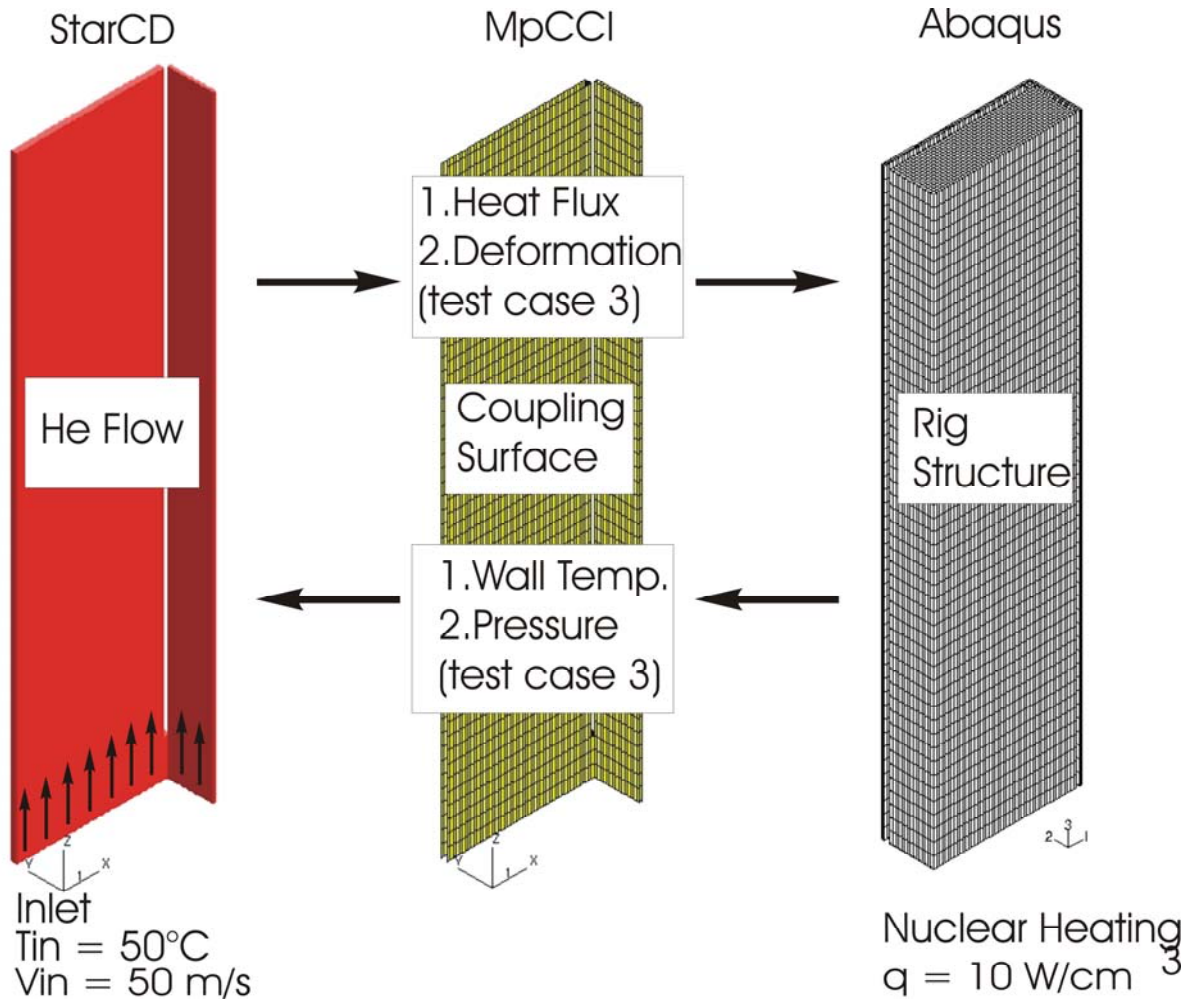


Fig. 2: Schematics for test cases 2 and 3.

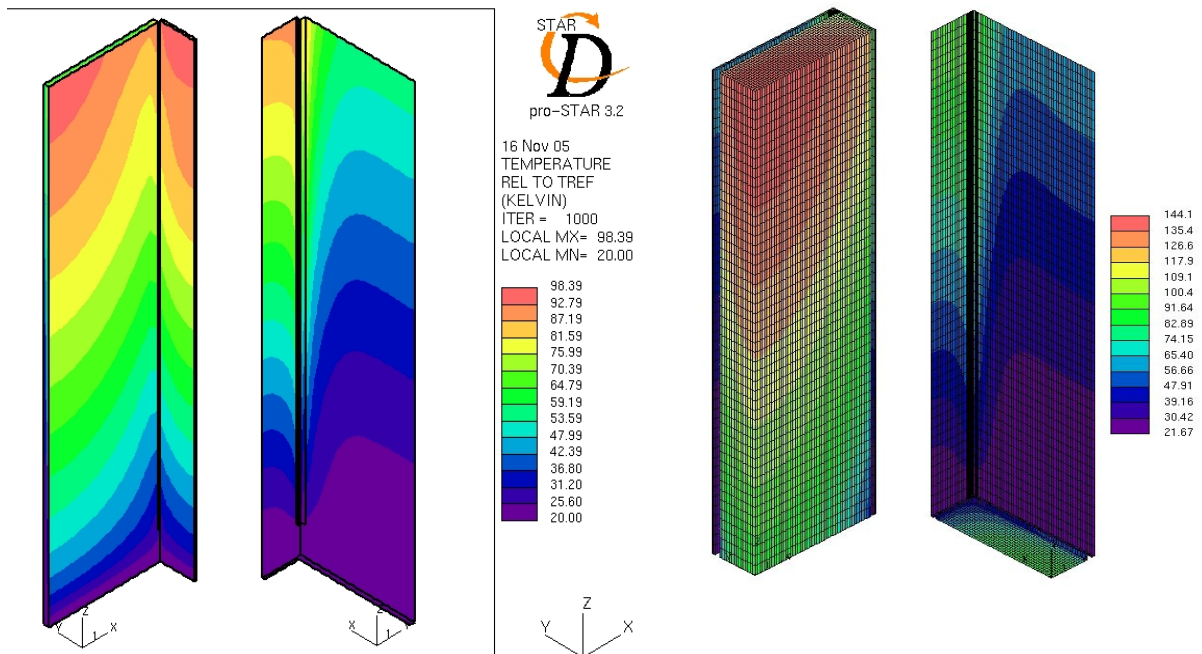


Fig. 3: Test case 2. Temperature profiles in the He flow calculated in Star CD.

Fig. 4: Test case 2. Temperature distribution in the Rig structure calculated with Abaqus:

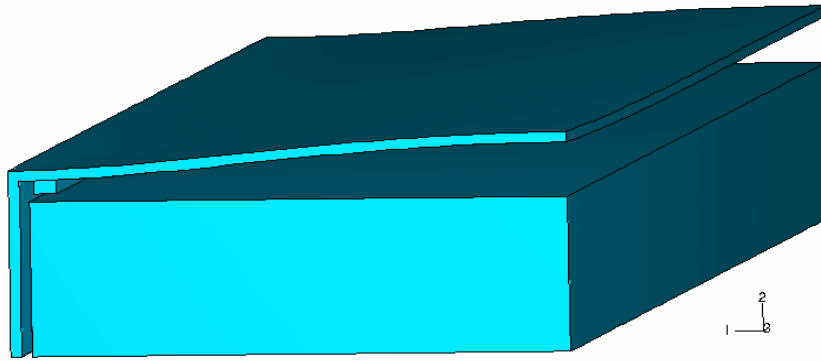


Fig. 5: Test case 3. Deformation of the rig structure by a fluid pressure of 3bar calculated with Abaqus (plotted with a magnification factor of 2).

Staff:

B: Dolensky  
S. Gordeev  
V. Heinzel

## TW4-TTMI-003 D 7 HFTM Component Manufacturing, Up-grading of the Helium-Loop

### Background and Objectives

For the generation of a materials database, definition of engineering rules and verification of materials performance in future fusion power reactors the IFMIF d-Li neutron source is accepted as the most promising irradiation facility. With IFMIF a fusion relevant radiation environment with accelerated testing could be provided.

The design of the test facilities has been advanced significantly, comprising neutronics, thermal and mechanical analyses.

The objective of the subtask was to finish the construction of the HFTM and to manufacture a triple heater capsule, a container and one 3-rig-compartment and to test the thermo-hydraulics in an upgraded Helium-loop. Due to budget limitations, non-availability of a low-pressure, high mass flow Helium loop as well as interaction with Target Facilities and MFTM the objectives have been changed to aim at the experimentally feasible test of one rig only.

### Manufacturing for HFTM and ITHEX experiment

The construction and design analyses of the HFTM rigs concentrated on the experimental feasibility within the ITHEX loop. To this end, two different concepts have been developed and are being manufactured.

The first experiment will make use of an adjustable test section (0 to 4 mm) with a rectangular cooling channel in IFMIF-like geometry. Both sides of the channel will be heated and equipped with thermoelements for the measurements.

The second experiment is aimed to test a HFTM-compartment equipped with a fully instrumented and assembled rig and two heated dummy rigs in order to cope with the expected conditions for the cooling channels. 54 thermoelements are attached to the dummy rigs. An additional rig foreseen for other analyses like micro-tomography is manufactured as well, the completion is expected at the end of the year.

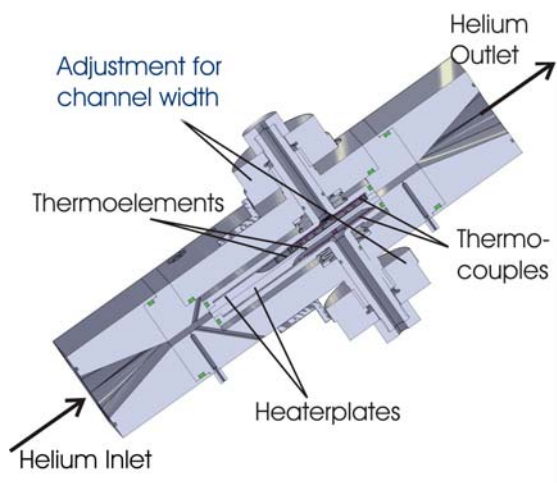


Fig. 1: CATIA drawing of the adjustable rectangular test-section for ITHEX.



Fig. 2: Parts for the ITHEX rectangular test-section: heater plates, thermocouples, and housing.

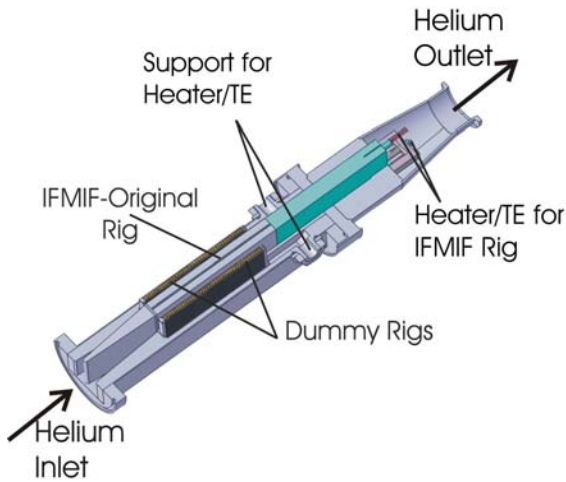


Fig. 3: CATIA drawing of the test-section comprising a HFTM rig accompanied by two heated dummy rigs.

### Upgrade and operation of the ITHEX coolant-gas loop

The ITHEX experimental facility provides a coolant gas circulating loop built from gas-tight components. The loop can be evacuated, and subsequently pressurized to a level of up to 0.4 MPa with gases from pressure bottles. The gas is circulated by two double stage sidechannel compressors controlled by frequency invertors.

The loop is instrumented with a coriolis massflow meter, thermocouples and Pt-100 resistive temperature sensors as well as pressure taps to determine the state of the working fluid at several locations. Since dilution by air has an impact on the data analysis, especially with helium gas as the working fluid, the gas purity is monitored by measuring the oxygen content. The fraction of diluting air is typically 100ppm, the limit for helium purity to accept an experiment for analysis has been chosen to be 1000ppm. The data analysis accounts for the measured impurity and calculates gas properties for the actual gas mixture.

The facility is further equipped with a data acquisition system to measure 36 thermocouple temperatures, a switching pressure scanner for 8 absolute pressures and 24 differential pressures and four adjustable direct current sources (300Vx10A) for electrical heaters.

Experiments were conducted employing an annular minichannel test section with a hydraulic diameter  $d_h=1.2\text{mm}$ . This test section is instrumented with electrical heaters and thermocouples within the cooled surfaces to measure the wall temperature profile in the thermal entrance section. The experimental conditions were varied in respect to the gas species ( $\text{N}_2$ , He), the inlet pressure  $p_1$ , the dimensionless heating span  $q^+$  and the Reynolds number  $Re$ , encompassing the range of parameters of operation of the IFMIF HFTM.

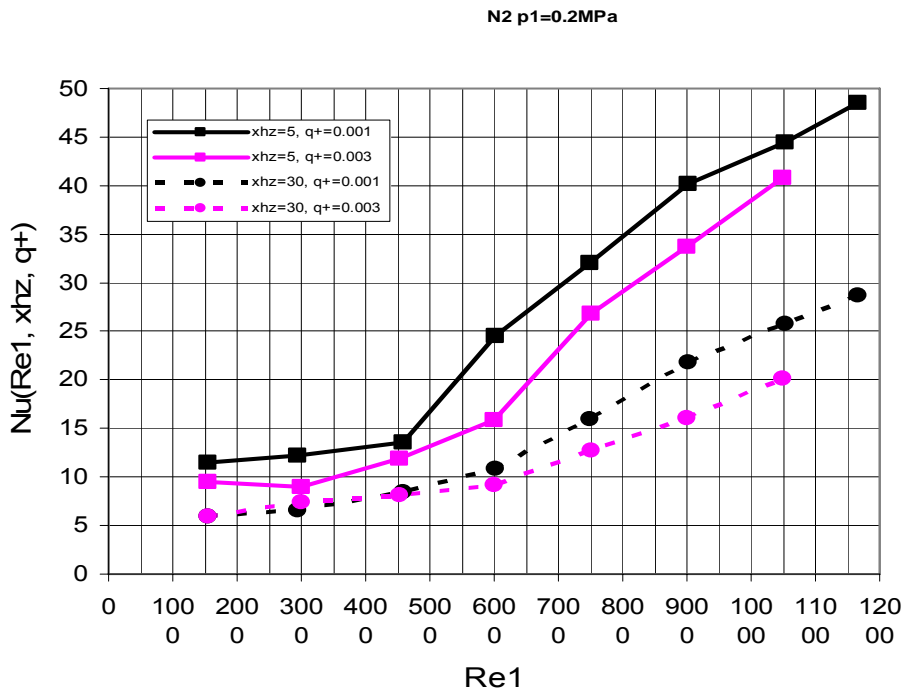


Fig. 4: Local Nusselt numbers derived from two ITHEX measurements with different dimensionless heating rates  $q^+$  plotted versus the entrance Reynolds number.

Local heat transfer coefficients have been evaluated from the experimental data. In fig. 4, local Nusselt numbers are plotted versus the channel entrance Reynolds number  $Re_1$  ( $Re$  before the heated section). The coordinate  $x_{hz}$  indicates the distance downstream of the beginning of the heated section of the surface. For the intermediate value of the dimensionless heating span  $q^+=0.001$ , a distinct increase of the heat transfer at the axial position  $x_{hz} = 5\text{mm}$  can be observed in the plot, indicating turbulent heat transfer for  $Re_1 > 4500$ . For the same axial position, but at a higher value of  $q^+=0.003$ , the level of the evaluated Nusselt numbers is generally lower, the transition appears less clear-cut and is delayed to a higher Reynolds number between 4500 and 6000. At a position further downstream at  $x_{hz}=30\text{mm}$ , the Nusselt numbers are lower, because of the growing thermal boundary layer. The difference between the high and the low heating rate can not be distinguished for low Reynolds numbers, the transition to turbulence is not clear-cut and appears near  $Re_1=6000$ .

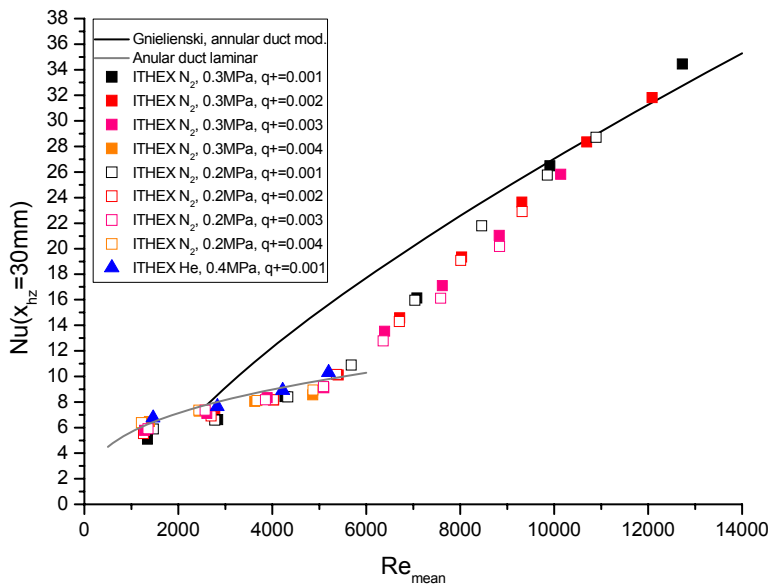


Fig. 5: Local Nusselt number in the thermally developed section for different experimental conditions plotted versus the local Reynolds number.

Nusselt numbers from experiments, as well as recommended correlations for the laminar and the turbulent Nusselt number, are plotted versus the local Reynolds number in fig. 5. The axial position considered here is  $x_{hz} = 30\text{mm}$ . The Nusselt number  $Re_x$ , calculated for the local state of the gas at the position considered, is lower than the entrance Reynolds number  $Re_1$ , because the viscosity increases with the rising temperature of the gas. The results of all experimental conditions compose to a narrow banded plot. Departure from the correlation for

laminar flow is observed for  $5000 < Re_x < 6000$ , the level of fully turbulent flow is reached for  $Re_x > 10000$ . Only a weak dependence of the Nusselt number on the heating rate  $q^+$  can be observed at  $x_{hz}=30\text{mm}$ . At high Reynolds numbers, the Nusselt number is higher for small values of  $q^+$ . The data is scattered for low Reynolds numbers. Experimental errors are due to heat losses to the environment, which are reduced when helium is employed, because the high heat conductivity of this gas effects a better heat transfer to the working fluid at the same Nusselt number than for the other gases.

Further experiments were conducted using a different assembly of the test section. By replacing the outer cylinder, the test section has been modified to allow the measurement of the incremental pressure drop in the channel. The pressure is measured every 5mm from the beginning of the channel using the pressure scanner. The outer wall of the annular flow domain, where the pressure taps have been drilled, can not be heated. Experiments were conducted either for adiabatic conditions, or with heating only of the inner surface of the annulus.

First departure of the friction factor derived from the adiabatic pressure loss measurements from the friction factor recommended for fully developed laminar flow in flat ducts has been observed at  $Re_1 = 4500$ . The value of the correlation for fully developed turbulent flow in flat ducts suggested by Beavers is met for  $Re_1 = 8500$  and exceeded for higher Reynolds numbers. The increased friction factor for Reynolds numbers  $Re_1 > 10000$  are attributed to the incipient effects of wall roughness.

It is concluded from the data for the adiabatic friction factor and the Nusselt number in the thermal entrance at low heating rates, that the critical Reynolds number for transition from laminar to turbulent flow is  $Re_c \approx 4500$  for the investigated annular minichannel geometry.

Further mechanisms, dependant on the dimensionless heating span  $q^+$ , deteriorate the turbulent heat transfer in the thermal entrance section, where the higher values of  $q^+$  shift the critical Reynolds number to higher values.

For the thermally developed flow ( $x_{hz} > 30\text{mm}$ ), the effective local Nusselt number can be calculated using the correlation for laminar flow in annular ducts up to  $Re = 6000$ . In the transitional range  $6000 < Re < 10000$ , the Nusselt number can be approximated by interpolating between the value of the correlation for laminar flow at  $Re = 6000$  and the value for the fully turbulent flow at  $Re = 10000$ . The influence of  $q^+$  is weak in the thermally developed flow, provided the effect of heating is already considered by calculating the Reynolds number for the local bulk temperature of the gas.

The ITHEX facility is also used to conduct experiments to study the developing flow field in flat minichannel testsections with Laser Doppler Anemometry (LDA). The scheduled measurements will investigate the development of turbulent flow in the hydraulic entrance section and allow direct comparison to numerical flow simulations.

To this end, a LDA system has been set up to satisfy the needs of spatial resolution imposed by the small length scales of minichannel flows. The setup of the LDA system is shown in fig. 6 . By employing a small focal length front lens, the measuring volume diameter has been reduced to  $25\mu\text{m}$ , which is sufficient to resolve the Kolmogorov length scale for  $Re=6000$ . An apparatus has been constructed to seed the flow with appropriate particles. These are selected according to their ability to follow the flow in the geometric deflection caused by the passage from the plenum to the minichannel, as well as to follow the turbulent motion of the flow at high frequency. The probe is positioned relative to the flow by a micron-resolving electronic positioning system. Preliminary measurements have been carried out to qualify the employed system, especially to test two different lens systems. The system will be employed to measure the flow field in flat channels with the gap width of  $1\text{mm}$ , which is the measure of the IFMIF HFTM cooling channels. Two different geometries of the entrance section will be studied.



Fig. 6: Setup of LDA system for minichannel measurements.

Staff:

F. Arbeiter  
B. Dolensky  
S. Gordeev  
V. Heinzel  
K.-H. Lang  
E. Stratmanns

Literature:

- [1] F. Arbeiter, T. Gehrlein, "LDA Messungen im Einlaufbereich Transitioneller Gasströmungen in flachen Minikanälen", in: Egbers, C. (ed.), Lasermethoden in der Strömungsmesstechnik : 13.Fachtagung, Cottbus, 6.-8.September 2005
- [2] F. Arbeiter, "Thermal-hydraulic investigations on minichannel cooling gas flows", Proceedings 6th World Conf. on Experimental Heat Transfer, Fluid Mechanics and Thermodynamics, April 2005: Kasagi, N. [ed.]

## TW4-TTMI-003 D 9 Evaluation and Validation of D-Li Cross Section Data

The objective of this sub-task was to improve the D-Li neutron source term calculation for IFMIF by updating the  $d+{}^{6,7}\text{Li}$  nuclear data evaluations and assessing the uncertainty of the neutron yields in IFMIF calculations with the McDeLicious Monte Carlo code [1]. A first set of such cross-section data was evaluated previously in a collaboration between FZK and INPE Obninsk [2]. Recent measurements of the double-differential  $d+{}^{6,7}\text{Li}$  cross-sections showed severe deficiencies of the neutron angular distributions and the inability to properly represent the population of residual nucleus excited levels. The measurements of the thick target neutron angle-energy spectra, on the other hand, revealed a significant overestimation of d-Li neutrons populating the low energy range. These results indicated the need to re-evaluate the  $d + {}^{6,7}\text{Li}$  cross-section data by applying a new methodology that takes into account all contributing nuclear processes such as compound nucleus and pre-equilibrium reactions, stripping and direct interactions.

### Data evaluation for the $d + \text{Li}$ reaction system up to 50 MeV

Many efforts were spent during the last decade to find and adjust appropriate nuclear models for the description of  $d + \text{Li}$  interactions in the energy range from a few to 50 MeV. The available  $d + \text{Li}$  data evaluation of Konobeev et al. [2] e. g. is based on the use of the intra-nuclear cascade model for non-elastic reactions, the Serber model for stripping processes and the diffraction approximation for elastic deuteron scattering. In the evaluation approach of this work, the following nuclear processes are assumed to take place when a deuteron collides with a lithium nucleus: elastic scattering, evaporation (i.e compound nucleus formation), pre-equilibrium processes, neutron/proton stripping and direct processes resulting in the excitation of specific residual nucleus levels. Fig. 1 shows the flowchart of the evaluation procedure.

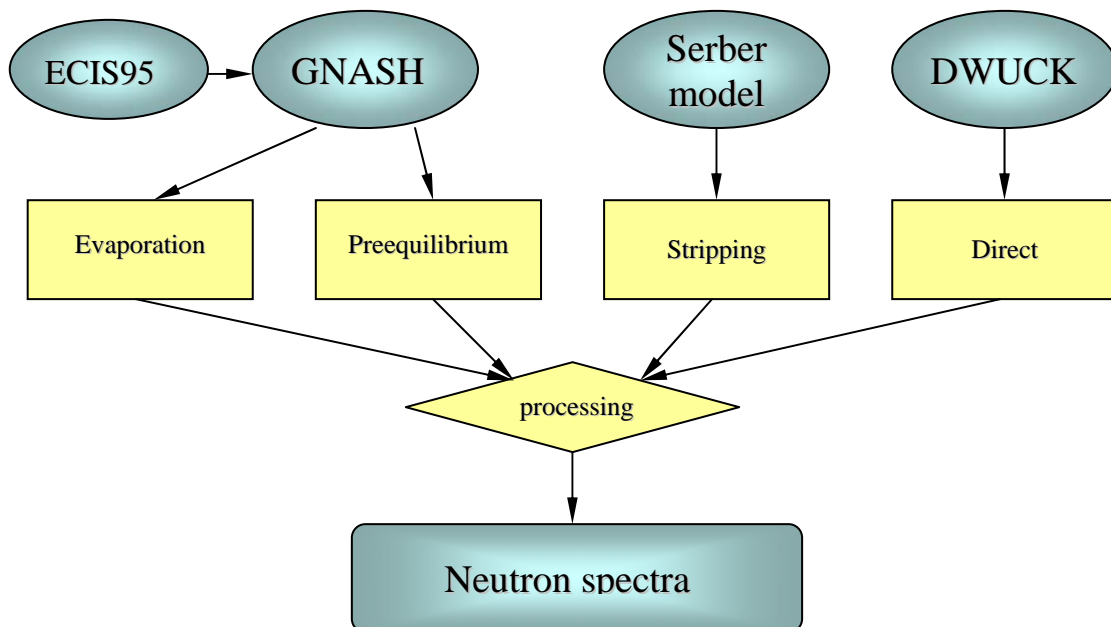


Fig. 1: Flowchart of the evaluation procedure.

For the deuteron elastic scattering, the diffraction approximation was proven to be inadequate, especially for the back angle scattering. As a suitable alternative, the use of a phenomenological optical model potential (OMP) was elaborated for  $d + {}^{6,7}\text{Li}$  interactions in the energy range up to 50 MeV. The resulting agreement of calculated angular distributions of elastically scattered deuterons with experimental data is very good thus suggesting the use of this OMP in the nuclear reaction cross section calculations.



Neutron emission is the most important reaction channel for applications to IFMIF. A proper neutron OMP must be available for the evaporation, pre-equilibrium and direct reaction models with neutrons in the entrance or exit channels. A combination of the Koning global neutron OMP and the Chiba local potential was shown to be suitable for neutron energies from 12 to 50 MeV and the energy range below 12 MeV, respectively. Slight modifications of the potentials were required to get good agreement of calculated and measured  $n + {}^9\text{Be}$  elastic scattering angular distributions. The Bechetti & Greenlees OMP was used for describing the emission of protons and tritons, and the Avrigeanu & Hodgson potential for the  $\alpha$  - particles.

The nuclear model calculations for the evaporation and pre-equilibrium reactions were performed with the GNASH code in combination with ECIS95. Double differential cross sections were produced using Kalbach systematics for angular distributions. The stripping processes were modelled on the basis of the Serber theory. Direct reactions were described with the DWUCK4 code which allows to calculate angular distributions for  $\text{Li}(d,n)$  reactions leading to the formation of the

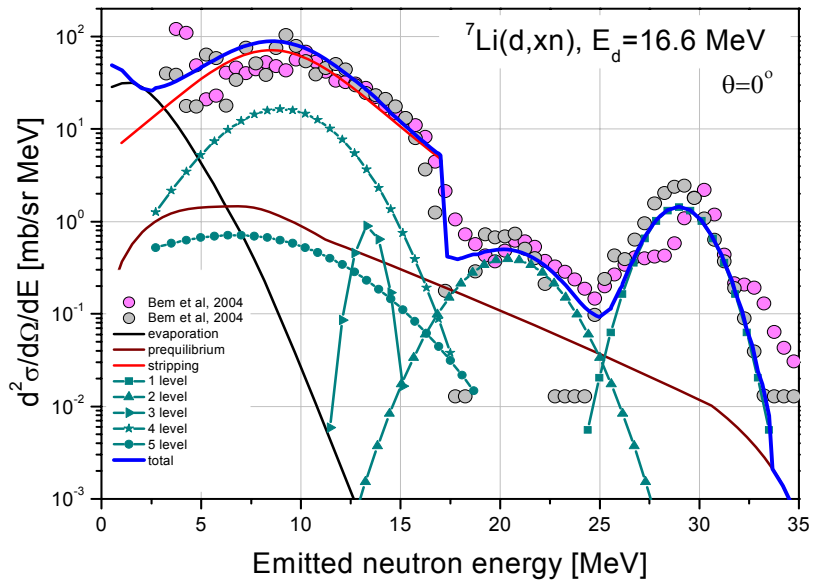


Fig. 2: Measured and evaluated  ${}^7\text{Li}(d,xn)$  double differential neutron emission cross section and its decomposition into reaction components for 16.6 MeV deuterons.

nucleus either in ground or excited states. The level scheme for  ${}^7\text{Li}$  isotope was represented by five excited levels, assuming that several levels with small width can be replaced by one “wide” artificial level. The neutron energy distributions for the direct reactions were calculated by spreading the cross section for a particular level over its excitation energy with Gaussian distribution, accounting for the level width. For 16.6 MeV incident deuterons, Fig. 2 shows the calculated double-differential neutron emission cross section and its breakdown into the different reaction components. It is revealed that the inclusion of direct interaction processes is essential for representing the structures of the emission cross-section at high neutron energies. This is due to the fact that the direct reaction mechanism is dominant for the emission of neutrons with energies above the deuteron incidence energy.

Results of the evaluated double-differential neutron emission cross sections and measured data are compared in Fig. 3 for deuteron incidence energies of 17 and 40 MeV.

The deuteron cross sections evaluated for  ${}^6\text{Li}$  and  ${}^7\text{Li}$  were stored on ENDF-6 formatted data files and processed into the ACE format for the McDeLicious Monte Carlo code by using a modified version of the NJOY-99 code system. The ENDF data files contain elastic scattering data (MT=2, MF=3 and MF=6) and secondary particle emission spectra (MT=5, MF=3 and MF=6) up to 50 MeV deuteron energy.

### Validation of the d-Li source term against thick lithium target neutron yields

A set of eleven independent experiments on thick lithium target yields is available for validation analyses including the recent measurements by P. Bém et al. at 16.3 and 17 MeV and M. Baba et al. at 25 and 40 MeV deuteron incidence energy. These experimental data sets

cover the deuteron energy range from 5 to 40 MeV and thus are well suited for benchmarking the IFMIF d-Li source term. The validation analyses were conducted on the basis of Monte Carlo calculations with the McDeLicious code which is capable of using the d-Li evaluated cross section data. For comparison, benchmark calculations were also performed with the semi-empirical d-Li reaction model of McDeLi the predecessor to McDeLicious, and the ISABEL intra-nuclear cascade model of the high energy particle Monte Carlo code MCNPX.

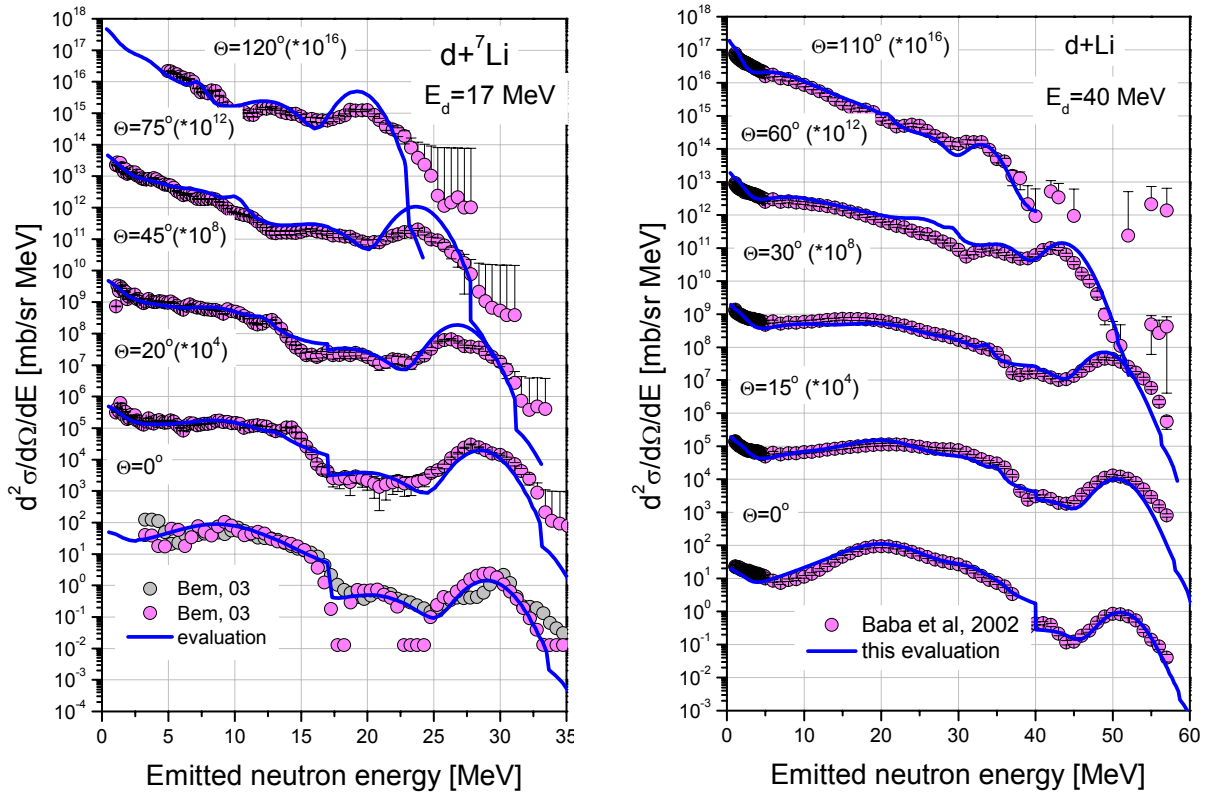


Fig. 3: Double differential neutron emission cross sections at 17 and 40 MeV deuteron incidence energy.

The analysis of the forward neutron yields from threshold up to 40 MeV deuteron energy, Fig. 4, shows that McDeLicious predicts the experimental results significantly better with the updated d-Li cross section data than with the original d-Li evaluation of the year 2001 [2]. The average deviation of calculated and measured neutron yield data was assessed to be around 10%. The McDeLi code shows worse agreement with the experimental neutron yields and is not capable to predict them below 15 MeV deuteron energy. The MCNPX code, on the other hand, underestimates the neutron yields by a factor 2 and thus fails to model this reaction with the required accuracy.

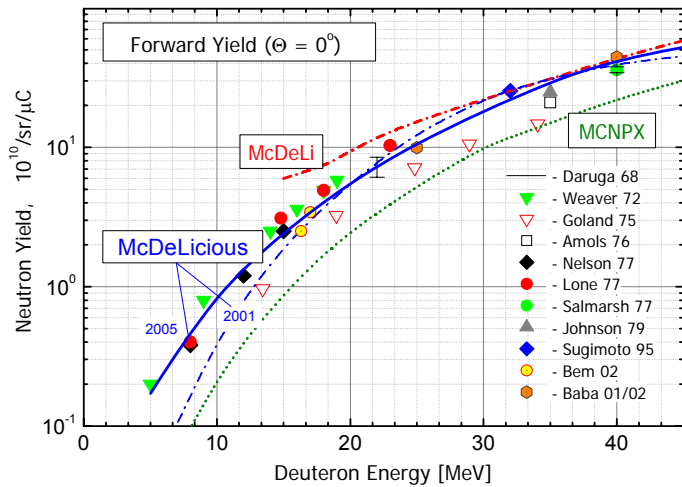


Fig. 4: Comparisons of measured and calculated thick lithium target forward neutron yields as function of deuteron incidence energy.

Measured double-differential neutron yields from thick lithium targets are available from the experiments of Baba et al (25 and 40 MeV deuteron incidence energy), Bem et al (17 MeV) and Sugimoto (32 MeV). The comparison of McDeLicious calculations with the measured energy distributions (double differential thick target neutron yields) demonstrates significant improvements achieved with the updated d-Li evaluation. As shown in Fig. 5 for the Baba experiments, both the absolute values and the shape of the energy spectra are reproduced with better accuracy. In particular it is seen that the humps in the high energy part of the neutron spectra, corresponding to the population of low lying states in  $^8\text{Be}$  due to the  $7\text{Li}(d,n)$  reaction, are well represented by the McDeLicious calculations with the newly evaluated d-Li cross sections data.

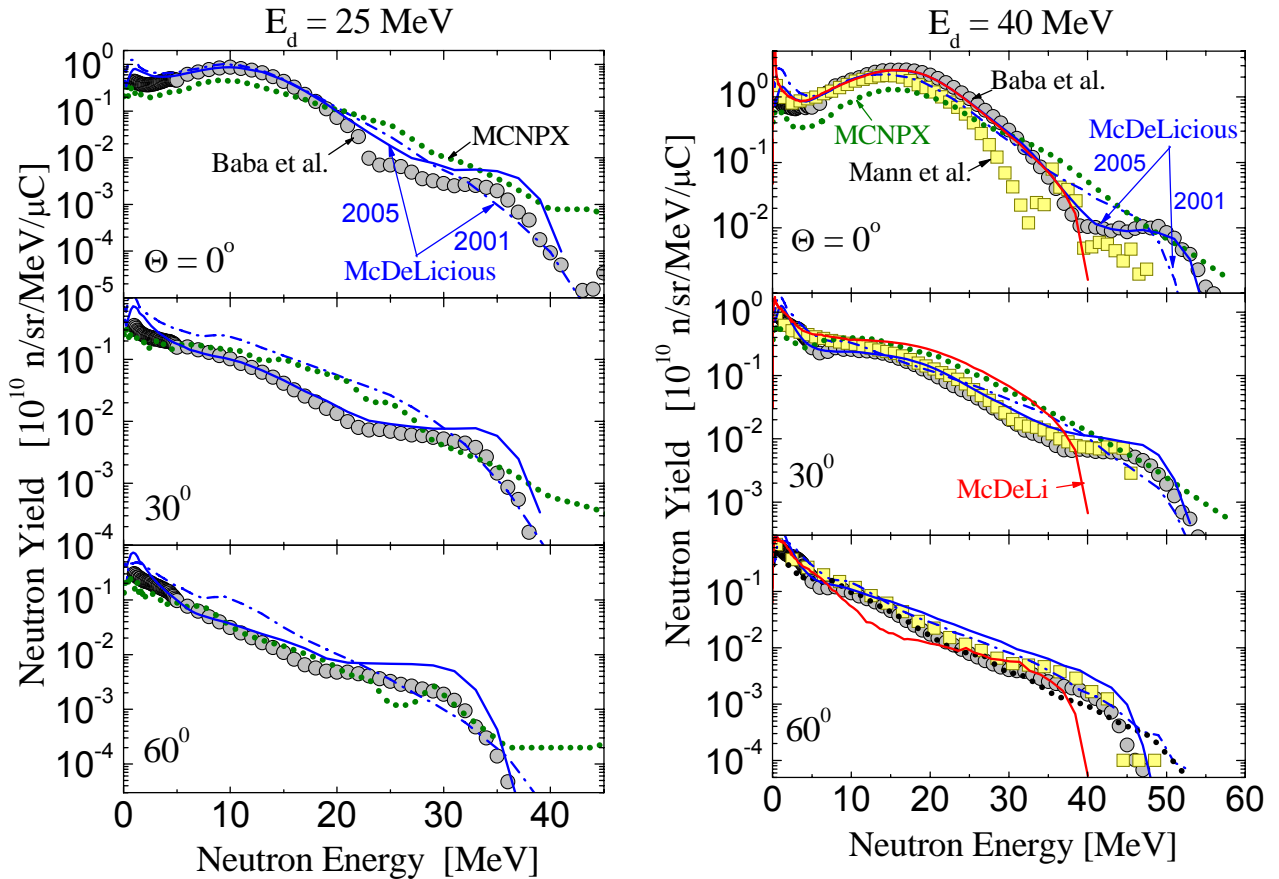


Fig. 5: Comparisons of calculated and measured thick lithium target forward neutron yield spectra at 25 and 40 MeV deuteron incidence energy.

Since IFMIF will be operated at 40 MeV deuteron energy and the material irradiation specimens will be located in the deuteron beam direction subjected to an angle of  $\pm 80^\circ$ , the accuracy of the thick Li target neutron yield data has a direct impact on the IFMIF irradiation parameters and the related uncertainties. It is therefore essential to arrive at a reliable and sound uncertainty assessment of the thick target neutron yields for IFMIF neutronics calculations. Such an assessment is possible on the basis of the new d-Li data evaluation and the recent measurement of M. Baba et al. performed at the Tohoku University using the AVF cyclotron and applying the time-of-flight (TOF) technique to obtain the neutron spectra at various angles between 0 and  $110^\circ$  at 40 MeV deuteron incidence energy. These measurements are considered state-of-the-art with the highest experimental accuracy currently achievable. Based on these measurements it is concluded that the double differential neutron yields at 40 MeV deuteron incidence energy can be calculated with a typical uncertainty of 20% when using the McDeLicious code with the newly evaluated d-Li cross section data sets.

Staff:

U. Fischer  
S. P. Simakov  
P. Pereslavtsev  
I. Schmuck

Literature:

- [1] S.P. Simakov, U. Fischer, U. von Möllendorff, I. Schmuck, A. Konobeev, P. Pereslavtsev, Advanced Monte Carlo Procedure for the D-Li Neutron Source Term Based on Evaluated Cross-Section Files, J. Nucl. Mat. 307-311 (2002) 1710-1714
- [2] A. Konobeyev, Yu. Korovin, P. Pereslavtsev, U. Fischer, U. von Möllendorff, Development of Methods for Calculation of Deuteron-Lithium and Neutron-Lithium Cross Sections for Energies up to 50 MeV, Nucl. Sci. Eng. 139 (2001) 1
- [3] U. Fischer, M. Avrigeanu, P. Pereslavtsev, S.P. Simakov, I. Schmuck, Evaluation and Validation of D-Li Cross-Section Data for the IFMIF Neutron Source Term Simulation, 12th Int. Conf. on Fusion Reactor Materials (ICFRM-12), December 4 – 9, 2005, Santa Barbara, California, USA

### TW5-TTMI-003 D 3

## Design of a Horseshoe Type Neutron Shielding Block Enveloping all Test Modules to Reduce further the Nuclear Inventory and the Gamma Dose Rate in the Rooms Surrounding the Test Cell

### Background and Objectives

The design of the test facilities has been advanced significantly, comprising neutronics, thermal and mechanical analyses.

The objective of the subtask was to assess the design of an additional shield surrounding the test modules in order to decrease radiation loads to the test cell walls. Based on nuclear calculations a thermo-hydraulic assessment including natural convection in the test cell should provide input for the further optimization of the shield layout.

### Nuclear heat generation in the IFMIF test cell walls

The geometry of the test cell including the horseshoe shielding used for nuclear heat calculations is shown in Fig. 1. This model was used to calculate the neutron and photon heating in the test cell walls using McDeLicious code for the IFMIF neutron source and transport simulation. For the further details see the task TW5-TTMI-003, Deliverable D 4.

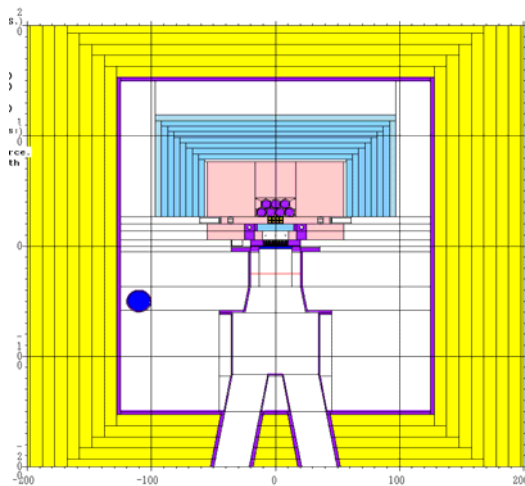


Fig. 1: Plan view of the IFMIF test cell with horseshoe neutron shielding block (shown in blue).

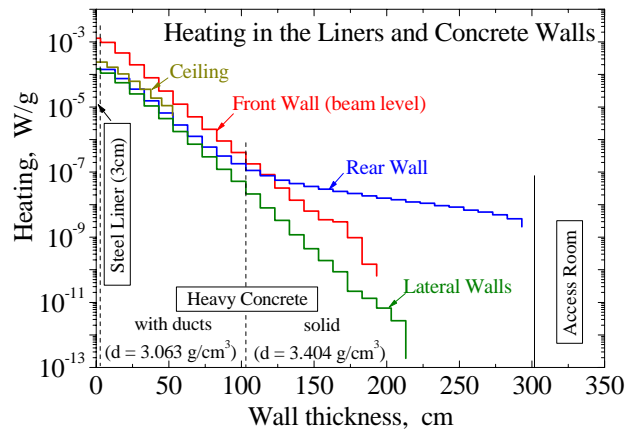


Fig. 2: The profile of nuclear heating in the IFMIF test cell walls due to the neutrons and photons.

Table 1 lists the results of calculations of nuclear heating in the steel liner (3 - 5 cm thick) and heavy concrete in the front (relative to the deuteron beam direction), lateral and rear walls of the test cell during IFMIF full power operation. It is seen that neutrons produce 30 kW of thermal energy, the main source being the Li loop (note that the deuteron beam generates 10 MW in the Li jet). The nuclear heat production in the steel liners and concrete walls is comparable. The calculations of heating density profile inside the walls (Fig. 2) has shown that it is an exponential function of the depth, that means the maximum thermal energy is released close to the surface of the walls.

Table 1: Nuclear Heating in the IFMIF Test Cell

Test Cell Component	Mass kg	Heat Density W/kg	Total Heat kW
<b>Wall Steel Liner: 3-5 cm thick (d = 7.6 g/cc)</b>			
Rear Wall	3444	0.15	0.51
Left Wall	3554	0.14	0.51
Right Wall	3554	0.15	0.53
Front Wall	1460	1.30	1.90
Floor	1932	0.27	4.41
<b>Sum over Liners</b>	<b>16906</b>		<b>6.48</b>
<b>Heavy Concrete Walls (d = 3.1 g/cc)</b>			
Front Wall	25634		3.994
Rear Wall	56149		1.415
Left Wall	68080		1.290
Right Wall	68080		1.352
Ceiling	15318		1.036
<b>Sum over Walls</b>	<b>217944</b>		<b>8.051</b>
<b>Li loop (d = 0.51 g/cc)</b>			
<b>Sum over Li-loop</b>	<b>1652</b>		<b>15.06</b>
<b>Energy Balance in the Test Cell :</b>			
<b>Total Heating in Cell by neutrons</b>			<b>29.59</b>
<b>d-Li neutron source power</b>			<b>131.00</b>
<b>Heating in Li target by deuterons</b>			<b>10000.00</b>

### Natural convection simulation with improved IFMIF Test Cell model

This work is carried out to estimate the natural convection heat transfer in the IFMIF test cell taking into account the nuclear heating of the surrounding walls and to find an acceptable solution for the shielding cooling strategy.

The volumetric heat deposition due to nuclear heating has been calculated as detailed in the preceding paragraph and is transferred with an interface user subroutine to the STAR-CD code used for thermo-hydraulic simulation. The concrete walls covered by the metal liner (3-5cm thick) from the inner side of the test cell are adopted for simulation. The cooling channels are foreseen in the concrete shielding to remove the nuclear heat. These channels are not simulated in detail, however, the following boundary conditions are applied: the external surfaces of the concrete shielding have a fixed given temperature, as well as the lithium loop elements. For the external surfaces of the concrete wall a temperature range of 30°C-50°C have been assumed, the lithium loop surfaces are kept at temperatures of 250°C and 300°C. Analyzing the volumetric heat deposition in the concrete walls, one can note that the intensity of the nuclear heating is decreased by more than one order of magnitude after a wall thickness of 30 cm, and is decreased by a factor of 20 – 30 after a wall thickness of 50 cm. Therefore, the calculation is done for concrete wall thicknesses of 30 cm and 50 cm.

Preliminary calculations show that the temperature of the concrete walls is unacceptable high if the lithium loop surfaces are not insulated even if the cooling surfaces in the concrete walls are located at the distance of 30 cm from the liner. The insulation layer (cellular glass type) of 50 mm thickness covering the hot surfaces results in significant decrease in the maximum temperature of the concrete shielding, but this temperature is still rather high.

To further decrease the concrete wall temperature a further variant of the cooling is proposed: the walls exposed to the highest heat load are cooled by two cooling surfaces located at different distance from the liner. The first cooling surface in the concrete (with the temperature of 30°C) is located in a depth of 10 cm from the liner and the second one (with the temperature of 50°C) is located at 30 cm from the liner for the wall-front-beam, upper-step-vertical and upper-step-horizontal walls (cf. fig. 3). With this option the temperature of the walls decreases significantly, but the maximum temperature of 100 °C is now observed in the ceiling and lower-step-horizontal and lower-step-vertical walls, which is still too high. In the next optimisation cooling surfaces are added in the lower-step-horizontal wall and partially in lower-step-vertical wall and ceiling. The results show that the maximum temperature of the concrete remains below 78°C (cf. fig. 3), which is acceptable. And finally, one more case is simulated with two cooling channels in the whole wall-front-beam, upper-step-vertical, upper-step-horizontal, lower-step-horizontal, lower-step-vertical walls and ceiling. The boundary conditions are the same as before. Different pressures of the helium in the test cell are also considered varying from 1 bar to 0.0001 bar. The typical results of velocity and temperature distribution are presented in fig. 4-5. The maximum temperature of the concrete wall does not exceed 80°C even at very low pressure. It should also be noted that the maximum temperature of the concrete is observed around the zones where the lithium loop tubes pass the concrete. To decrease the temperature in these zones the insulation thickness should be increased.

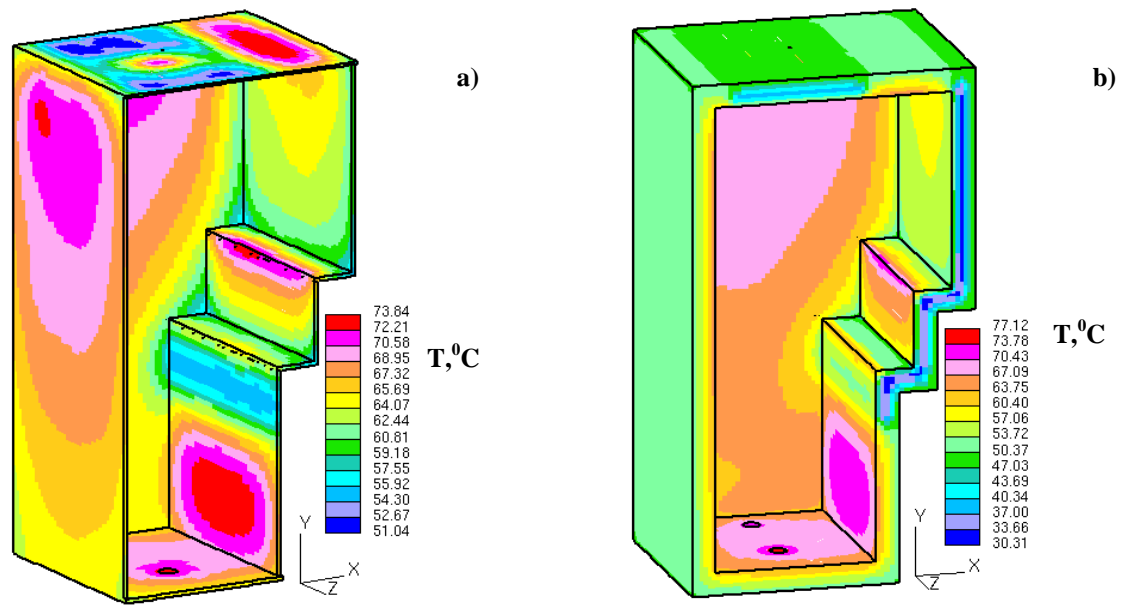


Fig. 3: Temperature distribution in the liner (a) and concrete (b) walls with two cooling surfaces in concrete walls located at 10 and 30 cm from the liner (in the wall-front-beam, upper-step-vertical, upper-step-horizontal, lower-step-horizontal and partially in lower-step-vertical walls and ceiling).

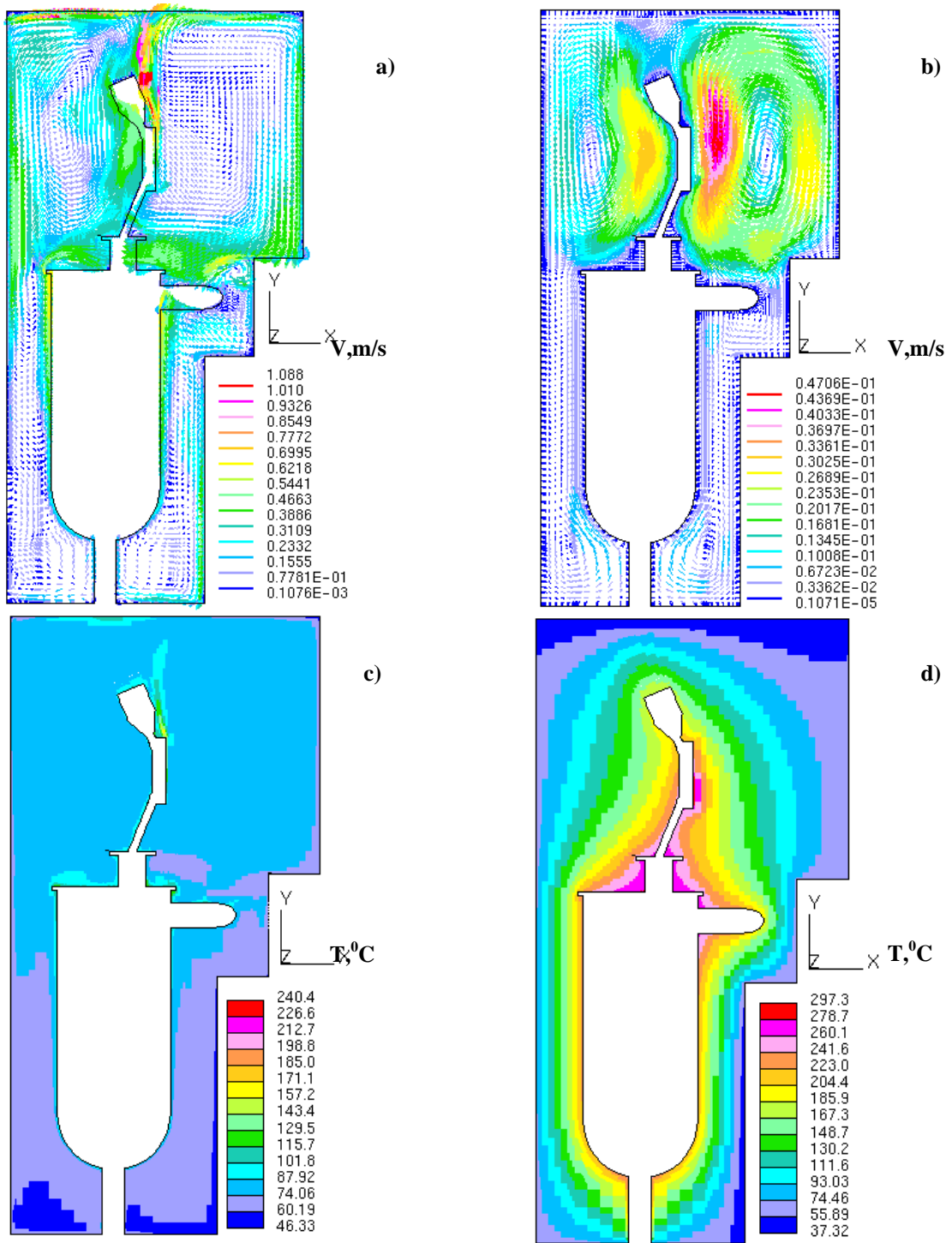


Fig. 4: Velocity (a, b) and temperature (c, d) distribution in the section of the test cell passing through the middle of the lithium tank. a, c – helium pressure of 1 bar ( $10^5$  Pa), b, d – helium pressure of 0.0001bar (10 Pa).



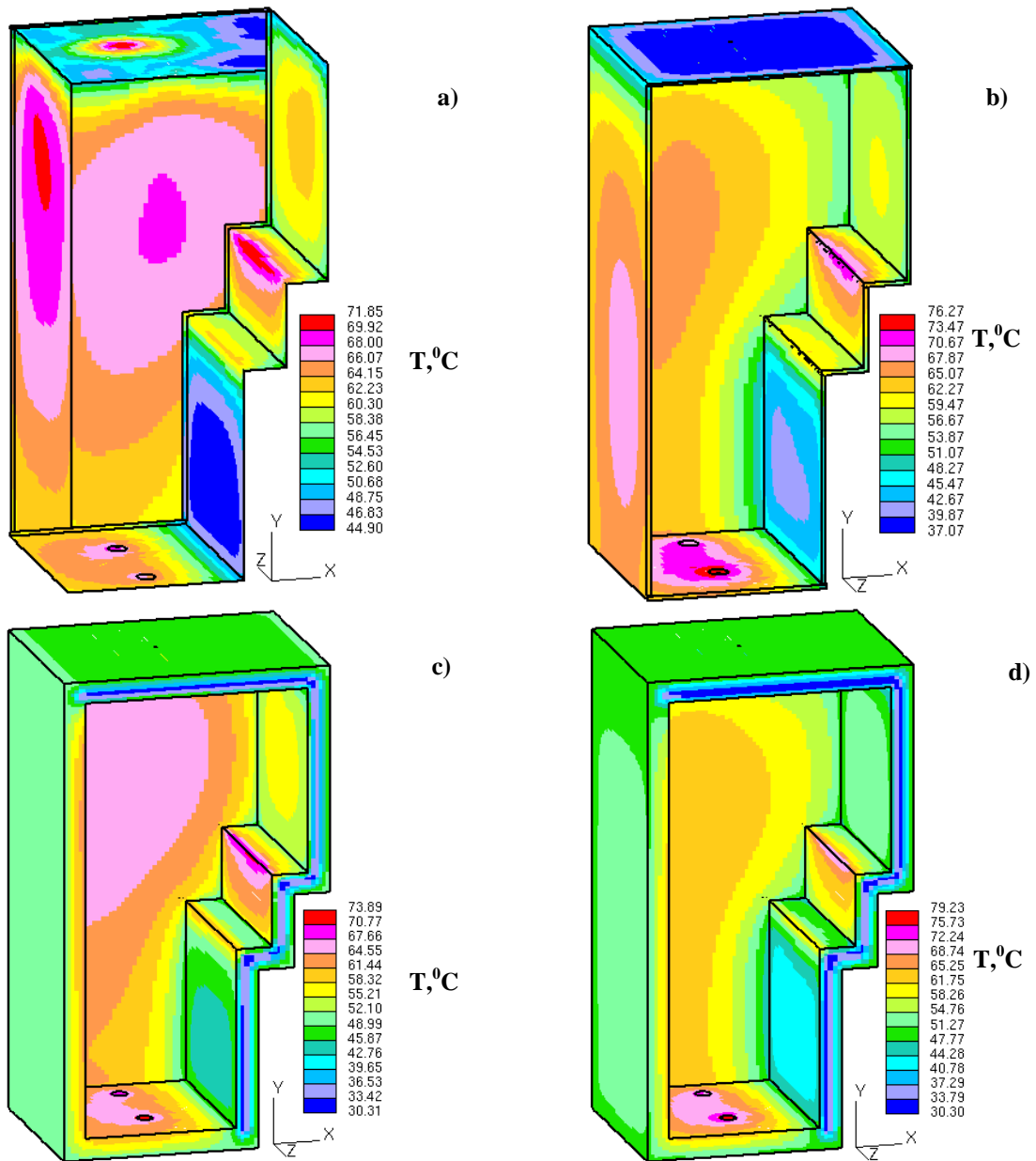


Fig. 5: Temperature distribution in the liner (a, b) and concrete (c, d) walls of the test cell. a, c – helium pressure of 1 bar (10<sup>5</sup> Pa), b, d – helium pressure of 0.0001 bar (10 Pa).

**Staff:**

S. Gordeev  
 V. Heinzl  
 S. Simakov  
 V. Slobodtchouk

**Literature:**

[1] S.P. Simakov, U. Fischer, A. Möslang, P. Vladimirov, F. Wasastjerna, P.P.H. Wilson. "Neutronics and Activation Characteristics of the International Fusion Material Irradiation Facility", Fus. Eng. and Des., v. 75-79 (2005), p. 813-817

[2] S.P. Simakov, U. Fischer, V. Heinzl, F. Wasastjerna, P.P.H. Wilson. "Evaluation of radioactive inventories in the IFMIF test cell", Jahrestagung Kerntechnik 2005 (Nürnberg, May 2005): INFORUM GmbH, 2005, p. 487 – 490

- [3] S.P. Simakov, U. Fischer, V. Heinzl, F. Wasastjerna, P.P.H. Wilson. "Reduction of radioactive inventories in the IFMIF test cell", presented at ICFRM-12, 4-9 December 2005, Santa Barbara, CA
- [4] V. Slobodtchouk, S. Gordeev, V. Heinzl, Draft report on „Natural convection simulation in the IFMIF test cell", Nov. 2005

## TW5-TTMI-003 D 4

### Calculation of Complete Nuclear Response through the Entire Test Cell with Consideration of an Additional Neutron Shielding Block

The objective of task TW5-TTMI-003, Deliverable 4, was to optimize the IFMIF test cell layout by including an additional horse-shoe type neutron shield around the test modules to reduce the radio-activity inventory and the heat loading in the concrete walls of the test cell. The shield block itself can be cooled during IFMIF operation and be removed if access to the test cell is needed. Due to neutron back-scattering effects such a block could also affect the nuclear responses inside the test modules which were already calculated in the previous task TW4-TTMI-003, Deliverable D5b. For this reason the present task also foresees the calculation of the 3D distribution of (a) the nuclear responses using the McDeLicious Monte Carlo code and (b) the activity inventory using suitable activation codes and activation data (IEAF-2001/EAF-2005).

#### Horse-shoe shielding block around the test modules

First of all, suitable materials for the shielding block were investigated with the objective to obtain a maximum reduction of the heat and the radioactivity generation in the test cell walls. The preliminary calculations have shown that the most efficient shielding materials for the IFMIF neutron spectra are WC, W,  $CB_4$  and  $ZrH_2CH_2$ . For example, a layer of 73 cm (maximum available space between the test modules and the walls) filled with such materials at 80% of the normal density will reduce the neutron and heating loading to the front wall by a factor 100 to 50. Finally, tungsten carbide (WC) was selected as shield material since it proved to be the most sufficient neutron attenuator.

The geometry of the horse-shoe shield is shown in Fig. 1. It consists of 40 cm thick plates to leave some space for the removal. The horse-shoe shield was integrated into the global MCNP model of the IFMIF test cell developed in the frame of task TW4-TTMI-003, Deliverable D5a (TEKES, Finland). The updated model was used to calculate the neutron loadings in the test cell walls and the nuclear responses in the test modules. In these calculations the IFMIF neutron source generation and transport simulation was described with the McDeLicious code using d-Li evaluated cross section data which were updated under task TW4-TTMI-003, Deliverable D2.

Table 1 lists the calculation results for the neutron flux and the nuclear heating in the steel liner (3 cm thick) and the heavy concrete (first 10 cm) in the front (relative to the deuteron beam direction), lateral and rear walls of the test cell during IFMIF full power operation. It is seen that the neutron loadings to the front wall are less than to the other walls already without horse-shoe shield. This is due to the attenuation of d-Li source neutrons by the test modules predominantly in downstream direction towards the front wall. The use of a horse-shoe shield around the test modules further decreases the neutron loadings to the front wall (by a factor 10 to 17 in the centre and by a factor 3 to 4 times when averaged over the whole surface), but has no effect on the lateral and rear walls. To get a reduction there the horse-shoe shield has to wrap the neutron sources from all sides.

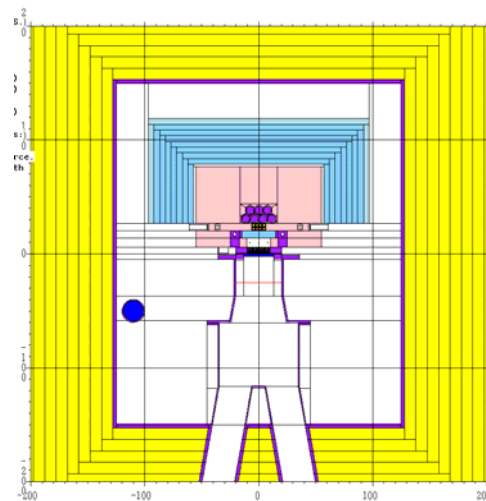


Fig. 1: Plan view of the IFMIF test cell with horse-shoe type shield (shown in blue) around the test modules.

The recalculation of the 3-dimensional spatial distributions of nuclear responses (dpa, heating, and gas production) inside the HFTM has shown that the horse-shoe shield in the present configuration has a negligible effect for these.

Table 1: Neutron flux and nuclear heating in the wall components of the IFMIF test cell as calculated at the center and average over the wall surface.

Loading	Front Wall		Lateral Wall		Rear Wall	
	Liner	Concrete	Liner	Concrete	Liner	Concrete
without horseshoe shield						
n-flux, $10^{11}$ n/cm <sup>2</sup> /s	10.2 - 10.9	- 6.1	24.1 - 6.8	15.8 - 4.3	32.9	29.6
Heating, W/kg	1.04 - 0.98	0.99 - 0.69	2.38 - 0.62	2.33 - 0.50	3.2	3.6
with horseshoe shield						
n-flux, $10^{11}$ n/cm <sup>2</sup> /s	1.1 - 3.2	- 1.8	23.7 - 6.3	18.2 - 4.0	33.4	30.1
Heating, W/kg	0.08 - 0.24	0.06 - 0.17	2.25 - 0.55	2.27 - 0.45	3.2	3.8
horseshoe shield performance (ratio "without shield" to "with shield")						
n-flux	9.3 - 3.5	- 3.2	1.0 - 1.1	1.2 - 1.1	1.0	1.0
Heating	13 - 4.1	17 - 4.1	1.1 - 1.1	1.0 - 1.1	1.0	1.0

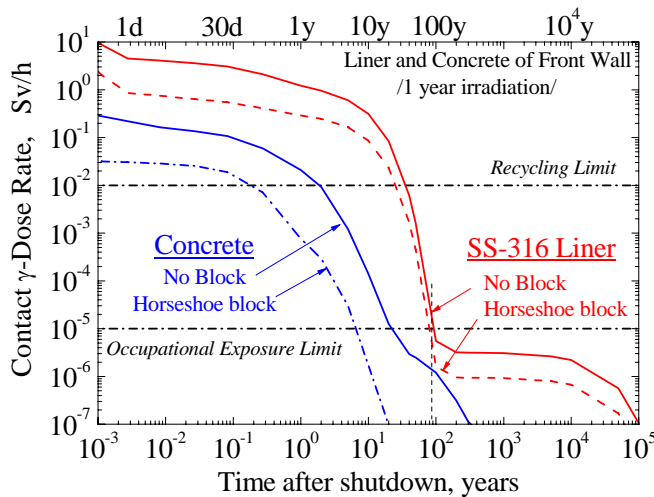


Fig. 2: The contact  $\gamma$ -dose rate in SS-316 liner and concrete wall of the front wall after 1 year irradiation versus the cooling time.

The time behaviour of the radioactivity after switching-off the IFMIF neutron source was calculated by the ALARA inventory code using cross sections from the Intermediate Energy Activation Files IEAF-2001. Fig. 2 shows the contact  $\gamma$ -ray dose rate versus the cooling time on the surfaces of the SS-316 steel liner and the heavy concrete of the front wall after 1 year of IFMIF full power operation. It is seen that the horse-shoe shield will reduce the contact  $\gamma$ -dose rate in the front wall materials by several factors. The waiting time for accessibility of the test cell by work personnel will be determined by the activation of the steel liner and is around 90 years.

### Reduction of Tritium production in the Li quench tank

The Li-quench tank contains 1.2 tons of Lithium. Recently it was shown that 1 gram of tritium per one full power IFMIF operation year will be generated in the tank due to neutron induced reactions. Inserting a neutron shield between the d-Li neutron source and the tank could reduce the tritium production rate. To study this, we integrated in the test cell model a 50 cm thick heavy concrete layer and a steel block above the tank as shown in Fig. 3. The calculations have shown that such a shield will reduce the tritium production by a factor 11, resulting in a final production rate of 0.1 g/fpy.

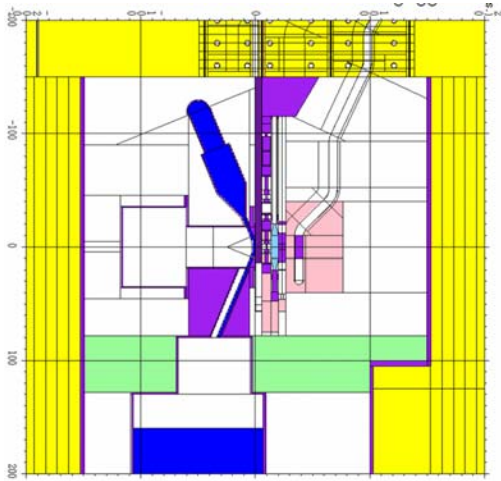


Fig. 3: IFMIF test cell vertical view with Li-tank neutron shielding: concrete layer (green) and steel at the tank top (pink).

### Assessment of the changes in the tritium and the helium production in the TRM

One of the objectives of this work was to determine the tritium, helium and damage production rates in beryllium irradiated in the Tritium Release Module (TRM) in the presence of a horse-shoe shield around the test modules. Helium is produced in the reactions  ${}^9\text{Be}(n,\alpha)$  and  ${}^9\text{Be}(n,2n)2\alpha$ . Since both reactions have thresholds above 1 MeV neutron energy, helium production in beryllium takes place only in the high-energy part of the neutron spectrum. The threshold for the direct tritium production through the  ${}^9\text{Be}(n,t){}^7\text{Li}$  reaction is even higher (about 11.6 MeV). However, tritium can be also generated through the two-step reaction  ${}^9\text{Be}(n,\alpha){}^6\text{He} \rightarrow {}^6\text{Li}(n,\alpha)\text{T}$  which, in particular,

can give a significant contribution for a soft neutron spectra. Due to the specific features of the neutron cross sections, the two-step reaction is effective only if the neutron spectrum shows both a high population of high and low energy neutrons (for the efficient production of  ${}^6\text{He}$  from Be and T from  ${}^6\text{Li}$ , respectively).

In the present work we have considered two main variants similar to that used previously, but in the presence of a horse-shoe shield block surrounding the test modules:

- the initial model with tungsten spectral shifter and extended graphite reflector (Fig. 4a);
- without creep-fatigue test module (CFTM) and tungsten spectral shifter, where the TRM was shifted upstream to the HFTM (Fig. 4b).

Calculations of neutron energy spectra were performed using updated McDelicious code (Fig. 5) and FISPACT-2005 radioactive inventory code for the subsequent calculation of the tritium production.

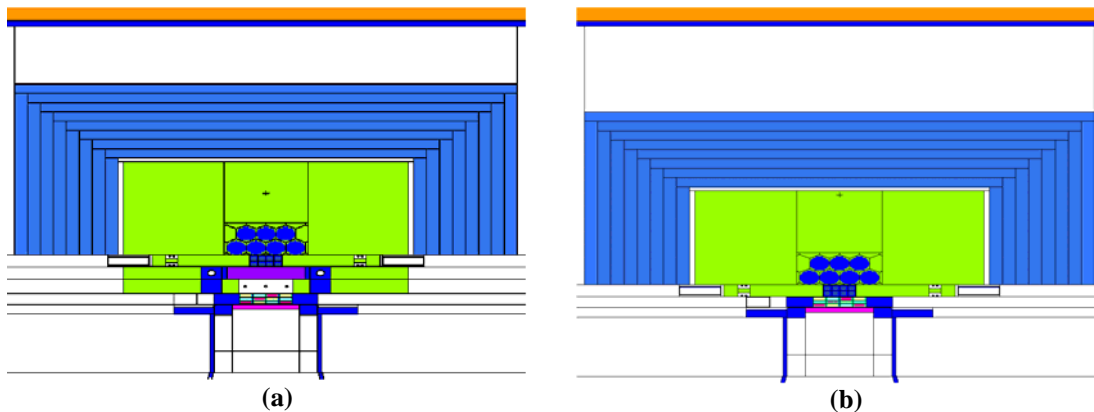


Fig. 4: Horizontal cut through IFMIF Test cell with the horse-shoe shield (blue) around the test modules. Variant (a) includes a CFTM and a W spectral shifter plate. In variant (b) both were removed and the whole TRM and the shielding block were shifted upstream.

The helium and tritium accumulation is shown in Table 2 as function of irradiation time. Some of the calculations were performed with FISPACT/EAF-2005 which became available only recently for activation calculations up to 60 MeV neutron energy. The new FISPACT/EAF-2005 results were shown to agree well with our previous results obtained with ALARA/IEAF-2001.

Comparison of gas production in IFMIF MFTM and HCPB fusion power reactor reveals that the helium production in the shifted TRM is at the same level as in the HCPB fusion reactor blanket, while the tritium production after one and two years irradiation time is slightly higher, but decreases after about five years. The integration of a shielding block slightly decreases the helium production for the initial and the shifted test module

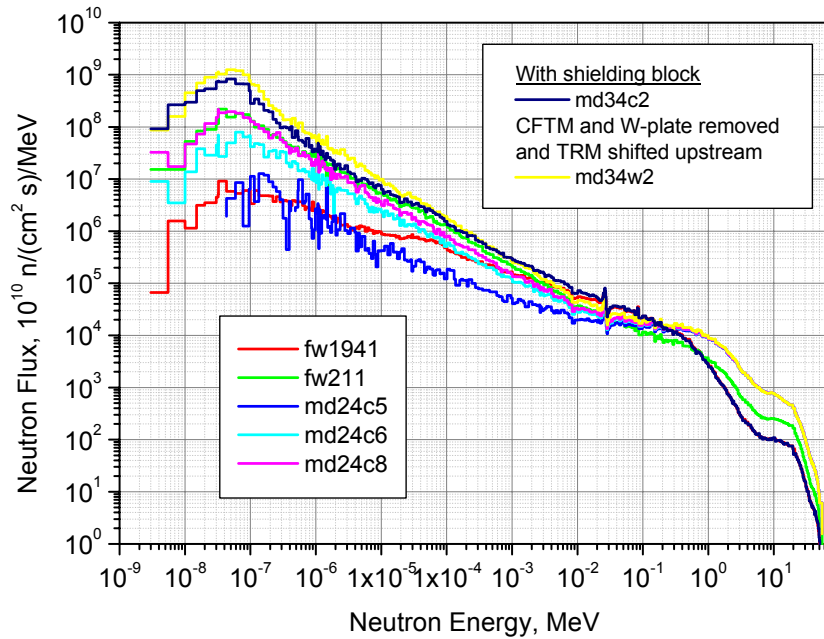


Fig. 5: Differential neutron spectra in the Tritium Release Module (TRM) applying various design variants of the IFMIF test cell. Spectra with the shielding block are labelled in the upper right legend

configuration, while the tritium production slightly increases for the latter. This results in a further decrease of the He to T production ratio. At an irradiation time of 4.6 years, however, the He/T ratio nicely fits to that of a fusion reactor.

Table 2: He and T production in Be when irradiated in the Tritium Release Module (TRM).

MFTM Config.	Variant	N flux n/cm <sup>2</sup> /s	He, appm			T, appm			He/T	
			1 y	2.28 y	4.57 y	1 y	2.3 y	4.6 y	1 y	4.6 y
<b>With CFTM and W moderator</b>										
No add. C fw19.6	ALARA	1.5·10 <sup>14</sup>	795	1821	3649	18.4	41.1	78.6	43.2	46.4
	FISPACT-2005		754	1719	3441	18.3	40.7	77.9	41.2	44.2
Shielding block md34c.2	FISPACT-2005	1.4·10 <sup>14</sup>	717	1634	3272	17.4	39.0	75.7	41.2	43.2
<b>With CFTM and without W moderator</b>										
add. C fw21.6	ALARA	1.7·10 <sup>14</sup>	1923	4407	8833	44.6	101	199	43.1	44.4
	FISPACT-2005		1827	4159	8312	44.3	99.7	195.7	41.2	42.5
<b>no CFTM, no W moderator, TRM is shifted upstream</b>										
no add C	md24c.5	3.7·10 <sup>14</sup>	5566	12749	25524	116	260	497	48.0	51.4
add. C	md24c.6	3.8·10 <sup>14</sup>	5581	12786	25607	117	264	514	47.7	49.8
extend.C	md24c.8	3.9·10 <sup>14</sup>	5584	12798	25639	118	269	534	47.3	48.0
Shielding block md34w.2	FISPACT-2005	4.1·10 <sup>14</sup>	5274	11974	23816	121	287	613	43.6	38.8
<b>HCPB Fusion Power Reactor Blanket</b>										
DEMO	ALARA	1.1·10 <sup>16</sup>	5656	12912	25825	85.5	247	683	66.1	37.8

## Conclusions

A study of the most efficient shielding materials for IFMIF was performed resulting in the selection of tungsten carbide for the horse-shoe type shield block surrounding the test modules. At 40 cm thickness this block reduces the neutron flux, the nuclear heating and the induced radioactivity by a factor 4 to 10 in the front wall but does not significantly affect the lateral and rear walls. Since the neutron loading and the nuclear heating to the front wall is lower than to the other walls even without this shield block, its inclusion in the design does not essentially reduce the total radioactivity or the nuclear heating produced in all test cell walls. It is also shown that the presence of the horse-shoe shield does not affect the nuclear responses inside the HFTM.

The integration of a 50 cm thick concrete/iron plate which shields the lithium quench tank from d-Li source neutrons reduces the tritium production in the tank from 1.0 to 0.1 g/fpy. Nevertheless the main source of tritium in the whole loop remains to be the deuterium-lithium reactions resulting in 6 grams of tritium generated per full power year.

It was also shown that the presence of the horse-shoe shielding block changes only slightly the helium and the tritium production in the Be samples in the TRM. The tritium production in the upstream shifted TRM is already higher than in the HCPB blanket of a fusion reactor even without the considered carbon reflector/moderator. Increasing the carbon moderator size results in an increased tritium production so that the He/T ratio further decreases. The most favourable design variant for the simulation of a proper He/T ratio after one year of irradiation would be that of an upstream shifted TRM without any carbon moderator. The shielding block increases the population of low energy neutrons and consequently decreases the He/T ratio. At an irradiation time of 4.6 years, however, the He/T ratio nicely fits to that of a fusion reactor. One could consider to remove the carbon moderator/reflector partly to fit the fusion reactor He/T ratio at earlier irradiation times.

### Staff:

U. Fischer  
V. Heinzl  
A. Möslang  
S.P. Simakov  
P. Vladimirov  
F. Wasastjerna (TEKES, Finland)

### Literature:

- [1] S.P. Simakov, U. Fischer, A. Möslang, P. Vladimirov, F. Wasastjerna, P.P.H. Wilson. "Neutronics and Activation Characteristics of the International Fusion Material Irradiation Facility", *Fus. Eng. and Des.*, v. 75-79 (2005), p. 813-817
- [2] S.P. Simakov, U. Fischer, V. Heinzl, F. Wasastjerna, P.P.H. Wilson. "Evaluation of radioactive inventories in the IFMIF test cell", *Jahrestagung Kerntechnik 2005 (Nürnberg, May 2005): INFORUM GmbH, 2005*, p. 487 – 490
- [3] S.P. Simakov, U. Fischer, V. Heinzl, F. Wasastjerna, P.P.H. Wilson. "Reduction of radioactive inventories in the IFMIF test cell", presented at ICFRM-12, 4-9 December 2005, Santa Barbara, CA
- [4] U. Fischer, M. Avrigeanu, P. Pereslavtsev, S.P. Simakov, I. Schmuck. "Evaluation and Validation of D-Li Cross-Section Data for the IFMIF Neutron Source Term Simulation" presented at ICFRM-12, 4-9 December 2005, Santa Barbara, CA
- [5] P. Vladimirov, A. Möslang. "Radiation damage conditions for ESS target hull and irradiation rigs", *J. Nucl. Mater.*, 343 (2005) pp.205-211
- [6] P. Vladimirov, A. Möslang, U. Fischer, S.P. Simakov. "Material Irradiation Conditions for IFMIF Medium Flux Test Module", presented at ICFRM-12, Santa Barbara, USA, December 4-9, 2005.

## TTMI-004 IFMIF – Design Integration

### TW5-TTMI-004 D 1 3D Radiation Shielding Analysis of all Rooms Surrounding the Test Cell using State-of-the-art Computational Tools

The objective of this sub-task was to assess the shielding performance of the IFMIF test cell with test modules surrounded by a horseshoe-type shielding block on the basis of accurate calculations of the dose rate distributions in the rooms surrounding the test cell.

A full 3D analysis of the shielding performance of the IFMIF Test Cell was performed to this end by making use of a recently developed computational scheme for coupled Monte Carlo/deterministic ( $S_N$ ) transport calculations [1,2]. The programme system makes use of the MCNP code for the Monte Carlo calculations and the three-dimensional  $S_N$  code TORT for the deterministic calculations.

This approach enables the use of the detailed geometry model of the test cell in the Monte Carlo calculation along with an accurate representation of the D-Li neutron source through the use of the McDeLicious Monte Carlo code. The neutron transport through the thick concrete walls surrounding the test cell is described by means of 3D  $S_N$  calculations with the TORT code using the boundary source distribution calculated by McDeLicious at the inner surface of the test cell wall. The geometrical model for the coupled MC/ $S_N$  calculation comprises two parts: the test cell with the D-Li neutron source for the Monte Carlo simulation and the maintenance/access room for the  $S_N$  calculations (Fig. 1). The model includes all sub-systems in the test cell such as the beam and target system, the lithium handling system, the high/medium/low flux test modules with surrounding horseshoe-type shield, the ceiling, the floor and the walls. The walls and floor are considered to consist of 3m thick heavy concrete and a 3cm thick steel liner on the inner side.

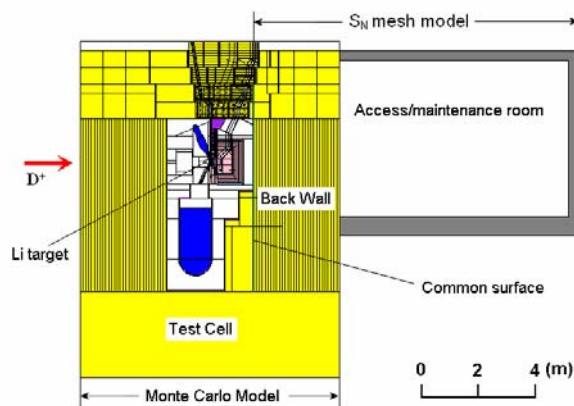


Fig. 1: Calculation model of the IFMIF test cell and the access/maintenance room with a horse-shoe type shield around the test modules.

Neutron and photon flux distributions were calculated across the back wall of the test cell and in the access/maintenance room using the approach described above. The dose rates were then obtained by multiplying the neutron/photon fluxes by flux-to-dose rate conversion factors.

Fig. 2 shows the profiles of the peak dose rates calculated across the back wall and the access/maintenance room. Two cases are considered, one with and one without a horseshoe shield around the test modules. The horseshoe shield consists of 40 cm thick slabs made of the efficient shield material tungsten carbide (WC) at 80% of the normal mass density. At the front of the back wall, the dose rate without horseshoe is almost 24 times higher than with horseshoe shield. The dose rate attenuates more than 9 orders of magnitude across the back wall with the horseshoe shield and more than 8 orders without the horseshoe. At the rear of the back wall the dose rate with the horseshoe shield is  $\sim 5 \mu\text{Sv/h}$ , which is well below



the design limit of 100  $\mu\text{Sv/h}$  for work personnel access. Without the horseshoe shield, the dose rate at the rear of the back wall is about 350  $\mu\text{Sv/h}$  thus exceeding the radiation design limit.

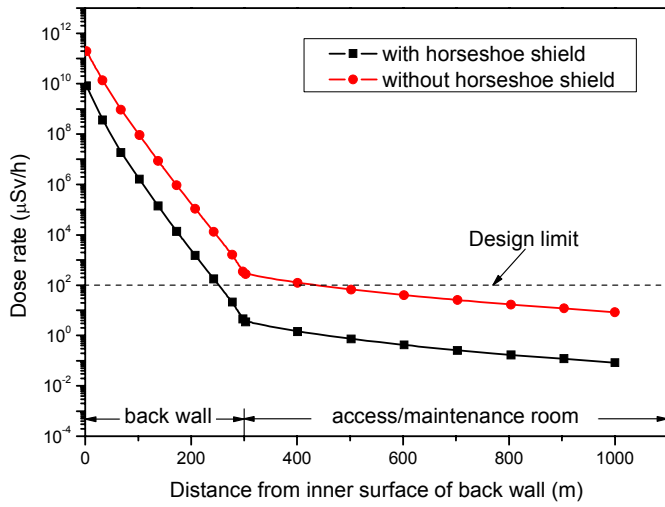
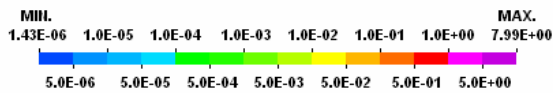
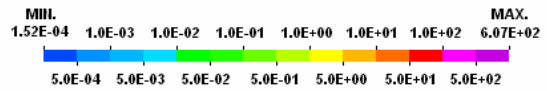


Fig. 2: Profiles of the peak total dose rates as function of the distance from the inner surface of the back wall at IFMIF full power irradiation.

Figs. 3 and 4 compare the three-dimensional dose rate distributions in the access/maintenance room with and without the horseshoe shield, respectively. The results demonstrate that the required dose rate limit for work personnel access to the access/maintenance room can be safely met during IFMIF operation assuming the test modules are surrounded by a WC horseshoe shield. Furthermore, the thickness of the back wall, made of heavy concrete, could be reduced to about 250 cm.



Unit: MicroSv/h



Unit: MicroSv/h

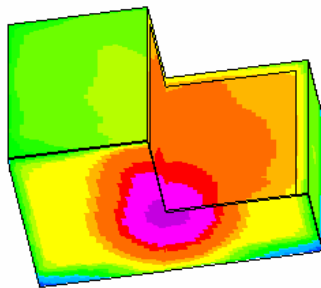


Fig. 3: Dose rate distribution in the access/maintenance room with horse-shoe shield.  
 Meshes: 62X, 44Y, 82Z  
 X=(-5.65E+02, 5.65E+02) Y=(-4.00E+02, 3.30E+02) Z=(4.43E+02, 1.203E+03)

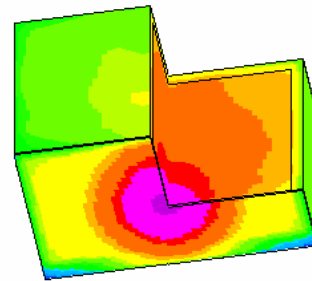


Fig. 4: Dose rate distribution in the access/maintenance room without horse-shoe shield.  
 Meshes: 62X, 44Y, 82Z  
 X=(-5.65E+02, 5.65E+02) Y=(-4.00E+02, 3.30E+02) Z=(4.43E+02, 1.203E+03)

**Staff:**

- U. Fischer
- Y. Chen (ASIPP, Hefei, China)
- S.P. Simakov
- F. Wasastjerna (VTT, Finland)

Literature:

- [1] Y. Chen, Coupled Monte Carlo-Discrete Ordinates Computational Scheme for Three-Dimensional Shielding Calculations of Large and Complex Nuclear Facilities, Forschungszentrum Karlsruhe, FZKA 7075, April 2005.
- [2] Y. Chen, U. Fischer, Program system for three-dimensional coupled Monte Carlo-Deterministic shielding analysis with application to the accelerator-based IFMIF neutron source, Nuclear Instruments and Methods in Physics Research Section A, Volume 551, Issues 2-3 (2005), 387-395.
- [3] Y. Chen, U. Fischer, S. P. Simakov, F. Wasastjerna, Shielding Analyses of the IFMIF Test Cell, 12th Int. Conf. on Fusion Reactor Materials (ICFRM-12), December 4 – 9, 2005, Santa Barbara, California, USA

## **Fuel Cycle**



## **GB8-VP 1 Cryopump Development and Testing**

### **GB8-VP 1 D 6 Effect of Strongly Sorbed Substances**

#### **1 Background and Objectives**

The Test facility for ITER model pump (TIMO) is used to demonstrate the qualification of the ITER-torus cryopump concept which is recommended as the reference design for ITER. The test programme with the 1:2 model cryopump covered the simulated ITER conditions with respect to gas flow, gas composition, gas pressure, time periods for heating up and cooling down, temperature of the panels during pumping, partial regeneration, and total regeneration.

One of the key points is the long term reliability of the cryopump. A major issue in this is the compatibility with high-boiling species, such as water and heavier hydrocarbons, which are still strongly bound to the cryosorbent at ambient temperatures. Water is a specified component in the torus exhaust gas and may originate at high levels from water leaks, hydrocarbons may be formed in the torus by plasma wall interaction or at the charcoal under presence of atomic hydrogen or due to radiochemical reactions initiated by the tritium decay [1].

Two major problems have to be solved in this context, namely what conditions are needed to regenerate these substances (this topic is dealt with in the parallel task TW3-TI-VP31), and what is the impact on the pumping speed of the cryopump. The reduction in pumping speed for the standard exhaust gas components (hydrogens and helium) due to the presence of strongly sorbed substances on the cryosorbent is called poisoning. To investigate this, a parametric test programme has been conducted comprising water, and two very heavy hydrocarbons (n-hexane and i-octane). These two species have already been investigated several years ago in the component test facility TITAN and it was shown there that the poisoning effect starts to become critical with octane, whereas it is still weak for hexane and any other hydrocarbons with less C content. From this point of view, octane is considered a worst case species. To derive the poisoning effect quantitatively, ITER relevant pumping speed tests for deuterium were performed with the cryopanel being pre-loaded with a defined amount of poisoning species (water, hexane, octane).

#### **2 Experimental Programme**

The aim is to pre-load the panel with defined amounts of the potentially poisoning substance. This species has to reach the panel to be fixed by sorption. Consequently, the loading has to be realised at ambient temperature, since all high molecular substances will immediately be frozen out at the entrance baffle under cold conditions. The technique shall be easy to perform, provide a small gas load that is built up homogeneously and uniform and not need too high calibration requirements so that the poisoning substance may be exchanged easily.

Three different approaches were chosen to meet the requirements [2]. The first approach (denoted method A [3]) was to use a bubble column to moisturise a helium gas stream until saturation and to inject this wet gas stream into the facility (against moderate vacuum of ~ 200 mbar) so that the moisture can adhere to the sorbent. This method provides a very accurate quantification of the dosed amount, however, involves uncertainties associated with the subsequent pump-down step, which leads to partial desorption, and was, consequently, not further followed. The alternative approach chosen was by direct evaporation of a connected liquid volume with the facility being already under high vacuum. Two procedures have been employed, either via the test vessel volume into the model pump (method B, with the inlet valve being open) or via the forepump line backwards into the model pump (method C, with the inlet valve being closed), see Fig. 1.

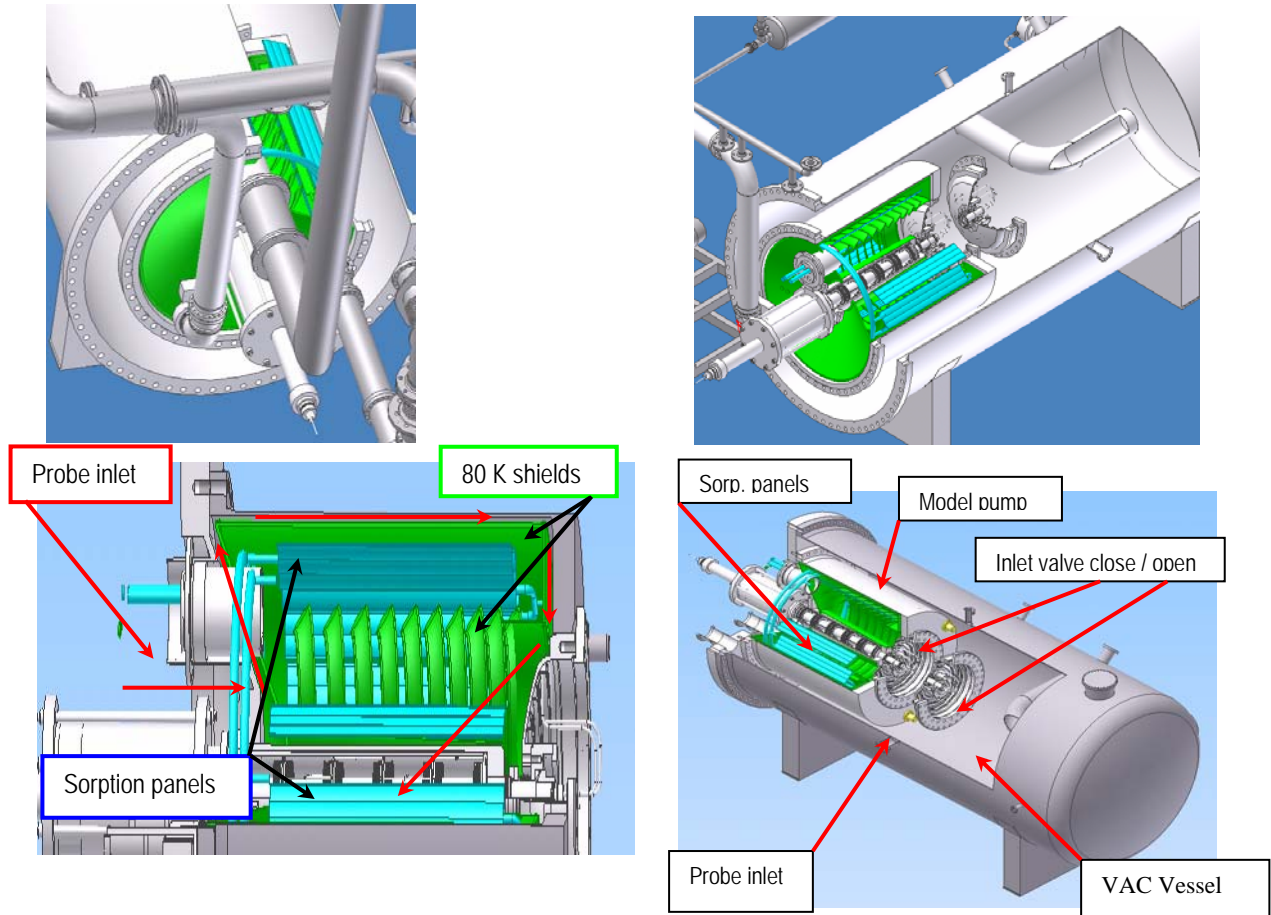


Fig. 1: Experimental arrangement for injection of the probe substance into the TIMO cryopump via the backside (method B, left) and via the front side (method C, right).

Table 1: Overview of the performed experiments.

Table 1 lists the experimental conditions investigated under this task. Given is the injected pre-sorbed amount, in total gravimetric and scalable specific units (related to the charcoal coated surface of 4 m<sup>2</sup>). Based on the specified ITER exhaust gas composition, a sorbed amount of 2.5 (mbar·l)/cm<sup>2</sup> would result after 10 cycles without total regeneration, which is the expected amount accumulated over one day. However, it is believed that the realistic contents of strongly sorbed substances are far below that value.

Investigated pre-sorbed substance	Sorbed amount	Dosing method
Water	Run #1: 3.2 g ≈ 0.1 (mbar·l)/cm <sup>2</sup>	A
	Run #2: 80 g ≈ 2.5 (mbar·l)/cm <sup>2</sup>	C
	Run #3: 190 g ≈ 5.9 (mbar·l)/cm <sup>2</sup>	C
n-Hexane	Run #1: 7.6 g ≈ 0.05 (mbar·l)/cm <sup>2</sup>	A
	Run #2: 380 g ≈ 2.5 (mbar·l)/cm <sup>2</sup>	C
i-Octane	Run #1: 100 g ≈ 0.5 (mbar·l)/cm <sup>2</sup>	B
	Run #2: 200 g ≈ 1.0 (mbar·l)/cm <sup>2</sup>	B
	Run #3: 300 g ≈ 1.5 (mbar·l)/cm <sup>2</sup>	B
	Run #4: 400 g ≈ 2.0 (mbar·l)/cm <sup>2</sup>	B
	Run #5: 400 g ≈ 2.0 (mbar·l)/cm <sup>2</sup>	C
	Run #6: 500 g ≈ 2.5 (mbar·l)/cm <sup>2</sup>	C

### 3 Results

In none of the experiments, any deterioration of the deuterium pumping speed was observed; the measurement was performed directly after contamination of the charcoal with the probe substance and subsequent cool-down. Fig. 2 illustrates the achieved pumping speeds with D<sub>2</sub> with the pump being pre-loaded with i-octane, which was regarded as most challenging

case. All results agree within the normal 5% experimental accuracy related to an average value of 1.79 l/(s·cm<sup>2</sup>) with the value of 1.75 l/(s·cm<sup>2</sup>) which holds for the uncontaminated, freshly conditioned pump, as measured at an early time of TIMO operation.

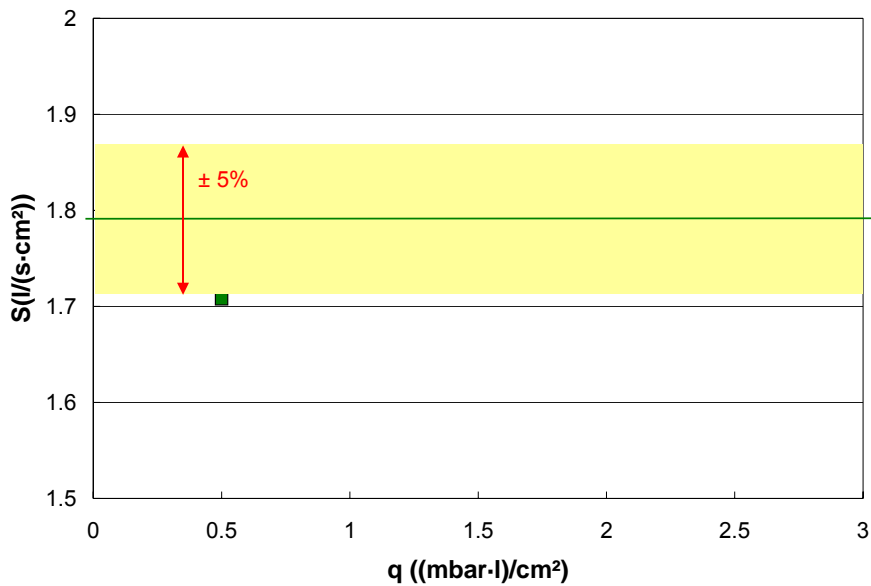


Fig. 2: Measured D<sub>2</sub> pumping speed tests at different pre-loadings of the cryosorbent with i-octane.

For all the deuterium pumping tests, the pumping speed was perfectly constant throughout the whole investigated pumping time. This indicates that there is no poisoning effect at all with respect to deuterium pumping, which is the reference pumping task. To validate this positive result, additional pumping speed tests with pure helium were performed, which is the most critical gas species to pump. Also these tests did not reveal any degradation [4]. As the final conclusion, no critical issues due to any poisoning effect are to be expected for ITER. The pumping case of i-octane, which has been considered to be critical in former times, did not indicate any limitation in pumping of strongly sorbed substances.

#### Staff:

Chr. Day  
A. Edinger  
H. Haas  
H. Jensen  
P. Pfeil  
R. Simon  
H. Stump  
J. Weinhold  
D. Zimmerlin

#### Literature:

- [1] Chr. Day, A. Antipenkov, I.-R. Cristescu, M. Dremel, G. Federici, H. Haas, V. Hauer, A. Mack, D.K. Murdoch, M. Wykes, Hydrogen inventories in the vacuum pumping systems of ITER, ISFNT-7, Tokyo, Japan, May 2005.
- [2] H. Haas, and Chr. Day, Final report, Internal Report, Forschungszentrum Karlsruhe, March 2005.
- [3] Chr. Day, B. Kammerer and A. Mack, The influence of water on the performance of ITER cryosorption vacuum pumps, Fusion Engineering and Design 51-52 (2000) 229-235.
- [4] H. Haas, C. Caldwell-Nichols, Chr. Day, A. Mack, and D.K. Murdoch, Study of poisoning effects with the ITER model pump during relevant operation cycles, ISFNT-7, Tokyo, Japan, May 2005.

## TW3-TTFF-VP 35

### Study of Cryopump Compatibility with Carbon Erosion Products

#### 1 Objectives

Predicting the amount and location of co-deposited hydrocarbon films is a major challenge for ITER. Recent studies have shown that only species with very small sticking probability may reach and stick along the inner surfaces of the pumping ducts [1]. When the inner surfaces are covered with a thin amorphous film, the hydrogen recombination coefficient may be significantly reduced so that atomic hydrogen and/or methane radicals could reach the cryopump region.

This task is dedicated to the analysis of the possible interaction between H atoms or CH<sub>3</sub> radicals and the activated charcoal sorbent in the cryopumps. It will investigate if the charcoal sorption properties will change due to the exposure to low sticking coefficient species and will identify the chemical species formed during such an exposure. The presence of any saturated hydrocarbon sorbed at the charcoal surface, which may act as promoter for a chemical reaction, will also be assessed. The saturated hydrocarbons, while not possible to get to the cryopump directly from the torus due to their high sticking coefficient, may be formed locally from radiochemical reactions in the presence of tritium, or originate from chemical reactions triggered by the radicals. Potential permanent deterioration of the charcoal performance will also be analysed. Recommendations and conclusions with respect to any needs for changes in the design for the cryopump system will be given.

#### 2 Experimental

The experimental work with radicals is accomplished and was performed in the Institute for Physical Chemistry of the Russian Academy of Sciences, Moscow (the future Institute for Physical Chemistry and Electrochemistry) [2]. They involve a radio frequency plasma induced discharge in a hydrogen/hydrocarbon gas mixture as source for atoms, radicals and excited molecules. The varied parameters include gas pre-loading of the charcoal sample, exposure time and catalytic contact material (quartz, stainless steel). The interaction of thermal hydrogen molecules and atoms with charcoal has been analyzed by sorption measurements (based on the stream technique [3]) at 77 K and thermodesorption (TDS) experiments at 77-300 K and 300-700 K, respectively. The experimental set up is shown in Fig. 1.

A cylindrical quartz reactor of 100 cm length and 1 cm radius was the main part of the setup. The pressure difference between inlet and outlet of the tube did not exceed 2 Pa. The reactor was pumped out by a rotary pump. An H<sub>2</sub> RF inductive-coupled discharge (frequency 20 MHz, specific power 0.1 W/cm<sup>3</sup>) in a flow of 6.9 sccm ( $3.1 \times 10^{18}$  H<sub>2</sub>/s) under a pressure of about 30 Pa has been utilized for production of atomic hydrogen. This corresponds to a molecular flow with  $Re \approx 1$  and  $Kn \approx 0.01$ . A plasma region of about 15 cm length was limited by a thin (100 μm) stainless steel grid. Hydrogen, deuterium and methane were used with a purity of 6.0. Three LN traps for deep purification of inlet gas from impurities were included, cf Fig. 1. The container with the ITER type charcoal was cooled by a fourth LN trap. The charcoal mass was 10-60 mg (10 to 100 single granules), depending on the actual experiment, conditioned by a vacuum bake-out at 620 K prior to the experiment.

The outlet of the quartz tube was equipped with a quadrupole mass-spectrometer with differential pumping by a turbomolecular pump, and a Pirani gauge. In terms of background, TDS evaluation and quantitative resolution, the whole experimental set-up was carefully calibrated with hydrogen, nitrogen, methane, and argon.



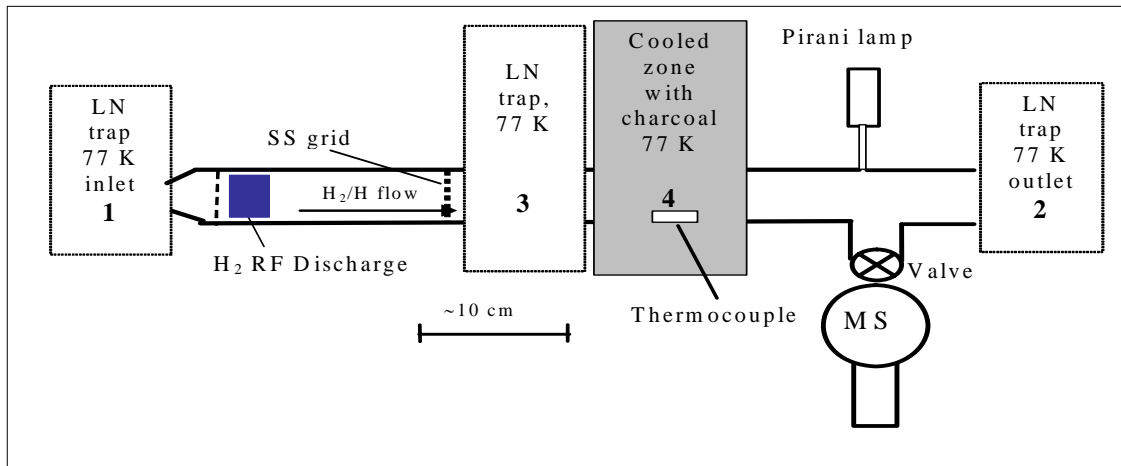


Fig. 1: *Top*: Scheme of the quartz gas flow reactor for experiments with charcoal in atomic/molecular hydrogen mixture at 77 K. Gas flow controllers were installed at the tube inlet.  
*Bottom*: Photos of H<sub>2</sub> RF discharge with cold LN traps (left), and the vacuum and gas analysis part with mass spectrometer and gauges.

For determination of the flows and atomic hydrogen concentration at the various tube regions solid carbon films were used ( $H/C=0.4$ ) deposited on silicon substrates. As the erosion coefficient of solid carbon films in the medium of atomic hydrogen is well known, measuring film areal densities before and after exposure in atomic hydrogen environment allowed to derive the erosion rate and, thus, the H (D) atom thermal flow ( $\sim 10^{16}$  H(D)/cm<sup>2</sup> s) and concentration ( $\sim 10^{11}$  H(D)/cm<sup>3</sup>) at the location of the charcoal. By this method, the hydrogen atom flow in the tube cross-section with charcoal was  $(2-30) \cdot 10^{-4}$  of the molecular hydrogen flow depending on the relative position of the atom source and the sample, and the hydrogen pressure. In most experiments, the atomic and molecular hydrogen ratio was about  $D/D_2=H/H_2 \approx 2 \cdot 10^{-4}$ .

## 2.1 Results for atomic hydrogen

The experimental concept for the tests with atomic hydrogen is shown in Fig. 2. Each sample was first characterised via a sorption measurement and a TD run in a reference experiment with molecular hydrogen. The samples were then exposed to atomic hydrogen (77 K, 30 Pa, in the afterglow zone of the discharge) over different time intervals, 0.5, 2, 3, and 4 hours, respectively. After that, the reference experiment was repeated to reveal the consequences of the exposure. From the adsorption-desorption experiments it was evident that irreversible hydrogen sorption takes place at charcoal exposure in the H(D)/H<sub>2</sub>(D<sub>2</sub>) gas mixture, leading to smaller amounts of hydrogen sorbed.

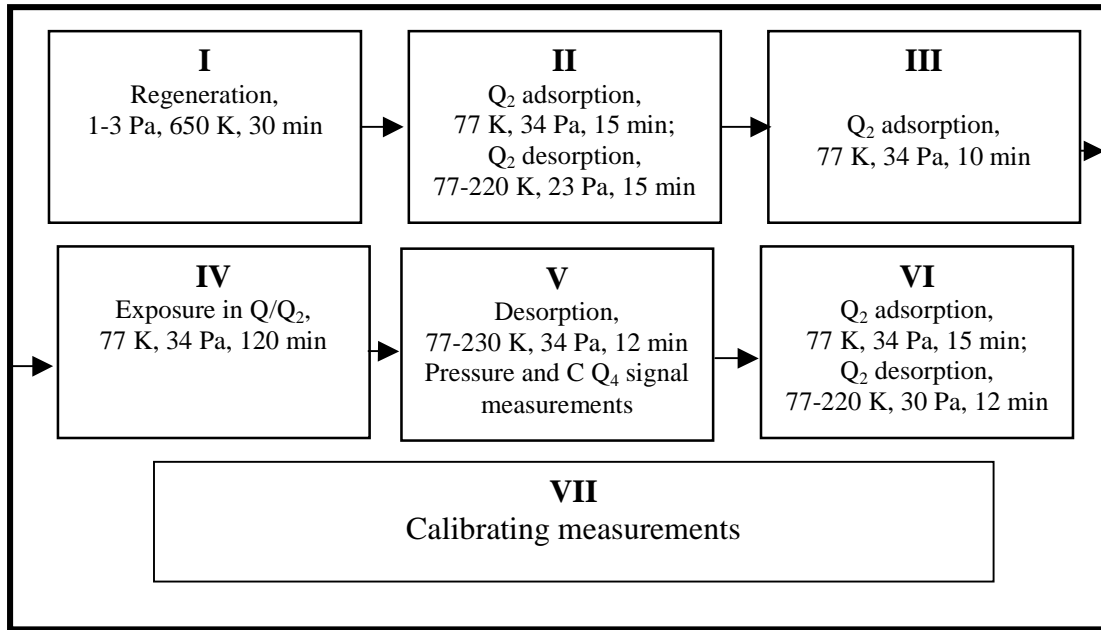


Fig. 2: Successive stages of in-situ in stream experiments. The tests were done with Q=H and D.

By gas analysis, there was clear indication for a formation of methane by interaction of atomic hydrogen (very similarly for protium and deuterium) with the charcoal. For the smaller samples (~ 10 mg), the numbers of formed methane (or deuteromethane) molecules and hydrogen atoms in the tube cross-section with the samples were close to each other, which means that the charcoal absorbs the majority of atomic hydrogen entering the tube cross-section (i.e. sticking coefficients close to unity) and transforms it in methane. Table 1 illustrates the influential parameters.

Table 1: Quantity of methane formed in reaction of the charcoal with the H/H<sub>2</sub> mixture at 77 K (P(H<sub>2</sub>)=35 Pa). Atomic flow was 2·10<sup>-3</sup> sccm.

Weight, mg	CH <sub>4</sub> yield (scc) at variable exposure time		
	1 h	2 h	2.5 h
10	7 granules: 0.017 9 granules: 0.024 12 granules: 0.072	---	0.08
20	0.02	0.038	---
52	0.03	---	---

The methane yield increased with the exposure time; for the experiments with deuterium, the CD<sub>4</sub> yield slightly exceeded the CH<sub>4</sub> yield in similar experimental conditions. The rate of methane accumulation was not directly proportional to the involved sample mass. These facts allowed to suppose that the methane formation is a reaction with sequential steps of hydrogen atom adding to “active” centres. It is possible that at one of the steps the absorbed molecular hydrogen also takes part in the

reaction on the “active” centre. For the heavier charcoal samples (~50 mg) the effects of charcoal interaction with H atoms were shadowed by the effects of molecular hydrogen sorption because of the relative insufficiency of atomic hydrogen flow. To verify this assumption, the same total amount of charcoal mass (10 mg) was constituted from different numbers of granules with different sizes, by that varying the active surface/mass ratio. It was revealed that this size effect is clearly dominating the methane formation yield in such a way that it becomes less pronounced with increasing charcoal mass involved.

When scaling this effect to ITER, it becomes very obvious that the methane formation and associated carbon consumption problem is uncritical. For the radical tests, the ratios of hy-

drogen flow related to charcoal mass was in the order of 1 sccm/mg, whereas at ITER, this number is of the order of  $4 \cdot 10^{-3}$  sccm/mg, more than 2 orders of magnitude lower.

## 2.2 Search for higher hydrocarbons

It is difficult to imagine the course of a consecutive chemical reaction on a certain active centre with final formation of methane without facilitated surface diffusion of the adsorbed hydrogen atoms. Consequently, other hydrocarbons of type  $C_2H_y$  are expected to be also formed at charcoal interaction with H/H<sub>2</sub> mixtures. However, it should be noted that under the typical conditions as given in Table 1, one molecule of formed methane corresponds to ~ 5000-10000 carbon atoms. In such conditions the probability of reaction between atomic hydrogen and methane is evidently quite low. Nevertheless, to study the reactions between adsorbed methane and atomic hydrogen in the charcoal, a series of experiments was performed in which methane was preliminary introduced in the charcoal sample at 77 K and a partial pressure of 25-30 Pa. Then, the methane atmosphere was replaced by hydrogen. After that the charcoal sample was exposed in H/H<sub>2</sub> mixture for 0.5-1.5 h.

To our surprise, at subsequent TDS analysis we did not find any other hydrocarbon besides methane (15 amu) or deuterated methanes (19 and 20 amu), respectively. The CD<sub>4</sub> yield was about 2-3 times higher than that in the analogous experiment but without preliminary CH<sub>4</sub> adsorption. This experiment has pointed at qualitative level that atomic deuterium forms CD<sub>4</sub> in a consecutive reaction with matrix carbon atoms; that means the reaction of atomic deuterium with adsorbed CD<sub>4</sub> proceeds with significantly lower probability than with the matrix. H and D atoms are captured by surface "active" centres and fail to notice the presence of considerable quantities of adsorbed methane.

In addition, tests with CH<sub>3</sub>-radicals (in form of H/H<sub>2</sub>/CH<sub>3</sub>/CH<sub>4</sub> mixtures) were performed which may add additional reaction pathways [3]. The charcoal turned out to be an effective sink for methyl. But also in this case, only methane was recorded in the mass spectrum during desorption.

In summary, the issue of higher hydrocarbon problem was not confirmed in any of the experiments performed, which is a very positive result for ITER.

## 2.3 Sorption isotherms

Most of the investigated samples have been characterised by sorption isotherms for H<sub>2</sub> and D<sub>2</sub> at 77 K before and after the exposure to the radicals, in the pressure range 10-50 Pa. This was to check if the consumption of carbon atoms from the matrix during formation of methane is associated with a loss of sorption capacity. The experiments revealed a certain decrease (in the range of few %), which however, is completely within the experimental error bound.

To validate this effect more closely, a batch of exposed charcoal was produced at IPC-RAS and shipped to FZK for future characterisation in the COOLSORP facility. Measurements under ITER relevant temperatures (4 K, 20 K, 77 K) and pressures are under way.

### Staff:

Chr. Day  
V. Hauer  
A.E. Gorodetsky  
A.P. Zakharov (Institute of Physical Chemistry RAS, Moscow)

Literature:

- [1] G. Federici, M. Mayer, G. Strohmayer, V. Chuyanov, Chr. Day, Journal of Nuclear Materials 337-339 (2005) 40-44.
- [2] A..E. Gorodetsky, S.P. Vnukov, R.K. Zalavutdinov, A.P. Zakharov, A.K. Buryak, A.V. Ulyanov, G. Federici, Chr. Day, Interaction of atomic hydrogen with charcoal at 77 K, IAEA Fusion Energy Conference 2004, IAEA, Wien, 2005.
- [3] A.E. Gorodetsky, R.Kh. Zalavutdinov, A.P. Zakharov, S.P. Vnukov, I.G. Varshavskaya, A.N. Makhankov, I.V. Mazul, G. Federici, Journal of Nuclear Materials 337-339 (2005) 892-896.

## TW1-TTF/VP 11 Torus Exhaust Cryopump Development and Testing

### TW1-TTF/VP 11 D 8 Design Modifications of ITER-Scale Pump

Within the final deliverable of this task a data base was prepared which is needed for the design the 1:1 torus cryopump [1]. It covers all results obtained in the tasks: GB8-VP1, TW0-T450, TW1-TTF/VP11, TW1-TTF/VP13, JW1-FT-6.1, TW2-TSS-SEA5.5, TW3-TI/VP31, and TW3-TTFF/VP33.

In the TIMO test bed at FZK, the model cryopump has been under extensive and fundamental investigation studying pumping, regeneration (thermal desorption pattern) and cryogenic aspects (heat load assessment, LOVA). The model pump cryosorbing panel area, which is from design point of view given by the required helium pump capacity, is composed of a number of identical cryopanel with a design that is similar for all ITER primary cryopumps. In parametric tests the regeneration with pure gases and gas mixtures were tested. It was experimentally shown that the cryopump can cope with light and higher hydrocarbons coming from reactions in the torus vessel or inserted as tracer materials for leak detection. The temperature levels needed for pumping, partial regeneration and total regeneration were defined.

TIMO was demonstrated to be a unique and versatile facility to test cryogenic vacuum components and sub-systems for ITER under ITER-relevant conditions in terms of gas flow, temperatures, pressures and cryogenic parameters. TIMO will be upgraded for testing of the prototype ITER torus exhaust cryopump (Task TW5-TTFF/VP58). Pumping tests in TIMO have validated the pre-calculated design values and have fully achieved the ITER requirements for non-active gases. The throttling characteristic of the front valve enables the control of the pressure in front of the pump and consequently the pressure in the divertor. Complementary tests under tritium in AGHS of JET have fully qualified the panel concept and confirmed the TIMO results [2, 3].

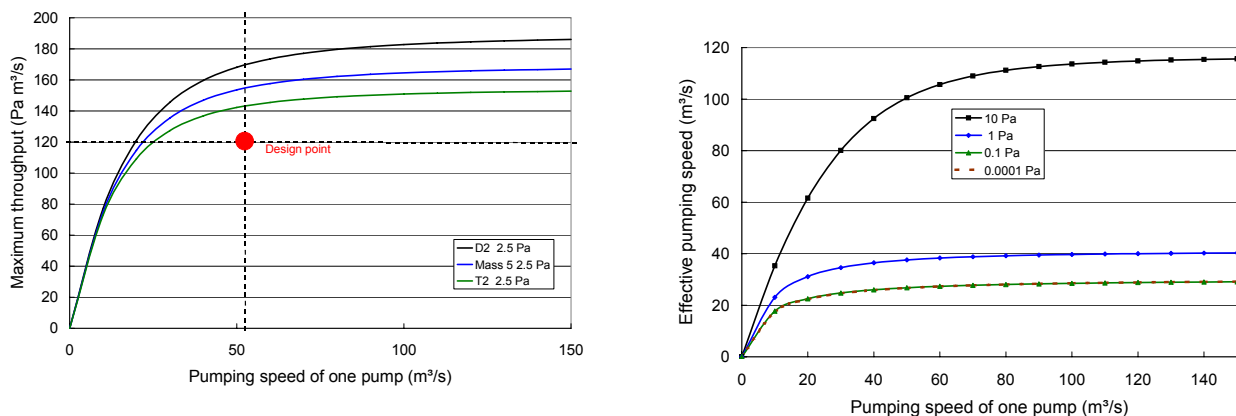


Fig. 1: Characterisation of the ITER torus exhaust primary vacuum pumping system as a function of the pumping speed of each of the torus cryopumps, calculated with ITERVAC. *Left:* Maximum throughputs for deuterium  $D_2$ , tritium  $T_2$  and a pseudo mass 5 gas, representing DT. 2.5 Pa is the smallest divertor pressure at which the required maximum throughput can be achieved. *Right:* Effective pumping speeds for variable divertor pressures. Molecular flow regime is achieved for pressures below 0.1 Pa.

As every vacuum pump is part of a vacuum system, the characteristics of the gas source and the conductance of the interconnecting divertor duct have been studied. The simulation codes ITERVAC for transitional flows, and MOVAK3D for molecular flows, both developed at FZK, are tools which have been employed to define the characteristics of the divertor duct and the connected torus cryopumps. Beyond that, the size of the cryopump in terms of pumping speed and pumping pressure can be optimised. Fig. 1 illustrates the performance of

the ITER torus exhaust primary vacuum pumping system, in terms of maximum throughput vs. pumping speed. Due to a significant conductance bottleneck in the divertor slots, there is a certain limit pumping speed beyond which an increase in pumping speed does not effectively increase the throughput anymore. This approach defines a target pumping speed of about 50-60 m<sup>3</sup>/s, which has to be chosen for the detailed design of the ITER-scale torus cryopump.

The main design issues which have to be fulfilled by the torus exhaust cryopumps are listed in Table 1. A speciality of the ITER cryopumps is the inclusion of an inlet valve, to control the throughput and to isolate the pump from the torus during regeneration. The inlet valve adds an additional degree of freedom to the pump control.

Table 1: Design issues in the development of the ITER-scale torus cryopump system.

Design driver	Solution
Different pump mechanisms for the different gases being pumped (re-sublimation vs. cryosorption).	The reference design shall include a pure He/H <sub>2</sub> -shot (100% sorption pumping). Minimize the dependency of pumping speed on gas species.
The gas throughput is variable and must be controllable.	Include an inlet valve for control.
Space limitations: The pump size is dictated by the given pump port diameter; the distance between the pumps' location and the gas source (divertor) is big.	Maximize pumping speed and pumping port conductance.
Harsh operating conditions (magnetic and electric fields, seismic and disruption loads, tritium compatibility, explosion safety requirements, neutron and activation, remote handling capability).	Develop a robust and maintenance-free design, include remote handling aspects.

Based on these targets, the ITER-scale cryopump could be designed in the limits of the available space [4]. Fig. 2 shows the original design of the TIMO model cryopump, characterised by an inlet valve which is opening towards the outside, compared with a candidate ITER-scale pump design with an interior valve, which was the valid design option over the last years.

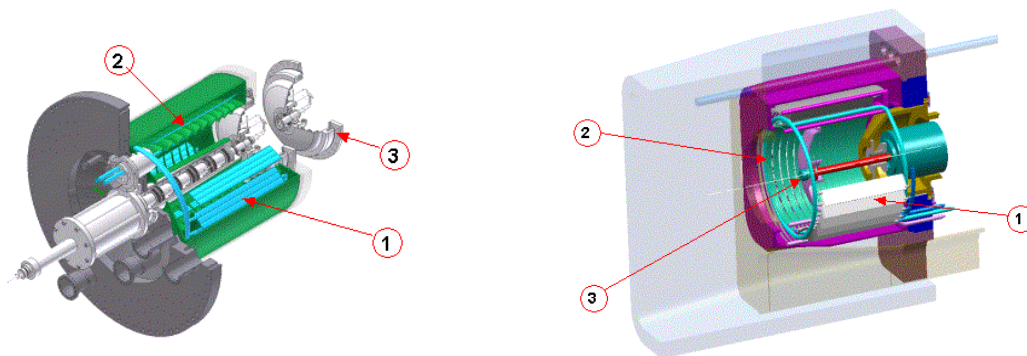


Fig. 2: Comparison of the TIMO model pump (left) and the ITER 1:1 torus exhaust cryopump (right) showing the pumping panels (1), baffles (2) and the inlet valve (3).

It has been shown that the pumping performance of a high throughput cryopump depends on throughput itself (as operating in transitional flow regime) and gas load. This is why these parameters, related to the pumping surface, were taken as scaling parameters between the model pump and the ITER 1:1 pump [5]. This yields a characteristic surface-related flowrate of  $2.5 \cdot 10^{-4}$  (Pa·m<sup>3</sup>)/(s·cm<sup>2</sup>), and a gas load of  $\sim 0.2$  (Pa·m<sup>3</sup>)/cm<sup>2</sup>; the requested surface-related pumping speed is  $\sim 1$  l/(s·cm<sup>2</sup>)

The efficiency of a cryogenic pump is characterised by the capture coefficient  $c$ , which is unity for a black hole under molecular flow conditions; in this theoretical case, all particles approaching the pump inlet cross-section are immediately captured. This integral effect, which is determined by the interior pump geometry, has to be considered separately from the panel-molecule interaction characterised by the sticking coefficient  $\alpha$ , which indicates the fraction of particles sticking to the cryosorbent surface related to all particles impinging on it. The sticking coefficient is, among other factors, defined by the sorbent type, its temperature, gas load and history and covers a range of factor 5 at 5 K conditions at the ITER type charcoal between close to unity (for DT) and only about 0.2 (for helium), as was learned from the TIMO tests. The current database for the ITER-reference charcoal as resulting from extensive testing in TIMO is summarized in Table 2 [5]. ).

Table 2: Comparison of initial (i.e. at zero gas load) sticking coefficients for fusion relevant gases at different temperatures for the ITER type charcoal.

	He	H <sub>2</sub>	D <sub>2</sub>	T <sub>2</sub>
At 5 K	0.35 0.25	0.6	0.9	1.0
At 7 K	0.17	0.5	-	1.0
At 12 K	0.03	0.3	0.85	-

The basic equations for pumping speed as a function of sticking coefficient and internal geometry were derived and numerically evaluated. The ITER torus cryopump design aims at the capture coefficient depending only very weakly on the kind of gas being pumped. This design target was

successfully met for the torus model pump, as illustrated in Fig. 3, which compares the model pump and the ITER 1:1 pump for three different valve openings. The maximum capture coefficient under molecular flow operation and at 100% valve opening was calculated to be 0.45 for the model pump, and even higher, about 0.65, for the ITER 1:1 pump (DN 800), respectively.

An important lesson learned in TIMO was that the pumping of a mixture containing helium is dominated by the helium fraction even at only some mol%. This is due to the generally significantly smaller sticking coefficient of helium compared to the one of the other mixture components, see Table 2; especially at elevated temperatures. This is no principle problem as it is included in the design of the ITER-scale pump, but limits the operational temperature range, as exemplified in Fig. 4 for a mixture containing 90% D<sub>2</sub>-base gas and 10% helium. At 5 K, there is sufficient safety margin against the design point, whereas at 8 K, the requirements can just be met. This is why the reference ITER cryopumping temperature is < 5 K (on top of the charcoal sorbent).

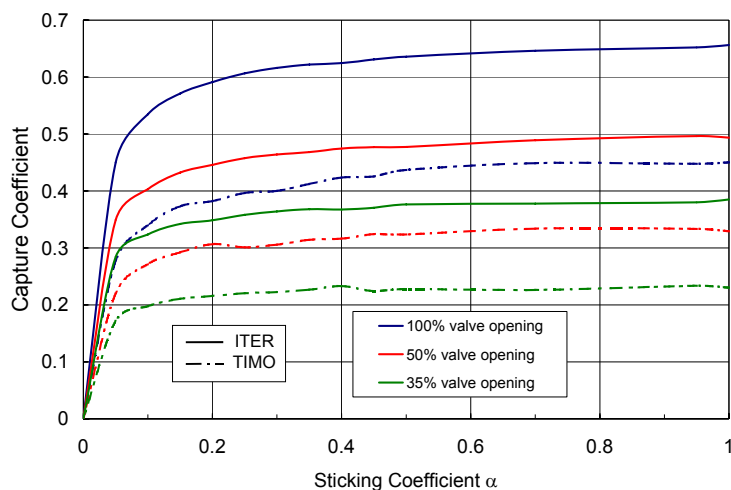


Fig. 3: Molecular flow capture coefficients for the model pump in TIMO (as experimentally validated) and the ITER-scale pump with interior valve.

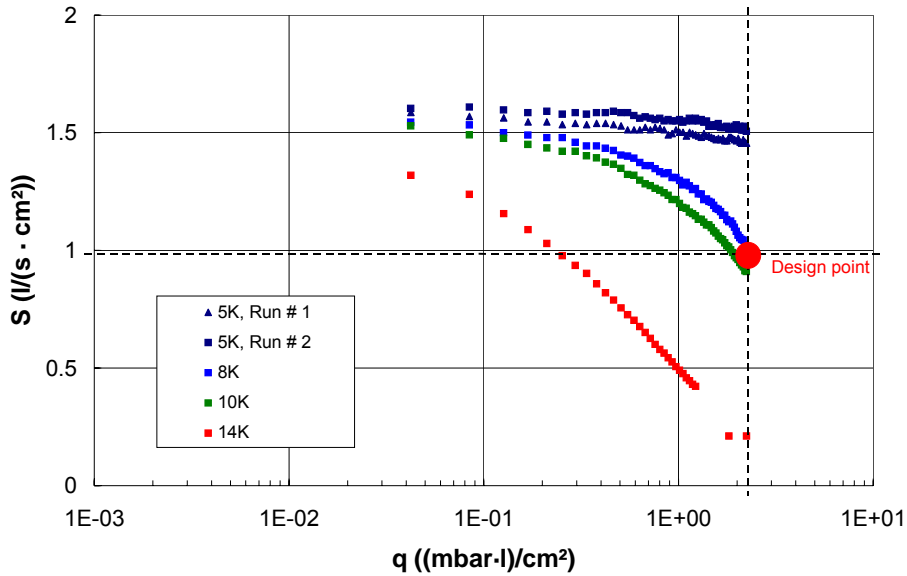


Fig. 4: Measured pumping speed curves for the model pump at elevated temperatures with a 90% D<sub>2</sub>-Base/10% Helium gas mixture.

Staff:

Chr. Day  
A. Edinger  
H. Haas  
V. Hauer  
H. Jensen  
A. Mack  
P. Pfeil  
R. Simon  
H. Stump  
J. Weinhold  
D. Zimmerlin

Literature:

- [1] A. Mack, Chr. Day, H. Haas, V. Hauer, Results of Testing the 1:2 Model Cryopump (Data Base for 1:1 ITER Torus Cryopump), Final report, Internal Report, Forschungszentrum Karlsruhe, July 2005.
- [2] Chr. Day, D. Brennan, P. Camp, H.S. Jensen, G. Jones, A. Mack, A. Miller, Fusion Science and Technology 48 (2005) 29-34.
- [3] D.K. Murdoch, I. Cristescu, Chr. Day, M. Glugla, R. Lässer, A. Mack, Material compatibility issues in fusion fuel cycle R&D and design, ICFRM-12, Santa Barbara, CA, US, Dec 2005.
- [4] [M. Glugla, D.K. Murdoch, A. Antipenkov, S. Beloglazov, I. Cristescu, I.R. Cristescu, Chr. Day, R. Lässer, A. Mack, ITER fuel cycle R&D, ISFNT-7, Tokyo, Japan, May 2005.
- [5] Chr. Day, A. Antipenkov, H. Haas, V. Hauer, A. Mack, D.K. Murdoch, M. Wykes, R&D and design for the mechanical and cryogenic vacuum pumping systems at ITER, European Vacuum Conference, Paris, France, April 2005, accepted for publication in *Vacuum*.



## EFDA/04-1173 Design and Procurement Specification for ITER Prototype Torus Exhaust Cryopump

### Background and Objectives

In the reference design of the ITER exhaust pumping system 8 cryopumps are foreseen to pump the torus via 4 ducts, see Fig. 1. The design of these cryopumps has to consider the different requirements for vacuum pumping, remote handling and safety, and provides strong interfaces to the surrounding environment on the ITER machine [1]. The nominal target pumping speed of the individual cryopump to be implemented was derived in a flow and throughput analysis of the complete system, using ITERVAC simulations (Task TW4-TTFF-VP47) [2].

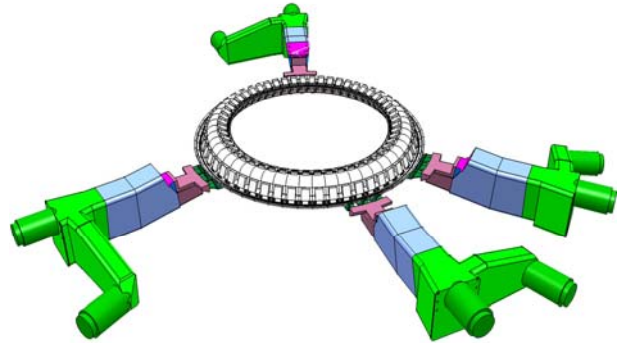


Fig. 1: ITER torus exhaust primary pumping system, showing the divertor system and the four duct connections towards the 8 cryopumps.

The aim of this task is the complete design of the prototype torus exhaust cryopump, including the mechanical construction, the calculation of pumping speed and thermohydraulic properties, the definition of operational parameters and the assessment of all safety issues. This design will be based on the extensive data-base which has been achieved in the TIMO campaigns with the model cryopump.

### General Design

The prototype torus cryopump is shown in Fig. 2. It is circular shaped with a maximum outer diameter of 1780 mm and a total length of about 2400 mm. The hydroformed 28 rectangular panels (1000 mm x 200 mm) offer in total a effective pumping area of 11.2 m<sup>2</sup>. The outer 80 K shields and the louvre baffle form an effective enclosure around the pumping panels against the heat radiation from inside and outside the cryopump. The pumping speed can be

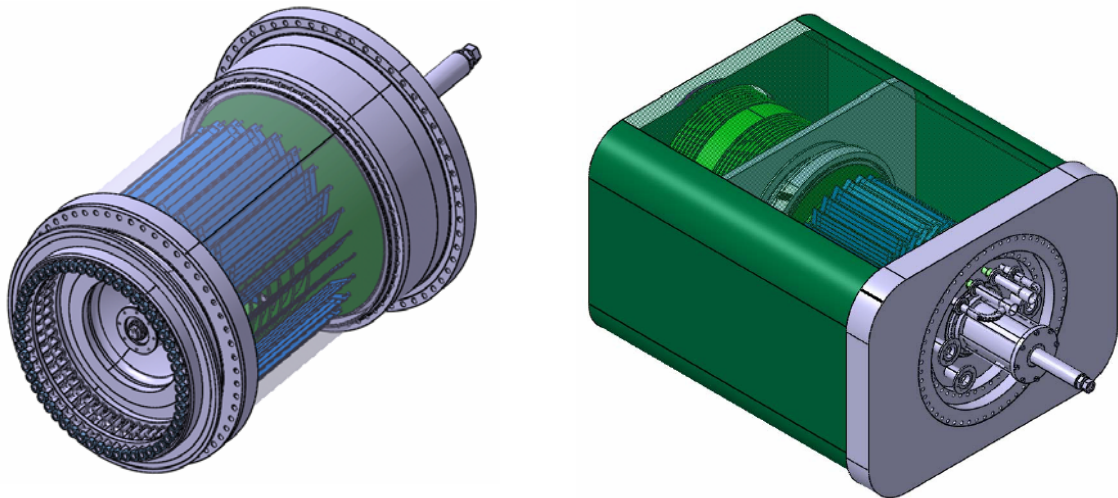


Fig. 2: Drawing of the prototype torus pump as single unit (left, without outer 80 K shield and housing) and as installed in the duct with the bellow (right).

varied by the main valve, which opens to the torus side with a maximum stroke of 500 mm. The valve inlet diameter is 800 mm.

The pump housing has openings, which provide connection between the pump interior volume and the duct volume. This increases the accessible volume in case of a oxy-hydrogen explosion in a LOVA event and, thus, helps to meet the requirements of maximum hydrogen deflagration pressure. This is also the reason why the pump has an adapter flange which seals between the pump housing and the duct. The valve actuator and a part of the valve shaft is removable to meet the remote handling requirements. The next step is the completion of the detailed design of the cryopump.

#### Staff:

Chr. Day  
H. Haas  
V. Hauer  
A.Mack  
R. Simon

#### Literature:

- [1] V. Hauer, Chr. Day, A. Mack, Design and Procurement Specification for ITER Prototype Torus Exhaust Cryopump - Preparation of input data, Deliverable 1, Internal Report, Forschungszentrum Karlsruhe, November 2005.
- [2] Chr. Day, A. Antipenkov, H. Haas, V. Hauer, A. Mack, D.K. Murdoch, M. Wykes, R&D and design for the mechanical and cryogenic vacuum pumping systems at ITER, European Vacuum Conference, Paris, France, April 2005, accepted for publication in *Vacuum*.

## TW5-TTFF-VP 51

### Mechanical Tests and Post-operational Examination of TIMO

Following more than five years of successful performance testing of the (50% scale) ITER model torus exhaust cryopump in TIMO, the next step of the programme will be the design, construction, installation and testing of a full scale ITER cryopump. Before dismantling of TIMO and adaptation of the infrastructure to accommodate the 1:1 scale pump two remaining activities had to be carried out in the existing TIMO facility. In 2005, these remaining experiments have been finished and disassembly of the TIMO facility has been started.

#### Cycling tests of the inlet valve

In order to investigate the tolerance of the inlet valve (particularly the sealing surfaces) to repeated opening and closing cycles, a campaign of multi-cycle tests was started. The valve worked properly throughout the whole TIMO campaign over the last 5 years. However, at an early stage of the cycling tests, considerable leakages were observed; the valve was not able anymore to close tightly. To find the reason for this malfunction, the valve was thoroughly inspected using an in-vessel viewing system. By this technique, no serious damages to the sealing surface could be recognized. But the visual check of the complete movement phase of the model pump inlet valve revealed that one pipe of the cooling water loop in the middle of the valve seat has obviously broken. The movie documentation showed clearly a blockage of the valve opening movement for the first  $\sim 50$  mm, possibly caused by a fixation bolt, resulting in a sudden jump out of the seat causing further oscillations during completion of the valve stroke. This issue will be analysed in full detail as part of the model pump dismantling and examination programme to be performed in 2006.

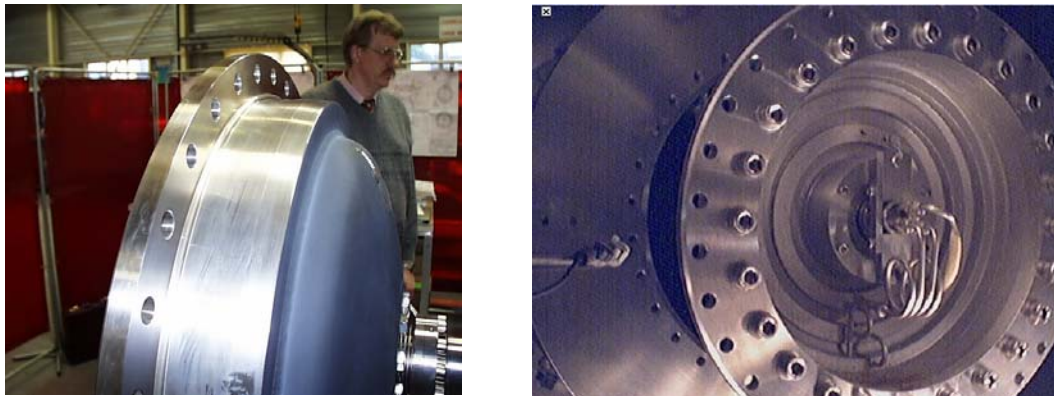


Fig. 2: Photo of the inlet valve before integration into the model pump (back in 1999), and a photo with the in-vessel viewing system of the valve as installed in the TIMO test vessel (2005), in fully opened position. A pipe break was detected in the cooling water loop in the centre of the valve.

#### Cryogenic safety tests

Under conditions of significant water or air inbreak from the torus into the pump, high rates of heat transfer to the 5 K pump components will occur, with the potential for overpressurisation of the SCHe circuits. In order to design the pressure relief system in ITER to cater for this, tests to determine the characteristics of the pressurisation (pressure level, pressure rise rate) were carried out. The tests aimed at measuring the pressure rise curves inside the SCHe loop vs. time at varied pressurisation rates of the vacuum vessel. The investigated pressurisation rates were between 0.3 and 4.7 mbar/s and chosen such to simulate the ITER torus LOVA reference accident (pressurisation rate of 2.3 mbar/s, [1]) with the pump being cold. The experimental limit as given by TIMO was the 18 bar burst disc pressure of the supercritical helium loop (normal operation pressure is 4 bar), and the use of nitrogen instead of air.

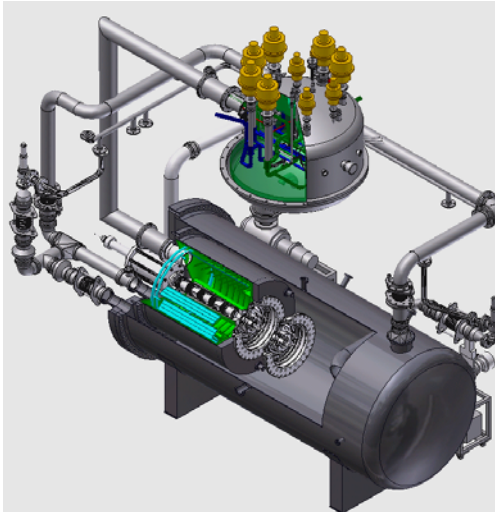


Fig. 2: 3D view of TIMO showing the piping between the cold valve box and the model pump in the test vessel.



Fig. 3: Photos of the used burst discs for the cryogenic safety test campaign at TIMO, showing that not all discs have burst properly.

The pressure increase rates were expected to be high, so that additional safety measures had to be integrated in the TIMO exhaust gas system. Fig. 2 shows the TIMO set-up as used for the tests.

The tests were performed in collaboration with CEA Grenoble, who are in charge of the design of the ITER cryoplants. Based on the TIMO experimental results, CEA tried to determine the heat loads on the TIMO 5 K system using the VINCENTA code, which was recently adopted by CEA Grenoble. CEA provided a series of burst discs at a nominal bursting pressure of 13 bar abs. In total, 10 tests were performed with measured pressure increase rates between 0.2 and ~ 8 bar/s. However, the measurements were difficult to evaluate due to the fact that the burst discs did not all work properly, see Fig. 3; part of them did not provide the full cross-section which lead to an undefined outflow situation. Fortunately, the experiment #10, with the strongest pressurisation rate representing the most adverse case, went fine, so that this was chosen to become the reference experiment for the VINCENTA analysis. This work is still going on at CEA [2].

#### Staff:

H. Haas  
H. Jensen  
A. Mack  
P. Pfeil  
H. Stump  
J. Weinhold  
D. Zimmerlin

#### Literature:

- [1] Chr. Day, H. Haas, Final report of task TW2-TSS-SEA5.5a: Safety related experiments to investigate air inbreak events in cryopumps, Internal Report # FE.5130.0046.0012/O, Forschungszentrum Karlsruhe, July 2004.
- [2] P. Gully, R. Vallcorba, nitrogen ingress tests and analysis in TIMO, Presentation at 11<sup>th</sup> ITER-EFDA-FZK Interface Meeting, October 2005, available at <http://www.ITER.org/bl> (ITER Technical Web Site, Pumping).

## TW1-TTF/VP 12 Performance Evaluation of Roots Blower with Ferrofluidic Seal System

### 1 Background and Objectives

The task objective was the investigation into the application of ferrofluidic seals in Roots blowers to reduce the potential for cross-contamination between process gas and lubricant, thereby enhancing tritium compatibility.

By the beginning of the reporting period the first tritium compatible Roots vacuum pump has been designed, delivered to FZK from UK Company Roots Systems Ltd. and tested with helium in the pumping chamber, at pulsating pressures replicating the conditions in the ITER roughing line. The goal of these tests was to validate the general feasibility of a ferrofluidic seal [1]. The seals remained intact with a low leak rate ( $\sim 10^{-7}$  mbar·l/s), but as the magnetic liquid was directly applied to the shaft, it was not possible to provide its required distribution among the cells and to avoid appearance of it in the pumping chamber, which is unacceptable for the tritium operation. This is why a new design of the seal (a cartridge – see Fig. 1) was implemented by the company FerroTec [2]. The replacement of the seals and a new testing series were done during 2005. The task has been completed.



Fig. 1: Ferrofluidic cartridge.

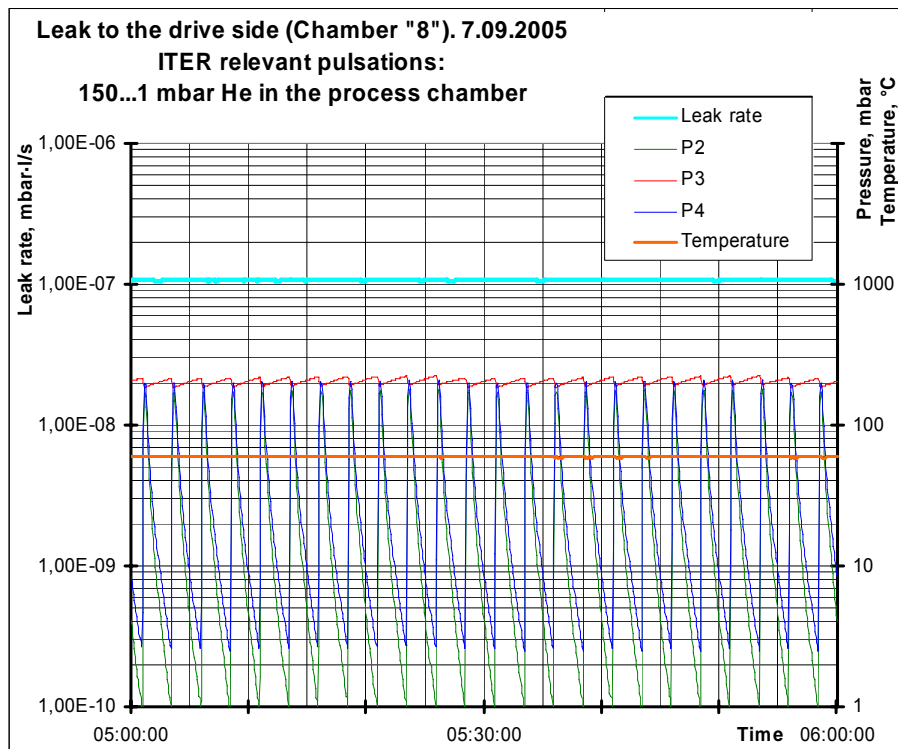


Fig. 2: Leak rate through two parallel ferrofluidic seals. ITER-relevant He pressure cycles. P<sub>2</sub> – inlet; P<sub>4</sub> – outlet; P<sub>3</sub> – buffer vessel.

## 2 Results

Having disassembled the pump, we have measured the axis position of the bearings and the ferroseals. We have revealed an unacceptably high eccentricity at the gear end: 0.04 and 0.06 mm, while the nominal gap in the seal is 0.05 mm. It was the reason of an initial high leak rate at this side. This failure was then eliminated by precise drilling of two new holes for the centring dowels.

Fig. 2 shows the leak rate measured in the lubricant containing chamber at the drive end of the test pump (through two parallel ferroseals) after a continuous run over four days. The helium pressure in the pump chamber was varied following the expected pressure pulsations in the ITER roughing line. The leak rate was on an acceptable level ( $\sim 10^{-7}$  mbar·l/s), stable and did not depend on the pressure pulsation and the working temperatures up to 65°C.

In order to complete the ferroseal validation it has to be tested on tritium. This test will be performed within 2006 in frame of a separate task (TW5-TTFF/VP53).

Based on the experience with the pilot 250 m<sup>3</sup>/h pump, the following modification issues towards an ITER scale pump can be recommended.

The internal shaft seals should be made as ferrofluidic cartridges. In order to assure a feasibility of these seals the circumferential velocity should be taken into account – see Fig. 3. With this regard, any type of a Roots pump which suits ITER capacity requirements can be equipped with a ferroseal. As a backing pump, a screw pump with cantilevered rotors has too large diameter of the shafts and the implementation of a ferroseal looks problematic.

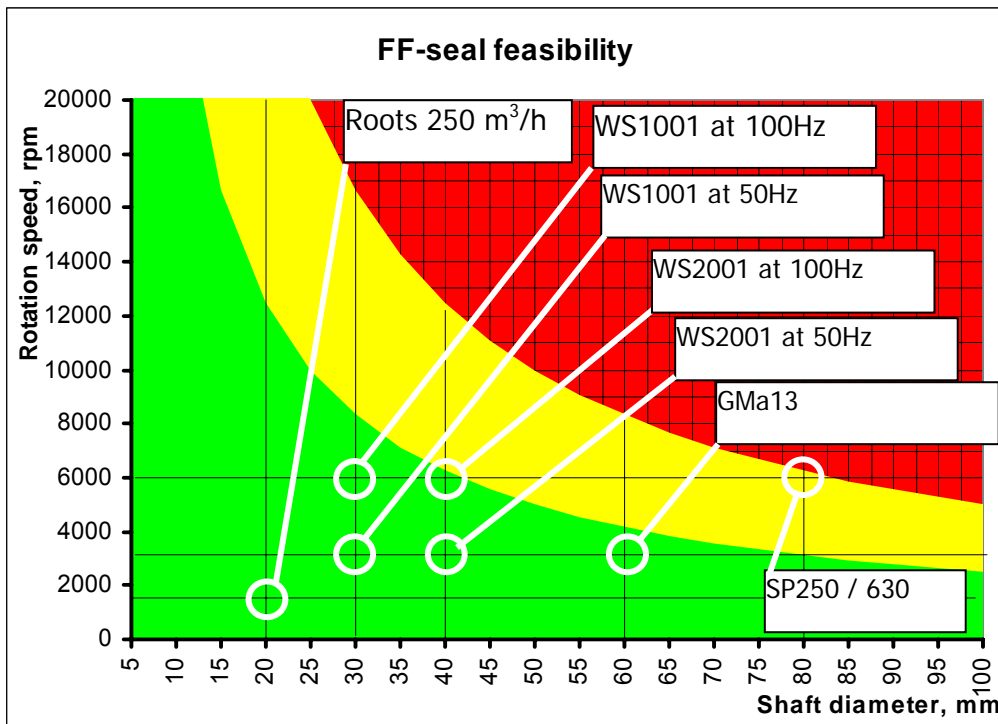


Fig. 3: Ferrofluidic seal applicability depending on the rotor velocity. The fields: green - feasible; yellow – not stable; red – not applicable. The indicated pumps are the pilot pump (Roots 250 m<sup>3</sup>/h), a nominal 1000 m<sup>3</sup>/h (WS1001), 2000 m<sup>3</sup>/h (WS2001) and 3000 m<sup>3</sup>/h (GMa13) commercial roots pump, and a screw pump SP (250 m<sup>3</sup>/h or 630 m<sup>3</sup>/h) as candidate last stage of the pump train.

An ITER pump with pumping speeds larger than the ones of the pilot pump (250 m<sup>3</sup>/h) allows for a better space allocation for these seals. At the same time the performance of a roots pump with hydrogen or helium is better on higher rotation speeds, and, in order to keep a diameter of a shaft not too large, it might be reasonable to limit on a single pump capacity

and to connect them in parallel, as well as to run them via frequency inverter on frequencies above 50 Hz. The ferrofluidic seals require a high eccentricity (<0.05 mm), thus the tolerances in the design of the pump housing and plates must be better than conventional ones. In addition some means have to be foreseen to control the pressure in the gear chamber because a ferroseal is practically tight.

To make the pump tritium compatible, all stationary seals should be metallic (better spring energised C-rings), the housing should be made of stainless steel or should be nickel coated from inside. No rotary seals to the environment are allowed, i.e. the drive should either have a magnetic coupling or be a canned motor. Budget prices for such developments have been obtained by commercial vacuum companies.

### 3 Final conclusions

- I. The ferrofluidic feedthrough of a cartridge type has proved its feasibility with helium and upon successful tritium tests in frame of a new task, it could be recommended for ITER roughing pumps' internal seals.
- II. An integration of a ferrofluidic feedthrough into a full scale high pumping speed roots or screw roughing pump requires additional R&D and would lead to significant increase in the cost in comparison with a catalogue pump or modified medium size pumping speed pump. A solution for the roots part of the forepump train is to provide the very high pumping speeds by a parallel–serial arrangement of medium size pumps. For the last stage (e.g. screw pump), the use of a conventional improved design of a shaft seal could still be considered.
- III. The successful tests of a relevant cartridge validates the concept of Roots blowers as the first stages of the ITER forepump train.

#### Staff:

A. Antipenkov  
A. Mack  
R. Simon  
H. Jensen  
R. Wagner

#### Literature:

- [1] A. Antipenkov, Chr. Day, R. Lässer, A. Mack, R. Wagner, Tritium pumps for ITER roughing system, Fusion Science and Technology 48 (2005) 47-50.
- [2] M. Glugla, D.K. Murdoch, A. Antipenkov, S. Beloglazov, I. Cristescu, I.R. Cristescu, Chr. Day, R. Lässer, A. Mack, ITER fuel cycle R&D, ISFNT-7, Tokyo, Japan, May 2005.

## EFDA/03-1095 Design of an ITER-sized Mechanical Pump Train

### 1 Background and Objectives

The aim of this task is a detailed design of an ITER relevant dry mechanical pump train as forepumping system for the cryopump systems of ITER. The tritium compatibility shall be realised with a ferrofluidic seal (further ferroseal) system, based on the results achieved in the R&D Task TW1-TTF/VP12 dealing with a modified Roots blower. The design shall include other (dry) pump concepts for the pressure range not covered by Roots blowers.

By the beginning of the reporting period the ITER operating requirements have been revised. The validation of a cartridge concept of a ferrofluidic shaft seal for a Roots blower has been started. The task was started with selection of an optimal roughing train for ITER (consisting of two Roots stages: 6000 and 2000 m<sup>3</sup>/h backed by a screw pump of 600 m<sup>3</sup>/h pumping speed) [1]. The performance of a Leybold screw pump SP630 on helium has been tested by the manufacturer, the result was negative, and there were no data for hydrogen.

The ITER roughing system shall fulfil the following major tasks, some of them not yet fully specified [2]:

#### 1. Roughing:

1.1 *Torus*. The volume 1350 m<sup>3</sup> should be evacuated from 1 bar down to at least 50 Pa within less than 60 hours.

1.2 *Cryostat*. The volume 8450 m<sup>3</sup> should be evacuated from 1 bar down to a cross-over pressure of ~10 Pa as fast as possible (no exact time is specified).

1.3 *Neutral beam vessel*. The volume 156 m<sup>3</sup> should be evacuated from 1 bar down to 10 Pa as fast as possible (no exact time is specified).

1.4 *Other services* (including guard volumes, diagnostics and high frequency heating and current drive waveguides). Roughing of these volumes should be achieved by the same roughing train. These clients do not dominate in the pumping speed definition of the roughing system.

#### 2. Evacuation of the desorbed gases during cryopump regeneration of the following high vacuum systems:

2.1 *Torus*. During continuous plasma operation, the torus cryopumps are regenerated in a staggered mode: Of a total eight cryopumps four ones are pumping and other four stand under one of sequential isochronous regeneration phases – evacuation being one of them. The roughing system has to evacuate the 7.5 m<sup>3</sup> volume of the cryopump from ~2 kPa down to 10 Pa cross-over pressure within 150 s via a ring manifold volume. The gas composition is a mixture of hydrogen isotopes (H<sub>2</sub>, D<sub>2</sub>, DT, T<sub>2</sub>), and He ash at 90 K regeneration, plus air and water-likes at 300 K and 470 K regeneration.

2.2 *Neutral beam*. Four NB units are working with either protium or deuterium. The high vacuum is maintained by cryopumps, which are subjected to different regeneration scenarios depending on the plasma operation scenario. For the most challenging scenario the accumulated deuterium during 3600 s at 18 Pa·m<sup>3</sup>/s flow rate has to be evacuated within 337 s from ~300 Pa down to 20 Pa. As these cryopumps are regenerated in not a staggered mode as the torus ones, it is possible to open the valve to the fore-line during warming-up phase and to consider an increased evacuation time



up to 500 s. For the operation on protium the flow rate is 35 Pa·m<sup>3</sup>/s, but in this case the evacuation time could be more relaxed.

2.3 *Cryostat*. Prior to cooling down the superconducting coils, two cryopumps evacuate the cryostat to 10<sup>-4</sup> Pa. The gas load is expected to be low and the regeneration time of these cryopumps is not significantly restricted, neither for regeneration of helium nor of the water-likes (leak detection).

2.4 *Other* (Guard, diagnostic and H&CD systems refrigeration cryopumps). These clients shall use the roughing system, which has been defined by other clients.

The vacuum technological design of the ITER forepump train has to reflect two major issues. Firstly, the pumps involved must provide a sufficiently high pumping speed for light gases, which is a problem for itself when it comes to dry systems, secondly, all train stages have to be tritium-compatible.

## 2 Major Results

All the requirements have been analysed. Two of them were selected to define the roughing system capacity [3]. The most critical is NB cryopump regeneration, for this task a roughing train of >6000 m<sup>3</sup>/h is needed (see Fig. 1). The second task is the torus cryopump regeneration. In ITER-2001 the evacuation time within the torus cryopump regeneration interval was defined as 75 s, and this task was dominant. Now the requirement of 150 s can be met with a roughing system of about two times less capacity than needed to fulfil the NB task.

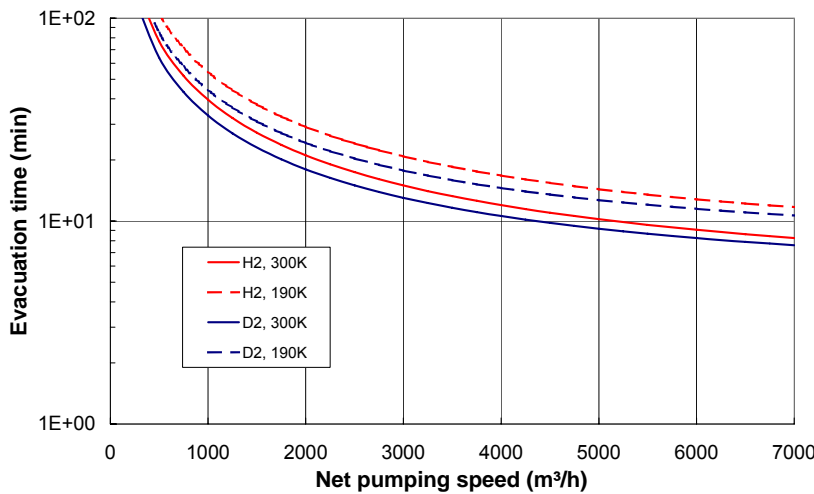


Fig. 1: Evacuation of the neutral beam cryopump during regeneration, calculated for H<sub>2</sub> and D<sub>2</sub> at two representative temperatures (partial and total regeneration). Target evacuation time is ~ 8 min.

With regard to the backing pump, the only commercially available tritium compatible pump of the required capacity is a scroll type NOR-METEX<sup>®</sup> pump. Failure of pumps of this type at JET is proven to be not because of inherent features of the pump, but likely due to exploitation failures. Unfortunately it became clear from the tests made at FZK in earlier times (FORTE and PETRA facilities) with helium, deuterium and protium, that the

NORMETEX<sup>®</sup> pump has a very poor performance with hydrogen in the case of exhaust to the atmosphere (for 150 m<sup>3</sup>/h pump an ultimate pressure is ~30 kPa, maximal pumping speed ~40 m<sup>3</sup>/h); it is therefore usually backed by a metal bellows pump.

The roughing train of a required capacity of 6000 m<sup>3</sup>/h and able to operate with hydrogen could consist of four roots stages backed a 150 m<sup>3</sup>/h scroll pump (see left diagram in Fig. 2). When the roughing train serves the torus cryopump during its 470 K regeneration, the water contents in the pumped gas can achieve a dew point. As a scroll pump is extremely sensitive to the liquid in the gas stream, a moisture trap will be needed at its entrance. Such a means is anyway needed to be compatible to safety events involving severe water-leaks.

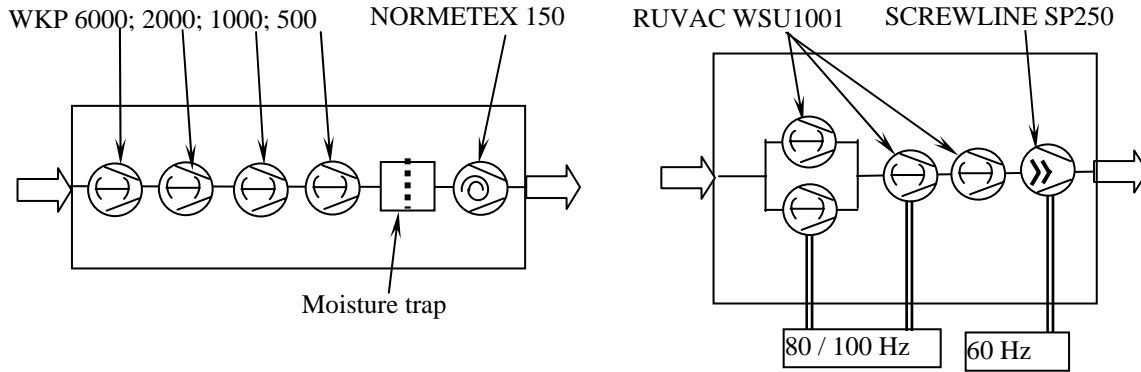


Fig. 2: Forepump train flow schemes. Principle set-up (left) and one candidate practical realisation (right).

In cooperation with the company Leybold Vacuum, tests of a screw pump SP250 with hydrogen were performed. Typically, this type of a pump requires purge gas for isolation of the lubricated volume from the process volume. In order to significantly enhance the pumping performance on light gases (helium and hydrogen), addition of gas ballast (typically N<sub>2</sub>) is very efficient. The purge gas streaming from the seal into the process gas assists the pumping performance as well. The pump SP250 has demonstrated much better results than SP630, especially running at 60 Hz supply.

For the application in the neutral beam test facility NBTF, where no tritium compatibility is requested, but similar requirements in terms of pump-down times, the pump train "RUTA" with roots pumps RUVAC WSU1001 running at ~80 Hz and a screw pump SP250 (see right diagram in Fig. 2) has been analysed and finally recommended (the train is assembled of catalogue units). SP250 and the roots pumps should be electrically fed via frequency inverters. During testing, it has been found that the roots and the screw pump performance on light gases is significantly enhanced with higher rotation speeds.

In the parallel task TW1-TTF/VP12 on tritium-compatible ferroseals, two main important conclusions have been drawn:

- 1) A ferrofluidic cartridge can be feasibly integrated in the roots pump as an internal seal between the pumping and gear volumes;
- 2) A Roots pump modification for the tritium operation will require very costly research and development works, and the modification of different pumps will lead to multiplication of the expenses.

Therefore, it is expedient to compose the forepumping train of one type Roots pumps only. The train proposed for NBTF (Fig. 2, right) does fulfil this requirement (only 1000 m<sup>3</sup>/h Roots). From that point of view, it could very well also be a solution for the ITER roughing system (pending additional tritium modification). Maximal effective pumping speed of this train is about 2800 m<sup>3</sup>/h. From pumping speed and capacity point of view, this forepump train set-up is able to meet the torus cryopump regeneration requirements completely and all but the most challenging of the NB cryopump regeneration requirements. The lay-out of this train is checked, it suits the place allocated for the ITER roughing system in the tritium building. For the case when during the NB cryopump regeneration the evacuation has to be achieved within 500 s, the roughing system should be equipped with a valve system, allowing for connection of two roughing trains in parallel.

A separate issue is the tritium modification of a screw pump. The pump has already aluminium housing; the stationary metallic seals can also be integrated. In opposite, the ferroseals seem to be not applicable for this pump, because the combination of the shaft diameter and rotation speed is out of the range of this seal workability. The development of this pump for

tritium shall be done in the frame of a separate task. The use of a conventional shaft seal should also be assessed as a fallback solution. This does not conflict with implementation of ferroseals in the roots pump, because the SP250 pump has cantilevered rotors, their shaft seals are at the high pressure side and they work at practically zero pressure difference. Moreover, no intensive gas exchange between the pumping and gear volumes can be expected, as at the last stage of the train there will be no effect of the inlet pressure pulsation.

### 3 Final Conclusions

The present task is completed. The following conclusions can be drawn:

1. The analyses of ITER requirements have defined the neutral beam cryopump regeneration to be the design driver. Nevertheless a smaller capacity train is recommended, being determined and designed for the torus cryopump regeneration and all but one NB regeneration case; for the one most challenging NBI service case, a connection of two trains in parallel could be foreseen. It looks reasonable to compose the Roots part of the train only of identical Roots units (serial, parallel).
2. It looks promising to use a screw as a backing pump with somewhat mitigated requirements to the internal inventory and migration of tritium.
3. A sound validation of the selected mechanical pumps for ITER will be provided on the NBTF, which is planned to be put into operation in 2009.
4. The selection of a backing pump is still an open issue (Scroll/Screw/Reciprocating piston) and needs further examinations.

One should note, that the development of a tritium compatible roughing train must be continued when ITER has achieved a complete specification. Design, and, correspondingly, regeneration requirements of the NB cryopump are still not frozen at ITER. Also, the fore-line geometry is still due to be updated. The philosophy of dedicated forepump trains and change-over valves of the roughing system is still under discussion within ITER. The requirements to the service vacuum are also not yet finally specified by ITER.

#### Staff:

A. Antipenkov  
Chr. Day  
A. Mack

#### Literature:

- [1] A. Antipenkov, Chr. Day, R. Lässer, A. Mack, R. Wagner, Tritium pumps for ITER roughing system, Fusion Science and Technology 48 (2005) 47-50.
- [2] J. How (Ed.), ITER Garching JWS, ITER Project Integration Document 2.0, September 2005.
- [3] Chr. Day, A. Antipenkov, M. Dremel, H. Haas, V. Hauer, A. Mack, J.C. Boissin, G. Class, D.K. Murdoch, M. Wykes, Validated design of the ITER main vacuum pumping systems, Fusion Energy Conference 2004, IAEA, Wien, 2005.

## **TW4-TTFF-VP 45**

### **Performance Assessment of Mechanical Pumps in Tritium Plant**

The Tritium Plant of ITER requires many vacuum pumps and compressors to move tritium and other gases within the plant and deliver gases to the torus and its subsystems, typically operating at about atmospheric pressure with relatively small volumes of gas. Several manufacturers produce mechanical pumps suitable for tritium operation and several models have been identified as candidates for the use in the Tritium Plant. Various pumps have been proposed for the ITER tritium plant by the designers. Rationalisation of the pump selections to as small a range of types as possible will bring benefits in operation, reliability and capital costs.

The objective of this task is to review the experience at tritium facilities, such as JET and TLK, and for selected pumps to be tested under representative conditions of the ITER Tritium Plant. Manufacturers' data for most pumps are either for discharge to atmospheric pressure (vacuum pumps) or for the inlet at atmosphere (compressors). The ITER Tritium Plant requires pumps that operate over conditions where the inlet and outlet pressures are variable.

The pumps to be tested have been identified and examples are available already at TLK except for a high pressure pump where an alternative arrangement will be examined using a combination of pumps types which are used in much greater numbers in the tritium plant, which will reduce capital costs and improve serviceability. An existing hydrogen rig has been modified to examine pumping parameters of several pumps that operate up to atmospheric pressure. One special pump, a Thales PR-130, was received at the end of 2004 and a modification of another existing inactive rig has been proposed to test this pump. The reason for this is that the PR-130 pump is designed to produce medium vacuum in the range of a few Pascals in combination with another pump. The pump has a limit on the inlet pressure and will be tested in a closed system. A report on deliverable 1 of this task was delivered in July 2005.

The selected pumps will be tested both to produce their pumping curves over a range of inlet and outlet pressures, first with helium and later with deuterium. Long term endurance tests will be carried out on pumps where firm data is not available. On the basis of the tests recommendations will be made, where appropriate, to change selected pumps to alternatives. It should be noted that none of the pumps selected are expected to survive the operational lifetime of ITER (20 years) if they are in (near) continuous operation. Pump recommendations will also be based on the assessed requirements for maintenance, or more likely replacement, of failed pumps in a glove box environment.

#### Staff:

C. J. Caldwell-Nichols  
S. Beloglazov  
R. Wagner  
S. Welte

## EFDA/04-1141 ITERVAC Conductance Modelling of ITER Torus Exhaust Pumping Ducts

### Background and Objectives

The reference design of the ITER exhaust pumping system is based on 8 cryopumps, connected via 4 ducts to the torus, each of them containing a pump in direct line of sight and a branched pump. For short pulses with a length below 400 s all pumps are pumping. For longer pulses the pumps have to be operated in a staggered mode with 4 pumps pumping and 4 always in regeneration.

The ITERVAC code was used for calculations of the flow in the complex torus exhaust pumping ducts. To do this, the ITER geometry was transformed into a network of defined elementary units, to define a mesh of block-cells. The main input parameters, gas properties, diverter pressure and the pumping speed of the cryopumps, have been varied in ITER relevant range. The outputs obtained are the maximum throughput from diverter into the pumps at isothermal conditions. With the work described here, the task could be finalized [1].

### Results of the system analysis

The simulations were done for two different pump scenarios. The first is the pumping at plasma operation [2]. The diverter pressure is typical between 1 and 10 Pa. The pumping speed of one pump was varied between 10 and 150 m<sup>3</sup>/s. In Fig. 1 the obtained maximum throughputs (for complete ITER) for deuterium are shown. In the same manner calculations were done for hydrogen, tritium, helium, nitrogen, neon, argon and a pseudo mass 5 gas.

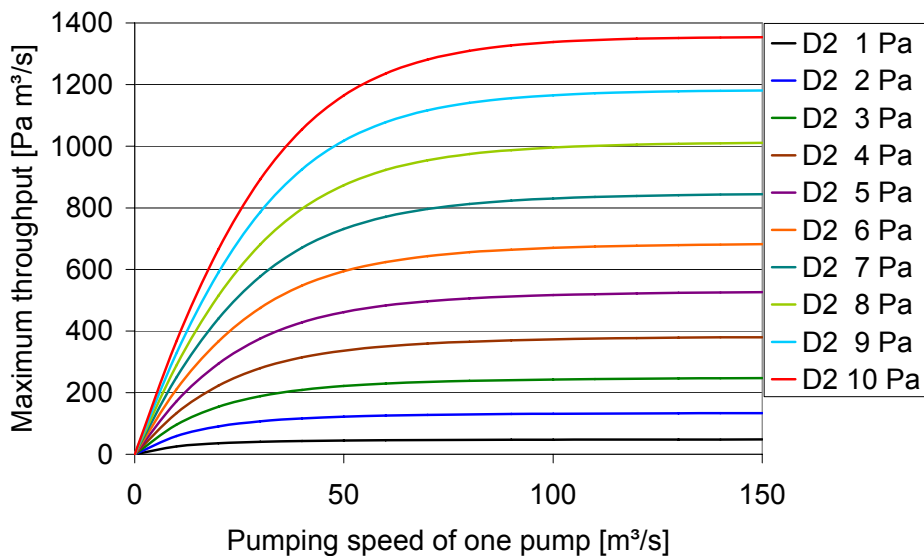


Fig. 3: Maximum throughput for pumping deuterium at diverter pressures between 1 and 10 Pa.

The pumping curves show the same behaviour: The throughput increases strongly with the pumping speed of one pump below 50 m<sup>3</sup>/s. Then the increase becomes slower and over 80 m<sup>3</sup>/s per pump the throughput change is very small. This behaviour is caused by the low conductance of the pumping duct in comparison of the pumping speed. The pressure profile of the duct identifies the pumping slots as the bottlenecks. Therefore the increase of the cross section of the pumping slots was investigated. The results show a relative increase up to 62 % for an increase in pumping slot area of 52 %. Such an increase is therefore strongly recommended to be able to pump the ITER maximum throughput at lower diverter pressures.

Fig. 1 is an important input for the optimum design of the 1:1 torus exhaust cryopump, which should consequently be designed for 50 to 80 m<sup>3</sup>/s nominal pumping speed [3]. With respect

to the absolute achievable throughputs, it becomes clear that a divertor pressure of about 2.5 Pa is needed to meet the ITER required throughput of 153 Pa m<sup>3</sup>/s. These results have already been incorporated into the latest version of the ITER PID [4].

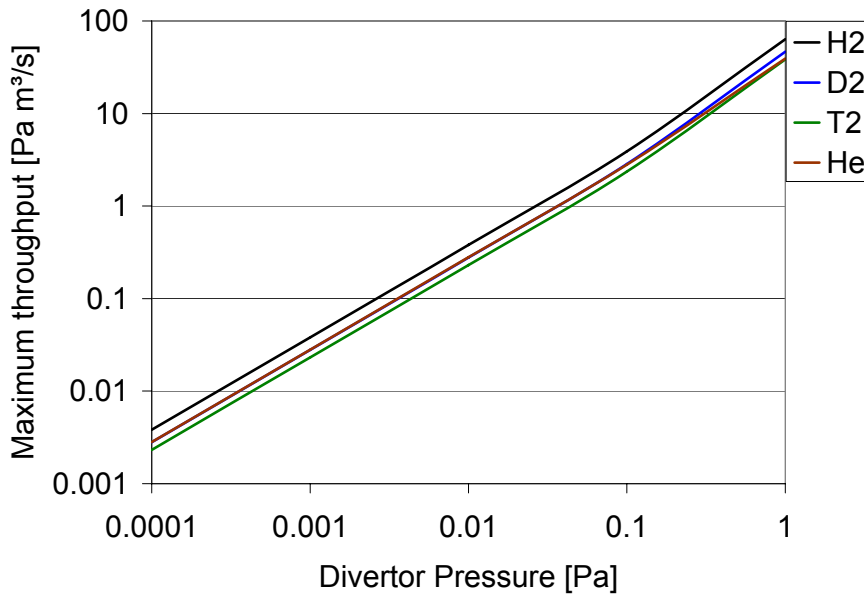


Fig. 4: Maximum throughput of the hydrogen isotopes and helium in the pressure range from 1 to 10<sup>-4</sup> Pa.

The second simulated pump scenario is the evacuating of the torus between two pulses. Here the pressure in the torus has to be decreased to 0.5 mPa in 1400s. In Fig. 2 the maximum throughputs in the pressure range between 1 and 10<sup>-4</sup> Pa are shown. The shape of the graphs are identical. The lowest throughputs are reached

for tritium, the highest for hydrogen. The calculated maximum flow in molecular regime of 28 m<sup>3</sup>/s is slightly below the ITER requirements of 30 m<sup>3</sup>/s. An enlargement of the cross section of the critical parts of the vacuum system, especially at the divertor, is therefore proposed. The required dwell pump down times can only be met, if the outgassing rate is reduced, the overall cross section of the pumping ducts is increased, the overall length of the ducts is reduced and/or the pumping speed in molecular regime is increased.

### Benchmark results

The ITERVAC code turned out to be a very powerful and versatile-to-use tool, which allowed, for the first time, a dedicated system analysis of the ITER vacuum pumping systems in the ITER-relevant transitional flow range. Due to the potentially very significant implications of the ITERVAC results on the ITER design, the code, which was developed only recently, must be benchmarked. An efficient benchmark has to include different geometries and different flow ranges. For a circular pipe, which is the simplest geometry, closed analytical solutions as well as many experimental data are available in the viscous flow regime. The molecular flow regime in all geometries can be very well and reliably treated by Monte Carlo methods, in case of a circular pipe, even closed analytical solutions are available. However, for the ITER relevant transitional flow range, even for the simplest geometry of a cylindrical pipe, experimental data are extremely scarce and do not seem to be very reproducible. Closed analytical solutions do not exist, but there are some approaches for direct solutions of the linearized Boltzmann equation, which have been applied to some simple channel shapes. With this background, three fields have been assessed for benchmarking:

1. Viscous flow through a circular and triangular equilateral channel: The average error found was in the order of 3%.
2. Molecular flow through several channel shapes (circular, square, triangular, rectangular) at varied length to diameter ratio L/d. The maximum error found here was 3%.

3. Transitional flow through a circular tube at varied L/d ratio (from orifice to very long). The ITERVAC results were compared with solutions based on the linearized Boltzmann equation [5], which are good for orifices and ducts with  $L/d > 10$ . For a long pipe the deviation of calculation against simulation found was about 20 % in some cases, only 5% in other cases. For a thin orifice a deviation of about 8 % was found at 10 Pa upstream pressure, increasing up to 40%, especially in the low diameter region, at an upstream pressure of 1 Pa, see Fig. 3.

In summary, the benchmark revealed a very good agreement of the ITERVAC code in viscous and molecular flow range. In transitional flow range, there are larger discrepancies, however without obvious trends. The ITER divertor duct system is characterized by channels with complex shape (conical, trapezoidal) and at short L/d (around unity). Unfortunately, there exist no other values in this region to which a thorough comparison could be drawn, neither experimental ones, nor theoretical based ones.

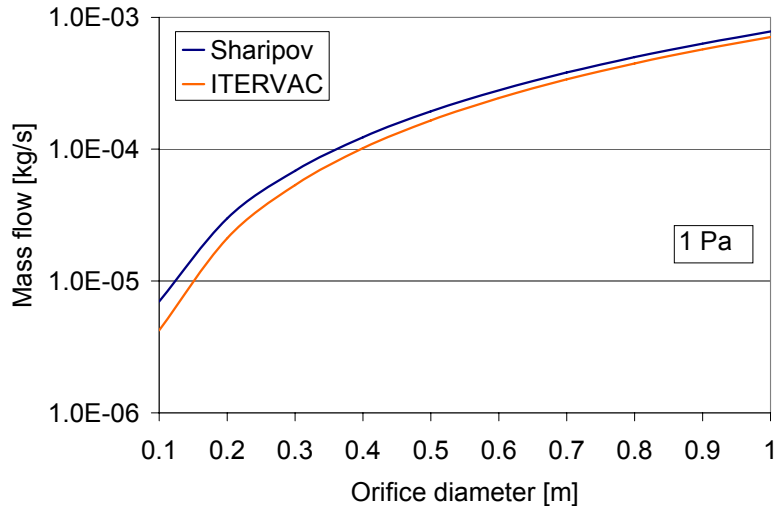


Fig. 3: ITERVAC results vs. calculated mass flows [5] through an orifice at an upstream pressure of 1 Pa (tritium, 273 K).

This is why it has been agreed to start a next step, which is the experimental verification of ITERVAC simulations with a new test rig TRANSFLOW (EFDA Task TW4-TTFF-VP57).

#### Staff:

Chr. Day  
V. Hauer  
A. Mack

#### Literature:

- [1] V. Hauer, Chr. Day, A. Mack, ITERVAC conductance modelling of ITER torus exhaust pumping ducts, Final report, , Internal Report FE.5130.0046.0012/V, Forschungszentrum Karlsruhe, August 2005.
- [2] Chr. Day, A. Antipenkov, H. Haas, V. Hauer, A. Mack, D.K. Murdoch, M. Wykes, R&D and design for the mechanical and cryogenic vacuum pumping systems at ITER, European Vacuum Conference, Paris, France, April 2005, accepted for publication in *Vacuum*.
- [3] Chr. Day, A. Antipenkov, M. Dremel, H. Haas, V. Hauer, A. Mack, J.C. Boissin, G. Class, D.K. Murdoch, M. Wykes, Validated design of the ITER main vacuum pumping systems, Fusion Energy Conference 2004, IAEA, Wien, 2005.
- [4] J. How (Ed.), ITER Garching JWS, ITER Project Integration Document 2.0, September 2005.
- [5] F. Sharipov, AIAA Journal 40 (2002) 10, 2006-2008.

## **TW5-TTFF-VP 57 ITERVAC Validation Test**

### **Background and Objectives**

The ITERVAC code, newly developed at FZK, has become an essential tool for the proper design of the ITER vacuum pumping systems which are at most locations operating in transitional flow regime, which is most difficult to assess. Thus, the standard vacuum formulae and Monte Carlo codes are not applicable. Modelling studies performed within the recent EFDA task TW4-TTFF-VP47 indicate that the ITER specified torus exhaust flow rate cannot be achieved at the lower end of the expected divertor pressure range with the present reference geometry of the divertor slots and ducts.

Because of the importance which is given to the calculation results of ITERVAC, the code must be extensively benchmarked. A theoretical benchmarking was done in the field of laminar and purely molecular flow, however, it has been found that literature data for (intermediate) transitional flow range, which is of major importance for the ITER conditions, are scarce and even not existing for geometries as complex as for the ITER vacuum pumping ducts [1]. In order to validate proposed design modifications, such as to increase the conductance of the path from the divertor to the torus exhaust cryopumps, which have to be made while respecting other functions of the design (e. g. shielding, structural strength of the cassette), an experimental confirmation of the modelling results is required.

This present task therefore aims to set up a test facility to provide a broad and relevant range of well defined experimental data which can be used to benchmark the code.

### **Experimental philosophy**

The philosophy of this approach is not in first line to investigate directly a 1:1 model of the ITER duct, as this would necessitate a huge facility with expensive instrumentation. It is rather foreseen to use different interchangeable test pieces which would be modelled by ITERVAC and the calculated results compared against predictions from the ITERVAC modelling calculations. Emphasis will be laid on the use of fairly complex geometries (conical, trapezoidal,...), culminating with a reduced scale (~1:5) model of the critical components of ITER. By that, covering a range of flowrates (in terms of Kn, Re and Ma numbers), confidence shall be gained with respect to the results obtained for the ITER geometry. This will enable designers to investigate parametrically potential improvements in conductance to be obtained by adjustments to the ITER geometry.

For scale-up, the characterisation of the flow regime is done by the Knudsen number, which is between  $Kn=0.5$  and  $0.01$  in transitional flow regime. Higher numbers indicates the molecular flow regime, lower ones the viscous flow regime. The soundness of a vacuum system in terms of gas throughput is characterised by the Mach number. Mach numbers close to unity indicate a potential bottleneck.

### **The new TRANSFLOW test rig**

The basic idea of the new TRANSFLOW test rig (Transitional Flow Experiments) is the measuring of the conductance of different channels in the transitional flow regime. The test rig can be separated into the dosing dome, two adapter flanges with the test channel in between and the pump dome. The dosing dome serves the purpose to produce an isothermal flow at a constant pressure difference through the test channel. The pump dome holds all pumps. Fig. 1 shows a 3D view and the P&ID of the planned rig. During measurement the wanted gas flow is dosed into the dosing dome via a mass flow controller. Different transducers register pressure and temperature inside the dome. The gas flow path comprises the first adapter flange, the test channel, the second adapter flange, the pump dome, and finally



the turbomolecular pumps with the forepumps. The 2 adjustable gate valves before the turbopumps can be used for reducing the pumping speed, and, by that, modifying the pressure and Kn range.

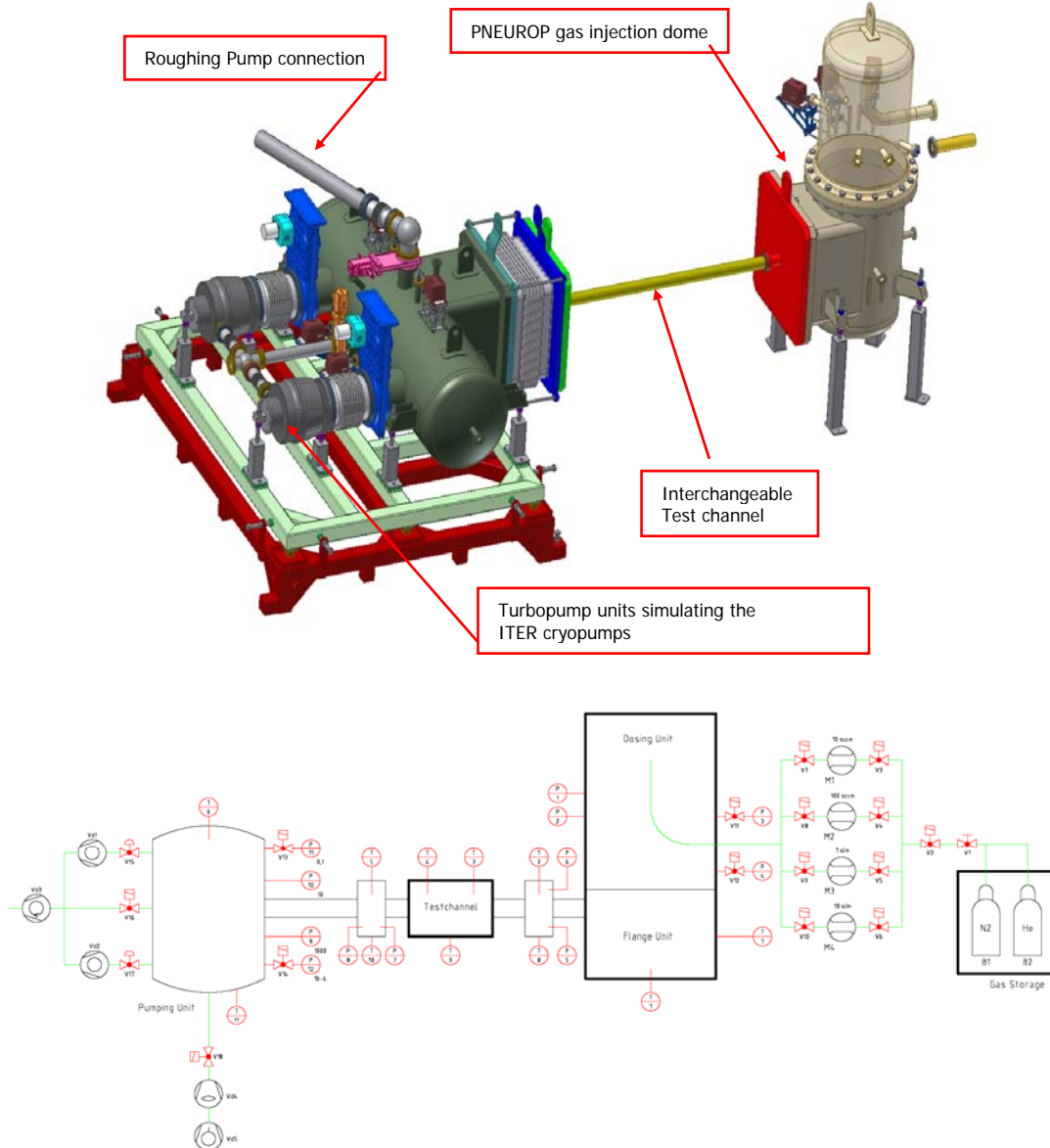


Fig. 5: 3D scheme and P&ID of the TRANSFLOW facility, to be set up at FZK.

The measurements will take place at isothermal conditions. The gases helium and nitrogen are used. The typical pressure inside the TRANSFLOW test rig is in between 100 and  $10^{-6}$  Pa. The temperature range is in between 20 and 200 °C. For temperature regulation a heating system of both domes, the adapter flanges and the test channel is foreseen.

All of the major facility components are under procurement, many have already been procured, such as the controllable DN250CF gate valves, two very large turbopumps (with 2600 l/s nominal pumping speed each), a 250 m<sup>3</sup>/h screw forepump, high precision pressure gauges etc. Both domes are under manufacturing in industry. In terms of piping, control valves and many other items, we could benefit from what was left by the FORTE facility. The SPS-5 data acquisition system was taken from the TIMO facility which is undergoing an up-

grade towards the S7 system. The TRANSFLOW data acquisition system will be based on a multichannel device with optical switch.

The facility will be set up on the location of the former FORTE facility, which has in the meantime been completely removed and dismantled (see Fig. 2). A detailed site plan has been elaborated and efforts are currently undertaken to provide the needed infrastructure (cooling water, electric power supply, lighting, compressed air). The electric cubicles needed for heating and control are also under preparation.

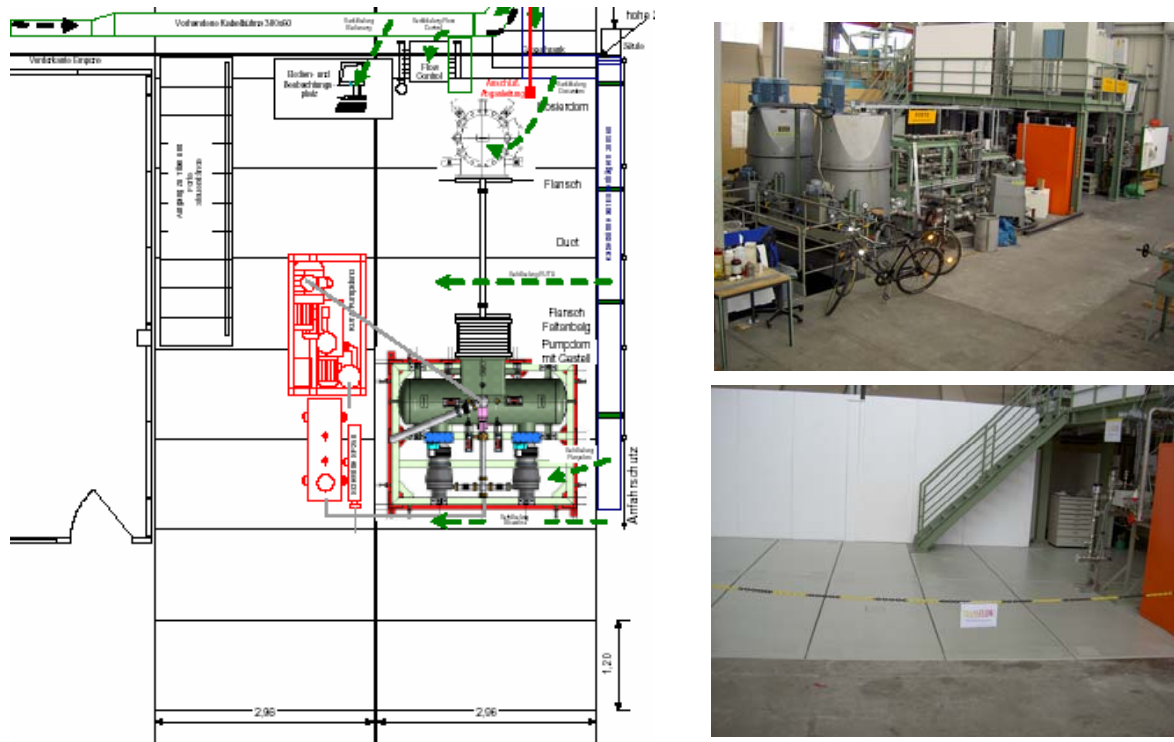


Fig. 2: Site lay-out and preparation of the TRANSFLOW facility in the experimental hall. The right side (*top*) shows the shut-down FORTE facility which was completely disassembled to provide space for TRANSFLOW (*bottom*).

Staff:

- Chr. Day
- V. Hauer
- H. Jensen
- A. Mack
- R. Müller
- P. Pfeil
- H. Stump
- J. Weinhold
- D. Zimmerlin

Literature:

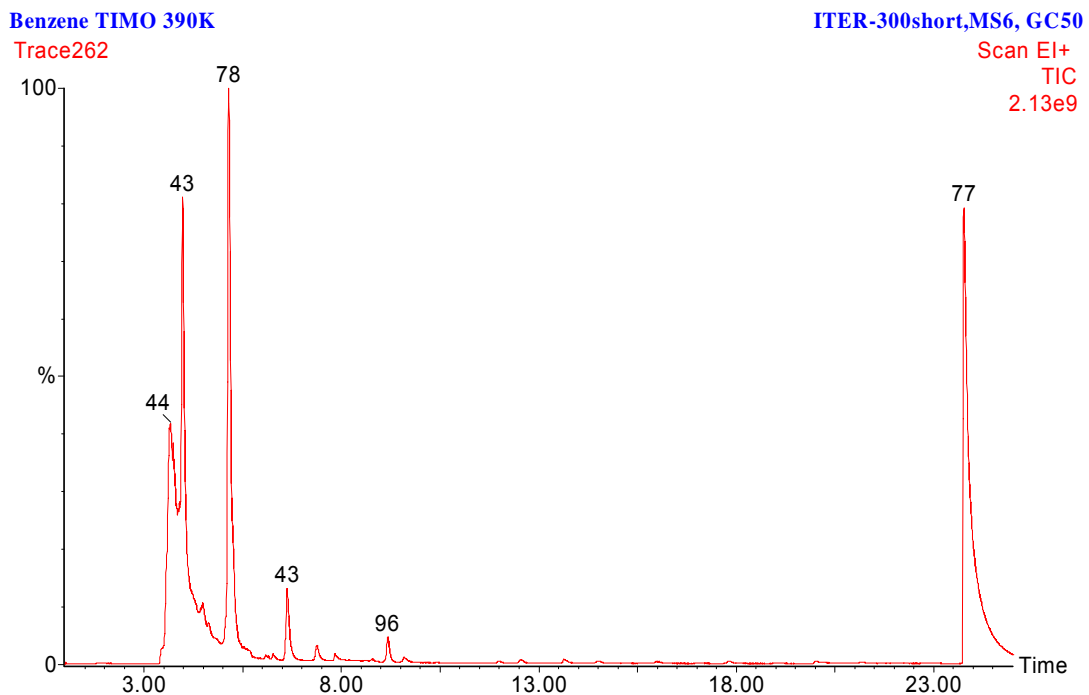
[1] V. Hauer, Chr. Day, A. Mack, ITERVAC conductance modelling of ITER torus exhaust pumping ducts, Final report, Internal Report, Forschungszentrum Karlsruhe, August 2005.

## TW0-T 450/01 Detection and Localisation of Leaks from Cooling Circuits

A method of locating leaks on ITER water cooling circuits is required which will be applied once a water leak into the torus has been confirmed. A proposed method is to add a tracer material into the water circuits and then analysing the exhaust from the ITER cryopumps for the tracer material. By isolating various parts of the cooling circuits and using several tracers it should be possible to locate any leak to a particular circuit and possibly to a sub-section of a circuit. The detector for this method is a gas chromatograph/mass spectrometer (GC/MS) combination which has been purchased and commissioned.

6 candidate tracer materials were tested by the end of 2004 on TIMO before work was halted for the re-configuration of TIMO. The results have been analysed indicating that at present the detection limit is about a factor of 100 greater than required to identify the location of a leak which is at the assumed ITER limit of detection of  $10^{-6}$  Pa.m<sup>3</sup>.s<sup>-1</sup>. However the GC/MS method has several orders of magnitude improvement possible, primarily because it is an off-line measurement based on accumulation techniques.

A gas chromatograph scan of a sample of gas produced from the regeneration of TIMO after poisoning tests using benzene as a trace material is shown below:

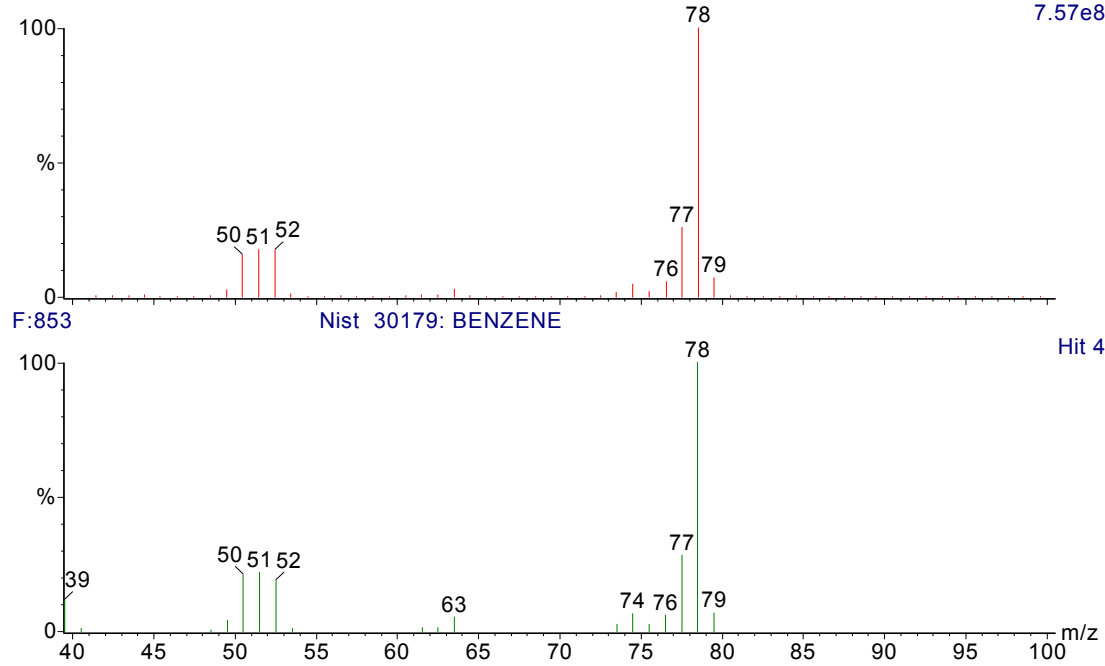


The mass spectrum of the peak at 5.15 minutes after background subtraction is shown below together with the fractionation pattern of benzene from a reference library of compounds.

Benzene TIMO 390K  
Trace262 1 (5.149)

ITER-300short,MS6, GC50

7.57e8



This identifies the peak as benzene and shows that after regeneration the cryopanel of TIMO have released the benzene. Other tracers positively identified in separate tests were hexane, toluene and xylene. In other tests octane and benzyl alcohol were not identified, most probably due to overload of the mass spectrometer which prevented correct detection. The method will be recommended as a method for leak localisation in ITER.

A paper on this work was presented at the SOFE 2005 conference at Knoxville, USA in September 2005 and a draft report on the final deliverable will be presented in December 2005.

Staff:

- C. J. Caldwell-Nichols
- C. Day
- H. Hass
- D. Zimmerlin
- J. Weinhold

## TW1-TTF/VP 13

### Compatibility of Leak Localisation Tracers with Cryopanel

#### 1 Background and Objectives

For ITER, a powerful and sensitive leak detection system is of utmost importance. Consequently, a multi-stage approach has been developed to meet the different leak detection requirements. One of the various strategies involved is for locating a leak in the cooling water circuits which is considered to be the most likely type of a leak into the vacuum vessel. Leak localisation will only be performed after a water leak has been noticed by poor plasma performance and confirmed.

A concept was proposed to add tracer substances at low concentrations which would be released in the gaseous phase in the event of a leak. These tracers would be pumped by the cryopumps and released during regeneration. They would then be detected by the global leak detection system located in the vacuum pump room which is connected to the torus roughing line and monitors the gases exhausted from the cryopumps. Due to the chemical species, the tracer substance will be released not after partial regeneration but after the less frequently performed (over night or over the weekend) regenerations at high temperature (450-470 K). The use of the cryopump would ensure a high sensitivity even for very small leaks due to their accumulation effect over the pumping operational time in between the regenerations.

Any substance to be used as a tracer must be investigated for compatibility with the cryosorption pumping concept. It has to be quantified what amounts of tracers accumulated to the panels can be accepted without leading to charcoal poisoning which would result in a deterioration of pumping performance. Different tracers may be added to the different sub-loops so that one becomes able to pinpoint the leak down to the component level. Therefore, several tracers have been proposed, ranging from lighter hydrocarbons over alcohols to aromatics.

#### 2 Experimental Programme

The experimental tests to exclude poisoning effects and confirm the regeneration within the available 450 K conditions were performed in the TIMO facility. Following the tests performed with light hydrocarbons (methane, ethane, propane), as reported in the last annual report, the programme was completed with higher hydrocarbons, which are liquid at ambient conditions.



Fig. 1: The two analytical devices used for monitoring the tracer gas release behaviour in TIMO: A GC-MS (in the front) and a stand-alone quadrupole MS (in the back).

As described under the task GB8-VP1, three methods were employed for how to inject the liquid probe tracer substances: Either via a bubble column, connected to the test vessel, using helium as carrier gas fed through a holdup of the liquid tracer (method A), or by direct evaporation, via the test vessel (method B), or from backwards via the roughing line (method C).

The standard analytic tool in TIMO to monitor the release behaviour of the candidate tracer species is a quadrupole mass spectrometer (128 amu in standard resolution). For detailed investigations in low concentration ranges, a gas chromatograph-mass spectrometer (GC-MS) combination has been procured and set into operation (cf

task TW0-T450), see Fig. 1.

The following candidate tracer substances have been investigated in this reporting period: 2-methyl-1-butanol, benzene, xylene, toluene, benzyl-alcohol, see Table 1. In those cases where the solubility of the tracers in water at ambient conditions was only very poor, so that the tracers with their high volatility would be preferably evaporated and, consequently, result in an unsatisfactory quantification of the dosed amount, tests with the pure tracers were performed. In addition, the higher hydrocarbons n-hexane and i-octane which have been characterised in terms of charcoal poisoning (parallel task GB8-VP1) have also been assessed

Table 1: Overview of the performed experiments.

Investigated tracer substance	Dosing method
2-methyl-1-butanol in water	A, C
Benzene in water	A
i-octane, pure	B, C
n-hexane, pure	A, C
Toluene, pure	B
Benzyl-alcohol in water	C
Xylene in water	C

for application as tracers. Each experiment comprised a pumping speed test for deuterium with the panels being pre-loaded with the tracer, followed by a complete reactivation of the pump at temperatures up to 450 K [1]. During reactivation, the release of the tracer was monitored as a function of panel temperature. For the reactivation tests, the GC-MS was applied together with the standard mass spectrometer. For each tracer substance, the individual GC-MS fingerprint could be determined and the qualitative release behaviour (in terms of ion currents) was monitored [2]. After some tests, a pumping speed test for helium was carried through subsequent to the reactivation procedure, to identify any permanent degradation of the pump performance, as helium is the gas most difficult to pump.

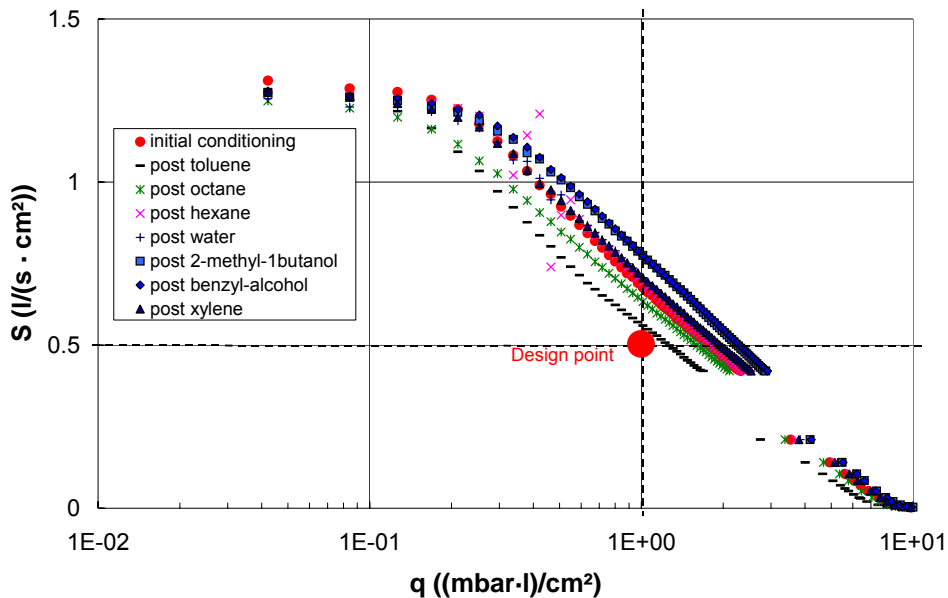


Fig. 2: Results of the helium pumping speed tests following regeneration of the tracer contaminated charcoal.

Fig. 2 illustrates the series of helium pumping speed tests performed. The curve denoted 'initial conditioning' was measured following a thorough bake-out and conditioning treatment in 2004, at an early stage of the campaign. It becomes obvious that there are no big deviations and no further deterioration relative to the conditioning phase; the curves seem to scatter around the one designating the status of fresh conditioning. The design point for pure helium operation can be clearly met. This indicates strongly that even for the heavy hydrocarbon substances, the reactivation can be performed quite successfully and no poisoning

appeared. No show-stoppers have been identified. The envisaged tracer technique for localisation of water-leaks looks to be fully compatible to the cryopump performance.

A quantitative evaluation of all test results will be made available in the next reporting period for completion of this task.

Staff:

Chr. Caldwell-Nichols

Chr. Day

A. Edinger

H. Haas

H. Stump

P. Pfeil

J. Weinhold

D. Zimmerlin

Literature:

- [1] H. Haas, C. Caldwell-Nichols, Chr. Day, A. Mack, and D.K. Murdoch, Study of poisoning effects with the ITER model pump during relevant operation cycles, ISFNT-7, Tokyo, Japan, May 2005.
- [2] C. Caldwell-Nichols, Chr. Day, H. Haas, M. Glugla, D.K. Murdoch, M.E.P. Wykes, SOFE, Knoxville, TN, US, September 2005.

## TW4-TTFD-TR 42 Analysis of Gases from Fusion Devices with Carbon PFCs

A knowledge of the expected impurity species and their respective concentrations is of primary importance for the design of Fuel Cycle systems (especially the Torus Exhaust Cryopump and Torus Exhaust Processing systems (TEP)) and in defining the parameters for related R&D. Of particular relevance to cryopumping are data on higher hydrocarbons (-C7 and above), water and other highly volatile. This is also of utmost importance with respect to tritium inventory control, as these species may have a high tritium content due to isotope exchange of the hydrogen atoms [1]. For TEP, the presence of elements such as S, halogens and other components which might poison permeators and/or catalysts is critical. While data from other devices could differ from ITER, it will still be a valuable indication which should be assessed for its relevance and, where considered necessary, investigated experimentally.

The ITER design has recently seen a significant reduction in fuelling rate, however the impurity content as specified for the exhaust gas mixture remained the same in absolute numbers. So, in the current design this quantity (33 (Pa·m<sup>3</sup>)/s impurity plus 120 (Pa·m<sup>3</sup>)/s fuel) does not seem to be reasonable anymore. It is therefore essential to quantify the composition and the amount of impurities. This task aims to provide confirmed input to the data base for the reference composition of the ITER exhaust gas, mainly focussing on the impurity fractions, which may have a negative impact on the performance of the ITER Fuel cycle system.

To achieve this, it was intended to collect gas samples and analyse them with mass spectrometric and/or gas chromatographic methods. Machines such as ASDEX and TEXTOR will be used as sources of the gas samples. For ASDEX, a wealth of mass spectrometric data (during shot and of the cryopump regenerated gas) is available (standard resolution), which is planned to be investigated. For TEXTOR, one pumping port is being equipped with a mass spectrometer to measure during the shots and with a sample device to collect gas samples via turbopumps, see Fig. 1. The samples are about to be analysed quantitatively by high resolution MS and GC-MS methods.

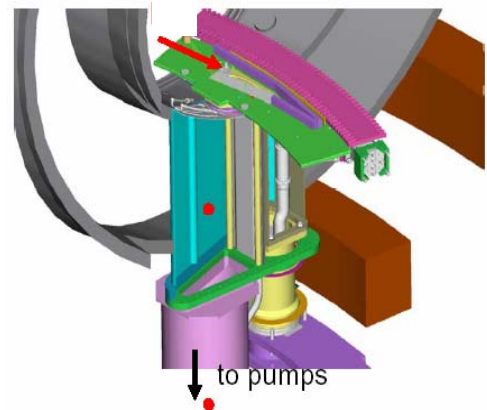


Fig. 1: Sampling duct for exhaust gas at a limiter machine (TEXTOR).

In a recent experimental approach undertaken in JT-60, traces of C<sub>2</sub> have been detected, but no higher hydrocarbons; the amount of exhausted C seemed to increase with rising temperature [1].

### Staff:

Chr. Day  
A. Edinger

### Literature:

- [1] Y. Kobayashi, K. Ksoke, A. Kaminaga, H. Nakamura, K. Tsuzuki, S. Higahijima, S. Konishi, Analysis of exhaust gas in JT-60 U operation, SOFE, Knoxville, TN, US, September 2005.



## EFDA/04-1217

### Operation of the Tritium Laboratory Karlsruhe (TLK)

The Tritium Laboratory Karlsruhe (TLK) is a semi-technical facility which was founded with the aim of establishing tritium handling techniques in Europe and to develop the technologies for the fuel cycle of future fusion reactors. Laboratory scale and technical scale experiments are conducted at TLK within the framework of the European Fusion Technology Program using realistic concentrations of tritium, tritiated gases and tritiated materials which will be characteristic of future fusion devices.

As a pre-requisite for experimental work, an infrastructure with subsystems such as a tritium storage system, clean-up system for the recovery of tritium, a hydrogen isotope separation system, an analytical system, and including confinement of tritium with tritium retention and monitoring systems was established [1]. These subsystems provide essential services to the fusion R&D work with tritium. TLK now has a license to hold 40 g of tritium and has gained a lot of experience in handling tritium since the first license was granted in 1993. In experimental area of around 1000 m<sup>2</sup> there are glove boxes with a total volume of about 125 m<sup>3</sup> which are available for the experimental R&D work at TLK.

The main duty of the TLK infrastructure operation during 2005 was to supply the tritium necessary for technical experiments, take back the tritium after the experiments are finished and to process the returned gases for reuse. Gram amounts of tritium have been supplied in several transfers to the CAPER experimental facility, particularly for the program to compare continuous mode and batch mode operation of the secondary loop of plasma exhaust gas-processing. In addition, 23 separation runs with the Isotope Separation System (ISS) have been carried out to separate and concentrate the tritium from the mixed hydrogen isotopes recovered from experiments. Accountancy was carried out for each transfer of tritium between subsystems and experiments by pVT-c measurements and calorimetry [2].

65 regenerations of molecular sieve beds from the different Tritium Retention Systems (TRS) of the glove boxes have been performed and 69 l tritiated water has been sent to the waste treatment department of FZK for disposal. From 2006 on tritiated water batches with more than 10<sup>10</sup> Bq tritium can no longer be sent to the waste treatment department. Therefore such water will need to be processed in the water detritiation facility which is currently being developed within the R&D program in a staged approach at TLK.

The program to modify the original facilities and systems after more than 10 years of operation continued throughout 2005. The local process control system for CAPER, which handles more than 300 sensors, actuators and controllers, was modified and the original Simatic S5 central process unit and signal groups were replaced by a Simatic S7 central process unit and decentralised periphery groups. The migration included a renewal of the operator interface based on the software package WinCC. This modification increased the availability and spare capacity for I/O and running time (CPU) and also ensures the operation of the local process control system for the next 10 years.

The ISS was also modified. After the upgrade of the system with a new column in 2000, essential parts of the old system and the new system were combined into a single ISS system which is controlled by one local process control system. This modification made the operation of the ISS much easier and also ensures its availability for the next 10 years.

A failed permeator in CAPER was disconnected from the process and moved to a repair box for inspection and to determine the cause of the failure. As a result of this work the glove box has become heavily contaminated with tritium-containing dust from the permeator; even the lines to the ionization chamber and the ionization chamber itself used to monitor the glove box atmosphere have been contaminated. Extensive work was, and still is, necessary to remove the contamination in the repair box.

Staff:

H-D. Adami  
U. Besserer  
L. Dörr  
H. Dittrich  
M. Göckel  
G. Hellriegel  
F. Kramer  
S. Krieger  
K. Nolte  
E. Porter  
F. Rehlinghaus  
P. Schäfer  
P. Schuster  
J. Wendel

Literature:

- [1] Dörr, L.; Besserer, U.; Glugla, M.; Hellriegel, G.; Hellriegel, W.; Schäfer, P.; Wendel, J.: The closed tritium cycle of the tritium laboratory Karlsruhe, Fusion Science and Technology, 48(2005) p. 262-67
- [2] Dörr, L.; Besserer, U.; Grünhagen, S.; Glugla, M.; Kloppe, B.; Sirch, M.; Hemmerich, J.L.: High resolution vacuum calorimeter, Fusion Science and Technology, 48(2005) p. 358-61

**TW1-TTF/TR 11  
Gas Processing during in-situ Tritium Recovery from PFC's**

**TW4-TTFD/TR 41  
Experimental Investigation of Undesired Side-reactions in PERMCAT**

**TW4-TTFD/TR 43  
Comparison of Batch and Continuous Operation Modes for the Impurity Processing Stage of the Tokamak Exhaust Processing System**

One of the key systems within the Tritium Plant of ITER is the Tokamak Exhaust Processing (TEP) system. However, exhaust gases from the vacuum vessel during D-D and D-T operation of ITER will certainly not be the only source for gaseous streams within the Tritium Plant from which deuterium and tritium need to be recovered. Besides the gases from other operational modes of the tokamak, such as deuterium or helium from Glow Discharge Cleaning (GDC) or the fluids from the retrieval of tritium from plasma facing components (PFC's) and co-deposits, various other sources within ITER will generate tritiated waste gases which have to be processed. Since ITER does not have a dedicated system for the treatment of gaseous wastes all the tritium needs to be recovered by the TEP system. Consequently the TEP system has many more duties than the name of this particular part of the ITER Tritium Plant may suggest.

The decontamination factor required for the TEP system is only defined for a short pulse of the D-T burn phase of ITER, is based on the ratio of tritium-inlet to tritium-outlet flow rates, and is specified to be  $10^8$ . Taking the gas composition and flow rates during the burn phase into account this decontamination factor can be translated into a target outlet concentration of  $\leq 10^{-4} \text{ g}\cdot\text{m}^{-3}$  (equivalent to  $\leq 1 \text{ Ci}\cdot\text{m}^{-3}$  or  $\leq 0.4 \text{ ppm}$  tritium). Off-gases from the TEP system shall be stacked via the Normal Vent Detritiation System (N-VDS) of ITER after intermittent storage for decay of  $\gamma$ -active species in dedicated tanks.

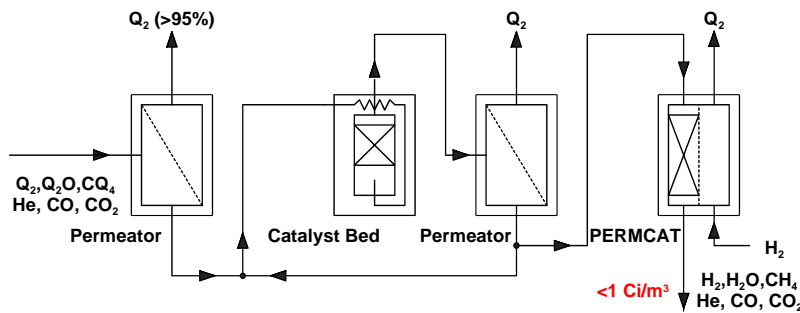


Fig. 1: Basic principles of the three step CAPER process for detritiation (Q=H, D, T).

The removal of tritium down to levels below 1 ppm from D-T streams containing also tritiated impurities such as water or hydrocarbons can only be achieved by multi-stage processes. Figure 1 shows the principle of the three step CAPER process for the TEP system of ITER.

The CAPER process employs a palladium / silver permeator as a first step ('impurity separation') to separate the bulk of un-burnt D-T fuel (tritium isotopomers) from the tritiated and non-tritiated impurities. The second step ('impurity processing') is carried out in a closed loop involving heterogeneously catalyzed cracking or conversion reactions combined with the permeation of hydrogen isotopes through another palladium / silver permeator to liberate and recover tritium from tritiated hydrocarbons or tritiated water. The third step ('final clean-up') removes almost all of the residual tritium by counter current isotopic swamping and is based on a so called permeator catalyst (PERMCAT) reactor. The PERMCAT reactor is a direct combination of a palladium / silver permeation membrane and a catalyst bed and has been specifically developed for final clean-up of gases containing up to about 1% of tritium in different chemical forms such as water, hydrocarbons or molecular hydrogen isotopes.

Depending upon the composition of the gas to be processed by the TEP system the first or even the first and second step of the CAPER process shall be bypassed and the gas directly fed into the second or third step, respectively. The interfaces to all the sources producing tritiated waste gases within the Tritium Plant and beyond (e.g. diagnostics) need to be defined before the capacity and throughput of the different TEP system stages can be finally laid out.

The design limiting case defining the required membrane surface area of the front-end permeators (first step of the TEP system) is the burn and dwell operational mode of ITER. The flow rate for deuterium glow discharge cleaning is specified to be  $100 \text{ Pam}^3\text{s}^{-1}$ , lower than the now reduced burn and dwell D-T feed flow rate of  $120 \text{ Pam}^3\text{s}^{-1}$ .

For the Final Design Report of ITER (FDR 2001) the bleed gas from the front-end permeators during the burn and dwell operational mode was considered to be the design limiting case for the second, and in turn for the third step of the TEP system. However, meanwhile the interfaces to the TEP system are becoming more and more detailed, definitely leading to reconsiderations for the capacity and throughput of the steps downstream of the front-end permeators. For example, each time the cryopumps are regenerated at higher temperatures water (and hydrocarbons) will be released at high partial pressures, and to avoid condensation and to protect the mechanical transfer pumps addition of an inert carrier gas is considered. Under this circumstances the gas load to the second (and third) step of the TEP system would be substantially higher than considered so far; in general cases other than burn and dwell are likely to become design limiting.

To experimentally investigate the individual steps of the TEP system and to demonstrate the overall process in an integral manner the so-called CAPER facility is operated at the Tritium Laboratory Karlsruhe (TLK). CAPER is a versatile semi-technical test rig with a typical tritium inventory of about 3 to 5 g, and a team of about 4 persons is required for experiments; its modular set-up allows different routing of gases, and a large number of control loops along with the comprehensive instrumentation installed permit a proper characterization of the chemical processes and components. The latter is particularly important to scale the process to ITER capacity and throughputs. A mock-up section within the CAPER facility is available and employed for the preparation of gases with different compositions, particularly tritium and tritiated impurity contents, as they are expected to appear from the various modes of tokamak operation and from operation of other systems of ITER. The CAPER facility is also an essential and central system within the closed tritium cycle of the TLK. All primary gaseous wastes arising from experiments at TLK are detritiated in CAPER. The integral tritium operation of the facility can therefore be considered as representative for the TEP system within the Tritium Plant of ITER.

The first step of the CAPER process was particularly investigated in view of the influence of different inert gas loads and the ample results of the parametric study previously reported. To finalize the current tasks recent experimental work was mainly focused on the second stage.

The second CAPER process step being a closed loop with a catalyst reactor ("Methane Cracker") and a palladium / silver "Permeator" can in principle be operated in two different modes. In the straightforward batch mode illustrated in Figure 2 the loop is filled with the gas to be detritiated from a "Storage Tank", which is then cycled for a certain period of time until the tritium

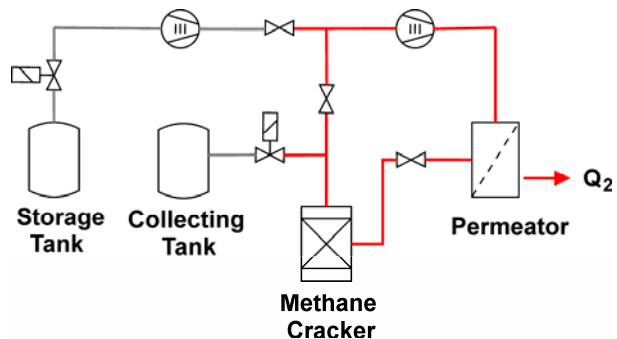


Fig. 2: Secondary CAPER process step operation in batch mode

ated from a "Storage Tank", which is then cycled for a certain period of time until the tritium

level is sufficiently lowered; finally the loop is emptied into the "Collecting Tank" to be ready for the next batch.

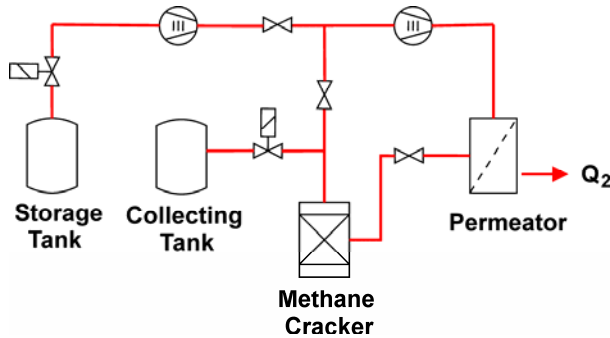


Fig. 3: Secondary CAPER process step operation in continuous mode.

Alternatively, as shown in Figure 3, gas to be detritiated can continuously be fed from the "Storage Tank" into the closed loop upstream of the "Permeator" at a flow rate much lower than the loop circulation flow rate, and the loop pressure is kept constant by a continuous withdrawal of gas downstream into the "Collecting Tank". Such a mode is thought to be easy to control and in comparison to the batch mode could have a higher throughput and maybe a reduced tritium inventory.

To compare in principle the batch mode with the continuous mode operation the evolution of the tritium concentration in the secondary loop with time as measured experimentally is shown in Figure 4 and Figure 5, respectively. After filling the loop and starting circulation of the gas the tritium concentration drops down from levels of almost 500 kCim<sup>-3</sup> (1.5 \* 10<sup>16</sup> Bqm<sup>-3</sup>) rather quickly, however then levels off and finally the tritium concentration is typically ranging between 50 and 100 Cim<sup>-3</sup> (63 Cim<sup>-3</sup> or 2.3 \* 10<sup>12</sup> Bqm<sup>-3</sup> in Figure 4).

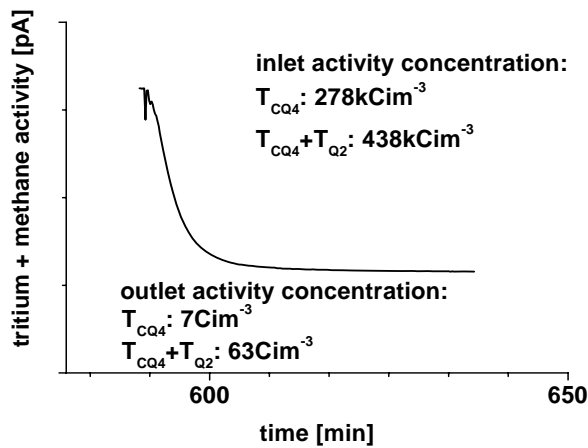


Fig. 4: Secondary CAPER process step operation in continuous mode.

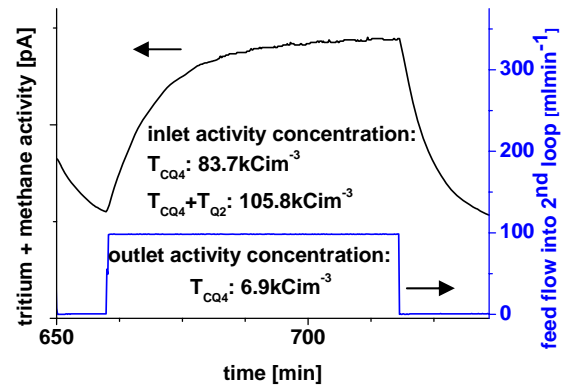


Fig. 5: Secondary CAPER process step operation in batch mode.

If tritiated gas is continuously fed into the secondary loop a steady state concentration is reached after a certain period of time. However, in the case shown the methane decontamination factor is only about 12 (from about 84 kCim<sup>-3</sup> to 7 kCim<sup>-3</sup>) for an inlet flow rate of about 100 mlmin<sup>-1</sup>. Once the feed flow is stopped the loop behaves as in batch mode and the tritium concentration drops down quickly.

As expected the steady state tritium concentration in the secondary loop increases stepwisely for a stepwise increase of the feed flow rate, as shown in Figure 6 and Figure 7. However, even though the concentration of tritium (bound in tritiated methane) in the feed is comparable for the two cases shown the decontamination factor is significantly different. For a feed flow rate of about 100 mlmin<sup>-1</sup> the decontamination factor is about 8 in the experiment illustrated in Figure 6, while the decontamination factor is slightly above 100 in the experiment shown in Figure 7.

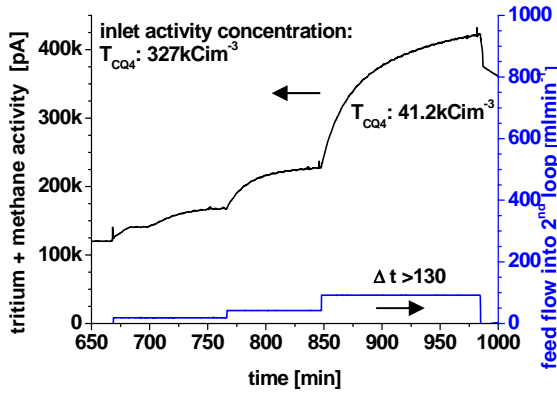


Fig. 6: Secondary CAPER process step operation in batch mode.

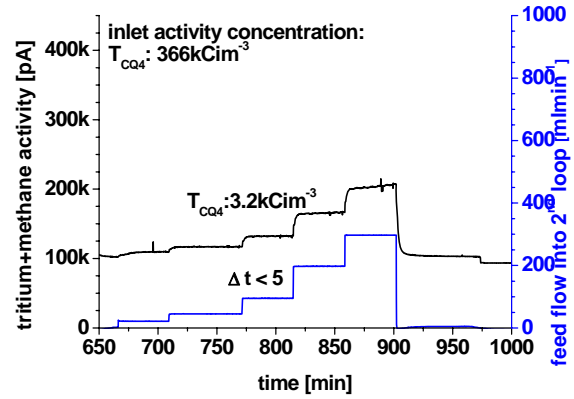


Fig. 7: Secondary CAPER process step operation in batch mode.

In a systematic approach the reason for such a behavior of the secondary loop was eventually found in the actual surface activity of the palladium / silver membrane of the permeator. Highest decontamination factors in continuous mode operation of the secondary loop have only been measured each time the permeator was treated immediately before a decontamination experiment with an oxidative gas, i.e. helium with 4% oxygen. Even at only 400 °C, the operation temperature of the permeator, palladium / silver has a certain catalytic activity to decompose methane and the carbon deposited thereby on the surface of the membrane partly deactivates it. Such a deactivation particularly reduces the apparent permeability of the membrane at low hydrogen isotope partial pressures, a regime in which the permeation flux is governed by the dissociative adsorption rather than by the solubility of hydrogen.

It was proven that the carbon deposited on the palladium /silver membrane surface can be removed with carbon dioxide (Boudouard reaction to carbon monoxide) or more efficiently with oxygen (conversion to carbon dioxide) to restore highest apparent permeabilities. However, by processing of gases containing methane the membrane becomes poisoned again soon and the decontamination factors in the continuous operation mode of the secondary loop are once more too low to comply with ITER requirements. It was therefore concluded that the continuous operation mode of the CAPER secondary loop is not an option for ITER.

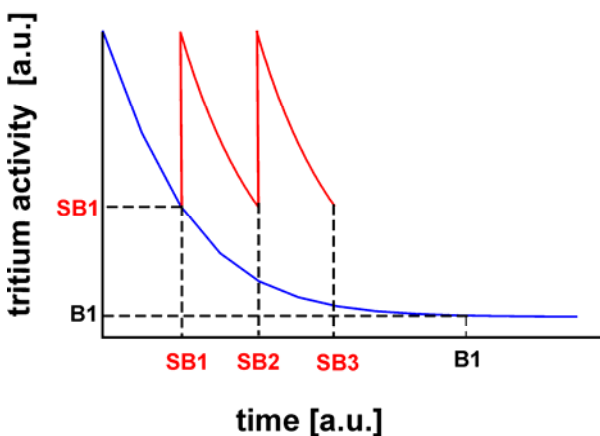


Fig. 8: Illustration of the short batch mode for the secondary loop operation of CAPER.

In an attempt to optimize the throughput of the secondary loop the operation time for a single batch was considered in detail. Essentially the gas to be detritiated can be circulated in the secondary loop until no further decontamination is achievable. On the other hand, the ultimate decontamination level is asymptotically approached and batch processing should therefore be stopped after the required decontamination is achieved. This leads to the so-called short batch mode operation of the secondary loop, as shown in Figure 8.

Once the design decontamination level of the gas is reached the loop can be emptied and filled again for the next step. Particularly in view of the superior performances measured for the PERMCAT component in the final clean-up stage of the CAPER process the short batch mode is the mode of choice for the secondary loop. Also, the palladium / silver membrane of the permeator is insensitive to partial poisoning by carbon deposition in this regime.

A comparison of the achievable throughput as a function of the decontamination factor between batch mode and continuous mode is given in Figure 9.

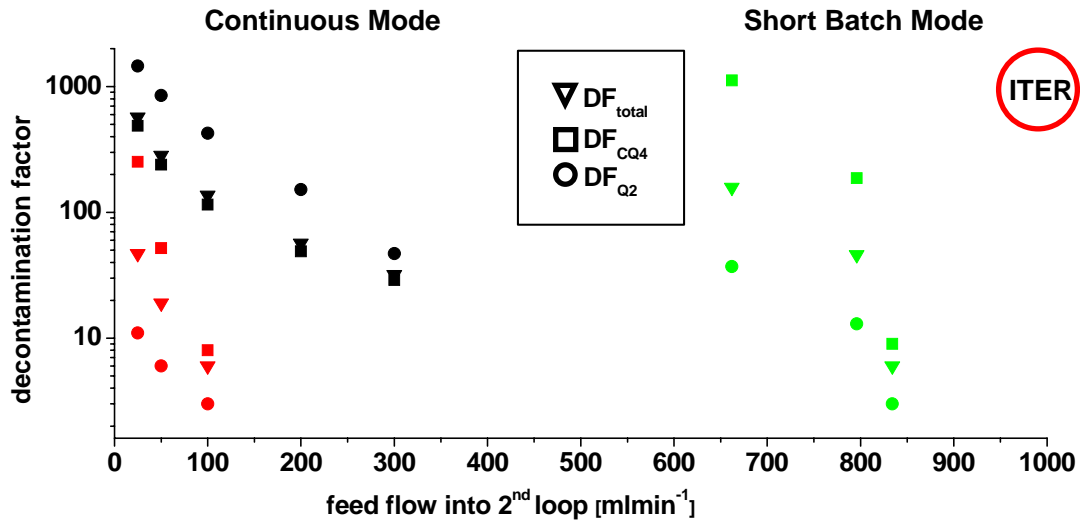


Fig. 9: Comparison of continuous mode with short batch mode operation of the second CAPER process stage.

One should bear in mind that the secondary loop was originally designed for 1/8 of the throughput and off-gas composition of NET, the small European precursor of ITER. With the short batch operational mode the secondary loop of the CAPER facility at TLK has almost 1/2 the capacity required for ITER.

The tritium experiments with the PERMCAT component currently installed in the CAPER facility have shown that the unit can be employed for final clean-up of tritiated gases with quite a variety of compositions. However, carbon oxides present in the feed gas are unavoidably converted to methane, and these unwanted side-reactions are reducing the throughput of the unit for a given decontamination performance. This should be taken into account when sizing the PERMCAT for the TEP system of ITER.

No reference process is chosen yet to recover tritium from flakes and co-deposits on PFC's. Most likely tritium will need to be recovered from highly tritiated water. Experiments with a single tube PERMCAT reactor with an improved mechanical design have proven the concept to process water vapor at high partial pressures. The experiments are ongoing.

Staff:

- B. Bornschein
- C. Corneli
- D. Demange
- M. Glugla
- K. Guenther
- H. Kissel
- T.L. Le
- P. Schuster
- K.H. Simon

Literature:

- [1] D. Murdoch, R. Laesser, M. Glugla, A. Mack, *ITER fuel cycle development: EU-PT activities*, Fusion Sci. Technol. 48, 3 (2005).
- [2] D. Corneli, B. Borschein, E. Fanghaenel, M. Glugla, K. Guenther, T.L. Le, K.H. Simon, Memory effects in measurement of low tritium concentrations as required for the outlet of the TEP system of the ITER fuel cycle, Fusion Sci. Technol. 48, 55 (2005).
- [3] B. Borschein, M. Glugla, K. Guenther, T.L. Le, K.H. Simon, S. Welte, Successful experimental verification of the Tokamak Exhaust Processing Concept of ITER with the CAPER facility, Fusion Sci. Technol. 48, 11 (2005).
- [4] K. Munakata, B. Borschein, D. Corneli, M. Glugla, *Numerical Simulation of membrane reactor for detritiation of plasma exhaust gas*, Fusion Sci. Technol. 48, 17 (2005).



## TW1-TTF/TR 31 Improvements to the Mechanical Design of the PERMCAT Component

The PERMCAT step is the final of the three-stage CAPER process and is being tested at TLK in a semi-technical facility used to demonstrate the feasibility and reliability for the tritium recovery not only from Tokamak exhaust streams but also from any other tritiated gases produced throughout the ITER Tritium Plant. The so-called PERMCAT component is a direct combination of a permeator made of palladium / silver membrane, which separates hydrogen isotopes from other gaseous species and a catalyst bed, the latter promotes isotope exchange reactions that liberate chemically bound tritium from molecules such as tritiated water or tritiated hydrocarbons. Permeation and isotopic exchange take place simultaneously in a countercurrent swamping mode, providing high decontamination ability by always keeping the outlet of the component at a very low tritium level. This high detritiation efficiency has been experimentally demonstrated and decontamination factors higher than  $10^4$  have been reached on different tritiated gaseous mixtures with single-tube and multi-tube PERMCAT membrane reactors.

Besides the physicochemical processes the mechanical stress of the membrane under normal or off-normal operations is another key issue that needs to be incorporated in further PERMCAT developments. Obviously the dilatation of palladium / silver membranes upon hydrogen uptake during permeation excludes to fix the membrane at both ends. For this reason the first generation of PERMCAT components involved finger-type membranes closed at one end, requiring additional capillary tubes and thus leading to a rather complex design implying a three-coaxial tubes configuration as shown in Figure 1. Moreover, it has been unfortunately observed that during off-normal operation, for example shut down of the heaters during hydrogen permeation, the PERMCAT performances can be dramatically spoiled. Since the performance loss is due to a permanent distortion of the geometry the function can not be restored after such an event.

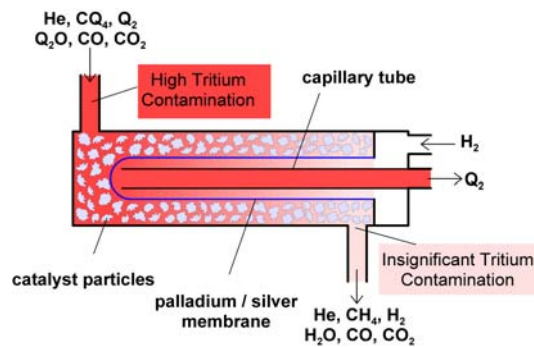


Fig. 1: Principle layout of three-coaxial tubes configuration (first PERMCAT design).

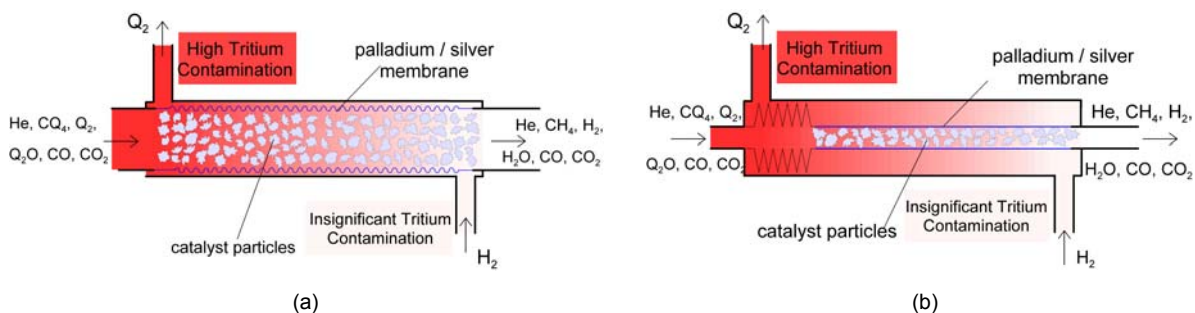


Fig. 2: Principle layout of two-coaxial tubes configuration (improved PERMCAT design).

In order to simplify the design and to improve the robustness of the PERMCAT component, different concepts have been proposed. One option is the use of bellows that could compensate the mechanical stresses that the membrane is subject to if fixed at both ends. For these purposes two different designs using a two-coaxial geometry are followed as depicted in Figure 2: (a) either by using a convoluted palladium / silver membrane acting itself as a bellow or (b) by adding a stainless steel bellow to a standard straight membrane. While the latter option takes advantages of commercially available parts, the first option requires an on request manufacture, which has been optimized to avoid cracks formation during the process.

Difficulties for the convolution production have been successfully overcome and sufficient numbers of new membranes were available for new PERMCAT production. Both options for improved PERMCAT designs will be tested on prototypes and hence four units for type (a) and one for type (b) have been produced in the main workshop of the Forschungszentrum.

The experimental proof of principle of the suitability for such improved PERMCAT designs has been engaged. It has been first verified on type (a) components that the high permeation and selectivity of the membranes are not affected by the convolutions. Then two units were filled with catalyst and put in series for further investigations about their ability and efficiency for gas processing. The first part of the experimental study concerns "cold" runs using water vapor ( $H_2O$ ) filled in the catalyst side while deuterium ( $D_2$ ) is used as the swamping gas. It is successfully observed that the water finally recovered contents up to 99% of deuterium proving that the convoluted design can be a candidate for future PERMCAT technical components. Because of the limited accuracy for the titration technique using an infra red spectrometer, measurements of decontamination factors higher than  $10^2$  are excluded. For that reason the next steps for experimental investigation will be performed with tritium in the CAPER facility that allows precise determination of very high decontamination factors. The same experimental study will be adopted for type (b) components.

In parallel a new installation was built with the aim to observe the varying length and mechanical behavior of palladium / silver tubes subject to hydrogen ambiances and thermal cycles. A first set of experiments were performed on finger-type membranes to study the contraction / expansion properties under hydrogen permeation at different temperatures. While thermal dilatation was measured closed to 0.5% at the normal operating temperature of 400 °C, expansions of up to 2.25% were observed at 50 °C as a result of hydrogen uptake by the membrane. In addition it was observed that under permeation conditions below 150 °C the membrane tends to bend significantly as shown in Figure 3, and secondly that hydrogen loading / de-loading cycles shortens the membrane (0.75%). However after these experiments the membrane remained leak tight. These observations will be useful to define the appropriate mechanical preloading of the bellows added in the improved PERMCAT designs. Next steps will focus on long-term hydrogen exposure at ambient temperature to learn more about possible failures of previous or future PERMCAT components.



Fig. 3: Deformation of a finger-type Pd / Ag membrane during  $H_2$  permeation at 100 °C.

Staff:

D. Corneli  
D. Demange  
M. Glugla  
T.L. Lee  
K.H. Simon  
S. Welte

## TW1-TTF/TEP 13A Self-Assay, Fast Delivery Tritium Storage Bed Development

### TW3-TTFD/TR 33 Determination of Isotopic Effect during Rapid Delivery from Storage Beds

The storage of the hydrogen isotopes as a metal hydride is considered to be one of the simplest, safest and most compact techniques. Such technique is implemented in the Storage and Delivery System of the ITER Tritium Plant for storage and supply of hydrogen isotopes and their mixtures. Parametric studies of a prototype technical scale storage bed is essential to meet ITER requirements: high safety standards, hydrogen supply rate as high as  $200 \text{ Pa}\cdot\text{m}^3\cdot\text{s}^{-1}$ , in-built tritium inventory accountability. Many technical issues shall be addressed starting from the selection of the proper getter material, designing of the getter containment to allow high heat loads and precise thermal accountability during determination of the tritium inventory.

A 1:1 ITER storage bed was designed and manufactured in the Forschungszentrum Karlsruhe. The Getter Bed (GB) is filled with  $\sim 1960 \text{ g}$  (13.0 moles) of zirconium-cobalt powder the current reference ITER material. However, the choice of ZrCo is increasingly criticized for a number of reasons. The amount of zirconium-cobalt is chosen such that GB can absorb 16.66 moles or  $100 \text{ g}$  of  $\text{T}_2$  resulting in  $\text{ZrCoT}_{2.6}$  tritide.

The storage bed is designed to perform in-situ accountability of tritium inventory. Therefore, calorimetric loop is included in the experimental setup to carry a helium flow through the stainless steel tube installed inside the ZrCo tritide powder containment. The tritium inventory of the storage bed can be evaluated based on the helium stream temperature increase picking up the decay heat of tritium. The tests of the in-situ accountability performance are ongoing. The initial calibration has been performed by simulating the heat generated by tritium decay using the electric heaters in the bed and recording of the He temperature increase.

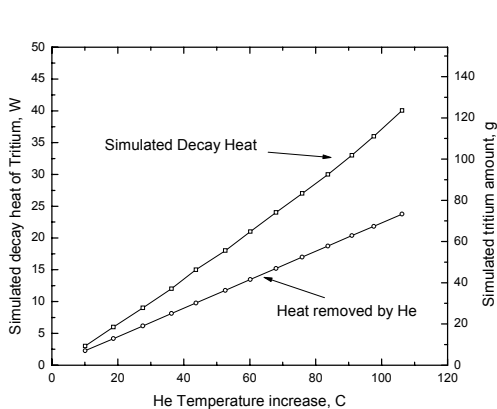


Fig. 1: Calibration curve (He flow 15 NI/min).

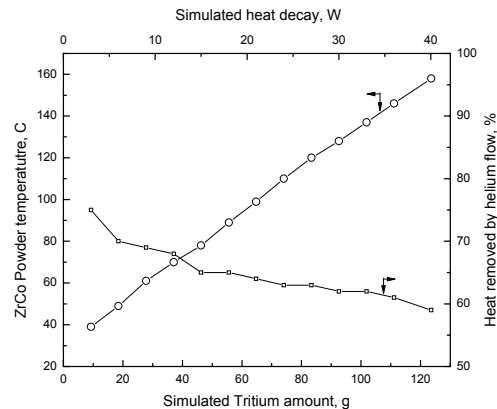


Fig. 2: Temperature increase of the ZrCo powder as function of tritium inventory.

During design and construction of the Storage Getter Bed priority was given to safety and to the achievement of the requested high supply rates. Lower priority was given to in-situ accountability. This means that intensive parametric studies are necessary to fully characterize performance of the accountability loop in order to give recommendations for optimizing of various parameters of the structural and functional components for the design of the final bed.

Under dynamic conditions, such as fast desorption of isotope mixtures from hydrogen storage getter beds, significant kinetic isotope effects might appear and mix up with the thermodynamic isotope effects in the metal hydride-hydrogen system, primarily depending on de-

sorption temperature interval and isotopic composition in the metal hydride. Kinetic isotope effect combined with the thermodynamic isotope effects may as well be of concern in the course of routine operation of the SDS. The composition of the hydrogen gas mixture supplied by the getter bed may be different from the one absorbed in the getter and may even change during unloading of the bed depending on the variation of the isotope effect with the actual amount of hydrogen isotopes stored in the bed. The purpose of the task TW3-TTFD-TR 33 is to determine these isotopic effects in the concentration range of the gas mixtures supplied from the ITER storage beds in comparison to the hydrogen composition absorbed in the getter beds. In many metals these effects exist in every metal hydride, but are usually small.

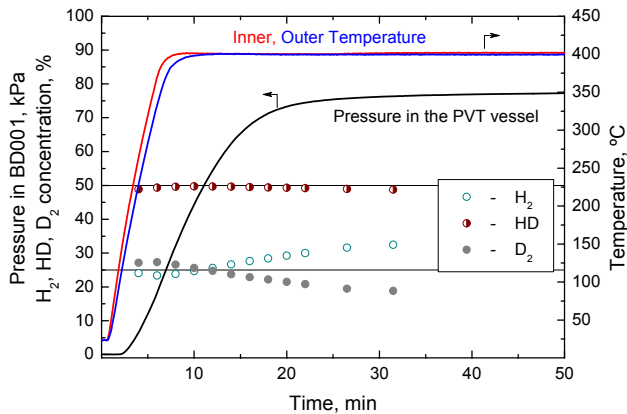


Fig. 3: Desorption of hydrogen deuterium/mixture from the storage bed.

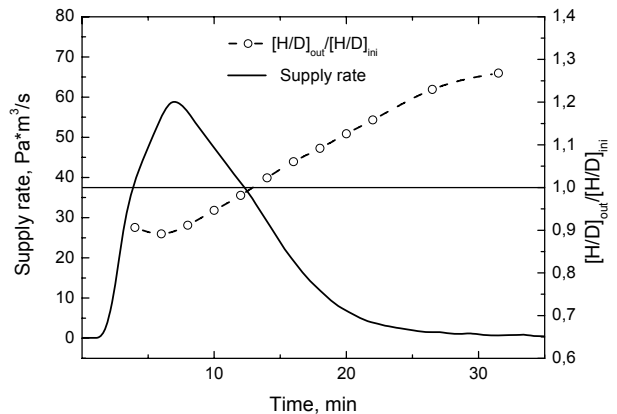


Fig. 4: H/D ratio in the outlet gas stream during fast deloading of the getter bed.

Figure 3 shows the variation of the hydrogen isotopes concentrations during the fast deloading of the stored equimolar hydrogen/deuterium gas mixture from the getter bed. At the beginning of desorption the deuterium concentration is higher than in the gas mixture loaded into the storage bed. After a certain time the deuterium concentration decreases below the initial value. Because the heavier isotopes are released preferably the zirconium-cobalt hydride/hydrogen system exhibits an inverse apparent isotope effect. It can be seen in Figure 4 that H/D ratio varies up to 20% from the one initially absorbed in the getter bed. Such an isotope effect will have an impact on the final design of the control system of ITER SDS in order to supply deuterium/tritium mixtures of required composition during the plasma shots. Experiments at different heating rates and various gas H/D/T ratios in the gas mixture are necessary to investigate systematically the isotope effects during loading and unloading of the zirconium-cobalt getter bed.

Additionally to the apparent isotopic effect under dynamic conditions investigation of the isotopic effect under thermodynamic equilibrium conditions is ongoing. The equilibrium pressures of protium and deuterium above  $ZrCoQ_x$  shall be determined for various temperatures in the pressure range between 0 and 0.11 MPa. In addition, the total atomic concentration  $x$  of hydrogen in the metal shall be changed with  $x$  being 0.5, 1.0, 1., 2.0 and 2.5 to determine the possible dependence on the total hydrogen concentration in the bed. However due to disproportionation behaviour of the  $ZrCo$  powder the experimental programme will be revised.

**Staff:**

- S. Beloglazov
- E. Fanghänel
- B. Kloppe
- R. Wagner

Literature:

S. Beloglazov, M. Glugla, R. Wagner, E. Fanghaenel, S. Gruenhagen "Investigation of isotope effects in the gas streams supplied by a 1:1 ITER storage bed using a micro gas chromatography", Fusion science and technology vol. 48 (2005) p. 67-71

## **TW4-TTFD/TR 44**

### **Inactive Tests of Selected Composition Control Loop Performance under Typical ITER Operating Conditions**

ITER will require various gas mixtures to be delivered to the torus subsystems, i.e. Gas Injection Systems, Pellet Injectors and Neutral Beam. The ITER Tritium Plant is to supply various gas streams to these systems, both hydrogen isotopes and impurity gases. For neutral beams pure hydrogen or deuterium is required. For gas puffing and pellet injection gas mixtures are required and ITER will have gas valve boxes to produce and control the composition of the final mixtures required for plasma operations. 7 gas valve boxes are planned for gas puffing and 6 for pellet injection, all of these will be outside of the ITER Tritium Plant.

The original task assumed that the ITER fuelling systems would require specific gas mixtures to be supplied to them from the Storage and Delivery System of the ITER Tritium Plant. Further, the gas mixtures could be required to vary with time according to the demands of ITER. Control loops were planned to provide these flows which would take into account changing conditions inside the ITER Tritium Plant (pressures in buffer vessels, compositions delivered from storage getter beds, etc.). Selected control loops were to be simulated in experimental rigs using components and control systems planned for ITER and their performance assessed. ITER has confirmed that the final mixing of gases will be performed at the gas valve boxes for gas puffing or for the pellet injectors and not in the Tritium Plant. The Tritium Plant is now required to supply basic mixtures of hydrogen isotopes and other gases to the gas valve boxes. The interface between the Tritium Plant and the gas valve boxes has to be defined, particularly the information of the gas compositions being supplied by the Tritium Plant.

The initial part of the task will be altered to examine the interaction of the Storage and Delivery System and the gas valve boxes to determine the optimum method of controlling the gas compositions supplied to ITER. Real-time information of the gases being supplied from the Tritium Plant may be necessary and this will require a device to perform gas analyses in the order of a second in order that feed-forward information can be sent to the controller for the gas valve boxes. A potential device has been identified and this will be proposed for testing in a re-defined task. The device is based on a quadrupole mass spectrometer with a fast sampling pumping arrangement to allow a representative sample of gas reach the quadrupole quickly and produce information for the gas valve box controller. The device is not tritium compatible and part of the investigation will be to propose changes required for operation with tritium. If a mass spectrometer is required then the investment will be beyond the resources originally envisaged and in this case the resources will need to be increased.

#### Staff:

C. J. Caldwell-Nichols

## TW1-TTF/TR 13 Extended Lifetime Tests of Specified Tritium Plant Components

### Background

Post service examination of several prototype tritium plant components is required to give design information for ITER components. Several components have already been investigated but a failed permeator from the CAPER facility of TLK remained to be examined for the cause of the failure.

### Objective of task

The failed permeator from CAPER had been transferred to a glove box dedicated to repair of tritiated components. The objective was to determine the cause of the failure of 4 of the 6 electrical heaters of the permeator as this is of prime importance to the design of similar ITER components. When the outer containment of the permeator was first removed there was a considerable release of tritiated gases which contaminated the glove box. As other urgent tasks had to be undertaken in the glove box which could not risk being contaminated, the glove box had to be decontaminated and a new ionisation chamber installed before the work on the permeator could proceed.

### Developments in 2005

When the outer containment of the permeator was re-opened there was again another large release of tritiated gases, suggesting that there was a surface which adsorbs gases and releases them when exposed to air. The heaters were mineral insulated metal sheathed co-axial cables which were wound around the permeator element and pre-heater section of the assembly. A heat shield had to be removed to reveal the heaters (fig. 1) and this involved cutting the inlet tube to the permeator element, resulting in a further but expected release of tritium into the glove box.



Fig. 1: Permeator element exposed showing the heater arrangement, discoloration of the foil.

Electrical test showed that the 4 heaters had failed in their hot zones by open-circuit breaks in the centre conductor and in 2 cases a partial short circuit to the sheath. The heaters were attached as bifilar pairs to the 2 heating zones of the permeator element (fig. 2) and covered with a thin stainless steel foil. The heaters had failed at the same locations in each pair, indicating a common mode failure. Between the securing straps that held the heaters to the permeator element the heaters had in many areas lifted off which would have reduced the heat transfer to the permeator element and the heaters would have then reached higher temperatures to maintain the required permeator temperatures. When the heaters were removed from the permeator this revealed that the sheath material of the heaters was very brittle and fractured during the removal process in several places (fig. 3). The conclusion was that repeated flexing of the heaters during operation due to thermal expansion had resulted in high stress levels which, together with a degree of hydrogen embrittlement, lead to failure of the sheath leading to failure of the centre conductor. The conclusion drawn was that all similar heaters in future will be conservatively rated and firmly secured in grooves cut in the device to be heated.



Fig. 2: Detail of heaters with covering foil removed showing gap between heaters and permeator tube.



Fig. 3: Heater removed from permeator showing brittle fracture of sheath.



Fig. 4: Cut into permeator element showing Pd/Ag tubes and black powder deposits.

Analysis of various samples of the permeator materials were made to produce an estimate of the tritium embedded in the permeator. A section of the permeator element was cut away and this revealed a considerable quantity of black powder had formed in the inlet volume of the permeator element (fig. 4), assumed to be mostly carbon from the dissociation of methane. Analysis showed that this powder contained a considerable inventory of tritium. The conclusion drawn was that future devices should take precautions against such powder spreading around a system. The inventory measurements gave a representative figure for the amount of tritium

that will remain in similar devices at the end of life even after in-situ detritiation techniques have been applied. Also it indicated the likely problems that will be encountered during decommissioning of the ITER Tritium Plant.

The draft report on the final deliverable for this task was presented in August 2005.

Staff:

C. J. Caldwell-Nichols  
N. Bekris  
U. Besserer  
H.-D. Adami  
F. Kramer



## **TW1-TTF/TR 16 Tritium Recovery from Ceramic Breeder Test Blanket Module**

During the last several years an intensive testing of the components for the tritium extraction system of the Helium Cooled Pebble Bed Test Blanket Module (HCPB-TBM) has been performed. In the present design of the HCPB-TBM tritium is extracted from the He purge stream in a two steps process: cryogenic trapping of water vapour followed by cryogenic adsorption of hydrogen isotopes. Experimental results describing the performance of the Cold Trap (CT) and the Cryogenic Molecular Sieve Bed (CMSB) at the flow rates as high as 1/6 of ITER requirements are published the mean time in referenced journals.

As far as the cryogenic Cold Trap is concerned the results achieved during parametric studies with CT show that water vapour concentrations lower than 0.1 vppm can be reached in the He stream at flow rates as high as  $1.0 \text{ m}^3 \cdot \text{h}^{-1}$  and initial water vapour concentration in the range of 10-300 vppm. In order to meet flow rates requirements of TBM the Cold Trap should be scaled up to be able to process helium streams at the rates up to  $12.0 \text{ m}^3 \cdot \text{h}^{-1}$ . However, based on the experimental results it was concluded that the present design can not be simply scaled to the full size ITER. This is true for all other CT's tested and reported in the literature by other groups. Therefore either full scale tests need to be taken into account or alternative process options, such as water vapour adsorption at room temperature using a molecular sieve bed.

### **Cryogenic Molecular Sieve Bed (CMSB)**

The performance of a CMSB was tested in a closed loop with process gas flow rates of up to  $2 \text{ m}^3 \cdot \text{h}^{-1}$  and hydrogen concentrations up to 2000 ppm. The adsorption capacity of the bed was found to be 9.0 mol at a hydrogen partial pressure of 110 Pa, in full agreement with the adsorption capacity measured by the volumetric method. Based on the results of parametric testing the design study is ongoing in order to scale up CMSB to meet the required throughput ( $12 \text{ m}^3 \cdot \text{h}^{-1}$ ). The fact that the mass-transfer zone was found to be relatively narrow (12.5% of the MS bed height) allows straight forward scaling up the CMSB to the ITER flow rates.

#### Staff:

S. Beloglazov  
R. Wagner

#### Literature:

- [1] N. Bekris, C. Caldwell-Nichols, E. Hutter, "Cold trap and cryogenic molecular sieve adsorber: components for tritium extraction from purge gas of the HCPB-breeder blanket for ITER", Fusion Eng. Design, **69** (2003), 21-25
- [2] N. Bekris, E. Hutter, J. Rodolausse, „Parametric studies and scale-up of a cold trap in the tritium extraction loop of a HCPB breeder tet blanket for ITER“, Fusion Scie. Technology, **41** (2002), 1009-1013
- [3] N. Bekris, E. Hutter, H. Albrecht, R.-D. Penzhorn, D. Murdoch, „Cold trapping of traces of tritiated water from the helium loops of a fusion breeder blanket“, Fusion Eng. Design, **58-59** (2001), 423-428
- [4] S. Beloglazov, N. Bekris, M. Glugla, R. Wagner, "Semi-technical cryogenic molecular sieve bed for the tritium extraction system of the test blanket module for ITER", Fusion science and technology vol. **48** (2005), 662-666

## TW4-TTFD/TR 46

### Design, Experimental Plan and Procurement of Cryogenic Distillation System for Isotope Separation Tests for ITER

A Cryogenic Distillation (CD) facility will be installed at TLK with the aim to investigate the trade-off between the Water Detritiation System (WDS) and the Isotope Separation System (ISS) for ITER, to analyze the behaviour and the performances of different components and to validate the modelling software related to the cryogenic distillation process. Design studies should establish the concept definition of the cryogenic distillation facility that will allow developing the engineering design of all subsystems of the experimental rig. A detailed design of the main components such as the cryogenic distillation column itself (including boiler, condenser and equilibrator), the refrigeration unit for the column condenser, the cold box layout and the layout of the enclosure for the equipment operating at ambient temperature will be provided as well.

In Figure 1 the block diagram of the TRENTA4 facility, under construction at TLK is shown. TRENTA4 is a combination of a WDS based on Combined Electrolysis Catalytic Exchange (CECE) and a CD process, allowing parametric studies for both combination and separately for each process. The configuration of the TRENTA4 facility is similar to the configuration of the proposed connection between the CD1 column and WDS for ITER.

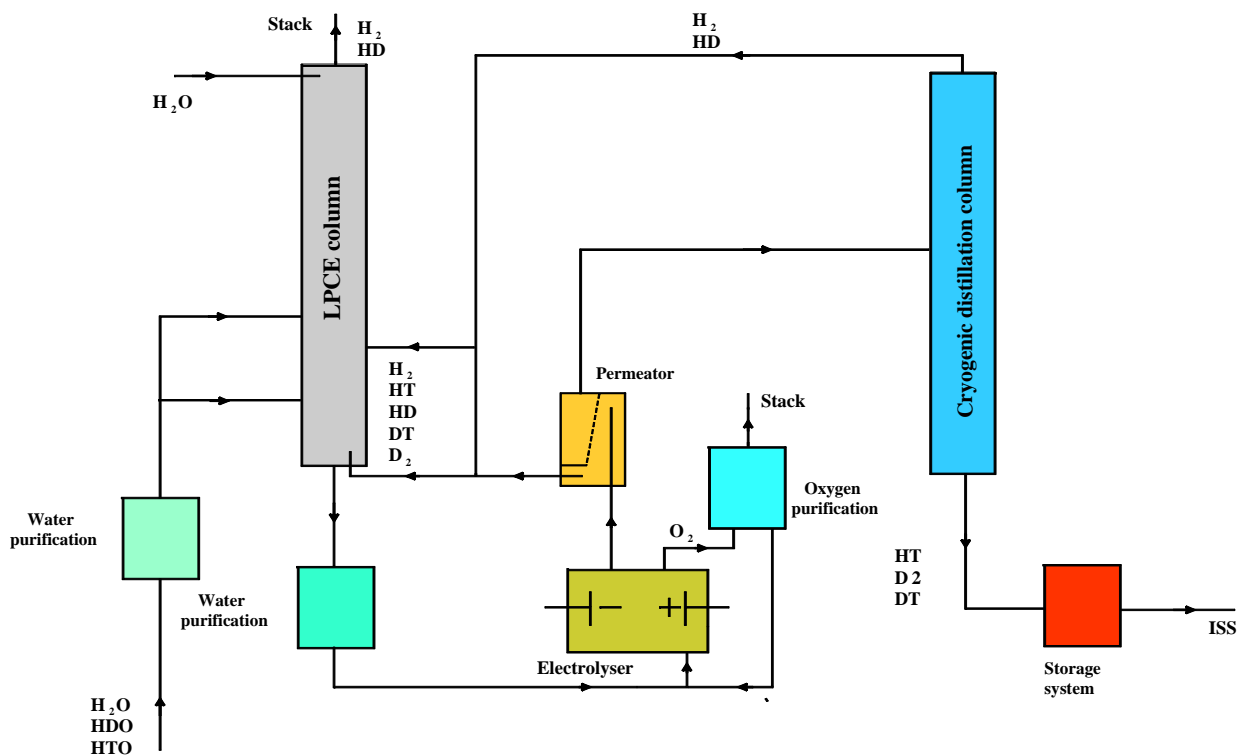


Fig. 1: TRENTA 4 configuration; CECE-CD facility at TLK.

The necessary development related to the CECE process is covered in the additional task TW4-TTFD-TR 47. The experimental programme for the CD facility will be focused on two kinds of tests:

- 1: Investigations of the separation performances of different packings in the cryogenic distillation process and validation of the steady-state mathematical modeling of the process. The separation performances of the cryogenic distillation process at very low tritium concentrations in mixture with deuterium and hydrogen will be experimentally proven in similar working condition as foreseen for the ITER-ISS CD1 from where the top product

should be discharged into the LPCE column of WDS. For this first case, 150 W are required at the temperature of helium stream from refrigeration unit in the range of 16-17 K.

- 2: Investigations necessary to validate the software for cryogenic distillation process during thermal transitory regimes along the CD column. The data base obtained on TLK cryogenic distillation facility will allow improving the dynamic modeling software taking into account the thermal fluctuations on different components. Therefore, the influence of thermal inertia of the column and other cryogenic components on separation performances of tritium, deuterium and hydrogen during transient regimes will be investigated in detail, namely regarded to the time response when rapid fluctuations in feed composition occur.

For this second experiment, the behavior of the combination of the cryogenic distillation column with the refrigeration unit will be investigated for both isotopic and thermal transitory regimes. Therefore, about 250 W at helium stream temperature below 20 K is required. Besides the isotopic composition and temperature measurements along the cryogenic distillation column, measurements of flow-rates and temperatures in the refrigeration will be performed as well.

The general configuration of refrigeration unit in combination with the CD column for hydrogen isotopes and its adjacent components is presented in Figure 2.

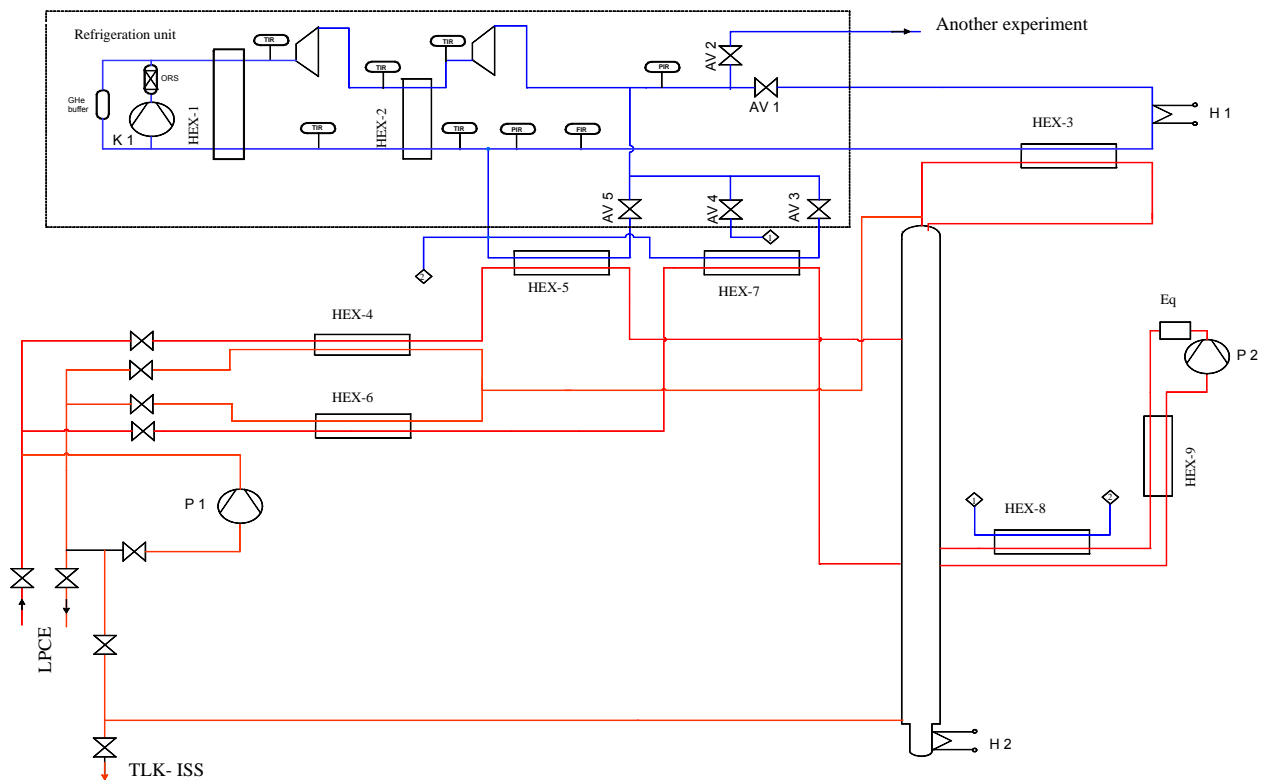


Fig. 2: Configuration of the CD system at TLK.

The refrigeration unit has to supply the cooling power necessary to cool down the condenser, the feed streams of the CD column and the hydrogen stream used in the chemical equilibrium loop.

The CD cold-box comprises the following main components:

- The CD column which for separation performances investigation may be filled with different types of packing. Several temperature sensors and sampling points located along the CD column allow transitory regimes investigation.

- The boiler necessary to provide the vapor stream inside the CD column.
- The condenser necessary for the uprising vapors condensation, connected to the main helium stream of the refrigeration unit.
- Four heat exchangers needed to cool down or to liquefy the two feeding streams of the cryogenic distillation column.
- One circuit to investigate the influence of chemical equilibration of the vapors at a certain location in the CD column on tritium and deuterium profile along the cryogenic distillation column.

Based on the available capacity of the CECE unit at TLK,  $90 \text{ mol}\cdot\text{h}^{-1}$  the throughput of the electrolyses, it is envisaged that a fraction of 50%-75% from the electrolysed tritium and deuterium enriched hydrogen stream will be processed in the CD column. Hence, the feed flow in the CD is in the range of 45-65  $\text{mol}\cdot\text{h}^{-1}$ , with a design feed flow of 65  $\text{mol}\cdot\text{h}^{-1}$ .

The average tritium activity of the tritiated water to be processed at TLK should be in the range of  $0.3 \times 10^{10} \div 20 \times 10^{10} \text{ Bq}\cdot\text{kg}^{-1}$ . In order to investigate simultaneous tritium and deuterium transfer, the hydrogen and deuterium content should be in the range of 10%  $\div$  90% atomic ratio with  $T_2$  in the range from  $1 \cdot 10^{-5}$  to  $1 \cdot 10^{-4}$  atomic ratio. The tritium enriched hydrogen and deuterium from the bottom of the CD column of TRENTA4 is envisaged to be sent to the existing Gas Chromatography (GC) based Isotope Separation System at TLK for final tritium recovery. Therefore, the enrichment of tritium from the feed concentration up to  $5 \cdot 10^{-3} \div 1 \cdot 10^{-2}$  atomic ratio is the duty of the enrichment section of the CD column. Related to the decontamination factor along the stripping section of the CD column, a depletion factor in the range of 10-100 is enough, as higher depletion factor have no significant influences in the separation performances of the LPCE column. Hence, the  $T_2$  concentration in the top product of CD column should be in the range  $1 \cdot 10^{-7} \div 5 \cdot 10^{-8}$  atomic ratio.

The characteristics of the TLK cryogenic distillation system are:

- Condensing power 150 Watt at 186 kPa;
- Two feed points located to divide the mass transfer part of the column into three equal sections and temperature measurements at each sampling point, necessary for investigations on dynamic behavior of the CD column;
- An equilibrator loop with flow capacity up to  $325 \text{ mol}\cdot\text{h}^{-1}$  allowing testing the ITER equilibrators at similar conditions (ratio vapor flow rate in CD column/equilibrator flow rate).
- Two inter-column liquid flow metering devices necessary for mathematical modeling validation, mainly on transient regimes.

Besides the conceptual design for the refrigeration unit and CD system, the detailed design of the facility has been completed. The following items have been developed:

- Process Flow Diagram and engineering description;
- Overpressure protection philosophy;
- Process and Instrumentation Diagram description;
- System interfaces have been defined;
- Lists of components have been provided (valves, pumps, temperature sensors, control loops, heat-exchangers, lines);

The refrigeration unit was manufactured, shown in Figure 3, and all interfaces with the cryogenic distillation cold-box have been established and prepared for functional tests. The design of the cryogenic distillation column was completed and the manufacture started. It is expected that the manufacture will be completed early 2006. The cold-box which will accommodate the cryogenic distillation column and other cold components such as heat exchangers was designed and the manufacture will be completed middle December 2005. The preparation activities to install all components of the cryogenic distillation system such as foundation for compressor, cranes for lifting of equipment, transfer lines between the refrigeration unit cold-box and the cryogenic distillation cold-box have been completed.



Fig. 3: The refrigeration unit for TRENTA facility.

The performance test of the refrigeration unit will be performed beginning 2006. The cooling capacity of maximum 250 W at 16.5 K is the target for the performance of the refrigeration unit. A dedicated heater for this test has been designed and is under manufacturing.

An integrated test of refrigeration unit and cryogenic distillation column will be performed until middle 2006.

#### Staff:

I. Cristescu  
I.R. Cristescu  
S. Welte  
W. Wurster

#### Literature:

- [1] I. Cristescu, Ioana R. Cristescu, L.Dörr, M. Glugla, G. Hellriegel, O. Kveton, D. Murdoch, P. Schäfer, S. Welte - TRENTA Facility for Trade-off Studies between Combined Electrolysis Catalytic Exchange and Cryogenic Distillation Processes, *Fusion Science and Technology* **48**, 97-102 (2005)

## TW4-TTFD/TR 47

### Upgrading of LPCE (Liquid Phase Catalytic Exchange) Column for Trade-off Studies between WDS and ISS

At the Tritium Laboratory Karlsruhe (TLK) a pilot water detritiation (WDS) facility shown schematically in Figure 1 is currently under design and installation to investigate the achievable decontamination factors and to characterize the behavior of the main components such as Liquid Phase Catalytic Exchange (LPCE) column and electrolyser at various experimental conditions.

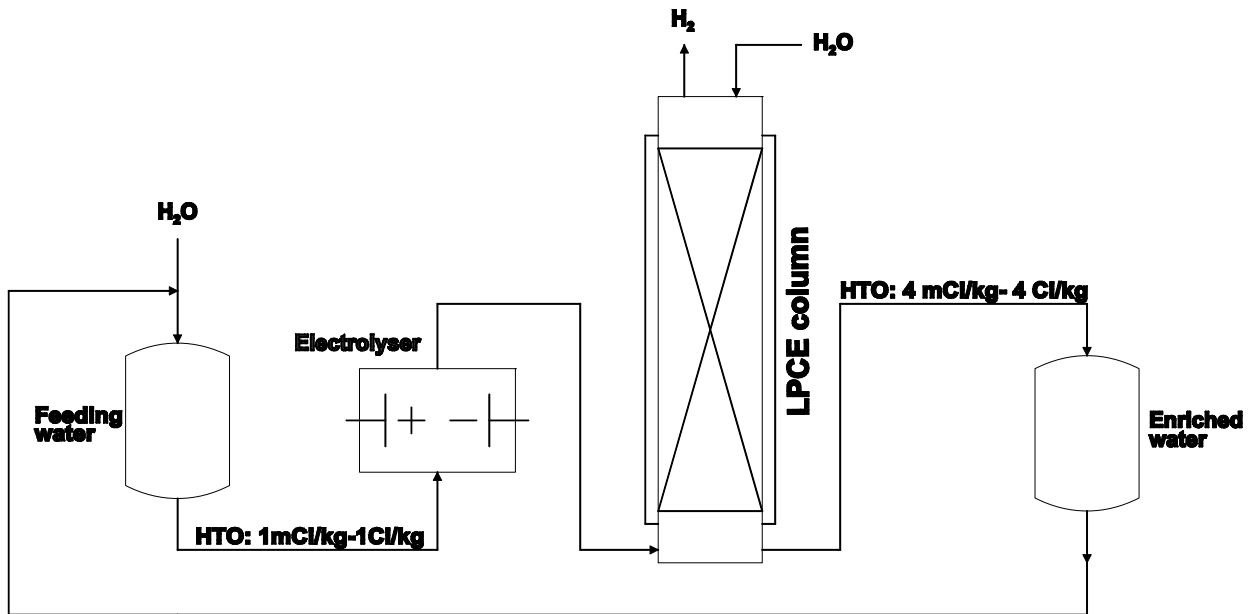


Fig. 1: Water Detritiation Facility at TLK.

The installation and commissioning of a 8 m long LPCE column, a boiler and a condenser has to be completed. Several feeding points along the LPCE column are to be provided, to allow different options for connection with the Cryogenic Distillation (CD) column and further with the TLK existing Isotope Separation System (ISS) for final tritium recovery. A preparatory unit to feed the electrolyser and the LPCE column in closed or opened loop have to be designed and commissioned. For the fraction of the gas provided by the electrolyser to be fed into the CD column, a hydrogen purification system based on a PdAg permeator has to be designed. A control and interlocking system has to be developed and integrated into the TLK control system. Overpressure and over temperature protection strategy will be defined and implemented. The new LPCE column (including packing and catalyst) and auxiliary equipment (including permeator, pumps, heat exchangers, hydrogen purification system, tanks, interconnecting tubing and control system) will be manufactured, installed and the system commissioned with hydrogen and deuterated hydrogen.

Based on previous experimental data, a LPCE column of 8 m length was designed with the target of a decontamination factor of  $10^4$  for tritium. The tritium activity in the water to be processed should be in the range of  $4 \times 10^6 \text{ Bq} \cdot \text{kg}^{-1}$  up to  $4 \times 10^{11} \text{ Bq} \cdot \text{kg}^{-1}$ .

The mechanical design of all components has been produced, and the main components such as the LPCE column itself, condenser, boiler, re-distributors have been manufactured and installed (Figure 2).

The stripping column for the tritium contaminated oxygen stream from the electrolyser has been designed, manufactured and installed.



Fig. 2: The LPCE column of TRENTA facility.

The control system for the LPCE column, oxygen stripping column and electrolyser unit was developed and is well advanced manufactured and commissioned.

The electrolysis unit consists of the two solid polymer electrolyzers of  $1 \text{ Nm}^3\cdot\text{h}^{-1}$  each and is already installed in a ventilated enclosure as shown in Figure 3. The two electrolyzers have been enhanced to allow tritiated water processing. Six vessels needed for closed loop operation of the CECE facility have been designed, manufactured and installed and can be seen in Fig. 3.

The separation performances of the LPCE column will be investigated under different operation conditions. For several parameters (e.g. pressure, temperature, and feed water composition) the experimental plan was developed. The plan for integrated testing of the two systems is currently under development in order to allow obtaining necessary experimental data for the decontamination factor achievable along the LPCE column when concentration fluctuations within the CD occur.

The upgraded LPCE column will be commissioned and the operation procedure for trade-off studies WDS-Cryogenic distillation will be developed.



Fig. 3: Ventilated enclosure for the electrolysis unit and feeding vessels.

The previous measurements of mass transfer performances of different catalyst/packing mixtures investigated at TLK showed dependence by deuterium presence in the LPCE process. The separation performances along the LPCE column will be measured against different operation conditions such as the feed composition, pressure and flow rates of gas, water and vapours along the column. The experimental results will be compared with the values predicted by a mathematical model developed at TLK.

#### Staff:

I. Cristescu  
S. Welte  
W. Wurster

P. Schäfer  
G. Hellriegel

#### Literature:

- [1] I. Cristescu, Ioana R. Cristescu, L. Dörr, M. Glugla, G. Hellriegel, O. Kveton, D. Murdoch, P. Schäfer, S. Welte - TRENTA Facility for Trade-off Studies between Combined Electrolysis Catalytic Exchange and Cryogenic Distillation Processes, Fusion Science and Technology **48**, 97-102 (2005)

## EFDA/04-1142 Development of a Procedure for Global Fuel Cycle Tritium Inventory Determination

The objective of the task is to develop an adequate procedure of tritium accountancy in the ITER Fuel Cycle, to identify any aspects that require further investigation, and to assess the times needed to carry out each step of the accountancy process.

In ITER, the Fuel Cycle, the Vacuum Vessel VV and the Hot Cell building will constitute a single tritium Material Balance Area (MBA).

The total MBA tritium inventory at any selected time ( $T_n$ ) can be derived as:

$$T_n = T_{n-1} - T_{Bu} - T_D - T_L - T_E + T_I + T_{Br} \quad (1)$$

$T_{n-1}$  is the total tritium inventory at previous determination,  $T_{Bu}$  represents the tritium burned,  $T_D$  is the tritium lost by decay,  $T_L$  represents the tritium leaving plant in effluent streams,  $T_{I/E}$  represents the tritium imported/exported from the plant and  $T_{Br}$  represents the tritium bred. Information about all these quantities will be available by monitoring and records.

On the other hand, the total tritium inventory can be divided into 4 categories:

$$T_n = M_{in} + T_{in} + M_{ex} + T_{ex} \quad (2)$$

Mobile in-vessel ( $M_{in}$ ) includes the fraction of the tritium in Plasma Facing Components (PFC) recoverable by selected routine methods and Torus cryopump residual tritium inventories (tritium trapped in impurities recoverable at high temperature regeneration).

Trapped in-vessel ( $T_{in}$ ) includes the firmly bound fraction of tritium in PFC's, flakes and dust.

Mobile ex-vessel ( $M_{ex}$ ) is considered to be tritium (in gas forms) within the Fuel Cycle (mainly buffer vessels from Tokamak Exhaust Processing TEP, Isotope Separation System ISS, Storage and Delivery System SDS and tritiated water in Water Detritiation System WDS and tritiated water holding tanks).

Trapped ex-vessel ( $T_{ex}$ ) includes tritium in flakes and dust removed from the VV (actually, part of the tritium can be recovered by adequate detritiation processes), components removed for maintenance (in transit casks and/or Hot Cell), material removed from components in hot cell processing, radwaste, permeation into Cooling Water System components and coolant, permeation into vessel walls and piping, etc. in the Tritium Plant (catalyst beds, cryosorbent panels, molecular sieve beds, other components).

The global tritium inventory determination comprises three major activities:

### 1. Recovery of the mobile Fuel Cycle inventories in SDS

As all the amount of tritium that can be withdrawn from other systems is fed into the ISS, it is necessary to evaluate the tritium inventory contained in the Cryogenic Distillation CD columns by milking down of tritium. In normal operation, deuterium and tritium inventory in ISS is significantly higher comparing with the hydrogen inventory. Therefore, tritium can be withdrawn from ISS by replacing it with additional deuterium that has to be fed into the system. Deuterium will be fed into the ISS through the feeding line used during normal operation to feed the plasma exhaust gas after purification in TEP. Several preliminary evaluations showed that it is possible to operate the WDS during the milking procedure; therefore, the  $H_2$  feed from WDS to the ISS will be kept as in the normal operation of the ISS.



During the milking operation, all the stream extractions will be stopped, excepting the hydrogen reject and the extraction stream that is used in normal operation for the enriched tritium (90%). This last stream will be used during the milking procedure to withdraw tritium, most of it in the form of DT. The withdrawn DT mixture will have a tritium content ranging from 90% at the beginning of the milking operation down to a target value, to be presented below. The aim is to reach during the milking an average concentration of 50% D-50% T of the extracted gas, to match the storage beds concentration existing in SDS.

The optimum procedure was established to be made from 2 steps:

**Step 1:** Extract an amount of tritium with an average concentration of 50% D-50% T.

At the beginning of the milking procedure, it was considered that the concentration profiles from the CD columns are those corresponding after several short pulses, therefore a total inventory of 22.8 mols of tritium. In order to avoid the introduction of additional deuterium (needed only for tritium inventory procedure and not actual during plasma shots) within the FC, D<sub>2</sub> from the SDS buffer vessel for NBI (H<0.5%, T< 200 ppm) will be fed into the ISS for the milking procedure.

Several simulations using TRIMO (task TW4 – TTFD- TR37.1) under 'tritium milking' scenario have been carried out. It was found necessary to add 43 mols of D<sub>2</sub> in order to remove a quantity of 21 mols of tritium at an average concentration of 50% D-50% T, the rest of the D<sub>2</sub> being used to replace tritium in the ISS as inventory. During the inventory procedure, the hydrogen reject maintains its quality as requested (T< 10<sup>-7</sup> at.).

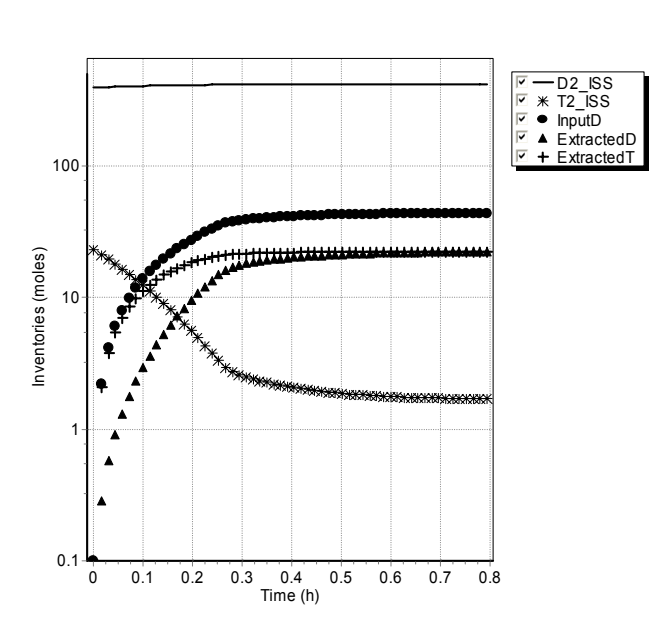


Fig. 1: Time variation of D and T inventory in ISS during step 1 of milking procedure

In Figure 1 the time evolution of D and T inventory in ISS, input D and extracted amount of D and T are plotted. At the end of the step 1, the target value of the tritium concentration in the extracted stream is 18%. During step 1, 42 mols of DT are collected, to be measured in 3 storage beds from SDS. After step 1, the remaining tritium inventory in ISS is 1.8 mols and the corresponding necessary time to carry on the milking would be approximately 1 hour.

**Step 2:** In step 2 the target is to operate the ISS in order to recover as much as possible tritium from the remaining inventory of 1.8 mols. Therefore, for this step, pure D<sub>2</sub> from bottles will be fed into the ISS.

Depending on the target value for the remaining T<sub>2</sub> inventory in the ISS, two

cases have been considered and the results are presented in Table 1. It has to be taken into account that presently 3 storage beds are available for D<sub>2</sub>(T) storage, and which can be used for tritium inventory measurement as they are also foreseen with in-bed calorimetry. This will be sufficient to recover tritium from ISS down to a residual tritium inventory of 0.1 g.

Table 1: Tritium milking from ISS

Time (hours)	Remnant T inventory (g)	T concentration (at.) in the bottom of CD4	Amount of D-T to be measured (mols)	Number of beds necessary for in-bed calorimetry	Average tritium concentration in D <sub>2</sub> (at.)
0.7	0.6	1%	29,1	2	6%
1	0.14	0.2%	45,7	3	3.8%

To be noted that all the evaluations presented above are heavily based on the values of the hold-ups of the CD stage, column, boiler and equilibrator loop as presented in Detailed Description Design of ISS.

In the specially designed beds of the SDS, calorimetric determinations of tritium are made by passing a helium stream of fixed mass flow rate through a closed circuit in each bed and measuring the temperature rise, using the value ( $0.324 \pm 0.0009$  W/g) for the decay heat of tritium. Experiments to characterize the bed performance are in progress, and it is expected that an accuracy of  $\pm 1\%$  can be achieved with a 24 h measurement duration.

## 2. Recover the mobile in-vessel tritium inventory in SDS

After the mobile ex-vessel tritium inventory determination has been made, a determination of the inventory of the mobile in-vessel tritium will be performed. The vessel walls should be conditioned and the torus exhaust cryopumps fully regenerated. Related to the residual inventory inside the cryopumps, they are envisaged to be regenerated at two high temperature levels: ambient temperature and 450 K to release water-like species and higher hydrocarbons. These gases shall be processed via TEP to eliminate the impurities and then via ISS. Following the milking procedure, a second inventory determination shall be made to determine the mobile in-vessel inventory and therefore also the effectiveness of the recovery procedures. After this step tritium will be measured by in-bed calorimetry in SDS.

## 3. Estimation of trapped inventories

After performing the procedures described above, the trapped tritium inventory in-vessel and ex-vessel can be computed from equation (2). The build up of tritium in specific components will be documented as operation of the ITER machine proceeds, to enable the evolution of these inventories to be correlated against operating parameters. When components are replaced, determinations of tritium inventory will be made to confirm or correct the data collected during operation. This will allow accurate estimation of the evolution of the various types of trapped ex-vessel inventories, hence trapped tritium in-vessel inventory will be possible to be calculated.

## Conclusions

A method for global tritium inventory determination in ITER has been developed. A logical flow chart with the necessary operations will be produced and the extent to which the necessary steps can be carried out in parallel, together with an assessment of time for each step, resulting in overall time estimate (a generic time-schedule) will be produced. This will be done in conjunction with the development of procedures to assess residual tritium inventories in process components after transfers to SDS.

Staff:

I. R. Cristescu  
Ch. Caldwell-Nichols  
I. Cristescu  
N. Bekris

Literature:

- [1] Ioana-R. Cristescu, I. Cristescu, D. Murdoch, L. Dörr, M. Glugla - *Tritium Inventory Assessment for ITER using TRIMO*, accepted for publication in *Fusion Engineering and Design*
- [2] D. Murdoch, Ioana-Ruxandra Cristescu, R. Lässer - *Strategy for Determination of ITER In-vessel Tritium Inventory*, *Fusion Engineering and Design*, **75-79** (2005) 667-671

## EFDA/04-1172

### Dynamic Modelling of ITER Tritium Inventory (TRIMO)

The use of a dynamic tritium inventory modeling code is essential for the design integration of the Fuel Cycle (FC) and other tritium-containing systems for ITER in order to minimize global tritium inventories as far as consistent with fulfilling the functions of the systems. A dynamic fuel cycle model was developed progressively in the decade up to 2000-2001 and was used as a basis for developing the TRIMO code, a valuable analysis tool for ITER for dynamic modeling of tritium inventories in the FC and Vacuum Vessel (VV). As the design for some systems from the FC (i.e. Vacuum pumping, Neutral Beam (NB) Injectors) have substantially progressed since 2001, new modules to reflect the current design of these systems have been developed.

TRIMO is hosted on a different software platform (Windows) and written in a different language (Delphi) to improve performance compared with the earlier CFTSIM code.

In the frame of the present task several topics have been addressed:

- A Water Detritiation System WDS model has been implemented and integrated into TRIMO.
- The Vacuum Pumping and NB Injectors models have been updated to agree with the current version of the ITER design requirements. Staggered torus cryopump operation for burntime pulses longer than 600 s have been implemented; new throughput values from vacuum pumping to Tritium Plant, NB Injectors regeneration philosophy (2002) for long and short pulses was implemented.
- A parametric model to account for tritium trapped in Torus and tritium trapped in impurities ( $\text{Q}_2\text{O}$  and  $\text{CQ}_4$ ) has been implemented.
- The uptake and delivery of gases by ITER scale getter storage beds was implemented in the Storage and Delivery system (SDS) model.
- Improvements to the Isotope Separation System ISS model have been made. The feed stream from Tokamak Exhaust Processing TEP to ISS has been now considered on vapor phase (for short pulse) or on gas phase (for long pulse) to account for possible warm-ups of the heat-exchanger in the feed stream during long dwell times. Also temperature differences in the returned streams from equilibrators have been considered.
- A user-friendly graphical interface was implemented.

An analysis related to the impact of the reduction proposed in the nominal fuelling rate (from  $200 \text{ Pa}\cdot\text{m}^3\cdot\text{s}^{-1}$  to  $120 \text{ Pa}\cdot\text{m}^3\cdot\text{s}^{-1}$ ) on individual systems and global inventory has been performed.

In Figure 1 the tritium inventories in the Fuel Cycle for short pulses computed with TRIMO are presented. In the case of a reduced fuelling rate there is a reduction in the tritium inventories for several systems, i.e. Vacuum Pumping, TEP, ISS. The necessary time to recover tritium from ISS in the case of  $200 \text{ Pa}\cdot\text{m}^3\cdot\text{s}^{-1}$  is 3600 s; at the reduced fuelling rate the necessary time to recover tritium from ISS is 5000 s. At a reduced fuelling rate the time to build the tritium inventory in ISS and achieve the required tritium quality will be longer.

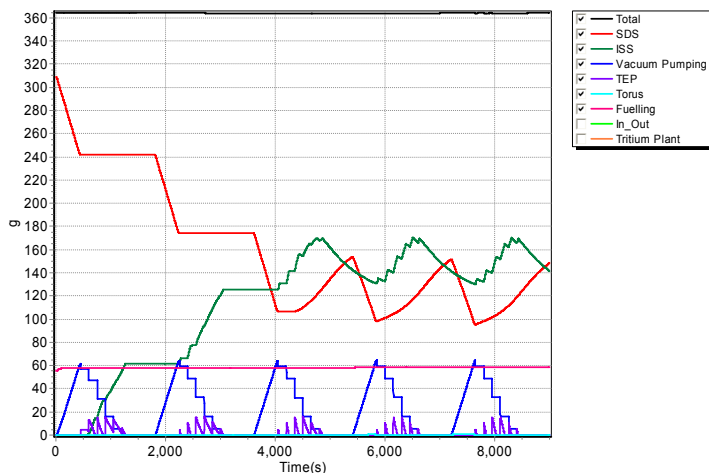


Fig. 1: Tritium inventories in the Fuel Cycle of ITER for short pulses.

In Figure 2 the tritium inventories in the Fuel Cycle for long pulses computed with TRIMO are presented. The maximum tritium inventory in the ISS for reduced fuelling rate is less or equal to the values of maximum tritium inventory for the 200 Pa·m<sup>3</sup>·s<sup>-1</sup>. The maximum tritium inventory in SDS per pulse decreases in time: This is due to tritium trapped in impurities as Q<sub>2</sub>O and CQ<sub>4</sub>, which in TRIMO is accounted for.

An analysis related to the influence of the reduced fuelling rate to the operation of the ISS (keeping the original configuration and cryogenic power) has been performed.

A first version of the TRIMO documentation was delivered as part of the present task, where the operational philosophy of the Fuel Cycle and the physical assumptions used to model the subsystems is described. In the documentation the graphical interface and the available graphical outputs of the code are also presented. TRIMO is conceived as a project with several units and the logical diagrams for these units and additional procedures are given in the documentation. Constants and functions describing various physical properties for tritium and mixtures are also contained in the documentation. The documentation will be permanently updated with the evolution of the code (and Fuel Cycle design) and is meant to be used as a stand-alone document.

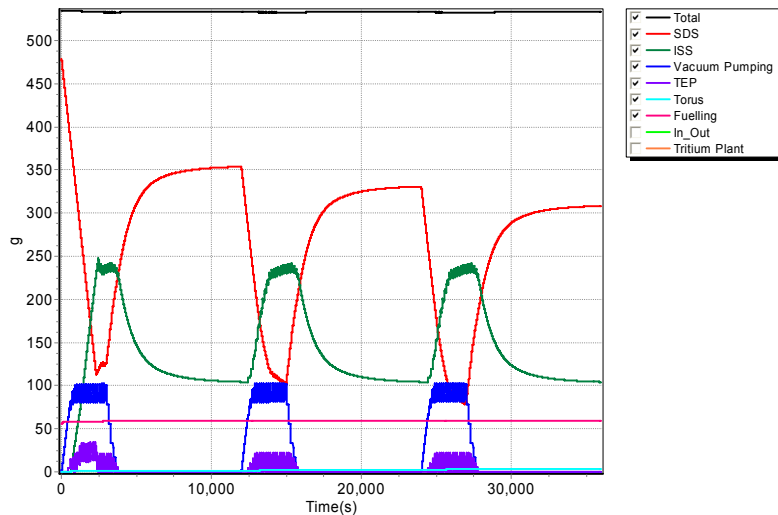


Fig. 2: Tritium inventories in the Fuel Cycle of ITER for long pulses.

Besides the 50% D-T fuelling scenarios, in the future other typical fuelling cases will be investigated with TRIMO to analyze the behaviour of the systems and the impact onto the dynamics of tritium inventories. A detailed model for TEP will be gradually introduced, which besides the performances of tritium recovery in TEP, will consider the dynamic of the gases (behavior of the feeding pumps of the permeators and the control system of the permeator) and therefore give a estimation related to the dynamic of the gases in TEP (i.e. residence time). Other developments of the code include a dynamic model for the WDS with a WDS-ISS connection and the consideration of a stream from the Hot Cells.

Staff:

I. R. Cristescu  
I. Cristescu  
Ch. Day  
V. Hauer  
A. Antipenkov

Literature:

Ioana-R. Cristescu, T. Busigin, L. Dörr, D. Murdoch - *ITER Dynamic Tritium Inventory Modeling Code*, Fusion Science and Technology **48**, 343-349 (2005)

## **EFDA/05-1237**

### **Development of ITER PRM and Standard Parts Catalogues in CATIA V5 for Tritium-containing Systems and Components**

The CATIA V5 *Equipment and Systems* is a workbench chosen to perform design and integration of the electrical, fluid and mechanical systems within ITER. The wide range of applications such as Piping & Instrumentation Diagrams (P&ID), Heating, Ventilation, Air Conditioning (HVAC) Diagrams, Piping Design, Tubing Design, HVAC Design, and Equipment Arrangement provides the ability for the upstream design process from the functional 2D design (P&ID, HVAC diagrams) to the 3D detailed design.

The Project Resource Management (PRM) is a framework of the project which on the one hand gives a tool to customize the working environment, on the other hand it organizes the design process to ensure design compliance with established standards, specifications, standardization, industrial conventions, terminology and practice. Feature Dictionaries, Catalogues for components as well as for standards and specifications are main parts of the CATIA V5 PRM.

An implementation of the *SmarTeam* software tools for data management gives a possibility to easy store, manage or share the data within a database of an engineering project. *SmarTeam* provides data management among the remote CAD offices to allow collaborative design and brings about a compatibility with the ITER data management system *Enovia*.

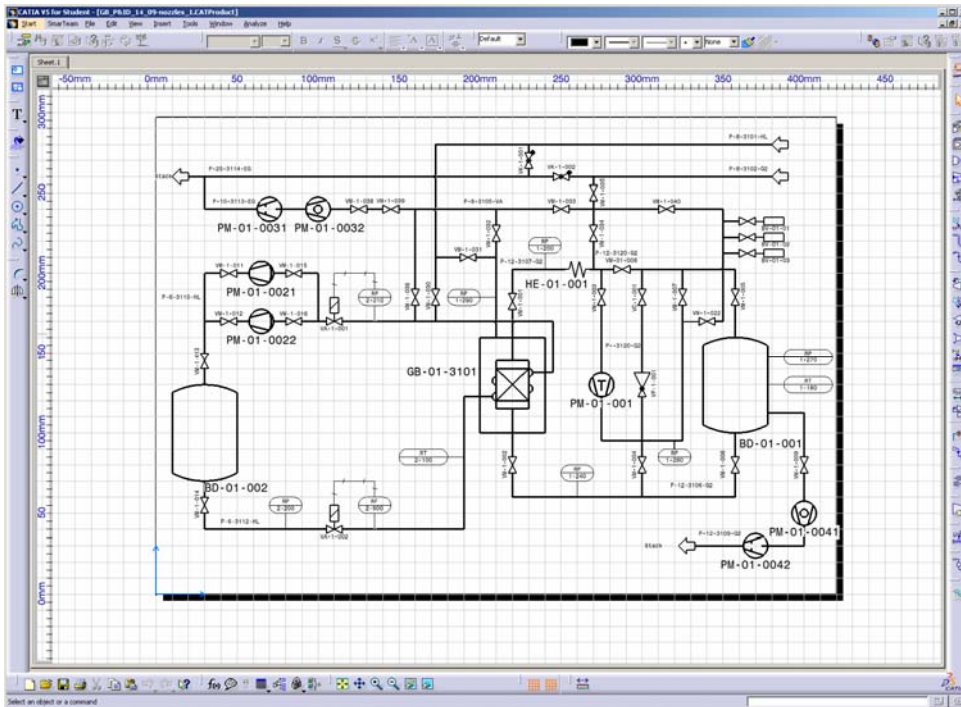
Knowledge in the areas of tritium processing, vacuum technology and systems engineering is required in order to customize CATIA V5 software tools to allow design and integration of the ITER Tritium Plant (TP) using full capabilities of the CAD system.

Customization of the CATIA V5 E&S includes:

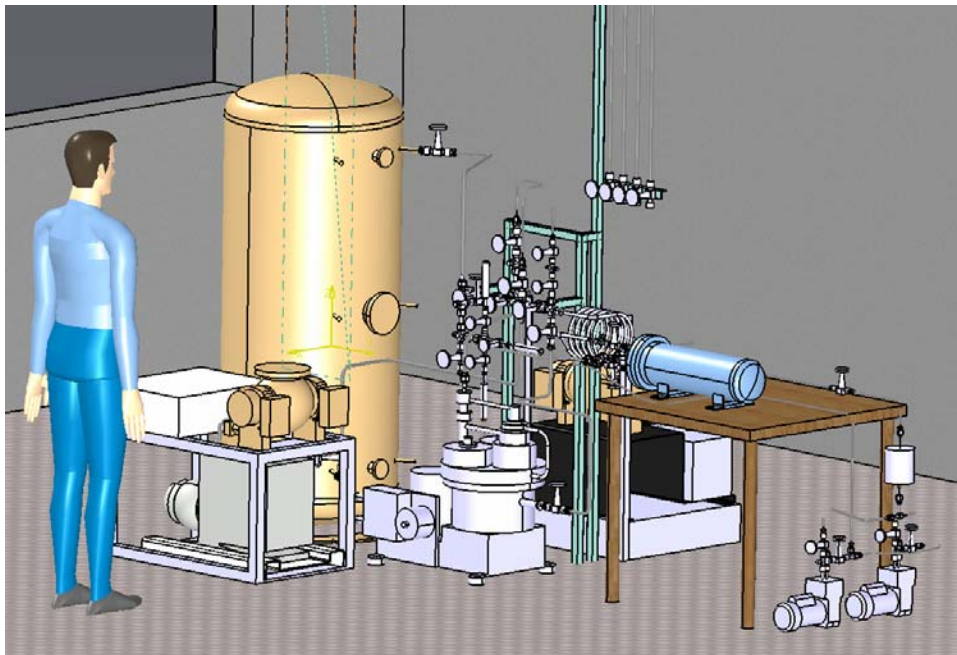
- Implementation of the industrial conventions, terminology and practice together with specific requirements of the ITER TP through the Project Resource Management system (PRM). The inputs required to build the PRM of CATIA V5 will be compiled from the ITER IT, from the experts in associations and from industrial consultants.
- Intensive testing of the tools in the frame of a pilot project
- Development of the standards parts catalogues for tritium containing systems
- Development of the methodology of design in the CATIA V5 E&S environment

Although the work on the development of the CATIA E&S PRM has been started not so long time ago significant progress has been achieved. The work is performed in close contact with ITER CAD Office in Garching in the frame of the co-development of CATIA E&S catalogues for the ITER systems. In order to support design activities for the catalogues development a collaboration between FZK and Fusion Centre in Moscow has been established.

A pilot project "Getter Bed" has been started in CATIA V5 E&S based on the existing experimental setup in Tritium Laboratory Karlsruhe. This project allows intensive testing and validation along the CATIA E&S PRM development and is used as a training environment for the education of young designers and engineers.



CATIA intelligent Piping and Instrumentation Diagram of the experimental setup



Detailed 3D layout in CATIA V5 E&S

Staff:

S. Beloglazov  
M. Gluga  
M. Lux  
R. Wagner  
V. Weber



**EFDA/05-1239**

**Development of a Resource-loaded Schedule for the Overall ITER Tritium Plant Integration**

The objective of the task is to develop the resource-loaded time schedule for the overall Tritium Plant Integration. The Tritium Plant design main activities will comprise designing of systems (Tokamak Exhaust Processing TEP, Isotope Separation System ISS, Water Detritiation System WDS, Storage and Delivery System SDS, Analytical System ANS, Atmosphere Detritiation System ADS, Vent Detritiation System VDS) and auxiliary systems with high degree of integration (Automated Control System ACS, Safety System SS, secondary containments).

The task covers the development of an integrated overall resource-loaded time schedule for the ITER Tritium Plant, based on inputs from systems design tasks to be provided by the responsible Participating Teams PT's.

The required time schedule for Tritium Plant Design and Integration is made in conjunction with the over-all time schedule for ITER. Eventually this activity should extend up to include the integrated plant commissioning to co-ordinate the installation and commissioning of the Tritium Plant systems with building construction, with infrastructure and with other interfaces.

The main activities monitored in the resource-loaded time schedule for the Tritium Plant are presented in Figure 1.

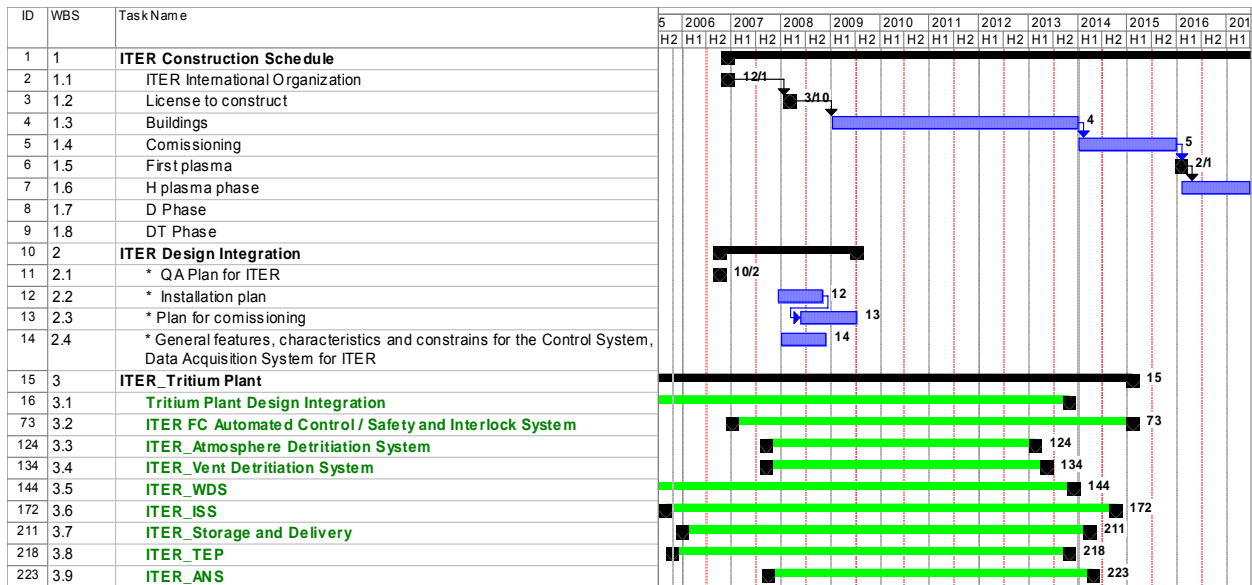


Fig. 1: Monitored activities for the Tritium Plant.

A total number of approx 220 tasks are currently monitored; the systems which are detailed more are the ones where EU-PT is responsible that are WDS and ISS. Considering on one hand the complexity of the Automated Control system and on the other hand the experience of EU related to this activity, this system was also thoroughly detailed.

As a common feature of the activities related to the design for sub-systems (VDS, ADS, WDS, ISS, ANS) the activity was split in tasks as shown in Figure 2. In this figure the time duration of each task is only approximate; on a case to case basis, depending on the complexity of the system itself and on the available human resources of each PT for a sub-system, various tasks from above can have longer or shorter time duration. Related to the logic behind, this is based on the principle of finishing the activity of 'Detailed design of a sub-system' as soon as possible, which means to maximise the number of tasks which can

be done in parallel (i.e. the activity of mechanical design can start when the PFD's are finished and also the 3D layout; however, the 3D layout will finish only when the P&ID's will be updated with the results of the HAZOP analysis and the safety analysis).

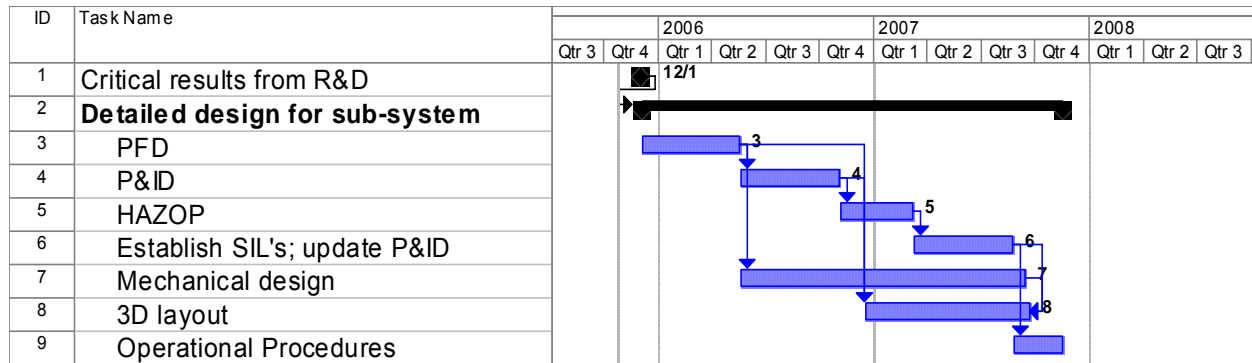


Fig. 2: Generic sequence of detailed design activities for a sub-system.

It is expected that a final HAZOP/FMEA analysis will be necessary at the end of the mechanical design activities. Unfortunately, Microsoft Project software does not allow recurrent connections, as this would create infinite loops. To overcome this limitation, it was adopted as a solution that the activities of mechanical design will need longer time; it is understood that under this task, a final check of the consequences of the mechanical design in the HAZOP analysis will be performed. The split of the detailed design in the manner shown above is dictated by the inputs needed for the Automated Control System and Safety System from each of the systems.

The resource-loaded time schedule for the Tritium Plant activities shows that inactive commissioning of the Tritium Plant might end in 2015. At this moment in time the major uncertainties in the time assessment for sub-tasks are due to:

- QA plan for ITER is not yet available;
- The requirements related to the Safety System for ITER are not known; if the IEC 61508 standard will be considered as unacceptable the tasks related to the Safety System will have to be re-evaluated;
- All the tasks related to installation and commissioning will have to be re-evaluated when the Installation plan and Commissioning plan will become available.

In the final report, an analysis of the necessary resources will be done, as the information will become available. This will be useful for the management to assess the necessary staffing and financial needs.

Staff:

- I. R. Cristescu
- M. Glugla
- I. Cristescu
- G. Hellriegel
- P. Schäfer

## **EFDA/05-1240**

### **Definition of the Interfaces between the Tritium Plant and the Torus Pumping, Neutral Beam Injection Pumping, and Fuelling Systems**

The objective of this task is to up-date the interfaces between the tritium plant and the torus pumping system, fuelling system, neutral beam injectors and wall conditioning system for each operation scenario of ITER. Based on several achievements as a result of R&D related to different subsystems of the tritium plant and systems which interface with the tritium plant, an up-date of these interfaces is necessary.

The interfaces will be characterized with respect to time evolution of the flow-rates, pressures and gas stream compositions during burn, dwell phases and wall conditioning.

In addition to the main duty of the tritium plant to process the hydrogenic streams for tokamak fuelling purposes and tritium inventory accountancy, different tritium contaminated gases have to be processed within the atmosphere detritiation system (ADS), which is part of the tritium plant. The interfaces of the above-mentioned system with ADS will be characterized as well.

Beside the normal operation, the tritium contaminated sources that may appear during maintenance activities or abnormal operation, which has to be processed within the tritium plant should be identified, and possibly quantified with respect to flow-rates and composition.

Based on the existing configuration of the mentioned systems the supply limits will also be established.

The Interfaces between the torus pumping system, fuelling system, neutral beam injectors and wall conditioning system and the tritium plant are under development. The tritium plant consists of the following subsystems:

- Tokamak fuel cycle subsystems
- Confinement and detritiation systems (ADS, ventilation detritiation system, glove box detritiation system, water detritiation system)
- Room depression systems
- Tritium monitoring systems (safety and area monitoring)
- Building ventilation systems (tokamak, tritium, hot cell, radwaste)
- Utilities (compressed air, normal & safety chilled water, breathing air)
- Contaminated drain collection and transfer system (tokamak, tritium, hot cell building, etc.)
- Electric power supply network (Class IV-A/B, III-A/B, II-A/B)
- Plant operation control and interlock

A tree structure configuration is implemented for the management of this task. The data management has been discussed and agreed during the Tritium Plant Working Group 3 meeting.

Some issues concerning the pellet injector system need further R&D activities. As the fuelling isotope mixture should be adjustable on pulse-by-pulse basis, between 100% D and 100% H during H/D phase operation, and between 100% D and 90% T during DT operation, the time evolution of gas composition delivered between the tritium plant and the fuelling system during burn and dwell should be quantified.

For the typical fuelling cases as shown in Table 1, the impact on the tritium inventory within the ISS is under investigation and operational procedures will be proposed.

Due to the requirement for GDC with deuterium the tritium plant has to process  $105 \text{ Pa}\cdot\text{m}^3\cdot\text{s}^{-1}$  deuterium. In order to recover tritium from the deuterium stream an appropriate feeding location on ISS is investigated and a dedicated operation procedure will be implemented.

Table 1: Typical fuelling cases for Tokamak operation.

Typical Fuelling cases	1	2	3	4	5	6	7	8
T/D ratio	25/75	40/60	50/50	50/50	60/40	70/30	75/25	90/10
D <sub>2</sub> flow rate	84	48	0	40	4	0	0	0
DT flow rate	6	42	120	30	66	50	30	0
Tritium flow rate	30	30	0	50	30	50	50	50
Total flow rate	120	120	120	120	100	100	80	50

The future activity will be focussed on the following items:

- ▶ The identified interfaces between the tritium plant and vacuum pumping, fuelling, neutral beam and glow discharge need to be updated during the process flow diagrams and detailed design developments of related systems.
- ▶ In order to define the design specifications for the tritium plant subsystems, the interfaces with other systems such as the hot cell, the test module blanket breeding, diagnostics, etc. and between the subsystems within the tritium plant have to be implemented.
- ▶ A “handbook of interfaces” may be generated if necessary.

Staff:

I. Cristescu  
A. Antipenkov

## **EFDA/05-1251**

### **Development of a Tritium Manual for ITER**

A Tritium Manual is required for use by ITER designers and operators as the prime source of relevant information on tritium properties, tritium processes in ITER, tritium compatible components, tritium safety, QA procedures and design guidelines for ITER systems that handle tritium. It will be mandatory to use components and devices for ITER tritium systems recommended in the manual and to follow procedures laid down in the manual.

The initial objective of the task is to initiate the construction of the ITER Tritium Manual on the ITER Baseline website in a format similar to the existing ITER manuals using the ITER Document Management System. The list of topics is agreed and the information has now to be assembled and authorised for inclusion in the Tritium Manual.

As the manual will need to be valid for up to 40 years the format will reflect this as far as can be foreseen, noting that over this period there will be many revisions and updates of the information and also that nature of information technology will change radically. The Manual will contain lists of recommended components from specific manufacturers that are to be used in the construction of ITER tritium systems.

The project started in September 2005 and the draft report on the first deliverable was presented in mid-October 2005. The information for the various sections will be assembled from contributors in the ITER Document Management System for approval.

#### Staff:

C. J. Caldwell-Nichols



## **Safety Analysis and Environmental Impact**





## TW5-TSS-SEA 3.5

### In-vessel Safety: Mitigation of Hydrogen and Dust Explosions

#### Objectives

In previous work, the problem of hydrogen and dust mixtures with air formed in the course of accidents in ITER has been addressed through analysis, small-scale experiments and code development mainly focused on hydrogen. About dust mobilisation and possible explosion, as well as on the reactivity of ITER dusts, only a restricted database is available. The proposed approach to evaluate the dust explosion hazard in ITER is to develop a semi-phenomenological code which allows modelling of the combustion/explosion process under ITER-typical conditions for the whole variety of the accident scenarios. The main objective of this work is to complete the experimental data on ITER-relevant dusts to support the code development/validation. The effective dust burning rates necessary for the combustion module of the code and their dependence on the dust particle size, dust concentration, and turbulence level are to be measured. Small-scale and medium-scale experiments will help in this work and will also allow to specify the conditions of large-scale tests, which could be necessary as the final step for reliable code validation for combined H<sub>2</sub>/dust explosion. Another activity on this way is to develop mitigation methods of the dust/hydrogen explosion hazard.

#### Status

In 2002-2004, the explosion behaviour of some ITER-relevant dusts – fine graphite and tungsten dusts and their mixtures – was studied using a standard method of a 20-l spherical combustion bomb. The dust explosion indices, i.e. maximum explosion overpressure and maximum rate of pressure rise, lower explosive concentration limits, and minimum ignition energy, were measured as functions of the dust particle size, dust-in-air concentration, and ignition energy. The tested dusts appeared to explode in wide concentration ranges generating overpressures about 5-7 bar; the minimum ignition energy was evaluated as 2 kJ. Further tests with 8 to 18 vol. % hydrogen added to graphite-dust/air mixtures showed the possibility of ignition of the cloud by a weak electric spark, if the hydrogen content is higher than 10 vol. %. At hydrogen concentrations higher than 12 vol. %, the combined hydrogen/dust/air explosion can generate rates of pressure rise higher than hydrogen/air alone. In the case of a strong ignition source, the dust-fuel constituent increases the hydrogen-relevant maximum explosion overpressure at any tested concentrations.

The tests on combined dust/hydrogen explosions have shown that, depending on the fuel concentrations, the mixture can explode in two stages: a first fast hydrogen explosion phase, followed by a slower dust explosion. This can proceed either like a dust cloud explosion initiated locally at the sphere centre by the hydrogen combustion, or like a volumetric dust cloud combustion initiated over the whole volume under the elevated pressure and temperature resulted from the hydrogen explosion. The former may feature the flame front propagating from the sphere centre outwards; the latter cannot have a characteristic flame front. To distinguish that, a unit to measure arrival-of-flame

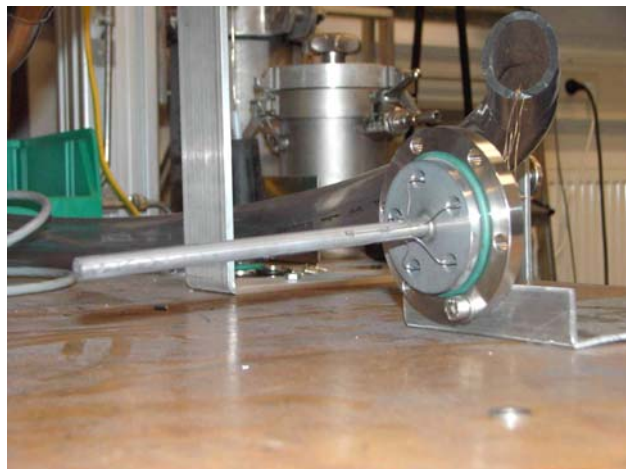


Fig. 1: Assembly to measure arrival-of-flame time. Flame sensors are 0.1 mm NiCr-Ni thermocouples.

times inside the sphere was designed, fabricated, and tested. The unit consists of an array of five 0.1mm NiCr-Ni thermocouples installed radially in the bomb (see Fig. 1). It is used in the tests with tungsten/hydrogen dust mixtures, which have been started this year.

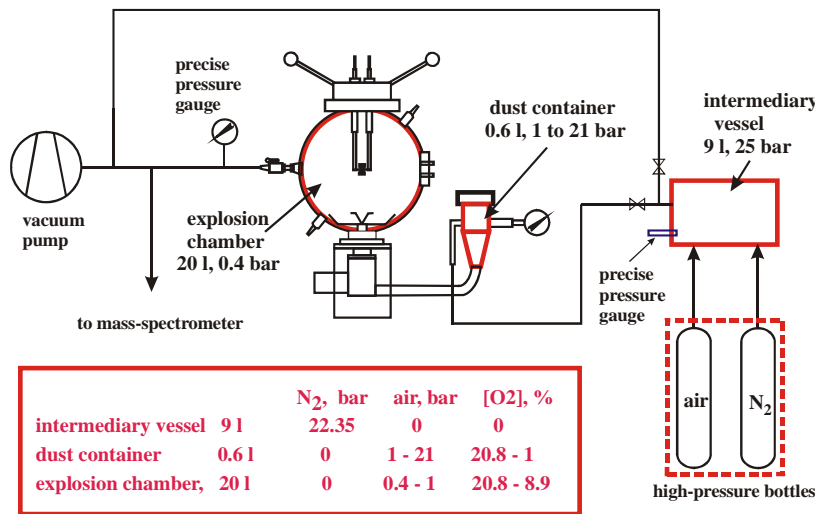


Fig. 2: Modified DUSTEX facility: gas filling system.

In 2005, tests have been started to support an inerting method to mitigate the hydrogen/dust explosion hazard in ITER. The limiting oxygen concentrations are measured for 4-micron graphite dust using the 20-l sphere method. As inerting gas, nitrogen is used. The DUSTEX facility has been modified accordingly (see Fig. 2). The gas-filling system has now an intermediary high-pressure vessel, where the  $N_2$ /air mixture is prepared by the partial-pressure method.

The DUSTEX facility has been equipped with a mass-spectrometer to measure the initial mixture compositions and the resulting concentrations of combustion products to better understand if the tested mixtures explode or barely burn out in the flame of the igniters. The oxygen content in the pre-explosion atmosphere is varied from normal 20.8 vol % to 10 vol. %. The tests are performed for 150, 200, and 300  $g/m^3$  dust concentrations. The tested mixtures are ignited by 2 or 10 kJ chemical igniters. In case of the weaker igniter, the maximum overpressure decreases from 5 bar at normal oxygen content (20.8 vol. %) to 0.5 bar at about 17 vol. %  $O_2$  (see Fig. 3). If the mixtures are ignited by the stronger 10 kJ igniter, 0.5 bar overpressure is observed down to 11 vol. %  $O_2$  (see Fig. 4).

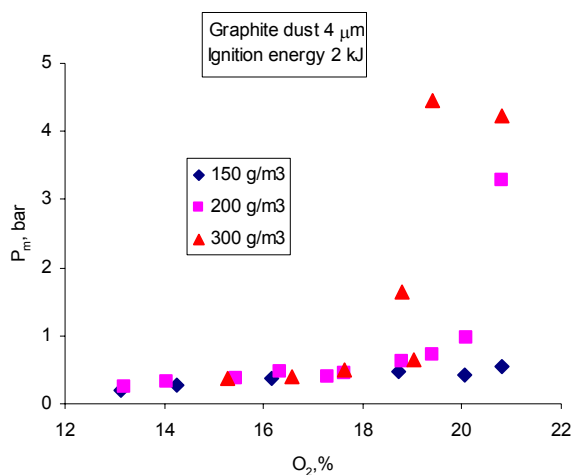


Fig. 3: Maximum explosion overpressure of 4  $\mu m$  graphite dust versus oxygen content. Ignition energy 2 kJ.

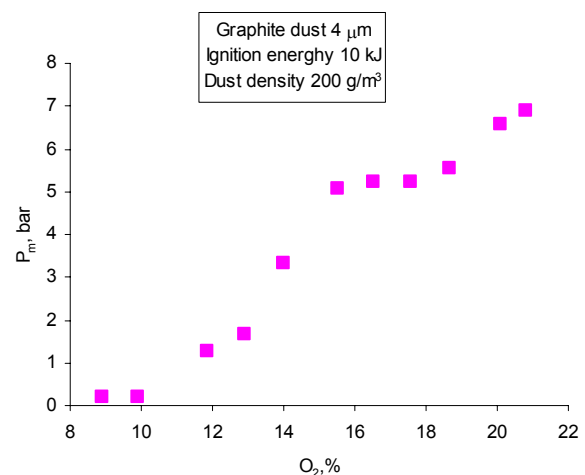


Fig. 4: Maximum explosion overpressure of 4  $\mu m$  graphite dust versus oxygen content. Ignition energy 10 kJ.

The development of another experimental technique was started in 2004 and continued in 2005, namely, the technique of open-end combustion tube. The goal is to measure efficient burning velocities the flame propagates with in the quiescent dust/air mixture under concern. The dust cloud is formed by dispersing a dust layer, initially deposited onto the tube bottom, with an array of compressed air jets from a dispersion pipe inside the tube near to the dust layer. After the dispersion, the dust cloud is ignited at the open end of the tube. As the combustion products can flow freely out of the tube, the flame propagates through an undisturbed

mixture. The flame propagation process is recorded, and the burning velocity is derived. For correct measurements, the spatial homogeneity of the dispersed dust cloud is important. A plastic tube of 2 m length and 15 cm inner diameter was designed and fabricated to test the dust dispersion characteristics (see Fig. 5). The dispersion tests were performed with fine graphite dust, resulting in dust cloud concentrations from 50 to 300 g/m<sup>3</sup>. The dispersion process in the tests was recorded with high-speed video (1000 frames/s). Some shots of the dispersion process with 100 g/m<sup>3</sup> graphite dust final density are presented in Fig. 6. The records demonstrate a good homogeneity of the dust clouds formed. First ignition tests have been started in this tube with strong chemical igniters or gas-burner as the ignition source.

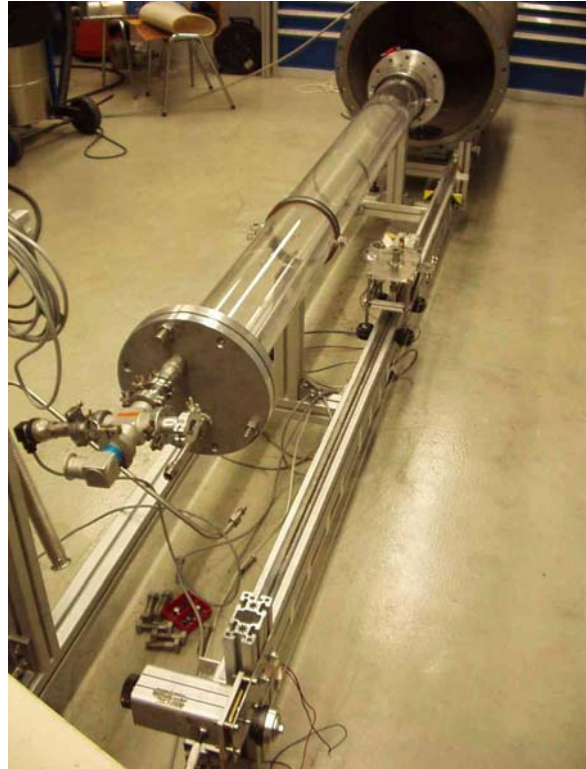


Fig. 5: Open-end tube to measure effective burning velocities in dust clouds.

A larger metal tube of 35 cm inner diameter and 2 m length is prepared for effective burning velocity measurements and to study scaling effects of flame propagation in dust clouds. The tube can be elongated up to 12 m. Furthermore, a metal version of the smaller 15 cm i.d. tube is being fabricated to perform effective burning velocity measurements in hydrogen/dust mixtures. The elaborated thin-thermocouple technique will be used to record the process of flame propagation.

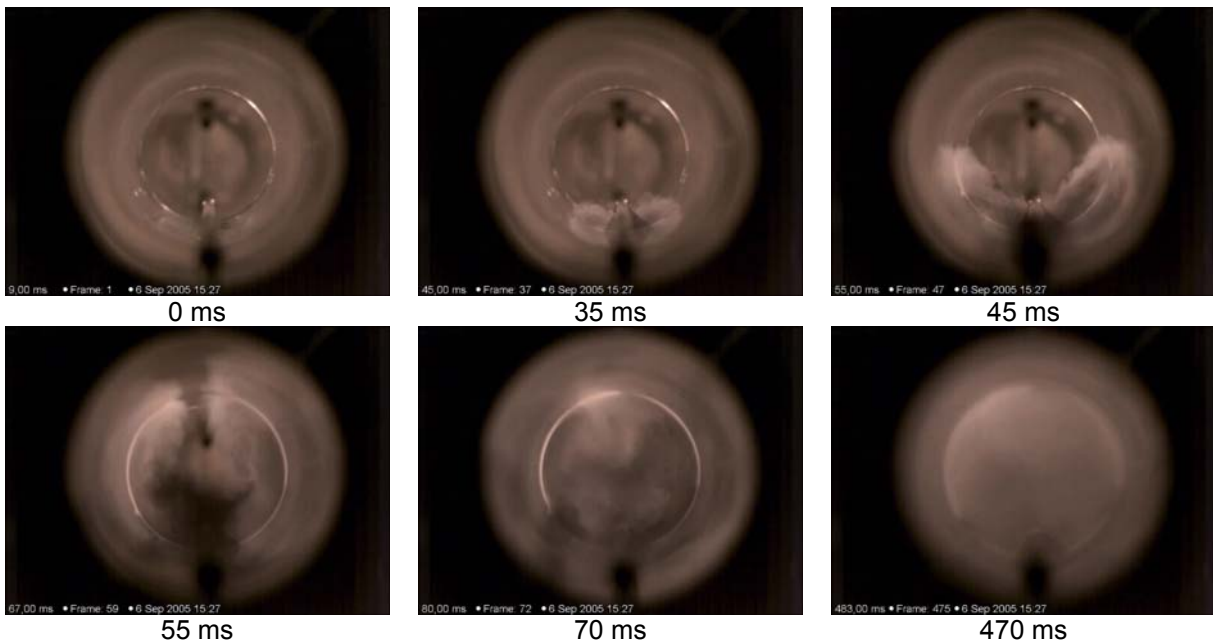


Fig. 6: Dust dispersion process with a dispersing pressure of 21 bar and a tube filling pressure of 0.6 bar. A portion of the tube is charged with the dust – from 70 to 90 cm from the open end. The final density of the dust is 100 g/m<sup>3</sup>.

## Outlook

- Measurement of the explosion indices of tungsten dusts in hydrogen-containing atmospheres in the DUSTEX facility.
- Measurements of effective burning velocities in graphite dusts in the 35 cm i.d., 3 m long open-end metal tube.
- Measurements of effective burning velocities in graphite dust/hydrogen mixtures in the 15 cm i.d., 2 m long open-end metal tube.

## Staff:

S. Baur  
W. Breitung  
A. Denkevits  
B. Kaup  
F. Prestel

A. Friedrich, ProScience  
K. Sempert, ProScience  
G. Stern, ProScience

## **EFDA/04-1194**

# **Hydrogen Deflagration/Detonation Analyses in ITER Cryopumps, Heating Neutral Beam, and Diagnostic Neutral Beam Boxes**

## **Introduction**

The safety assessment for ITER, performed as a Generic Site Safety Report (GSSR), demonstrated the strong inherent safety characteristics of fusion leading to much lower consequences in worst case accidents, compared to fission. The leading accident classes identified in the GSSR are:

- failure of coolant circuits (LOCA's),
- local breaches in the vacuum vessel (LOVA's)
- loss of power, and
- release of magnetic energy.

The task reported here addresses Loss-Of-Vacuum-Accidents (LOVA's) which belong to design basis accidents. Some of the accidents can lead to co-existence of combustible substances like hydrogen and dust with oxygen. Since an ignition source is difficult to exclude, combustion needs to be addressed to understand the potential consequences, and if necessary, to derive effective mitigation measures. Combustion processes require detailed analysis because they could create simultaneously

- high mobilization of the radiological inventory in the vessel (T, and C, Be, W dusts),
- increased leakage areas by local damage of the vacuum vessel and
- transient pressures above 1 bar.

The combination of these effects could cause venting of the vacuum vessel and potentially high radiological source terms. For radiological risk management and ITER investment protection, the prediction of combustion effects and possible mitigation measures are needed. Therefore a 3d code development for simulation of hydrogen and dust explosions in ITER was started. Meanwhile, accidents involving hydrogen combustion at conditions typical for ITER can be modeled with good precision. The codes for simulation of dust and combined hydrogen-dust explosions are under development, they have not yet reached predictive capabilities. The term "hydrogen" will be used here as synonym for all hydrogenic species ( $H_2$ ,  $O_2$ ,  $T_2$ ,  $DT$ ,...).

## **Achievements in 2005**

In 2005, the hydrogen risk related to Loss-Of-Vacuum-Accidents in ITER was investigated. The work addressed hydrogen distribution and combustion in modules which are connected to the ITER vacuum vessel:

- cryo-pumps,
- heating neutral beam injectors (HNB), and
- diagnostic neutral beam injectors (DNB).

Fig. 1 shows the ITER vacuum vessel with these extension volumes. In case of an air ingress, the cryogenic pumping panels would be warmed up. For temperatures above 50 K, the pumped hydrogenic species (H, D, T) are released and can form combustible mixtures with the air flowing in through the breach of the vacuum vessel. (In normal operation, the pumps are separated from the vacuum vessel and then regenerated by heating them above 100 K.) Hydrogen distribution and combustion analyses were performed for the above sub-systems of ITER.

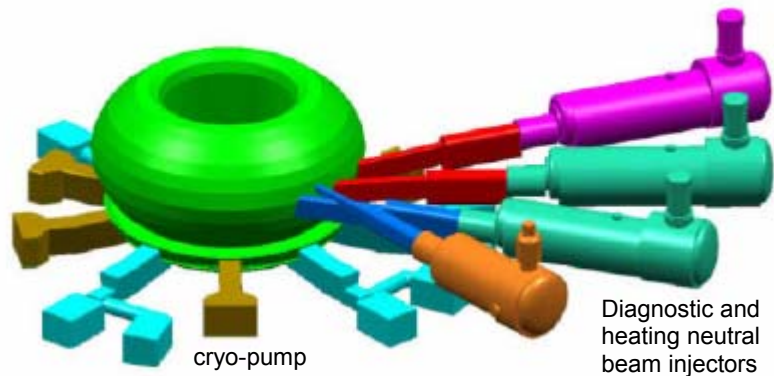


Fig. 1: ITER vacuum vessel with extension volumes for which a hydrogen analysis was performed.

### - Hydrogen analysis for ITER cryo-pumps

The cryo-pump was modeled as a horizontal cylinder with  $8.5 \text{ m}^3$  of free volume. Two boundary scenarios for air ingress were investigated:

- a) slow pressurization (1.5 mbar/s) simulating a leak in a port window of the vacuum vessel,
- b) fast pressurization (130 mbar/s), simulating a large leak in a cryo-pump seal.

The hydrogen inventory desorbing from the cryo-panels was assumed to be equal to the maximum pumping capacity (8 moles). The release kinetics of hydrogen under the given air pressurization rates was measured earlier in specific experiments in the TIMO facility of FZK (Day, Haas, ITP-FZK, 2004). In the slow case the release starts about 7 seconds after the begin of the air ingress and is completed 6 seconds later. In the fast case the corresponding times are about 2 and 3 seconds.

The transient air ingress and hydrogen release into the cryo-pump volume was modeled using the 3d code GASFLOW, which is being developed at IKET-FZK for hydrogen safety analysis. The computational grid used 28.000 nodes to represent the cryo-pump geometry (Fig. 2). Combustible mixtures developed only in the slow case, where almost the total  $\text{H}_2$  mass of 16 g is involved (Fig. 3). For the high air ingress rate, the desorbing hydrogen is strongly diluted during its release period and never reaches the flammability limit of about 4%  $\text{H}_2$  in air. The hydrogen is released with a temperature of 100 K. In case of the slow air ingress (1.5 mbar/s), at first a hydrogen-rich cloud forms in the cryo-pump which is then continuously diluted by the inflowing air. Fig. 4 shows the calculated hydrogen mol fractions in the cryo-pump 30 s after begin of air ingress. The total pressure at this time is about 57 mbar.

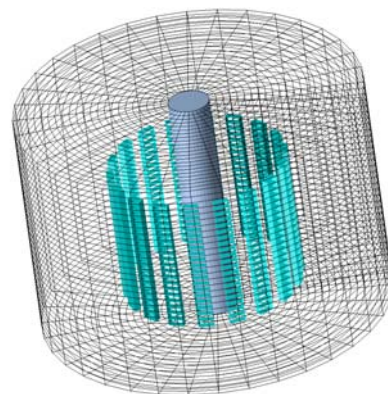


Fig. 2: Computational grid used for simulation of hydrogen release and mixing in a cryo-pump for case of a LOVA, GASFLOW code, 28.000 grid cells, cryo panels are shown in blue.

Mixtures which are able to support fast deflagration or detonation exist for about 1 min, thereafter only slow deflagrations with insignificant peak pressures are possible. A detailed risk evaluation using newly developed criteria showed that detonations which result in the

highest possible combustion pressures could occur only for an initial short time period during the air ingress, corresponding to the time interval between 10 and 20 s in Fig. 3. The hydrogen is fairly well mixed. Since an ignition time is difficult to postulate and not well defined, two combustion calculations were performed:

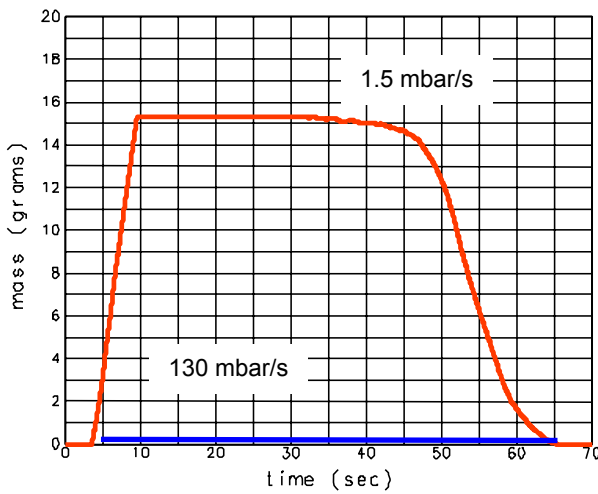


Fig. 3: GASFLOW result for the H<sub>2</sub> mass in a fast burning H<sub>2</sub>-air mixture (10.5-75% H<sub>2</sub>) in the cryo-pump during slow and fast air ingress. Combustible mixtures develop only in the slow case (1.5 mbar / s).

- 1) strong early ignition, leading to a detonation, and
- 2) late weak ignition, leading to a deflagration.

The second case results in slower flame speeds, but it starts from a higher initial pressure, compared to case 1. The net outcome with respect to the peak pressures generated in both cases was not obvious initially.

The detonation was simulated with the FZK code DET3D, using 1.4 million mesh cells (2 cm mesh size). Typical maximum peak pressures on the walls are 3-4 bars, with peak durations of the order of 0.1 ms (Fig. 5). Since these transient peak pressures are above the static design pressure of the cryo-pump housing (2 bar), a simplified structural response analysis using a single-degree-oscillator model was performed.

The resulting dynamic load factor was estimated to about 0.5, so that the maximum effective static pressure acting on pump walls is 4 bar x 0.5 = 2 bar, which is equal to the design pressure of the pump housing. The late ignition case, which was modeled with the FZK code FLAME3D, lead to a maximum pressure of only 0.65 bar, which is well within the design limit.

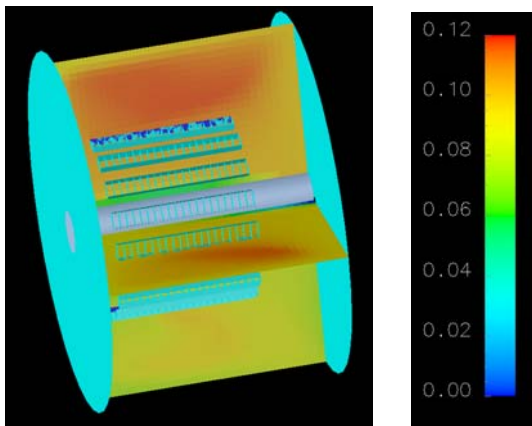


Fig. 4: Calculated hydrogen volume fraction in the cryo-pump at 30s after the beginning of the air ingress, for the case with slow air pressurization rate (1.5 mbar /s).

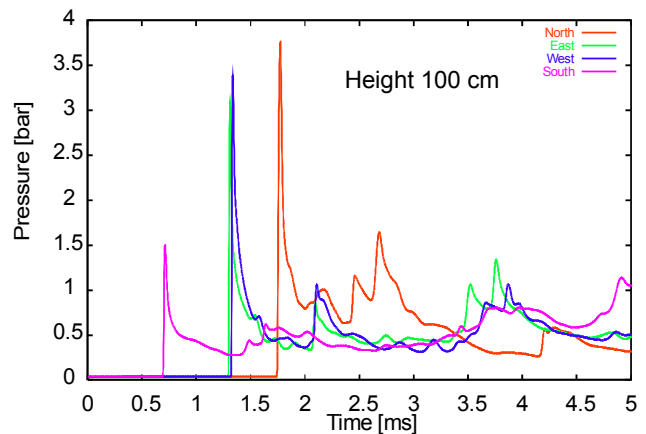


Fig. 5: DET3D results for typical wall pressures in case of detonation of the cryo-pump mixture. Initial gas distribution from GASFLOW, ignition assumed 10 seconds after the beginning of the air ingress.

Taking into account the rather conservative assumptions made, it can be concluded that loads from hydrogen combustion in the cryo-pumps of ITER which could develop during a LOVA will not exceed the design limits, however closely approach them. This means that the pumping capacity of cryogenic systems, which could in principle be increased above 8 mol of

hydrogenic species, should not be raised. Pumping capacity and structural limits of the current design are well balanced.

### - Hydrogen analysis for HNB modules

The HNB modules are modeled as horizontal cylinders with a total free volume of 127 m<sup>3</sup>, which is the current design value (Fig. 6). Since the internal structures occupy only about 15% of the total HNB volume, they were neglected in the distribution and combustion simulations. Only the case with slow air pressurization rate (1.5 mbar/s) was investigated. The inflow boundary condition on the near-plasma side was adjusted accordingly. A total hydrogen inventory of 48 moles was released, where most of this desorbs in room 2 (92 %), and only 8% in room 1. The release kinetics of the TIMO facility were again used in the simulation, because the same pumping technology is applied in cryo-pumps, HNB and DNB modules.

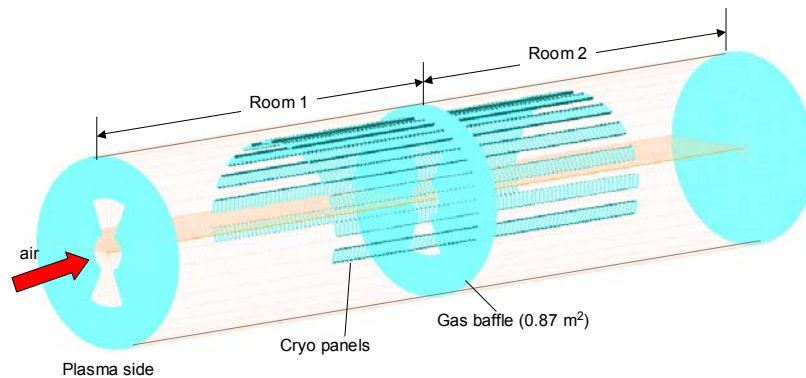


Fig. 6: Geometry model for HNB modules in form of a horizontal cylinder with a length of 15.6 m, and a diameter of 3.22 m.

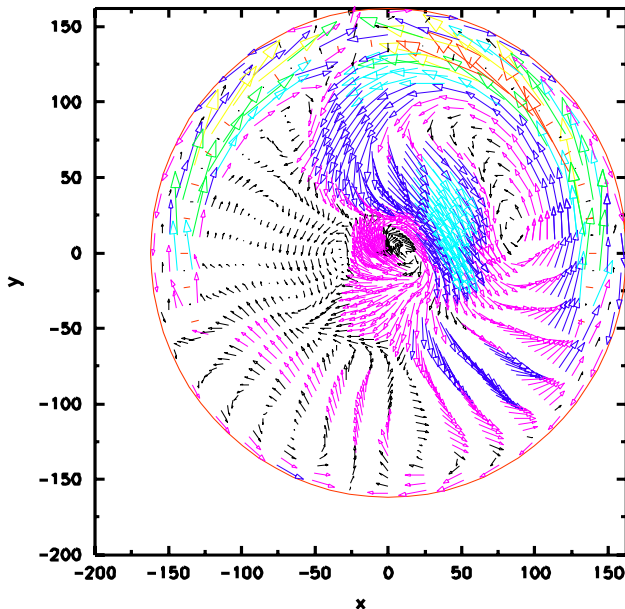


Fig. 7: Velocity field in HNB box, 8 s after the beginning of the air ingress, vertical cut 9 m from the near-plasma side opening. Velocities range from 1 cm/s to 3.5 m/s.

The GASFLOW geometry model used 190.000 cells. Fig. 7 gives an impression of the flow field in room 2 of the HNB box in form of a vertical cut, 9 m from the plasma side opening, 8 seconds after the begin of the air ingress. A strong upward convection of the released hydrogen can be observed at this time. The vector lengths in Fig. 7 are proportional to the flow velocities, which range from 1 cm/s to 3.5 m/s.

Fig. 8 shows the hydrogen concentration field 30 s after the air ingress. Hydrogen from room 1 has been swept to room 2 by the inflowing air. Initially, the hydrogen in room 2 raised to the top, but with increasing time the hydrogen was diluted and displaced to the lower half due to inflowing warmer air.

The risk evaluation for the time dependent mixture evolution showed detonable mixture compositions for a time period of about 20 s. To estimate the maximum possible loads from hydrogen-air reactions, a detonative combustion was simulated, using as a conservative ignition location the midpoint of the cylinder end plate (at 15.6 m axial position).



Figure 9 shows a plot of the maximum pressures obtained at a given position during the whole detonation process. The depicted plane is a vertical cut through the cylinder axis (see Fig. 6). Most of the wall surface is loaded with peak pressures below 2 bar; focusing of the detonation wave in the corner opposite to the ignition point can cause peak pressures of up to 4 bar in small local areas. These local transient loads are expected to have insignificant damage potential to the wall structure. Furthermore, inclusion of more internal components in the geometry model would destroy the symmetry and coherence of the detonation wave which is needed to create such high local pressures.

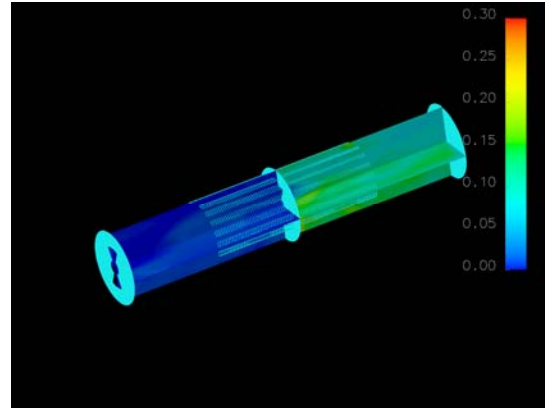


Fig. 8: Hydrogen distribution in the HNB module, 30 s after the beginning of the air ingress. Warm air rises to the top and displaces hydrogen to the bottom half of the HNB volume.

A deflagration of the mixture in the HNB volume was also simulated using the code FLAME3D. The resulting peak pressures were generally below 0.7 bar and reached 1.2 bar at most in focusing corners. Such peak pressures are well within the static design limit of the HNB box (2 bar).

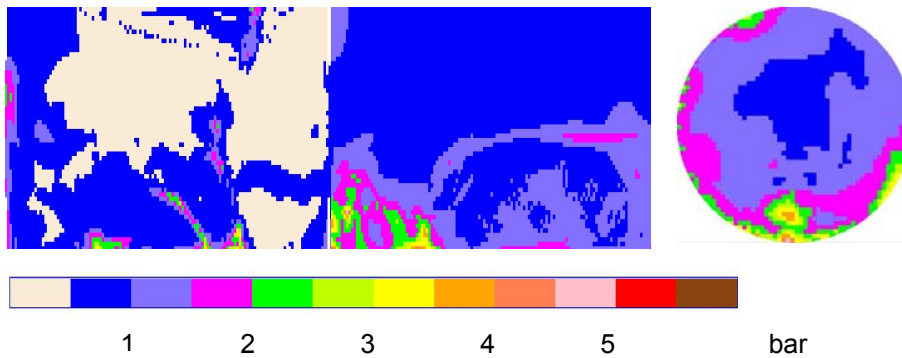


Fig. 9: Calculated maximum detonation pressures in the HNB volume. Most of the walls are loaded with peak pressures below 2 bar. Local focusing with higher peak pressures is expected to have negligible structural consequences.

The hydrogen distribution and combustion analysis leads to the conclusion that the peak pressures from combustion of desorbed pumped species will not jeopardize the integrity of the HNB housing. The HNB boxes appear to provide sufficient structural stability to serve as a barrier against release of radiological inventory (pumped tritium) to the ITER plant. A combustion event could however severely damage the interior components of the HNB module.

#### - Hydrogen analysis for DNB modules

A good general indicator for hydrogen risk and possible combustion pressures is the volumetric average hydrogen concentration, which characterizes the average energy density in the system after combustion (provided it is not oxygen limited). In case of the cryo-pumps this amounts to  $8 \text{ moles} / 8.5 \text{ m}^3 = 0,94 \text{ mol/m}^3$ , in case of the HNB boxes,  $48 \text{ moles} / (127 / 2) \text{ m}^3 = 0.75 \text{ mol/m}^3$  are obtained, and for the DNB boxes it is  $20 \text{ moles} / (86/2)\text{m}^3 = 0.46 \text{ moles} / \text{m}^3$ . The DNB case shows the smallest energy density, so that the peak pressures to

walls will be below the corresponding cryo-pump and HNB values. Compared to the cryo-pump situation, the average energy density in the DNB boxes is decreased by a factor of two. Hydrogen combustion in the DNB modules will therefore not create new risks, the peak pressures in ITER modules are limited by the cryo-pump and HNB results. According to the

ITER design team, all modules have a static pressure of 2 bar, so that the lower combustion pressures in the DNB case will not induce a risk for the structural integrity.

Staff:

W. Breitung

M. Kutznetsov

R. Redlinger

G. Necker, Pro Science

A. Veser, Pro Science

## **TSS-SEA 5.4 Busbar Arcs Behavior and Consequences**

### **TW5-TSS-SEA 5.4 D 1-3 Experimental Simulation in the VACARC Facility**

High power arcs at the ITER busbars are a possible threat to the cryostat wall which is part of the ITER containment. For licensing questions, this very improbable event must be investigated. Presently, no suitable numerical models with reasonable accuracy are available. Model development turned out to be difficult due to lacking knowledge of arc propagation and destruction behaviour. The VACARC busbar arc experiments are a continuation of the experimental contribution to the work on busbar arcs started with the MOVARC experiments in the frame of task TW3-TSS-SEA5.4. The main purpose of VACARC is the support of model development and model validation, however also experimental experience for possible full scale experiments is acquired. The VACARC setup is based upon a plasma spray device which had been taken out of service several years ago. The VACARC vessel is designed for vacuum conditions which allow for a more realistic simulation of the ITER cryostat conditions than MOVARC. Particularly, problems with the high sensitivity of arc column stability to gas flow are expected to be much lesser inside the vacuum chamber than in the 1bar argon protective gas atmosphere of MOVARC. The available powers will be almost one order of magnitude higher than in MOVARC thus providing a first hint on the scalability of the setup and the results. This is an important point with regard to model development and model validation.

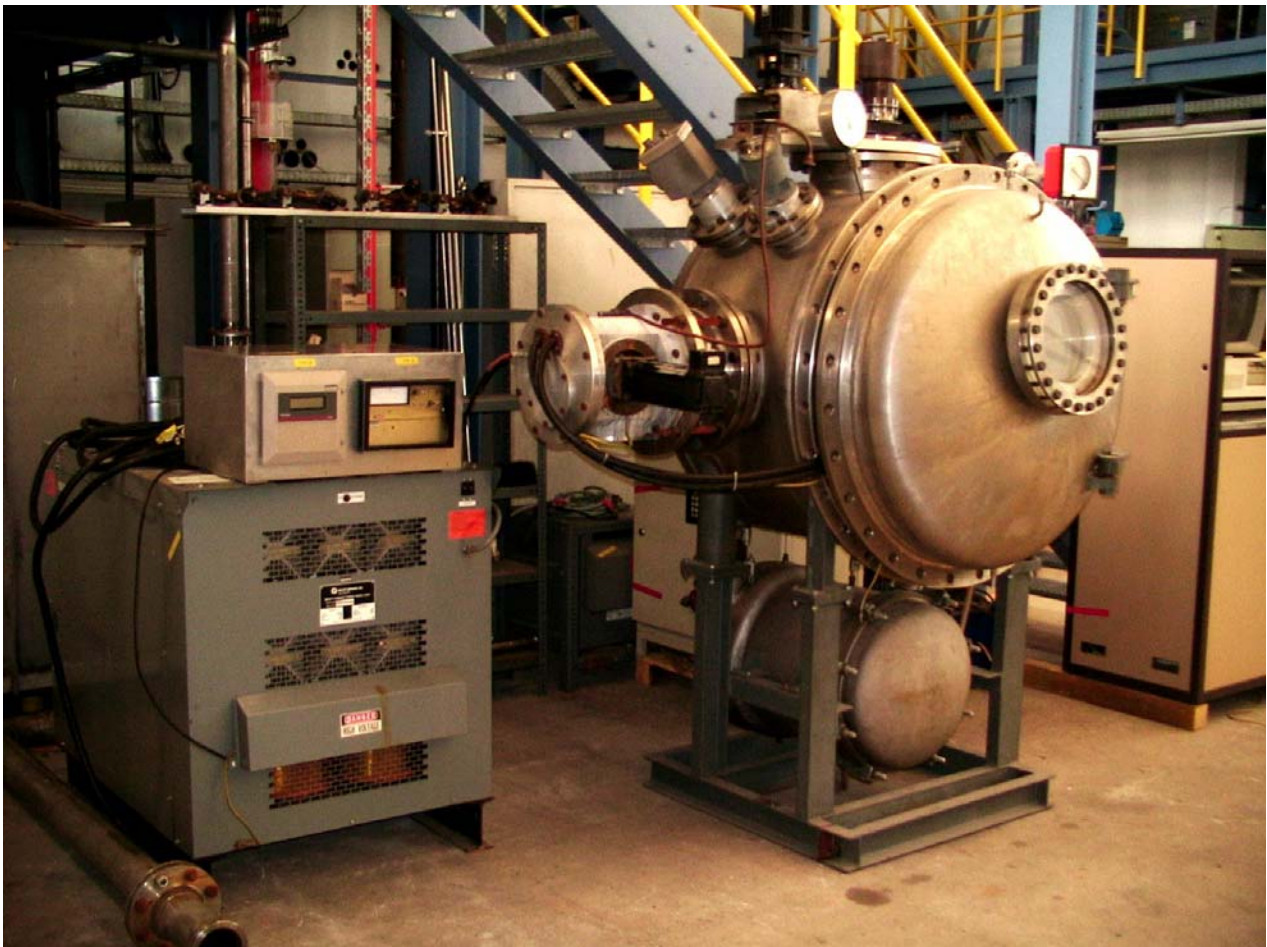


Fig. 1: Photograph of the vessel and the power supply (dark gray device on the left) foreseen for VACARC experiments.

The present status is that the main components for VACARC have been transferred from FZK-IHM to FZK-IRS. The vacuum pumps and the electrical connector box will be available for transfer as soon as the microwave furnace at FZK-IHM is replaced by a successor model.

The planning for the in-vessel components and the required 120kW-infrastructure is almost finished. The power converter could not be tested yet. If it will not work, the alternative option is to replace it by a stack of high power batteries.

Staff:

D. Klimenko

V. Pasler

**TW3-TSS-SEA 5.4 D 4  
Busbar Arcs Behavior and Consequences - Final report**

and

**TSS-SEA 5.5  
Validation of EU Safety Computer Codes and Models**

**TW4-TSS-SEA 5.5 D 8  
Report on Busbar Arc Model Development  
and**

**TW4-TSS-SEA 5.5 D 9  
Report on Arc Experiments for Support of Arc Model Development and  
Validation**

High power arcs at the ITER busbars are a possible threat to the cryostat wall which is part of the ITER containment. For licensing questions, this very improbable event must be investigated. Presently, no suitable numerical models with reasonable accuracy are available. Model development turned out to be difficult due to lacking knowledge of arc propagation and destruction behaviour. The MOVARC (MOVement of ARCs) experiments should clarify principle busbar arc behaviour at a small scale with regard to model development and validation. The experience from the experiments may also be valuable in the view of possible requests for full scale experiments from licensing authorities, if numerical efforts are not convincing. Additional information is expected from the VACARC experiments which will allow arcing under vacuum conditions.

During 2005, numerous experiments were performed with the MOVARC device. The experimental campaign provided important experiences and results for numerical approaches and for the further experimental investigations at larger scale. Basic and interesting findings are that the arc, driven by magnetic self-forces, propagates at a velocity of a few cm/s along the model conductor. The destruction is rather limited. Along the arc path, only a part of about 20% of the perimeter is molten into the insulation and the steel cover tube which simulate the busbar insulation and steel jacket. The copper core remains almost undamaged. During burning, the arc turned out to be very sensitive to even slight disturbances by convection or pollution of the metal surfaces. Particular measures were necessary to achieve stable arc burning. E.g., ceramic bricks were used to avoid convection. Even small amounts of hydrocarbons from cements or tapes turned out to produce enough black fallout on the metal surfaces to impact arc burning behaviour considerably. A relevant amount of hydrocarbons is located in the resin impregnation of the ITER busbar cable insulation.

The Steenbeck minimum principle says that an arc will choose the path of minimum energy release, which in practice would be a short and straight arc. These arcs are called stable. Stable arcs could be observed for currents up to 300A and powers up to about 15kW. In the experiments, this principle was easily overridden by convection or slight electrode pollution and long, bent arcs were observed unless the experimental conditions were controlled carefully. Arcs behaving like that are called unstable. However it turned out that the velocity of stable and unstable arcs of similar current and setup conditions was quite similar.

The use of MOVARC data for arc model development turned out to be difficult due to the large spread of data. The spread is partly caused by parameters which were unknown or not carefully controlled so far. Meanwhile, several deviations in experiments could be assigned to effects like insufficient protection against convection or slight corrosion of the electrode surfaces. Taking into account these findings, data correlations become visible. Surprisingly, not the arc power but the total arc voltage seems to have the strongest correlation to arc

propagation velocity. It is expected that increasing experience will give insight into further parameters unidentified so far, thus helping to enhance the accuracy of the evaluation.

Staff:

D. Klimenko  
V. Pasler

Literature:

- [1] V. Pasler: First report on feasibility of medium and large scale arc experiments for ITER safety investigations, June 2004, TW4-TSS-SEA5.5/D3.

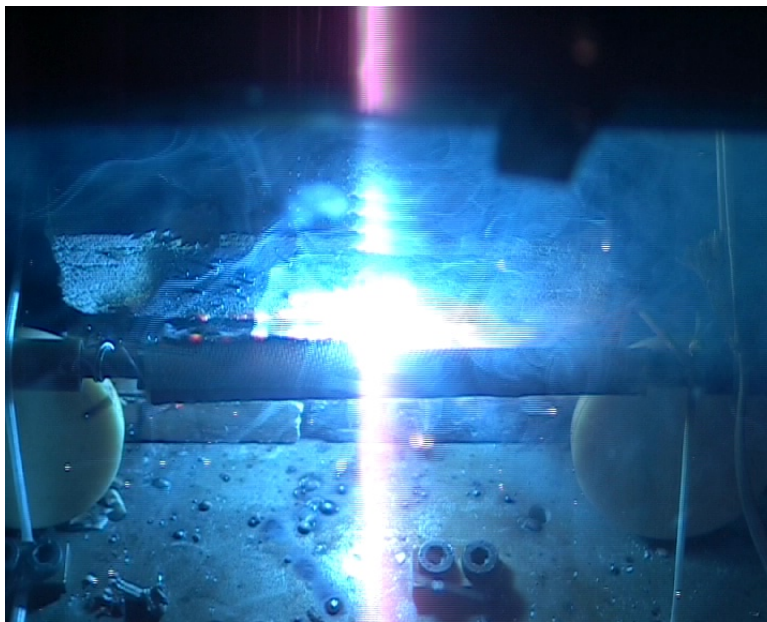


Fig. 1: Example #1, stable arc: A bright arc burning straight between the model conductor and the electrode moves from left to right at about 5.6cm/s.

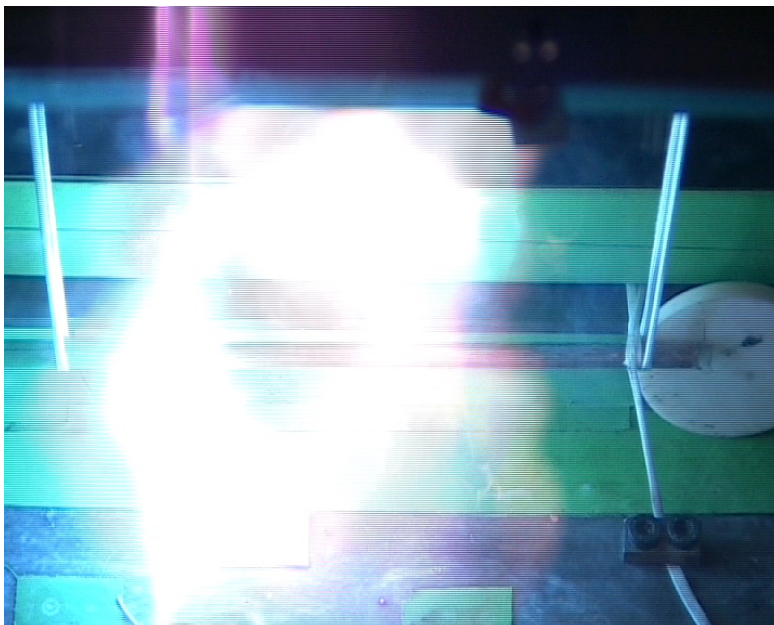


Fig. 2: Example #2, unstable arc: The arc column is bent into a long loop which causes arc voltage increase. In this experiment, the ceramic bricks which would hinder convection as shown in the above photograph of the stable arc are missing. Arc velocity and arc power are hard to estimate.

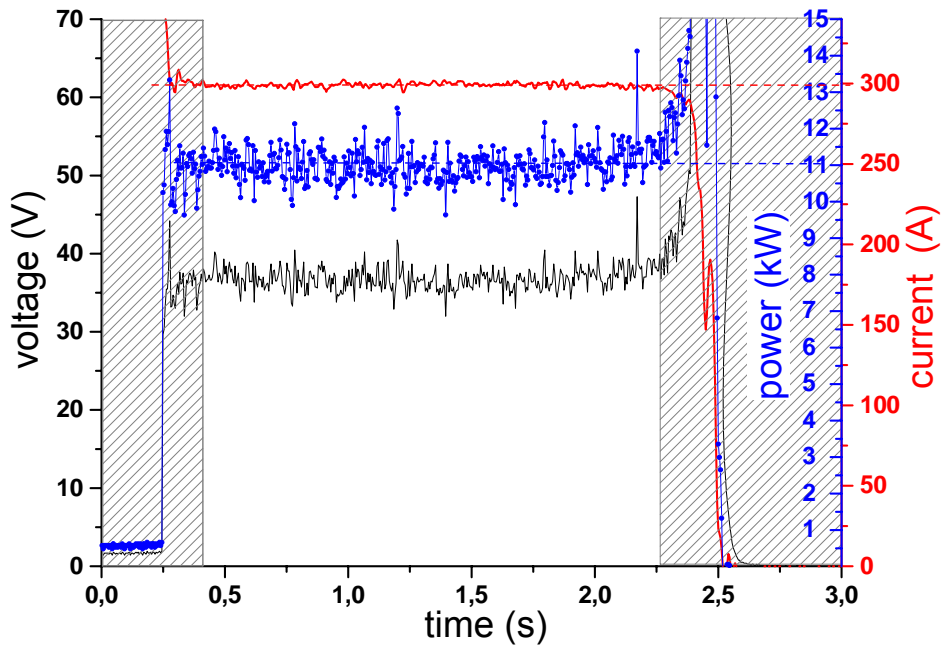


Fig. 4: Electrical data of example #1. Arc power data is quite regular. The arc velocity is calculated by dividing the unshaded time range by the total length of the model conductor.

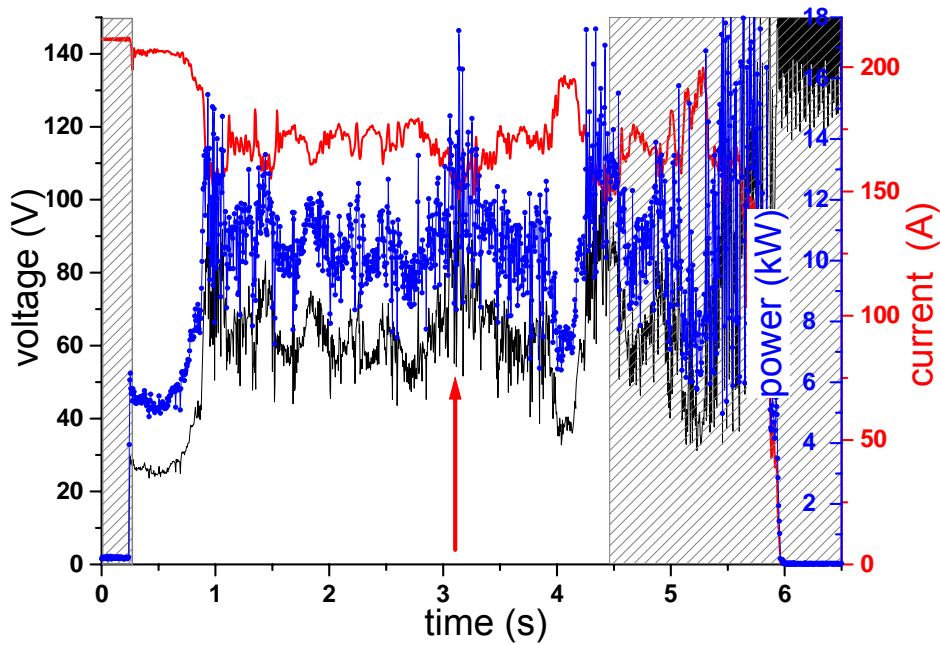


Fig. 5: Electrical data of example #2. The arc lost stability within the first second after ignition and did not recover again. The unshaded area indicates the time range for the arc passing the model conductor. The red arrow indicates the time when the photograph of example #2 was taken. The arc movement is much slower than for example #1.

## **TW4-TSS-SEA 5.5 D 7**

### **Report on MAGS Recalculation of EVITA Experiments including Noncondensables**

and

## **TW5-TSS-SEA 5.5 D 5**

### **Final Report on MAGS Recalculation of the EVITA Experimental Campaign 2005**

The EVITA condensation experiments at CEA Cardarache (France) are part of a long-term validation program for several safety codes, which are intended for usage in the licensing procedure for ITER. MAGS-CRYOSTAT represents the FZK contribution. EVITA is a 0.22m<sup>3</sup> stainless steel vessel that can be evacuated. A reservoir with an inlet system for steam and water injection and a nitrogen cooled cryogenic condensation plate are available for a campaign of condensation experiments. The apparatus is improved step by step to get closer to realistic ITER cryostat conditions.

In the calculations of non-cryogenic EVITA experiments with MAGS-CRYOSTAT, good results were received. However, the cryogenic experiments were difficult to analyse. After some changes to the experimental setup to optimize cooling and avoid unwanted heat barriers and flow effects, still no acceptable calculation results could be gained without using completely unjustified assumptions. A close analysis of the experimental data finally revealed the origin of these difficulties. From the presence of an ice layer at a vessel pressure above the mbar range, far away from the steam saturation line  $p(T)$ , it is obvious that nonequilibrium conditions are present during the experiment and the previously used equilibrium model cannot be expected to yield reasonable results. Another finding was that a considerable liquid condensation takes place on and around the insufficiently insulated nitrogen tubes in the partly separated volume of the vessel below the condensation plate. This volume separation is generated by a metal cover, the so called protective lid. The cover divides the vessel practically in two parts. The openings are large enough to guarantee pressure equilibrium in both parts, but temperatures are not necessarily equal.

A model taking into account nonequilibrium conditions as well as volume separation was developed during 2004. The model started to work reliably in early 2005. It combines nonequilibrium condensation based on a diffusion layer model with a division of the vessel into two subvolumes. In the volume containing the nitrogen cooled plate, nonequilibrium ice condensation takes place. In the second volume at almost equal pressure but different temperature, liquid condensation under equilibrium conditions is simulated at the nitrogen tube insulation. This model is able to describe the rather sensitive transient EVITA vessel pressure as well as the final condensate mass including the mass ratio of liquid and ice condensate.

Meanwhile, the EVITA experimental campaign proceeded with nitrogen used as an inert gas during steam injection and condensation. From a first data analysis, nitrogen seems to accelerate condensation, as final vessel pressures are lower compared to previous experiments with similar steam ingress but without nitrogen. The close to equilibrium correlation between cold bottom vessel parts and steam partial pressure is still observed. This strongly suggests that the combined nonequilibrium-two volume solution should also work to match experiments including inert gas. Required changes are expected to be restricted to modifications to the nonequilibrium cryogenic condensation model. Unfortunately presently no staff is available to perform this task.

#### Staff:

Y. Ke (until 3/2005)



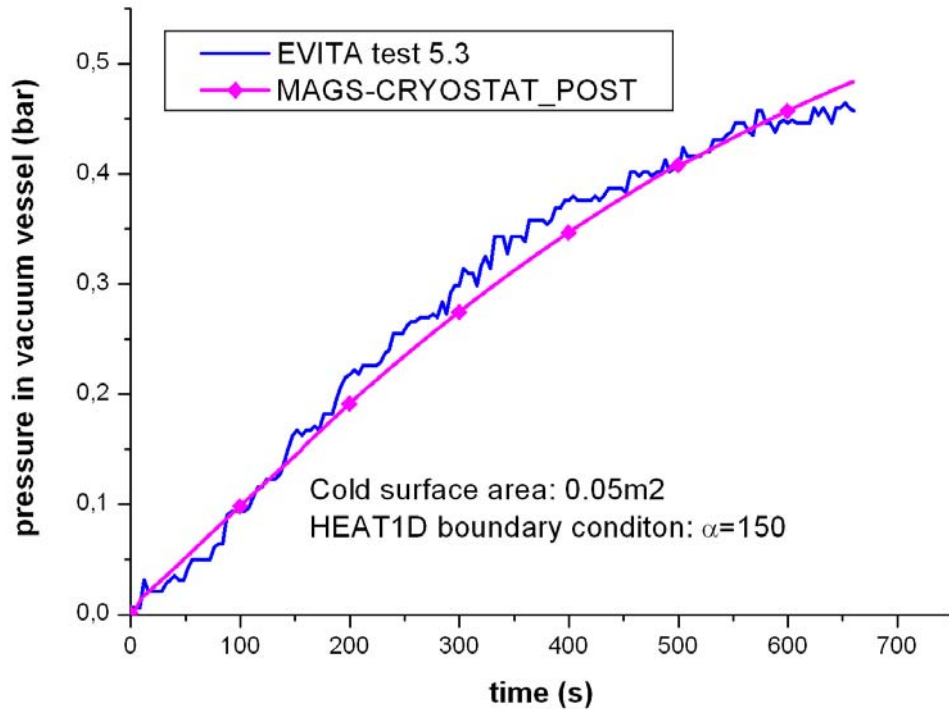


Fig. 1: Transient vacuum vessel pressure during EVITA steam injection test 5.3.

Table 1: EVITA steam injection test 5.3: comparison of experimental and calculated data.

	Average mass flow (g/s)	Injection time (s)	Injection mass (g)	Ice mass (g)	Liquid mass (g)	Vapour mass in VV (g) (Final pressure)
<b>Exp. data</b>	0.69	660	455.4	310	95 (on bottom)	50.0 (0.460 bar)
<b>Calculated</b>	0.714	660	471.3	311.6	103.0	54.3 (0.484 bar)

## **TW5-TSS-SEP 2**

### **Doses to the Public and Validation of UFOTRI**

#### **Objectives**

The objective of this task is to demonstrate the validation level of the computer codes used for the calculation of doses to the public in the case of radio nuclide release from a fusion reactor, and to calculate, on request by EFDA, in a consistent way such doses for given source terms, for realistic meteorological and siting conditions, for ITER (European site) and for fusion power plants. This comprises the enhancement of the "Fusion-Release-Target-Scoping-Tool" by the ingestion dose criterion for an easy assessment of all types of release targets and validation of UFOTRI in the frame of the EMRAS (Environmental Modelling for RAdiation Safety) international benchmark project including a comparison of concentration and dose criteria for the ingestion pathways.

#### **Work performed**

It is important to demonstrate, that potential radio nuclide releases from fusion power plants do not exceed internationally accepted intervention levels. In case of severe accidents, the radiological consequences have to be restricted to the vicinity of the plant and to times smaller than one year. Main safety targets for potential accidental releases to be compared with are European intervention levels for early (evacuation, sheltering) and late (relocation, food banning) actions and the regulations for European fission power plants. As the composition of realistic source terms is still open, a methodology has been developed to estimate the highest potential release which does not exceed the intervention levels. To this purpose, starting with the source terms as defined for the Power Plant Conceptual Study (PPCS) the contribution of each source term fraction to a particular dose target was calculated. Potential source terms from future fusion power plants mainly consist of activated dust (AP), activated corrosion products (ACP) and tritium in form of HT and HTO. Performing calculations for unit releases, an equation has been derived which allows further scaling of all three fractions so that the intervention level is not exceeded. This methodology has been developed in compliance with the European Utility Requirements.

As the number of calculations is large and the amount of data being processed and provided will be huge, and, as there is a certain possibility that the composition of a source term may change with time, a specific scoping tool was developed to allow an easy application for a particular case. This tool allows to

- load a particular scenario,
- load, modify or create a source term,
- and estimate the exhaust of the release targets for evacuation, sheltering, relocation and food banning.

The database of this tool contains nuclide specific doses and concentrations in food for the various release conditions. Each data set for one release condition includes information for all the four release targets. Only when a new release condition has to be investigated, additional calculations with UFOTRI and COSYMA would be necessary.

Microsoft EXCEL is used as basis for the tool. This allows an easy application as this software is widely distributed and a standard spreadsheet. Specific input forms will guide the user through the application function. In its present version, the tool was extended by the target ingestion dose and activity concentrations for the most important foodstuffs milk, leafy vegetables and wheat.

A draft report, describing the features of the scoping tool was delivered to the EFDA home team in October 2005.

The Tritium Working Group of the EMRAS project focuses on improving models of OBT formation and translocation in plants, animals and fish. Up to now seven different scenarios were proposed. FZK contributed with the UFOTRI code to the soybean and the hypothetical scenario.

The soybean scenario is based on experimental data collected at the Korean Atomic Energy Research Institute. Commercially available soybean was sown in May 2001 in 6 plastic pots (41cm x 33cm x 23cm high). Tritium exposure was carried out six times at different growth stages: July 2, July 13, July 30, August 9, August 24, and September 17. The pots were introduced into a glove box for the tritium exposure and the experiments were conducted under natural solar conditions, which resulted in high temperatures within the glove box. The surface of the soil was covered with vinyl paper so that uptake was only through the foliage. After exposure, the pots were placed in an open field among other soybean plants. UFOTRI performed well in the scenarios as stated in the draft report. *'All models over-predict the plant body HTO concentration in scenario 1 and 4 at the end of uptake, with UFOTRI giving best results. Soybean is mostly used for human consumption and the main target must be OBT at harvest. This must be predicted with comparable reliability in all reproductive stage. Accepting a factor 10 as a maximum miss-prediction allowed, only UFOTRI qualify (6 successes from 6 cases). All other models must be improved in various respects.'*

The objective of the hypothetical scenario is to analyse the consequences of an acute atmospheric release of tritium, by considering various pathways in terms of activity in biosphere compartments and products, as well as the contribution of the various forms of tritium (HT, HTO and OBT) to total exposure. The basic assumption is that 10 g of tritium is released over a period of 1 hr and the calculation period is 1 year. Results of the first predictions differed considerably so it was not possible to find consensus why model results diverged. Therefore, a new refined scenario will be worked out with additional endpoints to allow for a better comparison between the models.

### **Further work**

The model testing exercise in the frame of the EMRAS project will continue and the first draft report of the soybean exercise is expected for mid of 2006. Other exercises such as the hypothetical scenario will be refined end of 2005 and work will continue in 2006.

### **Staff:**

F. Fischer  
I. Hasemann  
W. Raskob



# **Power Plant Conceptual Study**



## TRP-001 He-cooled Divertor Concepts

### TW4 + TW5-TRP-001 D 2 Conceptual Design, Analysis, and Tests

#### Introduction

The 2005 divertor work programme (TW5-TRP-001) focused on the HHF He-loop experiments for the current optimised designs [1] (Fig. 1) HEMJ with jet impinging cooling and HEMS with a slot flow promoter for an enhanced convective cooling, respectively. The design goal is to withstand a high heat flux of at least  $10 \text{ MW/m}^2$ .

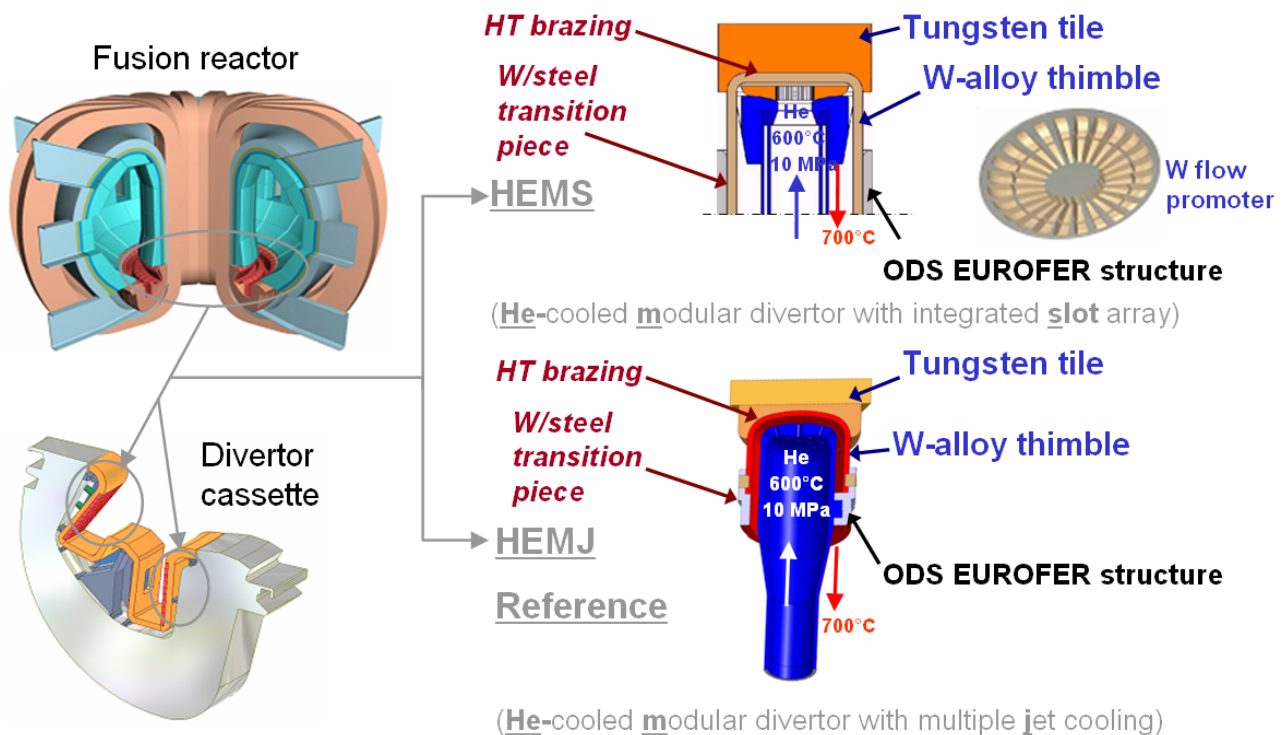


Fig. 1: He-cooled modular divertor designs HEMJ and HEMS.

#### Status of the conceptual design

The required high resistance of the armour material against high heat flux and sputtering led to the choice of tungsten as the most promising divertor material. W and W alloys possess a high melting point, high thermal conductivity, and relatively low thermal expansion. In addition, it is a low-activating material. Its disadvantages are a high hardness and a high brittleness, which make the fabrication of tungsten components comparatively difficult. Other disadvantages of tungsten are its poor values of ductile-brittle transition temperature (DBTT) and recrystallisation temperature (RCT), by which the operation temperature window of the tungsten structure is restricted. This temperature window and the ductility can be increased by adding fine oxide particles (ODS tungsten), with WL10 being regarded the most suitable option for the divertor design at present. The DBTT and RCT of a future W alloy under fusion neutron irradiation are estimated to be around 600°C and 1300°C, respectively, which were taken as the “design window” range in the following design work.

After detailed optimisations of both designs as well as screening tests in St. Petersburg, the HEMJ has been selected as reference solution and the HEMS as backup solution. This selection was also based on the fact that the HEMJ cooling finger unit can be manufactured

more easily. The main design principle common to both options (Fig. 1) is the use of hexagonal tiles of tungsten with a width over flats of 18 mm as a thermal shield and sacrificial layer (5 mm thick) which is brazed to a finger-like (thimble) structure made of a tungsten alloy, such as W-1%La<sub>2</sub>O<sub>3</sub> (WL10), having a size of Ø15 x 1.03 mm, thus forming a cooling finger unit. For reasons of reliability, the sacrificial tungsten tiles are separate components braced to the thimble in order to stop crack growth at the joining interface. The cooling finger units are fixed to the front plate (transition zone) of the supporting structure made of ODS steel (e.g. an advanced ODS EUROFER or a ferritic version of it) by means of e.g. brazing and/or a mechanical interlock. The divertor is cooled with helium at 10 MPa and inlet/outlet temperatures of 600°/700 °C.

For the HEMJ design in particular [2], a cartridge carrying the jet holes is placed concentrically inside the thimble, the number, size, and arrangement of the jet holes as well as the jet-to-wall distance (i.e. gap clearance between the cartridge and the thimble bottom wall) being decisive parameters that need to be further optimised. A conservative layout for a reference load case of 10 MW/m<sup>2</sup> leads to the nominal set of geometry: 27 holes (Ø 0.6 mm), jet-to-wall spacing 1.2 mm. In this case, a relatively large hole diameter was chosen at the expense of a reduced cooling capacity to avoid obstruction problems that may possibly be caused by contaminated helium gas.

The HEMS design employs a slot array made of tungsten as heat transfer promoter which is integrated at the bottom of the thimble by means of brazing to enhance the cooling surface and, hence, increase the heat transfer capacity. The thimble and flow promoter inlay can be manufactured in one piece, if a suitable processing method is available so that the brazing joint between them can be omitted.

CFD analyses (parameter study)

The computational fluid dynamics (CFD) analyses were performed with the FLUENT code focussing on the HEMJ design variants. In the calculations, the RNG turbulence model was applied. A reasonably higher mesh density in the near-wall turbulence region has been taken into account, leading to a number of about 2 million meshes for a 1/6 model of the divertor finger. An internal heating power of 17 MW/m<sup>3</sup> was assumed. The connection between the tungsten tile and WL10 thimble is postulated to be a perfect surface transition without any thermal resistance. The thermophysical properties of W and WL10 have been taken from the ITER handbook [3]. Helium coolant gas was considered as ideal gas. The surface of the flow channel wall is assumed to be hydraulically smooth. The nominal flow rate [2] was determined to be 6.8 g/s for one divertor finger.

Important parameters are the jet diameter D and the jet-to-wall distance H. A set of such parameter variations (beginning with J1-) is illustrated in Table 1. For the first category J1-a to J1-c the jet-to-wall distance H is varied between 0.6 and 1.2 mm, while keeping the jet diameter constant at 0.6 mm, a value that was reasonably chosen to be large to avoid the obstruction problem. The number of holes in this case amounts to 25, symmetrically distributed over three different pitch circles, with a centre hole of Ø1 mm as an

Table 1: HEMJ design parameters.

	Jet hole diameter D (mm)	Jet-to-wall distance H (mm)
J1-a	0.6	1.2
J1-b	0.6	0.6
J1-c	0.6	0.9
J1-c0.4	0.4	0.9
J1-d	0.7	0.9
J1-e	0.85	0.9



exception. In the second category J1-c to J1-e the jet diameter is varied from 0.6 to 0.85 mm at a constant jet-to-wall distance H of 0.9 mm. In the last category J1-f to J1-h the total flow cross section of the jet holes is kept constant at 10.4 mm<sup>2</sup>, the same level as J1-d.

The calculation results show that the above-mentioned reference HEMJ geometry J1-a can withstand 10 MW/m<sup>2</sup> as specified (Fig. 2). For a nominal mass flow rate of a cooling finger of 6.8 g/s, a value that allows to keep the He outlet temperature below the maximum permissible temperature of the steel structure of about 700°C, the maximum temperatures of the tungsten tile and the thimble (Fig. 3) amount to 1711°C (<~2500°C permiss.) and 1164°C (<1300°C permiss.), respectively. The mean HTC value amounts to 32 kW/m<sup>2</sup>K. The maximum He jet velocity is calculated to be about 260 m/s and the resulting pressure loss amounts to about 0.135 MPa. The corresponding pumping power is estimated to be 57 MW for the whole divertor, which corresponds to 9.8% of the total divertor power. At the same mass flow rate, the maximum thimble temperature could even be kept below the temperature limit for the W thimble of 1300°C under a heat flux of >12 MW/m<sup>2</sup>. A smaller mass flow rate of <5 g/s would also fulfil this boundary condition at 10 MW/m<sup>2</sup> with a lower pressure loss, if the operation temperature window of the steel structure material could be enhanced.

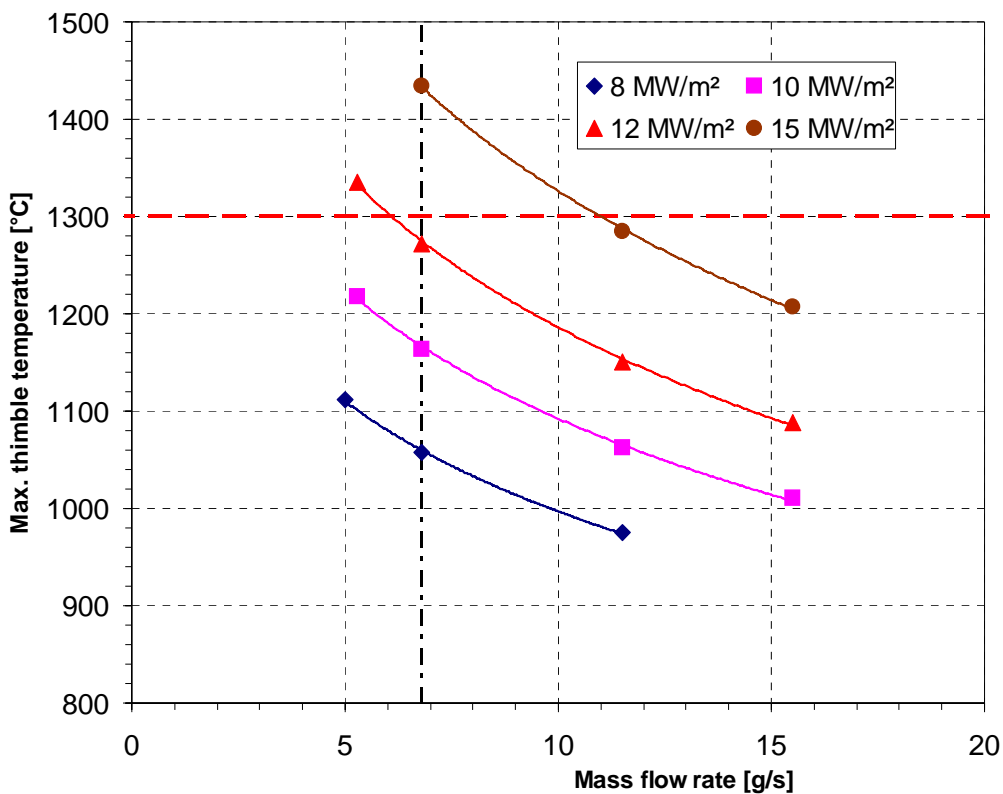


Fig. 2: HEMJ: Maximum thimble temperature as a function of mass flow rate and surface heat load for J1-a version.

The maximum thimble temperatures for the HEMJ versions J1-a through J1-e as a function of mass flow rate at a heat load of 10 MW/m<sup>2</sup> are illustrated in Fig. 4. It can be seen clearly that the larger the jet hole size is (e.g. J1-e versus J1-a), the higher is the maximum thimble temperature reached. In any case, the divertor performance of 10 MW/m<sup>2</sup> defined could be achieved at a nominal mass flow rate of 6.8 g/s with any HEMJ option, even with the weakest option J1-e, the pressure loss of which was smaller than that of J1-a by a factor of about 3.8. With an extremely small hole size that is reduced from 0.6 to 0.4 mm (J1c-0.4) the pressure loss will increase dramatically by a factor of about 4, although the maximum thimble temperature is significantly decreased by about 100 K.

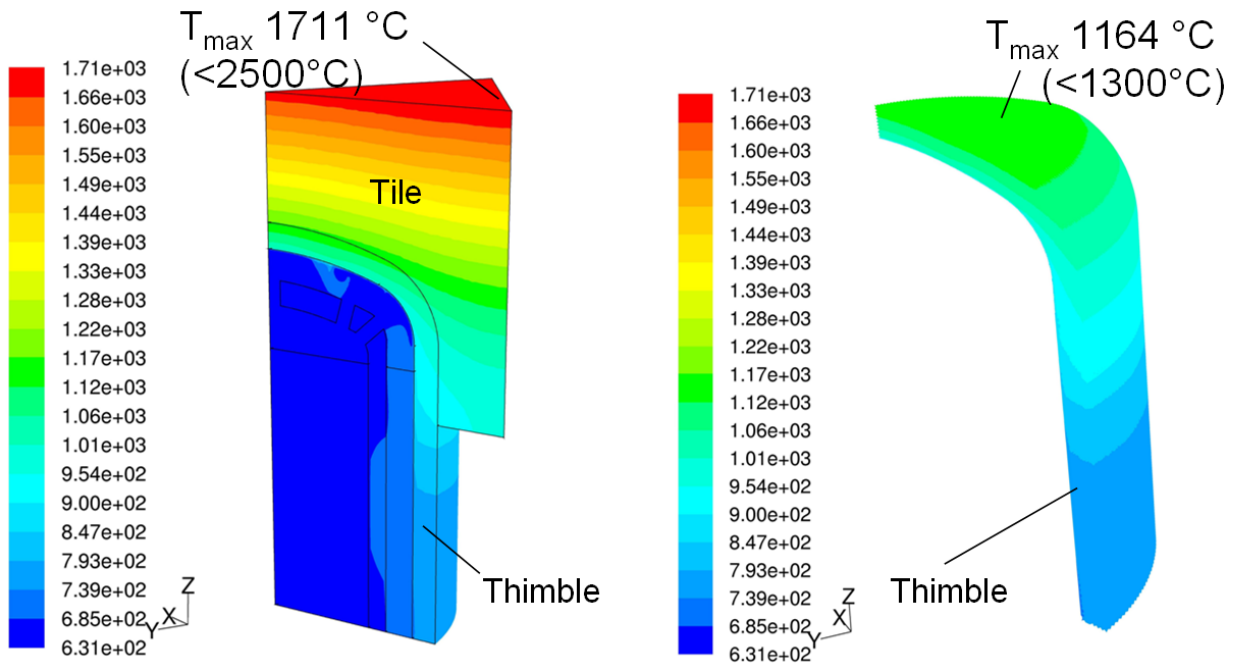


Fig. 3: Temperature distribution for the HEMJ reference case J1-a: heat load 10 MW/m<sup>2</sup>, mass flow 6.8 g/s, inlet pressure 10 MPa.

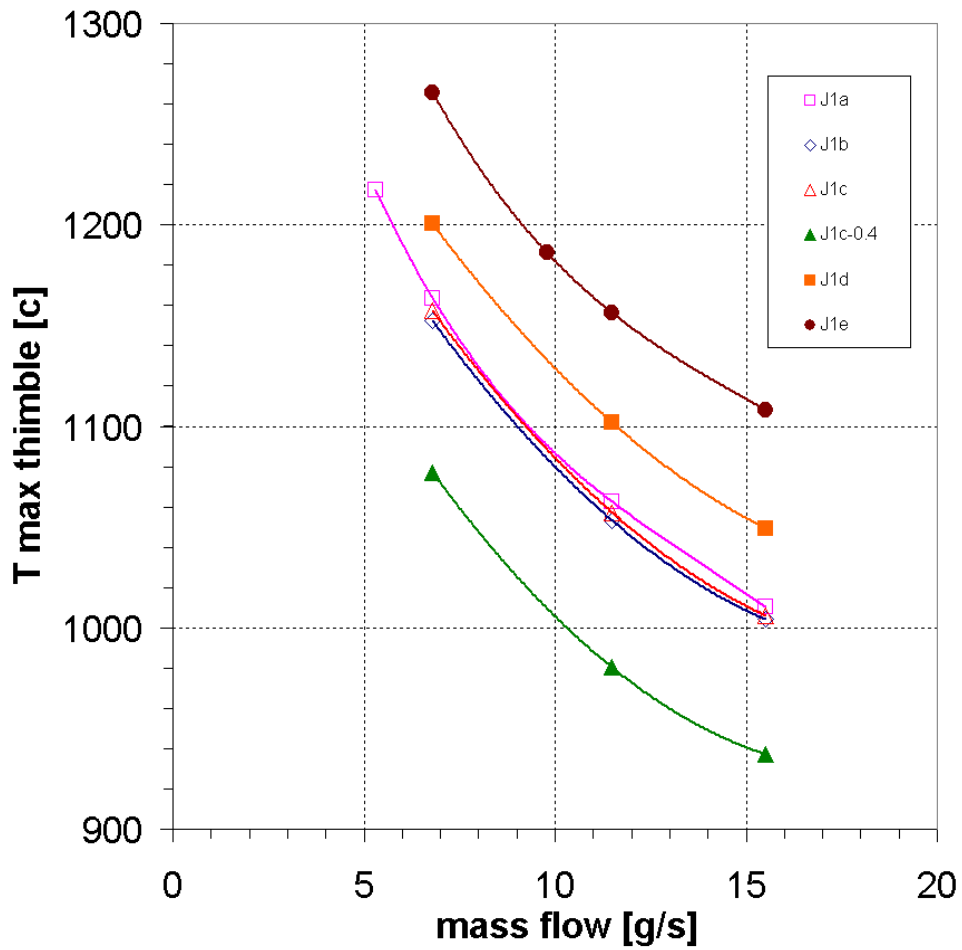


Fig. 4: Maximum thimble temperature for all versions of HEMJ as a function of mass flow rate at a heat load of 10 MW/m<sup>2</sup>.

## Summary of the GPF results

Prior to the HHF experiments in a helium loop at Efremov, which are now ready to start, thermo-hydraulic tests for design screening were carried out at the Efremov's gas puffing facility (GPF) [4] in 2005. The GPF experiments are based on a reversed heat flux method, i.e. hot helium (inlet/outlet temp. of 650°C/600-550°C) was pumped through the divertor mock-ups to estimate their thermohydraulic efficiency (pressure loss and HTC) when cooled by 100°C water coolant at the top of the thimble. The GPF experimental results (Fig. 5) show that the maximum performance of about 12.5 MW/m<sup>2</sup> was obtained for the HEMJ reference option and about 11 MW/m<sup>2</sup> for the HEMS design, respectively. The results for the HEMJ variants J-1a and J-1e agree well with the predicted values obtained from the CFD simulation calculations above.

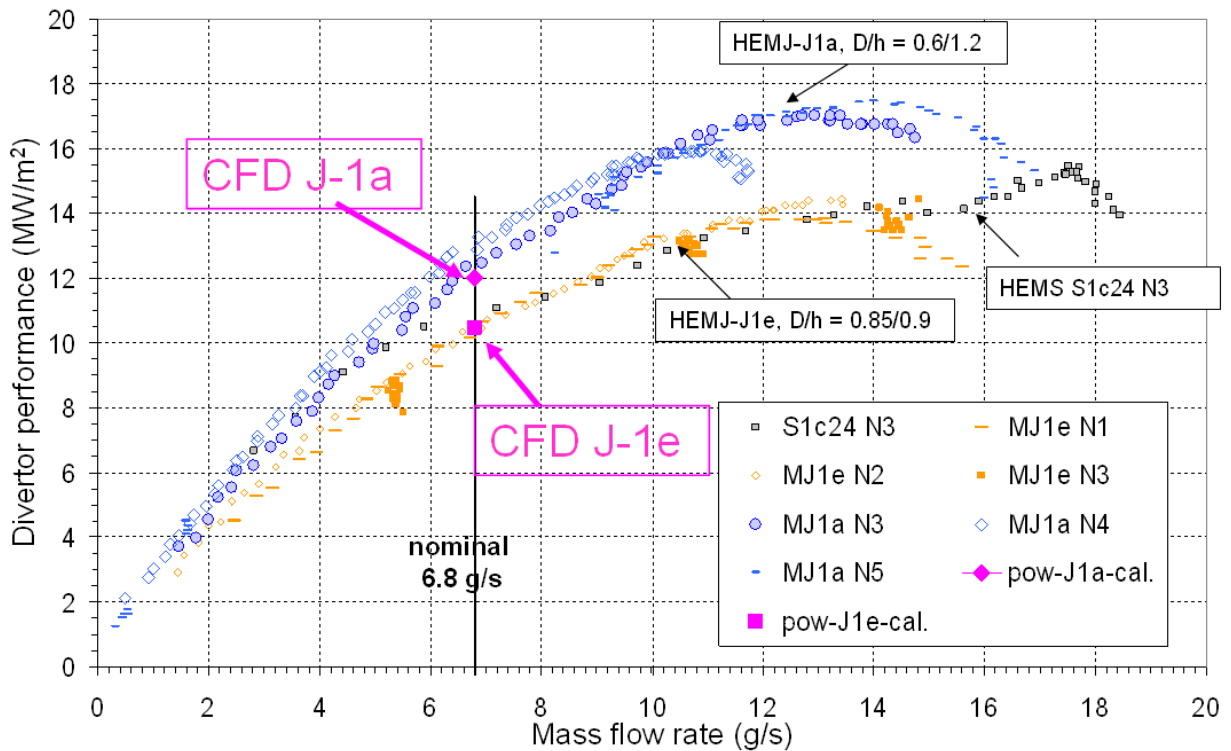


Fig. 5: Divertor performance of HEMJ variants J-1a, J-1e and one HEMS variant determined from the GPF experiments [4].

## The HEBLO experiments for CFD code validation

The HEBLO experiments for the HEMS design were carried out successfully. Post-calculations and evaluations are underway. The HEMJ mock-up has been integrated in the test section and connected to the HEBLO loop (Fig. 6). The whole hydraulic circuit and all equipment have been pre-tested successfully. Further experiments will start soon.

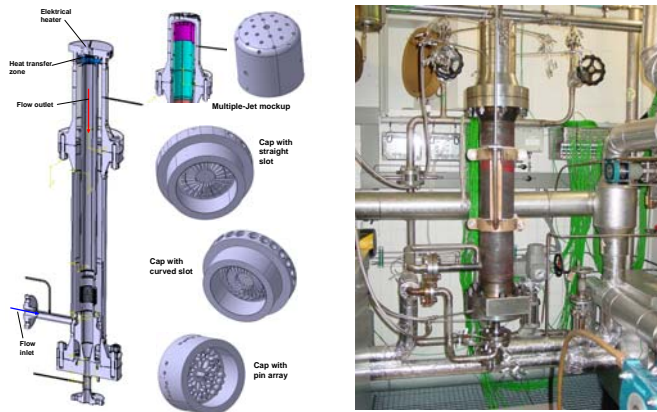


Fig. 6: The HEMJ test section mounted into HEBLO.

## Progress of joining technology



Fig. 7: W-W joint with real curved surface successfully tested with STEMET 1311® filler metal.

A series of technological breakthroughs [5] are necessary in order to achieve a functioning design. This concerns e.g. the joining technology for W-W and/or W-steel components as well as the fabrication technology for W structures and components. R&D in these technology areas have been carried out in cooperation with the Efremov Institute, St. Petersburg, Russia. The mock-up tests with W/W joints produced with STEMET 1311® filler metal (Ni-base, 16.0Co, 5.0Fe, 4.0Si, 4.0B, 0.4Cr,  $T_{br}$  1050°C)

have shown that these joints are reliable at temperatures in the joint of about 1200°C up to heat fluxes of 14 MW/m<sup>2</sup> (Fig. 7).

For W/steel joining, a first design of a transition piece (Fig. 8) with a Cu casting in the gap between W and steel (at 600°C, a vacuum-tight flexible seal) and an additional conical interlock was tested successfully. The first mock-up with a conic lock and WL10 thimble successfully survived 10 thermocycles between ~600°C and RT at the W-steel interface under an internal He pressure of 10 MPa. Based on these technological test results, a series of W 1-finger mock-ups have been manufactured for the EB tests in the TSEFEY facility at Efremov. The EB test results are expected to be reported in the first quarter of 2006.



Fig. 8: W-steel joint with conic lock and Cu casting successfully tested under thermocyclic and internal loadings.

## Progress of W structuring processes

The feasibility of the series fabrication of W and/or W alloy components required has not yet been demonstrated, since standard methods (e.g. milling) are not applicable to these materials due to their hardness and toughness. Two processing methods, namely, electrochemical milling (ECM) [6] and powder injection moulding (PIM) [7] are regarded promising, in particu-

lar in terms of mass production. First ECM results show that W parts produced by the ECM method have smooth surfaces without any surface damage (no microcracks), which is favourable for a reduction of peak stresses. The PIM process consists of many processing steps: feedstock compounding, injection moulding, debinding, and sintering. In the first PIM experiments with tungsten powder of 2  $\mu\text{m}$  particle size, first microstructured demonstrators, such as slot arrays and micro gear housings have been replicated. After sintering in a  $\text{H}_2/\text{Ar}$  atmosphere at  $\sim 2100^\circ\text{C}$ , a final density of  $\sim 95\%$  of the theoretical density was achieved with a carbon content of  $<0.003$  wt.%.

### Manufacturing of 1-finger mock-ups

Based on the knowledge gained from technological studies, 1-finger mock-ups to be tested in the helium loop & TSEFEY EB facility have been defined as follows:

#### Design:

- Reference: HEMJ / J-1a, 24 holes ( $D=0.6$  /  $h=1.2$ ), 1 centre hole ( $D=1\text{mm}$ )
- Backup: HEMS / S1-b,  $n = 24$ ,  $s = 0.3$  mm,  $h = 1.2$  mm

#### Materials:

- Tile: W, hexagonal SW=18mm (net 17.8mm), 5mm sacrificial thickness
- Thimble: WL10,  $D_a \times s = \text{Ø}15 \times 1.03$  mm
- Jet-cartridge: steel
- Structure: Eurofer

#### Joints:

- W-WL10: HT brazing, STEMET 1311®,  $T_{br} = 1050^\circ\text{C}$
- Transition WL10-steel: conic lock design with Cu interlayer

The manufacturing of the mock-ups consists of several steps (Fig. 9) with a final shaping of the tungsten tiles with and without castellation.

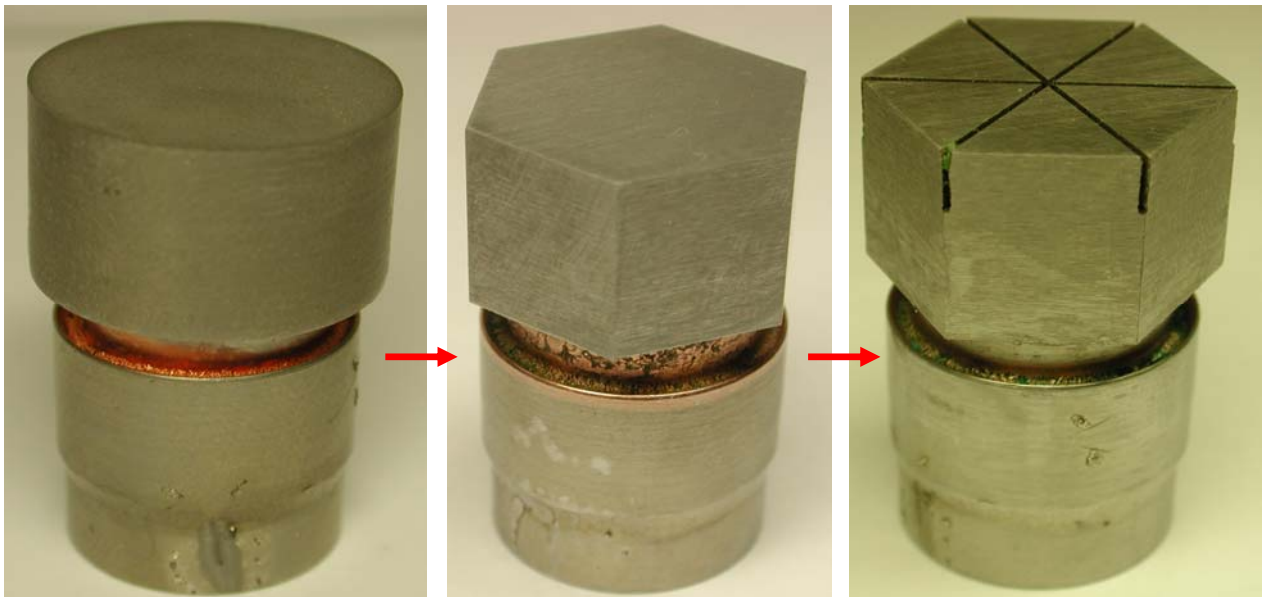


Fig. 9: 1-finger mock-up manufactured for the HHF tests.

## Conclusions and outlook

Work carried out in 2005 was aimed at technically investigating and manufacturing 1-finger divertor mock-ups for the HHF helium loop experiments at the Efremov Institute. Regarding the divertor conceptual design, HEMJ has been selected as reference solution and HEMS as backup solution, respectively. On this design basis as well as on the basis of the technological studies regarding e.g. the joining technology, the 1-finger mock-ups to be tested in the helium loop & TSEFEY EB facility have been defined and manufactured. The first stage of the helium loop will be completed soon, the TSEFEY electron beam facility has been installed. The first experimental outcomes can be expected in the first quarter of 2006. The next steps will focus on the completion of the 9-finger mock-ups and their tests in the second stage of the helium loop, which shall provide a sufficient mass flow rate.

### Staff:

J. Aktaa  
T. Chehtov  
S. Gordeev  
N. Holstein  
T. Ihli  
W. Krauss  
R. Kruessmann  
V. Piotter  
P. Norajitra  
V. Oberheide  
R. Ruprecht  
J. Weggen  
B. Zeep  
K. Zinn

### Literature:

- [1] P. Norajitra, R. Giniyatulin, T. Ihli, G. Janeschitz, P. Karditsas, W. Krauss, R. Kruessmann, V. Kuznetsov, D. Maisonnier, I. Mazul, C. Nardi, I. Ovchinnikov, S. Papastergiou, A. Pizzuto, P. Sardain, European Development of He-cooled Divertors for Fusion Power Plants, Nucl. Fusion 45 (2005) 1271-1276.
- [2] T. Ihli, R. Kruessmann, I. Ovchinnikov, P. Norajitra, V. Kuznetsov, R. Giniyatulin, An advanced He-cooled divertor concept, Fusion Engineering and Design 75-79 (2005) 371-375.
- [3] ITER Material Properties Handbook, S 74 MA 2, and G 74 MA 9 00-11-10 W 0.1, 2001.
- [4] I. Ovchinnikov, R. Giniyatulin, T. Ihli, G. Janeschitz, A. Komarov, R. Kruessmann, V. Kuznetsov, S. Mikhailov, P. Norajitra, V. Smirnov, "Numerical and experimental study of DEMO He-cooled divertor target mock-ups", 23rd SOFT, Venice, Italy, 20.-24.9.2004.
- [5] R. Giniyatulin, A. Gervash, W. Krauss, A. Makhankov, I. Mazul, P. Norajitra, "Study of technological and material aspects of He-cooled divertor for DEMO reactor", 23rd SOFT, Venice, Italy, 20.-24.9.2004.
- [6] W. Krauss, N. Holstein, J. Konys, I. Mazul, Investigation of fabrication methods regarding their impact on microstructure of W components to be used in a He-cooled divertor, Proceedings of the ISFNT-7, Tokyo, Japan, 22-27 May, 2005.
- [7] B. Zeep, S. Rath, T. Ihli, V. Piotter, R. Ruprecht, J. Haußelt, Powder injection molding of tungsten components for a He-cooled divertor, Proceedings of the 16th International Plansee Seminar, Reutte, Austria, 2005.

## TRP-002 DEMO Physics Studies

### TW5-TRP-002 D 2 Analysis of Total Radiation in Tokamak Reactor Scenarios

#### 1. Introduction

The aim of this task is to develop a modelling capability, based on a 2D plasma edge code (B2-EIRENE) and a 1.5D core transport code (ICPS), which allows the radiation fraction in tokamak reactor scenarios to be analyzed and characterized in terms of edge and core plasma parameters, in particular to quantify the core impurity contamination associated with a given level of radiation. The task is carried out with the integrated modelling as described in more detail in [1] and in a separate contribution to this Annual report [2]. Ongoing work for that task and also for the DEMO simulations is described in more detail in [3]. The task has just been active since the beginning of October 2005, so that results are still sparse and very preliminary.

#### 2. Core Plasma Modelling

The main thrust of the work carried out in the second part of the reporting period concerned modelling of DEMO in connection with an EFDA task agreement, using the model as developed for ITER simulation. Since this requires the addition of seeding with medium- to high-Z impurities to reduce the power entering the scrape-off layer, more detailed validation of neoclassical impurity accumulation becomes necessary. Accordingly, access to the ITER profile database has been established, and certain JET discharges have been chosen for more detailed examination, incorporating notably similar H-mode discharges with and without argon injection.

Examination of the database and first simulations of these discharges revealed anomalies in the data supplied to the database, unfortunately as regards the impurity and radiation profiles supplied to the database. This has been communicated to the scientist responsible for the data, and is presently being examined with a view to correcting the data. The validation therefore awaits the resolution of these discrepancies.

The geometric parameters chosen for the DEMO modelling task are similar to those of ITER as developed in the Conceptual Design Activity (1991) ( $B=5.7T$ ,  $R=8.1m$ ,  $a=2.8m$ ,  $\kappa=1.7$ ,

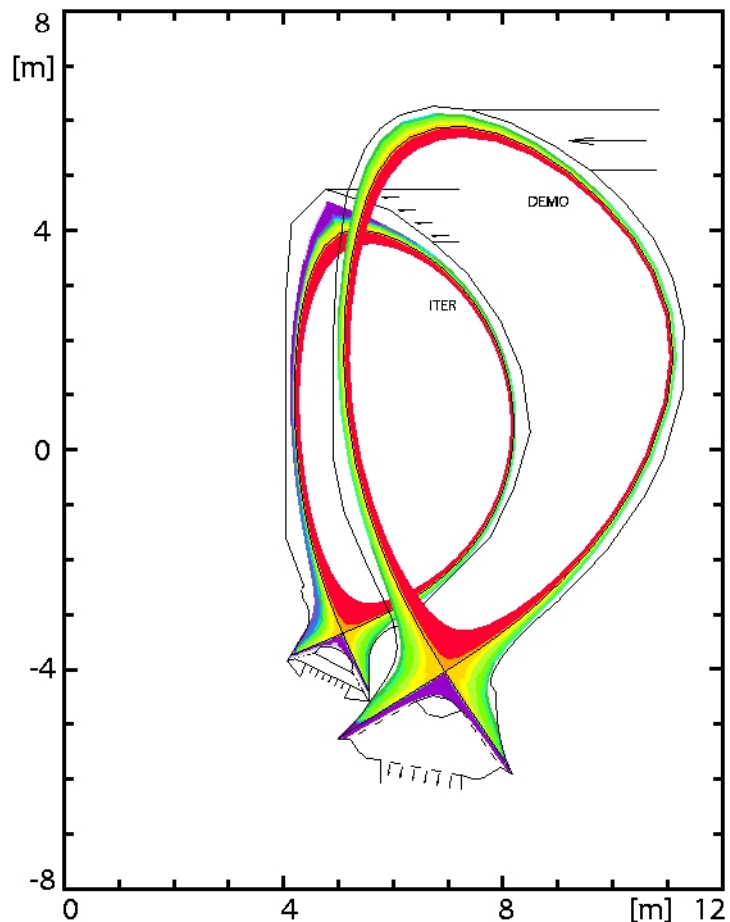


Fig. 1: Comparison of ITER and the larger prototypical DEMO geometry: Divertor and edge plasma is shown in colour.

$\delta=0.36$ ). Present modelling examines DEMO operation in ELMy H-mode with a  $q\sim 4$  ( $I=21$  MA) and a fusion power of  $\sim 3$  GW.

The transport model is as described in the separate contribution to this Annual Report [2], using MMM95 core transport. Pending the development of SOL scaling laws for DEMO parameters from 2-D modelling, the same scaling laws as for ITER are used to give the boundary conditions. This presumably ensures the correct functional dependence between the various quantities, while the numerical values remain to be determined.

First preliminary results indicate stable ignited operation with a pedestal temperature of  $\sim 4$  keV, requiring an average density of  $1.4 \times 10^{20} \text{ m}^{-3}$  for a fusion power of 3 GW. In the absence of impurity seeding, the power into the scrape-off layer is 450-500 MW, which can be reduced to a probably acceptable level of  $\sim 250$  MW by seeding with  $\sim 0.25\%$  argon or  $0.1\%$  iron. For these calculations, the impurity concentration is taken constant radially. After validation of the impurity accumulation model, neoclassical profiles of impurities will also be investigated. All values are subject to revision once the separatrix scaling laws for DEMO parameters are established.

## 2. Divertor Plasma Modelling

Using the geometry of Figure 1 and the model described in [1], [2], [3] (see in particular [2]), 2D modelling of the DEMO plasma has started. First results are being obtained with a model incorporating a full carbon wall and, for the moment, a simple neutral model, without the neutral-neutral collisions and molecular dynamics, particularly the ion conversion process (MAR) and elastic collisions of molecules with the plasma ions described in [2].

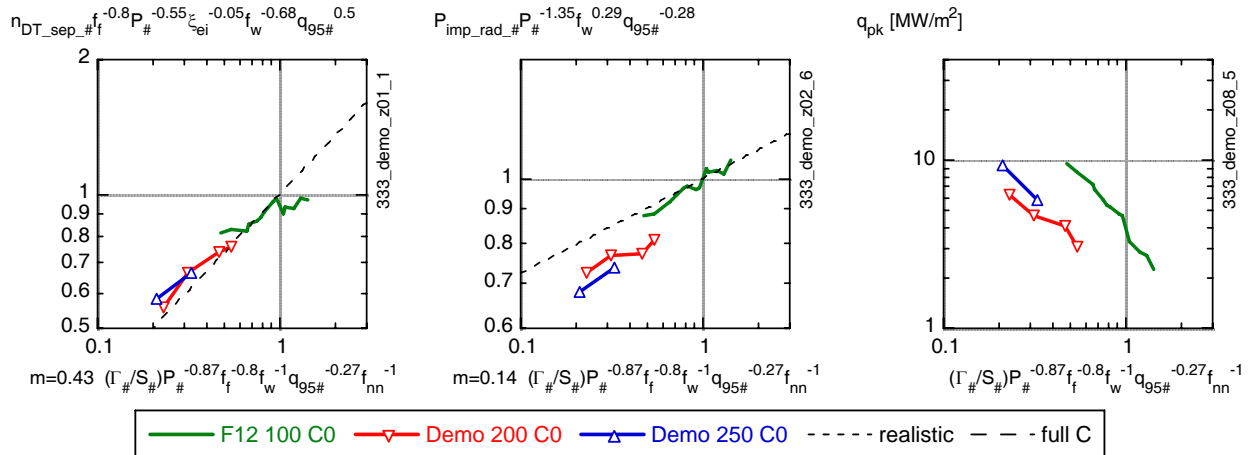


Fig. 2: a) Average DT density at the separatrix, b) Normalised impurity radiation c) peak power loading of the outer divertor vs. normalised divertor neutral pressure for ITER with 100 MW SOL power and for DEMO with 200 and 250 MW SOL power. See [1], [2] for definitions, normalisation and scalings.

In the preliminary runs established so far, most parameters fall near the ITER scaling in terms of the normalised divertor neutral pressure (see Fig. 2a for DT density at the separatrix and Fig. 2b for impurity radiation). The normalised peak power at the divertor plate is considerably lower than that of ITER. The absolute peak power at the divertor plate is shown in Fig.2c. As shown in previous publications (see references in [1], [2]), full detachment of the ITER inner divertor leg occurs at a normalised divertor neutral pressure of 1 (i.e. horizontal scale in Fig. 2 is 1). Although not shown here, there are preliminary indications that the normalised pressure for detachment for the inner divertor in DEMO has a lower value, about 0.5. If confirmed, this would mean that, at the same detachment state (normalised pressure 0.5 for DEMO and 1 for ITER), for the simplified model used here (full carbon wall, incomplete



neutral model), the peak power loading of the divertor plate in DEMO at 200-250 MW would be similar to that in ITER at 100 MW. This conclusion needs to be confirmed by further modelling, the point of detachment of the inner divertor needs to be confirmed, further power scans will be undertaken and the full neutral model and a more complete wall model will be applied.

## 5. Perspectives

The task has just started. Further work is indicated in the two sections above.

### Staff:

H. D. Pacher (INRS-EMT, Varennes, Québec, Canada)

G. W. Pacher (Hydro-Québec, Varennes, Québec, Canada)

A. S. Kukushkin (ITER International Team)

G. Janeschitz

I. Landman

S. Pestchanyi - with the collaboration of G. Pereverzev (IPP Garching).

### Literature:

- [1] Pacher H.D., Pacher G.W., in collaboration with ITER IT Garching, FZ Karlsruhe, Max-Planck-Institut für Plasmaphysik Garching, EFDA CSU Garching, "Divertor and core plasma modelling for ITER - Final Report June 2005", INRS Energie, Mat. et Télécom. Report, 2004, INRS-EMT-021-0605, June, 2005
- [2] Pacher H.D., Pacher G.W., in collaboration with ITER IT Garching, FZ Karlsruhe, Max-Planck-Institut für Plasmaphysik Garching, EFDA CSU Garching, "Divertor and core plasma modelling for ITER - Intermediate Report December 2005", INRS Energie, Mat. et Télécom. Report, INRS-EMT-025-1205, December, 2005, in preparation
- [3] Pacher H.D., Pacher G.W., "Divertor and Core Plasma Modelling for ITER", this Annual Report (Physics Section)

## TRP-009 He-cooled Divertor Test Module for ITER

### TW5-TRP-009 D 2 Testing suitable HEMS/HEMJ Prototypes in ITER

The intermediate-term goal of the He-cooled divertor development [1] is the completion of a test divertor module (TDM) which is envisaged to be tested in ITER from 2020 (Fig. 1). The scope of the TDM program includes the complete TDM design, further technological investigations as well as the HHF experiments for bigger parts of the divertor target in a larger helium loop to be built in FZK (i.e. HELOKA).

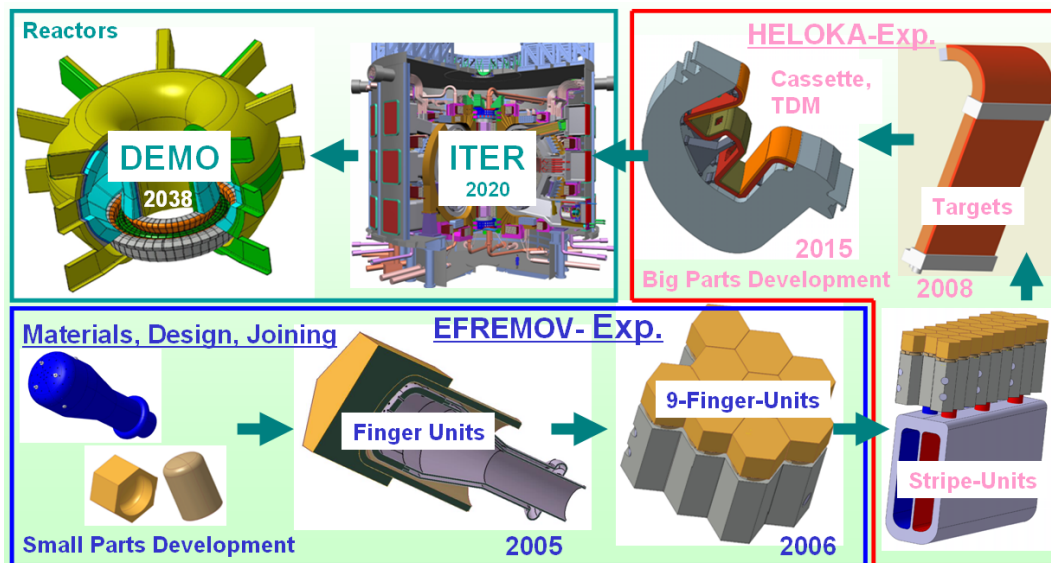


Fig. 1: Roadmap of the He-cooled divertor development.

Preparatory work has started for assessing the CATIA (version 4) computer model of an ITER divertor cassette (Fig. 2) regarding the cooling routes and the file conversion to CATIA version 5. The further step for the upcoming year shall be an assessment of the possibility of performing such an experiment with a helium-cooled test divertor module in ITER, i.e. the thermohydraulic assessment of a piping scheme and of the size of a helium cooling plant as well as checking whether the space available is sufficient and the experiment is compatible with ITER operation.

#### Staff:

R. Kruessmann  
P. Norajitra  
V. Oberheide  
R. Ruprecht

#### Literature:

- [1] P. Norajitra, R. Giniyatulin, T. Ihli, G. Janeschitz, P. Karditsas, W. Krauss, R. Kruessmann, V. Kuznetsov, D. Maisonnier, I. Mazul, C. Nardi, I. Ovchinnikov, S. Papastergiou, A. Pizzuto, P. Sardain, European Development of He-cooled Divertors for Fusion Power Plants, Nucl. Fusion 45 (2005) 1271-1276.

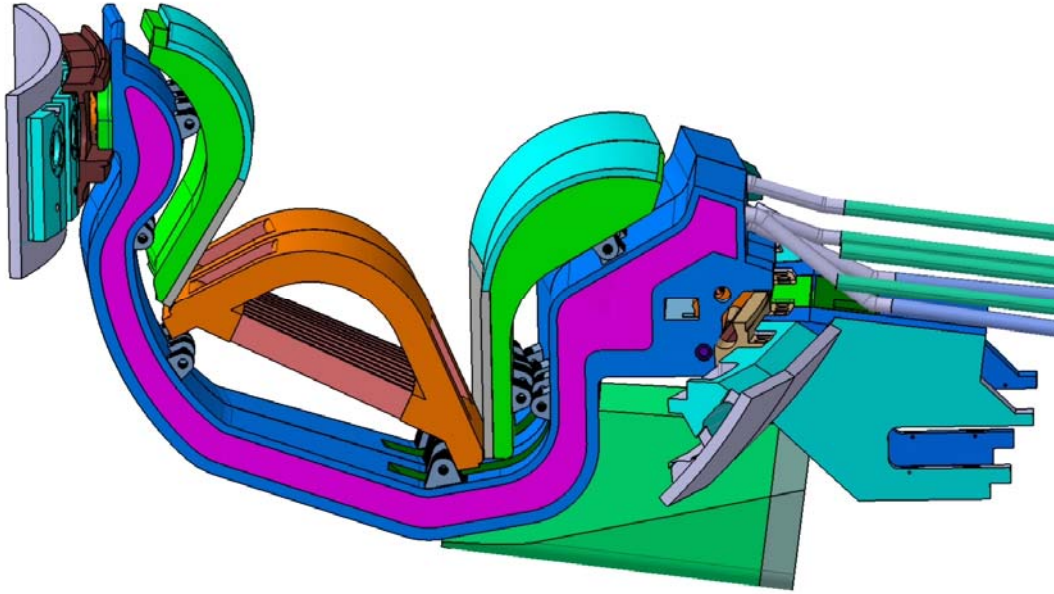


Fig. 2: ITER divertor cassette.



## **Tritium Inventory Control**



## **TW3-TI-VP 31**

### **High Temperature Regeneration Tests of the ITER Model Torus Cryopump**

#### **Task Objective**

The regeneration of the cryopumps is a key issue for the tritium inventory control for ITER [1]. To stay within the inventory limits, a multi-staged regeneration approach will be taken, comprising the regular regeneration stage at 100 K to release the hydrogen isotopes themselves, a second stage at ambient temperatures to release air-likes and light hydrocarbons, and a high temperature reactivation stage at 450-470 K to release any strongly sorbed substances such as water and heavy hydrocarbons. Especially the latter substances have a strong potential to build-up a high semi permanent tritium inventory in the cryopumps by isotope exchange. Although it could be shown that there will not result a significant poisoning effect from accumulated impurities (see tasks GB8-VP1 and TW1-TTF-VP13), from inventory limitation point of view it is essential to have an effective regeneration procedure available. The objective of this task was therefore to identify the temperature levels needed in order to release the accumulated impurities.

#### **Status**

Within the present task, representative species which are known to be difficult to regenerate, such as water, light and heavy hydrocarbons, aromatics and alcohols, were investigated quantitatively in the TIMO facility [2]. This was done in parallel to the water tracer substances programme (task TW1-TTF-VP13). The release pattern of these species was monitored by high resolution quadrupole mass spectrometry as reference device, in many cases in parallel with a GC-MS. Each reactivation test started from ambient regeneration, with deuterium from the preceding pumping test filling the closed pump volume to about 70 mbar. From this starting point, the temperature of the cryopanel system was increased in steps of about 30 K, and the gas composition was analysed. After having reached 470 K at all inner pump parts, the pressure was reduced by means of the forepumping system down to  $10^{-3}$  mbar in two steps with corresponding gas analysis to assess the effect of pressure reduction on gas release.

The experimental programme is finished, but the gas analysis log files still have to be evaluated. However, it can already be claimed that water is significantly released at temperatures of about 100 °C, below the maximum ones of 450 K. Even after very high amounts of sorbed heavy hydrocarbons, the regeneration at 450 K looks to be very efficient.

#### Staff:

##### Chr. Day

A. Edinger

H. Haas

J. Weinhold

D. Zimmerlin

#### Literature:

[1] Chr. Day, A. Antipenkov, I.R. Cristescu, M. Dremel, G. Federici, H. Haas, V. Hauer, A. Mack, D.K. Murdoch, M. Wykes, Hydrogen inventories in the vacuum pumping systems of ITER, ISFNT-7, Tokyo, Japan, May 2005, accepted for publication in *Fusion Engineering and Design*.

[2] H. Haas, C. Caldwell-Nichols, Chr. Day, A. Mack, and D.K. Murdoch, Study of poisoning effects with the ITER model pump during relevant operation cycles, ISFNT-7, Tokyo, Japan, May 2005.

## **EFDA/02-1019**

### **Detailed Design of a Water Detritiation Facility for JET**

The Water Detritiation System (WDS) for JET is based on the Combined Electrolysis Catalytic Exchange (CECE) process and is envisaged to work in combination with a new Cryogenic Distillation (CD) column with the aim to recover tritium contained in the processed tritiated water.

The main design requirements of JET-WDS are:

- To process 10 tons of tritiated water with  $\sim 1\text{Ci}\cdot\text{kg}^{-1}$  during one operation campaign of 2-3 months;
- To achieve a decontamination factor of  $10^4$  along the stripping section of the LPCE column;
- To deliver a tritium content in the bottom product of the CD column in the range of 0.5-1% atomic ratio to allow further separation by the existing gas chromatography (GC) or CD systems of JET-AGHS.

The preliminary evaluation of the JET-WDS process options has showed that any increase of the deuterium content in the feeding water affects the required lengths of the LPCE column and the composition of the feed stream into the cryogenic distillation column. Therefore, JET sampled twelve drums with tritiated water and approximately 60 ml from each have been sent to TLK to measure the deuterium content. The device used for these measurements was an FT-IR, calibrated for deuterium content in water in the range of 0.1% HDO up to 2% HDO in mixture with H<sub>2</sub>O. The deuterium content was found to be between 0.3-0.9% HDO.

The compilation of the design input data and an overall process flow diagram (PFD) with flow sheets giving detailed information of the flow rates, physical conditions, and chemical and isotopic compositions for each main stream between the various components have been completed.

In addition, the evaluation of process options for JET WDS has been completed and the HAZOP study Level 2 was undertaken during a meeting with the representatives from JET and TLK. The use of solid polymer membrane (SPM) electrolyser has been agreed upon in the reference design.

The main components of the JET WDS are described below.

#### **Front end and water purification system**

The tritiated water at JET is stored in drums of 205 liters. It is desirable to have a constant tritium concentration in the feeding water of the WDS during one campaign, therefore a feeding vessel was envisaged to be used. Before being fed into the LPCE column, the tritiated water has to be purified to avoid contamination of the catalyst/packing mixture. The purification system consists of two units working alternatively. The purification system was chosen according to the chemical analysis of tritiated water provided by JET.

#### **LPCE process**

The LPCE columns aim at transferring tritium and deuterium from the gas phase to the liquid phase in the counter current mode. The most efficient transfer is achieved by employing three phases in the process: gas phase, vapour phase and liquid phase. For this multiphase system, deuterium and tritium transfer occurs in the following two steps:



- A chemical reaction between the gas phase and the vapour phase takes place on a hydrophobic catalyst having as a result a higher concentration of deuterium and tritium in the vapour phase;
- Between vapour phase and liquid phase an equilibration takes place on packing separation as in the distillation process having as result an enrichment of heavier isotopes in the liquid phase.

Several combinations of catalyst-packing have been investigated at TLK. For the JET LPCE column, a combination based on SULZER structured packing and a hydrophobic catalyst developed at TLK is proposed to be used in a trickle bed exchange column.

In order to avoid hydrogen and tritium spilling from the LPCE columns, the flange connections between two sections of the LPCE columns have second containments, which allows both to detect and localize the leaks from the flanges and also to drain leaked water and to purge the area with nitrogen before dismantling the connections.

The LPCE columns have double walls, which allow thermal stability of the process by circulating heated water at the temperature of the streams within the column. Additionally, the second wall can be considered as a second barrier against tritium migration from the LPCE process.

### **Electrolyser**

In a WDS facility based on the CECE process, the electrolysis unit contains almost the entire inventory of tritium involved in the separation process. Usually the water hold-up of the electrolysis unit based on solid polymer electrolyte is three to five times larger than the water hold-up of the LPCE column. In the case of a KOH electrolyte, the water hold-up in the electrolysis unit is at least twenty five times larger than water hold-up of the LPCE column. The enrichment factor, defined as the atomic ratio between the tritium content in the water inside the electrolysis cell and the tritium content in the water fed into the electrolysis unit, together with the water hold-up in the electrolyser determine the tritium inventory contained in the electrolysis unit.

Similarly to the ITER design, for the JET-WDS an electrolyser based on solid polymer electrolyte has been chosen. This type was preferred instead of the classical one using KOH electrolyte due to the following main reasons:

- It avoids the  $K^+$  ions transportation into the packing and catalyst material that fills the catalytic exchange column.
- It has a lower inventory of tritiated water.
- There is no generation of additional tritiated waste (KOH electrolyte).

### **Oxygen and nitrogen purification system**

The oxygen purification system is needed to remove the hydrogen and tritiated water vapours from both oxygen and various nitrogen streams used to purge different subsystems of the WDS. The oxygen stream from the electrolysis cell is sent to a condenser, where it is cooled down to  $\sim 5$  °C and the condensed tritiated water vapours are collected. Due to the fact that both the oxygen stream and the nitrogen stream coming from the outer containment of the electrolyser contain hydrogen, approximately in the range 1000-5000 ppm  $H_2/H_2+O_2+N_2$ , the oxygen stripping column is equipped at the bottom with a catalyst bed with the aim to convert to water the hydrogen contained in the oxygen-nitrogen stream. Essentially tritium free oxygen-nitrogen is released at the top of the oxygen stripping column

and sent to stack. The stripping column is filled with structured packing of high efficiency, EX Sulzer type.

### Permeator

A combination between CECE and CD processes is necessary because the tritium content in the deuterium-hydrogen mixture from the electrolysis cell is only of maximum tens of Curies and cannot be recovered at this level by the existing GC from AGHS at JET. In order to feed the tritiated mixture deuterium-hydrogen supplied by the electrolyser a purification system is compulsory in front of the CD column. The permeation method is considered most suitable in order to achieve a very low oxygen concentration in the hydrogen-deuterium-tritium stream to be sent to the CD column.

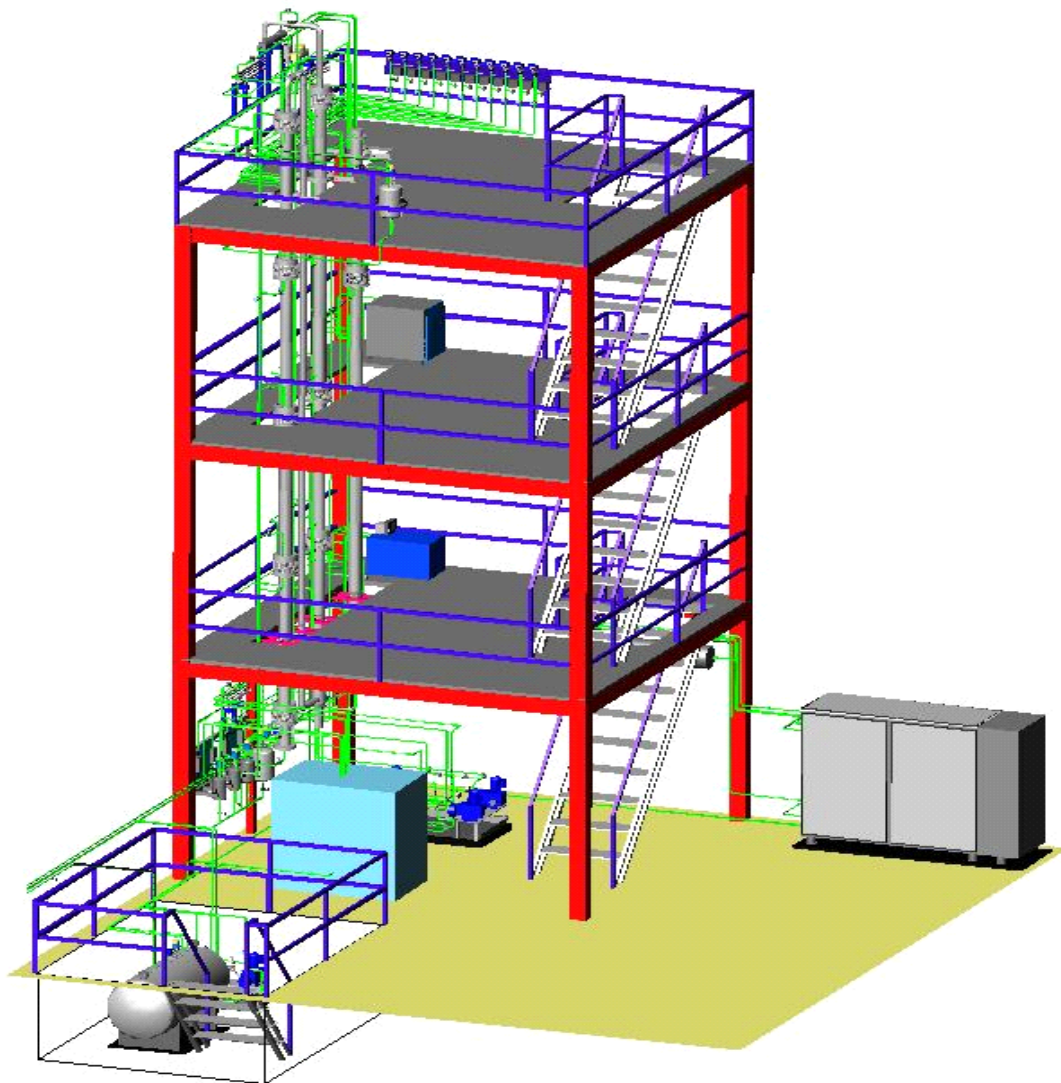


Fig. 1: 3D layout of WDS for JET.

The WDS will be accommodated in a new building, as an extension of the Active Gas Handling Building from JET. The following main groups of components have to be properly combined to minimize the required area for installation:

- The LPCE and oxygen/nitrogen stripping columns;
- The electrolyser;
- Storage vessel, pumps and purification units.

Based on the size established for each component during the design, the 3D layout of JET-WDS has been produced and is shown in Figure 1.

The piping and instrumentation diagrams (P&ID's), the mechanical design of all components of the facility, the general layout drawings showing equipment, piping and support location have been produced.

The cost estimation for JET WDS has been realized and the following items have been considered:

- Process and Mechanical Engineering
- Components
- Valves
- Piping
- Steel Construction, Miscellaneous
- Electric Equipment and Process Control System
- Installation
- Start-Up

The overall cost estimation of JET WDS is shown in Figure 2.

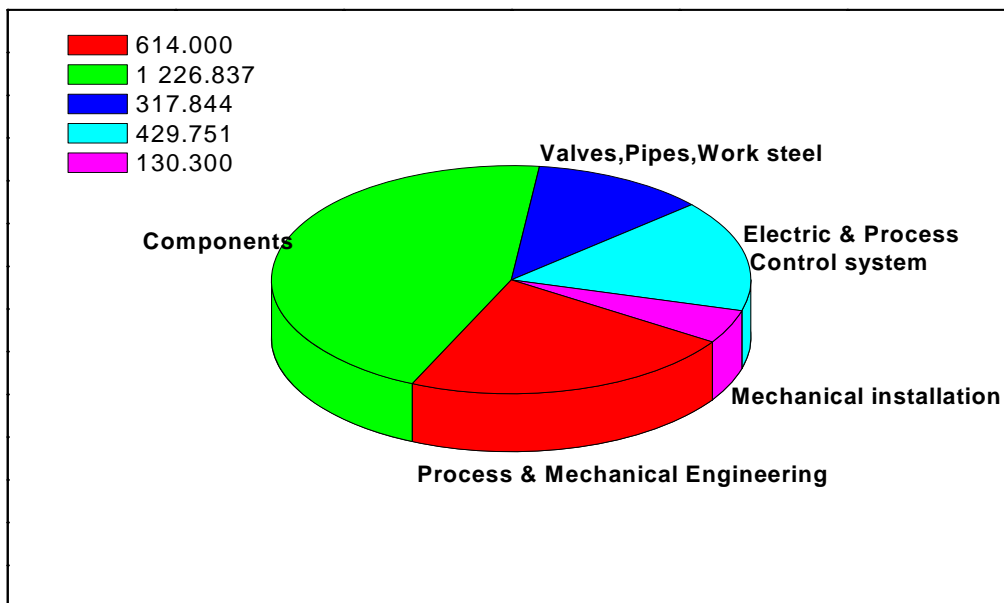


Fig. 2: Overall cost estimation of JET WDS.

**Staff:**

- I. Cristescu
- S. Welte
- W. Wurster
- A. Lazar, MEC Romania- EURATOM association
- M. Mustata, MEC Romania- EURATOM association



## **Design Support and Procurement**



## **EFDA/03-1100**

### **Detailed Engineering and Manufacturing Studies of the ITER Magnet System: Toroidal Field (TF) and Poloidal Field (PF) Coil Windings and Cold Test Facility**

#### **Background and Objectives**

1) Some critical areas of the TF winding need additional attention with respect to functionality and critical parameters. Especially He cooling inlets, interpancake joints, insulation details, terminal areas and instrumentation are reviewed by other contractors in the frame of this task. Forschungszentrum Karlsruhe will give special support by addressing issues in the field of low temperature high / voltage insulation and instrumentation.

2) In the actual ITER planning a cold test of finalized ITER coils is actually not foreseen. On the other hand large parts of the magnet community see this as not acceptable, pointing on the experience of other large projects (e.g. LHC or W7-X). As a consequence this task part shall evaluate in collaboration with CEA the boundary conditions and details of the need for a cold test facility. Possible scenarios for testing (prototype coil only, a few coils only, all coils, etc.) are evaluated including:

- Development of a cold test procedure and scenario to reach testing conditions relevant to the operation of the TF coils in the ITER machine.
- Preparation of the outline for the design of the cold test facility, including auxiliary equipment such as cryoplant and power supplies.
- A comparison of estimated costs of various testing scenarios is given (including the evaluation of re-using existing facilities or parts of them, as well as building a new facility on-site or off-site).

3) The manufacturing of the ITER radial plates (RP) is one of the most critical parts in the TF coil manufacturing with respect to technologic challenge and schedule. Therefore critical details will be reviewed in collaboration with industry (BNN) covering a manufacturing assessment of the basic sections of the TF radial plates, built as hot rolled plates or forged and cast sections, and the construction of the case sub-assemblies and the complete radial plates, including

- a cost comparison between different options.
- assessment of machining and manufacturing tolerances of case halves and radial plates.
- evaluation of non-destructive testing techniques for the construction and closure welds of the case sections.
- review and production of QA documents and quality control procedures.
- licensing aspects, such as acceptability of castings and inspectability of one-sided closure welds by ultrasonic technique.

#### **Results**

1) Regarding support in the evaluation of critical areas of the TF winding mainly the benefit from an inner electrical screen of the winding insulation of the PF conductor was discussed and found to be questionable. If a good method is found to produce a complete coverage this may cause problems during impregnation. Without a complete coverage or with hollow spaces the inner screen will not give clear signals but may cause trouble.

Forschungszentrum Karlsruhe recommend to use no inner screen and to use the available space for a reliable insulation.

2) A final cold test of completed ITER TF coils was found to be essential to ensure a functioning in ITER and to avoid large additional costs and delay in case of a coil problem [1].

The cold test of a complete ITER TF coil at 4.5 K at a reduced coil current of about 30 kA is the minimum option that has to be considered to ensure the functionality of the ITER TF coils. This test scenario allows to detect high voltage, leak, joint, sensor and cooling failure before installation into the ITER machine and therefore to avoid enormous disassembly and re-installation work and as consequence large additional costs and delay. In addition the proposed cold test facility (Fig. 1) allows to proof the cooling circuit planned for ITER and will allow to train the ITER staff when the cold test facility is built on ITER site.

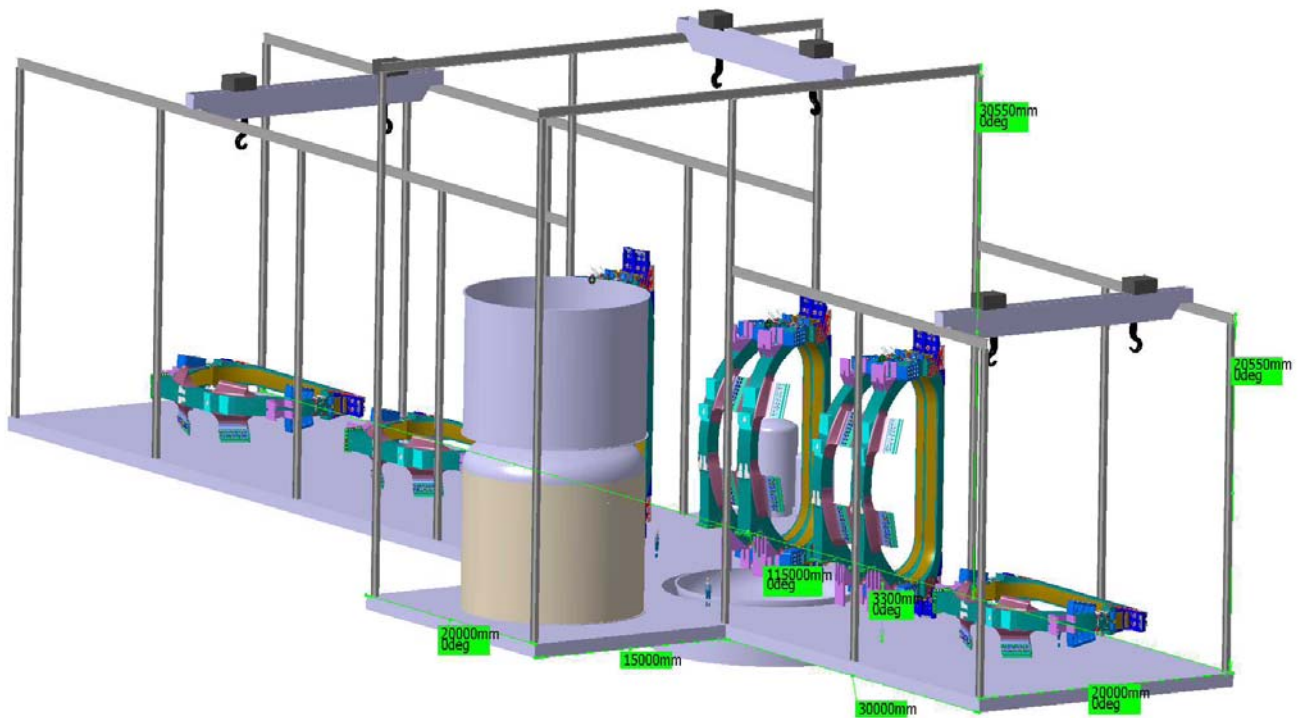


Fig. 1: Possible layout of a Cold Test Facility

The extension of the test to 68 kA would allow a comparison between coils by performing Tcs measurements. The results cannot be used to determine the "true" Tcs because the extrapolation from the too low fields and therefore necessary high temperatures is too difficult - but it can be used to compare coils and sort out coils with problems.

A single coil test is the simpler and cheaper solution. However, by comparing the necessary time of single coil and twin coil tests it is obvious that a twin coil test is very attractive. Using a ground floor cryostat the additive costs are affordable to ensure the functionality of the ITER TF coil without affecting the ITER schedule too much. In addition a twin coil test would offer the opportunity to test the dump circuit foreseen in ITER.

3) Concerning the manufacturing of the ITER radial plates two main concepts were found to be feasible when evaluating the manufacturing processes. Concept 1 consists of a pre-machining of segments with grooves, welding of the segments and final machining of the RP (Fig. 2). Concept 2 consists of a welding of not machined small segments to the D-shape of the RP and following machining of the surface and grooves (Fig. 3).



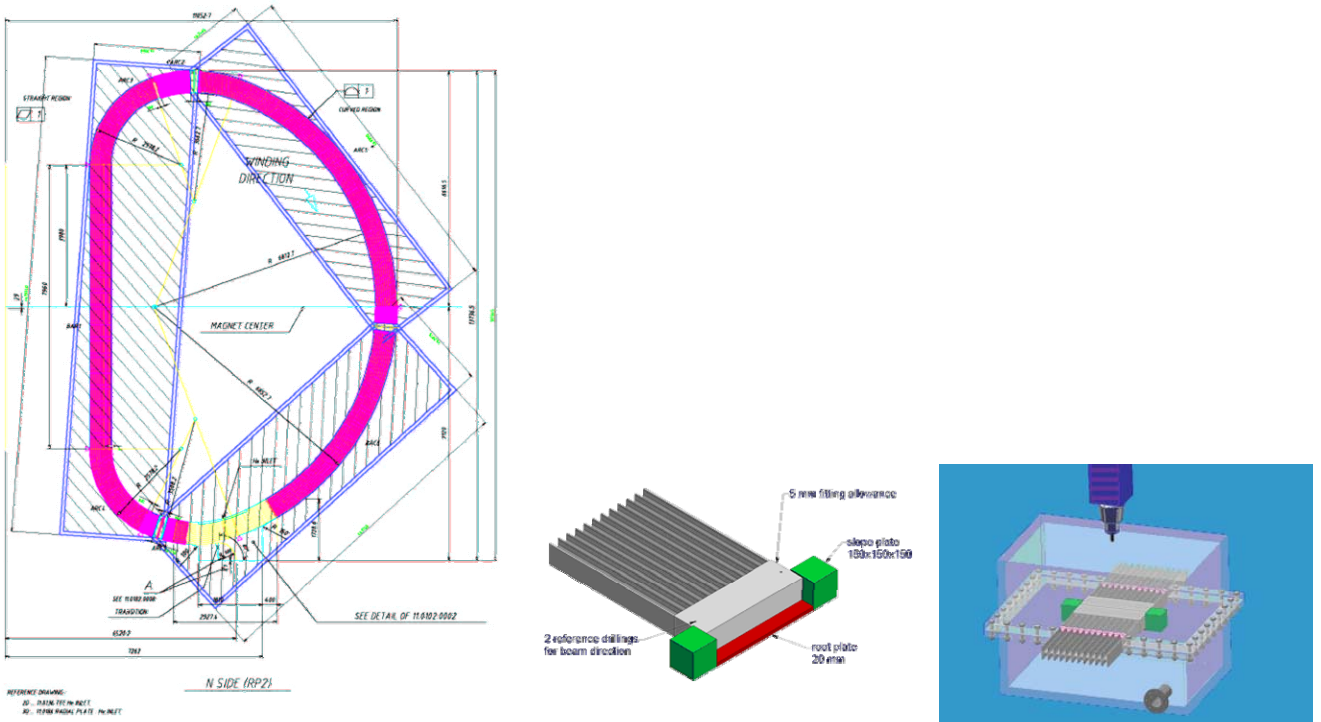


Fig. 2: Concept 1: Pre-machining of segments with grooves, EBW of the segments and final machining of the RP

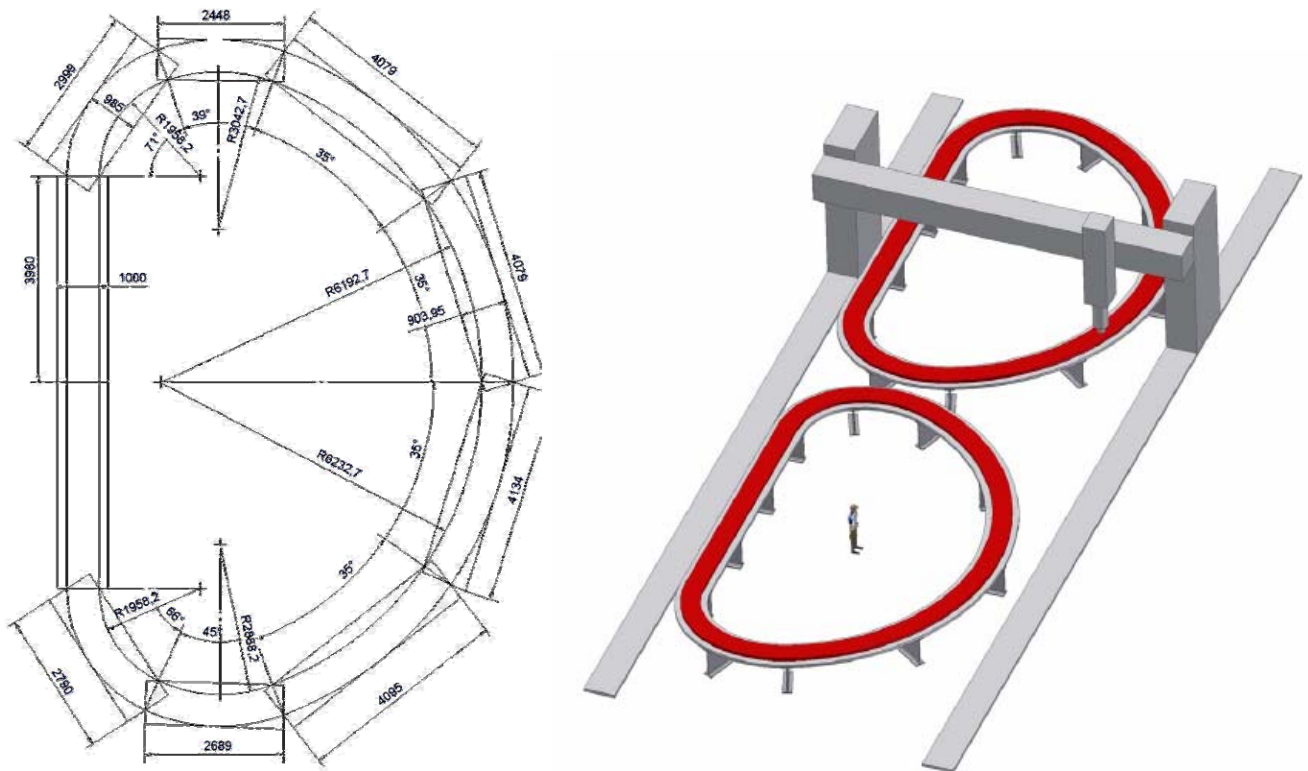


Fig. 3: Concept 2: Not machined small segments are TIG welded. Machining of surface and grooves on large machine.

Based on the results of the assessment of the different concepts and manufacturing techniques Concept 1 has much more advantages than Concept 2, even when it needs some more R&D before the start of the project.

Main advantages of Concept 1 are cost savings in terms of machine and labour and the time savings during machining that will lead to a keeping of the given time schedule. The

advantage of the time saving comes from the possibility to machine the three forged sections in parallel. This reduces the necessary time of 420 h for machining to about 140 h.

With the pre-manufacturing of the segments, Concept 1 gives the possibility to work with standard milling machines. This saves machine and labour costs. In case of problems during manufacturing it allows the supplier of the RP to do the work outside of his own factory on external machines. The savings in machining costs are much higher than the extra costs for the material.

From a technical point of view Concept 1 has the advantage that the inner leg section is forged in one piece. The inner leg is the region where, during later operation of the magnet, the highest stresses occur.

## **Summary**

The task has been finished and the final report issued.

A clear recommendation to install a cold test facility at ITER site for the test of fully assembled ITER TF coils can be given. This test facility will allow to detect high voltage, leak, joint, sensor and cooling failures before installation into the ITER machine and therefore to avoid enormous disassembly and re-installation risks and as consequence large additional costs and delay.

The evaluation of the manufacturing processes of the ITER radial plates showed that three pre-machined segments with grooves should be used that are electron beam welded to form the radial plate. The final machining of the joint regions is done using local electron beam welding chambers. This concept saves machining time because the three segments can be prepared in advanced on standard milling machines. In addition the inner leg which is the region where during later operation of the magnet the highest stresses occur is forged in one piece.

## **Outlook**

A decision to install a cold test facility has to be discussed in ILE.

Electron beam welded samples of 316LN steel with the specified higher content of N with a thickness of 120 mm should be manufactured. Welding tests on samples at cryogenic temperature should be done to check the strength values after welding. With these samples the parameters for the EBW should be optimised. Information about the shrinkage of the material will be obtained in addition during these tests.

In addition machining samples with the specified thickness should be prepared. This will give more information about the machining times, tool lifetime and possible distortions during machining.

## **Staff:**

W.H. Fietz  
S. Fink  
G. Zahn

## **Literature:**

- [1] Proposals for Cold Testing of the ITER TF Coil,  
P. Libeyre, D. Ciazynski, N. Dolgetta, J.L. Duchateau, F. Kircher, C. Lyraud, T. Schild, W. H. Fietz, G. Zahn  
Proceedings of the 19th Internat. Conf. on Magnet Technol. (MT-19), Sept. 18-23, 2005, Genova, Italy, to appear in IEEE Transactions on Applied Superconductivity

## **JET Technology**



## JW2-FT-2.9 Tritium Removal from JET Tiles

Carbon used presently as first wall material in fusion machines has as major drawback its relatively high erosion rate producing large amounts of eroded material which, associated with hydrogen isotopes, leads to the production of co-deposited layers. These layers immobilise substantial amounts of fuel material (deuterium/tritium) in inaccessible parts of the fusion machine and hence increasing the total tritium inventory of the machine.

The conditioning of graphite and CFC tiles collected from thermonuclear devices operated with tritium such as ITER, requires a process capable of achieving very high degrees of detritiation. This will be necessary in order to satisfy the current stringent regulations established for the conditioning and disposal of highly radioactive as well as chemically toxic waste. For low level waste (LLW) the maximum allowable tritium activity (in UK) is presently specified to be less than  $12 \text{ MBq}\cdot\text{kg}^{-1}$ . To achieve such low levels with tiles previously exposed to D-T plasmas it is estimated that decontamination factors (ratio of initial over final tritium activity) covering several orders of magnitude have to be realised.

With this aim an inductive heating facility using a Radio-Frequency (RF) inductive heating was tested at TLK to treat complete tiles. The Tritium Decontamination Experimental facility (TIDE) was used for that purpose and its efficiency was assessed by three different techniques, i.e. calorimetry, autoradiography and full combustion.

Basically the TIDE detritiation process contemplates a very rapid heating of carbon tile surfaces by the mean of induction heating. The basic principle behind heating by induction is that a very strong rapidly alternating magnetic field will induce eddy currents on any conductive material placed in the vicinity of that field. These eddy currents are then heating the metal (carbon tile) by induction. The amount of heating will depend:

- 1) On the field strength (and thus the amount of power running through the heating coil,
- 2) How quickly the field is changing (the heating coil power supply frequency), and
- 3) The degree of coupling between the induction coil and what is being heated (how close the objects are to one another, what their geometry is).

Prior to their detritiation by RF induction heating, the tritium content of the JET tile 1BN4 was measured by calorimetry while tritium depth profiles before detritiation were also determined by full combustion followed by liquid scintillation analysis of the collected water. Moreover, autoradiography or Imaging Plate (IP) technique was also used to evaluate the detritiation process using the following correlation between the PSL (Photon Stimulated Luminescence) signal, given by IP and the areal tritium activity provided by the combustion measurements according to the Tanabe's equation:

$$[1 \text{ MBq}\cdot\text{cm}^{-2}] = (1.2778 \pm 0.048) [\text{PSL}\cdot\text{cm}^{-2}]$$

The tritium content of the two parts of tile 1BN4 was estimated by calorimetry to be  $2.59 \pm 0.14 \text{ Ci}$ . In order to fit to the tile holder of the TIDE glove-box tile 1BN4 was cut in two pieces and the detritiation process was performed on 1BN4-a. During the first series of experiment the tile 1BN4-a was successfully heated twice, firstly at  $435 \text{ }^\circ\text{C}$  (25 cycles) and then at  $490 \text{ }^\circ\text{C}$  (15 cycles).

Comparison of the calorimetric measurements before and after the treatment allows an estimation of the detritiation process. Table 1 summarises all the calorimetric measurements performed on tile 1BN4 part a and b.

Table 1: Calorimetric measurements for tile 1BN4 before or after RF treatment. Lines 4 and 5 are obtained by adequate subtraction of lines 1 to 3.

	Tile	Calorimetric measurement	
		Ci	(GBq)
1	1BN4 a+b (before RF heating)	2.591 ± 0.143	(95.6)
2	1BN4 a+b (after RF heating)	1.088 ± 0.051	(40.3)
3	1BN4-b (not treated)	0.900 ± 0.035	(33.3)
4	<b>1BN4-a (before RF)</b>	<b>1.691 ± 0.147</b>	<b>(62.5)</b>
5	<b>1BN4-a (after RF)</b>	<b>0.188 ± 0.062</b>	<b>(7.0)</b>
	Tritium released		89%

After the second heating experiment the tritium activity of the tile was measured by autoradiography (Imaging Plates) and compared to the same image taken before the RF-heating.

Fig. 1 illustrates the autoradiography pictures taken after an exposure time of 20 min of the tile 1BN4-a.

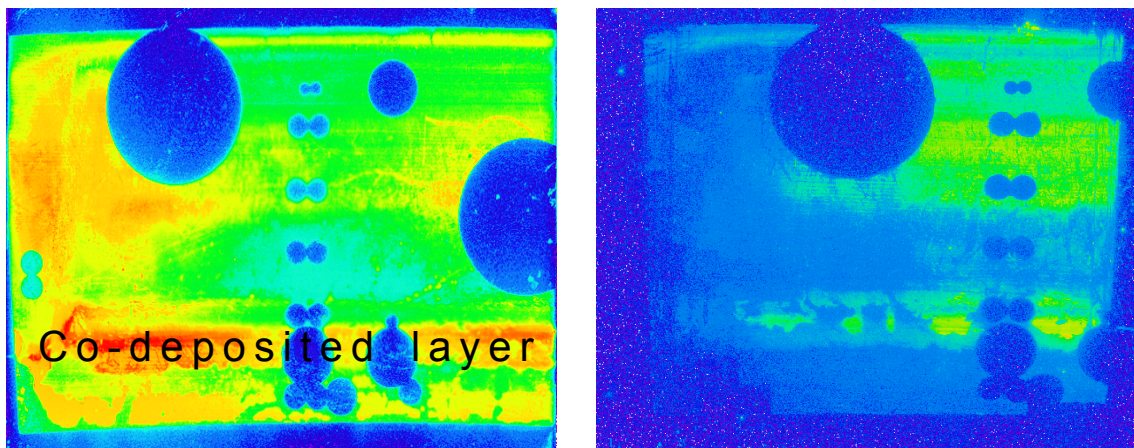


Fig. 1: Imaging Plate analysis for tile 1BN4-a.

**Left side:** before RF heating; **Right side:** after RF heating at 490 °C

The yellow and red areas of the tile surface indicate respectively, tritiated and highly tritiated areas of the tile. As it is clearly shown after the RF heating most of the tritium has been removed and only the region with the co-deposited layer is still visible. It is also noticeable that in the lower left part of the tile the tritium activity measured by PSL can hardly be distinguished from the background (in blue). On the other hand, the upper right part of the tile is less affected by the RF heating process. This is explained by the shape of the tile and the different geometry that we obtain during the displacement of the tile up and down in front of the heating coil. When the tile is in its lowest position the coil is facing the top of the tile and its respective distance is high (~2 cm), while when the tile is in its higher position the coil is facing the bottom of the tile and its respective distance is about 2 mm. As it was pointed out previously, the shorter the distance between the heating coil and the tile the higher the temperature and therefore, the higher the detritiation rate. Using Tanabe's equation mentioned above, it is possible to estimate the detritiation efficiency of the RF process.

At the distance of 38 mm starting from the left edge of the tile (in the toroidal direction) the surface tritium activity was estimated across the tile (in the poloidal direction) by reading the PSL signal before and after treatment. The reading of the tritium concentration found on the

surface of the tile across the poloidal direction is illustrated by a vertical line in Fig. 2 and Fig. 3 and the result is graphically represented on the right side of the same figures.

As it is illustrated in Fig. 2, before treatment the average tritium activity of the tile, at the distance of 38 mm in the toroidal direction, is approximately  $100 \text{ MBq}\cdot\text{cm}^{-2}$  with peak maximum in the co-deposited region of about  $1700 \text{ MBq}\cdot\text{cm}^{-2}$ .

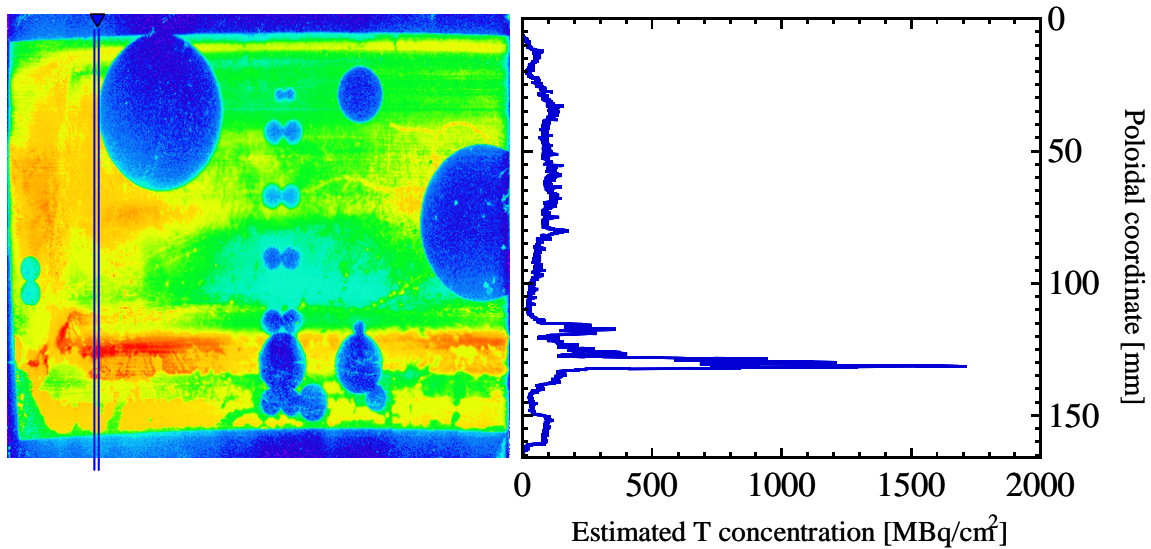


Fig. 2: **Left:** Picture obtained by IP for tile 1BN4-a before RF treatment.  
**Right:** PSL signal converted in  $\text{MBq}\cdot\text{cm}^{-2}$  taken at the toroidal distance of 38 mm.

After the RF heating the estimated tritium surface activity of the tile at the same position shows an average tritium concentration of about  $1 \text{ MBq}\cdot\text{cm}^{-2}$ .

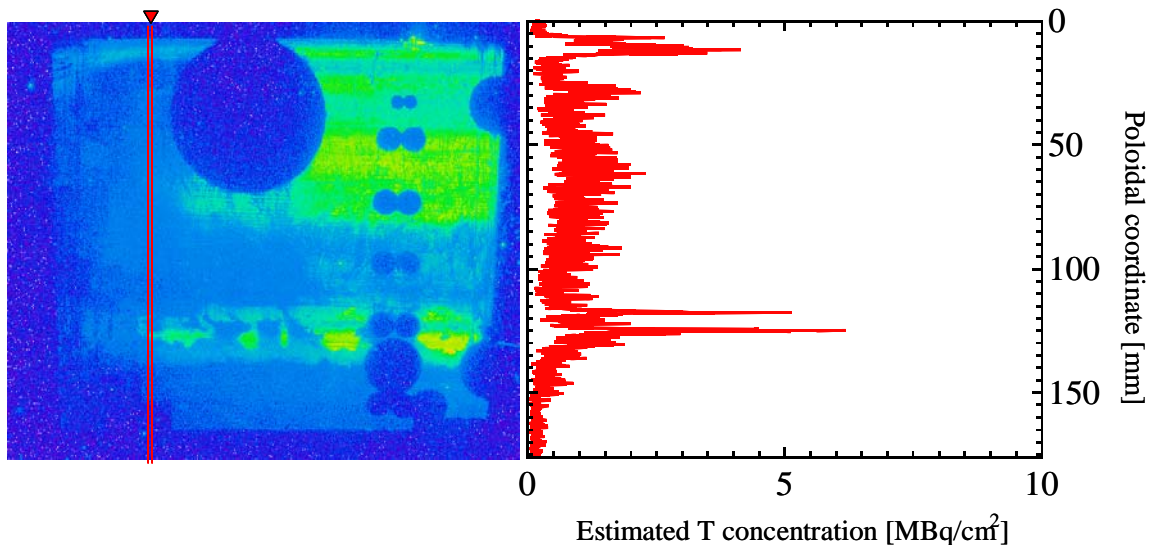


Fig. 3: **Left:** Picture obtained by IP for tile 1BN4-a after RF treatment;  
**Right:** PSL signal converted in  $\text{MBq}\cdot\text{cm}^{-2}$  taken at the toroidal distance of 38 mm.

Comparing the average surface activities of the tile, before ( $\sim 100 \text{ MBq}\cdot\text{cm}^{-2}$ ) and after the RF treatment ( $\sim 1 \text{ MBq}\cdot\text{cm}^{-2}$ ), observed for the same tile at the same location (38 mm toroidally), it appears that almost all surface tritium ( $>99\%$ ) has been released. On the other hand, comparing the peak maximum activities (see Fig. 2, 3), measured for the co-deposited layer of the tile, before ( $1700 \text{ MBq}\cdot\text{cm}^{-2}$ ) and after ( $6 \text{ MBq}\cdot\text{cm}^{-2}$ ) RF heating, we can estimate that a Decontamination Factor (DF) of about 280 was achieved.

Several cores were also retrieved before and after the induction heating using a hollow drill. From each cylinder the plasma exposed specimen was cut and combusted separately from the rest of the cylinder. Table 2 summarises the results obtained by the three techniques used to assess the efficiency of the RF heating process after the detritiation of tile 1BN4-a.

Table 2: Detritiation assessment of tile 1BN4 estimated by various techniques

Technique	Fraction of the re-leased tritium	DF
	(%)	
Calorimetry	89*	9
Autoradiography (IP imaging)	99**	100
Full combustion / liquid scintillation (for the surface samples)	99.5¥	185
Full combustion / liquid scintillation (for the bulk samples)	95¥	18

\* *the whole tile is considered*

\*\* *only the plasma exposed surface of the tile is considered*

¥ *only specific samples (or cylinders) are considered*

## Conclusions

Radio-frequency heating was successfully used as an ex-situ technique for the detritiation of entire tiles retrieved from JET. Autoradiography showed that using the RF technique more than 99% of total tritium inventory can be efficiently removed from a tile after several heating cycles at the average temperature of only 490 °C.

Compared to the heating process involving an open flame the RF technique has the advantage of heating the co-deposited layer from the reverse side and therefore compared to the flame treatment the generated temperature gradient is inverted. Indeed, during the RF treatment the temperature gradient is generated in the bulk of the tile (high thermal conductivity) and is conducted towards the surface, heating the co-deposit (low thermal conductivity) from behind. This has as main effect to avoid the diffusion of the released tritium into the bulk of the tile (redistribution). This was also observed experimentally. Indeed, after comparison of the combustion measurements obtained before and after RF heating, it has been noticed that the bulk tritium activity decreased significantly (95% of the bulk tritium was released) while at the same time more than 99% of the surface tritium is liberated. Nevertheless, the DF achieved by the RF treatment is not sufficient in order to qualify the method (as such) as a potential ex-situ detritiation technique. To reach the objective of LLW category waste, the tritium residual activity on the tile should not exceed the 12 kBq·g<sup>-1</sup>. However, it should be mentioned that the tile was heated at relatively low temperatures (maximum 490 °C) which is not enough to efficiently release the bulk tritium.

Finally, the three methods used to assess the RF detritiation process have their pros and cons, i.e. calorimetry allows a rough estimation of the complete tile, IP imaging allows an approximate estimation of the detritiation for the surface tritium, while full combustion associated to the scintillation analysis allows a very accurate measurements but of specific samples of reduced dimension (extrapolation needed).

## Staff:

N. Bekris  
D. Adami  
U. Berndt  
H. Dittrich  
L. Doerr  
B. Kloppe



Literature:

- [1] K.Sugiyama, T.Tanabe, N.Bekris, M.Glugla, J.P.Coad. Detailed tritium distribution on the JET Mk IIA divertor tiles. *Fusion Science and Technology* 48, (2005), 573.
- [2] T.Tanabe, K.Sugiyama, C.H.Skinner, N.Bekris, J.P. Coad. Tritium retention in the gap between the plasma-facing wall carbon tiles used in D-T discharge phase in JET and TFTR. *Fusion Science and Technology* 48, (2005), 577.
- [3] K. Sugiyama, T. Tanabe, K. Krieger, R. Neu, N. Bekris. Tritium distribution on plasma-facing tiles from AS-DEX Upgrade. *J. Nucl. Mat.* 337-339, (2005), 634-638

## JW4-FT-2.19 Endurance Test for the Catalyst-packing Mixture Proposed for Water Detritiation System at JET with FZK Mixture

The aim of the endurance test is to measure and compare both the separation performances of the catalyst-packing mixture and the chemical composition of the tritiated water after different exposure times (3, 6, and 9 months) in similar conditions as foreseen for the JET Water Detritiation System.

For this purpose an experimental setup comprising a column of 2 m length and 55 mm in diameter filled with the catalyst-packing mixture developed at the Tritium Laboratory Karlsruhe (TLK) was used for endurance testing. The catalyst-packing mixture is based on a hydrophobic catalyst, having platinum as the active element, and a structured Sulzer packing. In view of the tritium profile along the Liquid Phase Catalytic Exchange (LPCE) column envisaged to be built at JET going from  $1 \cdot 10^{12}$ - $5 \cdot 10^{12}$  Bq·kg<sup>-1</sup> at the bottom of the column down to  $2 \cdot 10^5$  Bq·kg<sup>-1</sup> at the top of the column, in the endurance test tritiated water of  $4 \cdot 10^{10}$  Bq·kg<sup>-1</sup> was used. The catalyst-packing mixture was exposed to tritiated water at the operation temperature and every three months the separation performance for both deuterium and tritium was measured. The performances of the catalyst-packing mixture was so far determined after two different exposure modes: catalyst-packing immersed in tritiated water and catalyst-packing mixture exposed to water-vapour as in a total reflux distillation process. Beside the separation performances measurements, the quality of water drained from the column after each exposure test have also been measured.

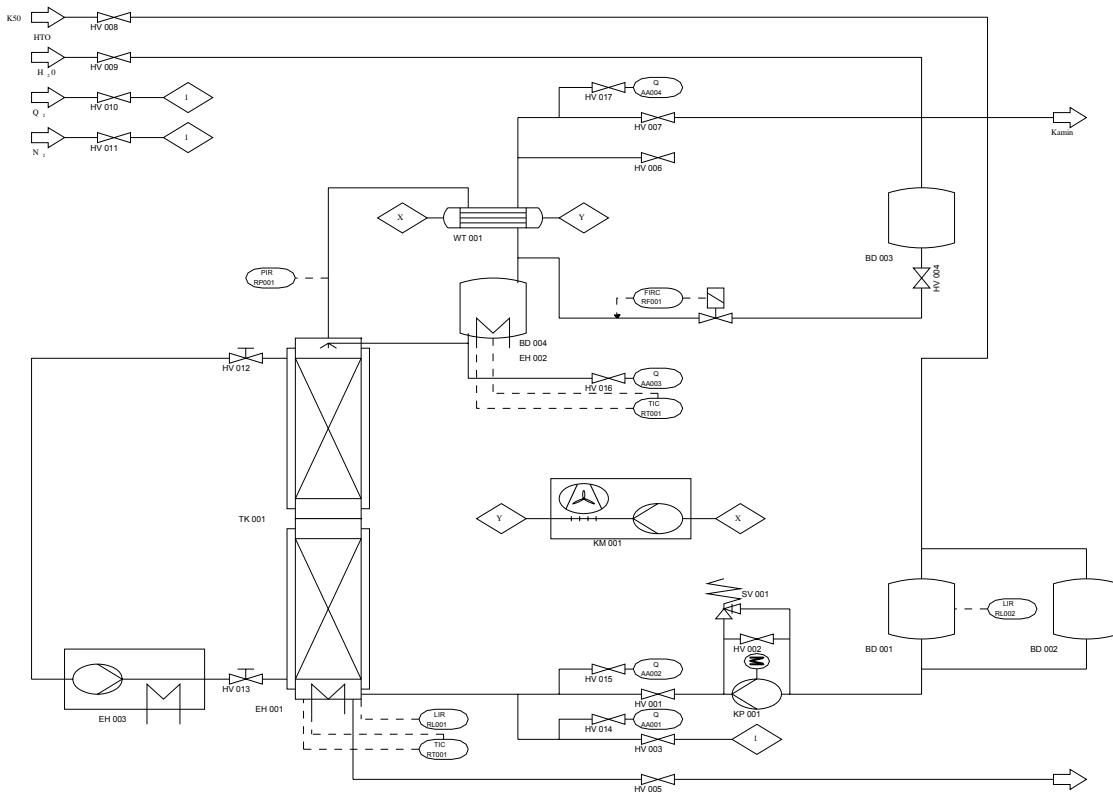


Fig. 1: Flow Diagram of the facility for the endurance tests.

The flow diagram of the experimental rig, which was connected to the TLK water detritiation facility is shown in Figure 1. The lower part of the experimental rig comprising the bottom of the LPCE column, boiler, pumps and IR spectrometer is shown in Figure 2. Since mid 2004, the LPCE column at TLK was continuously in operation for the endurance test. During the endurance testing period, the catalyst-packing mixture was exposed to tritiated water at 80 °C, in two different exposure modes:

- A. Catalyst-packing immersed in tritiated water;
- B. Catalyst-packing mixture exposed to water-vapour and tritiated hydrogen as in a total reflux distillation process.



Fig. 2: Experimental rig for catalyst/packing endurance test.

During the day shift, the LPCE column was in operation like a water distillation column; the vapours provided by the boiler have been condensed and returned as a reflux into the column. During this period, the catalyst was exposed both to tritiated vapours and tritiated hydrogen, HT species. At the end of the day shift, the hydrogen was removed from the column and stored in a vessel of the endurance rig. The LPCE column was filled with tritiated water pumped from the storage vessel, and the temperature of the column was maintained at 80<sup>0</sup> C during the night shift. At the end of the night shift, some part of the water was replaced gravitationally by hydrogen provided by a vessel of the experimental rig.

After 4, 6 and 9 months of continuous exposure alternating the two exposure modes, the separation performances such as the mass transfer coefficients have been measured at deuterium transfer. A hydrogen-deuterium mixture of 2% D/(H+D) was provided by two electrolysers at a throughput of 2 Nm<sup>3</sup>·h<sup>-1</sup>. The hydrogen-deuterium mixture was fed into the bottom of the LPCE column through the boiler that was saturated with water vapours. Along the LPCE column, an isotopic exchange took place between the saturated gas and demineralized water supplied in at the top of the column. The separation performances at deuterium transfer after operation with tritiated water are summarized in Table 1.

Table 1: Mass transfer coefficients at deuterium transfer during the endurance test.

Ratio Gas/Liquid	$K_{gv}(\text{kmol}\cdot\text{m}^{-3}\cdot\text{h}^{-1})$				$K_{lv}(\text{kmol}\cdot\text{m}^{-3}\cdot\text{h}^{-1})$			
	Starting value	After 4 months	After 6 months	After 9 months	Starting value	After 4 months	After 6 months	After 9 months
3.2	402	408	411	397	645	683	672	652

As it can be seen, no significant differences between the mass transfer coefficients have been obtained. The very small differences may be the result of the accuracy of flow rates and concentration measurements.

In addition to the test performed for deuterium transfer, one single tritium experiment was performed after the 9 months exposure period. Tritiated hydrogen of  $\sim 100 \mu\text{Ci}\cdot\text{m}^{-3}$  was supplied at the bottom of the LPCE column in countercurrent with demineralized water provided in at the top of the LPCE column. Enriched tritiated water was collected at the bottom of the LPCE column. The calculation method was similar with the one used for deuterium separation and the mass transfer coefficient was found to be:  $K_{gv} = 383 \text{ kmol}\cdot\text{m}^{-3}\cdot\text{h}^{-1}$  and respectively  $K_{lv} = 593 \text{ kmol}\cdot\text{m}^{-3}\cdot\text{h}^{-1}$  for a ratio gas to liquid of 3.2.

The chemical composition of water processed in the LPCE column during 9 months gives information related to the mechanical and chemical stability of mixture catalyst/packing in tritiated water environment. Therefore, water from the bottom of the LPCE column was sampled after 6 and 9 months of processing and the chemical composition was measured. In Table 2 a comparison between the chemical compositions of water after 6 and 9 months of processing and demineralized water is presented.

Table 2: Chemical composition of water during processing in the LPCE column.

Chemical element	After 6 months operation ( $\text{mg}\cdot\text{l}^{-1}$ )	After 9 months operation ( $\text{mg}\cdot\text{l}^{-1}$ )	Demineralized water ( $\text{mg}\cdot\text{l}^{-1}$ )
Fluorine	0.8	0.7	$\leq 0.3$
Chlorine	0.5	0.5	$\leq 0.3$
Sulfate	0.8	0.7	$\leq 1.0$
Phosphate	3.1	3.5	$\leq 1.0$
Acetate	0.2	0.2	$\leq 1.0$
Iron	0.2	0.2	$\leq 0.01$
Potassium	0.4	0.5	$\leq 0.01$
Phosphor	1.9	2.0	$\leq 0.01$
Silica	1.7	1.8	$\leq 0.01$
pH	7.0	7.0	5.6

The demineralised water of the composition shown in the Table 2 was used for the preparation of tritiated water used during the endurance test. 1 liter of tritiated water of  $\sim 10 \text{ Ci}\cdot\text{kg}^{-1}$  obtained after one molecular sieve bed regeneration at TLK was diluted with demineralised water to get  $\sim 10$  liters tritiated water of  $1 \text{ Ci}\cdot\text{kg}^{-1}$  used for the endurance test.

The deviation from the chemical composition of the demineralised water used for the preparation of tritiated water is quite low after 9 months processing in the LPCE column. Nevertheless, a purification unit is needed between the LPCE column and the electrolysis cells in order to keep the water conductivity below  $0.5 \mu\text{S}\cdot\text{cm}^{-1}$ . The data from the above table may be used as input data for the purification unit design.

#### Staff:

I. Cristescu  
I. R. Cristescu  
S. Welte  
W. Wurster  
L. Dörr

#### Literature:

I. Cristescu, I. R. Cristescu, L. Dörr, M. Glugla, D. Murdoch, S. Welte - *Long term performances assessment of a Water Detritiation System components*, accepted for publication in Fus. Eng & Des.

### **JW5-FT-3.11**

#### **Assessment of in-situ Detritiation in JET - OPL Tile Analysis**

The use of carbon-based materials for first wall components in any fusion machine results in the formation of eroded carbon material which after uptake of fuel material (deuterium and/or tritium) is co-deposited mainly on the remote and colder areas of the vacuum vessel such as the sub-divertor part of the machine.

A well defined physical or chemical description of these co-deposits is still not available therefore, they are reported in the literature, as a amorphous carbonaceous C:H layer, and referring to their  $sp^3$  hybridisation, sometimes as “diamond-like films”.

An elementary analysis of such co-deposited layers found on the JET divertor tiles, gave a D/C ratio of  $\sim 0.75$ . Such a high ratio could only be explained if the layers are composed by short chain of aliphatic carbons almost completely saturated with heavy hydrogen isotopes, i.e. carbon chains having a  $sp^3$  hybridisation and also having partially all bonds saturated with heavier hydrogen isotopes, such as  $C_2Q_xH_y$  ( $x+y=6$ ;  $Q= D, T$ ). In such compounds hydrogen is strongly bounded to the carbon.

Such films have been shown to contain high rates (3.3 g tritium per gram of material) of the in-vessel tritium retention, which would be very problematic in future fusion devices such as ITER. Indeed, calculations for ITER predict an accumulation of 10–20 g of tritium per 1000 s pulse whilst the maximum allowable in-vessel inventory for ITER is limited to only 350 g. It is therefore clear that the formation of such films has to be hindered or at least such films have to be removed as soon as they are formed. With this aim the development of techniques for the removal of such co-deposited material is a critical issue for the future development of ITER which will use carbon tiles on the strike points of the divertor.

Within a collaboration with the Princeton Plasma Physics Laboratory (PPPL) it could be proved that laser irradiation of Plasma Facing Components (PFC's) can be a powerful solution in terms of removing hydrocarbon films. Such a photonic cleaning represents a good candidate for the *in-situ* de-tritiation of plasma facing materials for ITER. Therefore, it was decided to test the method at JET during the shutdown of 2004. However, for contractual reasons, the laser photo-cleaning was replaced by high-power xenon flashlamps irradiation.

The photo-cleaning source uses a Xenon flashtube having an active length of about 50 mm and a 9 mm diameter and provides a high optical transmission in the UV and visible wavelength range. Several Outer Poloidal Limiter (OPL) tiles were irradiated by the flashlamp which delivered pulse lengths of approximately 140  $\mu s$  with a repetition time of up about 1 Hz at the maximum power density of 100 J per pulse (divertor tiles were treated at higher powers). During the flashlamp treatment the various tritiated gaseous by-products which were expected to be released under irradiation were monitored using an ionization chamber. However, the ionization chamber did not exhibit any noticeable change on the tritium released during the whole process.

To study the effectiveness of the flashlamp cleaning, 4 OPL tiles, i.e. 1 graphite and 1 CFC tiles together with the adjacent untreated tiles were shipped to the Tritium Laboratory Karlsruhe (TLK) for evaluation of their total tritium content and depth profiling, using calorimetry and full combustion respectively. Similar tiles were also analysed for their relative deuterium contents by Ion Beam Analysis (IBA). The IBA was carried out by UKAEA using the special glove-box facilities at Sussex University in Sussex, UK.

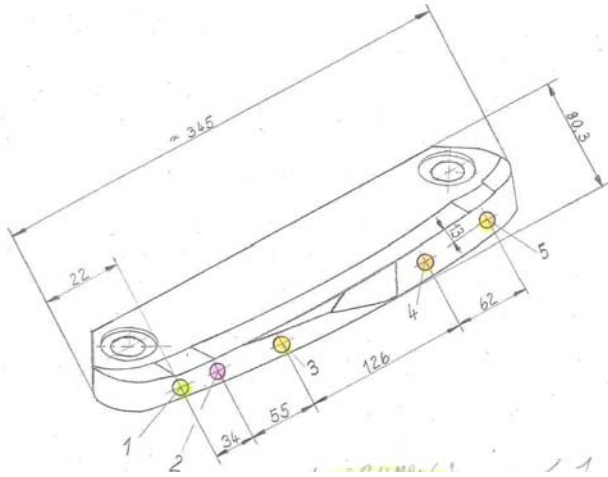


Fig. 1: Schematic view of a typical OPL tile. The cored cylinders used for combustion measurements are illustrated by the coloured circles.

To evaluate their tritium depth profile, several cylinders were cored from various locations of the plasma exposed surface of the tile as it is illustrated in Fig. 1.

Each cylinder was sliced in at least three smaller discs having a thickness of 1 mm and a diameter 7.8 mm each. The discs were numbered  $A_1$  to  $A_3$  starting from the plasma exposed side. Thus  $A_1$  represents the plasma exposed surface while the  $A_3$  is located into the bulk of the tile 3 mm below the  $A_1$  disc. All discs and the rest core were then combusted at TLK and their tritium content was measured by scintillation analysis. Table 1 shows the results for the 4 tiles.

Table 1: Overview of the tritium content for the plasma exposed surface of the 4 OPL's.

OPL Tile	CFC		Graphite	
	2B12T-160	2B12B-56	2B15B-5882	2B16B-top
	Untreated (T cm <sup>-3</sup> )	Treated (T cm <sup>-3</sup> )	Untreated (T cm <sup>-3</sup> )	Treated (T cm <sup>-3</sup> )
A <sub>1</sub> -Cyl-1	7.76 10 <sup>15</sup>	2.35 10 <sup>16</sup>	4.05 10 <sup>16</sup>	-
A <sub>1</sub> -Cyl-2	1.63 10 <sup>17</sup>	7.76 10 <sup>15</sup>	7.20 10 <sup>14</sup>	567 10 <sup>16</sup>
A <sub>1</sub> -Cyl-3	4.31 10 <sup>16</sup>	3.02 10 <sup>15</sup>	1.25 10 <sup>15</sup>	4.30 10 <sup>15</sup>
A <sub>1</sub> -Cyl-4	3.82 10 <sup>16</sup>	7.00 10 <sup>16</sup>	8.52 10 <sup>15</sup>	3.80 10 <sup>15</sup>
A <sub>1</sub> -Cyl-5	7.82 10 <sup>16</sup>	-	2.23 10 <sup>15*</sup>	-

- not a plasma exposed sample. Cylinder cored from the side of the tile

Surprisingly enough the tritium concentrations for the plasma exposed surfaces did not seem to be very much affected by the photon cleaning process at 100 J. Indeed, the differences in terms of tritium concentration before and after flashlamp treatment are minimal and sometimes the treated sample exhibit more tritium for the plasma exposed surface than the untreated one. These variations can only be attributed to the non homogeneous tritium distribution inside the vessel.

Comparing the tritium distribution throughout the tiles we may notice the following: Firstly, as it was pointed out by Table 1, comparing the CFC and Graphite's surface activities do not vary that much. In general, CFC seems to have a bit more tritium on the surface than the Graphite tile but this is most likely related to their relative location inside the vessel. Secondly, it is remarkable to see that the bulk tritium concentration for the CFC tiles is greater by factor five, to the corresponding tritium fraction for the graphite tile. This observation has been verified for the 4 tiles. It has been attributed to the different structure characterising both material and especially to the fibre structure of the CFC tiles which allows a better migration, of molecular tritium and "bigger" molecules such as methane, between the fibres

than graphite does. Indeed, for steric reasons (*steric hindrance*)<sup>1</sup> the migration of molecular species is more difficult between the graphite reticular planes.

Again, comparing the bulk tritium fraction for treated and the corresponding untreated tiles it is obvious that the flashlamp treatment did not have any noticeable effect.

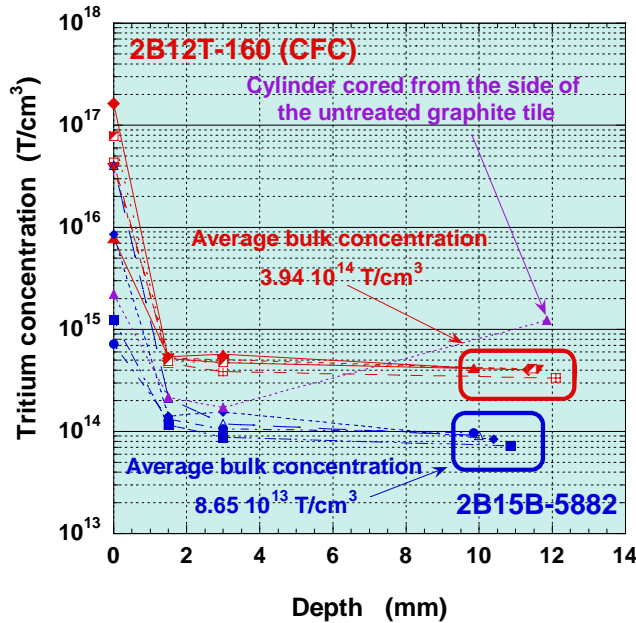


Fig. 2: Tritium depth profiles for the untreated CFC and graphite tiles 2B12T-160 and 2B15B-5882 respectively.

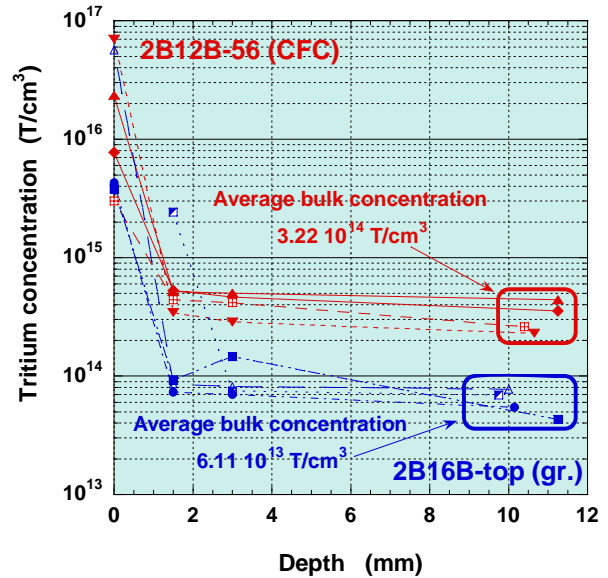


Fig. 3: Tritium depth profiles for the treated CFC and graphite tiles 2B12B-56 and 2B16B-top respectively.

## Conclusions and Outlook

Flashlamp photonic cleaning has been tested *in-situ* and at the Beryllium Handling Facility (BeHF) at JET. Several OPL tiles have been exposed to numerous pulses with a maximum power density of 100 J. To assess the efficiency of the detritiation method, four tiles, 1 graphite and 1 CFC and the adjacent untreated tiles have been sent to TLK. The tritium depth profiles measured for all tiles have shown that the tritium surface activity for both types of tiles is similar and it is depending on their relative location inside the vacuum vessel. Moreover, it has also been shown that the CFC tiles allow a better migration of molecular tritiated species most likely between the CFC fibres than graphite does. The photon cleaning treatment did not show any remarkable difference between treated and the corresponding untreated tile. Indeed, the combustion results revealed that the flashlamp treatment is almost inefficient when using a power density of only 100 J. This is also consistent with the data provided by the ionisation chamber during the photon cleaning treatment. Calorimetric measurements for the complete tiles are also planned for the near future. A direct comparison between the combustion and the calorimetric measurements will allow a final conclusion about the efficacy of the method.

<sup>1</sup> Steric effects as referred to in this report arise from the fact that the volume required for an easy migration of a chemical compound (molecular volume) is close to the available space left by the structural parameters of the material.

Staff:

N. Bekris

U. Berndt

A. Erbe

J. Ehrmann

Literature:

N. Bekris, J.P. Coad, R.-D. Penzhorn, S. Knipe, L. Doerr, R. Rolli and W. Nägele. Characterisation of flakes generated in JET after DD and DT plasma operations. J. Nucl. Mat. 337-339, (2005), 659-663



### JW4-FT-3.18 Assessment of in-situ Detritiation in JET

In the ITER fusion machine, carbon-based target materials are foreseen to be used in the divertor area. However, the use of carbon there is likely to be a major problem in terms of tritium retention in re-deposited carbon films. It is estimated that 5 g tritium per shot will be deposited to the first wall and therefore, detritiation of Plasma Facing Components (PFC's) of such tritium installations will play an increasingly important role in the future development of fusion. In this respect, it is important to develop a technology for the *in-situ* detritiation of the carbon tiles to meet the safety criteria for ITER which allow a total tritium amount into the vacuum vessel of 350 g. Fast and efficient tritium removal is needed for future DT machines with carbon plasma facing components. Photon cleaning is a potential detritiation method and has been applied on co-deposited layers of tiles retrieved from some smaller Tokamaks, such as the TEXTOR (Jülich, Germany) and Tore Supra (Cadarache, France) fusion machines. Depending on the power density applied, photon cleaning can work in two different modes, at low power (<200 J) it desorbs hydrogen isotopes from the deposited films, and at higher power densities (>200 J) it ablates the entire film.

To date the technique has been tested only in laboratory scale. However, to test the applicability to next step devices, an engineering scale demonstration of photon cleaning needed to be performed in situ. With this aim, during the JET 2004 shutdown several tiles of an Outer Poloidal Limiter (OPL) and the divertor region of the JET machine (Culham, UK), were treated *in-situ* or, in the beryllium handling facility (BeHF) at JET, by photon cleaning. In order to assess the efficiency of the H-removal process, 2 adjacent divertor tiles (one treated one untreated) were shipped to the Tritium Laboratory Karlsruhe (TLK) for evaluation of their total tritium content and depth profiling, using calorimetry and full combustion respectively. Similar tiles were also analysed for their relative deuterium contents by Ion Beam Analysis (IBA) methods. The IBA was carried out by UKAEA using the special glove-box facilities at Sussex University in Sussex, UK.

The flashlamp delivered to the divertor tiles, up to 300 J in ~140  $\mu$ s with a repetition rate of ~1 Hz. At the highest energies deposited material is ablated from the surface of the divertor tiles. The poloidal limiter tiles were treated at lower energies (<100 J), which was expected to desorb hydrogen isotopes rather than ablate the surface films.

By visual inspection, it appears that part of the deposited film (~100  $\mu$ m thick) on the divertor tiles, has been removed from the areas exposed at 300 J. Ion Beam Analysis showed that deuterium is absent from the very surface ( $1/2$  to 1  $\mu$ m in depth), but its level is similar to the untreated regions beyond the depth of ~7  $\mu$ m which was the maximum analysed depth.

The calorimetric measurements for the untreated 3BWG4B divertor tile and the treated 3BWG4A, are presented here.

Calorimetric measurements for the untreated divertor tile 3BWG4B (Fig. 1) gave an average total tritium activity of about  $1.619 \pm 0.080$  Ci or  $5.99 \cdot 10^{10}$  Bq, while the calorimetric measurement for the 3BW4GA treated tile (Fig. 2) estimated a total tritium

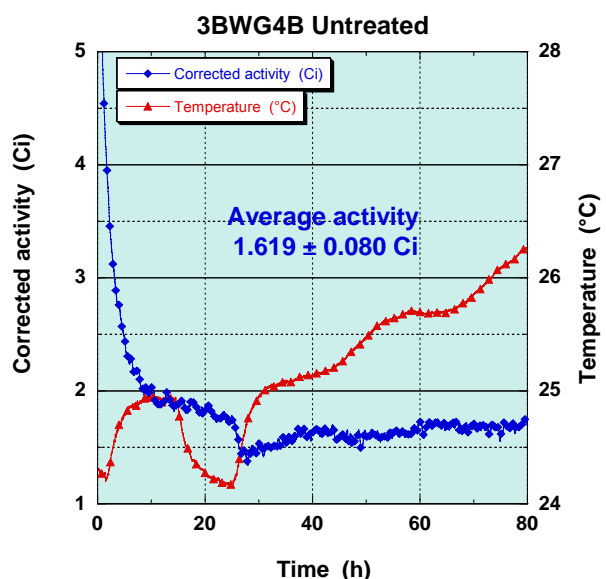


Fig. 1: Calorimetric measurement for untreated JET divertor tile 3BWG4B

content averaging  $1.089 \pm 0.041$  Ci or,  $4.03 \cdot 10^{10}$  Bq, i.e. 67% of the activity measured for the untreated tile.

As it is illustrated in Fig. 1, approximately 30 h are needed to allow the calorimeter reach an equilibrium i.e. give a stable value. Once the thermal equilibrium is reached the value given by the calorimeter remains remarkably stable even though the room temperature increased significantly. Normally the measurement is very sensitive to the room temperature but only when the tritium level is close to very low tritium levels ( $<0.5$  Ci). At higher tritium values, as it is illustrated here, the measurement is not affected by variation of the room temperature, if such a variation does not exceeds 2 to 3 °C.

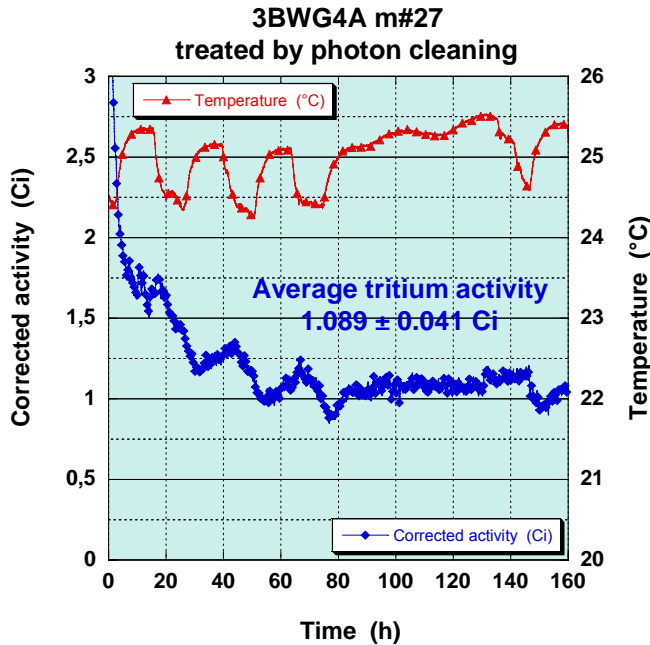


Fig. 2: Calorimetric measurement for treated JET divertor tile 3BWG4A

The measurements with the untreated tiles have been performed during the summer 2005 this explains why the room temperature increased up to 27 °C.

As it is illustrated in Fig. 2 almost 80 h are needed before the calorimeter reaches a thermal equilibrium. During that time it is also evident that the temperature variation of the room has an influence to the measurement. These temperature variations are related to the outside day/night temperature variation while the ventilation system is running. On the other hand, between 80 h to 130 h (week-end) the room temperature does not vary because the ventilation system is turned off during week-ends and therefore the room temperature remains constant during that time (variation  $\sim 0.5$  °C).

It must also be mentioned that approximately only one half of the 3BW4GA tile was treated by the flashlamp, namely the part of the tile which is lying on the inner divertor where it is located most of the co-deposited material. Moreover, the irradiation is performed by treating stripes of the tile along the toroidal direction having a width ranging between 10 mm to 40 mm. For each zone (stripe) the number of pulses or the power density is different, which makes very difficult to compare directly the treated and the adjacent untreated tile. However, assuming that both tiles had a similar initial tritium content, we may estimate that treating half of the tile by flashlamp, almost 33% of the total tritium was released or, speaking in terms of thickness of the co-deposited material, from the  $\sim 100$   $\mu\text{m}$  measured before irradiation approximately 30  $\mu\text{m}$  have been removed.

Presently, 8 cylinders were cored from tile 3BWG4A and from each cylinder the plasma exposed part was cut. Each cylinder is taken from the various irradiated zones and will be analysed by full combustion in order to evaluate the efficiency of the flashlamp detritiation method. The results will also be compared to the calorimetric measurements.

This first experimental attempt showed that the flashlamp treatment is able to ablate the co-deposited layer using an irradiation power of only 300 J. A second try is planned to be performed using the second tile 3BWG4B but at the higher power of 500 J.

Staff:

N. Bekris

L. Doerr

A. Erbe

B. Kloppe

G. Mangei

Literature:

- [1] S. Rosanvallon, N. Bekris, J. Braet, P. Coad, I. Cristescu, C. Grisolia, F. Le Guern, J. Likonen, G. Piazza, C. Poletiko, M. Rubel, J.M. Weulersse, J. Williams. Tritium related studies within JET Fusion Technology work programme. *Fusion Science and Technology* 48, (2005), 268
- [2] J.P. Coad, M. Rubel, N. Bekris, D. Hole, J. Likonen, E. Vainonen-Ahlgren and EFDA-JET Contributors. Distribution of hydrogen isotopes, carbon and beryllium on in-vessel surfaces in the various JET divertors. *Fusion Science and Technology* 48, (2005), 551
- [3] Y. Torikai, M. Matsuyama, N. Bekris, M. Glugla, P. Coad, W. Naegele, A. Erbe, N. Noda, V. Philipps, K. Watanabe. Tritium distribution in JET Mark IIA type divertor tiles analysed by BIXS. *J. Nucl. Mat.* 337-339, (2005), 575-579

## **JW5-FT-4.7**

### **CAD to MCNP Interface**

The Monte Carlo method allows the use of full and detailed 3D geometry representation for neutronics calculations. Geometry models for the Monte Carlo particle transport code MCNP are currently generated manually. This process becomes extensive and time consuming when geometry models for complex devices such as JET and ITER are to be prepared. An efficient solution is to shift the geometric modeling into a Computer Aided Design (CAD) system and use an interface programme for MCNP. Such an interface programme has been developed at FZK within previous JET fusion technology tasks (JW3-FT-5.6 and JW4-FT-5.14). The objective of the current task is to further develop the interface programme, aiming at a test release version.

The interface programme has been upgraded, tested and enhanced by new features. It is now able to access the CAD geometry, convert the data to the MCNP geometry representation and construct a complete MCNP model without the need of manual interactions. It provides capabilities for detecting and correction of errors in the CAD model as well as for the completion of the MCNP model by voids. The functionality of the basic components of the interface program have been tested using different CAD models. The main enhancements of the interface programme include the design and implementation of Graphical User Interface (GUI) components with their integration into an application programme with capabilities for visualisation, modelling and bidirectional exchange of the geometry data.

A final test release version of the interface programme is currently being assembled, including packaging and installation tools.

#### Staff:

H. Tsigé-Tamirat  
U. Fischer

#### Literature:

- [1] H. Tsigé-Tamirat, U. Fischer, P. Carman, M. Loughlin, Automatic Generation of a JET 3D Neutronics Model from CAD Geometry Data for Monte Carlo Calculations, Fus. Eng. Des. In Press, Corrected Proof, Available online 10 August 2005.
- [2] H. Tsigé-Tamirat, U. Fischer: CAD Interface for Monte Carlo Particle Transport Codes. The Monte Carlo Method: Versatility Unbounded in a Dynamic Computing World ; Proc.of the Conf., Chattanooga, Tenn., April 17-21, 2005 LaGrange Park, Ill. : ANS, 2005

## **JW4-FT-5.15**

### **Fully Automated Interface to Convert CATIA Files into MCNP Geometry Surfaces and Cells**

The overall objective was to develop an interface programme between a Computer Aided Design (CAD) system and a Monte Carlo (MC) particle transport code for accessing the geometric and topological data of CAD systems and then construct a geometry representation appropriate for MC particle transport calculations.

In the frame of the JET Fusion Technology Task JW4-FT-5.15, the interface programme developed at FZK for converting CAD to MCNP geometry representations has been further extended to allow a fully automated generation of MCNP models. The present version of the interface programme is able to access the CAD geometry, convert the data to the MCNP geometry representation and construct a complete MCNP model without the need of manual interactions. This includes the capability of detecting and generating voids as well as performing corrections of modelling errors. The interface includes capabilities for the visualization, modelling and exchange of the geometry data and is also capable to generate CAD geometry models from available MCNP input decks.

Successful test applications have been performed for a complete JET torus sector demonstrating its capability for the automated processing of the CAD data and their conversion into a geometry model for Monte Carlo calculations with the MCNP code. The converted geometry model has been validated by a stochastic calculation of the volumes by MCNP. The automatic conversion process was thus shown to reproduce the original CAD geometry properly.

#### Staff:

U. Fischer  
H. Tsige-Tamirat

#### Literature:

- [1] U. Fischer, H. Tsige-Tamirat, CAD Interface for MCNP, Final Report for JET Fusion Technology Task JW4-FT-15.5, March 2005.
- [2] H. Tsige-Tamirat, U. Fischer, P. Carman, M. Loughlin, Automatic Generation of a JET 3D Neutronics Model from CAD Geometry Data for Monte Carlo Calculations, Fus. Eng. Des. In Press, Corrected Proof, Available online 10 August 2005.
- [3] H. Tsige-Tamirat, U. Fischer: CAD Interface for Monte Carlo Particle Transport Codes. The Monte Carlo Method: Versatility Unbounded in a Dynamic Computing World ; Proc.of the Conf., Chattanooga, Tenn., April 17-21, 2005 LaGrange Park, Ill. : ANS, 2005

## JW4-FT-5.17 Simulation of Tritium Spreading in Controlled Areas after a Tritium Release Considering Inner Obstacles

The knowledge on tritium distribution in a confined area in case of a tritium spill and the knowledge of tritium removal rate are useful to determine the removal time for existing ventilation conditions in a tritium handling room, to design suitable detritiation systems and to identify effective monitor locations in a facility. The behaviour of tritium can be characterized by solving the dynamic equations of motion (the Navier-Stokes equations) coupled with the classical  $k-\epsilon$  turbulence model to simulate the ventilation in the room and mass diffusion for tritium spreading. The GASFLOW-II fluid dynamics field code, developed through a Los Alamos National Laboratory (LANL) – FZK co-operation, was used as the computational tool to solve the equations that describe the processes. The numerical results have been validated with experimental data collected on the experimental facility (Caisson) at the Tritium Process Laboratory (TPL) Japan.

The Caisson is a 12 m<sup>3</sup> stainless steel leak-tight box that is connected to a glove box housing the equipment to release tritium into the Caisson. The Caisson is connected to a membrane detritiation system with 4 volume exchanges per hour. The connection between the Caisson and the ventilation system is realized through a supply duct and an exhaust duct located below the ceiling. Seven ionisation chambers, designated TM0 to TM6 were installed in the Caisson for tritium concentration monitoring (Figure 1).

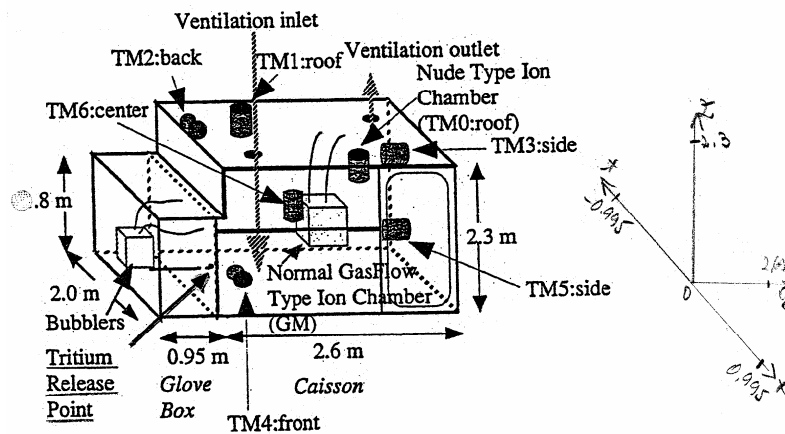


Fig. 1: Structure of the CATS and location of tritium monitors and tritium release point.

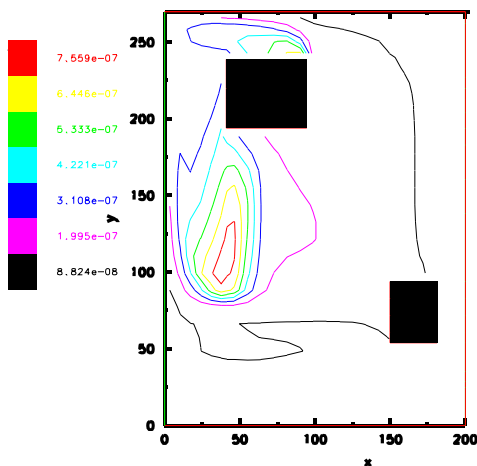


Fig. 2: Location of obstacles (case 2 and 3) and tritium plume immediately after the release

Five different cases with different obstacles (at half-height) and/or tritium release point locations have been investigated:

Case 1: Caisson without obstacles: tritium release point on the back wall;

Case 2: Caisson with 2 obstacles of approx. half-height, one under the supply duct, one under the exhaust duct; tritium release point on the back wall;

Case 3: Caisson with 2 obstacles, one under the supply duct, one under the exhaust duct; tritium release point from one of the obstacles, simulating a release from a glove-box;

Case 4: Caisson with 2 obstacles, one under the supply duct, one in parallel; tritium release point from 2<sup>nd</sup> obstacle, simulating an release from a glove-box, in opposite direction compared with case 3;

Case 5: Caisson with 4 obstacles, one under the supply duct, one in parallel, one under the exhaust duct, one in parallel; tritium release point on the back wall.

For all five investigated cases the value of the initial tritium release was 444 GBq. In case of a perfect mixing this will give an average tritium concentration of 37 GBq·m<sup>-3</sup>.

**Initial tritium behaviour (4 exchanges/hour)**

At this ventilation rate, it can be concluded that:

- The initial tritium behavior depends less on the obstacles numbers or locations but mainly on the tritium release point locations.
- In Case 3, where the tritium release point is located through a low ventilated area, huge local tritium concentrations are recorded by the monitors located in the neighborhood of the release (1200 GBq·m<sup>-3</sup> for TM6, see Figure 3).

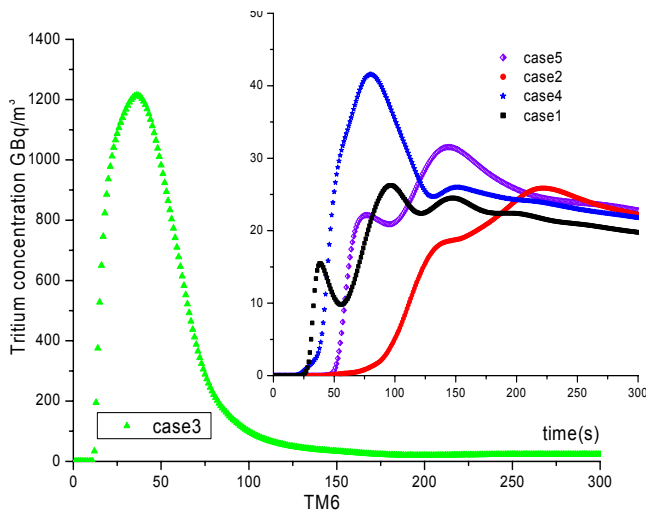


Fig. 3: Time variation of tritium concentration at location TM6

- In Case 4; where the tritium release is oriented towards an area with very good ventilation, all the monitors register a value of tritium activity of ~ 40 GBq·m<sup>-3</sup>, very close to an average of the tritium amount released in the Caisson.
- The presence of the obstacles has a very weak influence to the time when an almost constant concentration is attained in the Caisson (~300 s).
- The only location that records average values is TM4, situated under the supply duct where very good ventilation is assured.

The same investigation was done at a ventilation rate of one exchange/hour with similar conclusions

**Uniform ventilation**

Tritium behavior in the first period after the release is strongly depending on the velocity field in the ventilated area. A different configuration of ventilation ducts was considered, to obtain a more uniform velocity field in the Caisson. Instead of one ventilation duct, four ventilations ducts at equal surface area and equal with the surface of the inlet duct in the Caisson have been considered. Two of the four-inlet ventilation ducts are placed under the dent section of the Caisson (near the back wall) and the other two near the front wall of the Caisson. The outlet duct was placed in the Caisson centre, the cross section being kept constant as in the original

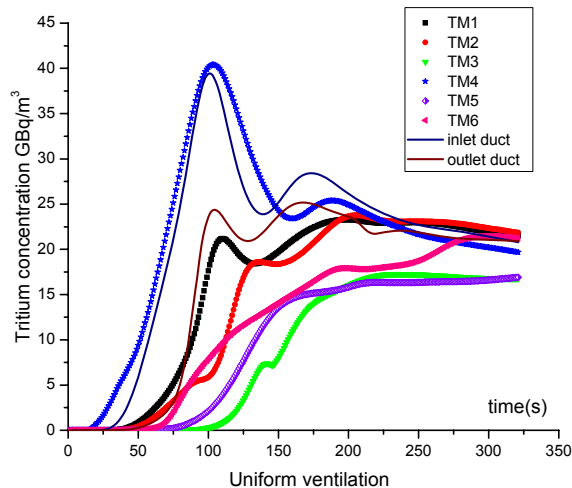


Fig. 4: Time variation of tritium concentration for uniform ventilation.

case of the Caisson.

In Figure 4, the time variation of the tritium concentration in the Caisson immediately after the release is plotted. It can be seen that in none of the locations of the Caisson, peaks of concentrations appeared as in the original case. In this case the maximum values as registered by the monitors are reflecting with a good accuracy the average tritium concentration in the Caisson that is  $37 \text{ GBq}\cdot\text{m}^{-3}$ . As only the ventilation distribution is changed from the initial case, keeping constant the ventilation flow rate, the total tritium removal time is not changed.

### **Conclusions:**

Tritium spreading in a ventilated area is strongly determined by the flow velocity field. Low ventilated areas and preferential flows can be created due to an inappropriate placement of ventilation ducts or due to the presence of obstacles. For these cases high gradients of tritium concentration are created in the case of a release. If such cases would occur in the ITER buildings, there is a high probability that some tritium monitors will trigger the signal to isolate the rooms and start the N-VDS (false alarms). It is expected that at lower ventilation rates, tritium will migrate in rooms in form of a plume, which means locally high values of tritium concentration can be recorded. The lower the ventilation rate, the longer the time in which these high local tritium concentrations will exist.

It was proven that best tritium monitor location that gives the best approximation of the average tritium concentration is the outlet duct.

It is therefore desirable and recommended that during the design of the ventilation system for ITER; an analysis of the velocity flow in the ITER buildings for a proposed configuration of the ventilation ducts should be done.

Not investigated here but important to be mentioned is that the influence of the water presence in the initial tritium release plays no role in the tritium distribution immediately after the release. The effects are however important in the tritium removal time. For future work, it is recommended that the problem of tritium spreading after an accidental release could be split into two phases: 1. An analysis of the tritium distribution after the release, to be investigated with a validated CFD code (GASFLOW) and 2. An investigation on the total tritium removal time considering the adsorption-desorption effects on the walls, as these effects become important after the time when perfect mixing in the ventilated area is attained.

### Staff:

I. -R. Cristescu  
J. Travis

### Literature:

Ioana-R. Cristescu, J. Travis, Y.Iwai, K.Kobayashi, D. Murdoch - Simulation of Tritium Spreading in Controlled Areas After a Tritium Release, Fusion Science and Technology, 48, 464-468 (2005)



## **JW5-FT-5.20**

### **Shutdown Dose Rate at JET Tokamak – Code Benchmark**

The objective of Task JW5-FT-5.20 is to validate the computational methods for shutdown dose rate calculations through the comparison with measured dose rates that will be recorded in a dedicated benchmark experiment on JET. The experiment, to be conducted by an experimental team of ENEA Frascati, is scheduled for D-D operation of JET only in 2006. The task schedule has been revised accordingly.

The task of FZK will be to analyse the experiment by means of the rigorous 2-step (R2S) approach, developed at FZK for the Monte Carlo based calculation of shut-down dose rates in 3D geometry [1].

The related task deliverables are on the adaptation of the JET MCNP model to the R2S requirements and pre-analysis (D4, due date: February 2006), on the R2S calculations for the benchmark experiment (D5, due date: June 2006), and on the data analysis and comparison of D1S/R2S experimental results (D6, due date: July 2006). Work on the adaptation of the JET MCNP model has not started since the related JET model (to be updated by ENEA, Frascati, for the experiment) is not yet available due to the revised task schedule.

#### Staff:

U. Fischer  
P. Pereslavitsev

#### Literature:

- [1] Y. Chen, U. Fischer, "Rigorous MCNP based shutdown dose rate calculations: Computational scheme, verification calculations and applications to ITER", Fus. Eng. Des. 63-64 (2002), 107-114.

## JW0-FT-6.1

### Impact of Tritium on the Performance of a Prototype Cryosorption Pumping Panel

This task is an essential complement to the parallel assessment of the pump performance of the ITER torus model cryopump in FZK, where the tritium fractions have been replaced by deuterium. The central objective of this task, being performed within the Task Force Fusion Technology at JET [1], is to study the interaction of tritium and tritiated gas mixtures with the panel, in terms of pumping performance, desorption characteristics and structural influences. The existing knowledge in this field is limited to qualitative results gained in other fusion devices and only one small scale phenomenological experiment. Together with the existing data for protium and deuterium, a sound assessment of any isotopic effect is aimed at.

Within this task, a Prototype Cryosorption Pump (PCP) was designed, manufactured and installed into an existing cryogenic forevacuum module of the Active Gas Handling System (AGHS) at JET. The PCP was first used in 2004 as regular pump during TTE, and then subjected to a parametric test programme [2]. The measured pumping behaviour for tritium and an equilibrated equimolar D<sub>2</sub>-T<sub>2</sub> mixture was excellent. It became obvious that the sticking coefficient for pumping tritium is close to unity, near the maximum possible. The pumping mechanism of tritium was clearly identified to be condensation. An important consequence of condensation pumping of T<sub>2</sub> is the potential risk of blocking the charcoal pores by formation of an ice layer on top. In this case the pumping speed for the species which have to be pumped by sorption, especially He, may drastically diminish. It has been agreed that a second experimental campaign will be started to better characterize and quantify this competing pumping situation.

The present reporting period was characterized by an extensive shut-down time of JET as well as a maintenance and non-availability phase of the cryoplant, and clear prioritization of AGHS to torus intervention work, so that the planned experiments have just started in December 2005.

Table 1: Air-purge results for conditioning of the PCP, after the tritium campaigns in 2004. Each cycle comprised filling with normal air and pump-down to medium vacuum (~ 100 mbar).

Air-purge cycle	Released activity [GBq]
#1	7.49
#2	7.96
#3	7.58
#4	1.16
Total	24.19

In preparation of the experiments, the PCP, which has seen a cumulative amount of ~ 0.3 g of tritium during the 2004 campaigns, was re-conditioned, first by air-purging and subsequent pump-down, in a later stage by bake-out to 475 K. By normal air purge, an initial activity in the order of ~ 8 GBq was measured for the whole pump filling. After only a few air purge cycles, the inventory could be reduced by one order of magnitude without any baking, see Table 1.

In September 2005, a first vacuum bake (at pressures between 0.1 and 0.01 mbar) was performed at 150 °C over one shift, which released 65 GBq. Over week-end (the PCP was pumped, but active heating switched off so that the temperature gradually decreased to ambient) additional 56 GBq were released. Upon that, a second vacuum bake (at same pressure levels as before) was performed at 200 °C (the maximum allowed for PCP due to the temperature sensors used) during ~ 4 hours, but no additional activity release was monitored. Following that, the residual activity was regarded to be sufficiently low, so that leak tests could be concluded successfully. Since then, no additional activity release was found. This means, the total amount of released activity was ~ 150 GBq and seems to have reached completion. A detailed treatment of this issue is expected from the detritiation assessment (via TDS measurements, total combustion, and isotope exchange with moist air) of the PCP panels after pump dismantling.

Staff:

Chr. Day

H. Jensen

D. Brennan (UKAEA)

P. Camp (UKAEA)

Literature:

- [1] C. Grisolia, S. Rosanvallon, N. Bekris, J. Braet, D. Brennan, B. Brichard, P. Coad, G. Counsell, I. Cristescu, Chr. Day, G. Ionita, J. Likonen, A. Perevezentsev, G. Piazza, C. Poletiko, A. Semerok, JET contributions to ITER technology issues, ISFNT-7, Tokyo, Japan, May 2005.
- [2] Chr. Day, D. Brennan, P. Camp, H.S. Jensen, G. Jones, A. Mack, A. Miller, Fusion Science and Technology 48 (2005) 29-34.



# **Heating Systems Technology Project**



## TW5-THHE-CCGDS2

### EC Coaxial Cavity Gyrotrons and Test Facility: Design, Support to the Industrial Development and Preparation of Technical Specifications

#### TW5-THHE-CCGDS2 D 1

#### Supervision of the Industrial Partner during the Procurement Contracts

In cooperation with European research institutions (CRPP, Lausanne; TEKES, Helsinki) and European tube industry (Thales Electron Devices (TED), France), the development of a 2 MW, 170 GHz coaxial cavity gyrotron, suitable to be operated in continuous wave (CW) as could be used for ITER, is going on. In summer 2004, EFDA has placed a contract at TED for the fabrication of a first industrial prototype of a 2 MW, CW, 170 GHz coaxial cavity gyrotron. The specifications and the design of components are based on results obtained on the 165 GHz coaxial cavity gyrotron at FZK [1,2]. Within the cooperation, the physical specifications and the design of the components for the industrial prototype are elaborated by the research institutions, and TED is responsible for the technological aspects. In the meantime all components have been designed and are under fabrication. A superconducting magnet has been ordered, and a test facility for the 2 MW, CW gyrotron is under construction at CRPP Lausanne. The first prototype is expected to be delivered in spring 2006, followed by the tests which may start in summer 2006.

In parallel to the industrial work, an experimental pre-prototype 170 GHz coaxial cavity gyrotron has been operated at FZK in order to verify the design of critical components of the prototype tube under relevant conditions. This experimental pre-prototype tube has the same cavity and the same quasi optical (q.o.) RF output system and a very similar electron gun. Due to limitation of the magnetic field to about 6.7 T, the operating voltage had to be reduced to values below 80 kV in order to be able to excite the  $TE_{34,19}$  mode at 170 GHz.

To validate the design and fabrication of the q.o. RF output system and its components a low power test facility with a 170 GHz,  $TE_{34,19}$  mode generator with very high mode purity has been prepared at FZK.

#### 2 MW, CW 170 GHz prototype of a coaxial cavity gyrotron for ITER

All components have been specified and the design has been finished. Based on this, TED converted the physical design into technical drawings which have been checked by the research institutions. Recently, as the last component, a collector suitable to dissipate 2.4 MW, CW power of the remaining electron beam has been designed. An axial sweeping coil system has been foreseen. A major problem is related to the influence of eddy currents in the collector walls on the beam sweeping along the collector surface. An aggravating factor is that the influence of the eddy currents is dependent on the temperature of the collector wall which is not known very well. In Fig. 1 the time averaged power density along the collector wall as designed for the prototype tube is shown for a sweeping frequency of 7 Hz.

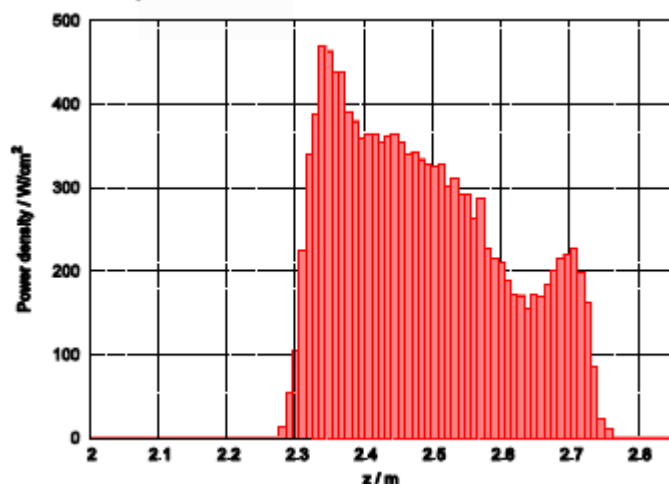


Fig. 1: Time averaged distribution of the power density along the collector wall for a total power of 2.4 MW and a sweeping frequency  $f_{\text{sweep}} = 7$  Hz.

## 170 GHz experimental pre-prototype coaxial cavity gyrotron

The pre-prototype gyrotron is of modular type, allowing an easy replacement of components (Fig. 2). The pulse length is limited to several ms mainly due to cooling conditions. The pre-prototype tube has the same cavity and the same quasi optical (q.o.) RF output system as designed for the industrial tube and a very similar electron gun. Since, as already mentioned, the magnetic field is limited to about 6.7 T in the available SC-magnet, the operating voltage had to be reduced to values below 80 kV in order to be able to excite the  $TE_{34,19}$  mode at 170 GHz. Due to the operation at lower voltages in comparison to the prototype, somewhat reduced RF output power is expected, depending on the magnetic field finally obtained.

### Experimental results

The experimental operation of the pre-prototype tube has been continued in 2005. The results obtained are summarized as follows:

- Parasitic low frequency oscillations:

Simulations of electromagnetic resonances of the whole gyrotron geometry have been performed with the code "CST microwave studio". The calculated resonance frequencies are in good agreement with the measured values. Further simulations with the code will be done for the geometry of the industrial prototype tube.

- Electron gun and electron beam:

The performance of the electron gun and electron beam has been found to be in agreement with the design objective as far as the properties have been observable during the gyrotron operation. Stable operation up to  $I_b \approx 80$  A and  $U_c \approx 80$  kV has been obtained without any indications of beam instabilities.

- Cavity and RF generation:

The nominal co-rotating  $TE_{-34,19}$  mode at 170 GHz has been excited stably in single-mode operation over a wide parameter range. However, the experimental results are not fully in agreement with calculations. In particular, the observed mode sequence is more dense than predicted by simulations, thus limiting the excitation range of the nominal mode to lower voltages than expected. An additional reason for the relatively low beam voltage is the magnetic field which is limited in the available SC-magnet to about 6.7 T. Recently, the influence of alignment of the electron beam, relative to the cavity axis, on the gyrotron operation has been studied. For that, the axis of the magnetic field has been aligned with respect to the mechanical axis of the gyrotron by measuring the concentricity of the electron beam relative to a circular capacitive probe placed on the cathode side of the cavity. In case of best align-

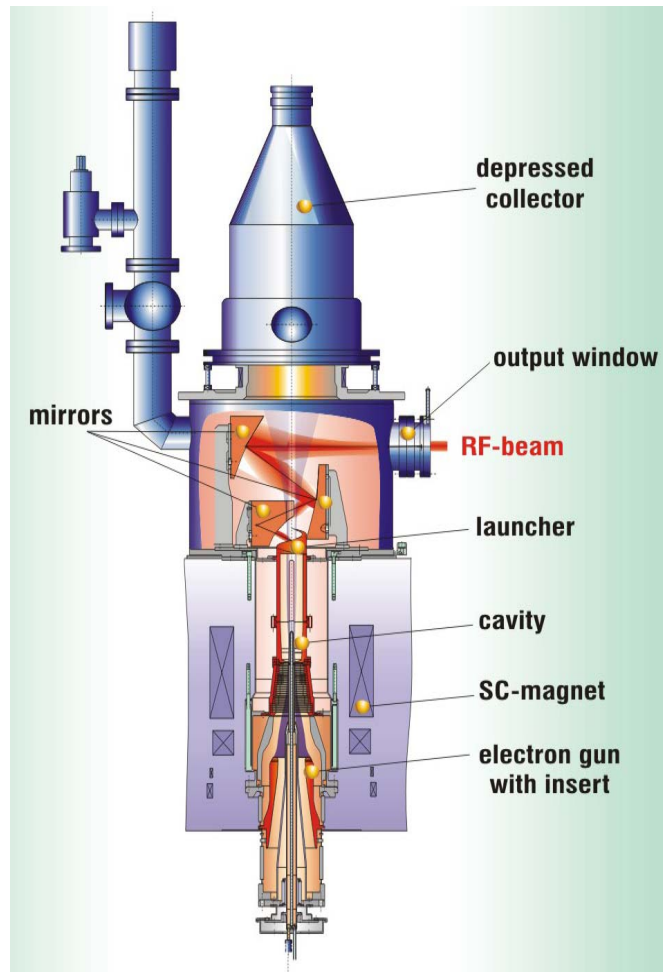


Fig. 2: View of the 170 GHz pre-prototype coaxial cavity gyrotron.



ment conditions the efficiency increased slightly from 20 % to 21.5 % due to a small rise of the beam voltage by  $\sim 1$  kV to 75 kV (Fig. 3). However, the observed mode sequence and range of oscillation is still in disagreement with theory. Further investigations, both experimental and theoretical, are needed.

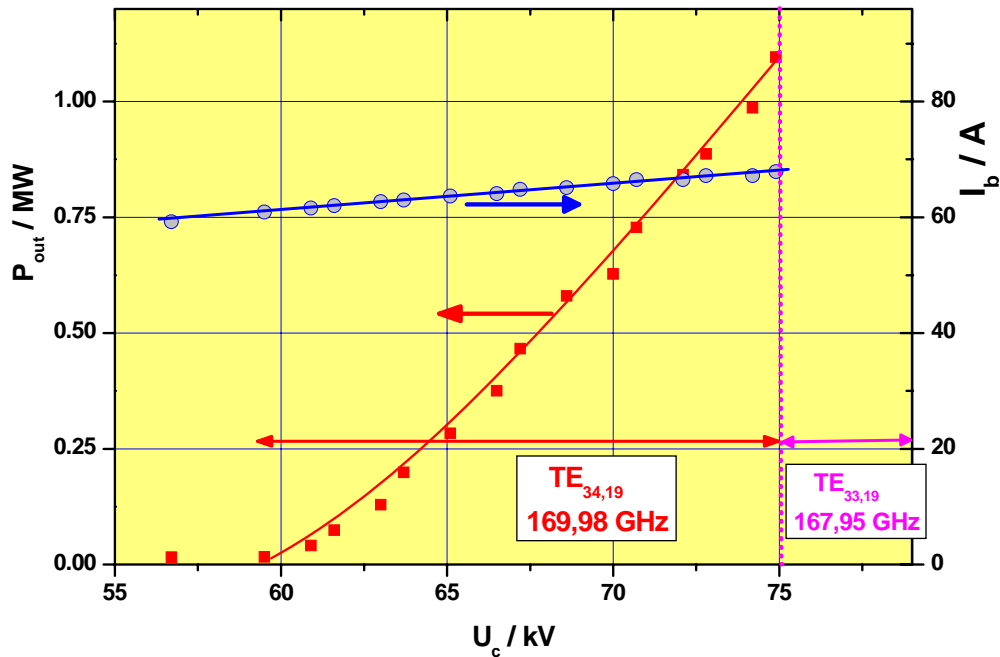


Fig. 3: RF output power and beam current versus cathode voltage at  $B_{cav} = 6.718$  T.

- Quasi-optical RF output system:

The performance of the q.o. RF output system has been studied both at low power levels ("cold") and at high power ("hot") with the gyrotron. A good agreement has been found between the "cold" and "hot" measurements and calculations. A mistake in the optimization of the mirrors has been discovered. Due to this, it became necessary to redesign the mirrors. "Cold" measurements performed with the redesigned mirrors are in good agreement with the design calculations confirming the reliability of calculations and the accuracy of fabrication. In the meantime, the correct mirrors have been installed in the pre-prototype tube. In the experiments to be performed next, the power distribution of the RF output beam and the amount of stray radiation will be measured.

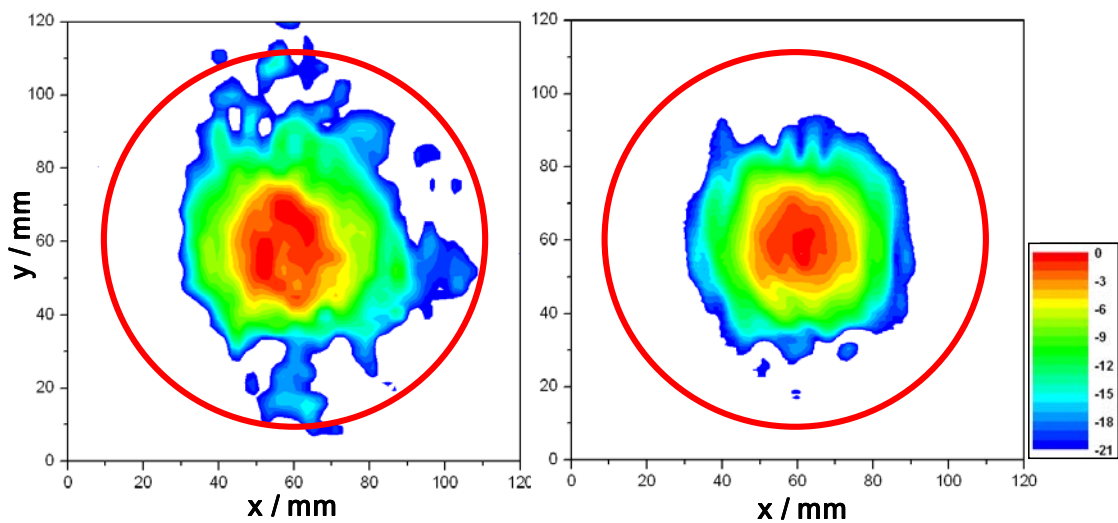


Fig. 4: Field pattern in the plane of the RF output window. Left side: calculations, right side: "cold" measurements. The aperture (96 mm) of the window is indicated

A low power test facility equipped with a very high quality  $TE_{34,19}$  mode generator is available for validation of the components of the RF output system manufactured for the first prototype gyrotron as well as for testing improved designs which are under development.

### **Summary and outlook**

The gyrotron performance in dependence of the accuracy of alignment has been investigated. A small increase of the efficiency has been obtained, however, the discrepancy in comparison with theory remained and requires further studies.

New mirrors for the q.o. RF output system have been designed, manufactured and tested at low power. The results are in good agreement with the design performance confirming both the design calculations and the fabrication accuracy. The facility for performing the low power tests is equipped with a very high quality 170 GHz,  $TE_{34,19}$  mode generator. The facility is ready for verification of the components of the RF output system under fabrication for the industrial tube. A further optimization of the launcher with a more accurate design code is in progress. As a result, an increase of the Gaussian content of the RF output beam and a reduction of the microwave stray losses is expected.

The design of a collector capable to dissipate a beam power up to 2.4 MW in CW has been elaborated. The wall loading is within the technical limits, thus the design has been accepted by TED for the prototype tube. The distribution of the power along the collector wall has been found to be quite sensitive to variations of the wall temperature. Thus, further optimization is needed to reduce this dependence.

### Staff:

A. Arnold (Uni Karlsruhe)  
G. Dammertz  
S. Illy  
J. Jin  
K. Koppenburg  
W. Leonhardt  
M.V. Kartikeyan (guest scientist)  
H.R. Kunkel  
D. Mellein  
B. Piosczyk  
T. Rzesnicki  
M. Schmid  
W. Spiess  
J. Szczesny  
M. Thumm  
R. Vincon  
X. Yang

### Literature:

- [1] B. Piosczyk, A. Arnold, G. Dammertz, R. Heidinger, S. Illy, J. Jin, K. Koppenburg et al., "Development of Steady-State 2 MW, 170 GHz Gyrotrons for ITER", 20th IAEA Fusion Energy Conf., Vilamoura, Portugal, Nov. 1-6, 2004
- [2] O. Loukscha, B. Piosczyk, G. Sominski, M. Thumm, D. Samsonov, "On Potentials of Gyrotron Efficiency Enhancement: Measurements and Simulations on a 4 mm Gyrotron", accepted for publ. in IEEE Trans. Plasma Science, 2005
- [3] B. Piosczyk, S. Alberti, D. Bariou, P. Benin, T. Bonicelli, G. Dammertz, O. Dumbrajs, et al., "Progress in the Development of the 170 GHz Coaxial Cavity Gyrotron for ITER", Proc. of VI int. workshop on "Strong microwaves in plasmas", 25 July – 1 August 2005, Nizhny Novgorod, Russia

- [4] B. Piosczyk, G. Dammertz, O. Dumbrajs, S. Illy, J. Jin, W. Leonhardt, G. Michel, et al., A 2 MW, 170 GHz coaxial cavity gyrotron – experimental verification of the design of main components ; 3rd IAEA technical meeting on "ECRH Physics and Technology for ITER", 2 - 4 May, 2005, Como, Italy
- [5] B. Piosczyk, T. Rzesnicki, G. Dammertz, O. Dumbrajs, S. Illy, J. Jin, W. Leonhardt et al., "170 GHz, 2 MW, CW Coaxial Cavity Gyrotron - experimental verification of the design", 30th Int. Conf. Infrared and Millimeter Waves, September 19-23, 2005, Williamsburg, USA.
- [6] T. Rzesnicki, J. Jin, B. Piosczyk, M. Thumm, G. Michel, D. Wagner, "170 GHz, 2 MW Coaxial Cavity Gyrotron - design verification of the new RF output system", 30th Int. Conf. Infrared and Millimeter Waves, September 19-23, 2005, Williamsburg, USA.
- [7] G. Dammertz, S. Illy, B. Piosczyk, M. Schmid, D. Bariou, "Collector sweeping systems for high power gyrotrons", 30th Int. Conf. Infrared and Millimeter Waves, September 19-23, 2005, Williamsburg, USA.
- [8] J. Jin, M. Thumm, B. Piosczyk, G. Dammertz, T. Rzesnicki, "Investigation of an Advanced Quasi-Optical Mode Converter for a Coaxial Gyrotron", 30th Int. Conf. Infrared and Millimeter Waves, September 19-23, 2005, Williamsburg, USA.
- [9] B. Piosczyk, G. Dammertz, R. Heidinger, K. Koppenburg, M. Thumm, "Development of multi-megawatt gyrotrons at Forschungszentrum Karlsruhe", Symp. on Fusion Engineering 2005, Sept. 26-29, 2005, Knoxville, USA,
- [10] C. Lievin, S. Alberti, A. Arnold, D. Bariou, P. Benin, T. Bonicelli, G. Dammertz et al., "Development of a 2-MW, CW Coaxial Gyrotron at 170 GHz for Electron-Cyclotron-Resonance-Heating in ITER", 5th IEEE Int. Vacuum Electron Sources Conference, April 2005, Nordwijk, Holland.

## **TW5-THHE-CCGDS2 D 6**

### **Upgrading of the Gyrotron Test Facility at FZK**

The deliverable D6 is part of the EFDA Technology work programme "Coaxial Cavity Gyrotron and Test Facility". In this frame, the high-voltage test facility at FZK will be upgraded for long pulse operation of 2 MW CW coaxial cavity gyrotrons and for short-pulse operation of Gyrotrons of even higher output power (about 3-4 MW). The power supplies have to be suitable to be operated at cathode voltages of  $-65$  kV (this is the voltage needed for gyrotrons with energy recovery) and at beam currents up to 80 A for about 10 s.

For short pulse operation (a few ms) of 3-4 MW gyrotrons (i.e., for DEMO), the HV power supply should be suited for operation at a cathode voltage of about  $-90$  kV and a beam current of 80 A. With energy recovery, an output power of about 3.5 MW would be possible.

#### **Results during 2005**

During experiments with the coaxial gyrotron it had been proven that the regulation tube of the HV power supply is able to handle currents of 80 A without harmful parasitic oscillations. At the beginning of this year, a study was launched in order to check the feasibility and the cost of the upgrade of the HV power supply with the above mentioned specifications. The study was performed by FEAG, and presented end of July 2005. Two key problems have been identified:

- 1.) The existing transformers are exposed to currents which are 2.7 times the design values. This leads to winding stresses which are 7 times higher than normal. No guarantees can be given by the suppliers for regular operation at such currents. However, during discussions with the company it was pointed out that many transformers are operated in pulsed conditions with similar stresses, and this was thought not to be a severe problem.
- 2.) A more serious problem was seen in the low frequency mains disturbances that could be caused on the entire 20 kV mains at FZK by the modified 12-pulse Thyristor HV-Supply. It was strongly recommended to perform measurements on this problem and to obtain a formal permission for the new operating parameters by the energy supplier EnBW, who are responsible for the energy distribution inside FZK.

The appropriate measurements have been performed by EnBW and by FZK. The measurements have shown that the mains disturbances will be within acceptable limits. On December 8, 2005 EnBW has confirmed that there are no objections on their part for the operation of the modified HV-power supply.

A "Single Tender Action" has been launched and the order for the upgrade will be issued as soon as the tender is received.

#### **Perspectives**

The work to be performed in 2006 is clearly described in the study report by FEAG. The work will be started at the beginning of 2006. There is a lead time of about 4 months for the delivery of the major components. The integration into the existing system is scheduled for May 2006, the commissioning and testing of the system for the first half of June.

#### **Staff:**

G. Dammertz  
M. Schmid

## TW3-THHN-NB-RF Cryopumps for the NBI-Testbed at IPP Garching

### Background and Objectives

IPP Garching is being charged to develop an efficient and reliable negative ion source for the ITER Neutral Beam Injection System. It was agreed to use the existing NBI-testbed L6 at IPP for this development work. However, with respect to pulse length, an upgrading of vacuum pumping was required. It has therefore been decided to replace the existing small capacity titanium sublimation pumps by a cryopump system to be connected with the ASDEX upgrade cryosupply. FZK has been responsible for this upgrade and could successfully finish the re-assembling and commissioning.

Table 1: Technical Specifications for the Cryopumps

Gas throughput:	$\sim 0 - 3 \text{ Pa m}^3 / \text{s} (\text{H}_2)$
Pumping speed of one cryopump:	$\sim 350 \text{ m}^3 / \text{s} (\text{H}_2)$
Pulse length of gas load:	3600 s
Pumping capacity:	$10^5 \text{ Pa}\cdot\text{m}^3$
Operating pressure:	Several $10^{-5}$ mbar
Max. leak rate (per pump)	$1 \times 10^{-7} \text{ Pa m}^3 / \text{s}$
Cryogenic media:	Liquid helium at 4.45K, 1.25 bar Liquid nitrogen at 80K, 1.3bar
Dimensions:	ca. 4400 x 1500 x 260mm (h x w x l)

The scope of the work was the development and manufacturing of a system of two cryopumps including the required cryo-, valve and intermediate storage systems for connection with the existing ASDEX cryo-plant according to technical specifications [1].

### Design work for the cryopumps and system description

The detailed design of the cryopumps has been finalised and the manufacturing drawings were generated using CATIA 5 to tender the fabrication of the cryopumps. Based on the thermodynamic and vacuum technological design of the cryopumps, the necessary cryogenic needs to fulfil the cooling requirements during all operation scenarios of the cryopumps have been met. Thus, the design of the cryosupply system for the independent operation of both cryopumps has been finalised, tendered and placed in order. The cryosupply system consists of the liquid helium cryostat, the valve box and the transfer lines for the cryogenic liquids and off gas systems. For all these components FZK supervised the manufacturing and was carrying out the quality control.

### Delivery of the cryopumps and commissioning at the test facility

Both cryopumps have been manufactured in parallel and the possibility to use a cryostat at the premises of the fabricator was taken to make the first cold tests to 77 K before they have been delivered to IPP. AT IPP the cryopumps have been integrated into the Neutral Beam Test Facility. After the successful final acceptance tests including a cold test and leak testing

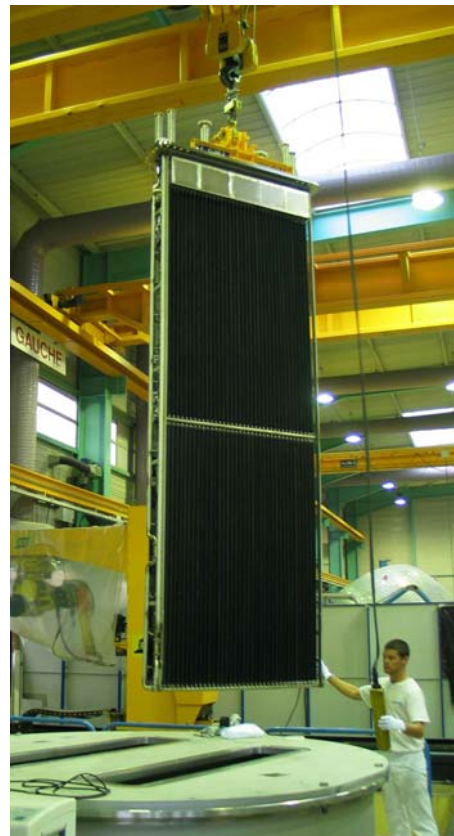


Fig. 1: IPP Cryopump when mounting into the test vessel

at 77 K the contract with the fabricator of the cryopumps could be finished and the integration of the cryosupply lines in the facilities of IPP was started.

### Commissioning of the helium cryostat and valve box



Fig. 2: 3D scheme of the cryostat with valve box for cryosupply.

The cryopumps are cooled by forced flow of liquid helium supplied by a circulation blower integrated into the helium cryostat. To ensure a proper mounting and operation of the circulation blower at low temperatures a preliminary examination of the operation was done by FZK. These tests with liquid nitrogen have been carried out at the manufacturers premises and could be effectually finished -- end of spring 2005.

### Integration and commissioning of the cryosupply in the test facility

Further tasks like the integration of an electrical break in the liquid helium transfer line and some changes in the run of the line were successfully finished. Proximately, the helium cryostat and the liquid nitrogen supply for the radiation shielding of the cryopumps were delivered and have been implemented into the test facility. A preliminary test and commissioning of the helium cryostat with the valve box was carried out without the cryopumps. This was done to test the operation of the cryosupply system and to simulate and improve the following operation scenarios with the cryopumps.

### Final commissioning tests of the cryopump system

The final tests have been carried out using the whole cryosupply system with both cryopumps in operation at the same time and also with each cryopump operated itself. For the main tests regarding the specification for

the cryopumps each cryopump has been operated alone. To demonstrate the compliance to the requirements given in the specification a predefined gas throughput of 20 mbar-l/s hydrogen ( $H_2$ ) over a period of 90 minutes has been pumped and the pumping speed has been measured during this period. The result is depicted in the diagram below. The pumping speed of about  $330 \text{ m}^3/\text{s}$  dropped less than 10% during the test, ending up with a gasload of more than 100 bar-l, that fulfils the requirements very well (see Fig. 3).

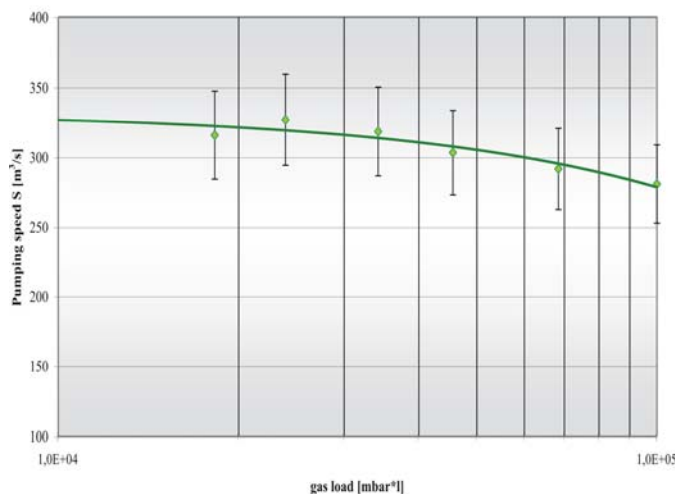


Fig. 3: The measured pumping speed during a period of 90 minutes fulfils the requirements of the test facility of IPP successfully.

## Detection of heat loads

The determination of the refrigeration heat loads of the cryopumps has been done to review the assessment of the heat loads included in the offer by FZK sent to IPP Garching. After finalizing the detailed design of the cryopumps an extensive calculation of the heat loads has been carried out. Herein the radiation heat loads have been calculated and the effect of the gaseous heat conduction during the nominal pumping and the regeneration of the cryopanel have been predicted. This procedure used various experimental results of the TIMO facility, so that the reliability of the calculations was significantly improved.

The radiation shieldings of the cryopumps are cooled by the vaporization of liquid nitrogen from a bath integrated within the cryopumps and supplied by a storage tank. The consumption has been detected by the measurement of the filling level in the storage tank and cross-checked with the measurement of the nitrogen off-gas flow. The calculated heat load on the radiation shieldings agrees very well with the measured heat load, see Table 2.

Table 2: Measured and calculated heat load on the radiation shielding of one cryopump.

77K circuits	Calculated	Measured
Heat load on the LN shielding	1900 W	1850 W

The determination of the heat loads of the 4.5K circuits requires to separate the heat load by the cryogenic supply - mainly given by the circulation blower - from the heat load given by the cryopumps. The integrated valve box gives the possibility to run both cryopumps together and also to operate each of them alone. Thus the measured overall heat loads that are including the consumption by the cryopumps as well as the consumption by the supply system consisting of the circulation pump and the cryostat with the valve box could be split into the contributions of each component. The liquid helium consumption of the cryostat is about 7 W which is a very good value for this size and design of cryostat. The resulting heat load on the helium circuits with the cryopanel is 38 W which is close to the calculated value of 41W. The heat loads are summarized in Table 3.

Table 3: Measured heat loads of the cryopump system and for the helium circulation blower.

4.5k circuits	Two cryopumps +circulation	One cryppump +circulation pump	One cryopump	Circulation blower
Measured heat loads	110 W	72 W	38 W +- 8 W	34 W +- 8 W
<i>Calculated heat load for one cryopump: 41 W</i>				

## Commissioning of the circulation blower

The detection of the heat loads together with the thermo-hydraulic behaviour of the cryopumps rendered also the efficiency of the circulation pump. The efficiency of the circulation blower is a very important design parameter for the future development of cryosupply systems and is also useful for the design of the ITER cryoplants where several of related blowers will be installed. The heat in-leak of the blower was determined with 34 W which is close to the heat load by one cryopump and shows the importance of the efficiency, which was determined to be about 50%. This efficiency agrees well with the results of other investigations on the properties of cryogenic circulation blowers of this design.

## Further Activities

The cryopump system was handed over to the NBI group of the Max Planck Institute IPP in summer 2005; since then it has been successfully in operation. The Neutral Beam Test Facility will be finally equipped with further beam line components to test different ion beam sources during ITER relevant time scales. The biggest improvement of the facility was realized by

the installation of the FZK cryopumping system to operate the beam line during long pulse operations of up to several hours.

Staff:

Chr. Day  
M. Dremel  
H. Jensen  
A. Mack  
P. Pfeil  
R. Simon

Literature:

- [1] M. Dremel, A. Mack, Chr. Day, H. Jensen, Cryosorption pumps for a Neutral Beam Injector test facility, Proc. CEC/ICMC, Keystone, CO, US, August 2005.



**EFDA/04-1185**

**The First ITER NB Injector and the ITER NB Test Facility: Progress in the Design**

**Background and objectives**

The design of the Neutral Beam (NB) system to be used in ITER and the results of the relevant R&D are described in the documents, which were produced at the end of ITER-EDA (July 2001). FZK is reviewing the design of the cryopump for the test facility of the first ITER NB Injector. Based on the final reports of the tasks TW1-TTF/D465-3 (February 2002) and TW3-THHN-IITF1 (November 2004, [1]), FZK is working further on the technical assessment and detailed design of the cryopumps and the conventional associated vacuum systems (forepumps, turbomolecular pumps). The updated key NB design-parameters and required pressures by given gas flows are summarized in Table 1.

Table 1: Design parameters.

Power delivered to the plasma per injector	16.5 MW
Beam Energy	1 MeV
Ion Species	H <sup>+</sup> , D <sup>+</sup>
Accelerated ion current	40 A
Average accelerated ion current density	200 A/m <sup>2</sup>
Current density uniformity over the extraction area	±10 %
Source filling pressure	0.3 Pa
Hydrogen source gas flow (max. flow)	7.5 Pa·m <sup>3</sup> /s
Hydrogen gas flow from neutralizer	31.6 Pa·m <sup>3</sup> /s
Hydrogen gas flow to Residual Ion Dump (RID)	2.5 Pa·m <sup>3</sup> /s
Required pumping velocity for hydrogen	3800 m <sup>3</sup> /s
Required pumping velocity for deuterium	2600 m <sup>3</sup> /s
Pulse lengths	≥ 3600 sec.

**Cryopumping concept for the Neutral Beam Test Facility**

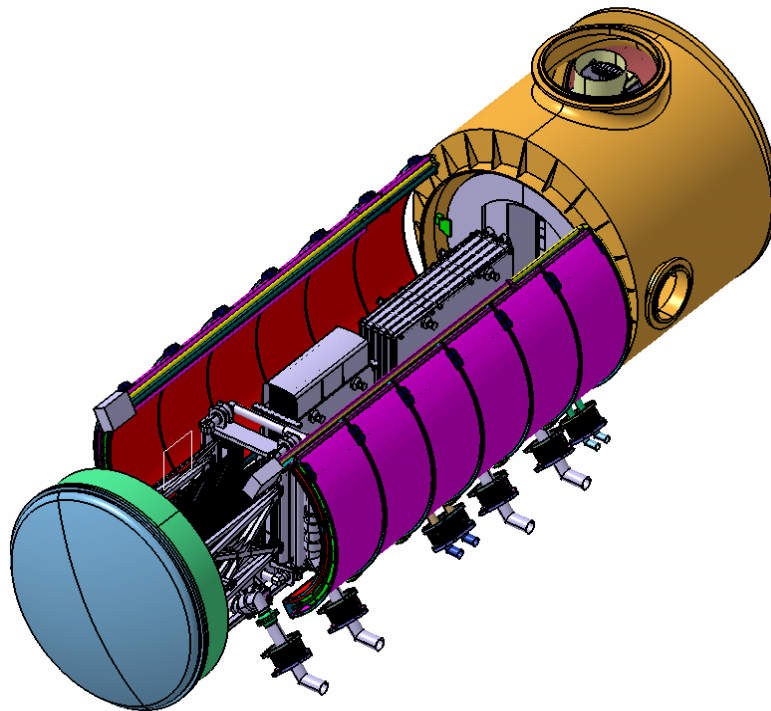


Fig. 1: CATIA5 drawings of the cryopump and the beam line components of the NBTF during the first phase in split configuration with top access to the beam line components.

The ITER relevant cryopump has a cylindrical shape opened to the bottom and surrounding the beam line components from top and sides. To improve the access to the beam line components during the first phase of the Test Facility for the first ITER Neutral Beam injector the cryopump will be split into two halves and will be installed on the sides of the beam line vessel (BLV) [2].

Thus, the top access through a large flange will strongly improve the assembly and disassembly procedures at the Neutral Beam Test Facility (NBTF). The ITER relevant design of the cryopump and the requirements for remote handling at the ITER site have been included in the design

of the cryopump for the Test Facility. For this reasons the entire cylindrical cryopump can be separated into six submodules to transport them with the transfer casks at ITER site. In each of these 6 submodules there are 36 cryopanel installed of which 18 are in a series connection. The design of the cryopump of phase 1 with the cryopump halves is shown in Fig. 1. The cryopump for phase 2, which includes the full requirements of the ITER relevant design for the ITER Neutral Beam injector, is depicted in Fig. 2.

### Cooling principles

The cryoplant design proposed by CEA Cadarache has foreseen a cooling of the cryopanel with a forced flow of ScHe at about 4.5 K inlet temperature and 6.5 K outlet temperature at a pressure of 4 bar. To reduce the heat-load, the cryopanel are only coated on the back-side facing to the 80 K walls, the front side facing to the blackened chevron baffle will be electro-polished.

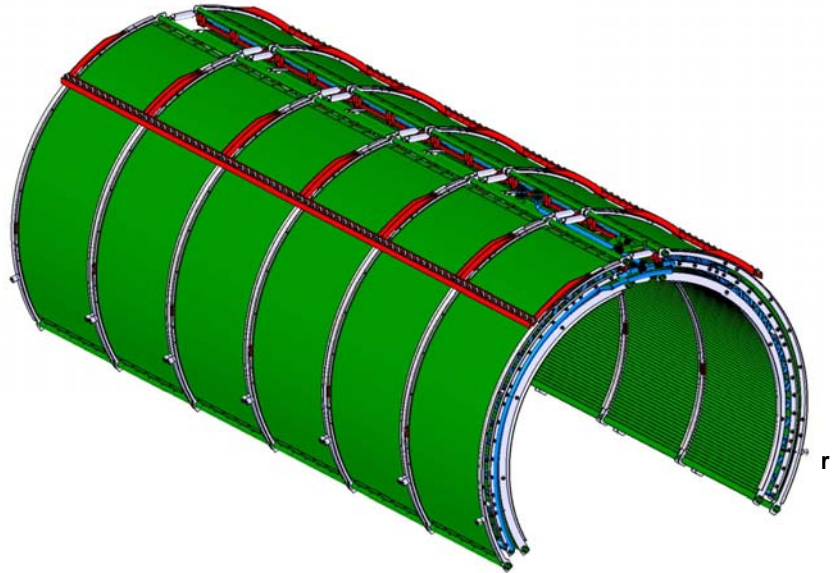


Fig. 2: CATIA5 drawing of the final design of the cylindrical cryopump for the ITER Neutral beam injector.

The radiation shields facing the outside in the direction of the BLV are closed radiation walls in quilted design. To the inner of the beam line, where the beam line components are installed, a blackened chevron baffle is integrated. Stainless steel plates that are cooled passively by heat conduction include front endings and bottom openings to protect the entire 4.5 K circuits from high temperature radiation. The shieldings are cooled by a forced flow of GHe at an inlet pressure of 17 bar and an inlet temperature of 68 K. The outlet temperature can increase up to 93 K, as, contrary to ITER, a Brayton cycle for cooling the shieldings of the cryopump is foreseen at NBTf [3].

### Design stage of the cryopump for the first ITER NB injector

Beginning from the former concept drawings of the ITER relevant cylindrical shaped cryopump, the detailed design of the cryopumps for both phases has been developed using CATIA5 for the construction, provided by the intense use of ANSYS strain analyses on the entire cryopump. Here, the mechanical and thermal loads on the cryopump have been simulated and critical design parameters could be improved in parallel to the construction drawings. Thus, the design of the first ITER relevant cryopump for the neutral beam injector has been far developed during 2005 [4].

### Thermo-hydraulic assessments

The detailed design stage of the cryopump determines the pipe routing of the cryogenic circuits of which thermo-hydraulic calculations about the pressure drop across the cryopumps were made. Based on these calculations the pipe routing has been improved to guarantee a reliable fluid distribution across the large cryopump, and the cryopant was adopted to thermo-hydraulic behaviour of the cooling circuits.

## **Updated thermal loads onto the cryogenic cycles**

For the different designs and all operation scenarios, the former calculations about the thermal loads have been adapted to the design changes during the ongoing task. An additional heat load was determined by the electron flux from the neutralizer entrance due to the impinging high-energy ion beam. Due to this, the resulting thermal loads onto the shielding are increased between 7.7 kW and 12 kW depending on the beam line arrangement. The resulting heat load during operation of the beam line can therefore reach about 30 kW. The heat loads on the 4.5 K circuits are increased by this effect from 160 W to a maximum of 260 W during the operation of the beam line. The needed changes on the cryopump and the cryo-plant have already been reintegrated during the design investigations.

## **Assessment of the gas distribution in the beam line vessel**

A neutral beam of molecules with a high energy is realized by the ionisation and subsequent acceleration of the molecules. The ionisation is done in the source by introducing a gas flow into a plasma chamber. The ionized molecules are afterwards accelerated up to high energy levels, but to introduce them into the torus plasma they must first pass the magnetic field surrounding the plasma. Therefore they need to be neutralized which is done by passing the ion beam through a gas cloud in the neutralizer. To ensure low ionisation losses of the neutralized beam the gas density after the neutralizer must be small. Finally the several gas sources and the cryopump lead to a gas profile in the neutral beam injector which determines the quality and efficiency of the neutral beam. Several investigations were done to calculate and analyse the gas profile to predict the behaviour of the beam line and, by that, improve the components. FZK started within this task calculations using the MOVAK3D computer code and ITERVAC code. ITERVAC can be a useful tool to predict the gas distribution of the neutral beam facility, because it covers gas flow calculations for arbitrary Knudsen numbers and geometries, as it is the fact in and around the beam line.

## **Experimental tests on hydrogen pumping with conventional forepumping systems**

The use of Roots pumps for the pump-down of the beam line vessel after openings and after a regeneration of the cryopump was proposed by FZK in the final report of TW3-THHN-IITF1. This proposal was based on assumed pumping speeds for hydrogen for the mechanical pumps and these pumping speeds were not proved. Therefore in a close co-work with the industry the behaviour for hydrogen pumping for combinations of screw and Roots pumps has been detected to give a more reliable and now detailed proposal about the fore-pumping system that would fulfil the requirements given at the NBTF.

## **Further Activities**

Based on the final reports of the previous task, the detailed design of the cryopump has been developed and was complemented by Monte Carlo simulations, thermo-hydraulic calculations and FEM analysis, as required. The work on the detailed design will go on to finalize a set of CATIA5 drawings for the cryopumps of both phases of the NBTF. The design will be based on detailed mechanical and thermal stress analysis and adapted to the results of the thermo-hydraulic assessments. A summary of the entire work will be given in the final report to be finished in 2006. FZK goes on with detailed calculations of the gas distribution for the complete injector considering molecular, intermediate and viscous flow regime by the use of ITERVAC computer code, which will be compared with Monte Carlo simulations.

Staff:

A. Antipenkov  
Chr. Day  
M. Dremel  
V. Hauer  
A. Mack  
R. Simon  
H. Strobel

Literature:

- [1] M. Dremel, The first ITER NB Injector and the ITER NB test facility: Design, EFDA Reference: TW3-THHN-IITF1, Deliverable 1.1, Cryo Pumping System, Available on: <http://efdasql.ipp.mpg.de/EUHandCD/NBI/>.
- [2] P. Zaccaria, S. Dal Bello, D. Marcuzzi, A. Masiello, J.J. Cordier, R. Hemsworth, A. Antipenkov, Chr. Day, M. Dremel, A. Mack, T. Jones, A. Coniglio, M. Pillon, S. Sandri, E. Speth, A. Tanga, V. Antoni, E. Di Pietro, P.L. Mondino, Fusion Engineering and Design 74 (2005) 255-259.
- [3] J.J. Cordier, R. Hemsworth, M. Chantant, B. Gravit, D. Henry, F. Sabathier, L. Doceul, E. Thomas, D. van Houtte, P. Zaccaria, V. Antoni, S. Dal Bello, D. Marcuzzi, A. Antipenkov, Chr. Day, M. Dremel, P.L. Mondino, Fusion Engineering and Design 74 (2005) 397-402.
- [4] M. Dremel, Chr. Day, A. Mack, H. Jensen, E. Speth, H.D. Falter, R. Riedl, J.J. Cordier, B. Gravit, D. Henry, P. Zaccaria, Fusion Engineering and Design 74 (2005) 205-209.

## **Physics Integration**



## ECR Heating and Current Drive – Step-Tunable Gyrotron Development

### 1. Introduction

Magnetohydrodynamic (MHD) instabilities are one of the main reasons for the limit of plasma confinement [1]. The stability is to a large extent determined by the distribution of plasma currents, and driving localized currents in a plasma is a very important tool to suppress current-driven instabilities and thus to optimize the performance of tokamaks. The suppression of plasma pressure limiting MHD instabilities (so called 'Neoclassical Tearing Modes') has been demonstrated successfully by localized electron cyclotron current drive (ECCD) at ASDEX-Upgrade, DIII-D and JT-60U.

The absorption of RF-waves with the angular frequency  $\omega$  is dependent on the resonance condition  $\omega - k_z v_z = \omega_c$ . Thus, the driving currents can be counteracted by an external current drive at different locations either by changing the injection angle or the RF-frequency.

For experiments on plasma stabilization at ASDEX-Upgrade (IPP Garching) with advanced electron-cyclotron-resonance heating (ECRH) and electron-cyclotron-current-drive (ECCD), multi-frequency tunable 1-MW long-pulse gyrotrons are highly needed. Two gyrotrons have been ordered by IPP Garching from "Gycom" in Russia. The first gyrotron operates as a two-frequency gyrotron at 105 GHz and 140 GHz (the single disk window is matched to these frequencies), the second one is designed as a multi-frequency gyrotron with different frequencies between 105 GHz and 140 GHz. As operating mode, the TE<sub>22,8</sub>-mode was chosen at 140 GHz. The frequency of 105 GHz corresponds to the TE<sub>17,6</sub>-mode [2-6].

### 2. Accompanying work at FZK

The TE<sub>22,6</sub>-gyrotron, existing at FZK, has been modified to operate in the TE<sub>22,8</sub>-mode like the industrial gyrotron. These tests are performed in order to be able to compare the results with obtained from the industrial gyrotrons. With the short-pulse gyrotron from FZK, fast step-tunability within 1 s in a range of 15 GHz had been proven very successfully. Beam tunnel, collector and the superconducting magnet system of the TE<sub>22,6</sub> gyrotron are used in the new experiment. The resonator, the quasi-optical mode converter and the output window had to be modified.

#### Gyrotron cavity

The behavior of a new resonator including uptaper was calculated and optimized with regard to broadband behaviour for modes of and between 105 GHz to 143 GHz. Few additional modes may also be excited at higher frequencies.

#### Quasi-optical mode converter

The quasi-optical mode converter of the gyrotron consists of a dimpled-wall antenna and a beam-forming mirror system optimized for nine modes from TE<sub>17,6</sub> to TE<sub>23,8</sub>. New results show, that a decrease of the inner diameter of the waveguide strongly improves the profile of the RF beam. Further, with the help of a new code, more complex structures of the waveguide antenna wall can be calculated. Thus, it was possible to find an optimised new design where the field amplitude is strongly decreased near the cut. This reduces the losses and the stray radiation considerably [7-12].

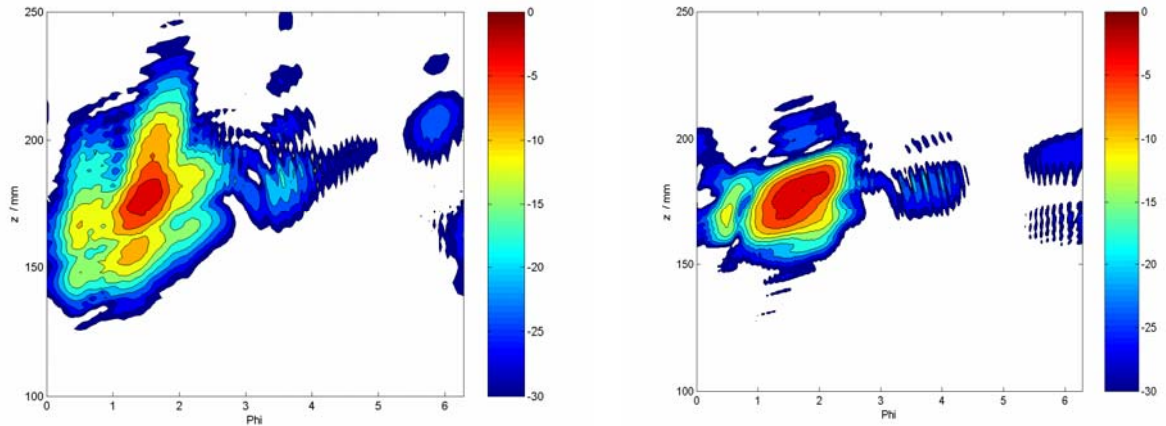


Fig. 1: Calculated radiation characteristics of the actual and improved launcher.

The first mirror is a large, quasi-elliptical one, the second and the third are phase-correcting mirrors. For further reduction of the stray radiation, the last two mirrors were redesigned. In the new design, the surfaces are curved in a way that the RF beam is matched better to the exit plane of the window. The new system will be fabricated in the beginning of 2006 and tested in low-power measurements to verify the theoretical results.

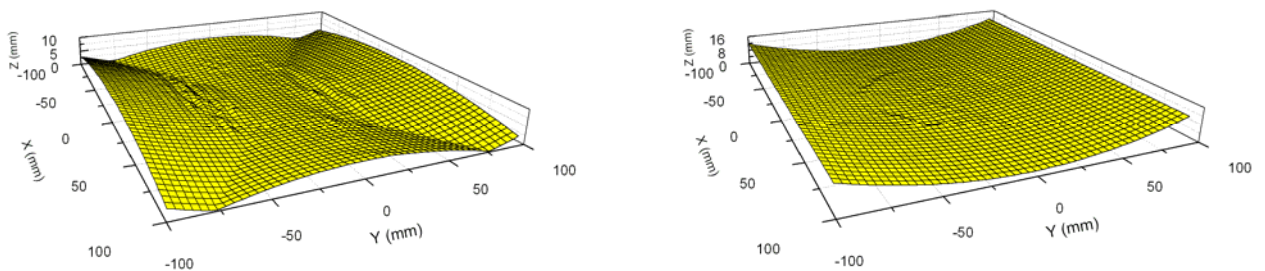


Fig. 2: Calculated surface contour of the mirror system. Left: 2<sup>nd</sup> mirror; right: 3<sup>rd</sup> mirror.

### CVD-diamond Brewster window

Efficient operation for the large number of operating modes at different frequencies is made possible by using a broadband diamond Brewster window fabricated by chemical vapor deposition (CVD). Due to the large Brewster angle, also the diameter of the disk has to be rather large in order to provide a sufficiently large aperture for the RF beam. One disk with a thickness of 1.7 mm and a diameter of 140 mm was developed by Element Six (formerly De-Beers) and already delivered. The disk had two cracks at the edge but nevertheless, there is a suitable elliptic area with a very low value of the loss tangent, which can be used for the elliptic shape of a Brewster window with an effective aperture of 50mm. An elliptic disk was cut from the original one.

Because of the ellipticity, the stresses during the brazing procedure are different from circular disks. These stresses were calculated to be higher by a factor of 1.3. To investigate whether a diamond disk will sustain these stresses, brazing tests will be performed with an existing smaller one. For this disk, the stresses are increased by a factor of 1.5 compared to an ellip-



tical one. In case of success, the 140 mm disk will be provided with copper cuffs, allowing to cool the disk at the edge.

As the diamond window will not be available during the next experimental phase (spring 2006), the gyrotron will be equipped with a quartz glass Brewster window of the same dimensions as the diamond Brewster window. This quartz glass Brewster window has been designed and manufactured in 2005.

#### Staff:

A. Arnold (Uni Karlsruhe)  
E. Borie  
H. Budig  
G. Dammertz  
I. Danilov  
R. Heidinger  
S. Illy  
K. Koppenburg  
H.-R. Kunkel  
W. Leonhardt  
D. Mellein  
B. Piosczyk  
O. Prinz  
M. Schmid  
W. Spieß  
M. Thumm  
X. Yang

#### Literature:

- [1] Zohm, H., M. Thumm: On the use of step-tuneable gyrotrons in ITER, Journal of Physics: Conference Series, 25, 274-282, 2005.
- [2] Leuterer, F., G. Grünwald, F. Monaco, M. München, H. Schütz, F. Ryter, D. Wagner, H. Zohm, T. Franke, G. Dammertz, R. Heidinger, K. Koppenburg, M. Thumm, W. Kasperek, G. Gantenbein, H. Hailer, G.G. Denisov, A. Litvak, V. Zapevalov: Status of the new ECRH system for ASDEX Upgrade, Fusion Eng. and Design, 74, 199-203, 2005.
- [3] Wagner, D., G. Grünwald, F. Leuterer, A. Manini, F. Monaco, M. München, F. Ryter, H. Schütz, H. Zohm, T. Franke, R. Heidinger, K. Koppenburg, M. Thumm, W. Kasperek, G. Gantenbein, G.G. Denisov, A. Litvak, V. Zapevalov: Current status of the new ECRH system for ASDEX Upgrade, Conf. Digest Joint 30th Int. Conf. on Infrared and Millimeter Waves and 13th Int. Conf. on Terahertz Electronics, Williamsburg, Virginia, USA, 2005, Keynote Paper, pp. 24-25.
- [4] Dammertz, G., S. Alberti, A. Arnold, V. Erckmann, G. Gantenbein, E. Giguët, R. Heidinger, J.P. Hogge, S. Illy, W. Kasperek, K. Koppenburg, H. Laqua, F. Legrand, W. Leonhardt, C. Lievin, R. Magne, G. Michel, G. Müller, G. Neffe, B. Piosczyk, M. Schmid, M. Thumm, M.Q. Tran: Development of a 1-MW, CW gyrotron at 140 GHz for electron-cyclotron-resonance-heating in fusion plasma devices, Proc. 6th IEEE Int. Vacuum Electronics Conference (IVEC2005), Noordwijk, The Netherlands, 2005, pp. 113-114.
- [5] Dammertz, G., A. Arnold, R. Heidinger, J. Jin, K. Koppenburg, W. Leonhardt, G. Neffe, B. Piosczyk, T. Rzesnicki, M. Schmid, M. Thumm, X. Yang, S. Alberti, J.P. Hogge, M.Q. Tran, I. Yovchev, V. Erckmann, H. Laqua, G. Michel, G. Gantenbein, W. Kasperek, G. Müller, K. Schwörer, O. Dumbrajs, D. Bariou, E. Giguët, F. Legrand, C. Lievin: High power gyrotron development at Forschungszentrum Karlsruhe for fusion applications, Conference Record-Abstracts, IEEE Int. Conf. on Plasma Science (ICOPS 2005), Monterey, CA, p. 110.
- [6] Koppenburg, K., A. Arnold, G. Dammertz, H.O. Prinz, M. Thumm, X. Yang: Recent results of the step-tunable 105-140 GHz, 1 MW gyrotron development at Forschungszentrum Karlsruhe, Conf. Digest Joint 30th Int. Conf. on Infrared and Millimeter Waves and 13th Int. Conf. on Terahertz Electronics, Williamsburg, Virginia, USA, 2005, pp. 291-292.
- [7] Yang, X., G. Dammertz, R. Heidinger, K. Koppenburg, F. Leuterer, A. Meier, B. Piosczyk, D. Wagner, M. Thumm: Design of an ultra-broadband single-disk output window for a frequency step-tunable 1 MW gyrotron, Fusion Eng. and Design, 74, 489-493, 2005.

- [8] Yang, X., A. Arnold, E. Borie, G. Dammertz, O. Drumm, K. Koppenburg, O. Prinz, D. Wagner, M. Thumm: New internal beam-forming mirror system for a multi-frequency 1 MW F-Band gyrotron, Proc. German Microwave Conf. – GeMiC 2005 -, Ulm, 2005, pp. 164-167.
- [9] Yang, X., A. Arnold, G. Dammertz, O. Drumm, K. Koppenburg, B. Piosczyk, D. Wagner, M. Thumm: Newly designed internal phase-correcting mirrors for a multi-frequency 1 MW gyrotron at FZK, Proc. 6th IEEE Int. Vacuum Electronics Conference (IVEC2005), Noordwijk, The Netherlands, 2005, pp. 127-130.
- [10] Prinz, H.O., A. Arnold, G. Dammertz, K. Koppenburg, M. Thumm: Investigations on mode converters for multi-frequency gyrotrons, Conf. Digest Joint 30th Int. Conf. on Infrared and Millimeter Waves and 13th Int. Conf. on Terahertz Electronics, Williamsburg, Virginia, USA, 2005, pp. 297-298.
- [11] Yang, X., A. Arnold, G. Dammertz, R. Heidinger, K. Koppenburg, B. Piosczyk, O. Prinz, D. Wagner, M. Thumm: Progress towards optimization of phase-correcting mirrors for a multi-frequency gyrotron, Conf. Digest Joint 30th Int. Conf. on Infrared and Millimeter Waves and 13th Int. Conf. on Terahertz Electronics, Williamsburg, Virginia, USA, 2005, pp. 618-619.
- [12] Prinz, H.O., A. Arnold, K. Koppenburg, M. Thumm: Development of a broadband real-time frequency measurement system for high power mm-wave gyrotrons, Proc. German Microwave Conf. – GeMiC 2005 -, Ulm, 2005, pp. 41-44.

## **Microwave Heating for Wendelstein 7-X**

### **Introduction**

Electron Cyclotron Resonance Heating (ECRH) has an inherent capability for plasma start up, localized heating and current drive and is of particular importance for stellarators. ECRH is thus foreseen as a basic heating system in the first operation stage of the stellarator Wendelstein 7-X (W7-X) with 10 MW heating power at 140 GHz in continuous wave (CW) operation [1]. The complete ECRH-system for W7-X will be provided by FZK, which in 1998 has established the team 'Projekt Mikrowellenheizung für W7-X' (PMW). The FZK responsibility includes the design, development, construction, installation and integrated testing of all components required for stationary plasma heating on site at IPP Greifswald. PMW also coordinates the contributions from IPF Stuttgart, which is responsible for the microwave transmission system and part of the HV-system, and from the team at IPP Greifswald, which is responsible for the in-vessel components and for the in-house auxiliary systems. In particular, a European collaboration had been established between the Forschungszentrum Karlsruhe, Centre de Recherche de Physique des Plasmas (CRPP) Lausanne, Institut für Plasmaforschung (IPF) of the University of Stuttgart, the Commissariat à l'Énergie Atomique (CEA) in Cadarache and Thales Electron Devices (TED) in Vélizy, to develop and build a prototype gyrotron for W7-X with an output power of 1 MW for CW operation at 140 GHz.

A contract between CRPP Lausanne, FZK Karlsruhe and Thales Electron Devices (TED), Vélizy, had been signed to develop and subsequently build a series of these continuously operated gyrotrons.

### **Measurements on the Prototype Gyrotron**

The major challenges of high power, high frequency gyrotrons are in the Ohmic heating of the cavity surface, in the dielectric losses in the output window, in the power capability of the collector and in the amount of stray radiation absorbed inside the gyrotron. The technical limit of the power density on the resonator surface is assumed to be 2 kW/cm<sup>2</sup> for CW operation. For this reason, high power gyrotrons are operated in high order volume modes with a large cavity [2].

A major breakthrough for a CW compatible source is the use of a diamond window fabricated by chemical vapor deposition (CVD), which allows the design and the operation of a CW tube at the 1 MW power level. The single-stage depressed collector brings the overall efficiency of the gyrotron in the 50% range and at the same time significantly reduces the thermal loading on the collector.

The long-pulse results of the measurements on the pre-prototype and the prototype tube were reported during the last years [3-5]. With the prototype, two problems had to be faced. The specified output power of 1 MW has not completely been achieved and the pulse length was limited to about 15 minutes even at reduced power of 534 kW. The reason for the limit in power is seen in a poor electron emitter quality (cathode) which leads to an inhomogeneous electron emission and thus to a poor beam quality. The limitation in pulse length was due to a pressure increase during the pulse which was caused by a temperature rise of the internal ion getter pumps. This temperature increase was proven by an infrared measurement after a long pulse.

To eliminate the limitation in output power for the series tubes, a better quality assurance of the emitter ring has to be performed before installing it into the gyrotron. To avoid the pulse length limitation, it was decided to use external ion getter pumps with better shielding against RF stray radiation.

The first improvement could be implemented still on the prototype tube. After the visual inspection which did not reveal any serious problems, the prototype was re-assembled with a new, qualified emitter. Measurements in short pulse operation showed an almost linear growth of the output power with increasing beam currents. At beam currents of 40 A, an output power of 1 MW could be achieved.

The technical limitation of the output power for the W7-X gyrotrons is mainly given by the limit of the power loading on the collector by the electron beam, though the power loading has already been reduced by an axial, normal-conducting magnet which is placed around the collector and is operated at 7 Hz. Higher frequencies are not effective due to the "skin effect". The manufacturer Thales has limited the power loading of the collector at 1.3 MW, which translates into an output power of 1,06 MW at an efficiency of 45%.

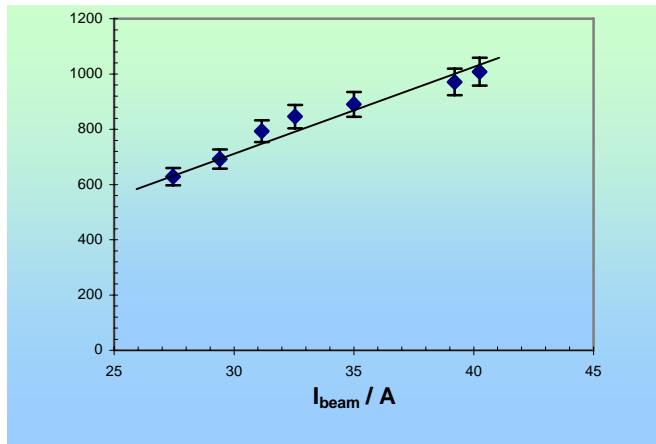


Fig. 1: Output power (in kilowatts) as function of electron beam current.

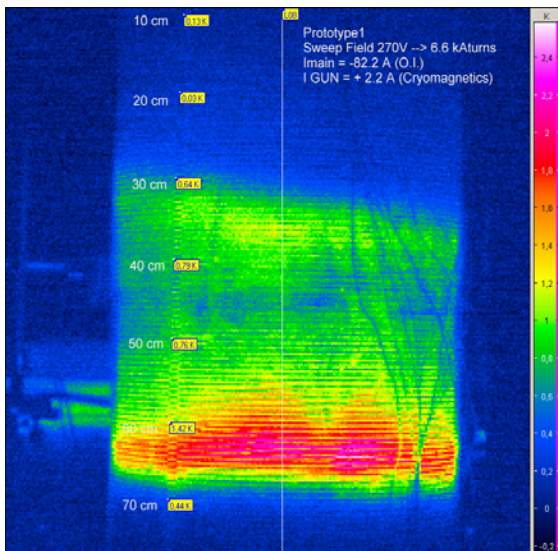


Fig. 2: The temperature distribution on the collector as a result of the electron deposition on the inner surface.

A radial sweeping system does not decrease the loading of the collector, but the system [6,7] is much simpler and cheaper. This is especially true as in the gyrotrons for W7-X, collectors which in the lower part are made of stainless steel are used. Therefore, 50 Hz could be used simplifying strongly the power supply of this system. Further, the system was designed in order to be operated at 220 V. The frequency of 50 Hz has the big advantage that the temperature modulation on the collector surface is strongly reduced and thus, also the problem of cyclic fatigue is decreased.

The system has been tested on the prototype, and it worked as expected. The results are in very good agreement with the theory. But apart from the simplicity, there was no improvement in performance as compared to the axial sweeping system. It is assumed that an im-

provement would be easily possible by a modulation of the amplitude or by a combination of axial and radial sweeping. It should be mentioned that this problem is extremely important for gyrotrons with even higher output like, e.g. the 2 MW gyrotrons with coaxial cavity for ITER. Measurements on an improved sweeping system will be performed during 2006.

### Series Gyrotrons

Seven series gyrotrons have been ordered from TED. Together with the pre-prototype tube, the prototype tube and the CPI-tube now operated at IPP Greifswald, ten gyrotrons will be available for Wendelstein 7-X. In order to operate these gyrotrons, eight more superconducting magnetic systems are necessary and have been ordered from Cryomagnetics, Oak Ridge, USA.



Fig. 3: First series tube at the test facility of Forschungszentrum Karlsruhe.

In the series tubes, the above mentioned difficulties concerning the output power and the pulse length limitation will be avoided. The emitter rings undergo a better optical quality assurance and temperature homogeneity check before they are installed inside the gyrotron. The ion getter pumps which were located inside the gyrotron in the prototype tubes are now placed outside. This results in a better shielding of the internal parts of the ion getter pump against RF radiation and heating. Further, the mirror box mostly exposed to RF has got a double wall structure for better cooling. Stainless steel parts with poor cooling are coated with copper to reduce the RF absorption.

The first series gyrotron had been delivered to FZK during February 2005. In short pulse operation, the behaviour of the output power was examined. The dependence on the electron beam current was similar to what had been found for the prototype after the exchange of the cathode emitter. At 40 A, a power of about 1 MW was measured; at 50 A even 1.15 MW. This dependence indicates the good emission properties of the cathode. The corresponding efficiencies

without depressed collector are 31 % and 30%, respectively. RF-field distribution measurements (perpendicular to the output RF-beam direction) were performed at different positions with respect to the window. The beam turned out to be shifted by 12 mm to the left (seen against beam direction) and 6 mm upwards. The Gaussian content was measured and calculated to be 97.5 % [8].

Due to neutralisation and expansion of the cavity, the parameters like the magnetic field in cavity and in the gun region are different in short and long pulse operation. The optimisation procedure for finding the operating parameters at high output power in long pulse operation was performed in 1s-pulses [9,10] assuming that the instantaneous power is well described by the frequency difference between the initial frequency and the instantaneous frequency (after one second). In a range of the magnetic field at the cavity between 5.52 - 5.56 T, no maximum for the output power was found. The power increased slightly with increasing magnetic field. In order to achieve the maximum output power, the accelerating voltage (this corresponds to the energy of the electrons inside the cavity) was adjusted and followed nicely the law that the ratio between magnetic field and the relativistic factor  $\gamma$  has to be constant.

A strong dependence of the output power on the electron beam radius inside the cavity has been found. The measurements were performed at a constant beam current of 40 A, but with optimising the electron beam radius inside the cavity. The desired mode can only be excited in a narrow range between 10.25 mm and

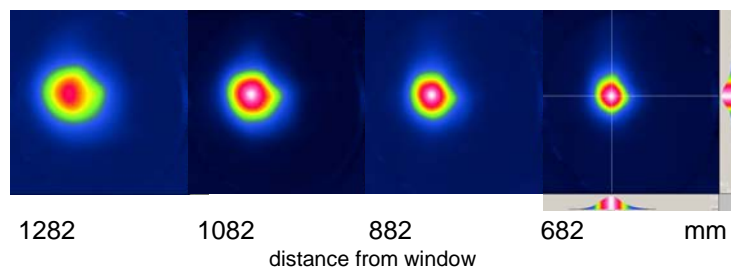


Fig. 4: Field profile measurements of the RF beam at different distances from the window.

10.43 mm radius. Increasing the voltage beyond this value leads to an excitation of neighbouring modes. At lower beam radii, arcing occurs, at higher radii a wrong mode (or the counter-rotating mode) is excited. The optimum value of the beam radius decreases slightly with decreasing cavity field and beam current.

In long pulse operation, the power was measured calorimetrically by the temperature increase of the cooling water of the RF-load. This load is placed at a distance of about 6 m from the gyrotron window. The RF beam is focused and directed into the load by means of two matching mirrors. In order to reduce the power loading on the surface, a set of polarizers are installed to produce a circularly polarized beam. The first matching mirror has a corrugated surface. A small amount of the RF beam is focused on a horn antenna with a diode detector to get a signal proportional to the output power. This signal, however, is not used for power measurements as the calibration procedure is complicated, and the calibration setting is rather unstably.

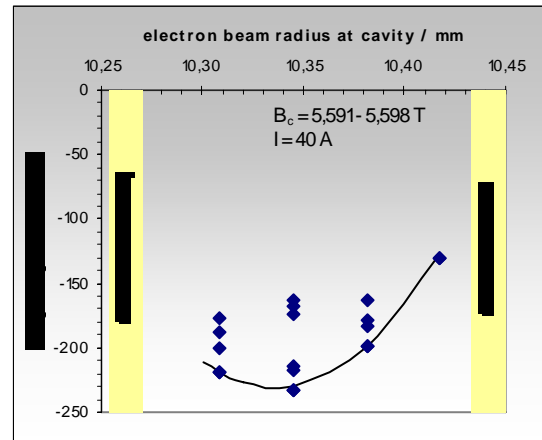


Fig. 5: Dependence of the frequency shift (as a measure for the output power) for different electron beam radii in the cavity.

In long pulse operation, the gyrotron was operated with depressed collector. The electrons are decelerated after the RF interaction by a negative voltage  $U_{\text{body}}$  which usually is chosen from between 25 and 30 kV (the cathode voltage is chosen at about -55 kV).

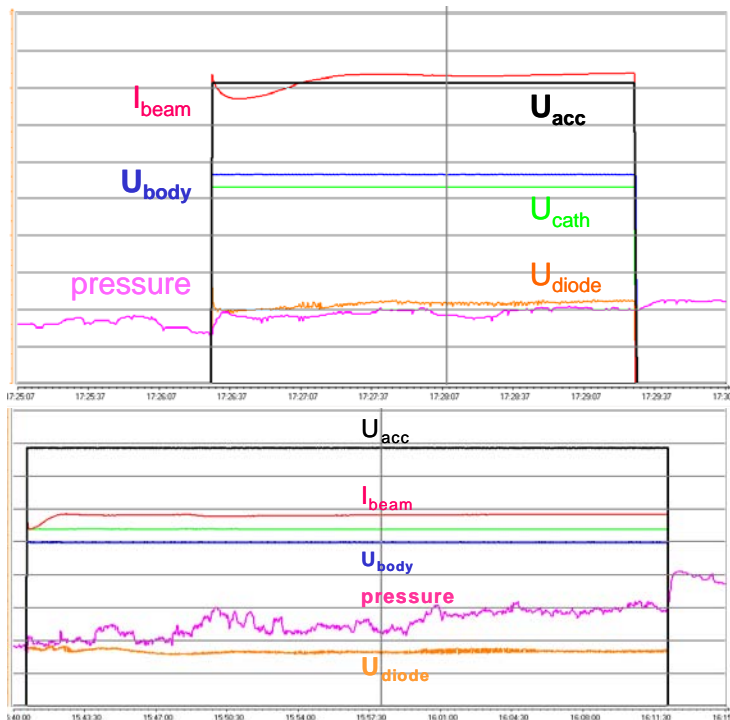


Fig. 6: Operation parameters for the 180 s, 922 kW (top) and the 1893 s, 570 kW pulse (bottom).

Fig. 6 shows the gyrotron operating parameters for a pulse length of three minutes (top) and 30 minutes (bottom) at reduced electron beam current. The beam current  $I_{\text{beam}}$ , the body voltage  $U_{\text{body}}$ , the accelerating voltage  $U_{\text{acc}}$ , the diode signal  $U_{\text{diode}}$  and the pressure inside the tube measured as the current of the ion getter pumps are depicted. The tube pressure is increasing very smoothly and stays well in the allowed operating range. The increase of pressure is less than a factor of two during three minutes.

The highest output power inside the load for a 3 min pulse was measured as 906 kW. Including the external stray radiation determined by the calorimetric measurement performed inside the microwave chamber, the total

power was 922 kW with an efficiency of 45%. With 906 kW inside the load, the specified value of 900 kW for the Gaussian content has been achieved.

The HV power supply available at Forschungszentrum Karlsruhe can only be operated up to three minutes at full power, but at reduced electron beam current (less than 30 A), longer pulses can be achieved. Fig. 7 shows the operating parameters for a pulse of about 31 minutes (1893 s) with an output power of 570 kW. It can be seen from the diode signal that the output power is very stable. The scale for the pressure is logarithmic with a factor of 1.8 per division. The pressure increase is lower than a factor of 2 ending up at about  $6 \cdot 10^{-9}$  mbar.

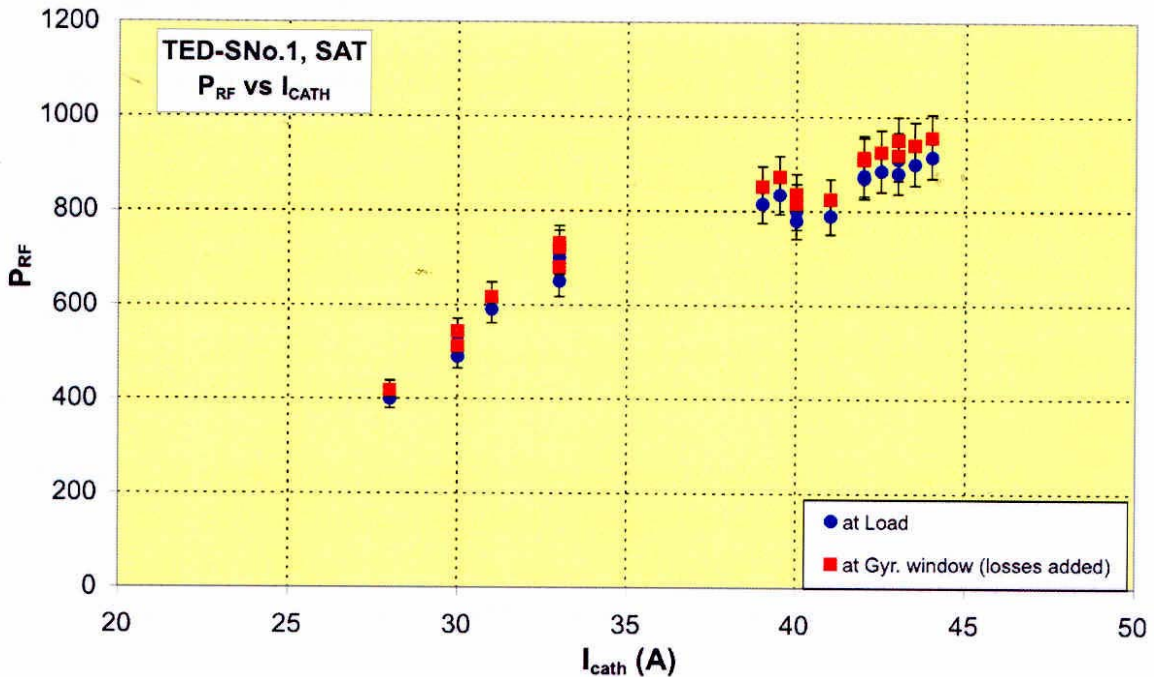


Fig. 7: Output power for different electron beam currents. This is an overview on the measurements performed at IPP at different pulse lengths. Extrapolating the measurements to higher currents, an output power of 1 MW could be achieved at 45 A. However, the collector loading does not allow this.

After the successful tests at the Forschungszentrum Karlsruhe, the tube was delivered to IPP Greifswald for tests at highest output power and a pulse length of 30 minutes. A directed output power of 865 kW was measured inside the load, and a total output power of about 920 kW was estimated taking the losses in the transmission line into account (world record in energy content). The tube was accepted. It is now protected and must not be switched on in order to avoid that the guarantee period starts running.

The second series tube was delivered to Forschungszentrum in November 2006. Short pulse experiments started recently. Up to now, an output power of 986 kW has been achieved. The experiment is going on.

Six of the eight superconducting magnet systems have been delivered to Forschungszentrum Karlsruhe or to IPP Greifswald. The first two systems were limited the in magnetic field to 5-7% above the operating field of 5.56 T (the specified value is 10%). The systems were accepted, but for the next ones the specified values were required. As a result of a slight change in design, the design value of 6.1 T was achieved for the next magnets.

The last two magnets are expected to be delivered at the beginning of 2006.

### Transmission line

The transmission line [11,12] consists of single-beam waveguide (SBWG) and multi-beam waveguide (MBWG) elements. For each gyrotron, a beam conditioning assembly of five single-beam mirrors is used. Two of these mirrors (M1, M2) match the gyrotron output to a

Gaussian beam with the correct beam parameters, two others (P1, P2) are used to set the appropriate polarization needed for optimum absorption of the radiation in the plasma. A fifth mirror (M3) directs the beam to a plane mirror array (beam combining optics: BCO), which is situated at the input plane of a multi-beam wave guide. This MBWG is designed to transmit up to seven beams (five 140 GHz beams, one 70 GHz beam plus an additional spare channel) from the gyrotron area (entrance plane) to the stellarator hall (exit plane). At the output plane of the MBWG, a mirror array separates the beams again and distributes them via CVD-diamond vacuum barrier windows to individually movable antennas (launchers) in the torus. To transmit the power of all gyrotrons, two symmetrically arranged MBWGs are used.

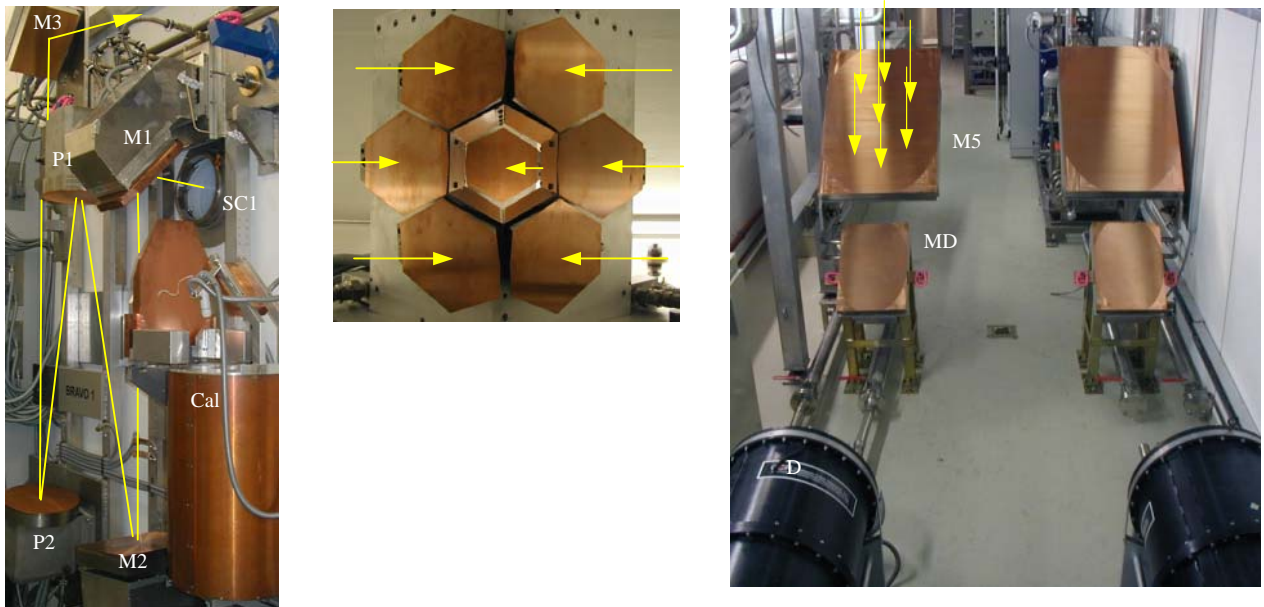


Fig. 8: View into the transmission duct of the ECRH system on W7-X. The left picture shows the matching optics M1, M2, and polarizers P1, P2, as well as M3, switch mirror SC1 and short-pulse calorimeter Cal for one gyrotron. In the middle, the beam combining optics (BCO) as seen from the first MBWG mirror M5 is displayed. Individual beams coming from M3 are impinging on the plane mirrors from left and right and are directed onto M5 of the MBWG system. The right picture shows a view into the beam duct with two large multi-beam mirrors M5 and the mirrors MD which can focus one selected beam into one of the CCR dummy loads D seen in the foreground.

All mirrors for the transmission system up to the torus hall are now installed. The design of the mirrors near the torus as well as their support and shielding structure has been continued. The design of the mirrors M14 was completed, and a set of 10 mirrors was ordered. In the frame of the long pulse tests of the prototype gyrotron from CPI and the first series tube from Thales, sections of the transmission line consisting of 7 mirrors could be tested successfully with a power of 900 kW for 30-minute pulses. No major problems were identified, however, it turned out that additional measures have to be taken to absorb stray radiation. High power tests of the MBWG are in preparation. These tests will employ retro-reflector mirrors, which – after forward transmission of the beam – reflect this beam back into the absorber load via another MBWG channel. The retro-reflectors are being manufactured and will be available early in 2006.

The short-pulse calorimeters have been installed in order to detect the output power of each gyrotron. Optimization of the power monitors continued. The integration of directional couplers into the mirrors next to the gyrotron (M1) is performed in context with the final machining of the reflector, which is done after the characterisation of the output beam during the acceptance tests of the gyrotrons.



## In-vessel-components

A motor driven movable prototype ECRH antenna had been fabricated. Its mechanical properties were tested. The push-pull rod drive mechanism provided a fast, precise and reproducible positioning over the total angular range required. Its reliability was successfully proven in a long-term loading with 10,000 cycles. Further, the compatibility of the motor-drive with the expected stray magnetic field of W7-X ( $<40$  mT) was tested. In parallel, a reliable cooling water supply inside the push-pull rods was developed. Two concepts were investigated: bellows integrated inside the universal joints and spiral pipes wound around the joints. Only the latter solution demonstrated a satisfactory reliability at cycling tests with the maximal bending angle. The spiral tubes are integrated into the prototype antenna presently. Therefore, integral reliability tests can be performed soon in the ECRH-stray radiation test chamber in vacuum conditions and with microwave loading. Based upon the present experience, a concept for the serial 10 ECRH-antennas was developed. The detailed design and fabrication is foreseen in 2006.

All CVD diamond disk vacuum windows were fabricated and delivered. The measurement of their microwave properties at the Institut für Materialforschung at the Forschungszentrum Karlsruhe was also completed.

## HV-systems

For the operation of the gyrotron with depressed collector, a precisely controlled beam acceleration voltage is necessary, which is supplied by the body voltage modulator. The beam current of the gyrotrons is controlled by means of the cathode heater supply, which is on cathode potential (about  $-55$  kV). In case of arcing inside the gyrotron, a thyatron crowbar protects the tubes from being damaged [13].



Fig. 9: HV control system for a gyrotron: It consists of a body voltage modulator and of a heater and thyatron protection unit. Left: HV control system for the W7-X gyrotrons (from left: modulator, crowbar and ignition coil. Right: Details of the HV modulator: Tube compartment with cooling hoses on HV isolators.

The fabrication of the body voltage modulators and the heating and tube protection unit by IPF Stuttgart is ongoing. Initial problems with voltage break-downs of the thyatron crowbars have been solved by a redesign of the external circuits of the thyatron. By the end of 2005,

four complete HV-control systems have been delivered to IPP Greifswald and were put into operation. Fig. 9 shows a complete HV system.

### **Auxiliary systems**

The water cooling systems for individual components like the RF-shielding tubes and the bypasses for the gyrotron collectors were installed and successfully tested. The software for operating the system has been installed.

The short pulse calorimeters have been connected to the water cooling system, and the second long-pulse RF-load as well.

The water cooling for the CPI-gyrotron has been fabricated and was tested in combination with the gyrotron. The cathode cooling (with air at the CPI tube) was modified in order to allow operation of the tube with oil cooling. This was necessary due to the high amount of stray radiation at the gun region of the CPI gyrotron. Further, this tube has to be run with oxygen-free water (differently from the other tubes from TED). The removal of oxygen has been prepared and is operating successfully. The three water circuits are now equipped with de-ionizers.

For all these installations, the controlling system and the visualization has been designed and installed. The visualization for the gyrotron operation has been improved and was integrated into the operation- and interlock system of IPP Greifswald.

### Staff:

IHM / FZK	IPF (University of Stuttgart)	IPP (Greifswald/Garching)
A. Arnold (Uni KA)	H. Babilon	B. Berndt
<u>G. Dammertz</u>	P. Brand	H. Braune
G. Gantenbein	G. Gantenbein	V. Erckmann (PMW)
R. Heidinger (IMF I)	M. Grünert	F. Hollmann
S. Illy	W. Kasperek	L. Jonitz
H. Kunkel	M. Krämer	H. Laqua
K. Koppenburg	R. Munk	G. Michel
W. Leonhardt	F. Müller	F. Noke
B. Mattern	P. Salzmann	F. Purps
D. Mellein	H. Schlüter	T. Schulz
G. Neffe	K. Schwörer	M. Weißgerber
B. Piosczyk	D. Wimmer	
U. Saller		
M. Schmid		
W. Spiess		
M. Stoner		
J. Szczesny		
<u>M. Thumm</u>		
C. Zöller		

### Literature:

- [1] T. C. Luce, "Applications of High-Power Millimeterwaves in Fusion Energy Research," IEEE Trans. Plasma Science 30 (2002) 734-754
- [2] B. Piosczyk, G. Dammertz, O. Dumbrajs, M. V. Kartikeyan, M. K. Thumm, and X. Yang, "165 GHz Coaxial Cavity Gyrotron", IEEE Trans. Plasma Science 32 (2004) 853-860 [2]

- [3] G. Dammertz, S. Alberti, A. Arnold, E. Borie, V. Erckmann, G. Gantenbein, E. Giguët, R. Heidinger, J. P. Hogge, S. Illy, W. Kasperek, K. Koppenburg, M. Kuntze, H. P. Laqua, G. LeCloarec, F. Legrand, W. Leonhardt, C. Liévin, R. Magne, G. Michel, G. Müller, G. Neffe, B. Piosczyk, T. Rzesnicki, M. Schmid, M. K. Thumm, and M. Q. Tran, "Development of multimewatt gyrotrons for fusion plasma heating and current drive", *IEEE Trans. on Electron Devices* 52 (2005) 808-817
- [4] G. Dammertz, S. Alberti, D. Bariou, P. Brand, H. Braune, V. Erckmann, G. Gantenbein, E. Giguët, R. Heidinger, J. P. Hogge, W. Kasperek, H. P. Laqua, C. Liévin, W. Leonhardt, G. Michel, G. Müller, G. Neffe, B. Piosczyk, M. Schmid, M. Thumm, "140 GHz high-power gyrotron development for the stellarator W7-X", *Fusion Engineering and Design* 74 (2005) 217-221
- [5] M. Thumm, "High power gyro-devices for plasma heating and other applications", *Int. Journal of Infrared and Millimeter Waves* 26,4 (2005) 483-503
- [6] G. Dammertz, S. Illy, B. Piosczyk, M. Schmid, D. Bariou, "Collector sweeping system for high power gyrotrons"; A comparison of different collector sweeping systems for high power gyrotrons", *Joint 30th Intern. Conf. on Infrared and Millimeter Waves and 13th Intern. Conf. on Terahertz Electronics*, Williamsburg, Sept. 19-23, 2005, 19-23
- [7] M. Schmid, G. Dammertz, S. Illy, M. Thumm, C. Liévin, "Transverse sweep collector system for the W7-X gyrotrons: Engineering and first results", 17th Joint Russian-German STC workshop on ECRH and Gyrotrons", Greifswald, May 30-June 4, 2005
- [8] M. Thumm, X. Yang, A. Arnold, G. Dammertz, G. Michel, J. Pretterebner, D. Wagner, "A high-efficiency quasi-optical mode converter for a 140-GHz 1-MW CW gyrotron", *IEEE Trans. on Electron Devices* 52,5 (2005) 818-824
- [9] G. Dammertz, A. Arnold, R. Heidinger, J. Jin, K. Koppenburg, W. Leonhardt, G. Neffe, B. Piosczyk, T. Rzesnicki, M. Schmid, M. Thumm, X. Yang et al., "High power gyrotron development at Forschungszentrum Karlsruhe for fusion applications", 32nd IEEE Internat. Conf. on Plasma Science, Monterey, California, June 18-23, 2005
- [10] G. Dammertz, S. Alberti, A. Arnold, D. Bariou, E. Borie, P. Brand, H. Braune, V. Erckmann, G. Gantenbein, E. Giguët, R. Heidinger, J. P. Hogge, S. Illy, W. Kasperek, K. Koppenburg, H. Laqua, F. Legrand, W. Leonhardt, C. Liévin, G. Michel, G. Müller, G. Neffe, B. Piosczyk, M. Schmid, M. Thumm, and M. Q. Tran, "Experimental results on the 140 GHz, 1 MW, CW gyrotrons for the stellarator w7-X", *Joint 30th Internat. Conf. on Infrared and Millimeter Waves and 13th Internat. Conf. on Terahertz Electronics*, Williamsburg, Sept. 19-23, 2005, 235-236
- [11] G. Gantenbein, W. Kasperek, G. Dammertz, V. Erckmann, M. Grünert, F. Hollmann, L. Jonitz, H. Laqua, G. Michel, F. Purps, T. Schulz, K. Schwörer, M. Weißgerber, "Progress report on the ECRH transmission line at the stellarator W7-X", *Joint 30th Intern. Conf. on Infrared and Millimeter Waves and 13th Intern. Conf. on Terahertz Electronics*, Williamsburg, Sept. 19-23, 2005, 427-428
- [12] W. Kasperek, P. Brand, H. Braune, G. Dammertz, V. Erckmann, G. Gantenbein, F. Hollmann, M. Grünert, H. Kumric, L. Jonitz, H. P. Laqua, W. Leonhardt, G. Michel, F. Noke, B. Plaum, F. Purps, M. Schmid, T. Schulz, K. Schwörer, M. Thumm, M. Weissgerber, "Status of the 140 GHz, 10 MW CW transmission system for ECRH on the stellarator W7-X", *Fusion Engineering and Design* 74 (2005) 243-248
- [13] H. Braune, P. Brand, R. Krampitz, W. Leonhardt, D. Mellein, G. Michel, G. Müller, J. Sachtleben, M. Winkler, W7-X ECRH teams at IPP; IPF and FZK, "HV-system for CW-gyrotrons at W7-X and the relevance for ITER", *Journal of Physics: Conference Series* 25 (2005) 56-65



## **Underlying Technology**



## Underlying Technology

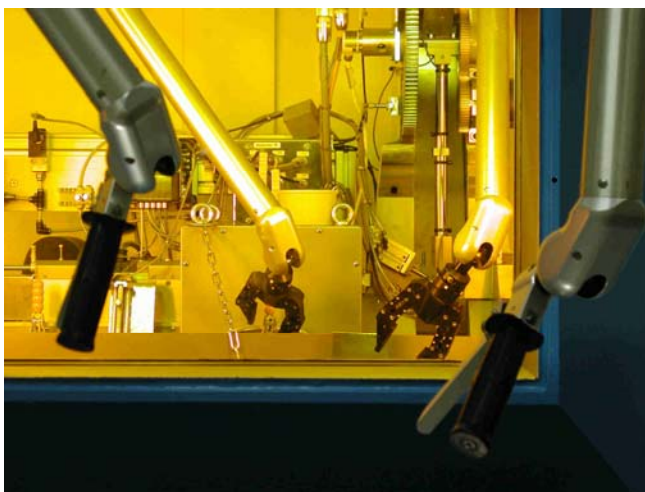
### Operation of the Fusion Materials Laboratory (FML)

The Fusion Materials Laboratory (FML) provides the infrastructure for the performance of tasks defined in the EFDA workprogramme related to the characterisation and testing of irradiated and non-irradiated materials. Methods such as optical and electron microscopy, tritium adsorption and desorption, He pycnometry and Hg porosimetry, crush load, micro hardness, creep, Charpy impact and tensile tests as well as long-time annealing tests are applied. The work includes Post Irradiation Examinations (PIE) of Reduced Activation Ferritic Martensitic (RAFM) steels (reference material for DEMO and ITER-TBMs), investigations on materials relevant for the HCPB blanket (ceramic breeder materials, beryllium) and Plasma Facing Materials (tiles) from tokamaks (JET, TFTR).

PIE on selected samples from the HFR1b and HFR1b experiments were carried out. Especially Charpy impact and tensile tests were performed and thereafter small cuts of the tested specimens for light optical, scanning and transmission electron microscopy were prepared and examined. The aim of the investigations was to study the irradiation effects on the mechanical and structural properties of these materials.

The investigation of blanket materials was continued with the characterisation of materials. Lithium orthosilicate pebbles were investigated by light optical microscopy and their porosity and deformation hardness were determined. Different batches of materials were characterised with respect to the influence of parameters of the fabrication process on the mechanical and structural properties. Adsorption and desorption experiments were done with irradiated beryllium pebbles to study the influence of the surface structure on the tritium kinetics. The characterization of pebbles from a uniaxially compressed metallic pebble bed for the determination of the mechanical parameters of the metallic pebble bed was continued.

Further samples from ASDEX, JET and TFTR carbon tiles were prepared for the investigation of tritium retention in these materials. In the TLK these samples were analysed. The irradiation experiments on tritium containing flakes from JET were continued with the radiation of a Co60-source to study the effect of the gamma-radiation on the desorption properties of the adsorbed tritium.



Charpy testing device in a lead shielded cell

Detailed results and consecutive analysis of the measurements are reported in the respective chapters of this report.

For the PIE the following equipment was used:

- Charpy impact and tensile testing devices;
- Light optical, scanning electron and transmission electron microscopes;
- Desorption device with high temperature furnace for tritium and helium release measurements;
- He-pycnometer and Hg-porosimeter;
- Sphere crush and creep testing apparatus.

In the frame of the FML upgrading programme, two new lead-shielded hot cells for materials testing and optical microscopy came into operation. New instrumented Charpy impact and tensile test machines and an indentation device have been implemented for the operation in these new hot cells.

### **Future activities:**

- Continuation of measurements as referred to above:
- PIE of the HFR II B irradiation phase: some 280 samples of steel, 15 dpa;
- Characterization of CFC tiles from TFTR;
- Characterization of new batches of ceramic breeder materials and beryllium.

### Staff:

P. Bariè  
J.Ehrmann  
A. Erbe  
M. Gilpert  
M. Holzer  
H. Jackisch  
S. Lautensack  
P. Lauterbach  
G. Mangei  
W. Nägele  
D. Reichmann  
H. Ries  
R. Rolli  
G. Rösch  
R. Schmidt  
H.-C. Schneider  
H. Steinle

### Literature:

- [1] H.-C. Schneider, „Entwicklung einer miniaturisierten bruchmechanischen Probe für Nachbestrahlungsuntersuchungen“, FZKA-Bericht 7066, September 2005
- [2] Möslang, A., Diegele, E., Klimiankou, M., Lässer, R., Lindau, R., Lucon, E., Materna-Morris, E., Petersen, C., Pippan, R., Rensman, J.W., Rieth, M., van der Schaaf, B., Schneider, H.C., Tavassoli, F., “Towards reduced activation structural materials database for fusion DEMO reactors“, Nuclear Fusion 45 (2005) 649-655
- [3] Y. Torikai, M. Matsuyama, N. Bekris, M. Glugla, P. Coad, W. Nägele, A. Erbe, N. Noda, V. Philipps, K. Watanabe, „Tritium distribution in JET MARK IIA type divertor tiles analysed by BIXS“, Journal of Nuclear Materials 337-339 (2005) 575-579
- [4] N. Bekris, J.P.Coad, R.-D. Penzhorn, S. Knipe, L. Doerr, R. Rolli, W. Nägele, “Characterisation of flakes generated in JET after DD and DT plasma operations“, Journal of Nuclear Materials 337-339 (2005) 659-663
- [5] J. Reimann, R.A. Pieritz, R. Rolli, “Topology of compressed pebble beds“, 7th ISFNT Conference, Tokyo (May 2005)
- [6] M. Matsuyama, Y. Torikai, N. Bekris, M. Glugla, A. Erbe, N. Noda, V. Philipps, P. Coad, K. Watanabe, “Applicability of BIXS to in-situ measurements of tritium retention in Plasma facing materials of ITER“, 7th ISFNT Conference, Tokyo (May 2005)
- [7] H.-C. Schneider, R. Rolli, J. Aktaa, “Small Fracture-toughness Specimen for Post-irradiation Experiments: Validation and Results“, accepted for ICFRM12, Dec. 4 - 9, 2005, Santa Barbara, Ca, USA
- [8] E. Gaganidze, H.-C. Schneider, B. Dafferner, J. Aktaa, “Embrittlement Behavior of Neutron Irradiated RAFM Steels“, accepted for ICFRM12, Dec. 4 - 9, 2005, Santa Barbara, Ca, USA



## Appendix I: FZK Departments Contributing to the Fusion Programme

FZK Department	FZK Institut/Abteilung	Director	Ext.
Institute for Materials Research	Institut für Materialforschung (IMF)	I. Prof. Dr. K.-H. Zum Gahr	3897
		II. Prof. Dr. O. Kraft	4815
		III. Prof. Dr. H. Haußelt	2518
Institute for Pulsed Power and Microwave Technology	Institut für Hochleistungsimpuls- und Mikrowellentechnik (IHM)	Prof. Dr. M. Thumm	2440
Institute for Nuclear and Energy Technology	Institut für Kern- und Energietechnik (IKET)	Prof. Dr. T. Schulenberg	3450
Institute for Reactor Safety	Institut für Reaktorsicherheit (IRS)	Prof. Dr. V. Heinzel (Acting Head)	2550
Institute for Technical Physics	Institut für Technische Physik (ITP)	Prof. Dr. P. Komarek	3500
Institute for Micro Process Engineering	Institut für Mikroverfahrenstechnik (IMVT)	Dr. K. Schubert	3114
- Tritium Laboratory Karlsruhe	- Tritiumlabor Karlsruhe (TLK)	Dr. M. Glugla	3226
Institute for Data Processing and Electronics	Institut für Prozessdatenverarbeitung und Elektronik (IPE)	Prof. Dr. H. Gemmeke	5635

### Contributing:

Institute for Nuclear and Particle Physics, Technical University of Dresden	Institut für Kern- und Teilchenphysik Technischen Universität Dresden	Prof. Dr. H. Freiesleben	+ 49 351/4635461
Max-Planck-Institute for Plasma Physics Berlin	Max-Planck-Institut für Plasmaphysik Berlin	Prof. Dr. G. Fussmann	+ 49 30/20366130
Institute for Applied Physics University of Frankfurt	Institut für Angewandte Physik J.W. Goethe-Universität Frankfurt	Prof. Dr. H. Klein	+ 49 69/7982 3489
Institut für Strahlwerkzeuge University of Stuttgart	Institut für Strahlwerkzeuge Universität Stuttgart	Prof. Dr. T. Graf	+ 49 711/6856841



## Appendix II: Fusion Programme Management Staff

<b>Head of the Research Unit</b>	Dr. G. Janeschitz	ext. 5460 e-mail: guenter.janeschitz@fusion.fzk.de
Assistant:	Mrs. M. Winkelmann	ext. 5461 e-mail: miriam.winkelmann@fusion.fzk.de
Secretariat:	Mrs. C. Hermsmeyer	ext. 5466 e-mail: carmen.hermsmeyer@fusion.fzk.de
<b>Program Budget, Administration, Reports, EU-Affairs</b>	BW. M. Henn	ext. 5547 e-mail: michael.henn@fusion.fzk.de
	Mrs. V. Lallemand	ext. 6461 e-mail: vera.lallemand@fusion.fzk.de
	Mrs. I. Pleli	ext. 8292 e-mail: ingrid.pleli@fusion.fzk.de
<b>Blanket and Divertor Development, Neutron Source, Reactor Studies, Public Relations</b>	DI. W. Bahm	ext. 5465 e-mail: werner.bahm@fusion.fzk.de
<b>Fuel Cycle, Structural Materials, Irradiations, Superconducting Magnets</b>	DI. S. Gross	ext. 5468 e-mail: sigurd.gross@fusion.fzk.de
<b>Quality Management, Resource Loaded Planning, Plasma Heating Technology, Physics, Safety Studies, Neutronics</b>	Dr. K. Hesch	ext. 5462 e-mail: klaus.hesch@fusion.fzk.de

**Address:**

**Forschungszentrum Karlsruhe GmbH  
Nuclear Fusion Programme Management  
Post Office Box 3640, D - 76021 Karlsruhe / Germany**

**Telephone No:**

**07247-82- Extensions .....**

**Telefax No:**

**07247-82-5467**

**world wide web:**

**<http://www.fzk.de/fusion>**



### Appendix III: Glossary

3D	Three-dimensional
3PB	3 Point Bending
6,7Li	<sup>6</sup> Li and <sup>7</sup> Li nuclei
AC	Alternating Current
ACE	A Compact ENDF data format for nuclear data (used for MCNP/McDeLicious)
ACP	Activated Corrosion Products
ACS	Automated Control System
ADS	Atomosphere Detritiation System
AGHS	Active Gas Handling System
AHTM	Averaged Heat Transfer Model
AISI 316L	Austenitic Steel
ALARA	Analytic and Laplacian Adaptive Radioactivity Analysis Code
ALTAIR	Fast Reactor Irradiation from CEA in BOR 60
ANS	Analytical System
AP	Activated dust
Ar/W	Annealing in Argon Atmosphere + Water Quenching
ARBOR-1	Fast Reactor Irradiation from FZK in BOR 60
ARBOR-2	Fast Reactor Irradiation from FZK and CEA in BOR 60
ASDEX	Axial-symmetrisches Divertor-Experiment
ASTM	American Society for Testing and Materials
BAM	Bundesanstalt für Materialforschung und -prüfung, Berlin
BD	Brittle Destruction
BIXS	Beta-induced X-ray Spectrometry
BLV	Beam Line Vessel
BOR 60	Fast Reactor at SSC RF RIAR
BU	Breeder Unit
CAD	Computer Aided Design
CD	Cryogenic Distillation
CEA	Commissariat à l'Energy Atomique
CECE	Combined Electrolysis and Catalytic Exchange
CERN	European Organization for Nuclear Research, Geneva, Switzerland
CFC	Carbon Fibre Composite
CFD	Computational Fluid Dynamic
CFTM	Creep Fatigue Test Module
CH-structure	Crossbar H-mode Structure

CICC	Cable in Conduit Conductor
CIEMAT	Centro de Investigaciones Energeticas Medioambientales y Tecnologicas (CIEMAT), Madrid ,Spain
CL	Current Lead
COSYMA	Code <u>S</u> ystem <u>M</u> aria
CP	Cooling Plate
CPS	Coolant Purification System
CRISM	Central Research Institute for Structural Material
CRPP	Centre de Recherches en Physique des Plasmas
CS	Central Solenoid
CT	Compact Tension
Cu	Copper
CVD	Chemical Vapor Deposition
cw	Continouous Wave
d	Deuteron
D	Diameter
D1S	Direct one-step method for shut-down dose rate calculations
DBTT	Ductile-to-Brittle Transition Temperature
DEMO	Demonstration Power Station
DF	Decontamination Factor
D-Li	Deuteron-Lithium (interactions, neutron source)
DN	Nominal Diameter
DNB	Diagnostic Neutral Beam Injector
dpa	Displacement per Atom
DT	Deuterium Tritium
DTL	Drift Tube Linac
DWUCK4	Nuclear Model Code (for direct reaction calculations)
EAF	European Activation File
EASY	European Activation System
EB	Electron Beam
EBW	Electron Beam Welding
EC	Electron Cyclotron
ECCD	Electron Cyclotron Current Drive
ECIS95, ECIS96	Nuclear Model Code (for coupled channel calculations)
ECM	Electrochemical Machining
ECRH	Electron Cyclotron Resonance Heating
EDX	Energy Dispersive X-Ray

EFDA	European Fusion Development Agreement
EFF	European Fusion File
ELM	Edge Localized Mode
EM module	Electro Magnetic Module
EMRAS	Environmental <u>M</u> odelling for <u>R</u> adiation <u>S</u> afety
ENDF	Evaluated Nuclear Data File
ENDF/B-VI	American Evaluation Nuclear Data File B, Version VI
ENEA	Italian National Agency for New Technology, Energy and the Environment
ENG	Frascati Neutron Generator
EUROFER 97	European RAF/M Steel
EVITA	Experimental Vacuum Ingress Test Apparatus
F82H mod.	Japanese RAF/M Steel
FBI	F = Force, B = Magnetic Field, I = Current
FC	Fuel Cycle
FE	Finite Element
FEG	Field Emission Gun
FEM	Finite Elements Method
FENDL	Fusion Evaluated Nuclear Data Library
FFT	Fast Fourier Transformation
FISPACT	Fusion Inventory Code
FM	Fracture-Mechanical
FML	Fusion Materials Laboratory
FNS	Fusion Neutron Source Laboratory, Tokai-mura, Japan
FP6	Framework Programme 6
FTTT	Fracture Toughness Tension Temperature
FW	First Wall
GC	Gas Chromatography
GC-MS	Gas Chromatography Mass Spectrometry Unit
GDC	Glow Discharge Cleaning
GNASH	Nuclear Model Code (statistical and pre-compound nucleus calculations)
GPF	Gas Puffing Facility
GRICAMAN	Grid Cap Manifold experiment
GTN	Gurson-Tvergaard-Needleman
GUI	Graphical User Interface
H&CD	Heating and Current Drive
HAZ	Heat Affected Zone

HAZOP	Hazard and Operability
HCLL	Helium Cooled Lithium-Lead
HCPB	Helium Cooled Pebble Bed
HCS	Helium Cooling System
He	Helium
HEBLO	Helium Blanket & Divertor Test Loop
HECOB	Heat Conductivity in Pebble Beds
HELICA	Helium-FUS3 Lithium Cassette
HELOKA	Helium Loop Karlsruhe
HEMJ	Helium-cooled Divertor Concept with Multiple Jet Cooling
HEMS	Helium-cooled Modular Divertor Concept with Integrated Slot Array
HETRA	Heat Transfer Experiment
HEX	Heat Exchanger
HEXCALIBER	Helium-Fus3 Experimental Cassette of Lithium, Beryllium Pebble Beds
HF	High Frequency
HFR	High Flux Reactor
HFTM	High Flux Test Module
HHF	High Heat Flux
HICU	High Neutron Fluence Irradiation of Pebble Stacks for Fusion
HIP	Hot Isostatic Pressing
HNB	Heating Neutral Beam Injector
HRS	Heat Rejection System
HRTEM	High Resolution Transmission Electron Microscope
HT	High Temperature
HT	Tritiated Gas
HTC	Heat Transfer Coefficient
HTO	Tritiated Water Vapour
HTS	High Temperature Superconducting
HV30	Vickers Hardness at 30 kp Load
IBA	Ion Beam Analysis
IEAF-2001	Intermediate Energy Activation File
IFMIF	International Fusion Material Irradiation Facility
IH-structure	Interdigital H-mode structure
ILE	ITER Legal Entity
IPF	Institut für Plasmaforschung, Universität Stuttgart
IPP	Max-Planck-Institut für Plasmaphysik



ISABEL	Intra-nuclear Cascade Model
ISO	International Organization for Standardization
ISS	Isotope Separation System
ISTC	International Science and Technology Center
ITER	International Thermonuclear Experimental Reactor
ITHEX	IFMIF Thermo-hydraulic Experiment
JEFF	Joint European Fusion Fission File
JENDL	Japanese Evaluated Nuclear Data Library
JET	Joint European Torus
JRC	Joint Research Center
KLST	Kleinstprobe acc. DIN 50 115
kN	Kilo Newton
Kn	Knudsen Number
LANL	Los Alamos National Laboratory
LAW	Parameter in ENDF Data Format
LCF	Low Cycle Fatigue
LDA	Laser Doppler Anemometry
LF	Low Frequency
LHC	Large Helical Coil
LHe	Liquid Helium
LLNL	Lawrence Livermore National Laboratory
LLW	Low Level Waste
LN	Liquid Nitrogen
LOCA	Loss of Coolant Accident
LOEM	Local Overheating Erosion Mechanism
LOVA	Loss of Vacuum Accident
LPCE	Liquid Phase Catalytic Exchange
LSE	Lower Shelf Energy
L-T	Longitudinal-Transverse
LTS	Low Temperature Superconducting
Ma	Mack Number
MAGS	Magnet Safety (Software module)
MANET I	Conventional 12 % Cr steel
MAT-DB	Material Data Bank
MBA	Material Balance Area
MC	Master Curve

McDeLicious	Monte Carlo Code for D-Li neutron generation and transport simulations
MCNP	Monte Carlo Neutron Photon (code for particle transport simulations)
MCNPX	Monte Carlo Code for multi-particle transport simulations (at high energies)
MCSEN	Monte Carlo Code for Sensitivity Calculations
MEKKA	Magneto-Hydrodynamic Experiments in Sodium und Potassium Karlsruhe
MF	Material File
MFTM	Medium Flux Test Module
MHD	Magneto-Hydrodynamics
MPa	Mega Pascal
Mpcci	Mesh-based parallel Code Coupling Interface
MS	Mass Spectrometry
MT	Material Type
NB	Neutral Beam
NB31	CFC (Carbon Fibre Composite) grades
NBI	Neutral Beam Injector
NBTF	Neutral Beam Test Facility
$N_f$	Number of Cycles to Failure
NIMONIC 90	Nickel Base Alloy
NJOY	Code for Processing Nuclear Data in ENDF Format
NRG	Nuclear Research and Consultancy Group, National Nuclear Research Institute of the Netherlands, Petten
NS31	CFC (Carbon Fibre Composite) grades
NT	Normalised and Tempered
N-VDS	Normal Vent Detritiation System
OBT	Organically Bound Tritium
ODS	Oxide Dispersed Strengthened
OKTAVIAN	Osaka University Neutron Generator
OM	Optimal Microscopy
OMP	Optical Model Potential
OPL	Outer Poloidal Limiter
OPTIFER	German RAF/M Steel
OSi	Lithium Orthosilicate
OST	Oxford Superconducting Technology
PAN-fibres	The NB31 fibres parallel to the surface
PCCv	Pre-cracked Charpy v
PCMC1	Personal Computer Memory Card International
PCP	Prototype Cryosorption Pump

PCS	Pressure Control System
PF	Poloïdal Field
PFC	Plasma Facing Components
PI module	Plant Integration Module
PIC	Port Cell Integration Cask
PICOLO	Pb-Li Corrosion Loop
PIE	Post Irradiation Examination
PIM	Powder Injection Moulding
Pitch-fibres	The NB31 fibres perpendicular to the surface
PMW	Projekt Microwellenheizung for W7-X
PPCS	Power Plant Conceptual Study
PPPL	Princeton Plasma Physics Laboratory
PRM	Project Resource Management
PT	Participating Team
Pt-PtRh-TC	Platinum Rhodium-Thermocouples
PWHT	Post Weld Heat Treatment
QA	Quality Assurance
R2S	Rigorous two-step method for shut-down dose rate calculations
RAF/M	Reduced Activation Ferritic Martensitic
RBS	Required Bond Strength
RCT	Recrystallisation temperature
Re	Reynolds Number
RF	Radio Frequency
RFQ	Radio Frequency Quadrupole
RP	Radial Plates
RT (HT)	Room (High) Temperature
SC	Single Crystal
Sccm	Standard-cm <sup>3</sup> /min
SCHe	Supercritical Helium
SCK	Studie Centrum voor Kernenergie, National Nuclear Research Institute of Belgium, located in Mol
SDC	Structural Design Criteria
SDS	Storage and Delivery System
SEM	Scanning Electron Microscopy
SICEMO experiment	Six Cell Mock-up Experiment
S <sub>N</sub>	Discrete ordinates of angular segmentation order N
SOL	Scrape-off Layer

SPICE	<b>S</b> ample Holder for <b>I</b> rradiation of Miniaturized Steel <b>S</b> pecimens Simultaneously at Different Temperatures
SPM	Solid Polymer Membrane
SS	Safety System
SSC RF RIAR	State Scientific Centre of Russian Federation Research Institute of Atomic Reactors
SULTAN	Superconductor Test Facility, Villigen, Switzerland
TBM	Test Blanket Module
T <sub>br</sub>	Brazing temperature
TBR	Tritium Breeding Ratio
T <sup>cc</sup>	Temperature in Cooling Channels
TCWC	Tokamak Cooling Water System
TD	Theoretical Density
TDM	Test Divertor Module
TDS	Thermal Desorption Spectroscopy
TED	Thales Electron Devices, Vélizy
TEKES	National Technology Agency (TEKES), Helsinki, Finland
TEM	Transmission Electron Microscope
TEP	Tokamak Exhaust Processing
TF	Toroïdal Field
TFTR	Tokamak Fusion Test Reactor (Princeton)
TIDE	<b>T</b> ritium <b>D</b> econtamination <b>E</b> xperimental Facility
TIG	Tungsten Inert Gas
TIMO	Test Facility for ITER Model Pump (located at FZK)
TITAN	Low Temperature Adsorption Test Facility
TLK	Tritium Laboratory Karlsruhe
TMF	Thermal Mechanical Fatigue
TORT	Three-dimensional S <sub>N</sub> transport code
TOSKA	Toroïdal Feld Spulentest Karlsruhe
TPL	Tritium Process Laboratory Japan
TRM	Tritium Release Module
TTE	Trace Tritium Campaign at JET
TUD	Technical University of Dresden
TZM	Molybdenum based Alloys
UCT	Uniaxial Compression Test
U-DW	Uniaxial Diffusion Weld
UFOTRI	Unfallfolgenmodell <u>T</u> ritium
UKAEA	United Kingdom Atomic Energy Authority

UMAT	User Material
USE	Upper Shelf Energy
V/V	Vacuum Annealing + Vacuum Cooling
VDS	Vent Detritiation System
VV	Vacuum Vessel
W	Tungsten
W La <sub>2</sub> O <sub>3</sub>	Tungsten Lanthanum Oxide Alloy
WC	Tungsten carbide
WDS	Water Detritiation System
WL10	Tungsten, Dispersion Strengthened with 1 wt.% La <sub>2</sub> O <sub>3</sub> Particles
WTZ	Wissenschaftlich-Technische Zusammenarbeit 01/577
XRD	X-Ray Diffraction
ΔDBTT	Difference of Unirradiated DBTT to Irradiated DBTT Values